SASEC 2023

SOUTHERN AFRICAN SUSTAINABLE ENERGY CONFERENCE

15 - 17 November 2023 | Boardwalk Hotel | Gqeberha | Eastern Cape

CONFERENCE PROCEEDINGS

ISBN 978-0-7972-1907-6

NELSON MANDELA UNIVERSITY

CENTRE FOR RENEWABLE & SUSTAINABLE ENERGY STUDIES

Stellenbosch UNIVERSITY IYUNIVESITHI UNIVERSITEIT

SOUTHERN AFRICAN SUSTAINABLE ENERGY CONFERENCE

15 - 17 November 2023 | Boardwalk Convention Centre | Gqeberha | Eastern Cape

Preface

The SASEC 2023 organising committee would like to extend a warm welcome to the Southern African Sustainable Energy Conference (SASEC) 2023. It is a pleasure to be a part of this prestigious event and engage with the sustainable energy community. The commitment of South Africa to the Just Energy Transition and to a more sustainable future is indeed commendable and is essential for the global transition to renewable energy and energy efficiency.

The diverse range of topics covered in this conference, including solar energy, biomass, wind energy, hydrogen and energy storage, reflects the growing importance of sustainable technologies. It is clear that this event will provide valuable insights into the latest developments and research in the field of renewable and sustainable energy.

We look forward to learning from the high-quality academic papers and the expertise of the keynote speakers, Dr Claudia Buerhop-Lutz and Mahandra Rooplall. Their contributions will undoubtedly add great value to the conference. We also look forward to hearing from our dinner guest speaker, Dr Morné du Plessis from World Wide Fund South Africa (WWFSA).

We also extend our gratitude to the Department of Science and Innovation (DSI), the South African National Energy Development Institute (SANEDI) and all the sponsors for their support to make this conference possible.

We are excited about the opportunity to network with fellow sustainable energy enthusiasts and contribute to the shared goal of building a more sustainable and green future. Thank you once again for your interest and attendance, and we look forward to the fruitful discussions and engagement at SASEC 2023.

Prof Ernest van Dyk
Conference Chair

Committees

ORGANISING COMMITTEE

Prof Ernest van Dyk (Chair)	Nelson Mandela University
Dr Frederik Vorster	Nelson Mandela University
Dr Chantelle Clohessy	Nelson Mandela University
Dr Jacqui Crozier McCleland	Nelson Mandela University
Ms Chanie Neveling	Nelson Mandela University
Ms Bailey Muir	PVInsight
Ms Inge-Rae Scholtz	Centre for Renewable and Sustainable Energy Studies
Ms Fhatuwani Mulaudzi	Centre for Renewable and Sustainable Energy Studies
Dr Richmore Kaseke	Centre for Renewable and Sustainable Energy Studies

REVIEW COMMITTEE

Alan Brent	Victoria University of Wellington
Alberto Julio Tsamba	Eduardo Mondlane University
Armand du Plessis	Stellenbosch University
Arnold Rix	Stellenbosch University
Ashmore Mawire	North West University
Azeem Khan	University of Cape Town
Béatrice Morel	University of Reunion
Benton Otieno	Vaal University of Technology
Bernard Bekker	Stellenbosch University
Chantelle Clohessy	Nelson Mandela University
Chantelle van Staden	Stellenbosch University
Dominique Grondin	University of Reunion
Don Fitzgerald	Stellenbosch University
Edson Meyer	University of Fort Hare
Ernest van Dyk	Nelson Mandela University
Frederik Vorster	Nelson Mandela University

REVIEW COMMITTEE

Golden Makaka	Fort Hare university
Hartmut Winkler	University of Johannesburg
Jaap Hoffmann	Stellenbosch University
Jacqui Crozier McCleland	Nelson Mandela University
Johan van der Spuy	Stellenbosch University
Johann Gorgens	Stellenbosch University
Johann Strauss	Stellenbosch University
Johannes Pretorius	Stellenbosch University
Karin Kritzinger	University of Pretoria
Ken Craig	University of Johannesburg
Kristy Langerman	University of Pretoria
Lawrence Pratt	CSIR
Michael Owen	Stellenbosch University
Michael Simon	University of Fort Hare
Michel Benne	University of Reunion
Mokhotjwa Simon Dhlamini	University of South Africa
Monphias Vumbugwa	Nelson Mandela University
Mukovhe Ratshitanga	Cape Peninsula University of Technology
Nnditshedzeni Eric Maluta	University of Venda
Petja Dobreva	UNAM
Pontsho Mbule	University of South Africa
Robbie Pott	Stellenbosch University
Warren Brettenny	Nelson Mandela University
Willem Le Roux	University of Pretoria
Zelalem Nigussa Urgessa	Nelson Mandela University

REVIEW OF PAPERS

All submissions to the Southern African Sustainable Energy Conference have undergone peer review by members of the Technical Review Committee. This includes an initial review of submitted abstracts and a second, full paper review of final submissions.

SOUTHERN AFRICAN SUSTAINABLE ENERGY CONFERENCE

Table of Contents

THE RECENT ACCELERATED PACE OF ROOFTOP SOLAR INSTALLATIONS IN SOUTH AFRICA

Hartmut Winkler[1]

[1] Dept. Physics, University of Johannesburg, PO Box 524, 2006 Auckland Park, Johannesburg, South Africa; Phone: +27-115594417; Fax: +27-115592327; E-Mail: hwinkler@uj.ac.za

Abstract: Worsening power shortages in South Africa have precipitated a faster move to alternative electricity supply technologies, especially solar rooftop generation. This study seeks to quantify and explore the timeframe of this growth in solar rooftop installations over the past few years through the inspection of the most recent as well as historical Google Earth imagery. The investigation also attempts to project the rate of embedded solar installations over the next few years, a poorly understood (yet key) factor in South African electricity demand models. Trends in commercial solar installations are analysed by examining bird's eye images of South Africa's larger shopping malls, also exploring whether there are regional differences attributable to site solar irradiance or other factors. Domestic solar installation growth in recent years is estimated by counting households with visible rooftop panels and determining the rate of increase in solar rooftop installations in the demographically well-studied Johannesburg suburb of Parkhurst. Aspects investigated include determining the extent to which rooftop installations have been optimally aligned to receive maximum solar irradiance. The study finds that shopping malls constitute ~60% of the embedded solar facilities with total capacity in the range 0.5-5 MW, and that the dramatic increase in solar installations in malls coincided with the stalling of the REIPPPP programme in 2015. The upturn in domestic household solar installations is much more recent, with the number of households with solar power having more than doubled in the last 10 months.

Keywords: commercial solar installation; domestic solar installation; solar rooftop; South Africa.

1. Introduction

South Africa enjoys some of the best conditions in the world for solar energy generation [1].

From around 2010, many countries around the world have experienced major booms in solar rooftop installations, even when climatic conditions did not favour this mode of electricity generation. This has been driven by the need to avoid electricity generation from greenhouse gas emitting fossil fuel sources, as well as a rapid drop in the cost of solar power generating equipment [2].

Compared to other countries, the move towards renewable energy has been unnaturally slow in South Africa. Reasons for this are complex and include government messaging that can sometimes be interpreted as anti-renewables. Its clearest manifestation is the stalling of the Renewable Energy Independent Power Producer Procurement Programme (REIPPPP), the flagship government initiative set up to drive the development of solar farms and other renewable energy projects [3]. As a result, only very few new large solar farm builds were started between 2015 to 2018.

The biggest inhibitor of a solar panel rollout has however been the until recently reliable and comparatively cheap supply of electricity by the state power utility Eskom. Eskom's vigorous expansion of the electricity grid into previously underserviced rural areas in the early 2000's also removed a key incentive for alternative sources of power supply in remote areas, a recognised niche for solar energy devices [4].

In the last few years the situation has however changed dramatically. Power cuts have progressively worsened to the point where they have become the daily norm [5], and electricity tariffs have been rising annually at well above the national inflation rate [6].

The last year in particular, when power shortages reached record levels and talk of a possible grid collapse entered public discourse, has seen a dramatic surge in the installation of rooftop solar panels. The boom is expected to be further boosted by the introduction of tax incentives to households that install solar power equipment domestically [7].

This study seeks to quantify the recent growth in solar rooftop installations in South Africa and better understand its drivers.

2. Analytical method

Given the dearth and unreliability of official statistics on rooftop installation, the research method followed here consists of two approaches. Firstly, I have compiled a list of large entities that have set up solar installations in the capacity range 0.5-5 MW on their operational properties (usually on the roof) [8]. These entities include factories, corporate headquarters, warehouses, farms, but above all shopping malls. Secondly, I have carried out an 'in-the-field' census of solar rooftop installations in residential suburb of Johannesburg. More details follow below.

In common to both approaches, I visually inspected bird's eye imagery accessed through the Google Earth© application in which solar installations are generally well visible. Furthermore, Google Earth also allows access to earlier imagery, thereby in many instances enabling the determination of the approximate date on which a solar installation was made.

2.1. Shopping mall survey

I have over the past few years built up a list of large solar power installations in South Africa where I have included every facility that could be identified from internet searches provided it had a reported capacity of 0.5 MW or above [8].

This list is extensive, and at present includes 229 entries in the category of private on-site installations in the range 0.5-5 MW. This collection will hereafter be referred to as the "Base List". Note that this Base List excludes larger solar farms with capacity of 5-100 MW such as the ones established under REIPPPP (details of which can also be found at [8]).

Importantly, the Base List is not complete, nor is it a statistically homogeneous sample. It is expected that it currently only contains about half of the actual solar facilities with capacities in the range 0.5-5 MW. It is going to exclude all facilities for which no information concerning their existence and capacity was discovered during the internet searches.

Another drawback of the information compiled in the Base List is that some facilities extended their capacities some time after the initial solar installations. An example is illustrated in Figure 1, where the initial solar capacity was more than doubled a few years later. The capacity listed in the Base List may therefore not be current one.

A further likely source of bias is that information on some of the latest solar installations have not been captured anywhere on the internet, either because the relevant websites have not been updated recently or because solar installations are no longer considered 'newsworthy'.

Despite this, the Base List constitutes a useful starting point for investigating the growth in solar installations in South Africa. Typical sources used in compiling the Base List include the recordals of completed solar projects found on the websites of many solar infrastructure developers. These are not expected to have any bias in favour of specific categories of clients (e.g. shopping malls versus factories). Note however that, while most such companies have a national footprint, they may operate with a regional focus. Despite the various reservations regarding potential bias, given the large number of entries listed in the Base List, the sample investigated may be considered as reasonably representative of South Africa's private solar power installations in the capacity range 0.5-5 MW.

Fig. 1. Examples of Google Earth images of a mall that underwent two phases of solar rooftop installations: Mams Mall, Mamelodi, Tshwane, 2018, 2021, 2023 (left to right).

The shopping malls listed in the Base List were then inspected in Google Earth imagery. In particular, the earliest image was identified in which the solar installations were visible. The year in which this image was taken was then recorded as the installation year of solar rooftop panels of the shopping mall in question. It is however possible that if the last image not showing any solar panels was in an earlier year, the actual installation happened earlier than assumed. Given that most shopping malls are in urban areas where Google Earth imagery is updated every few months rather than every few years, such instances should be infrequent and would not dramatically affect the values given in Table 1.

2.2. Domestic solar rooftop

In order to attempt to quantify the growth in domestic solar rooftop in South Africa, this study uses Google Earth images recorded periodically over the last few years to count households with installed solar panels in the Johannesburg neighbourhood of Parkhurst. This suburb was chosen due to its relatively high density compared to typical income, and as its character, demographics and even the residents' attitudes towards solar power have been well studied [9, 10, 11]. In particular, residents

in the suburb tend to have higher-than-average income and would also be more receptive to pro-environmental arguments and mitigating climate change. It is therefore the type of neighbourhood that would be expected to lead any national trends towards comprehensive solar rooftop installations.

Thirty street blocks in the suburb were chosen to constitute the sample of residential houses for this study. In common with the rest of the suburb, houses here mostly have roofs pitched at angles similar to the local latitude angle, meaning that a panel placed on a north-facing roof would face the Sun directly at solar noon around the time of the solar equinoxes. Only the properties on the southern side of the road were included, as the north-facing parts of the roof, where solar panels are most likely to be located, cannot be easily viewed when a house is north of a road. These southern sides of a street block usually consisted of 12 houses, although in isolated instances there were only 8 or 9 residential properties. Their location is illustrated in the Google Earth image displayed in Figure 2. The total count of residential houses in these 30 blocks amounted to 343.

Fig. 2. Google Earth image of Parkhurst, Johannesburg, illustrating in blue highlight the street blocks used to generate the sample for this study.

As with the shopping mall sample, the latest available Google Earth image covering Parkhurst (recorded in October 2022) was scanned for what looked like solar panels set up on the property. Thereafter imagery dating back to 2014 was inspected to determine the earliest image in which the solar panels are visible. The installation date was then assumed to be at the midpoint in time between the last image showing no sign of panels on the property and the earliest one where the solar installation is seen.

In order to quantify solar installations since the last Google Earth image of Parkhurst currently available, I walked along the street of all 30 street blocks and recorded all solar rooftop installations not seen on the Google Earth images. This exercise also formed an additional check of the correctness of the Google Earth-based solar panel installations – in some instances what looked like a set of photovoltaic panels turned out to be a solar water heating device. Furthermore, the walkabout showed that about 10% of the solar installations unambiguously identified in the Google Earth images were not visible from the street, mainly due to high walls.

3. Solar rooftop at commercial shopping malls

3.1. Trends in the installations timeline covering the last decade

The annual installations of solar rooftop capacity at shopping malls included in the Base List are recorded according to province in Table 1. The last three rows of Table 1 list the sum of the earlier rows from 2014 to 2023, the total installations (i.e. shopping malls plus other facilities with 0.5-5 MW capacity) on the Base List for each province, and the fraction of the Base List capacity made up by shopping malls in each province.

Table 1. Annual and provincial breakdown of the solar rooftop capacity (in MW) installed in the studied sample of South African commercial shopping malls (Note: 2023 data only runs up to August of that year).

(in MW)	GP	WC	KZ	L	other
2014	2.9	-	-	-	0.6
2015	-	1.3	-	-	1.0
2016	19.3	-	-	-	1.2
2017	9.7	3.8	-	1.6	4.6
2018	6.8	2.4	2.2	3.4	5.4
2019	4.5	2.3	4.2	-	6.4
2020	9.0	2.4	3.2	3.7	6.4
2021	6.2	0.6	2.1	1.9	1.5
2022	8.1	-	13.0	2.9	0.7
2023	1.2	-	3.2	-	1.4
Mall total	67.7	12.8	27.9	13.5	29.2
0.5-5MW	104.5	39.6	30.9	21.2	57.0
%(mall)	65%	32%	90%	64%	51%

Notes: GP – Gauteng; WC – Western Cape; KZ – KwaZulu Natal; L – Limpopo; 0.5-5MW – total provincial capacity of on-site, medium size (0.5-5 MW) installations included in the sample; %(mall) – the percentage thereof installed at shopping malls

While the entities in the other provinces given in the last column

are too small in number to extrapolate trends, it can be mentioned that these amounted to 11.2 MW, 7.4 MW, 4.2 MW, 4.0 MW and 2.4 MW in total in Mpumalanga, North-West, Northern Cape, Free State and Eastern Cape respectively.

The annual national total of solar capacity at shopping malls from the Base List is illustrated in Figure 3. One notes a big rise in installations in 2016, after which the annual installation rate initially remained relatively constant, but then fluctuated substantially during the years of the national lockdowns at the time of the Covid-19 pandemic. Installation rates for 2023 only cover part of the year and furthermore many of the projects completed in early 2023 might not yet appear on the web pages from which the Base List has been compiled. The value for 2023 should therefore not be considered in the further analysis.

It needs to be noted however that the initial rapid acceleration in the rollout of solar power generation facilities associated with shopping malls has not persisted. It appears rather that the average of ~20 MW added each year over 2016-2018 will be more or less maintained when considering 2020-2023 as a whole.

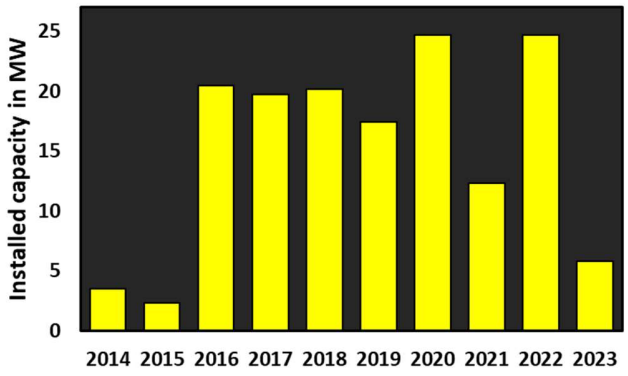

Fig. 3. Annual total installation of solar rooftop at the malls in the studied sample.

3.2. Trends observed in the rollout of medium-size solar installations

This study finds that nationally approximately 60% of all medium scale (0.5-5 MW) private on-site solar installations are located on the roofs (and occasionally parking shade ports) of large retail malls. Note that this excludes proper solar farms of 5 MW established as part of REIPPPP or 'wheeling' deals (where a company owns a solar farm far from its base location that feeds into the Eskom grid).

The fraction of shopping malls in the 0.5-5 MW capacity range differs substantially in some regions, with this figure as low as 32% in the Western Cape and as high as 90% in KwaZulu Natal. Possible reasons for this will be advanced later.

4. Domestic solar rooftop in residential areas

The outcome of the visual inspection of available Google Earth imagery for Parkhurst up to October 2022 and the in-the-field count of installations visible from the street in August 2023 are listed in Table 2.

Table 2. Solar rooftop installations in the 343 property sample in Parkhurst, Johannesburg.

Google Earth image date	Properties with new solar installed since last image	Monthly installation rate	Total properties with solar installed
2014 Jan	1	-	1
2015 Nov	3	0.13	4
2018 Mar	1	0.04	5
2018 Nov	2	0.25	7
2019 Jul	4	0.50	11
2020 May	7	0.70	18
2021 Apr	5	0.45	23
2021 Aug	3	0.75	26
2022 Apr	6	0.75	32
2022 Aug	8	2.0	40
2022 Oct	5	2.5	45
2023 Aug	51	5.1	96

4.1. Rooftop solar census

The total sample consisted of 343 properties that appeared to be residential households, although in some cases the properties might double up as small business operations. A minimum of 96 of these had solar rooftop panels installed, a penetration level of 28%. Of these, more than half had been installed in the 10 months between October 2022 and August 2023. Given that not all solar installations are visible from the street, it is probable that the true number of installations is just over 100, meaning a penetration level of about 30%. This estimate is based on the number of installations confirmed in the October 2022 Google Earth imagery that can however not be seen from the street, either because a property has high walls, or because the panels are on the roof of an outbuilding behind the main building.

The striking recent growth in domestic installations is evident in the plots in Figure 4. In this Figure, the green points represent the total number of households with rooftop panels installed, also

given in the last column of Table 2. The red triangles, also listed in column 3 of Table 2, represent the average number of installations per month for the period between the recording of the various Google Earth images. These were calculated by dividing the number of new installations since the previous image (given in column 2 of Table 2) to the number of months that passed between the date for that entry and the date for the previous image.

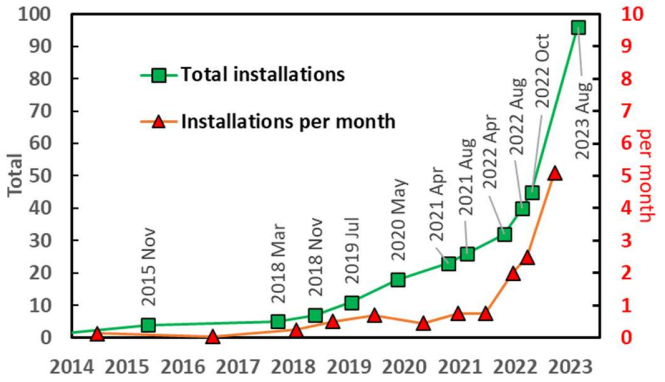

Fig. 4. Growth of domestic solar rooftop installations in Parkhurst, Johannesburg.

4.2. Rooftop solar panel orientation

The visual survey also allowed insights into the choices made regarding the solar panel alignment in residential homes.

Of the 96 properties with identified solar rooftop installations, 56 appeared to have all their panels aligned towards the north or close to north, facing the street (as seen in Fig. 2, the sampled streets run approximately east-west). For 10 properties all panels appeared to be aligned facing the morning Sun in the east, while in 12 instances all panels appeared to face towards the afternoon Sun in the west. The remaining 18 properties had panels facing in multiple cardinal directions. It is likely that a number of properties counted above as entirely north, east or west facing actually have panels tilted in multiple directions, as not all rooftop panels are readily visible from the street in some instances.

The Google Earth images and on-site inspections highlight that the area contains many high trees. Furthermore, some double-storey structures exist, and because of the small property sizes these can be located close to neighbouring houses. Trees and neighbouring structures cast large shadows, which would have impacted on a particular property's panel location decision and explains why comparatively many households chose to install their solar panels facing the morning or afternoon Sun rather than towards the normally optimal northern azimuth.

5. Discussion

5.1. The drivers of solar rooftop growth in South Africa

The timelines illustrating the growth of solar rooftop installations in Tables 1 & 2 and Figures 3 & 4, can be explained by the changing influence of driving factors.

Prior to 2016 there was relatively little interest in private solar installations, mainly due to financial considerations – electricity purchases from a then very reliable Eskom were cheaper than if this had been obtained through in-house solar power generation.

In 2016, with the effective suspension of large solar farm builds through REIPPPP, the nascent solar industry actively sought alternative customers, and found these in large private organisations that had become aware of the international trend towards generating electricity internally through solar rooftop installations. By then the cost of solar power had dropped to the point where large-scale installations could be shown to be financially advantageous.

When REIPPPP was resumed in 2018, major solar power developers again had the opportunity to engage in very large projects, and the previously accelerating rate of installations in the 0.5-5 MW range now stabilised. The economic downturn during the Covid-19 pandemic, including the associated uncertainty and loss of work hours due to lockdowns, may have even decreased the rate of solar installations for a while.

From 2022 onwards the South African power crisis worsened to the point where at times electricity was cut for as many as 12 hours a day. It also became clearer to the general public that the power crisis would not be resolved in the short term. This spurred a major move to install solar rooftop in domestic households, a sector that had up to that point been quite slow in making this leap. Reasons for this reluctance to embrace solar power technologies has been specifically studied in Parkhurst [11]. The sudden rise in solar installations in the Parkhurst sample from less than 1 installation monthly at the start of 2022 to over 5 new solar systems per month in 2023, highlighted dramatically by Figure 4, indicates that the inconvenience of power outages now outweighed the factors previously inhibiting the growth of solar power in the suburb.

The spike in solar rooftop installations in the year leading to June 2023 is also seen in estimated monthly installation figures released by national electricity utility Eskom [12]. Figures presented there projected a ~450% growth in South African solar rooftop capacity from just below 1 MW in March 2022 to about 4.4 MW in June 2023, although the accuracy of these figures cannot be easily confimed. Evidence of this trend is further seen in solar panel import figures, where the value of imports in the first six months of 2023 exceeded the 2022 annual total [13].

5.2. Regional differences

Contrary to perceptions that the Western Cape is leading the move to transit to renewable energy in the country, this study confirms previous findings that Gauteng is the province with by far the largest solar capacity installed [14], in this case in the form of medium-scale (0.5-5 MW) facilities, with 40% of the national fraction of Base List installations and more than double the fraction held by the Western Cape. It is difficult to see how this finding would change substantially if data from a complete census of solar installations became available.

Rooftop solar installations at shopping malls have been actively pursued around the country. These developments however only started in KwaZulu Natal in 2018, later than in other provinces, for reasons that remain to be clarified. Since then, the shopping malls in that province have however been some of the most actively movers towards solar power. In particular, Cornubia Mall in eThekwini and Boardwalk in Richards Bay now effectively have ~5 MW solar farms on their roofs [8].

The low percentage of shopping malls in the Western Cape is partly due to many installations in the 0.5-5 MW range on farms and food storage depots in that province [8].

5.3. Projections for further solar rooftop

It appears that by now the majority of larger shopping malls have installed some solar power capacity. Projections by retail groups themselves advocate the spread of this process to many malls that still do not have solar backup, e.g. [15]. At the same time, malls and other facilities with some solar capacity already installed are considering upgrades. Given the level of penetration already achieved, and with few signs that many facilities are projecting complete grid independence, it is likely that developments in the retail and corporate sectors will slowly saturate in the coming years. Accelerated growth is however still possible on farms, at mines and in industrial complexes.

While not explicitly investigated here, it is likely that the uptake in new solar installations seen in Parkhurst since early 2022 would have been a lot slower over the same period in lower income suburbs. This could however change given the opportunities for solar installation-linked loans by some financial institutions and the recent tax breaks offered by government [7]. The installation rate witnessed in Parkhurst this year would result in solar panel market saturation in the suburb within four years, and it therefore cannot be sustained.

This study also offers insights into the likely future spread of embedded power generation as a whole in South Africa. The Base List records facilities in the 0.5-5 MW range adding to a total capacity of ~250 MW, and this is in turn estimated to include about half of the actual solar facilities of that magnitude. The contribution by smaller installations (<0.5 MW) and individual sets of panels on domestic rooftops is even more difficult to estimate. Their total capacity can reasonably be expected to be of the order of the total installed capacity of facilities in the 0.5-5 MW range. That would imply that South Africa currently has an estimated 1000 MW of solar small embedded electricity generation capacity. This figure is three times higher than an estimated 330 MW suggested for 2020 [16]. Solar rooftop is therefore currently playing a more significant role in electricity production than previously assumed.

6. Conclusion

This paper highlights the increasing penetration of small scale solar rooftop installations in South Africa. It shows how medium scale (0.5-5 MW) solar installations, particularly at retail malls, multiplied manyfold after the stalling of the construction of large scale solar farms under REIPPPP. The major acceleration in domestic rooftop installations has only happened during the last year or two. It has been particularly noticeable in specific areas with relatively high income, but is bound to also strongly establish itself in medium income neighbourhoods due to offered financial incentives and the prospect of long-term savings.

Acknowledgements

This paper makes extensive use of current and historical imagery from Google Earth©.

References

[1] M. Suri, T. Cebecauer, A. J. Meyer, J. L. van Niekerk, "Accuracy-enhanced solar resource maps of South Africa", In *Third Southern African Solar Energy Conference*, pp. 450-456, May 2015.

[2] J. G. Wright, T. Bischof-Niemz, J. R. Calitz, C. Mushwana, R. van Heerden, "Long-term electricity sector expansion planning: A unique opportunity for a least cost energy transition in South Africa", *Renewable Energy Focus*, vol. 30, pp. 21-45, Sep 2019.

[3] M. L. Davies, "South Africa's contested transition to energy democracy: Lessons and struggles from the Renewable Energy Independent Power Producer Programme", Ph.D. thesis, CST, Stellenbosch University, 2021.

[4] R. Chidembo, J. Francis, S. Kativhu, "A review of the achievements, weaknesses, and challenges of rural electrification through Solar Home Systems in South Africa", African Journal of Development Studies, special issue, pp. 191-211, May 2022.

[5] W. Pierce, M le Roux, "Statistics of utility-scale power generation in South Africa: 2022", CSIR Energy Centre, https://www.csir.co.za/sites/default/files/ Documents/Statistics of power in SA 2022-CSIR-[FINAL].pdf (accessed 14 Aug 2023), Feb 2023.

[6] S. Moolman, "2022 update: Eskom tariff increases vs inflation since 1988 (with projections to 2024)", https://poweroptimal.com/ 2021-update-eskom-tariff-increases-vs-inflation-since-1988/ (accessed 14 Aug 2023), 2022.

[7] National Treasury, Republic of South Africa, "Solar panel tax incentive for individuals",https://www.treasury.gov.za/ documents/national budget/2023/2023 budget faqs - solar panel tax incentive.pdf (accessed 14 Aug 2023), 2023.

[8] H. Winkler, “South African solar power plant database”, https://hawiknowledge.org/solar_power_stations_2.html (accessed 13 Aug 2023).

[9] S. Rule, “Post-Apartheid Parkhurst: gentrification and deracialisation” In *Transforming rural and urban spaces in South Africa during the 1990s. Reform, Restitution, Restructuring*, Africa Institute of South Africa, vol. 10, pp. 225-248, 2002.

[10] P. T. Monare, N. Kotze and T. Morton McKay, “A second wave of gentrification: The case of Parkhurst, Johannesburg, South Africa”, *Urbani Izziv*, vol. 25, S108-121, 2014.

[11] T. McKay and D. Hendricks, “Pitiful rooftop solar uptake in sunny South Africa: A policy, funding and service delivery perspective”, *Frontiers in Sustainable Cities*, vol. 4, 969040, Sep 2022.

[12] Eskom, “Weekly System Status Report – 2023 Week 28 (10/07/2023 – 16/07/2023)”, https://www.eskom.co.za/wp-content/uploads/2023/07/Weekly_System_Status_Report_2023_w28.pdf, Jul 2023.

[13] S. Jacobs, “South Africa’s solar panel imports hit new record”, Daily Investor, https://dailyinvestor.com/energy/26209/south-africas-solar-panel-imports-hit-new-record/, Aug 2023.

[14] L. S. Waswa, B. Bekker, “Impact of PV small scale embedded generation on South Africa’s system demand profile”, In *Southern African Solar Energy Conference*, https://sasec.org.za/full_papers/90.pdf, Jul 2018.

[15] M. Arnoldi, “Growthpoint plans to double solar capacity by June”, Engineering News, Creamer Media, 6 Feb 2023.

[16] Sustainable Energy Africa (SEA) NPC, “Small-Scale Embedded Generation (SSEG): Guide for South African Municipal Distributors”, GIZ, https://pvgreencard.co.za/wp-content/uploads/2021/07/SSEG-final-digital.pdf, Jul 2021.

THE SOCIAL AND ECONOMIC POTENTIAL OF CLOSING THE LOOP ON PHOTOVOLTAIC (PV) MODULE WASTE

MN Crozier[1], C Schenck[2], JL Crozier McCleland[3] and EE van Dyk[4]

[1] University of the Western Cape, South Africa, Phone: +27 (0)84 271 3366, E-mail:4322394@myuwc.ac.za

[2] University of the Western Cape, South Africa, E-mail: cschenck@uwc.ac.za

[3] Nelson Mandela University; E-mail: Jacqueline.CrozierMcCleland@mandela.ac.za

[4] Nelson Mandela University; E-mail: Ernest.vanDyk@mandela.ac.za

Abstract: An unreliable energy supply is accelerating the transition to solar energy for South African industry and households. As solar photovoltaic (PV) module installations increase, so does the need to create systems to deal with the current and future e-waste produced. PV modules degrade in performance over the 20–25-year lifetime of the module with a normal power loss of less than 1% per year. However, early-life failures can occur if modules are damaged or are of poor quality and thus can degrade faster. With only limited recycling of PV modules occurring, a circular economy approach has yet to be developed in South Africa. A circular economy designs out waste, circulates materials at their highest possible value and is regenerative by design. Recycling is the least desirable of the circular economy activities due to the loss of value in the materials. Reuse and repair are potentially more ideal as they retain the product's inherent value. This paper places PV end-of-life within the context of South Africa's e-waste recycling and energy landscape. The potential benefits around business development and employment for a secondhand market in PV are referred to. The paper provides a context for understanding issues around PV Module reuse and repair in South Africa. *Keywords: Solar PV Modules; Reuse; Recycling; Circular Economy; End-of-Life; E-waste.*

1. Introduction

Renewable energy (RE) adoption is essential to meeting global carbon emission targets and mitigating climate change. Although solar PV energy systems offer great benefits, for it to be a truly sustainable option, attention must be placed on the components' entire life cycle, especially at end-of-life (EOL). There has been limited research on the potential adverse environmental and human health implications of unmanaged waste from PV energy systems [1]. Whilst this continues, solar PV cannot be considered a truly sustainable energy source. When e-waste, such as PV modules, is treated as a resource instead of waste, this will open up greater economic opportunities [2].

The study aims to explore the demand for PV reuse applications and the barriers and opportunities for employment creation in this field. This paper outlines the background to e-waste, the current energy landscape and PV module recycling in South Africa. It introduces the concepts associated with PV module reuse and provides a context on the need for a PV module reuse market. The study will include primary research through a survey to assess the e-waste and PV energy sectors' perceptions of barriers, enablers, and drivers for this circular economy solution. However, the survey results were unavailable at the time of writing this paper.

The structure of the paper includes a definition of the circular economy (Section 2), background to e-waste (Section 3), and the framework to consider findings on the reuse and repair of solar PV modules (Section 4). A brief overview of the South African solar energy landscape is provided in Section 5, and then issues around solar PV EOL and potential social and economic benefits are detailed (Section 6). The research gaps filled by the current work are described in Section 7 before concluding (Section 8).

2. The Circular Economy

A Circular Economy (CE) designs out waste and pollution, circulates materials and products at their highest value for as long as possible, and is regenerative, aiming to improve the environment, not just reduce negative impacts [3]. This is achieved through production and consumption practices that redesign, repair, remanufacture, refurbish, reuse or recycle materials. Thus, disposal should be the option of last resort for a product at its EOL. Global extraction, processing and manufacturing methods are linked to 62% of global greenhouse gas emissions [4]. Thus, exploring EOL solutions not only impacts waste and pollution levels but also reduces carbon emissions.

3. E-waste

Electronic waste or e-waste "…refers to discarded end-of-life and end-of-use electrical and electronic equipment (EEE)." [2, p. 52]. PV modules fall under EEE [5]. E-waste is the world's fastest-growing waste fraction. The Global E-Waste Monitor 2020 indicated that 53.6 million metric tonnes (Mt) of electronic waste (excluding PV waste) was generated in 2019, an increase

of 21% in 5 years[6]. The PV waste fraction was omitted from the calculation as ComTrade data was unavailable [6]. Drivers of e-waste are increasing levels of urbanisation and industrialisation globally and higher levels of disposable income, leading to higher consumption rates of EEE. South Africa generated 416 kt or 7.1 kg per capita of e-waste in 2019 [6]. Only 18 kt is estimated to have been recycled in 2015; however, waste statistics are unreliable thus, this is assumed to be an underestimate of e-waste recycling [7].

The South African e-waste supply chain relies heavily on informal waste pickers and small-scale recyclers for collection and dismantling. Estimates of waste pickers vary between 60 000 and 90 000, up to 215 000 [8]. Formal recyclers then will predominantly export to overseas processors [2].

E-waste is categorised as hazardous under South African law as it may contain toxic materials if disposed of incorrectly. Several legislative amendments have changed the environment for e-waste. The National Norms and Standards for Disposal of Waste to Landfill of 2013 banned e-waste from being disposed of at landfill sites [9] and took effect on 23 August 2021 [2]. South Africa has also moved from a voluntary Extended Producer Responsibility or EPR environment to a mandatory one. EPR is an approach to dealing with the negative impacts of waste through reassigning responsibility for the EOL of a product or its packaging to the producer. EPR legislation took effect on 5 November 2021, covering the lighting, electrical & electronic equipment and packaging sectors. This has implications for EEE product producers, importers and installers, including PV energy systems. Regarding the amendments to the National Waste Act, any person or company who imports or manufactures these items is responsible for their EOL management.

These are positive moves in terms of introducing a circular economy approach to e-waste, moving South Africa away from "the age of landfill" [2, p. 54] to the age of voluntary and now mandatory EPR.

Barriers experienced within the South African e-waste value chain include:

- An overwhelming percentage of e-waste in South Africa is exported due to a lack of infrastructure for processing these waste products [51]. The unfortunate *Catch 22* is that the small domestic market discourages companies from setting up e-waste collections, but the small domestic market is due to limited companies offering collections.
- Large volumes of valuable e-waste are lying in storage.
- Small recyclers face cash flow constraints and unreliable volumes
- Very high costs involved in formal e-waste certification.
- The lack of local product markets limits demand and local processing.
- At the disposal stage, high disposal costs are a cost for formal businesses and trigger illegal dumping [2].
- Cherry picking occurs [2], which is extracting only high-value and high-grade materials for recycling and leaving the waste fractions that are not economically viable for disposal.

Dumping unwanted components and burning plastic to access the high-value waste fractions[2] by informal collectors is a direct result of cherry picking. Informal recycling collectors lack storage facilities and equipment to break EEE, whilst plastics used in EEE have come in contact with flame retardant chemicals and thus cannot find a market to be recycled. This results in the inevitable and highly unfortunate consequences of dumping and burning e-waste. The presence of informal sector recyclers tackling PV waste is seen as a constraint to effective EOL management in countries such as China [10], as the informal sector lacks knowledge of the products and only recycles a small portion before discarding the remainder. The South African government's perspective is that the informal sector plays a vital role in the recycling value chain and should not be excluded but instead supported[11]. Thus, investigating how PV e-waste can also assist small-scale and informal recyclers is an important research area.

4. A Framework for Analysing Opportunities for Solar PV Module Repair and Reuse

Current literature has focused mainly on recycling as an EOL strategy for PV waste [1][15]. Themes in research have included studies on efficient EOL management strategies for PV energy systems using material flow analysis [13], as well as life cycle assessments of technologies [14], including concentrator photovoltaics [15]. Other studies have estimated the climate impacts of circular EOL for solar PV [16] or sought the perceptions of consumers and manufacturers on PV EOL [17].

Salim et al. [1] developed a conceptual framework for the solar energy system circular economy based on a systemic review of papers in the field. This framework illustrated in Figure 1 comprises Drivers, Barriers and Enablers.

The Drivers are why stakeholders would participate in a circular economy for solar energy systems, i.e., the opportunities. These are categorised into three clusters: economic, social and environmental [1].

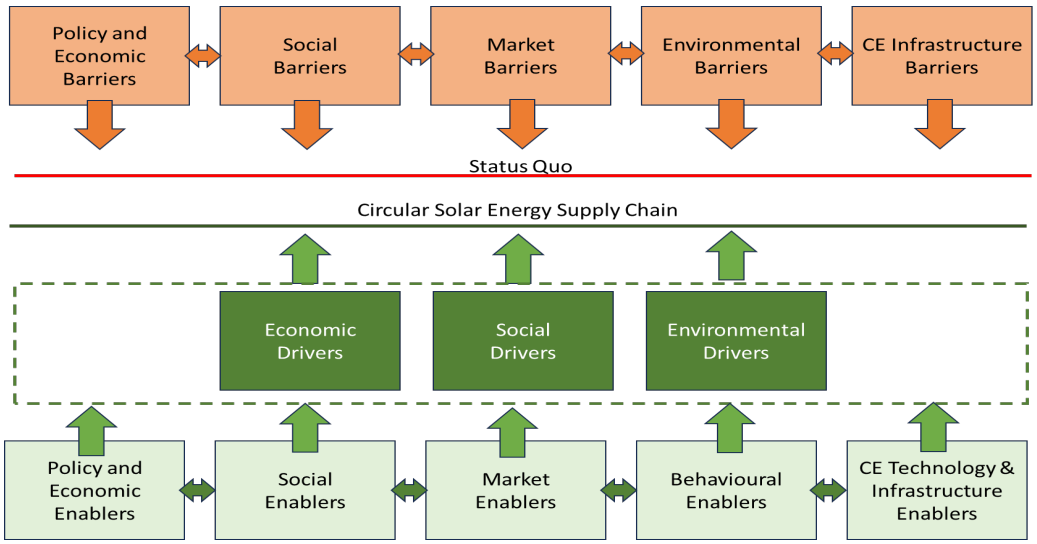

Fig. 1. Conceptual Framework for a Circular Solar Energy Supply Chain. Adapted from Salim et al.

Barriers are the limitations to implementing a circular economy for solar PV modules and battery energy storage systems (BESS) needs. These are summarised into five clusters:

- policy and economic;
- social;
- market;
- environmental;
- and recycling infrastructure.

The Enablers are the measures needed to overcome barriers to implement a circular economy for PV systems. The enablers are categorised into the following clusters: policy and economics, social, market, behavioural and recycling technology and infrastructure [1].

This conceptual framework offers a useful tool to analyse the findings of this research and for comparison with studies undertaken in other countries.

5. The South African Solar Energy Landscape

South Africa's energy mix heavily relies on coal at 72% of energy generation [18]. The push for RE transition has historically focused on Independent Power Producer agreements, which have allowed private energy companies to develop utility-scale PV plants in South Africa. Cumulative utility-scale PV power generation stood at approximately 2 371 MW in 2022[19]. Nationally, there has been growth in the energy services sector due to above-inflation electricity price rises, increased national energy insecurity due to persistent load-shedding, lower costs of RE generation, more favourable RE policy and regulations and new financing models[20]. Unreliable energy supply is leveraging the demand from industry and households to source alternative energy solutions. In 2022, South Africa experienced its worst year of load-shedding, with 208 days of power outages[21], with 2023 \ on track to beat this record. The South African solar energy market is expected to have a Compound Annual Growth Rate (CAGR) of 10.56% over 2022-2027 [22]. The country's cumulative solar PV capacity was 4 172 MW in 2021[19].

Rooftop solar for commercial/industrial, agricultural and residential applications grew by 60%, 45% and 30% CAGR, respectively, between 2020 and 2022 [19]. This sector's growth has been spurred due to changes in the regulatory environment. In 2022, energy generation capacity was added of between 800-900 MWp, valued at R7.5 billion. The rooftop solar market is expected to grow to a total capacity of 10 GWp by 2035, with a market value of approximately R100 billion [20]. In terms of employment, the expansion of energy services generates approximately 1250 jobs per 50MWp per year[20].

The majority of solar PV modules are imported, with minimal manufacturing occurring in South Africa[23]. There are, however, a few locally based manufacturers, such as ARTsolar, Ener-G Africa and Seraphim Solar.

6. Solar PV End-of-Life

South African households generally have poor recycling behaviours and low recycling rates of e-waste, at only 11% [24]. As solar PV modules become increasingly part of household and business electronics, developing accessible EOL options, educating consumers on responsible disposal, and enforcing anti-dumping and landfilling restrictions will become crucial.

Globally, over 6 000 square kilometres of solar PV modules have been installed [25, p. 39]. By 2050, global PV cumulative installed capacity will total 4 500 GW[26]. PV waste could exceed 10% of e-waste streams, with cumulative PV waste

conservatively estimated at 60 million tons by 2050 [26].

South Africa's cumulative PV waste is estimated to grow to between 8 500 tonnes and 80 000 tonnes by 2030 and between 750 000 and 1 million tonnes by 2050 [26]. These figures align with the Policy Adjusted Integrated Resource Plan (IRP) of 2019, indicating South Africa's goal for installed PV capacity by 2030 to be 8 288 MW[27].

To keep pace with the growing global demand for solar energy, this will increase demand for silver and indium materials, both critical raw materials. If global solar energy were to reach TW-scale power generation by 2050, at least half of global silver resources would need to be devoted to this application [25].

PV modules degrade in performance over the 20–25-year lifetime of the module. Typically, there is a power loss of less than 1% annually [28]. However, early-life failures can occur if modules are damaged or of poor quality. Then degradation can occur at a faster rate. Large PV plants will also repower, replace or upgrae modules to maximise production. So, even in the best-case scenario of all modules operating ideally and lasting their full-service lifetime, there is a potential for large volumes of PV waste at EOL.

the manufacturer. At EOL, landfill disposal would be avoided through parts reuse or recycling.

Recycling has thus far been the main circular economy strategy employed in the supply chain. However, recycling has a number of challenges, including financial viability and low concentrations of valuable metals within PV modules.

The capacity of PV recycling plants, the types of PV modules recycled[30], and the volumes of waste handled [13] were found to be critical aspects of the financial viability of PV module recycling. Only large industrial-scale or multi-use recycling plants were found to be financially feasible [30].

Globally, PV modules are unpopular for recycling, as 90% of the market are first-generation solar cells based on crystalline silicon technology, with low concentrations of valuable metals [31]. Recyclers are mainly interested in the remaining 10% of the PV market for recovering critical earth metals. However, the cost of recycling outweighs the value of recovered materials[31].

Another critical challenge in PV module recycling, as opposed to other e-waste, is the 20-year life span of PV modules. It thus takes time for recyclers to collect enough volumes of waste to make recycling viable [32].

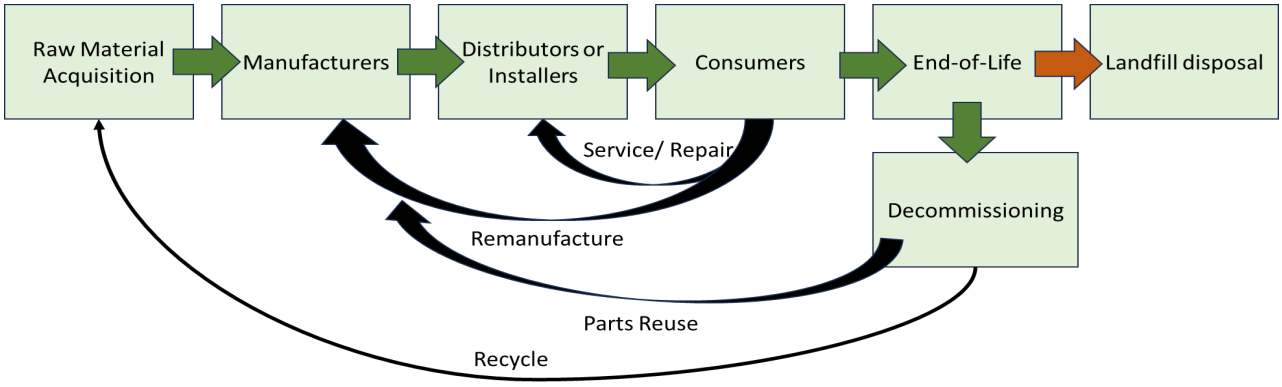

Fig. 2. Circular Supply Chain for Photovoltaic Systems adapted from [1, p. 540]

6.1. *A circular economy for PV modules*

A circular economy approach to EOL solutions for PV modules would consider options around reuse, remanufacturing and refurbishment, and designing for disassembly. Assessing opportunities for reuse aligns with the waste hierarchy outlined in South Africa's 2020 National Waste Management Strategy.

Electronic goods and their components in current circulation have a higher value than their component materials[29]. Thus, there are significant advantages to extending product lives and undertaking repair and reuse activities. Figure 2 offers an overview of what a circular economy for PV modules could look like. The diagram illustrates that consumers can access repair and maintenance services from installers and distributors before EOL. Alternatively, the unit could be remanufactured through

6.2. *Social and Economic Benefits of a circular economy for PV modules*

A circular economy transition that extends product lifespans is linked to improvements in the state of the environment, positive economic impacts and social benefits such as skills development[33]. Potential social and economic benefits that this study will be considering include:

- Job and business creation
- Access to testing to provide quality assurance to consumers
- Social justice through greater inclusion in energy transition

SMEs were identified as the stakeholders predominantly

responsible for solar PV reuse, remanufacturing and repair in the developing world [13]. Small business involvement in PV EOL activities was identified as a significant opportunity, especially around product repair, disassembly and remanufacturing [13]. There are also opportunities for new CE business models around remanufacturing, sharing and leasing [13] of PV modules. To take full advantage of any circular economy options around PV modules, the collection and sorting of this waste type needs to be improved, as with e-waste in general. Collection systems that have been recommended for e-waste in South Africa are trade-ins. The barrier to trade-ins is the difference in customers' perceived and actual market value of returned electronics. The opportunity is that it would unlock waste electronics in storage and create sustainable, consistent volumes for the CE businesses [34].

Employment in the construction and installation of commercial and industrial solar PV systems in South Africa was estimated to create between 5.3 and 8.0 full-time equivalent (FTE) jobs per MW[35]. In comparison, rooftop systems are projected to create between 6.1 and 9.2 FTE jobs per MW during construction and installation [35]. A CE for PV modules could support job creation in new areas of the value chain. European estimates indicate that 63 jobs are created per 1000 tonnes of collected electrical equipment waste [36]. In the US, electronics repair and remanufacturing could support 200 jobs per 1000 tonnes compared to 15 jobs for recycling that same amount [37]. Thus, in theory, reuse and repair should offer greater employment benefits in South Africa than recycling PV modules.

A key barrier for the reuse market is access to testing and certification of secondhand modules. The costs of current accredited testing services are prohibitively expensive and require expensive equipment. Crozier McCleland et al. [38], a paper emanating from this study, considers the development of repair and reuse criteria for PV modules. A key market challenge will be to ensure that modules can be accurately and cost-effectively tested, that they are safe for use, that consumers trust secondhand modules and that they can be supplied to the market at a reasonable price compared to new modules.

The United Nations Sustainable Development Goal (SDG) 7 is to 'Ensure access to affordable, reliable, sustainable and modern energy for all' [38]. Thus, access to RE should be available to all, and no communities should be left behind. The Just Energy Transition offers opportunities for new jobs, business, greater social justice, etc. [39]. This study asks whether a secondhand PV module market could place solar energy within the grasp of more households, especially low-income households in South Africa. Thus promoting social justice and inclusion in the RE transition.

7. Research Gaps and Study Methodology

Internationally, studies have focused on developed nations [13], experimental and modelling research methodologies, and the recycling aspect of PV modules. South Africa's informal sector, its exponential growth in solar PV and the geographical dispersion of utility-scale PV plants requires an analysis of its unique challenges.

Moyo et al. (2022) identified the need for more research in the field of e-waste in general in South Africa that focused on infrastructure, technology transfer and policy gaps. Research is needed considering solar PV modules at EOL beyond recycling and how reuse applications can have social and economic benefits. Researchers should consider consumer uptake of secondhand solar as well as the policy and legal ramifications in more detail. The focus of EOL PV module research globally has been in developed nations; who consider exporting decommissioned PV modules to the Global South a viable reuse alternative. Exporting low-quality PV modules to other countries can be considered dumping [33], especially if there are no systems for waste management within the recipient countries.

This study aligns with these identified gaps in the research. The study's methodology uses an exploratory research approach due to the limited information available on this topic within South Africa. A mixed methodology design using quantitative and qualitative data collection will occur simultaneously. At the time of writing this paper, ethics approval for a survey questionnaire and interview guide had been received. A survey will collect data from the energy sector on future demand for EOL services and the potential for reuse and repair. A semi-structured interview will be undertaken with e-waste recyclers working in PV recycling and key informants in the energy and e-waste sectors. The discussions will access data on levels of cooperation in the life cycle and barriers and drivers for reuse. The findings will be analysed within Salim et al. (2019) conceptual framework for a Circular Solar Energy Supply Chain (Figure 1). Thus providing a better understanding of how to develop a PV circular solar supply chain within South Africa with a focus on business and employment opportunities.

8. Conclusion

If a linear approach to producing, using and then discarding PV systems is maintained, it undermines the sustainability of this critical renewable energy source. The recent growth of South Africa's solar energy sector means larger volumes of modules that will one day need EOL solutions and increased volumes of current waste through faults and breakages. The need for an efficient EOL management system is more pressing considering the limited e-waste collection and recycling systems within

South Africa and developed nations' plans to export EOL modules to the developing world. The opportunities for reuse have had limited research attention and require an understanding of consumer preferences, regulatory frameworks, quality controls and market viability. The social and economic opportunities around a reuse market for PV include greater job and business creation across the value chain, informal sector integration, and greater access to RE, thus promoting a just energy transition and social justice.

Acknowledgements

The authors would like to acknowledge the support of the South African Technology Innovation Agency (TIA) in supporting the research on this topic.

References

[1] H. K. Salim, R. A. Stewart, O. Sahin, and M. Dudley, 'Drivers, barriers and enablers to end-of-life management of solar photovoltaic and battery energy storage systems: A systematic literature review', *Journal of Cleaner Production*, vol. 211, pp. 537–554, 2019, doi: 10.1016/j.jclepro.2018.11.229.

[2] T. Moyo, Z. Sadan, A. Lotter, and J. Petersen, 'Barriers to recycling e-waste within a changing legal environment in South Africa', *South African Journal of Science*, vol. 118, no. SPE, pp. 1–8, 2022, doi: 10.17159/sajs.2022/12564.

[3] Ellen MacArthur Foundation, 'What is a circular economy?', What is a circular economy? Accessed: Jul. 21, 2022. [Online]. Available: https://ellenmacarthurfoundation.org/topics/circular-economy-introduction/overview

[4] Circle Economy, 'The Circularity Gap Report 2019', The Platform for Accelerating the Circular Economy (PACE), 2019. Accessed: Jul. 19, 2023. [Online]. Available: https://www.legacy.circularity-gap.world/_files/ugd/ad6e59_ba1e4d16c64f44fa94fbd8708eae8e34.pdf

[5] V. Forti, C. P. Baldé, and R. Kuehr, 'E-Waste Statistics Guidelines on Classification, Reporting and Indicators', United Nations University, ViE – SCYCLE, Bonn, Germany, 2nd Edition, 2018. Accessed: Jul. 16, 2023. [Online]. Available: https://collections.unu.edu/eserv/UNU:6477/RZ_EWaste_Guidelines_LoRes.pdf

[6] V. Forti, C. P. Baldé, R. Kuehr, and G. Bel, 'The Global E-waste Monitor 2020: Quantities, flows and the circular economy potential', United Nations University (UNU)/United Nations Institute for Training and Research (UNITAR) – co-hosted SCYCLE Programme, International Telecommunication Union (ITU) & International Solid Waste Association (ISWA), Bonn/Geneva/Rotterdam, 2020.

[7] M. Lydall, W. Nyanjowa, and Y. James, 'Mapping South Africa's waste electrical and electronic equipment (WEEE) dismantling, pre-processing and processing technology landscape', Mintek, Johannesburg, Mintek External Report # 7574, 2017. Accessed: Jul. 16, 2023. [Online]. Available: https://www.itu.int/en/ITU-D/Environment/Documents/Events/2021/Fostering-E-waste-Management-across-Africa/weee_technology_landscape_assessment_report.pdf?csf=1&e=dWYDtB

[8] L. Godfrey and S. Oelofse, 'Historical Review of Waste Management and Recycling in South Africa', *Resources*, vol. 6, no. 4, Art. no. 4, 2017, doi: 10.3390/resources6040057.

[9] Republic of South Africa, *National norms and standards for disposal of waste to landfill: National Environmental Management: Waste Act 2008*. 2013. Accessed: Jul. 14, 2023. [Online]. Available: https://lawlibrary.org.za/akn/za/act/gn/2013/r636/eng@2013-08-23/source

[10] J. Yu, E. Williams, M. Ju, and C. Shao, 'Managing e-waste in China: Policies, pilot projects and alternative approaches', *Resources, Conservation and Recycling*, vol. 54, no. 11, pp. 991–999, 2010, doi: 10.1016/j.resconrec.2010.02.006.

[11] Department of Environment, Forestry and Fisheries (DEFF), 'National Waste Management Strategy 2020', Department of Environment, Forestry and Fisheries (DEFF), 2020. Accessed: Oct. 20, 2022. [Online]. Available: https://www.dffe.gov.za/sites/default/files/docs/2020nationalwaste_managementstrategy1.pdf

[12] Md. S. Chowdhury *et al.*, 'An overview of solar photovoltaic panels' end-of-life material recycling', *Energy strategy reviews*, vol. 27, pp. 100431-, 2020.

[13] A. Gautam, R. Shankar, and P. Vrat, 'Managing end-of-life solar photovoltaic e-waste in India: A circular economy approach', *Journal of Business Research*, vol. 142, pp. 287–300, 2022, doi: 10.1016/j.jbusres.2021.12.034.

[14] R. Contreras Lisperguer, E. Muñoz Cerón, J. de la Casa Higueras, and R. D. Martín, 'Environmental Impact Assessment of crystalline solar photovoltaic panels' End-of-Life phase: Open and Closed-Loop Material Flow scenarios', *Sustainable production and consumption*, vol. 23, pp. 157–173, 2020.

[15] A. Ziemińska-stolarska, M. Pietrzak, and I. Zbiciński, 'Application of LCA to determine environmental impact of concentrated photovoltaic solar panels—state-of-the-art', *Energies (Basel)*, vol. 14, no. 11, pp. 3143-, 2021.

[16] M. Goe and G. Gaustad, 'Estimating direct climate impacts of end-of-life solar photovoltaic recovery', *Solar energy materials and solar cells*, vol. 156, pp. 27–36, 2016.

[17] P. Nain and A. Kumar, 'Understanding manufacturers' and consumers' perspectives towards end-of-life solar photovoltaic waste management and recycling', *Environment, development and sustainability*, vol. 25, no. 3, pp. 2264–2284, 2023.

[18] ESKOM, 'Factsheet: Coal in South Africa', ESKOM, South Africa, 2021. Accessed: Jun. 23, 2023. [Online].

Available: https://www.eskom.co.za/wp-content/uploads/2021/08/CO-0007-Coal-in-SA-Rev-16.pdf
[19] E. Bellini, 'South Africa installed 1.3 GW of PV last year', *PV Magazine International*, Jul. 21, 2021. Accessed: Nov. 14, 2022. [Online]. Available: https://www.pv-magazine.com/2021/07/21/south-africa-installed-1-3-gw-of-pv-last-year/
[20] GreenCape, '2023 Energy Services Market Intelligence Report', GreenCape, Cape Town, South Africa, 2023. Accessed: Jun. 23, 2023. [Online]. Available: https://green-cape.co.za/wp-content/uploads/2023/04/ES_MIR_2023_DIGITAL_SINGLES.pdf
[21] S. Simpson, 'Load shedding tracker: A visualisation of power cuts over the years', The South African. Accessed: Jun. 23, 2023. [Online]. Available: https://www.thesouthafrican.com/news/load-shedding-tracker-how-many-days-2015-2023-outlier-visuals-breaking-11-january/
[22] Mordor Intelligence, 'South Africa Solar Power Market Size, Growth, Analysis (2022 - 27)'. Accessed: Oct. 25, 2022. [Online]. Available: https://www.mordorintelligence.com/industry-reports/south-africa-solar-energy-market
[23] K. Rivett-Carnac, 'Insights into the Solar Photovoltaic Manufacturing Value Chain in South Africa', TIPS; WWFSA, South Africa, 2022. [Online]. Available: https://tips.org.za/research-archive/sustainable-growth/green-economy-2/item/4441-insights-into-the-solar-photovoltaic-manufacturing-value-chain-in-south-africa
[24] Department of Environmental Affairs, 'National Waste Information Baseline Report', Department of Environmental Affairs, Pretoria, 2012. Accessed: Jul. 19, 2023. [Online]. Available: http://sawic.environment.gov.za/documents/1880.pdf
[25] Leiden-Delft-Erasmus Centre for Sustainability Circular Industries Hub, 'White paper: Critical materials, green energy and geopolitics: a complex mix', Leiden-Delft-Erasmus Universities, 2022. Accessed: Jun. 25, 2023. [Online]. Available: https://www.centre-for-sustainability.nl/uploads/cfs/attachments/Critical%20Materials_LDE%20White%20Paper_DEF20220627_0.pdf
[26] IRENA and IEA-PVPS, 'End of Life Management: Solar Photovoltaic Panels', International Renewable Energy Agency and International Energy Agency Photovoltaic Power Systems., Technical Report NREL/TP-6A20-73852, 1561525, 2016. doi: 10.2172/1561525.
[27] GreenCape, '2023 Large Scale Renewable Energy Market Intelligence Report', GreenCape, Cape Town, South Africa, 2023. Accessed: Jun. 23, 2023. [Online]. Available: https://green-cape.co.za/wp-content/uploads/2023/04/RENEWABLE_ENERGY_MIR_2023_DIGITAL_SINGLES.pdf
[28] D. C. Jordan, S. R. Kurtz, K. VanSant, and J. Newmiller, 'Compendium of photovoltaic degradation rates', *Prog. Photovolt: Res. Appl.*, vol. 24, no. 7, pp. 978–989, 2016, doi: 10.1002/pip.2744.
[29] D. Lazar, 'An Opportunity in the Circular Economy: E-Waste', *Energy Industry Review*, 2021. Accessed: Jul. 19, 2023. [Online]. Available: https://energyindustryreview.com/environment/an-opportunity-in-the-circular-economy-e-waste/
[30] F. Cucchiella, I. D'Adamo, and P. Rosa, 'End-of-Life of used photovoltaic modules: A financial analysis', *Renewable and Sustainable Energy Reviews*, vol. 47, pp. 552–561, 2015, doi: 10.1016/j.rser.2015.03.076.
[31] F. Cucchiella, I. D'Adamo, S. C. Lenny Koh, and P. Rosa, 'Recycling of WEEEs: An economic assessment of present and future e-waste streams', *Renewable and Sustainable Energy Reviews*, vol. 51, pp. 263–272, 2015, doi: 10.1016/j.rser.2015.06.010.
[32] J.-K. Choi and V. Fthenakis, 'Crystalline silicon photovoltaic recycling planning: macro and micro perspectives', *Journal of Cleaner Production*, vol. 66, pp. 443–449, 2014, doi: 10.1016/j.jclepro.2013.11.022.
[33] M. Pareek, 'Supply Chain of Second Life PV Modules for Reuse in Europe: Investigating Circular Service Models For Solar Power Industry', International Master of Science in Sustainable and Innovative Natural Resource Management (SINReM), Ghent University, 2022. Accessed: Oct. 04, 2023. [Online]. Available: https://www.semanticscholar.org/paper/Supply-Chain-of-Second-Life-PV-Modules-for-Reuse-in-Pareek/32f0e991fd794acd6674edfaffe096bf52d84d50
[34] R. Ichikowitz and T. S. Hattingh, 'Consumer e-waste recycling in South Africa', *South African Journal of Industrial Engineering*, vol. 31, no. 3, pp. 44–57, 2020, doi: 10.7166/31-3-2416.
[35] CSIR, 'Solar PV Industry Jobs Report', SAPVIA, 2021. Accessed: Dec. 06, 2022. [Online]. Available: https://www.sapvia.org.za/wp-content/uploads/2021/05/SAPVIA-PV-Industry-Jobs-Study-Report-COMBINED.pdf
[36] IRENA and ILO, 'Renewable energy and Jobs: Annual Review 2022', International Renewable Energy Agency and International Labour Organization, Abu Dhabi and Geneva, 2022. Accessed: Aug. 30, 2023. [Online]. Available: https://www.irena.org/publications/2022/Sep/Renewable-Energy-and-Jobs-Annual-Review-2022
[37] Rreuse, 'Briefing on job creation potential in the re-use sector', 2015. Accessed: Sep. 02, 2023. [Online]. Available: https://www.rreuse.org/wp-content/uploads/Final-briefing-on-reuse-jobs-website-2.pdf
[38] United Nations, 'Goal 7 Ensure access to affordable, reliable, sustainable and modern energy for all'. Accessed: Oct. 06, 2023. [Online]. Available: https://sdgs.un.org/goals/goal7
[39] Presidential Climate Commission, 'Just Energy Transition'. Accessed: Oct. 06, 2023. [Online]. Available: https://www.climatecommission.org.za/$PRIMARY_SITE_URL/just-energy-transition

PHOTOVOLTAIC MODULE TESTING: DEVELOPING A SOUTH AFRICAN CIRCULAR ECONOMY FOR PV MODULES

JL Crozier McCleland[1], M Vumbugwa[2], MN Crozier[3], EE van Dyk[4], FJ Vorster[5]

[1] Nelson Mandela University; +27 415044874; E-mail: Jacqueline.CrozierMcCleland@mandela.ac.za

[2] Nelson Mandela University; E-mail: Monphias.Vumbugwa@mandela.ac.za

[3]University of the Western Cape, South Africa, Phone: E-mail:4322394@myuwc.ac.za

[4] Nelson Mandela University; E-mail: Ernest.vanDyk@mandela.ac.za

[5] Nelson Mandela University; E-mail: Frederik.vorster@mandela.ac.za

Abstract: As South Africa experiences a dramatic increase in the uptake of solar energy so will Photovoltaic (PV) waste eventually increase either due to end-of-life or due to early failures. In the waste hierarchy, reduction and reuse are preferred to recycling or disposal. The ability to reuse or repair a PV module prevents the need for a new module from being manufactured which ultimately contributes to waste. This paper discusses the testing processes necessary to determine if PV modules can be reused, repaired or recycled at end-of-life. There are currently no standards for the testing of second-hand modules and the modules in this study are evaluated against the IEC 61215 Certification Standard. The testing includes Visual Inspection to identify module defects, Electrical Insulation to confirm module safety, Electroluminescence to detect invisible cracks and Maximum Power measurements to determine the module performance. These are compared to expected values for a module of that age to determine the module's suitability for resale or reuse. Where reuse is not possible repairs or refurbishments of PV modules are suggested and the safety of these repairs is assessed. If reuse or repair is nor possible then the PV modules are recommended for recycling.

Keywords: Photovoltaic; Circular Economy; PV Module Testing

1. Introduction

The Solar Photovoltaic (PV) market has increased dramatically in the past decade. By 2050 global PV cumulative installed capacity is expected to be 4 500 GW [1]. The growth in this industry has stressed the need to deal with expected PV waste and ensure that the limited resources needed in PV module production are conserved. PV waste is expected to contribute a substantial portion (>10%) of e-waste streams with cumulative PV waste conservatively estimated at 60 million tons [1]. A circular economy designs out waste, circulates materials at their highest possible value and is regenerative by design [2]. A circular economy approach to PV modules encourages reuse and repair and treats recycling as the least desirable option, preferable only to disposal.

PV module waste is generated at all four life stages of a PV module, these being [1]:

1. Production
2. Transportation
3. Installation and Use
4. End-of-life disposal.

In addition to this, module failures occur throughout the lifetime of a PV module, according to the "bath tub" curve, figure 1, the probability of early failures decreases with time and the failure rate will stabilise over the useful life and then increase at end-of-life (EoL)[3].

With the improvements in PV module efficiency, it can be financially viable to repower a system, and replace the operational modules with new modules [4]–[6]. This could introduce second-life modules into the market after only 15 years of plant operation.

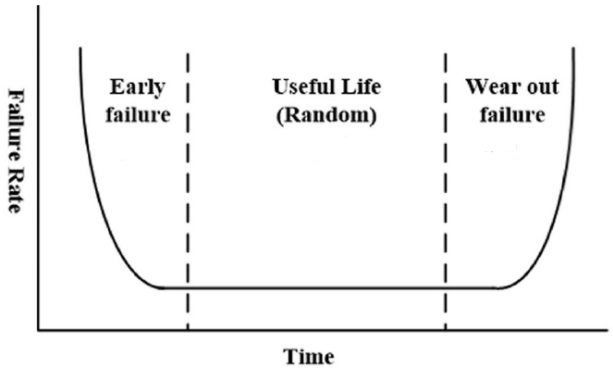

Figure 1: The Bathtub curve indicating the failure rate over the technical lifetime of the PV module[3]**.**

The issues of PV module waste and options for second-life modules are global and present in all countries with an established PV industry. Many countries expected to offset the cost of repowering by the sale of second-hand modules in developing countries in Africa and South Asia [1], [7], [8].

In line with international developments, the South African government acted by gazetting mandatory Extended Producer Responsibility legalisation for electronics [9]. This has created the necessity for any person or company who imports or manufactures PV modules to account for proper disposal and treatment of PV modules at end-of-life.

In South Africa, it is possible to recycle up to 96% of the mass of a PV module [10]. Internationally it has been proven that it is possible to separate the 99% of the PV module components allowing for the precious materials to be separated at high quality [11]. Although technically feasible to recycle PV modules, there remains limited demand for waste fractions from the most commonly sold PV modules in South Africa, thus recycling is constrained by financial and market feasibility.

Despite these advances in recycling, it is still preferable to reuse PV modules. Testing and sorting are important steps in diverting as much PV waste from disposal as possible and ensuring that modules are safe and reliable.

2. PV Market – South Africa

In South Africa, Independent Power Producer agreements have allowed private energy companies to develop utility-scale PV plants; with power generation of approximately 2 371 MW in 2022 [12]. The unstable national power grid which leads to rolling blackouts (loadshedding) has resulted in a dramatic increase in the uptake of PV, from the rooftop residential to the Commercial and Industrial market (C&I) market [13].

The predominant PV technology in utility-scale projects is crystalline silicon[14]. The trend of module production is towards larger modules with glass-glass (g//g) or bifacial structure [15]. The increasing size of modules can decrease the levelized cost of electricity (LCOE) by reducing the associated component costs, labour and handling but the disadvantage is that these modules are heavier and easier to damage during transport [16]. The increased size of the module means a failure in any component in a PV module results in the entire module failing and a larger volume of waste.

Thin-film technologies make up 12% of the installed operational utility scale REIPP projects and 555 MW is planned in bid windows 5 and 6 [14]. The size and degradation issues associated with thin-film modules mean they will contribute to the PV waste volumes. The specific technical challenges associated with testing thin-film modules are not addressed in this paper.

The reuse of PV modules could offset the costs of recycling broken and irreparable modules, making end-of-life management more cost-effective. Introducing new activities into the PV module value chain could spur new job creation and circular economy business development. A related conference paper by Crozier, Schenck, McCleland and van Dyk considers the social and economic opportunities that a reuse market for solar PV modules could offer South Africa [17].

3. Module Reliability and Degradation

The quality of a PV module is controlled by the manufacturer during the fabrication process, the modules are assessed against a certification standard which is designed to ensure a lifetime of 25 years [3].

In the real world, modules are exposed to stress factors (internal and external) that affect their performance and lifetime. These factors include the environmental conditions and internal factors such as the bill of materials (BOM) of the module [3]. These factors can result in module failures occurring before the predicted end of life.

In South Africa, due to the relatively young PV industry, there is limited research on early module failures from operational PV plants. Also due to the competitive industry, this information is not publicised. There have been published reports of large-scale backsheet failures of utility-scale PV plants which are less than 10 years old which indicates the potential for early-life module failures [18]. Recent studies indicate backsheet and polymer degradation is one of the cause of poor module performance in large-PV plants in South Africa [19], [20].

4. Sorting and Testing Process

The modules that the Sorting and Testing process applies to are End-of-life modules, modules with early failures, or module from repowered PV plants.

The testing process is outlined in figure 2, to ensure the safety and performance of the PV modules, and to be a guide to determine if PV modules are suitable for either reuse or recycling. Some modules will have the potential to be reused after repairs are completed. The feasibility of modules repairs is determined by the repair technology, the economic incentives, and skills available. Repaired modules or a representative sample will need to be retested before they can be reused and any repairs result in the process restarting at the first testing step as indicated in figure 2.

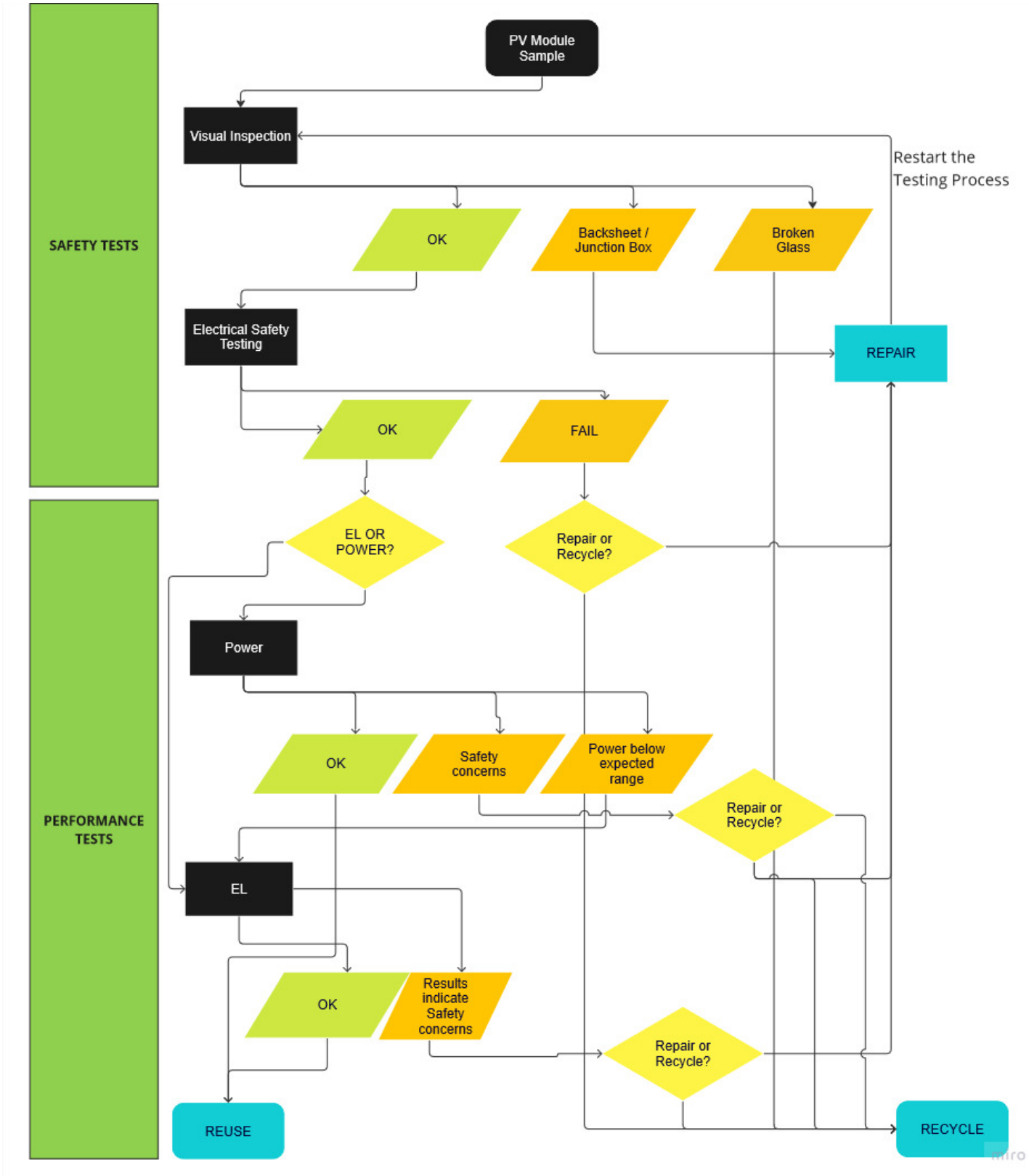

Figure 2: Basic outline of the PV testing process developed in this study. PV modules are guided through Safety (Visual Inspection, Insulation Resistance and Wet leakage) and Performance (Power and EL) testing with the outcome being either reuse or recycling.

4.1. Safety tests

4.1.1.Visual Inspection

Visual inspection is the first testing step required and is an important step in determining the reuse potential for PV modules. Broken glass is the most common module defect and is a result of poor module handling, transportation or severe weather conditions such as hail [3]. This failure is twice as likely with glass/glass (g/g) modules than with glass/backsheet modules [21]. There are limited repair options for broken glass, with procedures to fix the glass with applied resin only showing lab-scale testing feasibility [22]. Modules with broken glass are allocated for recycling.

The backsheet of the module can show visible signs of degradation including delamination, cracking, yellowing, and chalking [23]. Examples of backsheet damage are illustrated in figure 4. Burn marks are an immediate safety concern and should be flagged for further testing. Cracks or voids in the back surface can result in moisture ingress and a decrease in the insulation resistance of the PV module. In some situations, it is possible to repair a degraded back sheet by reapplying a back sheet film over the old film [24], [25]. This relatively simple repair might address the root cause of the backsheet damage, and it is not appropriate for burn marks nor will it undo the effect of moisture ingress through delamination.

Damage to the frame is normally due to mechanical stresses. If the frame is damaged with no damage to the glass, the module has the potential to be repaired.

Modules which have broken junction boxes or damaged external cables should be sorted for repair and further electrical safety testing. These failures include failed bypass diodes and are feasible to repair based on the module construction and the experience of field operators [6].

Figure 3: Examples of PV modules with broken glass

4.1.2.Electrical Insulation testing

The Insulation Resistance test and Wet Leakage tests are important safety tests and are designed to ensure that there is no current flowing between the cell circuitry and the frame [26]. Low insulation resistance has been linked to inverter shutdowns in the field, especially in the mornings when modules are wet with dew. This results in reduced production as these faults need to be clear before normal operation can resume [27]. These tests are conducted by applying a high voltage to determine the insulation resistance with the module either dry or in a shallow water bath. The challenges of this test is that it is time-consuming in both the setup time and the required test duration. It is however, very important to ensure the modules are safe for reuse.

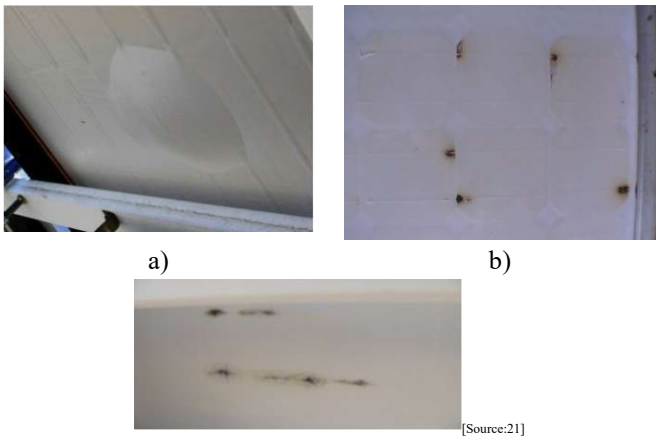

Figure 4: Image of module Back sheet defects including a)delamination, b)burn marks and d)cracks [23]**.**

4.2. Performance testing

It is a decision point in the testing process whether to do Maximum Power testing or Electroluminescence testing or both. Both tests give valuable information on the performance of the PV module. The module power gives an indication of the long-term reliability, so the Power test is prioritised if only limited testing is avaible.

4.2.1.Maximum Power Measurements

The Current-Voltage (I-V) characteristics of a PV module are measured using a Solar Simulator that meets the requirements of the IEC6064-9 Ed3. In this study, a full spectrum long pulse A+A+A+ LED flasher was used. The parameters measured include; Maximum Power (P_{MAX}); short-circuit current (I_{SC}); open-circuit voltage (V_{OC}), current at maximum power (I_{MPP}) and Voltage at maximum power (V_{MMP}). These parameters give an indication of the degradation and failures present in the modules and are needed for future PV installation design [28].

The Solar Simulator is an expensive piece of equipment and the more cost-effective alternative is an I-V curve tracer which can only be used outdoors under natural sunlight. The disadvantages are increased measurement uncertainty and less control of environmental conditions.

Figure 5 shows the I-V curves of two 540W PV modules.

Module 1 has an IV curve that does not indicate any defects or failures and the P_{MAX} measured is 542.7W, which is in the expected range for a new module. Module 2 has a step in the I-V curve which indicates cell damage within the module and the measured P_{MAX} is only 470.9W.

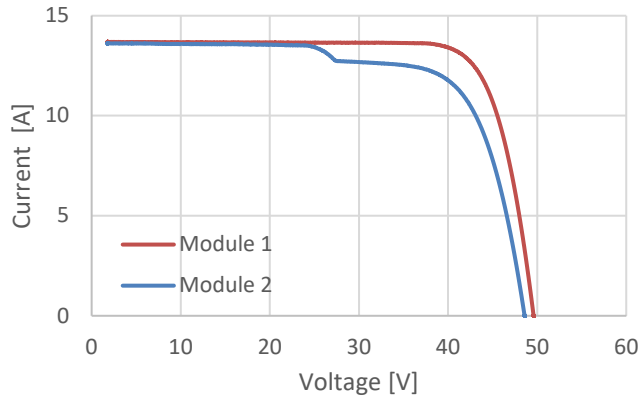

Figure 5: IV curves of two 540W PV modules. Module 1, modules has an expected I-V curve shape and Module 2 has a step indicating the module has damaged cells.

Using a digital multimeter (DMM) to measure the module's I_{SC} and V_{OC} is possible and this is often offered as a solution to measuring PV module performance at a hobbyist/consumer level as the equipment is inexpensive. It can be used to confirm that module is functional, however, as can be seen in figure 5, just measuring the current and voltage would not give you the full picture of the power loss. The decreased V_{OC} gives an indication that cells are not operational in the module, however, the resolution of the DMM might not detect the relatively small decrease.

4.2.2.Electroluminescence

Electroluminescence (EL) imaging of photovoltaic modules is an imaging technique that can identify cracks, disconnected busbars, shunting and other cell defects [29]. The process can be done at two bias levels; 1) with injected current at 110% Isc, used for detecting cracks and defects, and 2) 10 % Isc for detecting Potential induced degradation (PID) shunting, Light and elevated temperature-induced degradation (LETID) effects. EL imaging can be done on-site, either with modules on the racks at night or for module removed from rack in a dark- room.

Figure 6 shows examples of EL images for the two 540W modules that were introduced in figure 5. In Module 1, figure 6 a), there is a single cell cracked, which due to the cell multi-busbar configuration has minimal effect on the power output. In comparison module 2, figure 6 b), has an entire row of cells damaged, as confirmed by the I-V curve results.

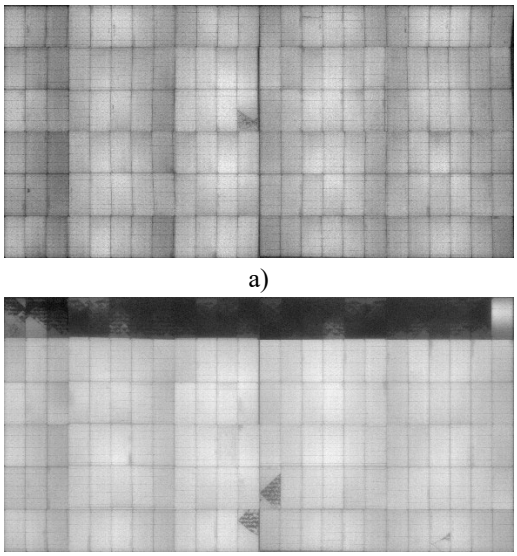

a)

b)

Figure 6: EL images of a) Module 1, with one cracked cell visible and b) Module 2 with several cracked cells visible.

4.3. Process

4.3.1.Thresholds of Acceptance

The levels that are determined to be acceptable can be set based on the requirements of the end use and hopefully would be based on some minimum standards/regulations set for PV module reuse. In the absence of these, initial simplified acceptance criteria are detailed in Table 1.

Table 1. Test acceptance levels for the Sorting/ Testing Criteria

TEST	– OK –
Visual Inspection	Mechanically sound with no visible safety concerns.
Electrical Insulation Testing	Meet the minimum requirements of IEC61215 [26].
Power	Above expected power output based on the manufacturer-given degradation rate and age of the module.
Electroluminescence (EL)	No cell cracks that would prevent the module from operating normally or result in localised heating.

The Power acceptance should also account for the fact that even if the module is below the expected manufacturer warranty it could still operate at a lower power for years to come. It is

important to give some form of expected lifetime for a module. Modules that do not meet the stricter lifetime requirement could be given a much short lifetime, two years for example to ensure appropriate costing for the PV system.

These thresholds are suggested and will be refined based on further research.

4.3.2. Repairs

The option for repairs has been included in the process as it is a vital step to ensure that modules are diverted from recycling. The cost-effectiveness of repairs remains to be seen and further investigation is required.

5. Conclusions

PV module testing has been identified as an important step in the safe reuse of PV modules and diverting them from disposal on landfill. The challenges in this process include the lack of testing standards and the costs involved in testing. These costs would make testing for PV module second life out of reach of normal rooftop solar customers, unless either an incentive, subsidy or penalties for incorrect disposal are applied. There are also opportunities to reduce the complexity of testing to make testing more accessible and financially feasible. The ideal testing process is outlined in figure 2, based on the test process described in the IEC 61215 standard. However, in terms of PV reuse and recycling the costs of completing all the tests described on every module would be prohibitive. Solutions to this include streamlining of test processes, using the most cost-effective equipment, reducing the time needed for testing and testing samples that can be extrapolated to the batch.

Encouraging a reuse market in South Africa not only requires thorough quality control mechanisms such as testing, but policy frameworks, government and industry support and a financially viable business model.

Acknowledgements

The authors would like to acknowledge the support of the South African Technology Innovation Agency (TIA) in supporting the research on this topic. The authors wish to acknowledge PVinsight (pty) LTD for providing lab access, and use of their solar simulator to this project.

References

[1] IRENA and IEA-PVPS, "End of Life Management: Solar Photovoltaic Panels," International Renewable Energy Agency and International Energy Agency Photovoltaic Power Systems., Technical Report NREL/TP-6A20-73852, 1561525, 2016. doi: 10.2172/1561525.

[2] Ellen MacArthur Foundation, "What is a circular economy?," *What is a circular economy?*, 2022. https://ellenmacarthurfoundation.org/topics/circular-economy-introduction/overview (accessed Jul. 21, 2022).

[3] M. Aghaei *et al.*, "Review of degradation and failure phenomena in photovoltaic modules," *Renewable and Sustainable Energy Reviews*, vol. 159, p. 112160, May 2022, doi: 10.1016/j.rser.2022.112160.

[4] S. Herceg, M. Fischer, K.-A. Weiß, and L. Schebek, "Life cycle assessment of PV module repowering," *Energy Strategy Reviews*, vol. 43, p. 100928, Sep. 2022, doi: 10.1016/j.esr.2022.100928.

[5] J. A. Tsanakas *et al.*, "Towards a circular supply chain for PV modules: Review of today's challenges in PV recycling, refurbishment and re-certification," *Prog Photovolt Res Appl*, vol. 28, no. 6, pp. 454–464, Jun. 2020, doi: 10.1002/pip.3193.

[6] A. Heide, L. Tous, K. Wambach, J. Poortmans, J. Clyncke, and E. Voroshazi, "Towards a successful re-use of decommissioned photovoltaic modules," *Progress in photovoltaics*, vol. 30, no. 8, pp. 910–920, 2022.

[7] DCCEEW, "Wired for Change: Regulation for small electrical products and solar photovoltaic systems waste Department of Climate ChangeWired for Change: Regulation for small electrical products and solar photovoltaic systems waste Department of Climate Change," Department of Climate Change, Energy, the Environment and Water, Canberra, Austrailia, CC BY 4.0., Jun. 2023.

[8] CPVA, "Reclaimed PV Panels Market Assessment Industry Report," Apr. 2023.

[9] Department of Environment, Forestry and Fisheries (DEFF), "National Waste Management Strategy 2020," Department of Environment, Forestry and Fisheries (DEFF), 2020. Accessed: Oct. 20, 2022. [Online]. Available: https://www.dffe.gov.za/sites/default/files/docs/2020nationalwaste_managementstrategy1.pdf

[10] D. M. Williams-Wynn, "Solar panel recycling : not a dark art after all," *Resource*, May 2020.

[11] N. Martin, "New environmentally friendly solar panel recycling process helps recover valuable silver," *UNSW Newsroom*, Jul. 20, 2023. [Online]. Available: https://newsroom.unsw.edu.au/news/science-tech/new-environmentally-friendly-solar-panel-recycling-process-helps-recover-valuable

[12] E. Bellini, "South Africa installed 1.3 GW of PV last year," *PV Magazine International*, Jul. 21, 2021. Accessed: Nov. 14, 2022. [Online]. Available: https://www.pv-magazine.com/2021/07/21/south-africa-installed-1-3-gw-of-pv-last-year/

[13] GreenCape, "2023 Energy Services Market Intelligence Report," GreenCape, Cape Town, South Africa, 2023. Accessed: Jun. 23, 2023. [Online]. Available: https://green-cape.co.za/wp-content/uploads/2023/04/ES_MIR_2023_DIGITAL_SINGLES.pdf

[14] "IPP Project Database." [Online]. Available: https://www.ipp-projects.co.za/ProjectDatabase

[15] A. Metz, M. Fischer, and J. Trube, "International Technology Roadmap for Photovoltaics (ITRPV) 8th edition:," 2016.

[16] W. Gu, T. Ma, S. Ahmed, Y. Zhang, and J. Peng, "A comprehensive review and outlook of bifacial photovoltaic (bPV) technology," *Energy Conversion and Management*, vol. 223, p. 113283, Nov. 2020, doi: 10.1016/j.enconman.2020.113283.

[17] M. Crozier, C. Schenck, J. Crozier McCleland, and E. van Dyk, "The Social and Economic Potential of Closing the Loop on Photovoltaic (PV) Module Waste," presented at the Southern African Sustainable Energy Conference, Nelson Mandela Bay, Nov. 2023.

[18] “Reports of backsheet failures at 75 MW Mulilo Sonnedix Prieska solar farm in South Africa,” *PV Magazine International*, Feb. 11, 2020. [Online]. Available: https://www.pv-magazine.com/2020/02/11/reports-of-backsheet-failures-at-75-mw-mulilo-sonnedix-prieska-solar-farm-in-south-africa/

[19] “Polymer Degradation in Different Climate Zones - Impact on Performance and Operation in South Africa and Germany,” presented at the the EU PVSEC 2023, the 40th European Photovoltaic Solar Energy Conference and Exhibition., Lisbon, Portugal.

[20] “Investigating the Phenomenon of Backsheet Chalking in a Multi-MW Plant in South Africa,” presented at the 40th European Photovoltaic Solar Energy Conference and Exhibition, Lisbon, Portugal, Sep. 2023.

[21] “2023 PV Module Reliability Scorecard,” PVEL. Accessed: Aug. 16, 2023. [Online]. Available: https://scorecard.pvel.com/download-the-scorecard/

[22] M. P. M. Tas and W. G. J. H. M. Van Sark, “Experimental repair technique for glass defects of glass-glass photovoltaic modules – A techno-economic analysis,” *Solar Energy Materials and Solar Cells*, vol. 257, p. 112397, Aug. 2023, doi: 10.1016/j.solmat.2023.112397.

[23] M. Köntges, S. Kurtz, C. Packard, U. Jahn, K. A. Berger, and K. Kato, *Performance and reliability of photovoltaic systems: subtask 3.2: Review of failures of photovoltaic modules: IEA PVPS task 13: external final report IEA-PVPS*. Sankt Ursen: International Energy Agency, Photovoltaic Power Systems Programme, 2014.

[24] Y. Voronko *et al.*, “Repair options for PV modules with cracked backsheets,” *Energy Sci Eng*, vol. 9, no. 9, pp. 1583–1595, Sep. 2021, doi: 10.1002/ese3.936.

[25] Rolf Frischknecht, Keiichi Komoto, and Taisuke Doi, “Life Cycle Assessment of Crystalline Silicon Photovoltaic Module Delamination with Hot Knife Technology,” IEA-PVPS T12-25:2023.

[26] “Terrestrial photovoltaic (PV) modules: design qualification and type approval. Part 2, Test procedures.” 2021.

[27] G. Wang, Y. Jiang, Y. Wei, H. Gong, and J. Zhu, “STUDY ON INSULATION RESISTANCE TEST OF PV MODULE FOR THE 28TH EU PVSEC 2013”.

[28] F. J. Vorster and E. E. Van Dyk, “Current-voltage characteristics of high-concentration, photovoltaic arrays,” *Prog. Photovolt: Res. Appl.*, vol. 13, no. 1, pp. 55–66, Jan. 2005, doi: 10.1002/pip.563.

[29] U. Jahn, M. Herz, M. Köntges, D. Parlevliet, M. Paggi, and I. Tsanakas, *Review on infrared and electroluminescence imaging for PV field applications: International Energy Agency Photovoltaic Power Systems Programme: IEA PVPS Task 13, Subtask 3.3: report IEA-PVPS T13-12:2018*. Paris: International Energy Agency, 2018.

EFFECTS OF CELL SHADING LEVEL ON THERMAL AND ELECTRICAL CHARACTERISTICS OF A POLY-CRYSTALLINE PV MODULE UNDER DIFFERENT OPERATIONAL I-V POINTS

Monphias Vumbugwa[1], Jacqueline Crozier McCleland[2], Frederik Vorster[3] and Ernest van Dyk[4]

[1] Nelson Mandela University, Physics Department, P.O.Box 77000, Summerstrand 6031, Port Elizabeth, South Africa; Phone: +2741-504-4989; Fax: +2741-504-2574; Monphias.Vumbugwa@mandela.ac.za,

[2] Nelson Mandela University; Jacqueline.CrozierMcCleland@mandela.ac.za, [3] Nelson Mandela University; Frederik.vorster@mandela.ac.za,

[4] Nelson Mandela University; Ernest.vanDyk@mandela.ac.za

Abstract

Photovoltaic (PV) modules deployed in the field experience changes in load conditions, soiling and shading levels. These dynamic operating conditions affect the interpretation of thermal imaging and electrical characterisation measurements. This study investigates the dynamics of the operational current and voltage (I-V) and thermal characteristics of a poly-crystalline PV module and individual cells to understand the behaviour of the cells at different cell shading levels and module operational voltages. When the module operates at maximum power voltage (V_{MP}), the voltage of a shaded cell becomes negative (reverse bias) at a shading level of 8% and the temperature of the whole cell is elevated. The operational temperature of a shaded cell increases when the shaded cell area is between 8 to 40% reaching a peak temperature when the shaded cell area is between 40 and 50%. The cell's temperature decreases for shading levels 50 to 100% when the bypass diode of the substring containing the shaded cell appears to be activated. When the operational voltage of the module is $<V_{MP}$, a small shading level of 4% causes reverse biasing of the shaded cell, while at operational voltages $>V_{MP}$, the cell becomes reverse biased by shading levels ≥50%. A cell can easily be mismatched, operate in reverse bias, and cause abnormal thermal signature when the module's operational voltage is $<V_{MP}$ unlike when operational voltage is $>V_{MP}$. Therefore, when a PV module is shaded, it is beneficial for the operational point to be $>V_{MP}$, since the mismatched cells will not become abnormally hot to cause detrimental effects such as module back sheet damage, cracks, risk of fire and increased module degradation rate. This work gives valuable information which can advance the interpretation of thermal images and I-V curves of PV modules.

Keywords: poly-crystalline cells; cell mismatch; current-voltage characteristics; thermal signature

1. Introduction

The series connected poly-crystalline silicon cells of a conventional PV module require all the cells to be electrically equally matched to generate the expected maximum power. However, when operating in the field, the performance and efficiency of the cells and modules can be influenced by environmental factors such as temperature, soiling and shading. These environmental factors shift the operational maximum power point (MPP) of individual cells, modules and strings and can result in current and voltage mismatch [1][2][3]. Since the MPP always shifts, the inverters in PV systems will ensure the supply of optimum power to the load by constantly tracking the MPP of PV module strings [4][5][6]. One of the main consequences of mismatch is the inability of cells to produce the same current with the result that underperforming cells are forced to operate at lower voltages, or even negative (reverse bias) voltages, resulting in performance degradation of the PV module [7][8][9]. This study investigates the effects of changing cell shading levels and module's operational point on the thermal and electrical characteristics of a poly-crystalline PV module.

PV modules installed in the field can experience shading due to soiling, bird droppings, trees, poles, buildings and nearby structures. Shading due to soiling is dynamic in nature and is unavoidable since PV modules are installed outdoors at an inclination for optimum capture of solar radiation and conversion efficiency. The inclination angle can result in the wind-blown dust settling on and shading the cells. Shading can cause reverse biasing and heating up in affected cells when the shaded cells dissipate electrical energy generated by good cells. This results in a current mismatch between the cells and substrings [10][11][12], and causes non-uniform temperature distribution in the modules enabling the bad cells to be located as hot cells on Thermal Infrared (TIR) images [13][14]. The effects of abnormally hot cells is lessened by using the bypass diodes incorporated in the PV modules. The bypass diodes minimise the abnormal heating effect on bad cells by providing a current path around the affected substring [15]. However, if the bypass diode continuously conducts the current produced by the string and no corrective action is taken then it will eventually get damaged and the scenario can result in fire when the cells overheat [16].

Regular inspection of PV modules is crucial for the early detection of anomalies in solar cells which can develop and impact on the performance of the modules, return on investment and cause safety issues. Unmanned Aerial Vehicle (UAV) based TIR imaging is an inspection technique widely applied in large PV plants since it is cost-effective and is conducted in-situ, while the plant is operating at irradiance levels above 600W.m^{-2}. TIR imaging is carried out under clear sky and low wind conditions with the angle of capture almost perpendicular to the plane of the modules to avoid reflections [14][17][18][19]. One of the outcomes of the interpretations of TIR images is an attempt to quantify the energy loss in PV plants associated with the abnormal thermal signatures identified in TIR images. No standard procedure has yet outlined the quantification of energy loss related to TIR images of underperforming modules since the interpretation of TIR images remains a challenge. The effective judgement and interpretation of thermal signatures in PV modules remain a challenge since many factors such as operational conditions, the emissivity of a target object, thermal reflections, capturing angle, etc., can influence TIR images [20][21]. Being able to detect, identify and quantify the severity of cell anomalies, cost-effectively, on operational PV modules is essential for a reliable, efficient and safe system. Therefore, detailed information regarding the behaviour of individual poly-crystalline silicon PV cells under different shading levels can be obtained when TIR images of the modules are captured under different modules' operational voltages with a concurrent recording of the electrical characteristics of individual cells.

2. Experimental procedure

Figure 1 shows the experimental setup for measuring the operational electrical characteristics of a poly-crystalline silicon PV module and individual cells in the module. The module consists of series connected cells that are arranged in three substrings SS1, SS2 and SS3 with a bypass diode across each substring.

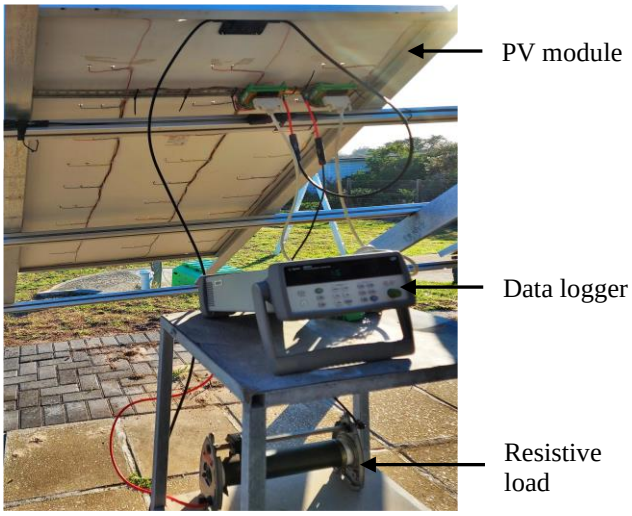

Fig.1: The poly-crystalline silicon PV module set up for TIR imaging and voltage measurements of individual cells.

Individual cell contacts were made to the module to measure each cell's voltage and thus monitor cell mismatch. EL imaging was performed with a MBJ mobile-Lab 3.0 unit to check for any EL features and if any cracks were introduced when contacts were made.

The measurements were recorded when cell-shading levels of 4 to 100% were applied on one cell while the module was receiving irradiance of 700 - 1000W.m^{2}. Different sizes of the opaque shading material were accurately cut and placed, one at a time, on the front side of the cell, to shade a definite area, 4-100%, of the cell while recording the measurements. Figure 2 shows a visual image of the module with a shading of 60% on cell 51 in substring (SS) 3.

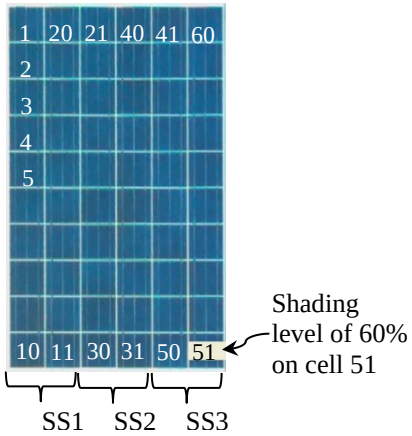

Fig.2: Visual image of the poly-crystalline module showing cell numbering in substrings SS1, SS2 and SS3, and partial shading on cell 51.

TIR images of the module were recorded concurrently with the cell voltage measurements while the module was operating at different voltages: 13.0V, 28.0V, 30.0V and 33.0V. The

operational voltages were achieved by varying an external resistive load.

The electrical measurements were recorded using a data logger (Agilent 34972A) at 5-second (s) intervals with an uncertainty of approximately 1 µV [22]. TIR images of the module were captured, as recommended by Jahn et al. [14], after adjusting the resistive load, thus changing the module's operational voltage. The TIR camera (FLIR T620) was positioned at 4 meters above the module's front surface with the angle of capture almost perpendicular to the module's front surface to keep away from reflections [14][18].

3. Results

Figure 3 shows the EL images of the module recorded at (a) high current (110% I_{SC} - High EL image) and (b) low current (10% I_{SC} – Low EL image) to identify pre-existing cell anomalies that can cause inherent mismatch. There are minor cracks on cells 1, 20, 47 and 52 which run diagonally across the cell and were observed before and after making cell contacts. Cells 1, 20, 47 and 52 are enlarged in Figure 3(c), (d), (e) and (f), respectively, so that the cracks in the cells can be noticeable. All fingers of the cracked cells appear to be connected to the busbars and there are no dark or isolated cell parts, thus the cracks did not impact the performance of the module. There are no dark cells on the Low EL image, hence no shunt paths or PID are present on the cells.

Figure 4 shows the voltage measurements as well as thermal characteristics of the individual cells that were recorded simultaneously when the module's operational voltage was 28.0 V (V_{MP}) and while shading cell 51 between 4 to 100%. The figure shows the correlation between the operational voltage of the shaded cell and its thermal characteristics. The graphs show the operational voltages of the 60 cells in the module while cell 51 was shaded. When cell 51 is shaded at 4%, its operational voltage is reduced to 0.31V from 0.53V, signifying a mismatch due to the partial shading. The operational temperature of the whole-cell 51 is not influenced by the small 4% shading, but a hot strip is seen on cell 51 on the TIR image (a) due to the difference in emissivity of the module glass (0.92) and the opaque shading material (paper: cardboard 0.81) [23]. The shading material radiates higher thermal energy than the module glass and hence appears hotter on the TIR image (a).

When the shading area is increased from 8 to 100% on cell 51, it significantly affects the operational voltages of individual cells. At an 8% shading level, the voltage of cell 51 becomes negative (reverse bias) and the cell starts dissipating some of the module's generated electrical energy. When the cell becomes reverse-biased, the temperature of the whole-cell 51 increases. The temperature increases up to a shading level of 40%. As the shading level increases to 40%, the voltage of the shaded cell 51 becomes more reverse biased. The temperature of the cell was measured on the unshaded part of the cell on the TIR image.

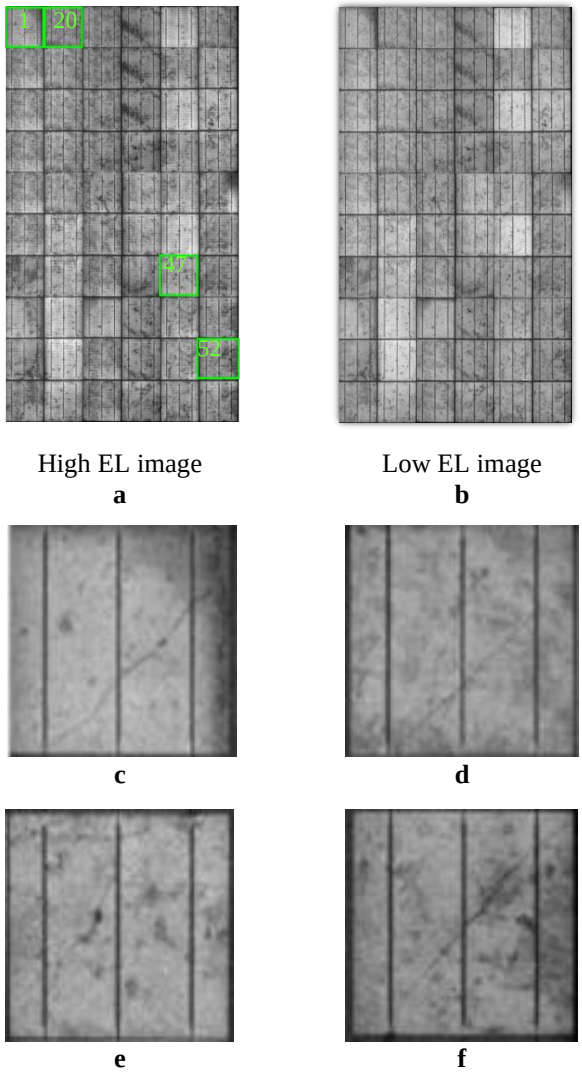

Fig.3: EL images of the polycrystalline PV module taken at (a) 110% and (b) 10% of the I_{SC}. Cells 1, 20, 47 and 52 are enlarged in (c), (d), (e) and (f) respectively.

Smaller changes in voltage of cell 51 occur from a shading level of 50% to 100%. The operational temperature of the shaded cell increased with the shaded area between 8 to 40% reaching a peak between 40 and 50%. The cell's temperature decreased for increased shading levels of 50 to 100% when the bypass diode of the substring containing cell 51 appears to be activated. The bypass diode diverts the module current around the shaded substring, SS3, as evidenced by an increase in the junction box temperature containing the bypass diodes and a small increase in the temperature of the whole substring SS3. The substring SS3 is now at an elevated temperature compared to the other two substrings SS1, and SS2 because much of the solar radiation incident on substring SS3 heats the cells instead of generating electrical energy. TIR images in Figure 4(e), (f) and (g) show that the substring SS3 is at an elevated temperature compared to substrings SS1 and SS2. The main focus of this study is to analyse the behaviour of cell 51 under different shading levels and changing the module's operational voltage. The behaviour (current and voltage characteristics) of the unshaded cells is

discussed by Vumbugwa et. al. 2020 [3] when similar results were obtained after shading a cell.

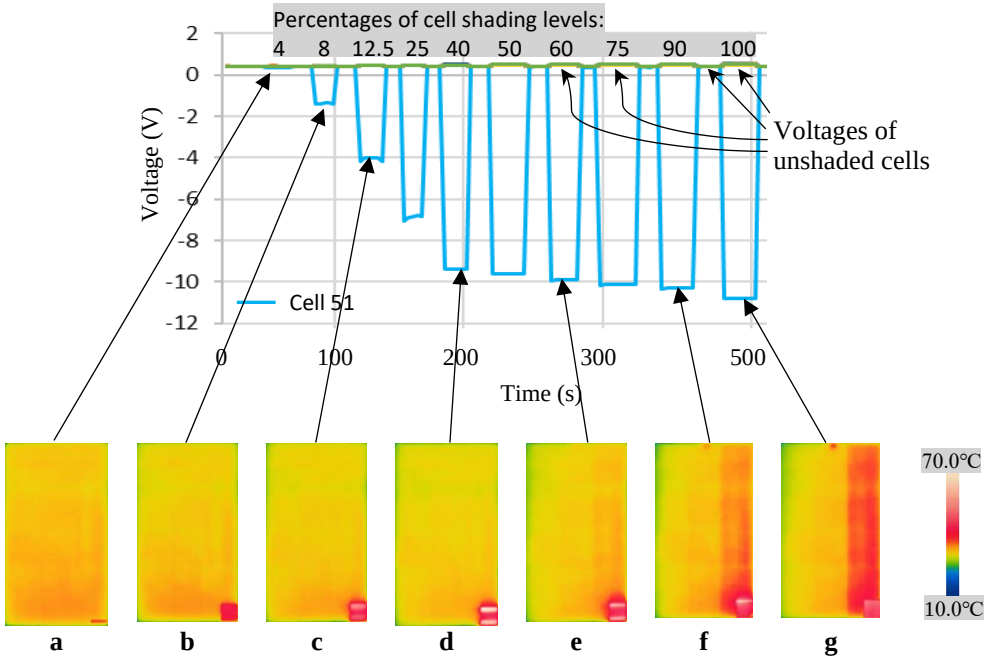

Fig.4: Cell voltage measurements together with TIR images taken when the module was at maximum power point and cell 51 was under different shading levels.

Figure 5 shows the effects of the shading levels, 4-100%, on cell 51's voltage when the module's operational voltage is (a) 13.0V, (b) 28.0V, (c) 30.0V and (d) 33.0V. When the module's operational voltage is 13.0 V, Figure 5(a), the voltage of cell 51 becomes negative for all the shading levels 4-100%. Thus, cell 51 operates in reverse bias when the shading levels of 4-100% are applied to the cell. The trends of cell 51's voltage in Figures 5(a) and (b) are similar, however, the cell operates at different negative voltages for the shading levels of 4-25%. An example showing the difference is when the cell is 8% shaded, and is highlighted with a dotted red rectangle in Figure 5(a) and (b). When the module's operational voltage is 13.0V, Figure 5(a), the reverse bias voltage caused by the 8% shading level on cell 51 is -7.6V, while the same shading level resulted in the cell operating at -1.37V for a module operating voltage of 28.0V. Thus, the impact on reverse biasing due to partial shading is influenced when the module's operational voltage is shifted. When the module's operational point is $<V_{MP}$ and closer to I_{SC}, the impact of shading on the electrical characteristics of the cell becomes severe.

The operating voltages of cell 51 when the shading levels of 4-100% were applied, at different module's operational voltages, are shown in Table 1. At each module's operational voltage, the minimum shading level which causes cell 51 to operate in reverse bias is different. When the operational voltage is 13V, the minimum shading level of 4% will cause the shaded cell 51 to operate at -5.10V, while when the module's operational voltage is close to V_{OC}, e.g. at 30V and 33V, the minimum shading levels to reverse bias the cell are 50% and 75%, respectively. Thus, when the module's operational voltage is $<V_{MP}$, a small shading level of 4% causes cell 51 to operate in reverse bias, but the same shading level cannot reverse bias the cell when the module's operational voltage is $>V_{MP}$. The highlighted, red-dotted rectangle in Figures 5(c) and (d) shows the impact of a shading level of 90% on the voltage of cell 51 when the module's operational voltage is 30V and 33V. When the shading level is 90%, cell 51 is reverse biased to -10.3V and -8.47V at the module's operational voltage of 30.0V and 33.0V, respectively. Thus, the shading cause less impact on the performance of the cell when the module's operational voltage is closer to V_{OC}.

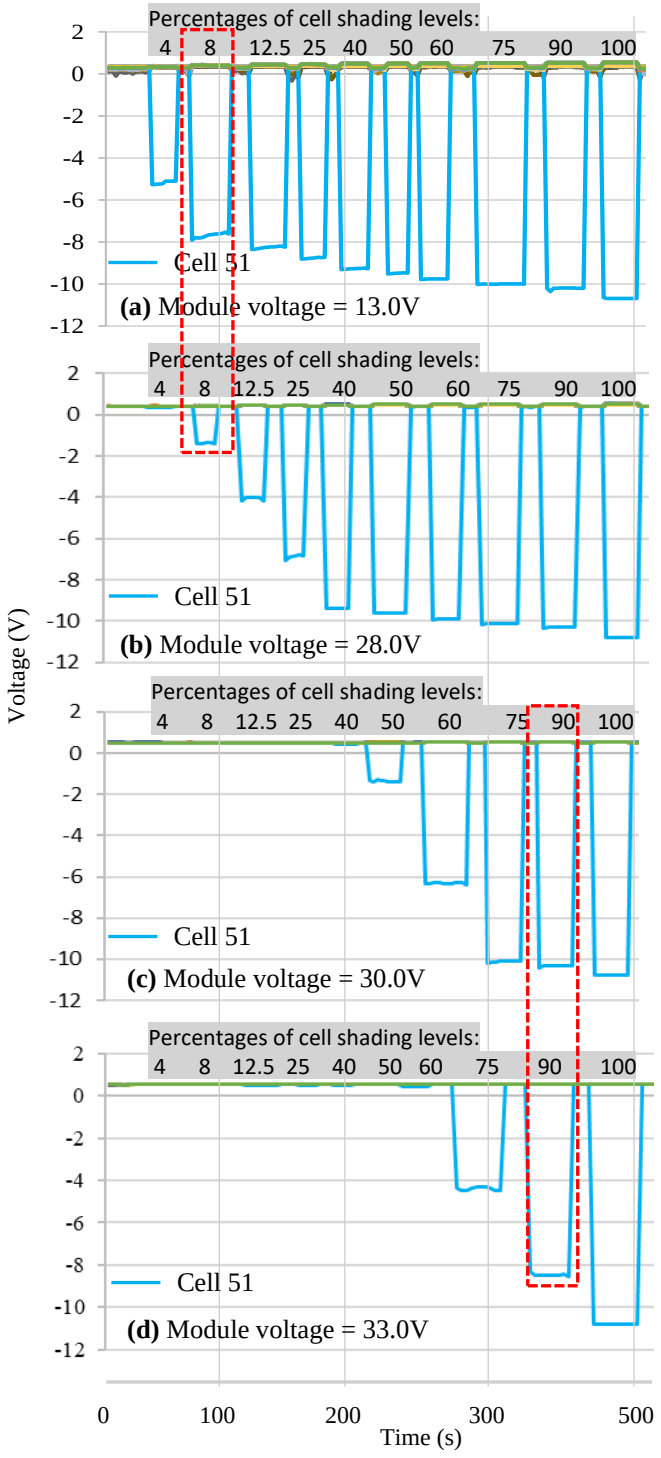

Fig.5: Cell voltage measurements taken when cell 51 was under different shading levels, 4-100%, at module's operational voltage of (a) 13.0V, (b) 28.0V, (c) 30.0V and (d) 33.0V.

Figure 6 shows the graphical representation of the results in Figure 5 and Table 1. The figure shows that when the module's operational voltage is 13.0V, blue graph, all shading levels cause cell 51 to operate with negative voltages, as previously discussed. The green graph shows the voltage of cell 51 when the module is operating at 28V. For this graph, cell 51 is forward biased (positive voltage) for a shading level of 4%, the other shading levels, 8-100%, resulting in cell 51 being reverse biased (negative voltages). For the module's operational voltages of 30V and 33.0V (black and red graphs), cell 51 is reverse biased when it is under shading levels of 50-100% and 70-100%, respectively. Therefore, the impact of shading on the voltage of cell 51 is less when the module's voltage is closer to V_{OC}.

A current mismatch between good and bad cells in a module can easily occur when the module's operational point shifts from MPP towards I_{SC}, along the module's I-V curve, and is unlikely to occur when the module's operational point shifts towards V_{OC}. At operational points <MPP, the modules deliver a large current and a significant current mismatch and energy dissipation can occur [24], such that the small shading level of 4% can easily cause the whole cell to become abnormally hot and be seen on TIR images. The same small shading level on a cell cannot cause energy dissipation when the module operates at closer to V_{OC} due to minimal current mismatch.

It is shown in Figure 4 and also explained by Vumbugwa et. al. 2020 [3], that when a cell operates with a negative voltage, the whole cell appears abnormally hot on TIR images and its temperature increases with an increase in reverse bias voltage to a point when the bypass diode on the substring containing the shaded cell is active. In the study, by Vumbugwa et. al. 2020 [3], the effect of cell shading levels on the voltages of the unshaded cells is illustrated and explained. When a PV module is partially shaded, or underperforms, it is beneficial for the operational point to shift towards V_{OC}, since the bad cells will not become abnormally hot to cause detrimental effects such as module back sheet damage, cracks, risk of fire and increased module degradation rate. The bad cells in a mismatched module, operating in a string, will easily get reverse biased and appear abnormally hot on TIR images when the module's operational point is less than its MPP. However, when the module's operational point is >MPP, the bad cells will not appear abnormally hot on TIR images as the cells may not be operating with negative voltages. When the operational point of a mismatched module shifts towards V_{OC}, along its I-V curve, the bad cells will not be reverse-biased and appear as good cells on TIR images. This scenario can mislead decision-making during TIR inspections of PV modules in PV plants.
modules.

Table 1: Cell 51 voltage measurements

Module's operational voltage (V)	Cell shading level (%)									
	4	**8**	**12.5**	**25**	**40**	**50**	**60**	**75**	**90**	**100**
13.0	-5.10	-7.66	-8.23	-8.76	-9.25	-9.48	-9.76	-9.99	-10.2	-10.6
28.0	+0.51	-1.37	-4.01	-6.81	-9.36	-9.60	-9.90	-10.1	-10.3	-10.7
30.0	+0.53	+0.53	+0.53	+0.53	+0.53	-1.41	-6.33	-10.1	-10.3	-10.8
33.0	+0.53	+0.53	+0.53	+0.53	+0.53	+0.53	+0.50	-4.34	-8.47	-10.8

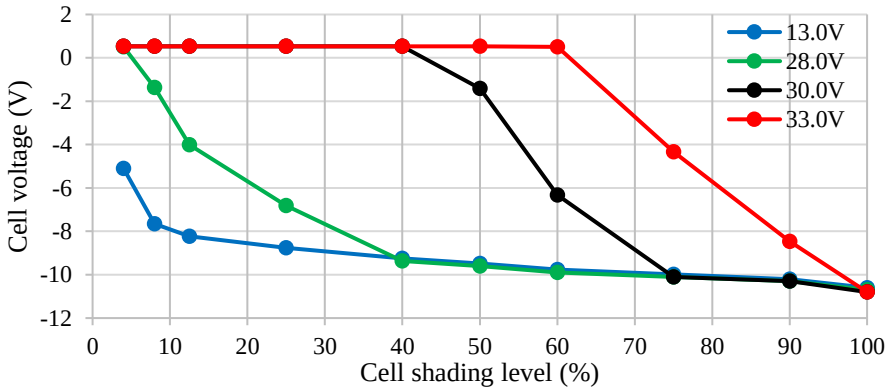

Fig.6: Graphical representation showing forward and reverse bias voltages on cell 51 at different module's voltage and when the cell was under shading levels of 4-100%.

4. Conclusions

In this study cell shading levels of 4-100% were applied on one cell of a poly-crystalline PV module when the module was at different operational voltages: 13V, 28V, 30V and 33V. At 13V, a small shading level of 4% could reverse bias cell 51, but for higher operational voltages of 28V, 30V and 33V, the cell could only operate under reverse bias conditions when bigger shading levels were applied. The shift in the module's operational voltage causes the change in the current and voltage operational point of mismatched cells and influences current mismatch and dynamics of abnormal thermal signatures. A current mismatch is influenced when the module's operational point shifts from MPP. The bad cells can easily emerge on TIR images when the operational voltage shifts towards I_{SC} unlike when the operational voltage shift towards V_{OC}, along the I-V curve. Thus, the level of current mismatch will determine when a bad cell emerges as a hot cell on TIR images since the shading level which causes the shaded cell to change from positive (generating power) to negative voltage (dissipating power) depends on the module's operational point. If the operational point of the module shifts towards V_{OC}, bad cells can be missed on TIR images, due to minimal current mismatch, and can mislead decisions when TIR inspections are carried out in the field. The detailed information in this paper can add value to the operations and maintenance of PV modules when TIR imaging inspections are conducted for long-term reliability and hence an improved return on investment of the PV plants.

Acknowledgements

The authors gratefully acknowledge the South African Department of Science and Innovation, Nelson Mandela University and PVinsight (Pty) Ltd for the necessary facilities and financial support for the research.

References

[1] A. K. Devarakonda, N. Karuppiah, T. Selvaraj, P. K. Balachandran, R. Shanmugasundaram and T. A. Senjyu, "Comparative Analysis of Maximum Power Point Techniques for Solar Photovoltaic Systems," *Energies*, 15, 8776, 2022. https://doi.org/10.3390/en15228776.

[2] K. Hasan, S. B. Yousuf, M. S. H. K. Tushar, B. K. Das, P. Das, Md. S. Islam, 2021. Effects of different environmental and operational factors on the PV performance: A comprehensive review. Wiley Online Library, https://doi.org/10.1002/ese3.1043.

[3] M. Vumbugwa, F. J. Vorster, J. L. Crozier McCleland and E. E. van Dyk, "Effects of changing partial cell shading on the electrical and thermal characteristics of crystalline silicon photovoltaic module," *Sol. Energy* vol. 240, pp. 147-156, 2020, https://doi.org/10.1016/j.solener.2022.05.031.

[4] S. Saravanan and N. B. Ramesh, "Maximum power point tracking algorithms for photovoltaic system – A review," *Ren. and Sust. Ener. Rev.*, vol. 57, pp. 192–204, 2016, doi: 10.1016/j.rser.2015.12.105.

[5] S. Sengar, “Maximum Power Point Tracking Algorithms for Photovoltaic System : A Review,” *Res. India Publ.*, vol. 4, no. 2, pp. 147–154, 2014.

[6] Z. Zandi and A. H. Mazinan, “Maximum power point tracking of the solar power plants in shadow mode through artificial neural network,” *Complex Intell. Syst.*, vol. 5, no. 3, pp. 315–330, 2019, doi: 10.1007/s40747-019-0096-1

[7] S. Bowden and C. Honsberg, “PVCDROM | PVEducation.” [Online]. Available: http://pveducation.org/pvcdrom, (accessed 23 August 2021).

[8] M. Köntges, S. Kurtz, C.E. Packard, U. Jahn, K. Berger, K. Kato, T. Friesen, H. Liu and M. Van Iseghem, (2014). Review of failures of photovoltaic modules, IEA-Photovoltaic Power Systems Programme, IEA-PVPS, 2014. https://iea pvps.org/wp content/uploads/2020/01/IEAPVPS_T13 01_2014_Review_of_Failures_of_Photovoltaic _Modules_Final.pdf.

[9] A. Al Mansur, M. Ruhul Amin, and K. K. Islam, “Performance comparison of mismatch power loss minimization techniques in series-parallel PV array configurations,” *Ener.*, vol. 12, no. 5, 2019, doi: 10.3390/en12050874.

[10] M. Vumbugwa, J. L. C. McCleland, E. E. van Dyk, F. J. Vorster, and T. J. Serameng, “Effects of current mismatch due to uneven soiling on the performance of multi-crystalline silicon module strings,” *Journal of Energy in Southern Africa*, vol. 31, no. 1, pp. 62–72, 2020, doi: 10.17159/2413-3051/2020/v31i1a7571.

[11] A. D. Dhass, N. Beemkumar, S. Harikrishnan, and H. Muhammad Ali, “A Review on Factors Influencing the Mismatch Losses in Solar Photovoltaic System,” *Hind. Int. Jor. Photo*, vol. 2022, 27, 2022, https://doi.org/10.1155/2022/2986004.

[12] J. L. Crozier, E. E. Van Dyk, and F. J. Vorster, “Identification and characterisation of performance limiting defects and cell mismatch in photovoltaic modules,” *J. Energy South. Africa*, vol. 26, no. 3, pp. 19–26, 2015. http://www.scielo.org.za/scielo.php?script=sci_arttext&pid=S1021-447X2015000300003&lng=en&nrm=iso.

[13] C. Buerhop, L. Bommes, J. Schlipf, T. Pickel, A. Fladung, I. M. Peters, “Infrared imaging of photovoltaic modules: a review of the state of the art and future challenges facing gigawatt photovoltaic power stations,” *Prog. Energy*, 4, 042010, 2022.. https://doi.org/10.1088/2516-1083/ac890b.

[14] Jahn, U., Herz, M., K¨ontges, M., Parlevliet, D., Paggi, M., Tsanakas, I., Stein, J.S., Berger, K.A., Ranta, S., French, R.H., Richter, M., Tanahashi, T., 2018. Review on Infrared and Electroluminescence Imaging for PV Field Applications IEA-Photovoltaic Power Systems Programme, IEA-PVPS. https://iea-pvps.org/wp-content/uploads/2020/01/Review_on_IR_and_EL_Imaging_for_PV_Field_ApplicatioNs_by_Task_13.pdf.

[15] P. Bauwens and J. Doutreloign, “Reducing partial shading power loss with an integrated Smart Bypass,” *Sol. Ener.*, vol. 103, no. 5, pp. 134–144, 2014, doi: http://hdl.handle.net/1854/LU-4430511.

[16] A. Pandian, K. Bansal, D. J. Thiruvadigal, and S. Sakthivel, “Fire Hazards and Overheating Caused by Shading Faults on Photo Voltaic Solar Panel,” *Fire Technol.*, vol. 52, no. 2, pp. 349–364, 2016. doi: 10.1007/s10694-015-0509-7.

[17] FLIR Systems, “User’s manual FLIR T6xx series,” 2013. [Online]. Available: https://www.instrumart.com/assets/FLIR-T620-T640-Manual.pdf.

[18] C. Buerhop, T. Pickel, M. Dalsass, H. Scheuerpflug, C. Camus, and C. J. Brabec, “aIR-PV-check: A quality inspection of PV-power plants without operation interruption,” in *43th IEEE Photovoltaic Specialist Conference Proceedings*, Portland, 5-10 June 2016, Piscataway, NJ, IEEE, 2016 pp. 1–5, doi: 10.1109/PVSC.2017.8366365.

[19] J. A. Tsanakas, L. Ha, and C. Buerhop, “Faults and infrared thermographic diagnosis in operating c-Si photovoltaic modules: A review of research and future challenges,” *Renew. Sust. Ener. Rev.*, vol. 62, pp. 695–709, 2016

[20] C. Buerhop, H. Scheuerpflug, R. Weißmann, “The Role of Infrared Emissivity of Glass on IR-imaging of PV-Plants,” in: 26th European Photovoltaic Solar Energy Conference (EUPVSEC) Proceedings, Hamburg, 5-9 September 2011. https://doi.org/10.4229/26thEUPVSEC2011-4AV.1.39.

[21] Buerhop, C., Pickel, T., Dalsass, M., Scheuerpflug, H., Camus, C., Brabec, C.J., 2016. aIR-PV-check: A quality inspection of PV-power plants without operation interruption. In: 43rd Photovoltaic Specialist Conference (PVSC), Proceedings, Portland, 5-10 June 2016. https://doi.org/10.1109/PVSC.2016.7749909.

[22] Agilent Technologies, “Agilent 34970A/34972A Data Acquisition Switch Unit User’s Guide,” 2012, [Online]. Available: https://testworld.com/wp-content/uploads/user-guide-keysight-agilent-34970a-34972a-daq.pdf.

[23] Electronic Temperature Instruments Ltd (eti), “EMISSIVITY TABLE,” [Online]. Available: https://thermometer.co.uk/img/documents/emissivity_table.pdf. (accessed July 15, 2023).

[24] H. Wei, L. Fengshou, J. Jie, Z. Shengyao and C. Hongbing, “Safety Analysis of Solar Module under Partial Shading,” *Int. Jor. Photo*,vol. 2015, 907282, 2015, http://dx.doi.org/10.1155/2015/907282

A COMPARATIVE EVALUATION OF HEAT DISSIPATION FACTORS FOR OPEN-RACK AND FLOATING SOLAR PHOTOVOLTAIC INSTALLATIONS

[1]Brendan Willemse, [1]Shaun Nielsen, [1]Johannes Pretorius, [1]Michael Owen, [2]Arnold Rix

[1]Department of Mechanical and Mechatronics Engineering, [2]Department of Electrical and Electronic Engineering, Stellenbosch University Private Bag X1, Matieland, 7602, Stellenbosch, South Africa

E-mail: 22635122@sun.ac.za, 19050089@sun.ac.za, jpp@sun.ac.za, mikeowen@sun.ac.za, rix@sun.ac.za

Abstract:

Estimation of solar photovoltaic (PV) module operating temperature is an important component of accurate PV system simulation and design. Faiman's module temperature model provides a simple method of estimating PV module operating temperature using empirical heat dissipation factors (HDFs) and is widely used in PV simulation. This paper presents HDFs for open-rack and floating solar PV (FPV) configurations based on measurements collected on installations near Stellenbosch, South Africa. The paper allows for direct comparison of the HDFs for these different PV configurations under similar solar and ambient conditions. Differences in the thermal characteristics of the configurations are thus highlighted and potential design factors that influence FPV's heat dissipation are outlined.

Keywords: module temperature; open-rack PV; floating photovoltaic (FPV); Faiman model; heat dissipation factors

1. Introduction

It is well known that photovoltaic (PV) systems are susceptible to efficiency losses when exposed to high module operating temperatures. Various methods have therefore been developed to accurately predict the operating temperatures of PV systems. Faiman's [1] model is commonly used to model the heat dissipation of PV modules by correlating the wind speed, ambient temperature, and plane of array (POA) irradiance to the operating module temperatures. Faiman's model has been shown to be relatively accurate across a wide range of PV technologies and climatic operating conditions [2] and provide comparable accuracy to more complex models [3].

Heat dissipation is a critical factor in PV system performance as it directly impacts the modules' temperature and thus efficiency. Different PV configurations (e.g., ground-mounted open-rack, building-attached or floating) experience unique thermal operating conditions and thus display distinct heat dissipation characteristics. For example, ground-based open-rack systems, typically used for large-scale operations (such as utility-scale or commercial PV installations), facilitates relatively uninhibited airflow around the panels. Natural air currents and wind can thus reach and cool the modules and relatively low module temperatures are expected.

Floating solar PV (FPV) systems are installed on the surface of still water bodies and are an emerging technology that can be used in regions with limited land resources for ground-based open-rack PV installations. FPV systems can also contribute to water security (they reduce the amount of water loss due to evaporation throughout the day [4]) and can be coupled with hydropower systems, reducing the cost of renewable energy generation [5]. In theory, these systems should offer improved heat dissipation due to the proximity to a cool water body and some research has shown that FPV systems can be more efficient than ground-based systems [6]. However, there is limited literature on the thermal behaviour of these water-based systems. A method to specifically determine the heat dissipation factors (HDFs) and cell temperature of FPV systems is presented in [7]. The model shows acceptable correlation to measured values however it has not been extensively validated for FPV technology. Dörenkämper et al. [8] modelled the HDFs of FPV systems to determine the impact of different float designs and climates on the HDFs of FPV.

This paper utilizes the Faiman model to predict the heat dissipation factors (HDFs) for a ground-based open-rack PV and FPV system operating in close proximity (and thus under similar operating conditions), enabling a direct comparison between the thermal behaviour of the two technologies. By analysing the heat dissipation characteristics of FPV configurations, valuable

insight into their respective efficiencies and potential design considerations can be gained.

2. Experimental Setup and Methodology

The test sites are located in the Western Cape province of South Africa, with a straight-line distance of 12.7 km between the two sites (see Fig. 1). The region is characterised by a Mediterranean climate with an average maximum summer temperature of 25℃ and minimum winter temperature of 9℃ [9] and high solar resource, 1 649 kWh/kWp [10].

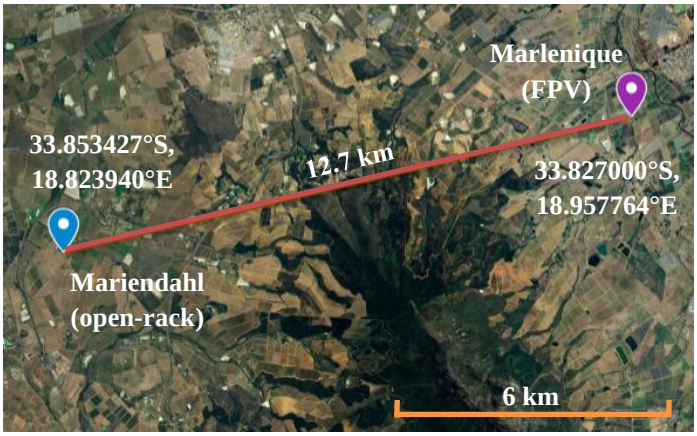

Fig. 1. Geographical map of PV installations

2.1. Open-Rack Installation Details and Data Gathering

The open-rack PV installation monitored in this work is shown in Fig. 2, and located at Mariendahl farm outside Stellenbosch, South Africa. Two PV modules (CS3W-420P) were mounted at a fixed tilt angle of 31°, facing North. The module is rated with an efficiency of 19% and a nominal module operating temperature (NMOT) of 42±3 ℃. The modules were connected in series to a 136 Ω 4 A resistive load, allowing the modules to operate in a closed-circuit condition during the test period.

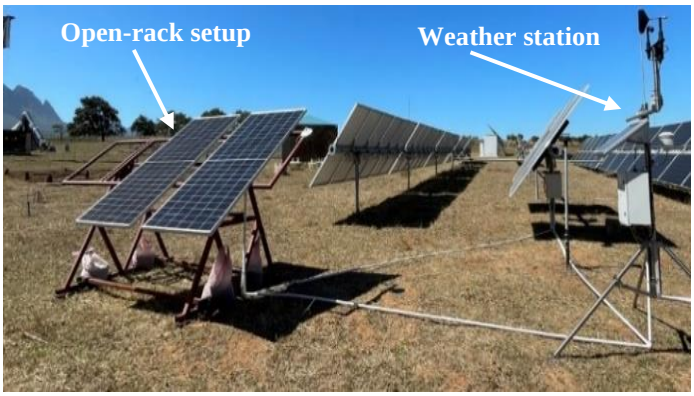

Fig. 2. Mariendahl open-rack system

Two T-type thermocouples were attached to the back side of each module using aluminium tape, positioned at a central and corner cell respectively (similar to Faiman [1]). All module temperature data was logged at one-minute intervals using a Lord TC-Link 200 and recorded using a Lord WSDA Base Station and SensorConnect software. Ambient temperature, wind speed and POA irradiance were collected from a weather station installed near the open-rack structure shown in Fig. 2. Ambient temperature was measured with a shielded HygroVUE5 digital temperature sensor. Wind speed and direction were measured with a R.M. Young 03002 wind sentry and vane. The POA irradiance was measured with a Kipp & Zonen CMP10 pyranometer installed on the open-rack structure, in-plane with the modules.

2.2. FPV Installation Details and Data Gathering

The FPV system is located at Marlenique Estate, Stellenbosch, South Africa (Fig. 3). The PV system consists of 10 x 18 PV modules (CS6U-320P modules) at a fixed tilt angle of 16°. The modules are rated with an efficiency up to 16.97% and a nominal operating temperature (NOCT) of 45±2 ℃. Charge controllers ensure that the modules operate at their maximum power point.

The temperature of the centre module in the Northern row is measured. This module was chosen since its operating environment is likely to be most similar to the open-rack case (limited packing effect in the FPV array), ensuring a comparable assessment to the open-rack experiment.

Fig. 3. Marlenique FPV system

The module and ambient temperatures were measured using a RSPRO PT100 and Campbell Scientific CS109 thermocouple respectively. Two module thermocouples were taped slightly offest from the back face's centre position. The system's equipment was instrumented by the Institute for Energy Technology (IFE) in Norway, therefore the system configuration differs somewhat from the open-rack installation.

Fig. 4. Weather station at FPV installation

The wind speed measurement was taken with a Gill Windsonic wind sensor, while the POA irradiance was measured using a Kipp & Zonen CMP10 pyranometer that is installed in-plane with the PV module tilt angle. The pyranometer and wind speed sensor were both attached to a GeoSun weather station (Fig. 4). The weather station is attached to a mast at the back of the array and stores the data in 1-min intervals. Additionally, the ambient temperature is measured at the centre of the array.

2.3. Data Processing

Thermal models that evaluate the heat dissipation factors for PV modules often assume steady state conditions. Rapid fluctuations in operating conditions therefore degrade the accuracy of the models and filtering is applied to limit the analysis to times of relatively stable conditions. Such filtering is standard practice for thermal measurements on PV modules and an IEC standard [11] has also been developed that describe the measurement and filtering requirements.

For our data, the application of the filtering practice (specifically the filtering of wind) according to the standard resulted in a major reduction in acceptable data points on the open-rack system, and in contrast virtually no difference in the data for the FPV system.

In light hereof, and as our paper determines heat dissipation factors according to the Faiman model, we decided to implement the same filtering strategy as the original paper by Faiman [1]. This strategy does not filter based on wind data, and applies the following:

- Data is stored as 5-min averages.
- Only days with clear sky conditions (i.e. only minor observable irradiance fluctuations) are to be considered.
- Analysis period between 10 am and 2 pm.

For the open-rack installation the module temperature was calculated by averaging the two thermocouple measurements for each module. Out of a potential 92-day testing period between 2023/03/30 and 2023/06/29, data from 29 days with clear skies provided a total of 2330 useable data points.

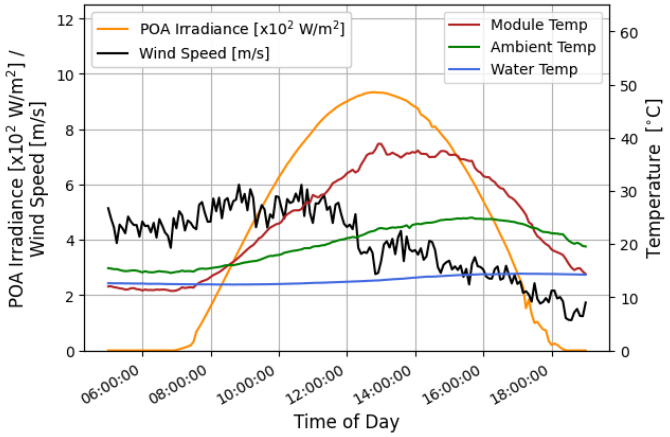

Fig. 5. Unfiltered clear sky data for the FPV site

The GeoSun weather station at the FPV site also reported the average values of the two module thermocouples. During an analysis period of 58 days (2022/08/31-2022/10/28) for the FPV installation, only 13 days had clear sky conditions, resulting in 610 useable data points. The impact of clear sky filtering on the FPV data is illustrated in Fig. 5 (unfiltered) and Fig. 6 (filtered).

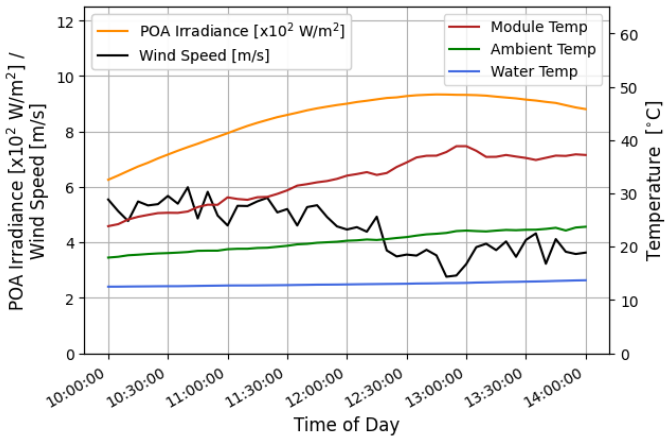

Fig. 6. Filtered clear sky data for the FPV site

2.4. Faiman Module Temperature Model

The thermal model proposed by Faiman [1] utilizes meteorological data as inputs and is based on the Hottel-Whillier-Bliss [12, 13] equation. The modified equation by Faiman decomposes the overall HDF into two components: a constant factor (U_0') and a wind-dependent factor (U_1'). The combined effects of radiation and natural convection heat transfer are represented by U_0', while forced convection heat transfer via wind is represented by U_1'. Faiman relates these parameters to the module and ambient temperatures (T_{mod} and T_{amb}), POA irradiance (H), and wind speed (v_w).

$$\frac{H}{U_0' + U_1' \cdot v_w} = T_{mod} - T_{amb} \quad (1)$$

HDFs are determined from experimental measurements of temperature, POA irradiance and wind speed by linear regression.

3. Results and Discussion

3.1. Environmental Conditions

To evaluate the similarity of the environmental test conditions for the two sites, histograms of the POA irradiance, wind speed and ambient temperatures are presented in Fig. 7 and 8, over the respective test periods. The variables are normalized with respect to the open-rack configuration's maximum values. The open-rack configuration measured values of $H_{max} = 1175.2\ W/m^2$, $v_{w,max} = 6.37\ m/s$, and $T_{amb,max} = 32.8\ ℃$.

The FPV site exhibited higher average wind speeds, whereas the open-rack site consistently encountered a broader range of wind speeds. Both sites maintained similar POA irradiance values throughout the day, with slightly elevated values on average observed at the FPV site. Unlike the open-rack site, the FPV site did not reach the maximum POA irradiance. On average, the FPV site also recorded higher ambient temperatures during the day, although it did not reach the peak temperature observed at the open-rack site. The distribution (negatively skewed) of the ambient temperature for the FPV site can be attributed to the fewer available data points for the analysis period in comparison to the open-rack analysis period. Overall, the disparities in environmental conditions were deemed acceptable for facilitating a direct comparison.

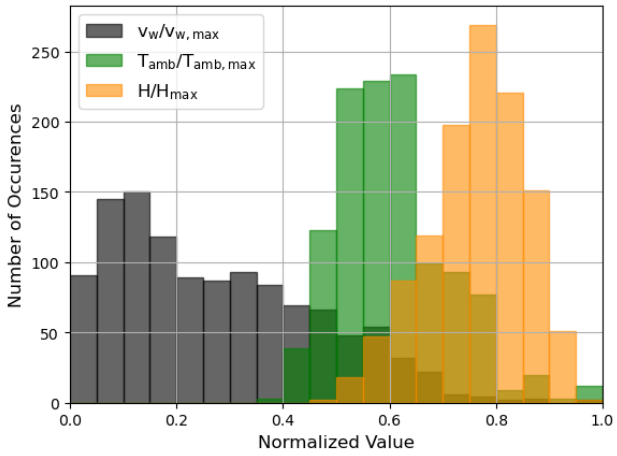

Fig. 7. Open-rack normalised environmental conditions

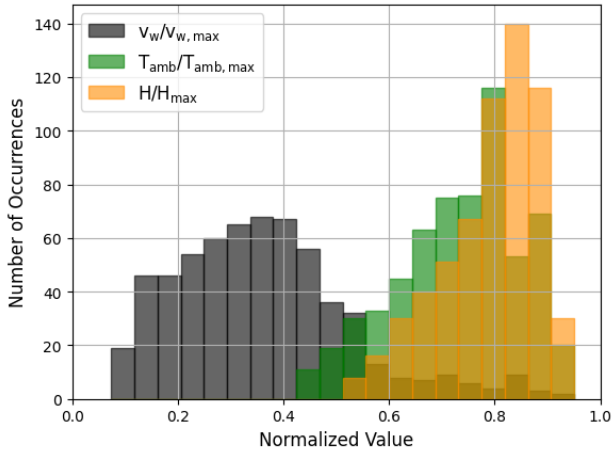

Fig. 8. FPV normalised environmental conditions

3.2. Open-Rack PV Results

The results for the open-rack configuration are shown in Fig. 9. The U_0' and U_1' values ($25.70\ W/m^2K$ and $9.90\ Ws/m^3K$ respectively, with $R^2 = 0.79$) compare well to those initially determined by Faiman [1] ($U_0' = 25\ W/m^2K$, $U_1' = 6.80\ Ws/m^3K$, $R^2 = 0.63$) and open-rack experiments conducted at Stellenbosch University [14] ($U_0' = 26.5\ W/m^2K$ and $U_1' = 5.2\ Ws/m^3K$ at a tilt angle of 23°).

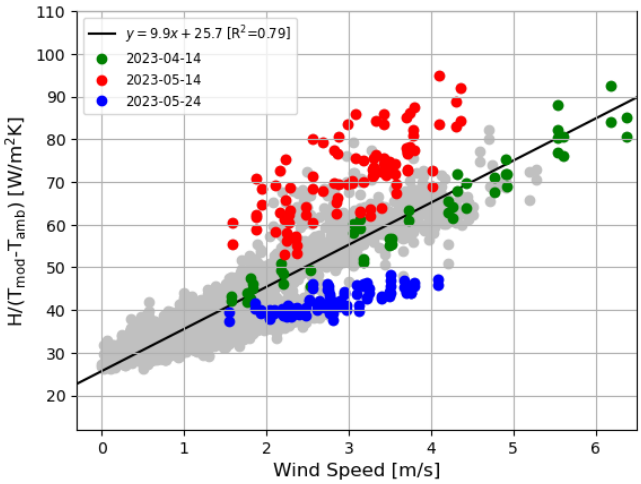

Fig. 9. Open-rack HDF curve

From the 29 clear sky days, data from three different days are highlighted in colour in Fig. 9, and their behaviour and influence on the dataset are examined. In the figure, we observe two outlier days (red and blue) and one trend-aligned day (green) for the open-rack system.

For the day represented by green markers, the increasing trend in HDF aligns with a gradually increasing wind speed (over a large range) throughout the day. Little fluctuation in instantaneous wind speed (limited gusts) during this period

results in little HDF variation around the trendline.

The magnitude of POA irradiance, wind speed and ambient temperature are similar for the days represented by the red and blue data. There is however greater fluctuation in wind speed for the day in red versus the day in blue, causing the respective difference in scatter on the graph. Despite the similar atmospheric conditions, module temperatures for the blue data are higher. As a result, $H/(T_{mod} - T_{amb})$ is lower due to the higher denominator, causing the data points to sit below the trendline. It is our hypothesis that the difference in module temperature between these two days can be ascribed to a difference in wind direction.

A comparison between the measured and predicted (using the HDFs and Eq. 1) module temperatures is shown in Fig. 10. The model predicted the measured temperatures with a root-mean-square error (RMSE) of 2.56 ℃. This compares well with the RMSE of 1.86 ℃ obtained by Faiman [1] and 1.7-2.5 ℃ in [5].

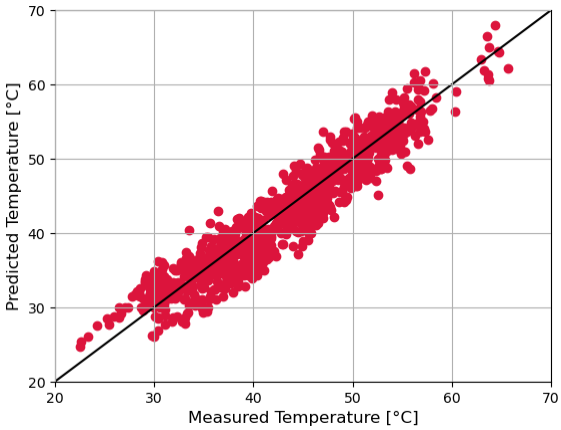

Fig. 105. Open-rack temperature prediction

3.3. FPV Results

Fig. 11 shows the FPV results. The coefficient of determination value of the fitted data is reasonably high (R^2 = 0.73). However, it is worth noting that the FPV analysis had fewer data points available compared to the open-rack experiment and the smaller sample size may impact the results of the comparison. The regression analysis yielded values of 19.62 W/m^2K and 10.91 Ws/m^3K for U_0' and U_1' respectively.

Similar to Fig. 9, Fig. 11 also highlights the placement of HDF data in colour for three individual days from the total of 13 clear sky days collected. The behaviour of the red data can be explained by extremely high wind speeds cooling the module temperature to below 40 ℃. This causes the temperature gradient between the module and ambient air to be small, which causes $H/(T_{mod} - T_{amb})$ to be higher than the norm.

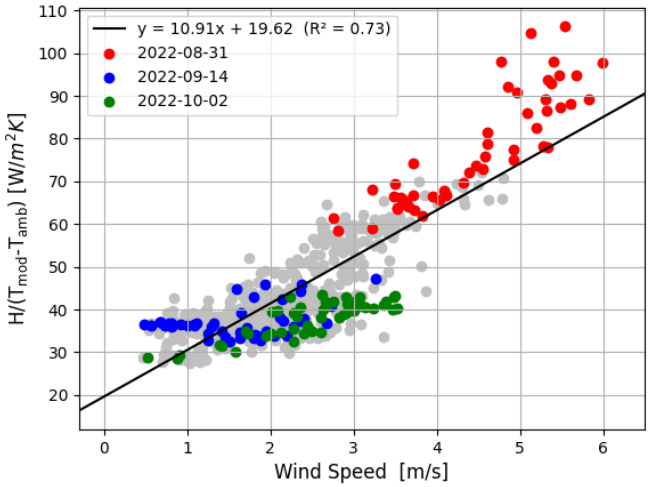

Fig. 11. FPV HDF curve

A comparison (not shown) of the conditions for the green and blue data indicates a steady, moderate wind speed for the day in green, with a lower, gradually increasing wind speed for the day in blue. Even though the wind speed for the green data is higher, a higher module-to-ambient temperature difference is observed. The blue data also shows a higher sensitivity to the lower wind speed compared to the effects of wind on the day in green. Here, it is again our postulation that wind direction plays a role.

The mean module temperature prediction for the FPV system has an RMSE of 3.72 ℃. The quality of the model's prediction versus the measured module temperature can be seen in Fig. 12.

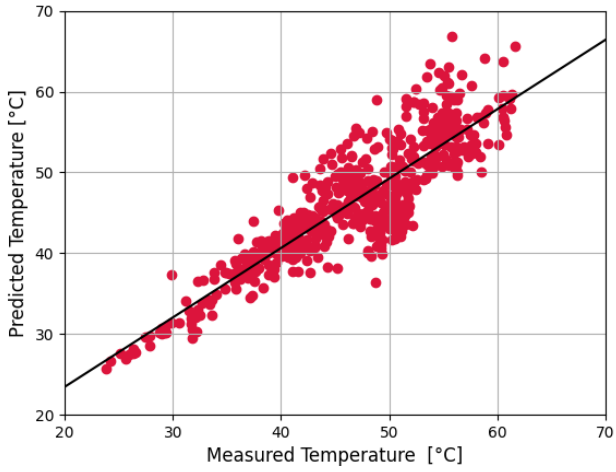

Fig. 12. FPV temperature prediction

The FPV HDFs found in this work compare relatively well to values reported in [8]. In [8], two distinct FPV systems were evaluated: one featured a closed float design and variable tilt panels ($U_0' = 24.4$ W/m^2K and $U_1' = 6.5$ Ws/m^3K with R^2 = 0.57), while the other employed a more open float array with a fixed panel tilt of 12° ($U_0' = 18.9$ W/m^2K and $U_1' = 8.9$ Ws/m^3K with R^2 = 0.58) in the Netherlands and Singapore

respectively. Data for each of these systems have been recorded on-site between 2017-2019. Additionally, two ground-based systems served as references near the two FPV sites: one in an open-rack configuration with a fixed panel tilt of 22° ($U_0' = 13.0$ W/m^2K and $U_1' = 5.4$ Ws/m^3K with R^2 = 0.52) and the other was a rooftop-mounted system ($U_0' = 18.9$ W/m^2K and $U_1' = 8.9$ Ws/m^3K with R^2 = 0.58) with a 10° panel tilt angle, located in the Netherlands and Singapore, respectively. The FPV system in Singapore is similar in configuration to the system considered in this work, except for the larger tilt angle at the Stellenbosch site (16°). Dörenkämper et al. [8] identified a significant influence of wind speed on the HDFs and concluded that higher wind speeds over open water, as well as the cooler air near water bodies, constitute the primary contributors to enhanced heat dissipation in FPV systems.

3.4. Discussion of PV Configuration Results

The U_1' value for the FPV system is higher than that of the open-rack configuration (10.91 Ws/m^3K compared to 9.90 Ws/m^3K). This is expected, due to higher wind spends carrying colder air [8] over FPV panels than for ground-based systems. When comparing the HDFs determined in this work, the FPV shows a lower U_0' but higher U_1' compared to the open-rack configuration. The higher wind dependent HDF (U_1') aligns with the findings of [8] and the that the water provides cooler ambient conditions around the installed modules. However, the lower FPV U_0' (19.62 W/m^2K compared to open-rack's 25.7 W/m^2K) value is somewhat unexpected and points to the need for FPV systems to be carefully configured if the full potential of lowering their operating temperatures are to be realized (as noted in [15]).

In this case, the FPV panels are less inclined than the open-rack system (16° compared to 31°). Lower tilt angles are typically chosen to mitigate wind loading on the system, but they may inadvertently impede natural convection heat dissipation. Furthermore, the presence of the float or the design thereof may further impact the ventilation of the back surfaces and, critically, prevents the back surface from being exposed to the cool water surface. The radiative heat loss from the back surface of the panels in the FPV case may thus be poorer than in the open-rack case.

It is important to note that the connection of the open-rack modules to a load resistor does not necessarily mean that these modules were operating at their maximum power point, in contrast to the FPV modules which were controlled to operate at maximum power. It is expected that the HDFs of the open-rack system would increase if they were to operate at their maximum power point, as the module temperatures should theoretically drop due to greater power evacuation from the modules while POA irradiance and ambient temperature would remain the same. The HDFs for the open-rack installation in this study are therefore likely to be relatively conservative.

3.5. Single Day Direct Comparison

To gain a deeper insight into the different thermal behaviours of the two PV configurations, a comparison is performed on a day with similar environmental conditions (POA irradiance, ambient temperature, and wind speed) as shown in Table 1.

Table 1. Environmental conditions for single day comparison

FPV - 2022/09/12			
	MIN	**MAX**	**MEAN**
Module Temp [°C]	28.9	46.5	40.7
Ambient Temp [°C]	14.5	18.4	16.6
$T_{mod} - T_{amb}$ [°C]	14.4	28.1	24.2
POA Irradiance [W/m^2]	637.5	983.3	885.3
Wind Speed [m/s]	0.80	2.65	1.39
$U_0' + U_1' \cdot v_w$ [W/m^2°C]	-	-	36.58
Open-rack - 2023/06/10			
Module Temp [°C]	29.3	42.6	38.2
Ambient Temp [°C]	14.6	17.7	16.2
$T_{mod} - T_{amb}$ [°C]	14.7	24.9	22.0
POA Irradiance [W/m^2]	598.1	892.4	813.7
Wind Speed [m/s]	1.23	2.48	1.78
$U_0' + U_1' \cdot v_w$ [W/m^2°C]	-	-	36.99

The data analysis reveals that the effective heat dissipation (represented by $H/(T_{mod} - T_{amb}) = U_0' + U_1' \cdot v_w$) for the two systems are virtually equivalent. This evaluation for a single day of similar conditions shows that, despite the lower averaged U_0' value obtained for the FPV system compared to the open-rack system, comparable heat dissipation from the FPV can be achieved.

4. Conclusion

The aim of the study was to compute and compare the HDFs according to Faiman's [1] thermal model for open-rack and FPV systems operating under similar environmental conditions. Experimental measurements were taken at an open-rack and FPV solar installation, both of which are located near Stellenbosch, South Africa. The measurement data for the two PV installations were filtered according to the method prescribed in [1].

The experimentally determined HDFs for the open-rack PV system align well with values reported in the literature [14], and the predicted temperature demonstrated an RMSE of 2.56 °C, indicating a reasonably accurate model. The value found for the wind-dependent HDF was consistent with values found in

literature [8] for FPV systems. However, the results of the FPV experiment revealed a lower U_0' than expected, with RMSE of 3.72 ℃ for the predicted temperatures. This suggests that, under low wind conditions, FPV systems dissipate heat less effectively than open-rack systems.

When comparing the thermal behaviour of the open-rack and FPV system on a day with similar environmental conditions, it was found that the FPV system's heat dissipation is comparable to that of the open-rack configuration.

The FPV system's relatively small tilt angle and float design were identified as potential contributing factors affecting the wind-independent heat dissipation, leading to higher-than-expected module temperatures, on average, compared to the open-rack configuration. This idea is further reinforced with the varying HDFs found in literature [8] for different FPV system designs. The floats used can affect the view factor the back of the FPV module experiences when radiating heat to the water.

In conclusion, the study highlights the importance of considering various design elements in FPV systems to optimize heat dissipation and module performance. By understanding the impact of tilt angle, float design, and module positioning on heat dissipation, researchers and designers can better enhance the thermal behaviour of FPV systems, maximizing their energy efficiency and overall performance.

Acknowledgements

The author would like to thank Scatec for providing the funding required to conduct this research and IFE for providing the necessary FPV data.

References

[1] D. Faiman, 'Assessing the outdoor operating temperature of photovoltaic modules', Progress in Photovoltaics: Research and Applications, vol. 16, pp. 307–315, Feb 2008.

[2] E. Barykina and A. Hammer, 'Modeling of photovoltaic module temperature using Faiman model: Sensitivity analysis for different climates', Solar Energy, vol. 146, pp. 401–416, 2017.

[3] Koehl, M., Heck, M., Wiesmeier, S., and Wirth, J., 'Modeling of the nominal operating cell temperature based on outdoor weathering', Solar Energy Materials & Solar Cells, vol. 95, pp. 1638-1646, 2011

[4] K. K. Agrawal, S. K. Jha, R. K. Mittal, and S. Vashishtha, 'Assessment of floating solar PV (FSPV) potential and water conservation: Case study on Rajghat Dam in Uttar Pradesh, India', Energy for Sustainable Development, vol. 66, pp. 287–295, Jan 2022.

[5] World Bank Group, *Where Sun Meets Water: Floating Solar Market Report—Executive Summary*, 2018, [Online]. Available:https://documents.worldbank.org/en/publication/documents-reports/documentdetail/579941540407455831.

[6] A. M. K. L. Abeykoon, G. M. L. P. Aponsu, H. M. B. I. Gunathilaka, and H. A. V. Nadeera, 'Effect of temperature on the photovoltaic characteristics of polycrystalline silicon solar cells at hambantota solar power plant', Solar Asia 2018 Int. Conf. National Institute of Fundamental Studies, Kandy, Sri Lanka, Jan 2018.

[7] D. Lindholm, T. Kjeldstad, J. Selj, E. S. Marstein, and H. G. Fjaer, 'Heat loss coeffients computed', Progress in Photovoltaics: Research and Applications, vol 29, pp. 1262-1273, July 2021.

[8] M. Dörenkämper, A. Wahed, A. Kumar, M. de Jong, J. Kroon, and T. Reindl, 'The cooling effect of floating PV in two different climate zones: A comparison of field test data from the Netherlands and Singapore', Solar Energy, vol. 219, pp. 15–23, May 2021.

[9] Weather Spark, *Average Weather in Cape Town, South Africa, Year Round*, 2019. [Online]. Available:https://weatherspark.com/y/82961/Average-Weather-in-Cape-Town-South-Africa-Year-Round

[10] A. Rix, K. Kritzinger, I. Meyer, and J.L. van Niekerk, "Potential for distributed solar photovoltaic systems in the Western Cape Province," Centre for Reneweable and Sustainable Energy Studies, 2015. [Online]. Available: https://www.crses.sun.ac.za/files/research/publications/technical-reports/WCG%20PV%20Report%20Final%5B1%5D.pdf

[11] Photovoltaic (PV) module performance testing and energy rating – Part 2: Spectral responsivity, incidence angle and module operating temperature measurements, IEC 61853-2 International Standard, Edition 1.0, Aug 2016.

[12] H. C. Hottel, A. Willier, 'Evaluation of Flat Plate Collector Performance'. Transactions of the Conference on the Use of Solar Energy, vol. 2, Part 1, University Of Arizona Press, pp. 74, 1958.

[13] R. W. Bliss, 'The Derivations of Several "Plate-Efficiency Factors" Useful in the Design of Flat-Plate Solar Heat Collectors', Solar Energy, vol. 3, pp. 55, 1959.

[14] M. Owen, J. Pretorius, B. Buitendag, and C. Nel, 'Heat dissipation factors for building-attached PV modules', International Heat Transfer Conference, Cape Town, South Africa, IHTC-17, ID-416, 2023.

[15] D. Lindholm, J. Selj, T. Kjeldstad, H. Fjær, and V. Nysted, 'CFD modelling to derive U-values for floating PV technologies with large water footprint', Solar Energy, vol. 238, pp. 238–247, May 2022.

AGRIVOLTAIC SYSTEMS: TECHNO-ECONOMIC ANALYSES OF POTENTIAL PV CONFIGURATIONS FOR SOUTH AFRICA

Nicholas C Chapman[1], Prof Alan C Brent[2], and Imke H de Kock[3]

[1] Department of Industrial Engineering, Stellenbosch University, Stellenbosch, South Africa; Cell: 082 886 8305 E-mail: 20823983@sun.ac.za

[2]Sustainable Energy Systems, Victoria University of Wellington, Wellington, Aotearoa New Zealand and Department of Industrial Engineering, Stellenbosch University, Stellenbosch, South Africa; E-mail: alan.brent@vuw.ac.nz

[3] Department of Industrial Engineering, Stellenbosch University, Stellenbosch, South Africa; E-mail: imkedk@sun.ac.za

Abstract: Agrivoltaic systems offer the opportunity of utilising the solar resource of South Africa effectively without reducing agricultural productivity. A previous Geographic Information System (GIS) analysis has shown that less than 2% of agricultural land that is suitable for agrivoltaic systems (around 400,000 hectares) could potentially double the current annual electricity generation in the country. Most of the opportunity lies with livestock farming and maize production in the central provinces, but orchards and vineyards in the Western Cape Province may also be an option. This study summarises techno-economic analyses that were undertaken for agrivoltaic systems that are deemed (technically) the most viable for three types of farming operations, namely: grazing, maize and orchards. The results show LCOE values in the range of R1.08 to R1.72 per generated kWh. Compared to available import and export tariffs values across the provinces indicates that agrivoltaic systems may well be a feasible option for farmers in South Africa.

Keywords: Agrivoltaics; economic analysis; agriculture; utility-scale PV; South Africa.

1. Introduction

South Africa has seen significant growth in the solar energy sector (see Figure 1) with generation increasing from 2 TWh to around 7.6 TWh from 2014 to 2019 [1].When it comes to land use for utility-scale photovoltaic (PV) systems there is a risk of ground mounted PV (PV-GM) systems taking up perfectly good arable land that could be used for farming, or possibly negatively effecting natural ecosystems.

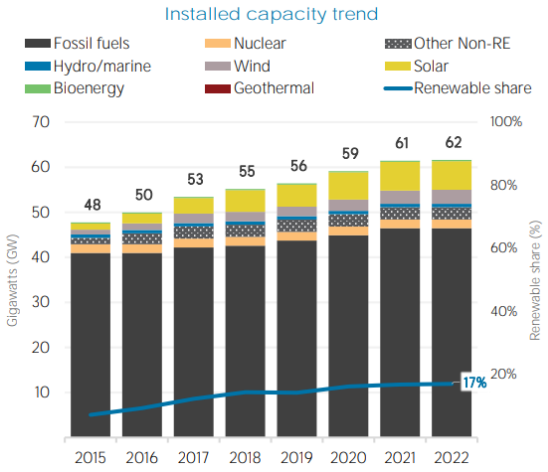

Figure 1. Installed Capacity in South Africa [2].

Agrivoltaic systems seek to address this issue by combining farmland and PV, thereby reducing or eliminating the negative effects on the land and, in some cases, improving the productivity of the soil [3]. This is done by reducing the panel density and elevating the PV system off the ground to lessen the system's effect on the environment or crops below. This can take many forms and each implementation depends entirely on the context in question, which will decide the panel density and height for example.

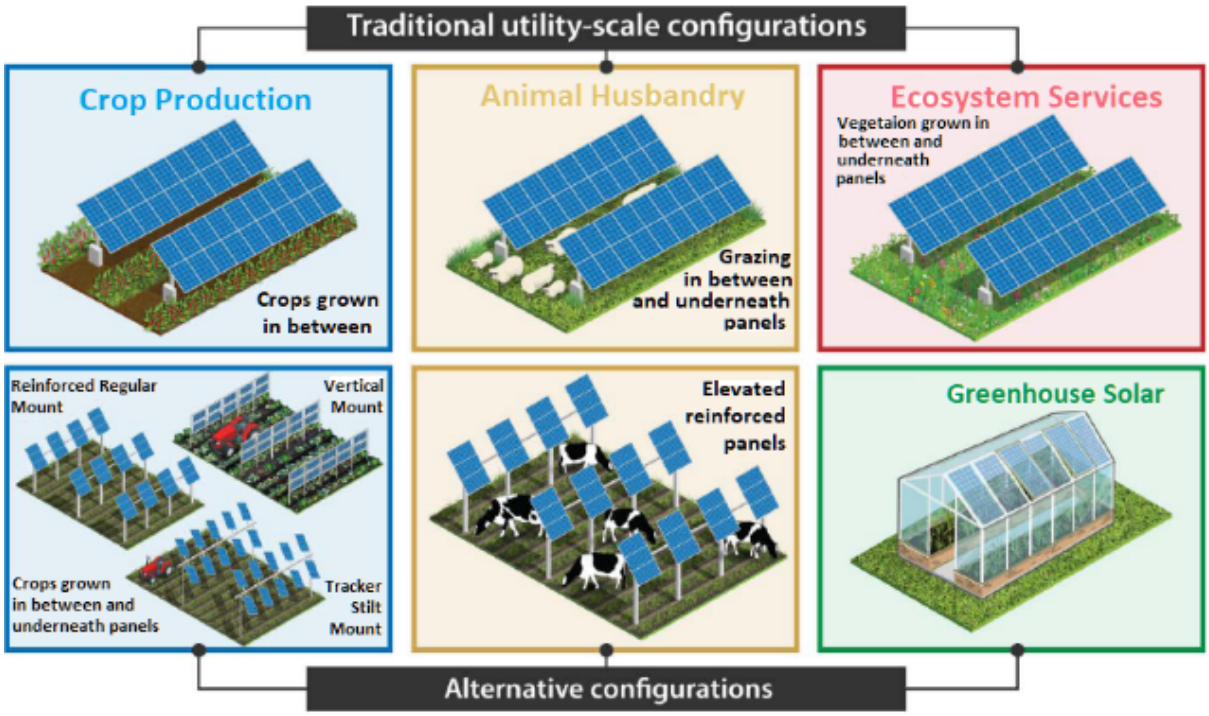

Figure 2. Types of agrivoltaic systems that have been deployed commercially [3].

Examples of possible agrivoltaic configurations are shown in Figure 2, although there are a vast number of different implementations that can be used depending on the agricultural operations.

The purpose of this paper is to analyse the techno-economic feasibility of implementing grazing, maize, and orchard agrivoltaic systems in South Africa – the largest opportunities identified from a previous GIS analysis [4]. For the analyses the Levelized Cost of Electricity (LCOE) metric is used and compared to South African electricity tariffs to evaluate payback periods and the Return on Investments (ROIs).

2. Methods

2.1. Crops chosen

Grazing was chosen as it accounts for most of the farmland in the country [4]. However, it should be noted that most of this land is not formally cultivated and often remote compared to other farmed crops. Maize was chosen as it uses the largest area of arable land in South Africa and offers many locations for utility-scale PV projects to be implemented [4]. However, maize is shade-intolerant meaning module arrangements must be of low density. Fresh fruit production only makes up around 0.5% of the suitable land [4]. However, it does account for over 50% of agricultural exports and the potential implications of agrivoltaic systems on the productivity of this sub-sector is therefore also of interest.

2.2. Agrivoltaic technical configurations

For grazing operations, the PV modules need to be positioned at least 2.8 metres above the ground to prevent damage from the cattle. Shading is not as much of an issue as compared to crops, but some sunlight is needed for the pasture. A panel density, or land cover area, of 30% was considered, although higher densities can be used. Maize operations need to allow clearance for farming equipment, so the modules need to be positioned 4.5 metres above the ground. Alternatively, vertical bi-facial modules can be used to reduce infrastructure costs. Due to the shade-intolerance of maize a panel density of 15% or less is required to minimise crop yield losses. Orchards require at least 5 metres of clearance due to the height of the trees. Due to the shading of the trees vertical modules cannot be used as with maize. However, their shade-tolerance means that panel densities of 30% can be used between the rows of trees.

All these configurations can benefit greatly from solar tracking systems. The flexibility of positioning allows for mitigation against wind damage, clearance for vehicles by going fully vertical or horizontal not like what is observed in Figure 2. Control over microclimates under the modules can also be achieved, be it for frost protection by trapping humidity, soil water retention, or the

control of unwanted vegetation that would otherwise form under the panels [4][5].

For the analysis three configurations that incorporate solar tracking with a single portrait (1P) panel arrangement and at a height of 5 metres (to allow a minimum height of around 3.5 metres at the lowest point of tracking) were considered to simplify the calculations and reduce the variables: 30% panel density (for beef and dairy farming/grazing), 15% panel density (for maize farming), and 30% panel density (for orchard farming/fruit). 1P is used based on standard industry practice for agrivoltaic systems and 5 meters is used to satisfy the minimum height requirement of all three agricultural operations. Figure 3 provides examples of operational systems elsewhere.

Figure 3. 1P tracking systems used for grazing and orchard operations. Top [6], Bottom [7].

2.3. Economic analysis

To evaluate the economic performance of a PV system the LCOE (Levelized Cost of Electricity) metric is primarily used:

$$LCOE = \frac{\sum \text{costs over lifetime}}{\sum \text{electrical energy produced over lifetime}} = \frac{\sum_{t=1}^{n} \frac{I_t + M_t}{(1+r)^t}}{\sum_{t=1}^{n} \frac{E_t}{(1+r)^t}} \quad (1)$$

With I_t the investment expenditure in year t, M_t the operations and maintenance costs in year t, E_t the electrical energy generated in year t, r the discount rate, and n the lifetime, namely 30 years.

Having an LCOE less than the electricity import tariff means that over its lifetime it will be worth more than importing power from the grid. Having it higher means that there is no economic incentive to invest in projects, as there will be an insufficient ROI (Return on Investment). This is not accounting for other incentives such as carbon emissions reduction and backup power if the grid is not available for periods of time.

CAPEX, a component of the LCOE calculation, is also an important consideration. Due to the modularity of PV installations this value can to some degree be scaled to fit the project, albeit with LCOE values not scaling down linearly.

The CAPEX and LCOE values per hectare for the three scenarios are calculated across multiple locations where the farming operations are primarily distributed in the respective province. These values are then compared to utility-scale PV systems in South Africa, as well as agrivoltaic systems in other countries.

3. Techno-economic analysis

3.1. Costs of PV system

While it is possible to calculate the hardware for an agrivoltaic system in terms of modules and inverters, rack mounting for agrivoltaic systems range in cost depending on the situation. Labour costs also vary considerably between projects.

As such, where possible, costs are expressed in terms of cost per unit, but certain “soft costs” are rather expressed in terms of a percentage of the total project or other components over time where relevant.

3.1.1. Cost assumptions

The cost assumptions are summarised in Tables 1 and 2.

Table 1. Specifications of each scenario.

	Grazing	Maize	Fruit
No. of modules	1160	1160	580
Capacity (kW)	649.6	649.6	324.8
Inverters (per ha)	0.54	0.54	0.27

Table 2. Cost assumptions across all scenarios.

	Min	Max	Comment
Discount rate	6% [8]	8% [9]	
Racking costs	10% [9]	25% [9]	Of project
Soft costs* [8]	35%	37%	Of project
PV degradation [9]	0.5%		Per year
Lifespan	30		Years
module cost** [10]	R7.00	R8.50	Per Watt
Inverter cost [11]	R1.25	R1.50	Per Watt
Inverter replacement in year 15	7% [9]		Of initial CAPEX
Operational costs per year [8][9]	1.5%	5%	Of project

* Soft costs refer to costs that are not attributed to hardware, e.g. modules, racking and inverters. These costs include construction and services such as labour and planning.
**Prices may be higher or lower than stated, due to different sellers or macro-economic changes.

3.1.2. Cost calculations

Calculating the initial capital cost from the figures outlined in Tables 1 and 2 ranges of R9.8 million to R14.2 million per hectare – for a 30% panel density – and R4.9 million to R7.1 million per hectare – for a 15% panel density – are obtained from:

$$\mathbf{InitialCapital} = \frac{\mathbf{Panels+Inverters}}{\mathbf{1\text{-}\%(SoftCosts+Racking)}} \quad (2)$$

For operational costs the replacement of all inverters in year 15, as well as a percentage cost for all hardware as outlined in Table 2, were considered:

$$\mathbf{Operations/yr} = 0.05 * InitialCapital + InverterReplacement \quad (3)$$

Where inverter replacement is 7% of initial capital in year 15.

Yearly costs of R494.2 thousand to R713.1 thousand per hectare – for a 30% density – and R249.7 thousand to R359.1 thousand per hectare – for a 15% coverage – are obtained.

Combining all these costs gives a ZAR/Watt value range of R38.12 to R54.97 for 15% panel density, with the 30% values only differing slightly.

3.2. Comparison with reported values

3.2.1. Utility-scale PV systems in South Africa

Utility-scale PV systems in South Africa have large ranges for ZAR/Watt values due to the year and conditions they were constructed, as well as the contractor used. The De Aar Project and Jasper Project [12][13] reported values of R43.37/W and R27.43/W respectively, with rough LCOE estimates assuming a 20-year lifetime of R1.37/kWh and R0.64/kWh. These projects were both built in 2014, which shows that economic values at this scale can vary considerably.

Estimates from industry sources have put the current ZAR/Watt value closer to R12/W for an installation of around 75 MW (see acknowledgements).

3.2.2. Agrivoltaic systems in other countries

There are plenty of examples of overseas agrivoltaic implementations and the costs differ from project to project, with most ground mounted PV systems ranging from R23/W to R34/W compared to agrivoltaic systems, which typically range from R25.6/W to R37.6/W [3][14][15][16], although for specific projects costs as high as R44.74/W have been reported [3] (the reported ranges for grazing and maize agrivoltaics are provided in Table 3). It can therefore be assumed that, on average, an agrivoltaic system will cost at least 11% more than a ground mounted PV system due to the additional costs of the racking system.

Table 3. Reports of similar agrivoltaic projects.

Scenario	Low	High
Grazing [9]	R30.72/W	R33.72/W
Maize [4][5]	R24.67/W	R30.89/W

By comparison the ZAR/W values from the analyses in this paper are much more conservative with the upper reported values of overseas installations being close to the lower estimate of the calculations. This implies that the cost estimates are extremely conservative, and the lower estimate of CAPEX is closer to real world values. However, it is better to overestimate the CAPEX values to ensure the projects financial goals are achieved.

3.3. LCOE calculations

Using Solargis [17] the values for PV output per month were simulated, based on municipalities located in each province (see Figure 4). These values are for a 15% coverage, but similar values can be expected for a 30% coverage.

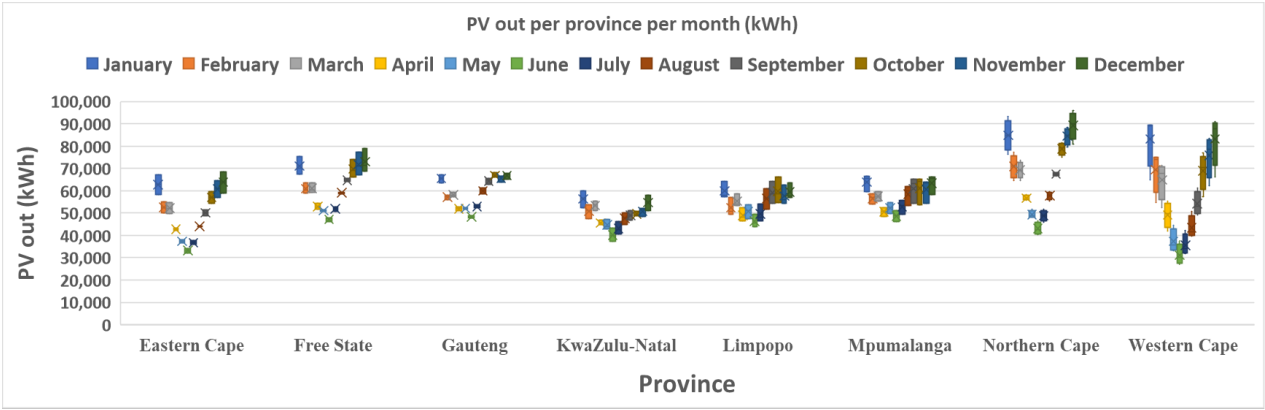

Figure 4. Simulated PV output (kWh/month) for the provinces of South Africa.

LCOE rates are shown in Figure 5 for each province based on average seasonal values. The best-case is calculated with the lower end of the cost estimates using the highest irradiation data out of the locations chosen. While the worst case uses the higher end of the cost estimates and the worst irradiation data of the locations chosen. This was done to establish a range of realistic LCOE values.

The lowest average LCOE is R0.97 and the highest R1.55 per kWh, across the different provinces, with the lower estimate falling between the Jasper and De Aar projects [12][13] and the higher estimate exceeding the De Aar project by about 13%. As these LCOEs mostly reflect conventional utility-scale PV systems, if an 11% increase is included for agrivoltaic systems these values increase to R1.08 and R1.72 per kWh respectively.

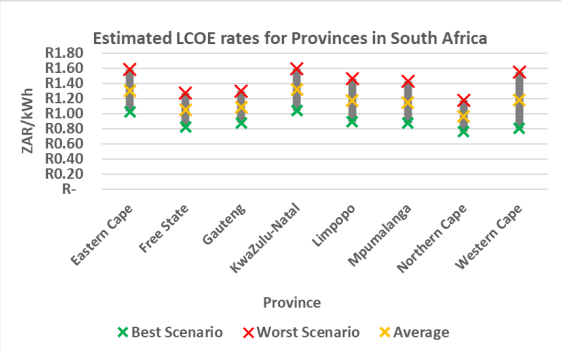

Figure 5. Estimated LCOE rates for provinces in South Africa.

3.4. ROI and payback periods

3.4.1. Tariff rates and cost of electricity

Unfortunately, there is very little information on export tariffs for most provinces. The one exception is the Western Cape Province, which has almost the same number of entries as all the other provinces combined. As shown in Figure 6 a few of the provinces only had a single entry. The average was found to be R0.89/kWh and R1.01/kWh for the high and low seasons respectively.

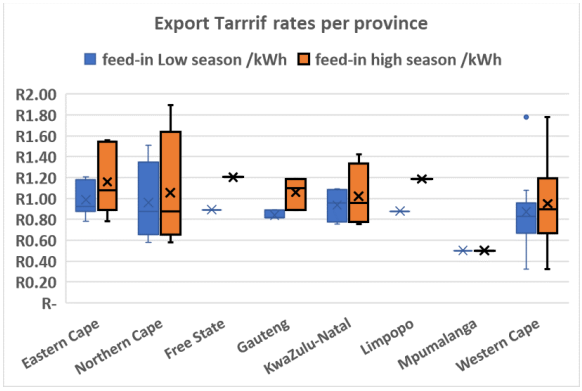

Figure 6. Tariff export rates for each province in South Africa.

When it comes to import tariffs there is a wide range across each municipality. For simplicity the analyses considered an average commercial import tariff of R1.33/kWh and an agriculture import price of R1.88/kWh based on the Eskom 2020/21 pricing sheet [18].

3.4.2. ROI and payback period calculation

Assuming the system will have a lifetime of 30 years and that there will be no major changes to tariff structure for export tariffs and that import tariffs will grow at a rate of 7% per year based on averaged historical data from 2017 to 2021, and without considering the discount rate or inflation, this gives payback periods of 5 and 13 years for import values of R1.33/kWh and R1.88/kWh respectively, and ROI values of 244% and 616% respectively. This assumes all the electricity generated by the agrivoltaic systems are used on site without any electricity being fed back into the grid.

Assuming all the electricity is exported to the grid with a municipality compensation of R0.89/kWh and R1.01/kWh (averages for low and high seasons respectively), which increases at the same rate as the import rates, payback periods of 10 to 21 years and ROI values of 147% to 308% are obtained. This assumes that all electricity is exported and sold back to the municipality, and none is used on site.

4. Conclusion

Techno-economic analyses have been undertaken on agrivoltaic systems in South Africa using the LCOE metric.

Based on the calculations, it is estimated that agrivoltaic systems will cost between R38.12 and R54.97 per Watt installed, and LCOE values are in the range of R1.08 to R1.72 per generated kWh.

These values will result in payback periods of 5 to 13 years and have ROIs of 244% to 616% if all the electricity is used as a substitute to electricity from the grid, or alternatively payback periods of 10 to 21 years and ROIs of 147% to 308% if all electricity is exported back to the grid at average municipal export rates.

While these estimates may be useful for estimating the viability and costs of installations in a broader sense it does not consider each individual location, climate, and municipal rate for the area. Installations across the country may therefore deviate substantially from the average value range used in cases of low irradiation or possibly poor/good municipal export/import rates. What is more, the project cost breakdown is not based on average projects costs for parts such as racking.

Future research could include better import tariff data for provinces besides the Western Cape Province, as well as more accurate cost/unit breakdowns of the racking system as a function of other parameters such as height. Multiple calculations could also be run per location and municipality, and then averaged to better represent the values for each location's tariff system and irradiance.

5. Acknowledgements

The authors acknowledge and appreciate the inputs from the CSIR Energy Research Centre for providing installation costs for current utility-scale PV systems.

References

1. International Renewable Energy Agency (IRENA), "Energy profile South Africa", https://www.irena.org/-/media/Files/IRENA/Agency/Statistics/Statistical_Profiles/Africa/South%20Africa_Africa_RE_SP.pdf (accessed Jul. 22, 2023).
2. International Renewable Energy Agency (IRENA), "Regional trends", https://www.irena.org/-/media/Files/IRENA/Agency/Statistics/Statistical_Profiles/Africa/South-Africa_Africa_RE_SP.pdf (accessed August. 15, 2023).
3. K. Horowitz, V. Ramasamy, J. Macknick, and R. Margolis, "Capital costs for dual-use photovoltaic installations: 2020 benchmark for ground-mounted PV systems with pollinator-friendly vegetation, grazing, and crops", *NREL*, 2020. doi:10.2172/1756713
4. A.C. Brent, N. Chapman, and I.H. de Kock, "Agrivoltaic systems: Potential opportunities for South Africa, *AgriVoltaics*, Daegu, South Korea, 2023.
5. P. Juillion, G. Lopez, *et al.*, "Shading apple trees with an agrivoltaic system: Impact on water relations, leaf morphophysiological characteristics and yield determinants", *SSRN Electronic Journal*, Sep. 2022. doi:10.2139/ssrn.4045895
6. Ilana Newman "Agrivoltaics Offer Dual Use on Land Used for Solar Energy Development", https://dailyyonder.com/agrovoltaics-offer-dual-use-on-land-used-for-solar-energy-development/2023/07/19/ (accessed Aug. 17, 2023).
7. Sun'Agri, "Arboriculture: La Pugere", https://sunagri.fr/en/project/the-la-pugere-experimental-station/ (accessed Aug. 17, 2023).
8. A. Pandarum, ""Price parity" of solar PV with storage?", Ameu, https://www.ameu.co.za/Price_Parity_of_Solar_PV_with_Storage_-_A_Pandarum.pdf (accessed Aug. 6, 2023).
9. A. Vaughan, A.C. Brent, M. Fitzgerald, J. Kueppers, and E. Wright, "Agrivoltaics: Integrating solar energy generation with livestock farming in Canterbury", Our Land and Water National Science Challenge, AgResearch, Aotearoa New Zealand, 2023.
10. EnergyTech Store, "Canadian solar panel 455W super high power mono perc hiku", https://energytechstore.co.za/canadian-solar-panel-455w-mono-perc-hiku/ (accessed Aug. 6, 2023).
11. SMA Solar Technology AG, "Solar inverters", https://www.sma.de/en/products/solar-inverters (accessed Aug. 6, 2023).
12. Power Technology, "Jasper Solar Photovoltaic Power Plant", https://www.power-technology.com/projects/jasper-solar-photovoltaic-power-plant/ (accessed Aug. 3, 2023).
13. Power Technology, "Power plant profile: Solar capital De Aar 1, South Africa", https://www.power-technology.com/marketdata/power-plant-profile-solar-capital-de-aar-1-south-africa/ (accessed Aug. 3, 2023).
14. G. Di Francia, and P. Cupo, "A cost–benefit analysis for utility-scale agrivoltaic implementation in Italy", *Energies*, vol. 16, no. 7, p. 2991, 2023. doi:10.3390/en16072991
15. A. Agostini, M. Colauzzi, and S. Amaducci, "Innovative Agrivoltaic Systems to produce sustainable energy: An Economic and Environmental Assessment," *Applied Energy*, vol. 281, p. 116102, 2021. doi:10.1016/j.apenergy.2020.116102

16. S. Schindele, M. Trommsdorff, *et al.*, “Implementation of agrophotovoltaics: Techno-economic analysis of the price-performance ratio and its policy implications”, *Applied Energy*, vol. 265, p. 114737, 2020. doi:10.1016/j.apenergy.2020.114737
17. Solargis, “Solar Irradiance Data”, https://solargis.com/ (accessed Aug. 3, 2023).
18. Eskom, “Historical average prices and increase”, https://www.eskom.co.za/distribution/wp-content/uploads/2022/04/Historical-average-prices-and-increase_v20210903_13h00_no-links_External.xlsx (accessed Aug. 3, 2023).

MODELLING THE INFLUENCE OF REFLECTED LIGHT ON THE REAR SIDE OF A BIFACIAL PV MODULE.

Mayur Rabadia[1] and Arnold J. Rix[2]

Department of Electrical and Electronic Engineering, Stellenbosch University, Stellenbosch, South Africa

E-Mail: [1]21556415@sun.ac.za, [2]rix@sun.ac.za

Abstract: This paper focuses on modelling the influence that the reflected light spectrum has on the rear side of a bifacial PV module. The front and rear-facing spectrums as well as current-voltage (I-V) curves for the front and rear side are measured for a bifacial PV module on two different surfaces (white gravel and grass). The five parameters of a single diode model are then extracted from the measured I-V curves and two new factors are proposed that can be used with the conventional way of modelling the rear side to improve yield forecasting. The results demonstrate that the photocurrent (I_{ph}) is the most influenced factor with varying reflected spectrums. Notably, on white gravel and grass surfaces, there is an improvement in modelling the I_{ph} parameter by 61.7% and 87.4%, respectively, compared to conventional methods. These results contribute significantly to the accurate modelling of the rear side of bifacial PV modules.

Keywords: Bifacial technology; rear-side modelling; reflected light spectrum; spectral response

1 Introduction

Over the last few years, bifacial photovoltaic (PV) modules have had a remarkable growth in the solar industry, due to the fact that the rear side can contribute 25% of the total power. It is predicted that the technology will account for 17% of the global PV module market in 2024 [1]. Therefore, with such a huge potential of the technology in the near future, accurately forecasting the yield is important for system balancing, but also to reduce the investment risk.

Plenty of research has been done on predicting the power output of monofacial PV modules using analytical and numerical approaches [2, 3, 4, 5]. These models predict the front-side power of a PV module accurately and can also be utilized for bifacial PV modelling. However, with inadequate research done on the rear side modelling, it is still difficult to accurately predict the total power contribution of a bifacial PV module. The authors in [6, 7] have recently carried out experiments on various surfaces and modelled the bifacial PV module as a double- or single-diode model connected in parallel. To account for the power contribution from the rear side of the module, they multiply the rear irradiance by the bifaciality factor provided in the module datasheet. The bifaciality factor introduces inaccuracies since the datasheet does not provide a fixed value but rather a range. To predict the reflected spectrum, the author in [8] proposes a bifacial spectral factor (BSF) that combines the front and rear spectral impact. This factor requires the determination of photon flux density which is a property that is not easily derived.

Nevertheless, the author in [9] rather came up with a different electrical model for bifacial PV modules. The model includes two current sources for the front and rear sides, controlled by two factors X_1 and X_2. These factors account for the contribution of bifaciality and errors caused by the I-V (X_1) and irradiance (X_2) measurements. The author in [10] proposed an electrical model with additional series resistance to compensate for the non-linearity of the bifacial PV systems and concluded by identifying the need for additional research on the effects from the rear side.

The conventional methods used to predict the power output of the rear side include employing either a constant albedo value of 0.2 or using a measured average albedo value for different surfaces. To calculate the measured albedo, a pyranometer is placed away from the module, then the irradiance is measured with the pyranometer facing up and then down. The albedo value is then calculated from these measurements and the average is obtained [11].

This research work aims to adapt the already existing analytical model in literature coupled with two new proposed factors (irradiance albedo modifier and spectral response modifier) to better predict the power output of the rear side. The reflected light spectrum is analysed and factors for two different surfaces are deduced that can be utilized with the measured rear spectrum for enhanced rear-side power prediction. Section 2 and 3 describe the experimental setup and the procedure to calculate the proposed factors. Section 4 discuss the results obtained when using the proposed factors compared to other rear-side modelling techniques, and finally, the work is concluded in Section 5.

2 Experimental setup

Figure 1 shows the practical setup of the LONGi Solar LR6-72BP-350M bifacial module with a module height of 1.3 m above ground. As it is noticeable, the setup was modified to have an increased height, to mitigate the effects of bypass diode activation for lower module heights due to the uneven distribution of reflected light on the rear side, which further makes the rear side modelling complex and reduces the power produced from the rear side. To measure the current-voltage (I-V) curves, a SOLAR I-Ve tracer is used, while for spectrum measurements, a Spectrafy SolarSIM-G spectrometer, with a spectral resolution of 1 nm in the range of 280 nm to 4000 nm is used. The electrical characteristics of the bifacial PV module according to the datasheet are shown in Table 1 [12]. The experiments were carried out on clear sky days and on two different surfaces shown in Fig. 2. The measured reflected light spectrum of these two surfaces varies significantly and this research delves deeper into this matter.

Fig. 1: Experimental setup

(a) White gravel pavement **(b) Grass**

Fig. 2: Types of surfaces

Table 1: Bifacial PV module's datasheet electrical characteristics at STC

Testing condition	Front	Rear
Maximum power - P_{mpp} $[W]$	350	263
Voltage at maximum power - V_{mpp} $[V]$	39.4	40.2
Current at maximum power - I_{mpp} $[A]$	8.89	6.54
Open circuit voltage - V_{oc} $[V]$	47.2	46.8
Short circuit current - I_{sc} $[A]$	9.39	7.19
Module efficiency [%]	17.8	13.3
Bifaciality	$\geq 75\%$	

3 Methodology

A significant emphasis is placed on accurately modelling the photocurrent, I_{ph}, parameter for the rear side. Even a minor absolute difference between the modelled and measured current on the rear side yields a substantial percentage of current error compared to the same absolute difference for the front side. I-V curves for front-facing up (FFU), rear-facing up (RFU) and rear-facing down (RFD), as well as the Sun's spectrum (front-facing spectrum) and the reflected spectrum (rear-facing spectrum), are measured for the two different surfaces. The FFU, RFU and RFD I-V curve traces were taken while the other side of the module is covered with a black plastic sheet. Using the *curve_fit* function in Python's *scipy.optimize* package (version 3.10.4), the five parameters of a single diode model shown in Equation (1) are extracted.

$$I = I_{ph} - I_s \left[\exp\left(\frac{V + R_s I}{a}\right) - 1\right] - \frac{V + R_s I}{R_{sh}} \quad (1)$$

where I_s is the diode saturation current, R_s and R_{sh} are the series and shunt resistance respectively, a is the modified ideality factor ($a = \frac{nN_s kT}{q}$), n is the ideality factor, N_s is the number of cells in series, $k = 1.38 \times 10^{-23} J/K$ and $q = 1.6 \times 10^{-19} C$ refer to the Boltzmann's constant and elementary electron charge respectively, while T is the cell temperature in Kelvin.

The parameters extracted for RFU, are then used to model the I-V curves for RFD. Thus, the only parameter required to accurately model the rear side is I_{ph}, which is greatly influenced by the reflected spectrum. Two new factors are proposed in this study and are integrated with the formula shown in Equation (2), to calculate I_{ph}.

$$I_{ph} = I_{ph,STC} \left(\frac{\alpha G}{G_{STC}}\right) [1 + \mu_{Isc}(T - T_{STC})] \quad (2)$$

where α is a correction factor that can be replaced with an irradiance albedo modifier or spectral response modifier. The albedo in POA or constant albedo is then used to calculate G to model the rear irradiance. μ_{Isc} is the temperature coefficient of I_{sc}, T is the module temperature, G is the rear irradiance measured, $G_{STC} = 1000\ W/m^2$ and $T_{STC} = 25\ ^\circ C$ is the irradiance and cell temperature at Standard Test Conditions (STC).

Equation (3) describes an accurate way to calculate the current using the spectrum. This equation is used to deduce the proposed factors.

$$I_{ph} = \int_{\lambda_0}^{\lambda_1} \text{SR} \times \text{Solar Spectrum} \times \text{A}\ \ d\lambda \quad (3)$$

where SR is the spectral response and A is the area of a cell, solar spectrum is the measured front-facing or rear-facing spectrum, λ_0, λ_1 is the range of wavelength of the spectrometer.

3.1 POA albedo

The plane of array (POA) albedo is measured in this research (ρ_{POA}), which differs from the conventional albedo discussed previously. The total irradiance on a collector surface (G) consists of direct beam irradiance (G_{direct}), diffuse irradiance ($G_{diffuse}$) and reflected irradiance ($G_{reflected}$).

$$G = G_{direct} + G_{diffuse} + G_{reflected} \tag{4}$$

The front and rear irradiance ($G_{\_f,meas}$ and $G_{\_r,meas}$) at POA can be determined using Equation (5) and (6), respectively [13].

$$G_{\_f,meas} = G_{direct}\left[cos\beta sin\Sigma cos(\phi_S - \phi_C) + sin\beta cos\Sigma\right] + \left[G_{direct}C\left(\frac{1+cos\Sigma}{2}\right)\right] \tag{5}$$

$$G_{\_r,meas} = \left[G_{direct}C\left(\frac{1-cos\Sigma}{2}\right)\right] + G_{direct}\rho(C+sin\beta)\left(\frac{1+cos\Sigma}{2}\right) \tag{6}$$

$$C = 0.095 + 0.04sin\left[\frac{360}{365}(n-100)\right] \tag{7}$$

where G_{direct} is the beam insolation at the Earth's surface, β is the altitude angle, ϕ_S and ϕ_C is the solar and collector azimuth angle respectively, Σ is the module tilt angle, ρ is the ground reflectance, C is the sky diffuse factor and n is the day number.

The reflected component has a minimum contribution to the front side, while the beam irradiation is not exposed on the rear side, thus, these components are neglected in the equations. For the rear side, the complement of the tilt angle is used viewing the rear side as if it were the front side.

The albedo at POA, graphically illustrated in Fig. 3, is used in this research for modelling the rear side and it is calculated using Equation (8).

$$\rho_{POA} = \frac{G_{\_r,meas}}{G_{\_f,meas}} \tag{8}$$

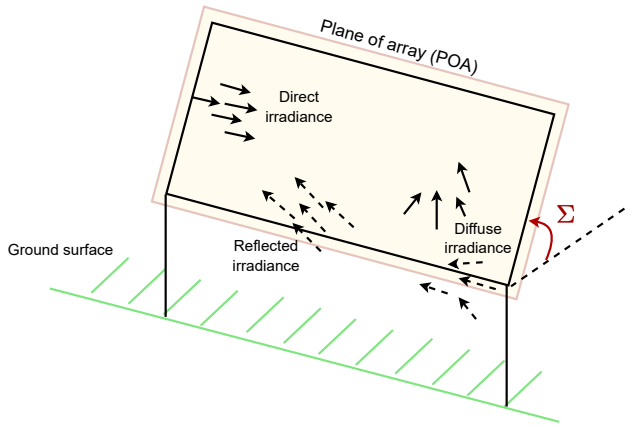

Fig. 3: Measuring albedo at POA

3.2 Irradiance albedo modifier

The irradiance albedo modifier is derived by scaling the front-facing spectrum with the reference SR of the cell technology. The reference SR is the scaled SR such that, $I_{ph,calc}$ using Equation (3) is equal to the $I_{sc,meas}$ for FFU. The irradiance albedo modifier can be calculated as follows:

1. Calculate the current ($I_{ph,calc}$) using Equation (3) with the measured rear-facing spectrum and reference SR. Compare the current with the measured current ($I_{sc,meas}$) for RFD.
2. Scale the reference SR until the error between $I_{ph,calc}$ and $I_{sc,meas}$ is at a minimum. When the error is achieved, this scaled SR is what will be used for the rest of the procedure.
3. Note down the measured total rear-facing irradiance. $G_{\_r,meas}$ is equal to the area under the measured rear spectrum.
4. Using the measured front-facing spectrum, calculate the current ($I_{ph,calc}$) using Equation (3) with the scaled SR obtained in step 2. Compare the current with the measured current ($I_{sc,meas}$) for RFD.
5. Scale the front-facing spectrum until the error between $I_{ph,calc}$ and $I_{ph,meas}$ is at a minimum. When the error is achieved, note down the area under the scaled front-facing spectrum, which will give the total front-facing irradiance ($G_{\_f,scaled}$).
6. Determine the irradiance albedo modifier by calculating the ratio between $G_{\_f,scaled}$ and $G_{\_r,meas}$

The above procedure can be repeated for several experiments and the average value of the irradiance albedo modifier for different surfaces can be calculated using Equation (9).

$$\text{Irradiance albedo modifier} = \frac{G_{\_f,scaled}}{G_{\_r,meas}} \tag{9}$$

The irradiance albedo modifier accounts for the mismatch in the modelling, due to the different shapes of front and rear-facing solar spectrums, that is used as a single irradiance value. Therefore, this factor corrects the POA albedo discussed in the previous section, as shown in Equation (10).

$$G_{f,scaled} = \text{Irradiance albedo modifier} \times \rho_{POA} \times G_{f,meas} \tag{10}$$

3.3 Spectral response modifier

The spectral response modifier is derived by scaling the reference SR of the cell technology with the front-facing and different rear-facing spectrums. To calculate this factor the SR of the cell technology is scaled because the solar spectrum is measured and the area of a cell is constant. The spectral response modifier can be calculated as follows:

1. Calculate the current ($I_{ph,calc}$) using Equation (3) with front-facing spectrum and reference SR. Compare the current with the measured current ($I_{sc,meas}$) for RFU.

2. Scale the reference SR until the error between $I_{ph,calc}$ and $I_{sc,meas}$ is at a minimum. When the error is achieved, note the scaling factor (k_{RFU}), by which the reference SR was scaled. This can be mathematically represented as shown in Equation (11).

$$I_{sc,RFU} = \int_{\lambda_0}^{\lambda_1} k_{RFU} \mathrm{SR_{ref}} \times \text{Solar Spectrum}_{\text{front}} \times \mathrm{A}\ d\lambda \tag{11}$$

3. Repeat steps 1 and 2, for RFD on different surfaces with respective measured rear-facing spectrum. Note the scaling factors for different surfaces (k_{RFD1}, k_{RFD2}). This can be mathematically represented as shown in Equation (12)

$$I_{sc,RFD} = \int_{\lambda_0}^{\lambda_1} k_{RFD} \mathrm{SR_{ref}} \times \text{Solar Spectrum}_{\text{rear}} \times \mathrm{A}\ d\lambda \tag{12}$$

The above procedure can be repeated for several experiments and an average value of the scaling factors (k_{avg}) can be obtained. The spectral response modifier can now be calculated for different surfaces as shown in Equation (13). This factor considers the spectral information of the irradiance and SR of the cell technology.

$$\text{Spectral response modifier}_{(i)} = \frac{k_{RFD,avg(i)}}{k_{RFU,avg}} \tag{13}$$

where i denotes the different number of surfaces. This spectral response modifier can then be used in Equation (2) to calculate the contribution of I_{ph} from the rear side.

3.4 Accuracy indicators

For this paper, about 20 experiments were carried out on two different surfaces. The current error between the measured and modelled, root mean square error (RMSE) and mean bias error (MBE) shown in Equation (14), (15) and (16) respectively, are the metrics used to validate and compare different ways of modelling the contribution of I_{ph} from the rear side. The RMSE value provides insight into the accuracy of the measured data when compared to the corresponding predicted data, while MBE provides information regarding under- or overestimation of the predicted data when compared to the measured data.

$$\text{Error}(\%) = \frac{I_{mod} - I_{meas}}{I_{meas}} \times 100 \tag{14}$$

$$\text{RMSE} = \sqrt{\frac{\sum_{i=1}^{N}(p_i - o_i)^2}{N}} \tag{15}$$

$$\text{MBE} = \frac{\sum_{i=1}^{N}(p_i - o_i)}{N} \tag{16}$$

where p_i and o_i are the predicted and measured values, respectively, N is the data set size.

4 Results and discussion

In this section, the results obtained from modelling the contribution of I_{ph} for the rear side, with different α factors used in Equation (2) are discussed. Fig. 4 shows an internationally recognized spectrum at STC according to the American Society for Testing and Materials (ASTM G-173) and the International Electrotechnical Commission (IEC 60904-03) [14]. The ASTM G-173 and IEC 60904-03 spectrums are almost similar, and therefore the ASTM G-173 spectrum is compared to a spectrum measured by the spectrometer used for the experiments. It can be seen that there is a close resemblance between the measured spectrum and the ASTM spectrum. The slight difference can be explained because the measured spectrum has a total irradiance of 1003 W/m^2 compared to STC. Therefore, all the results rely on spectrum measurements that conform to international standards.

4.1 POA albedo

Figure 5 shows the varying albedo measured at POA for different surfaces. POA albedo was calculated using Equation (8). The average value of the measured albedo is then used in Equation (2) to model I_{ph} for the rear side. The average albedo on white gravel and grass was 0.154 and 0.137 respectively.

4.2 Irradiance albedo modifier

Figure 6 shows the scaled front-facing spectrum so that when the SR is overlaid on the scaled front-facing spectrum, $I_{ph,calc}$ is equal to the measured current for RFD on two different surfaces at a specific time stamp. The irradiance albedo modifier of a surface is then calculated using Equation (9). Fig. 7 shows the variation of the irradiance albedo modifier on different surfaces. The average irradiance albedo modifier on a white gravel surface is 0.9976, while on grass it is 1.0732.

These irradiance albedo modifiers are then used in Equation (2) to model the contribution of I_{ph} from the rear side. As ex-

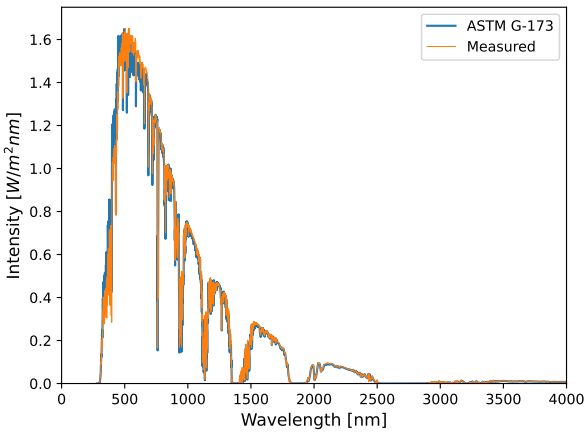

Fig. 4: Meas vs ASTM spectrum

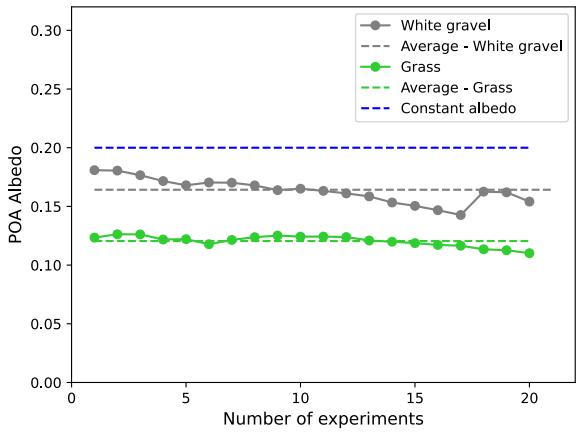

Fig. 5: Measured POA albedo vs constant albedo

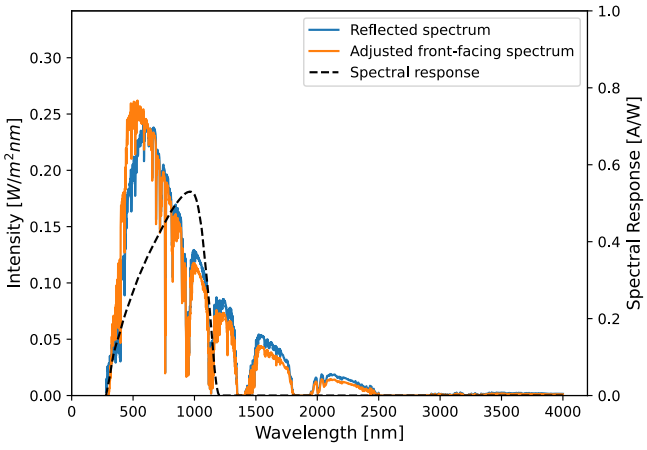

(a) White gravel pavement

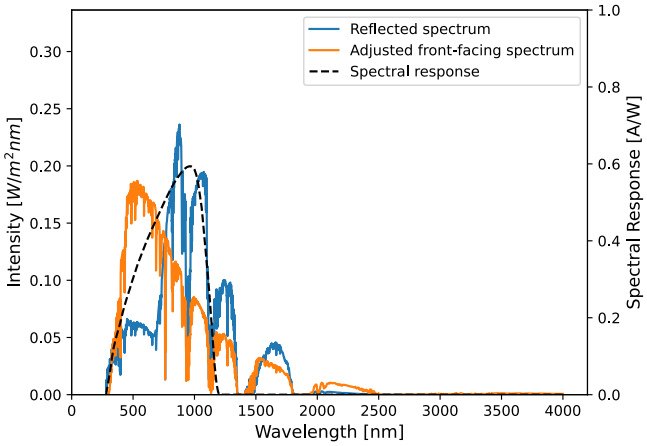

(b) Grass

Fig. 6: Illustration of irradiance albedo modifier calculation utilizing scaled front-facing and rear-facing spectrum for different surfaces.

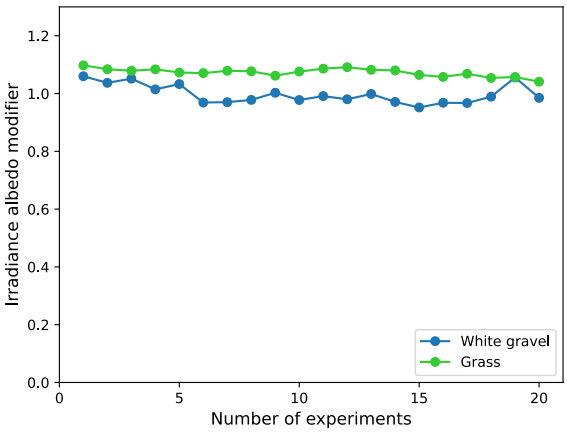

Fig. 7: Irradiance albedo modifier over different surfaces

pected, the ratio of $G_{\_f,scaled}$ and $G_{\_r,meas}$ for the white gravel surface is closer to 1 than the grass surface, and this is due to the reflected spectrum of the white gravel surface having a shape similar to the front-facing spectrum, thus not much irradiance correction is done by the irradiance albedo modifier, while the reflected spectrum of the grass surface is much more a red-shifted spectrum and therefore the irradiance albedo modifier accounts for the mismatch in irradiance, due to differences in the shape of the spectrum.

4.3 Spectral response modifier

Figure 8 shows the variation in the scaling factors (k_{RFU} and k_{RFD}) for RFU and RFD on different surfaces, respectively. The average values of these scaling factors are summarized in Table 2. The spectral response modifier for the two different surfaces is then calculated using Equation (17) and (18). These spectral response modifiers are then used in Equation (2) to calculate the contribution of I_{ph} from the rear side.

$$\text{Spectral response modifier}_{(\text{White gravel})} = \frac{0.745}{0.7918} = 0.9409 \quad (17)$$

$$\text{Spectral response modifier}_{(\text{Grass})} = \frac{0.8348}{0.7918} = 1.0543 \quad (18)$$

4.4 Comparison of different α values

Various ways of modelling the rear side's current contribution are summarized in Table 3. For each method, the current error,

Table 2: Average value for scaling factor k

Experiment	k value
RFU	0.7918
RFD (White gravel)	0.745
RFD (Grass)	0.8348

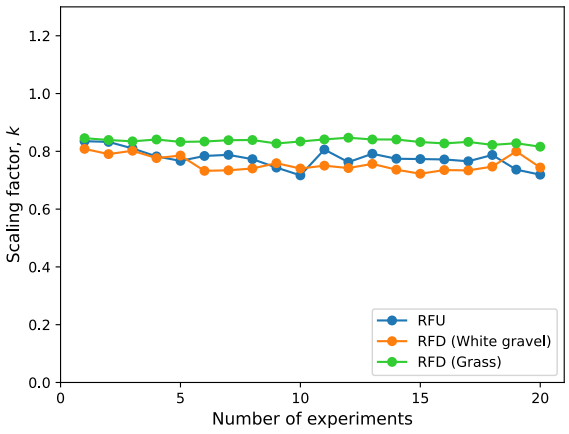

Fig. 8: Scaling factors (k) for different experiments

RMSE and MBE are calculated to validate the model's accuracy. Fig. 9 shows the current error between the modelled and measured I_{sc}. A positive current error and MBE mean that the model overestimates the measured current, while a negative error indicates an underestimation. To quantify the errors, Table 4 shows the RMSE and MBE values.

It is evident that using a constant albedo of 0.2 can lead to higher inaccuracies of modelling the rear side current. While in Fig. 9 it can be observed that when the current is modelled using the irradiance albedo modifier and the measured rear irradiance, the current error for the white gravel surface is almost similar. This is because both the scaled front and rear-facing spectrum look similar, thus not much scaling is required when calculating the irradiance albedo modifier. However, for the grass surface, since the front and rear-facing spectrums are different, the irradiance albedo modifier yields an accurate current prediction than the measured irradiance, because the irradiance albedo modifier accounts for the difference in the irradiance due to different shapes of front and rear- facing spectrums.

From the two proposed factors, the spectral response modifier gives the most accurate results with RMSE of 0.0339 A and 0.0112 A for white gravel and grass surfaces, respectively. It also overestimates the current by only 0.0201 A and 0.0021 A on white gravel and grass surfaces, respectively. Neglecting the shape of the reflected spectrum is equivalent to using the measured rear irradiance when modelling the current contribution from the rear side. This can be observed in Fig. 6b, where the two spectrums have different shapes but the same irradiance values. However, the spectral response modifier considers the spectral information of the spectrum, and the results show that considering the spectrum using the proposed spectral response modifier can improve the modelling accuracy by 61.7% and 87.4% on white gravel and grass surfaces, respectively. There is a significant improvement in the model even for a slightly different reflected spectrum from the front-facing spectrum (white gravel surface). These values are significantly

Table 3: Different ways of modelling the rear-side current I_{ph}

Method	α factor value
Spectral response modifier	0.9409 (White gravel) 1.0543 (Grass)
Irradiance albedo modifier	0.9976 (White gravel) 1.0732 (Grass)
POA albedo	0.154 (White gravel) 0.137 (Grass)
Constant albedo	0.2
Measured rear irradiance	1

Table 4: RMSE and MBE for different ways of modelling rear-side current I_{ph}

	White gravel		Grass	
Method	RMSE [A]	MBE [A]	RMSE [A]	MBE [A]
Spectral response modifier	0.0339	0.0201	0.0112	0.0021
Irradiance albedo modifier	0.0862	0.0819	0.0312	-0.0303
POA albedo	0.0827	0.0266	0.0327	0.0147
Constant albedo	0.2556	-0.2455	0.1207	-0.1169
Measured rear irradiance	0.0886	0.0845	0.0890	-0.0883

lower than the other factors used to model the rear side current. The spectral response modifier shows the significance of taking the spectral information into account and the effect it has on the rear side modelling of a bifacial PV module.

5 Conclusion

In this paper, the methodology with practical experiments is presented to model the current contribution of the rear side. Two new factors (spectral response modifier and irradiance albedo modifier) are introduced and compared with other factors widely used for modeling I_{ph}. Based on the analysis and findings presented in the paper, the following conclusions can be drawn.

The irradiance albedo modifier is calculated by scaling the front-facing spectrum, while the spectral response modifier is calculated by scaling the SR of the cell technology. These factors are then coupled with a well-established equation in the

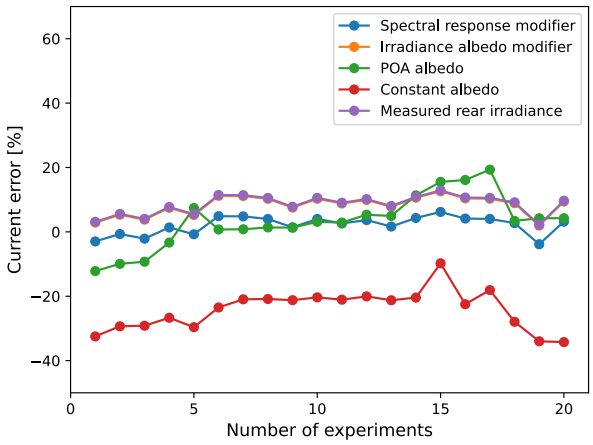

(a) White gravel pavement

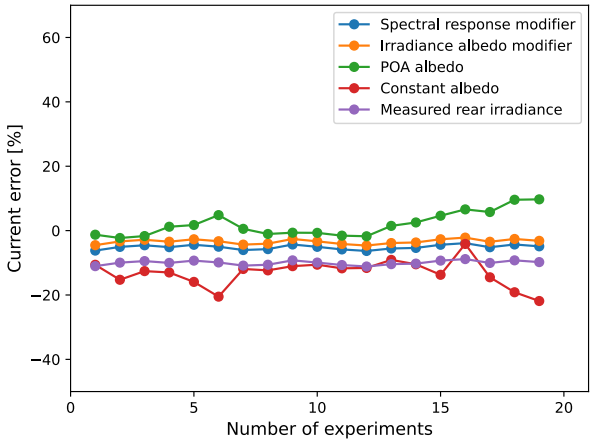

(b) Grass

Fig. 9: Current error of various α factors on different surfaces.

literature that can model the I_{ph} parameter of a single diode model. Along with the proposed factors, three other methods (POA albedo, constant albedo, and measured rear irradiance) are used to model the current contribution from the rear side.

The results show that the spectral response modifier produces the most accurate way to model the I_{ph} parameter with an improvement of 61.7% and 87.4% on white gravel and grass surfaces, respectively, compared to the other methods used. The primary emphasis resides in the spectral response modifier producing accurate results over using measured irradiance value. This suggests that the shape of the reflected spectrum does influence the rear side modelling of a bifacial PV module. The proposed spectral response modifier does take into account the shape of the reflected spectrum, as compared to the measured rear irradiance used, which does not take into consideration the shape of the spectrum.

However, more experiments need to be conducted on different surfaces that exhibit colors (except white and black surfaces). This would ensure that the reflected spectrum is much different than the front-facing spectrum.

References

[1] L. Rodríguez, "Bifacial modules: the future of solar pv? a comprehensive guide on financial and technical performance of the next hot thing in solar," January 2022.

[2] F. J. Toledo, J. M. Blanes, and V. Galiano, "Two-step linear least-squares method for photovoltaic single-diode model parameters extraction," *IEEE Transactions on Industrial Electronics*, vol. 65, no. 8, pp. 6301–6308, 2018.

[3] A. Senturk and R. Eke, "A new method to simulate photovoltaic performance of crystalline silicon photovoltaic modules based on datasheet values," *Renewable Energy*, vol. 103, pp. 58–69, 2017.

[4] W. Long, T. Wu, J. Jiao, M. Tang, and M. Xu, "Refraction-learning-based whale optimization algorithm for high-dimensional problems and parameter estimation of pv model," *Engineering Applications of Artificial Intelligence*, vol. 89, p. 103457, 2020.

[5] B. Nayak, A. Mohapatra, and K. B. Mohanty, "Parameter estimation of single diode pv module based on gwo algorithm," *Renewable Energy Focus*, vol. 30, pp. 1–12, 2019.

[6] J. Louw and A. Rix, "Modelling and simulation of bifacial pv modules by implementing the ray tracing technique," Master's thesis, Stellenbosch, South Africa, 2020. URL: http://hdl.handle.net/10019.1/107857.

[7] K. Ganesan, D. P. Winston, S. Sugumar, and S. Jegan, "Performance analysis of n-type pert bifacial solar pv module under diverse albedo conditions," *Solar Energy*, vol. 252, pp. 81–90, 2023.

[8] E. Mouhib, P. M. Rodrigo, L. Micheli, E. F. Fernández, and F. Almonacid, "Quantifying the rear and front long-term spectral impact on bifacial photovoltaic modules," *Solar Energy*, vol. 247, pp. 202–213, 2022.

[9] D. Hong, J. Ma, K. L. Man, H. Wen, and P. Wong, "Prediction of i-v characteristics for bifacial pv modules via an alpha-beta single double-diode model," in *2022 IEEE Energy Conversion Congress and Exposition (ECCE)*, pp. 1–5, 2022.

[10] E. M. Ahmed, M. Aly, M. Mostafa, H. Rezk, H. Alnuman, and W. Alhosaini, "An accurate model for bifacial photovoltaic panels," *Sustainability*, vol. 15, no. 1, 2023.

[11] M. Chiodetti, A. Lindsay, P. Dupeyrat, D. Binesti, E. Lutun, R. Khalid, and S. Mousel², "Pv bifacial yield simulation with a variable albedo model," in ., 06 2016.

[12] LONGi Solar, "Longi lr6-72bp 350-370w solar panel datasheet," 2018.

[13] G. M. Masters, *Renewable And Efficient Electric Power Systems*. hoboken, New Jersey: John Wiley and Sons, Inc., second ed., 2013.

[14] D. Meyers, "Review of consensus standard spectra for flat plate and concentrating photovoltaic performance," September 2011.

CURRENT-VOLTAGE CHARACTERIZATION OF BIFACIAL MODULE WITH A SINGLE LIGHT SOURCE SOLAR SIMULATOR

S.D.E. Ndzonda[1], J.L. Crozier McCleland[1], R.M. Dix-Peek[1*], M. Vumbugwa[1], E.E. van Dyk[1]

[1] Nelson Mandela University, University Way, P. O. Box 77000, Gqeberha, 6031, South Africa; Phone: +27415042233; Email: s214353052@mandela.ac.za

Abstract

Bifacial photovoltaic (bPV) modules are designed to absorb light on both the front and rear surfaces to generate electricity, and as a result bPV modules have a better yield and can improve the Levelized Cost of Electricity (LCOE) of photovoltaic (PV) installations. The factor by which the output of the bifacial module is increased compared with a monofacial PV module is called the rear irradiance driven Power Gain. The two surfaces of a bPV module differ in collection efficiency and this difference depends on the cell technology used in the module. The electrical parameters of each surface of a bPV module are measured at standard testing conditions (STC) as explained in the technical standard IEC TS 60904-1-2: 2019. These parameters included Maximum Power (P_{max}), Short-circuit Current (I_{SC}) Open circuit voltage (V_{OC}) and the ratios of these parameters give the bifaciality coefficients ($\varphi_{P_{max}}$, $\varphi_{I_{SC}}$, $\varphi_{V_{OC}}$) of a bPV module. These measurements are made indoors using an indoor solar simulator and outdoors using a portable I-V curve tracer. The results are comparable given the associated measurement uncertainty of each method. This paper outlines the advantages and disadvantages of each method and critically examines the limits and challenge of each method.

Keywords: Bifacial photovoltaic module; bifacial module characterisation; rear irradiance driven power gain yield

1. Introduction

Photovoltaic (PV) technology converts sunlight directly into electricity using the photovoltaic effect, and produces no harmful by-products during operation. The electricity in PV systems is generated by absorption of light by PV cells, which is "a specialised semiconductor diode with a large barrier layer exposed to light" [1]–[4]. The junction separating the p-type and n-type layers of the diode is much larger compared with the thickness of the n- and p-type layers, and the first (emitter) layer in the path of light is thinner than the second (base) layer to allow more light to reach the base layer. The type of the base layer in a PV cell (whether n-type or p-type) is used to indicate if a cell is n-type or p-type [2]. Electrical contacts are printed on the front and rear surfaces of PV cells to conduct the generated current to power external circuits. Fig. 1 is a simplified diagram comparing the structures of a standard (monofacial) p-type PV cell and a bifacial PV cell [5]. In the monofacial PV cell the rear electric contact covers the entire back surface of the cell, while in the bifacial PV cell the rear electrical contact is exactly like the front surface contact. The front electric contacts are in a grid pattern to allow light to enter the cell [5]. The anti-reflection coating (ARC) reduces the amount of light reflected at the surface of the PV cell. The n-type layer has free electrons in the crystal, and in the p-type layer the free charge carriers are holes due to doping with group III elements [3]. The depletion layer forms when the electrons and holes recombine to establish a region devoid of free charge carriers. The depletion layer extends into the n-type and p-type layer and is important to the operation of the PV cell due to the potential barrier that is established there.[3]

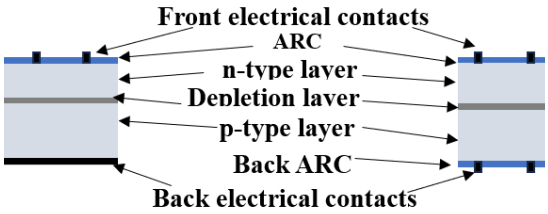

Fig. 1: A simplified diagram of a standard PV (p-type) cell compared to a bifacial PV cell [5].

The efficiency of PV cells is between 10% and 33% depending on cell technology [3]. PV technology researchers always seek ways to improve efficiency of PV cells, and one way of making high efficiency cells is by making bifacial PV cells that absorb light on both surfaces by having grid-type electric contacts on the rear surfaces like on the front surface[6] - [7]. There exists different architectures of bifacial PV cells. The p-type cell architectures are: passivated emitter rear contact (PERC), passivated emitter rear locally-diffused (PERL), double-sided buried contact solar cell (DSBCSC) and the n-type solar cells structures are: passivated emitter rear totally diffused (PERT), heterojunction with intrinsic thin layer (HIT), interdigitated back contact (IBC) and tunnel oxidated passivated contact

*Current affiliation: Eversci Pty Ltd, ross@eversci.com

(TOPCon). The two bifacial PV (bPV) cell surfaces generate current using the same junction.

In a bifacial module the two surfaces do not generate current with the same efficiency due to the difference in dopant concentration of the emitter and base layers, their different lengths from the depletion zone and the possibility the different application of the anti-reflecting coating on the front and rear surfaces [8].

The bifaciality coefficient is generally higher in n-type cells than in p-type cells. For PERC and DSBCSC the bifaciality coefficient is in the range (70 – 80%), for PERL (80 – 85%), and for n-type cells IBC (70 – 80%), PERT and TOPCon (80 – 85%), and HIT (95 – 100%) [7].

Fig. 2 is an equivalent circuit diagram for a bifacial PV cell: the front surface and rear surface (indicated by subscripts ***f*** and ***r*** respectively) are connected in parallel. Each surface of a bifacial cell generates current proportional to the incident irradiation using the same junction.

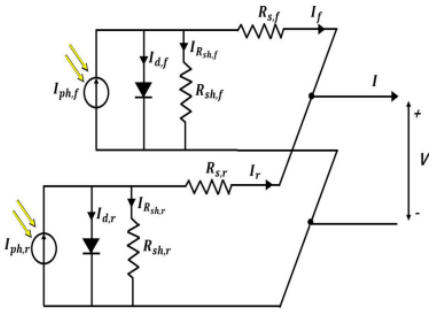

Fig. 2: Equivalent circuit diagram for a bifacial PV cell [10].

The short-circuit current (I_{SC}) and open-circuit voltage (V_{OC}) of bifacial modules are given by equation (1) and equation (2) [7]:

$$I_{SC} = I_{SC,r} + I_{SC,f} \tag{1}$$

$$V_{OC} = V_{OC,f} + \frac{V_{OC,r} - V_{OC,f} \ln\left(\frac{I_{SC,f} + I_{SC,r}}{I_{SC,f}}\right)}{\ln\left(I_{SC,r} / I_{SC,f}\right)} \tag{2}$$

PV cells typically have open-circuit voltage of about 0.5 V, to obtain a desired electrical output multiple PV cells can be connected either in series or parallel. Cells connected in series will sum the voltages of all the cells, but the current of the connected cells will equal current of a cell with the lowest current. For cells in parallel the currents will add but the total voltage will equal voltage of a single cell.

The ratios of the electrical parameters of the rear surface to the front surface of bifacial modules are called bifaciality coefficients (φ). The bifaciality coefficients of I_{SC} ($\varphi_{I_{SC}}$), V_{OC} ($\varphi_{V_{OC}}$) and of maximum power P_{max} ($\varphi_{P_{max}}$) are given by equations (3) – (5), respectively:

$$\varphi_{I_{SC}}(\%) = \frac{I_{SC,r}}{I_{SC,f}} \times 100 \tag{3}$$

$$\varphi_{P_{max}}(\%) = \frac{P_{max,r}}{P_{max,f}} \times 100 \tag{4}$$

$$\varphi_{V_{OC}}(\%) = \frac{V_{OC,r}}{V_{OC,f}} \times 100 \tag{5}$$

The bifaciality coefficient φ of a bifacial PV module is then given by the minimum of the power and current coefficients, equation (6):

$$\varphi = \min\{\varphi_{I_{SC}}, \varphi_{P_{max}}\} \tag{6}$$

The standardised method for characterization of bPV is covered in the International Electrochemical Commission (IEC) TS 60904-1-2 (Edition 1.0 2019-01) based on the work of previous research [9]–[15]. The measurement of the Current-Voltage (IV) characteristic curve of bPV modules can be performed indoors in two ways, using a single light source to characterize each face individually or with two light sources, one illuminating each surface simultaneously. In both cases characterization is done at standard testing conditions (STC) of irradiance intensity of 1000 W·m^{-2}, module temperature of 25 °C and air mass of 1.5. During characterization with a single light source, the irradiance on the second surface not being characterised does not exceed 3 W·m^{-2}. The setup for double side illumination is more complex and expensive. The IEC TS 60904-1-2 also allows for the measurement of the IV curves outdoors in natural sunlight [7]. The power rating of bifacial PV modules is based on the performance of the front surface only. The contribution of the rear surface to the total electrical power generation for each unit of rear irradiance is expressed by a parameter called the rear irradiance driven power gain yield, $BiFi$.

2. Methodology

The aim of this study was to characterize bifacial PV modules by measuring the electrical performance at different irradiance levels. The measured electrical parameters are then used to determine bifaciality coefficients. The BiFi of one bifacial module is also determined. The modules used in this experiment are LONGi bifacial modules (LR4-72H BD-430M), p-type monocrystalline PERC 430 W peak modules. The specification of the module is given in Table 1.

Table 1: Module specification for the LONGi modules used in the experiment.

	LR4-72H BD-430M
P_{max} (W ± 3%)	430
I_{sc} (A)	11.09
V_{oc} (V)	49.6
I_{mpp} (A)	10.44
V_{mpp} (V)	41.2
Efficiency (%)	19.2
Bifaciality: (%)	≥70

A module was tested by PVinsight, the PV testing laboratory based in the Gqeberha and at Fraunhofer-ISE in Freiburg, Germany. The purpose of this was to use this module as a reference module for the solar simulator calibration.

2.1. Procedure – Measurements at Standard Test Conditions (STC)

For the indoor characterization, a full spectrum long pulse A+A+A+ LED flasher was used. The rating of the solar simulator means that the spectrum (300-1200 nm) meets Class A+ according to IEC6064-9 Ed3, with spectral coverage 94% (± 3%) and spectral deviation 43% (± 3%). The Long-term instability is less than ± 1% and the non-uniformity of the light source is less than ± 1%, meeting Class A+ according to IEC6064-9 Ed3. The technical specifications of the solar simulator can be found in [16]. The irradiance range of the simulator is 200 - 1000 $W \cdot m^{-2}$ configurable in steps of 200 $W \cdot m^{-2}$. Current software limitations prevent smaller irradiance level increments and measurements at irradiances above 1000 $W \cdot m^{-2}$ were not possible at the time of the tests.

The testing procedure for a single surface of a bifacial module using a single light source is illustrated in Fig. 3. A non-reflective surface and baffles are used to ensure that no more than 3 $W \cdot m^{-2}$ of stray irradiance reaches the other surface not under test. The procedure is repeated on both sides of the module.

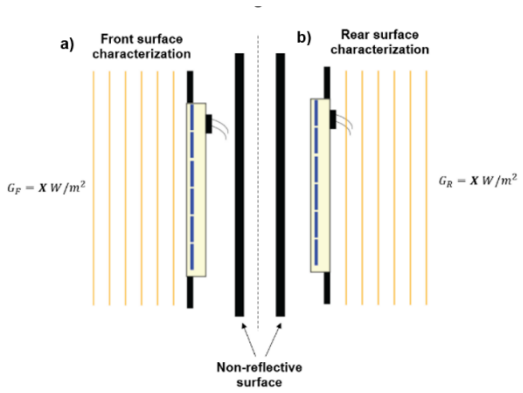

Fig. 3: The setup for characterization of a bifacial PV module with a single light source. The non-reflective surface behind the module prevents reflection of stray light to the surface not being characterized [19]. a) front surface illumination , and b) rear surface illumination

The MBJ Mobile lab 5.0 simulator is shown in Fig. 4, with a bifacial module loaded for testing. In the image black foam sheets have been used underneath the module to ensure that there is no stray light on the surface not under test. The temperature of the module is measured using IR sensors mounted underneath the module. While the foam is in place the temperature of the module cannot be accurately measured so the module is temperature stabilised prior to test (25°C ± 2°C) and the system temperature reading are manually confirmed with a temperature sensor.

For I-V measurements the simulator will flash the module, records the measured electrical output, and corrects the data to STC measurements, according to IEC 60891 [17]. This process is repeated with the rear surface, though care must be taken to ensure the cabling does not create additional shading. In total, four modules were tested in the solar simulator.

Fig. 4: The solar simulator used for indoor characterization of bPV module, with a module loaded and ready to be tested.

The alternative to indoor measurements using a solar simulator is to test modules outdoors using an I-V curve tracer. A Solmetric PVA-1500V4 analyser was used. The modules were mounted on a mobile frame

to be able to move to different surfaces and also allowed to change the tilt angle. The irradiance is measured on the front surface using the Solmetric Irradiance sensor, which also measures module temperature and tilt angle. The rear irradiance was not measured. To ensure no stray incident light, a black cloth was laid on a cardboard to form a non-reflecting cover for the face not being measured. Fig 5 shows, a) the front and b) rear faces of the bifacial module used in the experiment, mounted on the frame while taking the measurements. While measuring the respective IV curves, the module is tilted with irradiance perpendicular to the module surface.

a) b)

Fig. 5: The setup for outdoor characterization of a) Front surface and b) rear surface of a bifacial PV module.

The PVA-1500V4 was used to record the IV characteristic curves, with multiple measurements obtained for each part of the experiment. The tilt was kept constant throughout the experiment, and the measurements were taken in quick succession to ensure near constant temperature and irradiance. The temperature was measured at the rear surface of the module, however, this does present challenges when measuring the complete (rear and front) module output as the temperature sensors (k-type thermocouples) can shade the rear surface cells and effect the results. The temperature sensors were positioned in ways to minimise this effect on the module results. However, in measuring the front side the effect of shading is not a concern. Covering of the back surface increases the rear surface temperature but provided the sensor is correctly applied the temperature corrections will account for this.

The procedure in testing standard IEC TS 60904-1-2 (2019-01)[18], for measuring individual face performance was adapted for outdoor testing of the bifacial module.

When testing the rear surface (Fig. 5b) it is important to ensure that the shading on rear surface is limited, the cabling should be clamped to prevent additional shading. In both indoor and outdoor measurements, the frame shades the back surface of the module, as indicated in Fig. 6.

Fig. 6: Challenge of module self-shading when characterizing the rear surface due to the module frame and module cables.

2.2. Procedure – Determination of Bifaciality and Rear Irradiance Power Gain (BiFi)

The Bifaciality coefficients of the modules are calculated using equations (3) – (6) from the measurements at STC.

The procedure for measuring the BiFi is described in IEC TS 60904-1-2: multiple low irradiance levels G_{r_i} are used to determine the equivalent irradiance $G_{E,r}$, equation (7), and φ is the bifaciality of the bifacial PV module.

$$G_{E,r}(G_r) = G_f + \varphi \cdot G_r \qquad (7)$$

The front surface of the bifacial PV module is characterized with the equivalent irradiances to measure maximum power P_{MAX}. The P_{MAX} is plotted as a function of the rear-side irradiance. The $BiFi$ is the slope of this plot.

The measurement of the rear irradiance driven power gain yield, $BiFi$, with a single light source is determined using the procedure outlined in IEC TS 60904-1-2 and requires equivalent irradiance levels $G_E > 1000\, W \cdot m^{-2}$. The equivalent irradiance G_E is calculated with equation (7), and the maximum power output at equivalent irradiance is measured on the front surface. These measurements were made by Fraunhofer and serve as a reference to the measurements made in this study. The solar simulator used in this study is limited in the irradiance levels that can be tested above $1000\, W \cdot m^{-2}$.

The power output for rear surface P_r measured at low irradiances can be added to the Power output of the front surface at STC to determine the Power output of the entire module, see equation (8). This is a simplified approach that can in implemented when there are limitations in the irradiance levels available to test modules.

$$P_{r+f_{STC}} = P_{f,STC} + P_{r,100} \qquad (8)$$

Now $P_{r+f_{STC}}$ is plotted against rear irradiance to determine $BiFi$.

The results for bifacial characterization using procedures given in IEC TS 60904-1-2 (2019) done at Fraunhofer are included to compare with the results of the adapted procedure for the determination of $BiFi$.

3. Results and Discussion

3.1. Single surface characterization

The results for the indoor and outdoor characterization of a bifacial PV module at STC are recorded in Table 2. The results are comparable when the measurement uncertainties are considered.

Table 2: The measured results for the characterization of the front and rear surfaces of a bifacial PV module.

	Indoor			Outdoor		
	Front			Front		
	Measured Value	±	*Uncertainty*	*Measured Value*	±	*Uncertainty*
$P_{max}(W)$	430.6	±	3.0%	428.29	±	5.45%
$I_{sc}(A)$	11.16	±	2.5 %	11.20	±	2.5%
$V_{oc}(V)$	49.15	±	0.7%	49.87	±	1.35%
$I_{mpp}(A)$	10.57	±	2.5 %	10.60	±	2.5%
$V_{mpp}(V)$	40.75	±	0.8%	40.41	±	1.35%

Fig. 7 shows the IV curves of the front surface of the modules for the indoor and outdoor measurements.

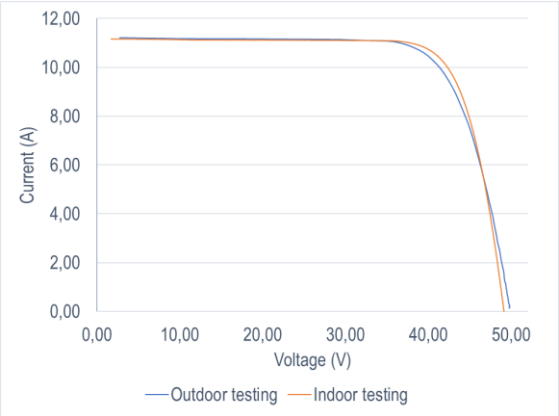

Fig. 7: The current-voltage measurements of the front face of the bifacial module measured indoor and outdoor corrected to STC.

The most notable deviation is the variation between the V_{OC} measurements. As V_{OC} is highly temperature dependant this could be attributed to the uncertainty in temperature measurements in both indoor and outdoor measurements.

The rear surface IV curve for irradiances from 200 to 1000 W·m^{-2} are shown in Fig. 8.

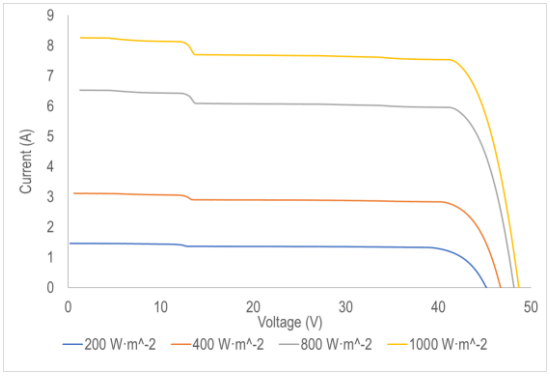

Fig. 8: The rear surface IV curve measured indoors at irradiances from 200 - 1000 W·m^{-2}.

The bump in the curves is attributed to the shading from the frame and occurs at the same voltage on the curves at the different irradiances. At lower irradiances the effect of the rear surface shading is less significant, indicating that in normal operation the losses due to frame shading will be small.

3.2. Determination of Bifaciality

The Bifaciality coefficients are calculated using the indoor measurements and the equations (3) – (5). The results are given in Table 3. The average of multiple modules of the same type is taken as this is the recommendation of IEC TS 60904-1-2. This average is compared with the result reported by Fraunhofer for a single module. The results are comparable. NMU (Nelson Mandela University) determined a bifaciality of 73.6%, and 74.1% at Fraunhofer ISE, which is within the expected range for PERC modules [7].

Table 3: The calculated Bifaciality coeffecients for a sample of identical modules measured at STC compared with the same module type measured at Fraunhofer.

	MODULE				MEAN	FRAUN-HOFER
	1	2	3	4		
$\varphi_{I_{SC}}$	75.1%	75.9%	77.3%	75.6%	76.0%	74.8%
$\varphi_{P_{ma}}$	73.1%	73.6%	74.3%	73.4%	73.6%	74.1%
$\varphi_{V_{OC}}$	99.0%	99.0%	99.1%	98.9%	99.0%	98.9%
φ	73.1%	73.6%	74.3%	73.4%	73.6%	74.1%

To determine the rear irradiance driven power gain yield, $BiFi$, using the standard procedure, the results measured at Fraunhofer were used with low rear

irradiance levels of 100 W·m^{-2} and 200 W·m^{-2} and bifaciality coefficient of 74.1% are input into equation (7), (with equivalent irradiances of 1000 W·m^{-2}, 1078 W·m^{-2} and 1148 W·m^{-2} respectively). The irradiance levels used to determine the BiFi for the calculated bifaciality coefficient are given in Table 4. The measured maximum power at these equivalent irradiances is then plotted against the rear irradiances in Fig. 9. The gradient equals the $BiFi$ of the module, which is 0.314 as summarised in Table 5.

Table 4: The calculated Pmax for the effective irradiance measurements for a sample measured at NMU.

φ [%]	G_r [W·m^{-2}]	G_E [W·m^{-2}]	P_r [W]	$P_{MAX,STC}$ + P_r[W]
74.1	0	1000		433.3
	100	1074.1		
	200	1148.2	52.4	485.70
	400	1296.4	116.3	549.60

With the adapted procedure, the rear surface was measured at irradiance levels G_r of 200 W·m^{-2} and 400 W·m^{-2}. By adding the maximum power output of the front face $P_{STC,f}$ to the maximum power measured on the rear surface P_r at G_r (equation (8)), the effective power output can be determined with the front surface receiving 1000 W·m^{-2} and the rear surface 200 W·m^{-2} or 400 W·m^{-2}. Table 4 indicates the calculation of this effective power output. These measurements are plotted on same axis with measurements of the equivalent power of front surface. The two sets of measurements are plotted in Fig. 9. The slope of the graph equals the BiFi of the module is 0.29.

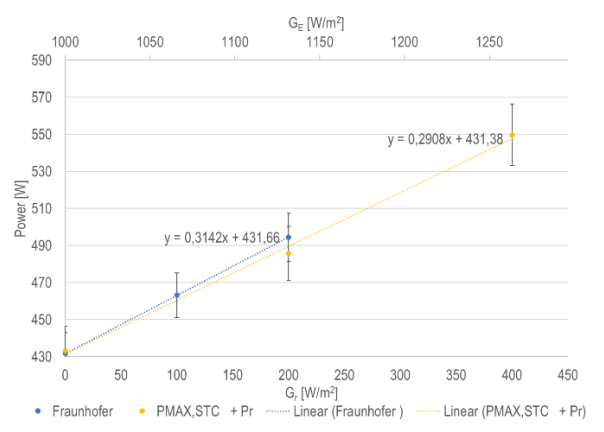

Fig. 9: P_{MAX} plotted as a function of rear irradiance in order to calculate the rear irradiance-driven power gain yield, $BiFi$, measured on bifacial modules at NMU and at Fraunhofer ISE.

The $BiFi$ calculated with the non-standard procedure is 10% less than the $BiFi$ measured at Fraunhofer ISE, which has an uncertainty of 21%.

Conclusion

The front and rear surface measured power output can be measured individually by isolating the surface under test. This process allows the bifaciality coefficients to be measured and compared with those stated by the manufacturer. This process is time consuming and can only be done on a sample of modules.

The measuring of the electrical power output of bifacial modules requires a standardised procedure with a controlled test setup that can provide results that are meaningful to the real-world operation of the module. The challenges encountered when determining the rear irradiance driven power gain yield parameter $BiFi$ using the published procedure inspired the development of an adapted procedure using the available equipment to calculate the $BiFi$. The $BiFi$ was determined for the same module at Fraunhofer using the published procedure and at NMU using an adapted procedure. The $BiFi$ determined with the adapted procedure is within one standard deviation of the value determined with the standard procedure, which shows compatibility of the two methods. The BiFi gives an indication of how much electrical power will be generated by the rear surface for each unt of irradiance absorbed by the rear surface when a bifacial module is receiving light in both surfaces simultaneously.

It is possible to measure modules in indoor or outdoor tests and get similar results which are within measurement error. The measurements uncertainties for outdoor measurements due to the variable conditions outdoor are larger than indoor measurements. The method used to determine the $BiFi$ is an acceptable compromise when it is not possible to use the high irradiance levels for the equivalent irradiance method, or in the absence of a dual light source for bifacial characterization.

Acknowledgements

The authors wish to acknowledge PVinsight (Pty) Ltd for providing lab access, use of their solar simulator and staff resources to this project.

References

[1] P. Hersch and K. Zweibel, “Basic Photovoltaic Principles and Methods,” Golden (Colorado), Feb. 1981.

[2] J. Klaus, Olindo Isabella, A. Smets, R. van Swaaij, and M. Zeman, “A Student Introduction to Solar Energy,” Delft, Sep. 2014.

[3] K. Mertens, “A comprehensive and up-to-date tutorial on all aspects of photovoltaic technology

Technology and Practice Photovoltaics Photovoltaics Mertens."

[4] Heinrich. Haberlin and H. Eppel, *Photovoltaics : system design and practice*. Wiley, 2012.

[5] W. Gu, T. Ma, M. Li, L. Shen, and Y. Zhang, "A coupled optical-electrical-thermal model of the bifacial photovoltaic module," *Appl Energy*, vol. 258, Jan. 2020, doi: 10.1016/j.apenergy.2019.114075.

[6] E. Lorenzo, "On the historical origins of bifacial PV modelling," *Solar Energy*, vol. 218, pp. 587–595, Mar. 2021.

[7] W. Gu, T. Ma, S. Ahmed, Y. Zhang, and J. Peng, "A comprehensive review and outlook of bifacial photovoltaic (bPV) technology," *Energy Conversion and Management*, vol. 223. Elsevier Ltd, Nov. 01, 2020. doi: 10.1016/j.enconman.2020.113283.

[8] B. G. Bhang, W. Lee, G. G. Kim, J. H. Choi, S. Y. Park, and H. K. Ahn, "Power Performance of Bifacial c-Si PV Modules with Different Shading Ratios," *IEEE J Photovolt*, vol. 9, no. 5, pp. 1413–1420, Sep. 2019, doi: 10.1109/JPHOTOV.2019.2928461.

[9] B. Burger, L. Friedrich, C. Kost, S. Nold, and S. Philips, "Photovoltaics Report," Freiburg, Jul. 2021. [Online]. Available: www.ise.fraunhofer.de

[10] D. McCauley and R. Heffron, "Just transition: Integrating climate, energy and environmental justice," *Energy Policy*, vol. 119, pp. 1–7, Aug. 2018, doi: 10.1016/j.enpol.2018.04.014.

[11] G. Raina and S. Sinha, "A holistic review approach of design considerations, modelling, challenges and future applications for bifacial photovoltaics," *Energy Conversion and Management*, vol. 271. Elsevier Ltd, Nov. 01, 2022. doi: 10.1016/j.enconman.2022.116290.

[12] J. P. Singh, A. G. Aberle, and T. M. Walsh, "Electrical characterization method for bifacial photovoltaic modules," *Solar Energy Materials and Solar Cells*, vol. 127, pp. 136–142, 2014, doi: 10.1016/j.solmat.2014.04.017.

[13] B. Newman *et al.*, "COMPARISON OF BIFACIAL MODULE LABORATORY TESTING METHODS." EU PVSEC 2017.

[14] P. Ooshaksaraei, K. Sopian, R. Zulkifli, M. A. Alghoul, and S. H. Zaidi, "Characterization of a bifacial photovoltaic panel integrated with external diffuse and semimirror type reflectors," *International Journal of Photoenergy*, vol. 2013, 2013, doi: 10.1155/2013/465837.

[15] T. S. Liang, D. Poh, and M. Pravettoni, "Challenges in the pre-normative characterization of bifacial photovoltaic modules," in *Energy Procedia*, Elsevier Ltd, 2018, pp. 66–73. doi: 10.1016/j.egypro.2018.09.006.

[16] G. Razongles *et al.*, "Bifacial Photovoltaic Modules: Measurement Challenges," in *Energy Procedia*, Elsevier Ltd, Aug. 2016, pp. 188–198. doi: 10.1016/j.egypro.2016.07.056.

[17] C. Duran, "Bifacial Solar Cells : High Efficiency Design, Characterization, Modules and Applications." [Online]. Available: http://nbn-resolving.de/urn:nbn:de:bsz:352-205361

[18] "MBJ Mobile Lab 5.0 Field of Application." [Online]. Available: www.mbj-solutions.com

[19] Iec, *Photovoltaic devices-Part 1-2: Measurement of current-voltage characteristics of bifacial photovoltaic (PV) devices*. 2019. [Online]. Available: www.iec.ch

[20] International Electrochemical Commision, *Photovoltaic devices-Part 1-2: Measurement of current-voltage characteristics of bifacial photovoltaic (PV) devices*, IEC TS 60904-1-2. Geneva: International Electrochemical Commision, 2019. [Online]. Available: www.iec.ch

THERMAL CHARACTERISTICS OF AN INDIRECT SOLAR DRYER FOR DRYING BANANAS

Ashmore Mawire*[1], Masodi Ramokali[1], Molebogeng Mothupi[1] and Maarten Vanierschot[1,2]

[1]North-West University, Material Science, Innovation and Modelling (MaSIM) Research Focus Area, Department of Physics, Mmabatho 2745, Mahikeng, South Africa, *E-mail 1: ashmore.mawire@nwu.ac.za, E-mail 2: masodiramokali@gmail.com, E-mail 3: mothupimolebogeng@gmail.com

[2]KU Leuven, Department of Mechanical Engineering, Group T Leuven campus, Celestijnenlaan 300, B-3001, Heverlee, Belgium, E-Email: maarten.vanierschot@kuleuven.be

Abstract: Post-harvesting losses are predominant in developing countries due to inadequate food preservation methods. Open sun drying usually used by small-scale subsistence farmers in the developing world is inefficient since the quality of the product is reduced due to under or over-drying in the sun. Additionally, environmental factors such as rain, wind, and dust have a negative impact on the quality of the dried products. To cater to the drawbacks of open sun drying, an indirect solar dryer is designed and experimentally evaluated for drying bananas. The dryer is evaluated under two experimental conditions. The first drying condition involves drying bananas during two 8 h periods of good solar radiation on two consecutive days. Secondly, the solar dryer is tested for a continuous 24 h period to study the overnight characteristics of the dryer. To evaluate the thermal characteristics, the thermal profiles in six drying trays are measured with K-type thermocouples during the drying process. The six trays are in three levels (top, middle, and bottom), and there are two trays per level (left and right). Each tray has two thermocouples making a total of twelve measurement positions in the dryer. The moisture ratio is also used to evaluate the thermal characteristics in the drying chamber. The maximum temperatures attained for both days in the 8 h sunny period tests in the top trays are around 48 ºC. For the 24 h test, the maximum temperature at the top trays is around 50 ºC. The drying process continues even when the drying tray temperatures drop drastically overnight to minimum values between 6-8 ºC for the 24 h test. The final average moisture ratios for the 16 h and 24 h tests are comparable showing values of around 26 % and 32 %, respectively. This indicates that the solar drying process can be continuously done for 24 hrs without much moisture rebuild. A storage system can effectively improve the drying process overnight.

Keywords: Bananas; Indirect solar dryer; Thermal characteristics

1. Introduction

Food security in developing countries is a very important issue that requires a sustainable food supply chain to alleviate hunger [1]. Food shortages are made worse in developing countries due to high birth rates, poor food preservation techniques, and natural disasters such as floods and droughts [2-3]. Close to 1.3 billion tonnes of food are lost annually as reported by the Food and Agriculture Organization (FAO) [4]. One effective way to reduce post-harvesting losses is the drying of food which is a generally energy-intensive process. The simplest method used in the developing world is open sun drying which has several disadvantages. Disadvantages include non-controlled drying resulting in under and over-drying and food contamination due to dust, rain, wind and over-exposure to direct solar radiation [5]. Open sun drying is also a labour-intensive process requiring constant monitoring in a very large open area for large amounts of food, and food tends to reabsorb moisture if it is left for a long period thus losing its colouring and nutritional value.

A method of addressing the shortcomings of open sun drying is solar drying using both direct and indirect modes. Different types of solar dryers have been developed in recent years as reported in the recent comprehensive review papers on solar dryers[6-9]. Solar dryers have been used in recent years to dry fruits and vegetables [10], sugarcane [11], and meat [12]. Fruits are grown widely by commercial or subsistence farmers in Africa and Asia. Fruits also grow naturally in these regions, and solar dryers have been used to dry grapes [13], apples [14], bananas [15], mangoes [16] and pineapples [17] to extend their shelf-life. Although some recent work has been on the solar drying of bananas [18-21], there is still room for improvements to optimize the solar drying process. The aim of this paper is thus to evaluate a novel indirect solar dryer for drying banana slices. The novel aspects investigated include having DC fans attached at the top of the

collector to reduce the pickup of dust and measuring the thermal profiles in 12 different locations inside the drying chamber to fully understand the thermal behaviour during solar drying. Experimental results for two tests are presented in this paper. The first test involves drying the bananas for two consecutive days of good solar radiation conditions for periods of 8 h. The second test involves continuously drying bananas for a 24 h period (9 am on day 1 to 9 am on day 2). The results obtained will be useful for improving the solar drying of bananas.

2. Experimental setup and method

Isometric and cross-sectional schematics of the novel solar dryer are shown in Figs. 1 and 2. The dryer is a scaled-up experimental version of the one reported recently by Tegenaw et al. [22]. The width and length of the collector are 1.164 m and 1.740 m, respectively, and the highest point of the ground to the collector is around 3 m.

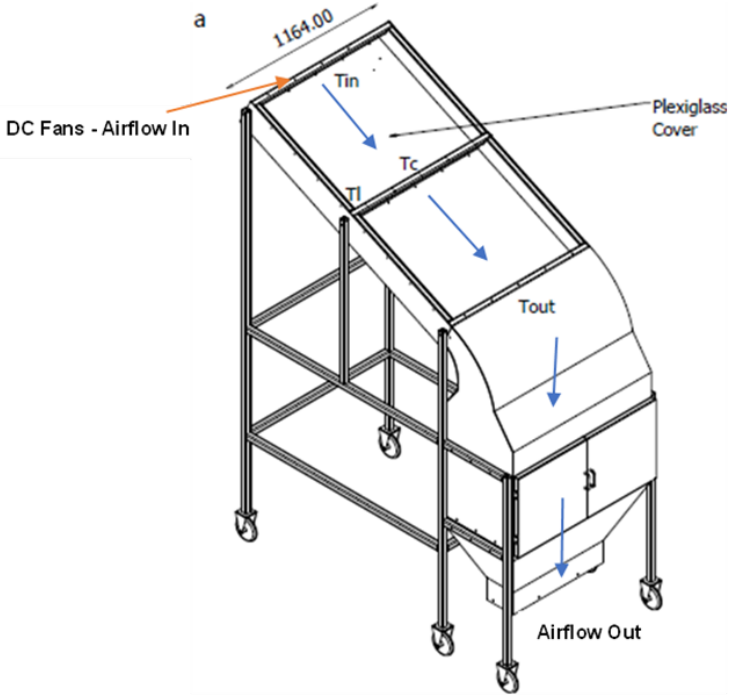

Fig. 1. An isometric view of the novel solar dryer

A stainless-steel absorber plate absorbs solar radiation incident on the collector, and this solar thermal energy is extracted using six computer CPU cooling DC fans that are connected to the inlet of the collector. The hot air from the outlet of the collector heats the drying chamber trays. A DC power supply or a solar panel with a battery and a charge controller can be used to power the fans. The DC power supply is used in the reported experiments to power the fans since the charge controller has a thermal switch that shuts off the fans after 4 hrs of continuous running. A DC supply supplies a maximum current of around 0.4 A which corresponds to an average airflow velocity of around 0.20 m/s in the drying chamber.

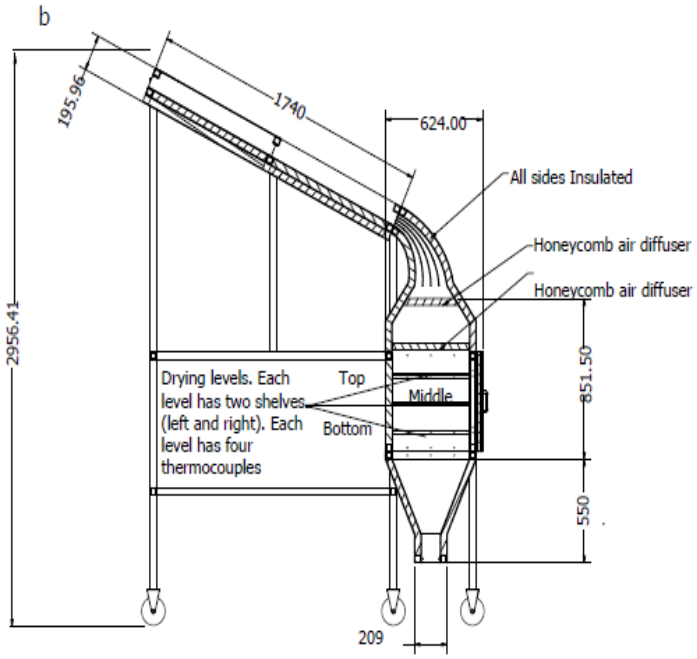

Fig. 2. A side cross-sectional view of the novel solar dryer

The inlet (Tin) and outlet (Tout) temperatures are measured with two flat K- thermocouples with an accuracy of ± 2 ºC are placed centrally on the absorber plate on the inlet and outlet ends of the collector (See Fig. 1). Two other flat K- thermocouples are placed on the central axis of the collector to measure the central collector temperature (Tc) and the left-hand side (Tl) collector temperature on the central axis. Two honeycomb diffusers before the drying chamber (See Fig. 2) uniformize the airflow velocity and improve the heat transfer to the drying chamber.

The drying chamber consists of three drying levels (top, middle, and bottom) as shown in Fig. 2. Each level comprises left and right compartments (trays) making a total of six trays inside the dryer. Four K-thermocouples (accuracy ± 2 ºC) are placed on each level to measure the temperature distribution on the left and right trays. A drying tray without bananas together with the measuring thermocouples is shown in Fig. 3, while the one loaded with banana slices in an experimental trial is shown in Fig. 4.

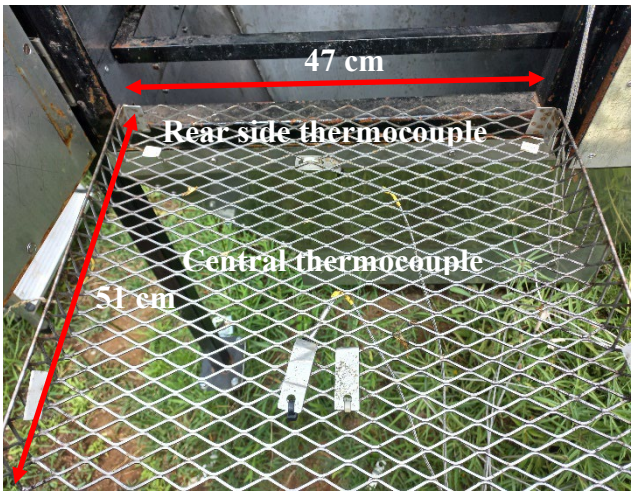

Fig. 3. Empty drying tray showing the central and rear side thermocouples.

Fig. 4. The loaded tray with banana slices with a 1 mm wire mesh that was placed on top of the drying tray during a drying experiment.

To prevent the banana slices from dropping down since the pore size of the mesh in a tray was in some cases greater than the diameter of the slices, a wire mesh with a pore size of 1 mm had to be added on top of the tray mesh as shown in Fig. 4. Each tray is about 51 x 47 cm. Each tray has a thermocouple placed at the centre and close to the central rear side edge from the door opening. To prevent the growth of microorganisms, bananas are first treated with lemon juice. Each tray contains around 120-130 circular banana slices (disks) with thicknesses ranging from 4.5-5 mm. The diameters of the slices ranged from 25-30 mm, and 10 bananas are placed in each tray making a total mass of around 530 g in each tray. The total mass of the bananas in the six trays is around 3.18 kg.

To measure the airflow velocity inside the chamber, a Testo 450i thermal anemometer with a measuring range of 0-30 m/s, a resolution of 0.01 m/s and an accuracy of ± 0.01 m/s for a range of 0-2 m/s is used. It is placed centrally in between the top trays shown in Fig. 4. A Kipp and Zonen CMP11 pyranometer with a 95 % response time of less than 5 s is used to measure the incident global solar radiation on the collector. A Mastech 625 B anemometer (range-0.8-30 m/s, resolution- 0.01 m/s, accuracy ± 2 %) is used to measure the wind speed during experimental tests. A Hession digital temperature and humidity meter (accuracy ±5 %, resolution 1 %) is used to measure the relative humidity in the drying chamber.

The first test involves drying the bananas for two consecutive days of good solar radiation conditions for periods of 8 h. The second test involves continuously drying bananas for a 24 h period (9 am on day 1 to 9 am on day 2). During the drying experiments, the data from the thermocouples and the pyranometer are automatically logged to the computer using an Agilent 34970 A data logger. The other remaining measurements are taken manually every hour. The total mass of the bananas is measured every hour by opening the dryer so that the moisture ratio can be estimated. The moisture ratio is estimated [23] as:

$$MR = \frac{M - M_{eq}}{M_0 - M_{eq}} \approx \frac{M}{M_0}, \quad (1)$$

where M is the moisture content, M_{eq} is the equilibrium moisture content and M_0 is the initial moisture content. M_{eq} is much less than M and M_0 therefore it can be neglected as indicated in Eq. (1).

3. Results and discussion

Fig. 5 shows the solar radiation, wind speed, and collector thermal profiles during a solar drying test on two consecutive days of generally good solar radiation conditions. The first 8 h period of the test started at 9 am on 1 November 2021 and it ended at 5 pm. The second drying period of the test was on 2 November 2021 during the same time interval, and the total test period was 16 hrs. The maximum global solar radiation of around 1240 W/m^2 for both testing periods occurs around 3-4 hrs from the commencement of the drying process (Fig. 5A). The first testing period shows instances of slight clouds just after 5 hrs, however, the average solar radiation values for periods 1 and 2 are comparable (970 and 1005 W/m^2). Windspeeds for both test periods fluctuate up and down for the duration of the experiments. The maximum wind speed is close to 5 m/s for the first test period whereas for the second test period, it is around 2.5 m/s. The average wind speed in the 16 h test is around 1.40 m/s. Fig. 5B shows the collector and ambient temperatures. The collector temperatures for day 1 follow the same trajectory of the solar radiation, and the cloudy period after 5 hrs since well depicted by the drop in the collector temperatures. A maximum

outlet collector temperature close to 80 ºC is achieved on day 1, and the corresponding maximum inlet temperature is around 40 ºC. It can be observed that the middle centre of the collector achieves higher temperatures values than the middle far left section suggesting better heat transfer at the centre of the collector. In contrast to the plots of day 1, day 2 shows slightly higher collector temperatures which also vary in a similar manner to the solar radiation. The inlet temperature for day 2 starts at a lower temperature compared to day 1 due to recording the temperature after switching on the fans. The middle central region of the collector is heated more effectively compared to the far-left central region which shows lower temperatures suggesting more heat losses at the left edge of the collector. An unexpected rise in the inlet collector temperature at around 11.2 h during day 2 for test 2 causes the other collector temperatures to also rise. This rise is likely attributed to a drop in the airflow velocity in the collector which causes the inlet temperature to rise as the airflow velocity was manually controlled at the set power supply current.

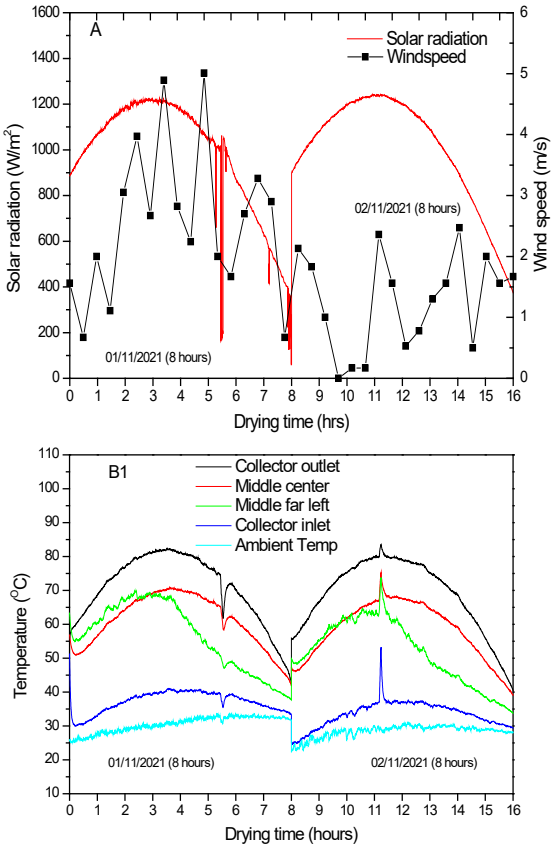

Fig. 5. (A) Global solar radiation and wind speed profiles and, (B) collector and ambient temperatures for 16 hrs in two consecutive sunny days of drying with an average drying airflow velocity of 0.20 m/s.

The average ambient temperatures for the two test periods of 30.5 and 28.4 ºC, respectively are comparable. Even with the slightly lower ambient temperatures on day 2, the collector temperatures are higher due lower windspeeds which reduce heat losses from the collector.

Fig. 6 shows the drying chamber thermal profiles for the top, middle, and bottom trays.

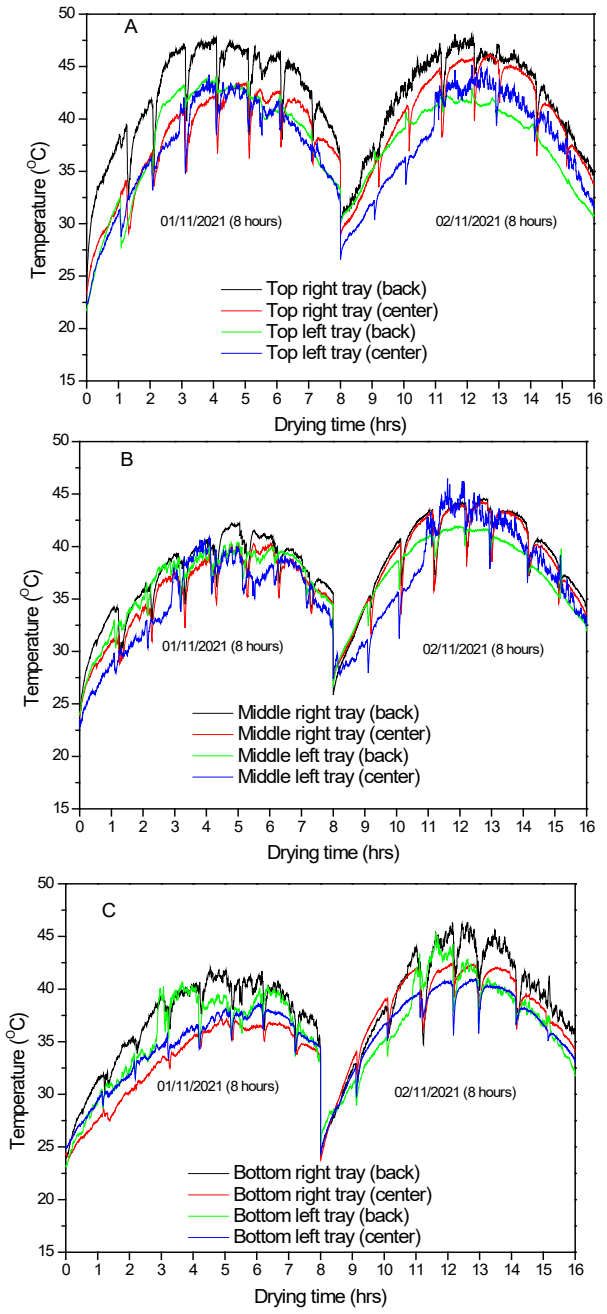

Fig. 6. Temperature profiles of the (A) top trays, (B) middle trays, and the (C) bottom trays for 16 hrs on two consecutive sunny days of drying with an average drying airflow velocity of 0.20 m/s.

Hourly fluctuations in the thermal profiles to lower temperatures are due to opening the drying chamber doors to measure the mass of the banana slices that are used to estimate the moisture ratio. For the top tray, it is seen for both test periods that the top right back section (black trace) achieves higher temperatures than the other sections. This is due to the outlet port from the honeycomb diffuser being closer to the top back section. For the middle trays, the temperature profiles are more comparable, however slightly higher temperatures are seen on day 2 of the test due to the slightly higher average solar radiation conditions. For the bottom trays, the right back section shows slightly higher temperatures, and higher temperatures are achieved on day 2 like the middle trays. For both test days, the thermal profiles also follow the same trajectory as the solar radiation of rise, peaking, and falling. The maximum temperatures achieved in the drying chamber for day 1 for the top, middle and bottom trays are 48, 43, and 43 ºC, respectively. For day 2 with comparable higher but comparable solar radiation conditions and lower wind speeds, the maximum temperatures are 48, 46 and 46 ºC for the top, middle, and bottom trays, respectively. The relative humidity reduces in the drying with an increase in the drying chamber temperatures as the solar radiation increases. It drops from 35-15 % on day 1, and from 30-15 % on day 2.

Fig.7 shows the solar radiation, wind speed, and collector thermal profiles for a 24 h testing period from 3-4 November 2021 using an average drying chamber airflow velocity of 0.20 m/s. The maximum solar radiation in the test is around 1250 W/m^2, and the average solar radiation during the sunshine hours on day 1 is around 980 W/m^2. The solar radiation starts to rise after 20 hrs on day 2 achieving a maximum value close to 900 W/m^2 at the end of the 24 h drying process. The wind speed fluctuates during the solar drying period, and it shows a maximum value of around 5.8 m/s at around 3.5 hrs of the drying process. During night-time hours, there is very little wind blowing. The maximum collector outlet temperature achieved is around 84 ºC, and the middle center section shows higher temperatures than the middle-left section like the 16 h test. After 8 hrs of solar drying, the collector temperatures drop to minimum temperatures of around 15 ºC during overnight drying. The collector temperatures also start to rise on day 2 with rise in the solar radiation. The average ambient temperature is around 32 ºC during the solar drying period. The ambient temperature drops to a minimum of around 15 ºC at night.

Fig. 8 shows the thermal profiles in the drying trays for the 24 h test. Slightly higher top tray temperatures are achieved in test 2 compared to 16 h test due to the slightly higher collector outlet temperatures as result of a lower wind speed variability. The back right top and bottom trays show higher temperatures than the other sections during the solar drying process like the 16 h tests. The maximum temperature achieved at the top trays is around 50 ºC. The maximum temperatures attained in the middle and bottom are both close to 44 ºC. Due to the drop in the collector temperatures during night-time drying, the thermal profiles in the trays also drop significantly. The minimum temperatures attained in the top, middle and bottom trays are around 7.5, 6.5. and 6.0 ºC, respectively. The highest temperatures in the top and bottom trays (top and bottom right back) show the greatest drop during night-time solar drying suggesting more pronounced heat losses in these two sections. In a similar manner to the collector temperatures, the thermal profiles of the drying chamber begin to rise after 20 hrs due to the rise in solar radiation. The relative humidity for the 24 h case drops from 40-15 % in the first 8 hours of drying. After that. it gradually rises from 15-45 % from 8-22 hrs before dropping from 45-25 % between 22-24 hrs.

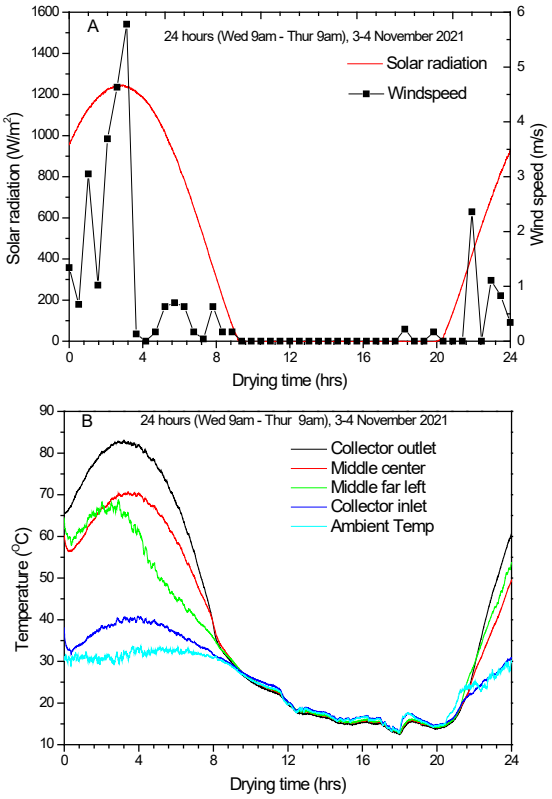

Fig. 7. (A) Global solar radiation and wind speed profiles and, (B) collector and ambient temperatures for 24 hrs drying with an average drying airflow velocity of 0.20 m/s.

To quantify the effectiveness of the dryer, the average moisture ratios in the six trays for the two tests are presented in Fig. 9. The 16 h test shows a slightly faster drop in during the first 4 hrs of drying which is probably attributed to non-uniform drying rates in the drying chamber because of different aiirflow regimes in the different sections of the dryer. This has to be

investugated in future woirk. At 4 hrs of drying, the moisture ratio for the 16 h test is around 56 % whereas that of the 24 h test is around 62 %. At the end of 8 h, the moisture ratios are around 38 and 45 % for the 16 h and 24 h tests, respectively. Even though there is no solar radiation after 8 hrs, the drying process continues in the 24 h test with the moisture ratio attaining a value of 32 % at the end of 24 hrs. On the other-hand, due to the sunny period after 8 hrs for the 16 h test, the moisture ratio shows a lower value of around 26 %. The results of the 24 h test suggest that it is possible to improve the performance with the use of thermal energy storage (TES) due to the continuous drop in the moisture ratio regardless of the lower chamber temperatures and the increase in the relative humidity. The airflow velocity has a more significant effect on the drying process than the relative humidity since the moisture cotinues to be removed regardless of the higher relatuve humidity.

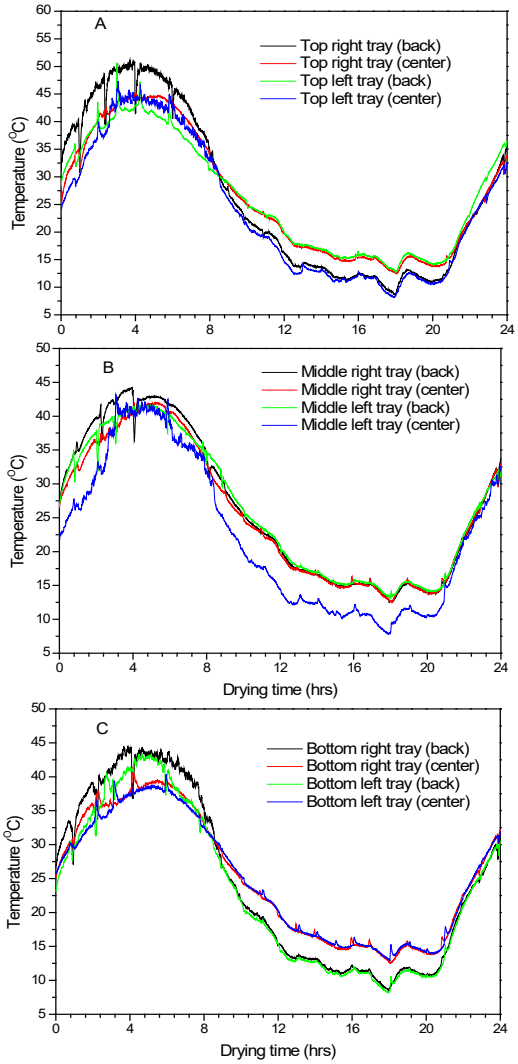

Fig. 8. Temperature profiles of the (A) top trays, (B) middle trays, and the (C) bottom trays for 24 hrs of drying with an average drying airflow velocity of 0.20 m/s.

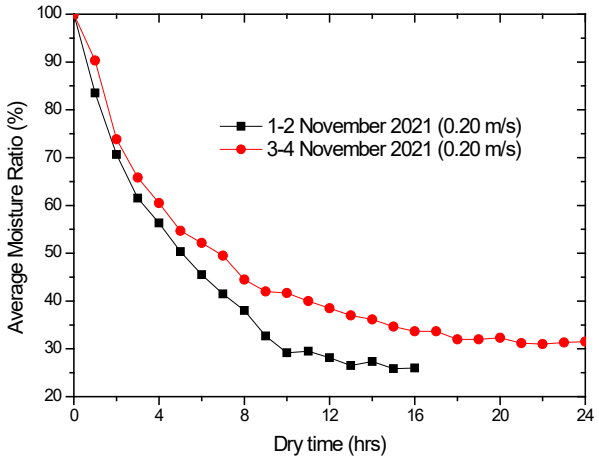

Fig. 9. Average drying chamber moisture ratios for the 16 and 24 h tests using an average drying airflow velocity of 0.20 m/s.

4. Conclusion

An indirect solar dryer was experimentally evaluated for drying bananas under two experimental conditions. The first drying condition dried bananas during two 8 h periods of good solar radiation for two consecutive days. The second drying condition was continuous 24 h drying to evaluate the overnight characteristics of the dryer. The thermal characteristics were evaluated by measuring the thermal profiles in six drying trays using two thermocouples per tray. The moisture ratio was also used to evaluate the thermal characteristics in the drying chamber. The maximum temperatures attained for both days in the 8 h sunny period tests in the top trays were around 48 ºC. For the 24 h test, the maximum temperature attained at the top trays was around 50 ºC. The drying process continued regardless of the overnight drop in the drying tray temperatures to minimum values between 6-8 ºC for the 24 h test. The final average moisture ratios for the 16 h and 24 h tests are comparable showing values of around 26 % and 32 %, respectively. This indicates that the solar drying process can be continuously done for 24 hrs since the airflow velocity has a more significant effect on the drying process than the relative humidity since the moisture continues to be removed regardless of the higher relative humidity. A storage system can effectively improve the drying process overnight since higher temperatures can be achieved with stored thermal energy irrespective of the increase in the relative humidity.

Acknowledgements

The authors would like to acknowledge VLIR-UOS, Belgium

under South Initiatives 2020 project (Project No: ZA2020SIN306A101) for funding to carry out the research. The authors also acknowledge the Instruments Making Department of the North-West University for fabricating the experimental setup, in particular the head of the Department, Mr Thys Taljaard.

References

[1] Rudel T.K., Meyfroidt P. (2014). Organizing anarchy: The food security–biodiversity–climate crisis and the genesis of rural land use planning in the developing world. Land Use Policy 36, 239-247.

[2] Rahman M.D., Khan I., Field D.L, Techato K., Alamen K. (2022). Powering agriculture: Present status, future potential, and challenges of renewable energy applications. Renewable Energy 188, 731-749.

[3] Awad A. (2023). The determinants of food insecurity among developing countries: Are there any differences? Scientific African 19, e01512.

[4] Gustavsson J., Cederberg C., Sonesson U. (2011). FAO Global food losses and waste. extent causes and prevention, Rome 1-37,

[5] Kamarulzaman A., Hasanuzzaman M., Rahim N.A. (2021). Global advancement of solar drying technologies and its prospects: A review. Solar Energy 221, 559-582.

[6] Mugi V.R., Das P., Balijepalli R., Chandramohan V.P. (2022). A review of natural energy storage materials used in solar dryers for food drying applications. Journal of Energy Storage 49, 104198.

[7] Udomkun P., Romuli S., Schock S., Mahayothee B., Sartas M., Wossen T., Njukwe E., Vanlauwe B., Müller J. (2020). Review of solar dryers for agricultural products in Asia and Africa: An innovation landscape approach. Journal of Environmental Management 268, 110730.

[8] Lingayat A.B., Chandramohan V.P., Raju V.R.K., Meda V. (2020). A review on indirect type solar dryers for agricultural crops – Dryer setup, its performance, energy storage and important highlights. Applied Energy 258,114005.

[9] Srinivasan G., Rabha D.K., Muthukumar P. (2021). A review on solar dryers integrated with thermal energy storage units for drying agricultural and food products. Solar Energy 229, 22-38.

[10] Getahun E., Delele M.A., Gabbiye N., Fanta S.W., Demissie P., Vanierschot M. (2021). Importance of integrated CFD and product quality modeling of solar dryers for fruits and vegetables: A review. Solar Energy 220, 88-110.

[11] Embong R., Shafiq N., KusbiantoroA., Nuruddin M.F. (2016). Effectiveness of low-concentration acid and solar drying as pre-treatment features for producing pozzolanic sugarcane bagasse ash. Journal of Cleaner Production 112, 953-962.

[12] Chaouch W.B., Khellaf A., Mediani A., Slimani M.E., Loumani A., Hamid A. (2018). Experimental investigation of an active direct and indirect solar dryer with sensible heat storage for camel meat drying in Saharan environment. Solar Energy 174, 328-341.

[13] Essalhi H., Benchrifa M., Tadili R., Bargach M.N. (2018). Experimental and theoretical analysis of drying grapes under an indirect solar dryer and in open sun. Innovative Food Science and Emerging Technologies 49, 58-64.

[14] Ullah F., Kang M. (2017). Impact of air flow rate on drying of apples and performance assessment of parabolic trough solar collector. Applied Thermal Engineering 127, 275-280.

[15] Janjai S., Lamlert N., Intawee P., Mahayothee B., Bala B.K., Nagle N., Muller J. (2009). Experimental and simulated performance of a PV-ventilated solar greenhouse dryer for drying of peeled longan and banana. Solar Energy 83, 1550-1565.

[16] Koua K.B., Fassinou W.F., Gbaha P., Toure S. (2009). Mathematical modelling of the thin layer solar drying of banana, mango, and cassava. Energy 34, 1594-1602.

[17] Bala B.K., Mondol M.R.A., Biswas B.K., Das Chowdury B.L., Janjaic S. (2003). Solar drying of pineapple using tunnel drier. Renewable Energy 28,183-190.

[18] Amer B.M.A., Hossain M.A., Gottschalk K. (2010). Design and performance evaluation of a new hybrid solar dryer for banana. Energy Conversion and Management 51, 813-820.

[19] Nabnean S., Nimnuan P. (2020). Experimental performance of direct forced convection household solar dryer for drying banana. Case Studies in Thermal Engineering 22, 100787.

[20] Hegde V.M., Hosur V.S., Rathod S.K., Harsoor P.A., Narayana K.B. (2015). Design, fabrication, and performance evaluation of solar dryer for banana. Energy, Sustainability and Society 5, 23.

[21] Pruengam P., Pathaveerat S., Pukdeewong P. (2021). Fabrication and testing of double-sided solar collector dryer for drying banana. Case Studies in Thermal Engineering 27, 101335.

[22] Tegenaw, P.D., Mawire, A., Ramokali M., Mothupi M., Vanierschot M. (2021). Experimental measurement of heat transfer in a solar powered food dryer. Southern African Sustainable Energy Conference (SASEC2021), Spier, Stellenbosch, South Africa.

[23] Djebli A., Hanini S., Badaoui O., Haddad B., and Benhamou, A. (2020). Modeling and comparative analysis of solar drying behavior of potatoes, Renewable Energy 145, 494-1506.

DEVELOPMENT OF A PILOT LOW TEMPERATURE SOLAR THERMAL CO-GENERATION SYSTEM FOR WATER DISTILLATION AND ENERGY GENERATION

Jacobus G. van Zyl[1], Michael T.F. Owen[2], and Gerald Müller[3]

[1] Stellenbosch University – Solar Thermal Energy Research Group (STERG); E-Mail: cobusvanzyl123@gmail.com

[2] Stellenbosch University, 1 Joubert Street, Stellenbosch, 7600, South Africa; Phone: +27-713596654; E-Mail: mikeowen@sun.ac.za

[3] University of Southampton; E-mail: g.muller@soton.ac.uk

Abstract: A solar-thermal system for co-generation of distilled water and energy was investigated in a collaborative study by the University of Southampton and Stellenbosch University. The system utilises a condensing engine, using solar-generated steam at ~1 atm (abs) and a vacuum generated by condensation. The study entailed the design, manufacture, commissioning and testing of a 6.5 kW_{th} prototype system. From on-sun testing, the average daily specific energy consumption (SEC) for water distillate production was 2125 kWh_{GTI}/m^3; and the average daily theoretical solar-to-mechanical energy conversion efficiency was 0.79 %. The SEC was determined to be significantly higher than existing alternatives such as solar PV reverse osmosis, and the energy generation significantly lower compared to commercial solar power technology (e.g. solar PV). As such, the performance and experience gained with the prototype suggest this system is not feasible.

Keywords: co-generation; compound parabolic collector; desalination; solar thermal energy; steam expansion;

Nomenclature

A_{ap}	[m^2]	Aperture area
c_p	[J/kg K]	Specific heat capacity
d_o	[mm]	Outer diameter
ΔT	[K]	Change in temperature
η_{coll}	[%]	Collector solar-to-thermal efficiency
η_0	[%]	Optical efficiency
η_{th}	[%]	Thermal efficiency
GTi	[W/m^2]	Global tilt (in-plane) irradiance
GTI	[kWh/m^2]	Global tilt (in-plane) irradiation
L_{coil}	[m]	Boiler heat-exchanger coil length
$\dot{m}_{st}$	[g/s]	Steam mass flowrate
P_{eo}	[bar (abs)]	Condenser (engine exhaust) pressure
P_s	[bar (abs)]	Cylinder inlet pressure
$\dot{Q}_b$	[W]	Boiler heat gain
$\dot{Q}_u$	[W]	Collector useful heat gain
r_{exp}	–	Expansion ratio
SEC	[kWh/m^3]	Specific energy consumption
T_{in}	[°C]	Outlet temperature
T_{in}	[°C]	Inlet temperature
V_c	[m^3]	Condensate volume collected
V_{clear}	[m^3]	Clearance volume (clearance height x bore area)
V_{exh}	[m^3]	Exhaust volume (exhaust port height x bore area)
$\dot{W}_o$	[W]	Mechanical output power

1 Introduction

In the global transition towards renewable and sustainable energy systems and equitable supply of energy and water resources, Southern Africa is a region of particular interest. This region has large rural populations, who often lack access to energy and clean water, while boasting abundant clean energy resources, including a notable solar resource. In a collaborative effort, Stellenbosch University (SU) and the University of Southampton (UoS) are investigating a low-temperature solar thermal co-generation system for combined water distillation and energy generation. The system couples a compound parabolic solar thermal collector, for steam generation (and thus distillation) at ~1 atm (abs), with a reciprocating steam expander (developed by UoS) to provide a theoretically simple, robust and safe co-generation system. In a parallel study, Reed and Owen [1] simulated the potential performance of the system and concluded that the system was unlikely to be competitive with alternatives such as solar photovoltaic-powered reverse osmosis (PV-RO) and direct PV power generation. Their work included several simplifying assumptions and requires data for validation. Despite the questionable feasibility of the system, the component performance and technical challenges facing the operation of such a system remain interesting. This paper presents the system concept and describes a 6.5 kW_{th} prototype developed at SU. At

the time of writing, the steam expander was not yet operational and this paper includes results from the testing of the solar thermal system, and a preliminary (theoretical) analysis of the overall system output and efficiency.

2 System Description

Figure 1 shows the layout of the experimental system. The system consists of two primary sub-systems. The solar steam generation system (SSGS) includes the solar collector array, the boiler and the feed water supply tank. The condensing engine includes the reciprocating steam expander and condenser.

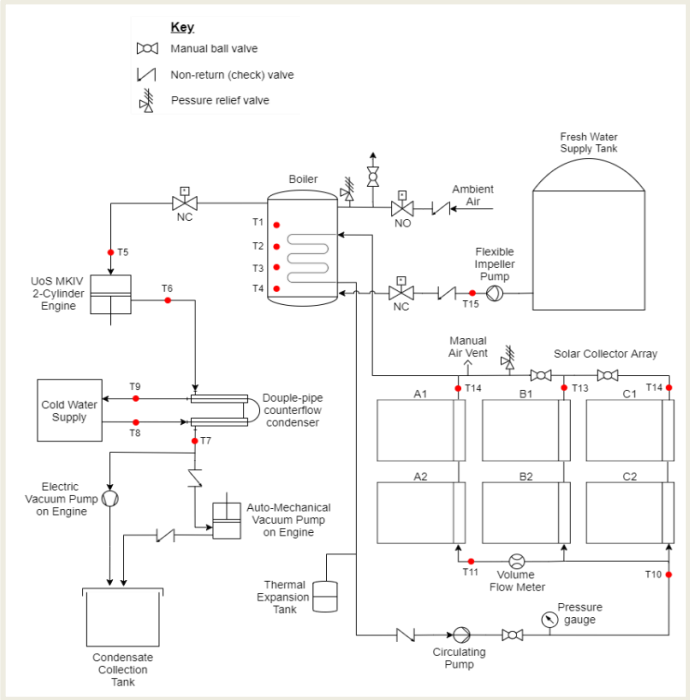

Figure 1 System P&ID

Details of the measurement equipment used in the study are given in Table 1. In addition to the measurement equipment shown in Figure 1, a pyranometer was installed on the collector mounting frame for direct measurement of global tilt irradiance (GTi), condensate volume flow was measured manually at regular intervals to determine the condensate production rate, and pressure transducers were used in the boiler, engine, and condenser.

Table 1 Measurement equipment

Equipment	Measurement	Resolution/ Accuracy
T-type thermocouples x15	Temperature	Error < 1°C. 10-s intervals.
DMP 331 pressure transducers x4	Absolute pressure	Error < 0.35 %. 10-s intervals.
Winsmeter TH7 volume flowmeter x1	HTF volume flowrate	Error < 0.6 %. 10-s intervals.
KIPP and ZONEN CMP6 pyranometer x1	GTi	Error < 5%. 10-s intervals.
Laboratory measuring beakers x3	Volume of condensate	5-mL resolution.

2.1 Solar Steam Generation System (SSGS)

The system uses six external compound parabolic concentrating (XCPC) solar thermal collectors (Figure 2) connected in three parallel rows of two collectors each (see Figure 1). These non-tracking, non-imaging concentrating collectors utilize global (beam + diffuse) tilt solar irradiance to heat the heat transfer fluid (HTF) circulating through the collector array in a closed loop. Liquid water (pressurized to avoid boiling in the collector loop itself) provides a safe, affordable, and readily available HTF.

Figure 2 Solar collector array before pipe insulation

Each XCPC consists of three metal-glass evacuated tubes, with aluminium parabolic reflectors (aperture area A_{ap} = 2.41 m^2, concentration ratio 1.4 [2] and rated optical efficiency 57%). The evacuated tubes enclose a pentagon-shaped fin and U-shaped copper absorber tube, both coated with a selective absorber coating (absorptivity 93-97 %, emissivity 3-7 % [2]). The collector array was mounted on a large frame and fixed at 30° inclination, facing north.

The collector efficiency is defined in Equation (1),

$$\eta_{coll} = \frac{\dot{Q}_u}{GTi \cdot A_{ap}} \quad (1)$$

where $\dot{Q}_u$ is the useful heat gain (sensible) calculated from the measured enthalpy change in the HTF – Equation (2).

$$\dot{Q}_u = \sum_{i=A}^{C} \left(\dot{m}\, c_p\, \Delta T_{io}\right)_i \qquad (2)$$

where *i* represents row A, B or C in Figure 1, $\dot{m}_i$ is the HTF mass flowrate through the two collectors in the respective row, $c_{p,i}$ is the specific heat capacity of liquid water at the bulk mean temperature (mean of row inlet and outlet temperatures), and $\Delta T_{io,i}$ is the temperature rise over the row (e.g. $T_{14} - T_{10}$ for row C in Figure 1).

Steam is generated indirectly in a 70-litre kettle-type boiler (see Figure 3) with a helical coil heating element (L_{coil} = 9 m, d_o = 25 mm) carrying the HTF from the solar collectors. The boiler and collector were sized together to operate in the nucleate boiling regime, with the boiler pressure being approximately 1 atm (abs) and always below 1.5 bar (abs). Indirect steam generation was selected to limit fouling in the solar absorber tubes and facilitate easier maintenance through periodic blowdown and cleaning of the boiler.

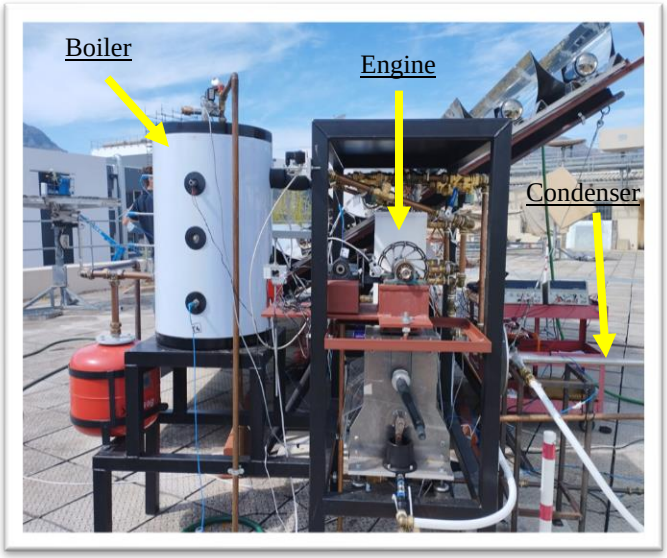

Figure 3 Side view of the system showing the boiler, engine and condenser

The boiler is equipped with various temperature and pressure sensors (the latter controlling the valve between the boiler and the engine); a pressure relief valve (for passive safety); a vacuum breaker; a blowdown port; and connectors for the HTF, feedwater, and steam.

The heat gain by the boiler is equal to the sensible heat loss of the HTF as it passes through the coil, determined using the total HTF enthalpy change through the helical coil – Equation (3).

$$\dot{Q}_b = \dot{m}\, c_p\, (T_{in} - T_{out}) \qquad (3)$$

Feedwater is supplied from a 500-litre storage tank by a pump controlled by a float switch in the boiler. The water level in the boiler is kept relatively constant to avoid large influxes of cold water and quenching of the boiler pool.

The SSGS was sized to supply the engine with steam at a rate of 4.36 L/s at 1 bar (abs), equating to 2.56 g/s of saturated vapor The sizing was done using a collector-boiler model constructed in MATLAB, for a clear day with a peak GTi of 900 W/m^2, (which is the overall average daily peak for the test location taken from data for the year 2021 [3]).

2.2 Condensing Engine

A two-cylinder uniflow condensing engine (reciprocating steam expander and condenser) was designed to generate mechanical power from the steam supplied by the SSGS. The steam expander was designed by UoS and manufactured by SU.

2.2.1 Reciprocating steam expander

The piston-cylinder steam expander is shown in Figure 4 (100 mm bore diameter, 160 mm stroke, 3.7 mm clearance height, and 10 mm exhaust port length).

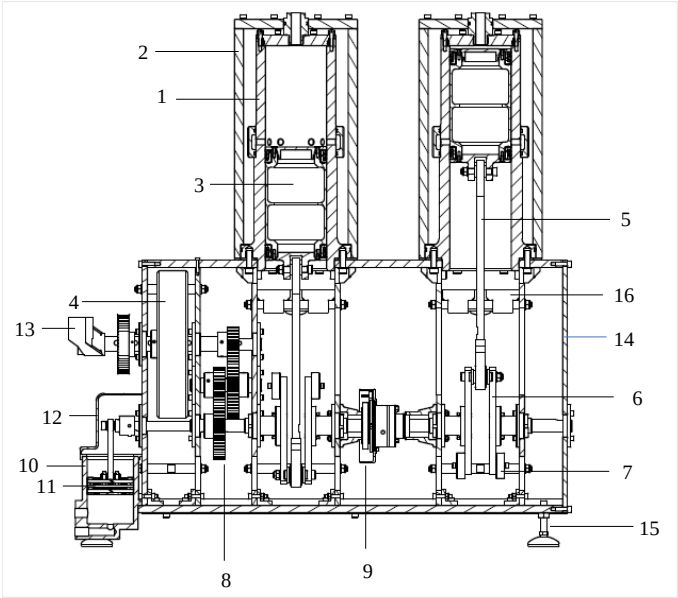

Figure 4 Engine CAD (by UoS) front view, partial section

The major components in Figure 4 are: (1) cylinder, (2) cylinder jacket, (3) piston assembly, (4) flywheel, (5) conrod, (6) crank, (7) counterweight, (8) gear train, (9) position sensor assembly, (10) auto-mechanical vacuum pump (AMVP) cylinder, (11) AMVP piston assembly, (12) AMVP housing, (13) starter handle, (14) aluminium frame and bearing housings, (15) adjustable feet, and (16) drip tray.

2.2.2 Basic Operating Principles

The engine was designed to operate between 60 and 120 rpm. A

single revolution of the engine includes one downstroke and one upstroke for both pistons, which equates to a single revolution of the crankshaft and four revolutions of the output shaft. During engine operation, steam is injected alternately into the top of cylinder 1 and 2, prompted by the engine position sensor. Each cylinder has both a supply and exhaust solenoid valve at its inlet, in addition to the exhaust ports in the cylinder which are exposed at the bottom of the downstroke.

The motive force for the engine is the pressure difference across the piston (bottom surface exposed to ambient, top surface exposed alternately to steam / vacuum). The thermodynamic cycle, illustrated in Figure 5, begins with the piston at TDC (5).

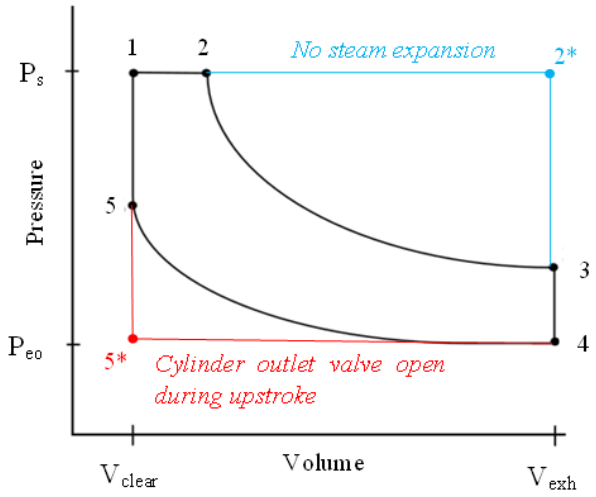

Figure 5 P-V diagram for full condensing engine cycle

The inlet valve opens and steam is supplied, initially at ~1 bar (5-1), before the downstroke begins. The piston is pulled downwards by the momentum of the engine (the pressure on either side of the piston is similar at this stage). The inlet valve remains open for the initial part of the downstroke (1-2, constant pressure). If the valve is closed, then the cycle follows an isothermal expansion process (2-3), with a steam jacket around the cylinder providing the additional heat input. Expansion ratios up to 1:43 are theoretically possible. Alternatively, the inlet valve can remain open for the downstroke, in which case there is no expansion (2-2*, expansion ratio 1:1). Towards the end of the downstroke, the exhaust ports are exposed and the steam is instantaneously evacuated into the condenser (3-4), which operates under vacuum. The pressure inside the cylinder is now sub-atmospheric and the piston is driven upwards by atmospheric pressure acting on the bottom surface of the piston. The exhaust solenoid valve at the top of the cylinder can be closed (4-5) or open (4-5*) during the upstroke.

2.2.3 Condenser

The condenser is critical to the operation of the condensing engine since it maintains the vacuum that results in the net pressure difference across the piston during the upstroke (and thus the motive power). SU's laboratories are equipped with a simple water-cooled, counterflow, double-pipe heat exchanger supplied with cooling water from a water reticulation system (WRS) at ~50 L/min, of sufficient rating. While unlikely to be practical for the eventual system, this condenser provided a convenient solution for the prototype demonstration.

At start-up, an electric vacuum pump is used to evacuate air from the condenser, engine piping and boiler. Once the system is running, the vacuum in the engine is maintained by the AMVP, driven off the engine crankshaft. When the AMVP piston moves upward it creates a vacuum in the AMVP cylinder, drawing the condensate from the condenser. On its downstroke it discharges the condensate into the condensate collection tank.

The volume of collected condensate (V_c) is measured and the Specific Energy Consumption (SEC, kWh/m^3) of the system – Equation (4) – is used to assess and benchmark the water production efficiency of the system.

$$\mathbf{SEC} = \frac{\mathbf{GTI} \cdot \mathbf{A_{ap}}}{\mathbf{V_c}} \qquad \mathbf{(4)}$$

2.3 Engine Power and Efficiency

The engine performance is measured using the thermal efficiency (η_{th}) defined in Equation (5),

$$\boldsymbol{\eta_{th}} = \frac{\dot{\mathbf{W}}_\mathbf{o}}{\dot{\mathbf{Q}}_\mathbf{b}} \qquad \mathbf{(5)}$$

which is the ratio of mechanical power output to boiler heat gain. The thermal efficiency of the engine was estimated using a linear relationship between the thermal efficiency and engine expansion ratio: r_{exp} = 1 to 4, corresponding to η_{th} = 2 to 5.5 %, derived from measured data obtained by UoS [4]. The mechanical power output was therefore inferred using Equation (5) and the measured heat input, with a variable thermal efficiency determined at each time step using Equation (6).

$$\mathbf{r_{exp}} = \mathbf{max}\left[\mathbf{1}\,;\,\frac{\mathbf{2.56\ g/s}}{\dot{\mathbf{m}}_\mathbf{st}}\right] \qquad \mathbf{(6)}$$

3 Results

Results for three 8-hour SSGS performance tests (14, 16 and 18 February 2023) are reported here. The generated steam was passed through the piping and solenoid valves that connect the SSGS to the engine and the engine to the condenser (to emulate

the real pressure losses in the system). Issues with maintaining vacuum have prevented successful operation of the engine to-date. Theoretical engine output is thus estimated based on the expected thermal efficiency and measured SSGS performance. Tests were carried out at SU's Solar Rooftop Laboratory (33.92810°S, 18.86540°E). Test results are extended to theoretically estimate annual yield from the system.

3.1 Solar Input

All three days of testing are considered good solar days during the global-south summer. Figure 6 presents the measured GTi distribution. Cloudy periods on 14-Feb are excluded from this analysis (dashed lines in the figures) as they add no further value to the conclusions drawn.

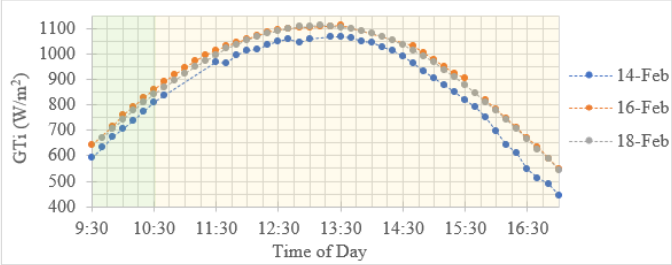

Figure 6 Measured global tilt (in-plane) irradiance

The section highlighted in green in Figure 6 is the ramp-up period during which the boiler water is sensibly heated to its saturation temperature. The in-operation period, when the boiler was generating steam, is indicated in yellow. The peak GTi on 14, 16 and 18 February were 1065, 1110 and 1110 W/m^2, respectively.

3.2 System Output

Figure 7 shows the steam generation rate for the three test periods. Steam was generated at (or above) the required rate of 2.56 g/s during the middle part of the day for all three tests (2-3 hours), reaching a maximum of 2.65, 2.79, and 2.85 g/s; with a mean value of 2.10, 2.10, and 2.25 g/s on 14, 16, and 18 February, respectively. Seeing as the tests were conducted on good solar days, the results suggest the SSGS would require upsizing to meet the required rate during winter and to increase the duration of full-load generation during summer. The inclusion of thermal energy storage (TES) to store the excess thermal energy during peak solar hours may be of benefit. Furthermore, as with any solar powered system, the variable rate of heat input, and associated variations in steam generation (and condition) in this case, would need to be accounted for through careful valve control and / or energy storage to result in steady operation of the engine.

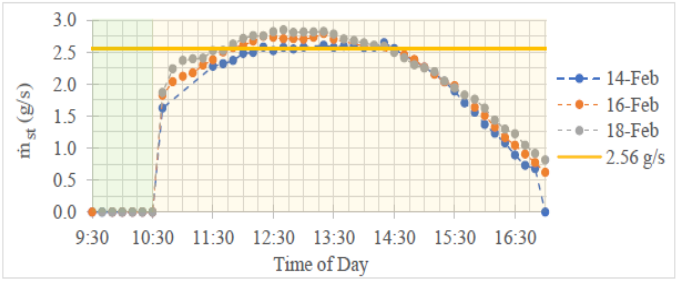

Figure 7 Rate of steam production

The average daily SEC was 2125 kWh$_{GTI}$/m^3, with the hourly distribution shown in Figure 8.

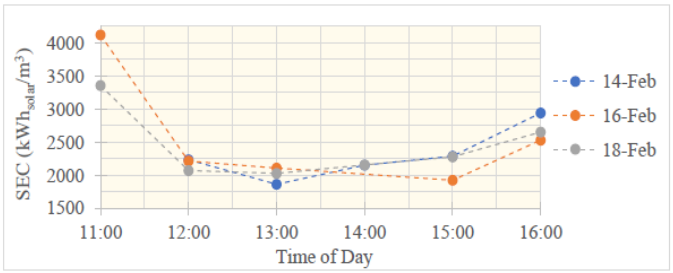

Figure 8 Solar-to-distillate specific energy consumption

Furthermore, the inferred mechanical power output is presented in Figure 9, which gives an average daily solar-to-mechanical energy conversion efficiency of 0.79 %.

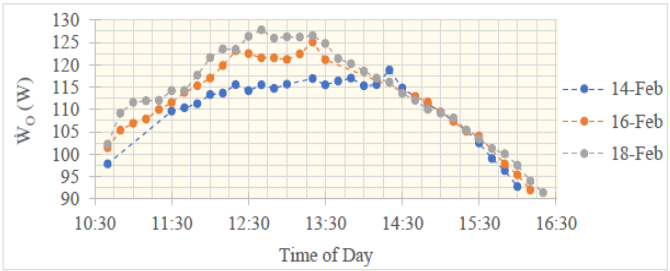

Figure 9 Theoretical mechanical power output

3.3 Annual Performance

Based on the average daily SEC and solar-to-mechanical efficiency, the annual water and power production were estimated using monthly satellite GTI data for the test location from SOLARGIS [5]. The total annual GTI for the test location is 2149.7 kWh$_{GTI}$/m^2. The system is estimated to produce an annual specific mechanical power output of 17.1 kWh/m^2, with the monthly distribution illustrated in Figure 10, which also shows the electrical output assuming a mechanical to electric efficiency of 80 % [6], as well as the monthly distillate production, equating to an annual output of 1012 L/m^2 and average daily output of approximately 2.8 L/m^2.

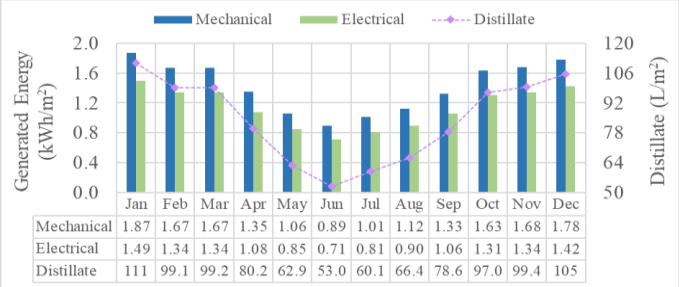

	Jan	Feb	Mar	Apr	May	Jun	Jul	Aug	Sep	Oct	Nov	Dec
Mechanical	1.87	1.67	1.67	1.35	1.06	0.89	1.01	1.12	1.33	1.63	1.68	1.78
Electrical	1.49	1.34	1.34	1.08	0.85	0.71	0.81	0.90	1.06	1.31	1.34	1.42
Distillate	111	99.1	99.2	80.2	62.9	53.0	60.1	66.4	78.6	97.0	99.4	105

Figure 10 Monthly specific mechanical power and distillate production

To assess the practicality / feasibility of the system investigated in this study, a comparison is made to a solar PV-powered co-generation system consisting of a PV-RO water purification system (SEC as low as 4 kWh_{solar}/m^3 [7, 8]) and generating additional electricity (PV module efficiency 15 % [8]). The systems are sized to generate ~50 kWh_e/month (Free Basic Electricity grant in South Africa [9]) in winter (average of 127.1 kWh_{GTI}/month) at the test location.

The results of the comparison are shown in Table 2 and indicate that the investigated system is not feasible since a PV-powered alternative is significantly more compact to produce the same amount of electricity and cean water, makes use of much less complex and more mature technology, and will cost significantly less based on total size. The total required PV aperture area is 2.75 m^2 compared to 62.7 m^2 in XCPC aperture area for the system investigated in this study.

Table 2 Comparison with solar PV

System ID	Solar PV		This System
Total Collector Area (m^2)	2.62	0.12	62.7
Approx. Number of Collectors/Panels	2-3		26
Average Electrical Energy Output (kWh/month)	50	–	50.6
Clean Water Output (L/month)	–	3900	3900

4 Conclusion

This paper describes a novel solar thermal clean water and energy co-generation system. A 6.5 kW_{th} prototype was developed as part of this work and this paper presents measured results for the steam / distillate production along with theoretical energy generation predictions. At the time of writing, the engine was not operational and getting the full system to operate has proven challenging. The results obtained show the SEC and solar-to-mechanical energy efficiency are notably poor compared to commercially available technologies such as solar PV reverse osmosis and PV power generation, suggesting that this system is not technically feasible. Furthermore, the investigated system is notably more complex and expensive. The condensing engine is nonetheless an intriguing prospect for waste heat recovery (avoiding the need for a dedicated solar thermal steam generation system) and the XCPC collectors have shown good thermal performance and are of interest for industrial process heat applications.

5 References

1. Reed, M., Owen, M. 2023. Simulation of a Novel Combined Water Purification and Electricity Generation System. *17th International Heat Transfer Conference*, Cape Town, 14 – 18 Aug 2023.
2. Artic Solar Inc. 2021. External Concentrating Parabolic Collector (XCPC). Available: https://articsolar.com/wp-content/uploads/2017/08/XCPC-Specifications-102716-Copy-1.pdf
3. Brooks, M., du Clou, S., van Niekerk, J., Gauche, P., Leonard, C., Mouzouris, M., Meyer, A., van der Westhuizen, N., van Dyk, E. & Vorster, F. 2015. SAURAN: A New Source for Solar Radiometric Data in Southern Africa. Journal of Energy in Southern Africa. 26:2–10. Available: https://sauran.ac.za/.
4. Müller, G., Chan, C.H., Gibby, A., Nazir, M.Z., Paterson, J., Seetanah, J., Telfer, M., Tsuzaki, T., Walker, C. & Yusof, F. 2018. The condensing engine: A heat engine for operating temperatures of 100 °C and below. Proceedings of the Institution of Mechanical Engineers, Part A: Journal of Power and Energy. 232(4):437–448. DOI: 10.1177/0957650917736455.
5. SOLARGIS. 2022. Solar Resource Maps and GIS Data for 200+ Countries and Regions. Available: https://solargis.com/maps-and-gis-data/download/world.
6. Müller, G. & Howell, C. 2021. Comparative analysis of ORC and condensing heat engines for low grade waste heat recovery. Applied Engineering. 5(1):29–35. DOI: 10.11648/j.ae.20210501.15.
7. Stillwell, A.S. & Webber, M.E. 2016. Predicting the specific energy consumption of reverse osmosis desalination. Water (Switzerland). 8(12). DOI: 10.3390/w8120601.
8. Rashid, F., Saleem, E.A., Kashif Mehmood, E. & Faizan Rashid, E. 2019. The efficiency of solar PV system. Proceedings of the 2nd International Multi-Disciplinary Conference. Available: https://www.researchgate.net/publication/334277230.
9. Department of Energy. 2012. A survey of energy-related behaviour and perceptions in South Africa. Available: https://www.energy.gov.za/files/media/Pub/Survey%20of%20Energy%20related%20behaviour%20and%20perception%20in%20SA%20-%20Residential%20Sector%20-%202012.pdf.

UPGRADING THE COMPRESSOR STAGE OF A SOLARISED MICRO GAS TURBINE

Michael Fivaz[1], Johan van der Spuy[2], and Hano van Eck[3]

[1] Solar Thermal Energy Research Group (STERG), Department of Mechanical and Mechatronic Engineering, Stellenbosch University, Joubert Street, Matieland 7602, Stellenbosch, South Africa; Phone: +27736842438; Email: 21555931@sun.ac.za

[2] Solar Thermal Energy Research Group (STERG), Department of Mechanical and Mechatronic Engineering, Stellenbosch University; Email: sjvdspuy@sun.ac.za

[3] Department of Military Technology, Stellenbosch University; Email: hvaneck@sun.ac.za

Abstract: A solar-hybrid gas turbine combines the environmental advantages of concentrating solar power (CSP) with the capabilities of a micro gas turbine's (MGT) continuous high-power output. A variety of options are available to improve MGT's performance and efficiency, with the primary focus being on its compression stage. An upgraded compressor stage for an existing solar-hybrid application MGT testbench is presented. MGT engines commonly feature a centrifugal compressor stage due to higher per stage pressure ratios being achieved compared to single stage axial configurations. The existing operational solar-hybrid MGT testbench, operates at low efficiency. The impeller of the MGT is redesigned by first simulating the existing impeller in a computational fluid dynamics (CFD) simulation and comparing the results to its existing performance charts. It is then redesigned with a one-dimensional (1D) mean line code and simulated in CFD to evaluate performance improvement. The new design is further improved by increasing the geometrical tolerances of the impeller stage's tip gaps to the finest achievable manufacturing tolerance of 0.3 mm. This improvement increases the simulated pressure ratio and efficiency of the MGT compressor from 1.482 to 1.55 and 78.3% to 84.2%, respectively. The MGT testbench predicted overall output power improves by 22.7%, from 18.078 kW to 22.186 kW. Due to a redesigned impeller and finer impeller clearance tolerance requirements, both the impeller and shroud cover need to be re-manufactured. This enables the centrifugal compressor to provide its optimal performance based on geometrical limitations.

Keywords: Centrifugal compressor design; Micro gas turbine; Solar-hybrid gas turbine.

1. Introduction

South Africa is blessed with some of the highest Direct Normal Irradiance (DNI) levels in the world, with certain regions receiving more than 9 kWh/m^2 each day, equating to 3 287 kWh/m^2 annually according to [1]. These high DNI zones in South Africa, particularly in the Northern Cape, are regarded to be relatively remote, with few human settlements and dry, flat landscapes. As a result, this area is particularly suitable for harnessing the sun's energy for renewable energy generation.

A small-scale concentrating solar power (CSP) system based on the Stellenbosch University Solar Power Thermodynamic (SUNSPOT) cycle (proposed by [2]), has been investigated at Stellenbosch University's Mechanical and Mechatronic Engineering Department. The SUNSPOT cycle integrates a conventional CSP plant with a Brayton cycle gas turbine generator, offering the benefits of a hybrid system. This cycle is represented in Fig. 1 below, where the Brayton cycle is coupled to the CSP plant through the combustor and turbine.

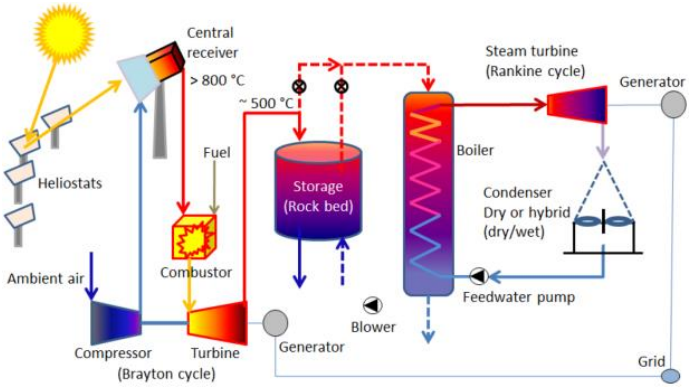

Fig. 1. The SUNSPOT cycle (proposed by [2])

Sunlight is reflected onto a central receiver tower by heliostat mirrors, which transports heat to the gas turbine that generates a significant amount of heat on its own. This heat is then transferred from the gas turbine to a storage facility, where the

remainder of the cycle functions as a traditional CSP plant. That is, steam is produced by a boiler and used to drive a steam turbine, which generates electricity through a generator. The remaining work produced by the gas turbine is transferred to another generator and contributes to overall electricity generation. The performance of the gas turbine generator is therefore essential to the overall efficiency of the SUNSPOT cycle.

The micro gas turbine (MGT) testbench, designed and built by [3] and intended for use in a solar-hybrid application, has a twin-spool and twin-shaft configuration. The gas generator and power turbine sections were developed by using BorgWarner K31 and K44 turbocharger models respectively. The K44 model, which initially served as the power turbine, is replaced by another K31 model that offers a better operating point for the engine. Therefore, both the gas generator and power turbine sections now feature the same K31 model. The tubular style combustion chamber was designed and built by [4] for an MGT engine similarly to the K31 turbocharger setup. This MGT engine is depicted in a flow diagram in Fig. 2 below, with the central receiver system omitted because the focus of this work is on the MGT engine.

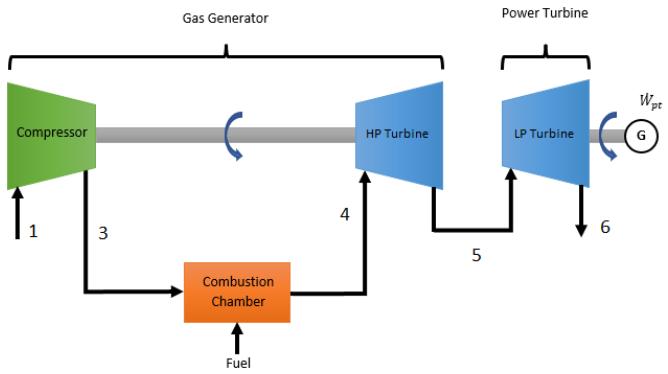

Fig. 2. Layout of twin-shaft MGT system (acquired from [5])

The K31 model, acting as the gas generator, includes the compressor and high pressure (HP) turbine. Whereas the other K31 model, acting as the power turbine, includes the low pressure (LP) turbine and output power section. This K31 model's compressor is omitted since it acts purely as a load for the LP turbine to drive, which will later be replaced with a generator. The inlet and outlet of each stage is labelled, and the compression stage, which is the primary focus of this paper consists of a centrifugal impeller and a diffuser separated by point 2.

According to [6] a centrifugal impeller uses centrifugal force to propel fluid outwards, where the fluid's energy increases through raising static pressure and velocity levels. As it exits the impeller, the diffuser converts kinetic energy into pressure energy.

This paper investigates the effect of upgrading the compression stage of the twin-shaft MGT testbench engine, on overall system performance and operating efficiency. This is accomplished by redesigning the compressor's centrifugal impeller and diffuser using a one dimensional (1D) mean line code. On the new design, a computational fluid dynamic (CFD) simulation is carried out to provide compressor performance charts that allow the performance of the system to be analysed and compared to the existing one. A model of the engine has been developed in a fluid network simulation program by [7], which is used to evaluate the overall improvement of the new compressor design.

Previous research on designing centrifugal compressors focused mostly on acquiring a design methodology and testing the new design on an MGT engine for performance improvement evaluations. This design methodology entails first replicating the original impeller's geometry, then subjecting it to a CFD analysis and comparing the performance results to the original. Subsequently, a new impeller design is optimised using the 1D mean-line code to achieve the desired performance. The improved pressure ratio and efficiency performance charts of the new impeller design, obtained from its CFD analysis, are then tested and compared to those of the replicated design.

2. Flownex® Model

Flownex® (2022b), a fluid network simulation program, is used to model different properties such as mass flow, pressure, and temperature, as well as any other fluid properties required for performance analysis of a system. It solves the mass, momentum, and energy conservation equations to acquire the results. The Flownex® program constructs a network representing a system by using component icons made up of nodes, elements, and boundary conditions. The settings for each of these components can be adjusted to correctly portray the fluid conditions and the engine's size proportion.

2.1. Twin-Shaft MGT Flownex® Model

The twin-shaft micro gas turbine (MGT), developed by [3], was successfully modelled using Flownex® by [7]. This model's nodes, elements, and boundary conditions are presented in Fig. 3. It has been altered from its original layout to be superimposed on the flow diagram in Fig. 2.

The components of the compressor's inlet mimic a bellmouth, with the fluid adjusted to precisely match that of ambient air entering the engine. It is powered by a high pressure (HP) turbine, which is represented by a rotating shaft element, and its outlet is connected to the combustion chamber.

The addition of fuel to the inlet of the combustion chamber

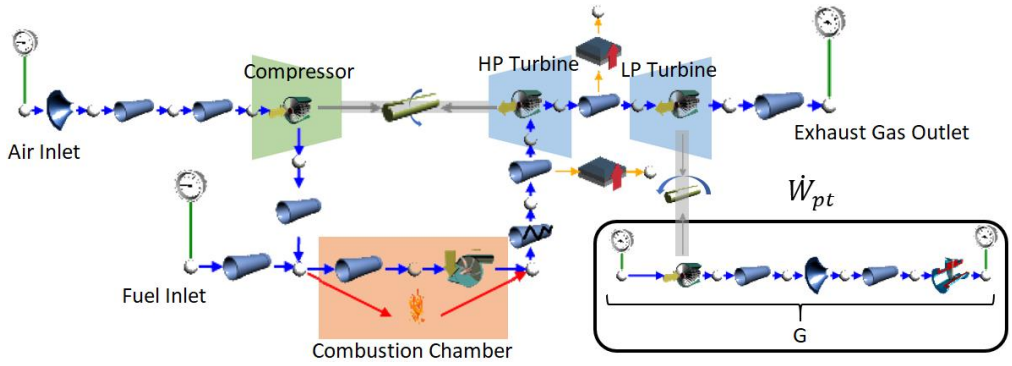

Fig. 3. Flownex® model of twin-shaft MGT (Adapted from [7])

represents an increase in the mass flow rate of fluid going through. To depict the behavior of internal combustion, the combustion chamber is made up of a pipe, a pump, and an adiabatic flame element. The outlet of the combustion chamber is connected to the HP turbine via a resistive network pipe and a heat transfer element which indicates friction and heat loss.

The outlet of the HP turbine is connected to the low pressure (LP) turbine via a heat transfer pipe element, also indicating heat loss. Its outlet is open to the atmosphere, as defined by the boundary condition.

The LP turbine is intended to power a generator that generates electricity; however, this model incorporates a load compressor which the LP turbine drives. This load compressor, which is likewise linked with piping elements, serves as a load for the LP turbine, which is regarded as the overall engine output power.

2.2. Compressor Maps

Compression and efficiency performance charts (compressor maps) portray the relationship between pressure ratio and mass flow rate, with superimposed rotational speed curves and efficiency contours. These compressor maps are what define a specific compressor in Flownex®, where the data is interpolated and any operating points within the compressor range can be predicted. Fig. 4 shows a compressor map labelled with all the essential components.

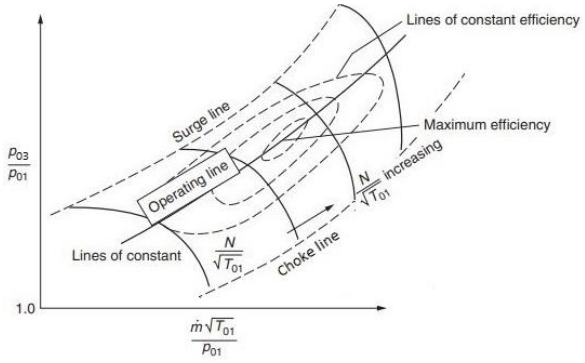

Fig. 4. Compressor map (acquired from [6])

The subscripts 1 and 3 refer to the compressor's inlet and outlet, respectively, with the suffix 0 indicating stagnation (total) conditions. The vertical axis label is the pressure ratio, $\frac{P_{03}}{P_{01}}$, plotted as a function of $\frac{\dot{m}\sqrt{T_{01}}}{P_{01}}$ for fixed values of $\frac{N}{\sqrt{T_{01}}}$. The constant efficiency islands are calculated using Eq. (2), derived in [6] from the pressure ratio (Eq. (1)), where k is the specific heat ratio of air, yielding the ideal running point regions.

$$PR_{C(T-T)} = \left(\frac{P_{03}}{P_{01}}\right) \tag{1}$$

$$\eta_{C(T-T)} = \frac{\left(\frac{P_{03}}{P_{01}}\right)^{\frac{k-1}{k}} - 1}{\left(\frac{T_{03}}{T_{01}}\right) - 1} \tag{2}$$

At the upper pressure ratio, the stall point region is where the constant speed curves end and the compressor becomes unstable. The choke point region is when the constant speed curves become vertical and no increase in $\frac{\dot{m}\sqrt{T_{01}}}{P_{01}}$ can be achieved at these lower pressure ratios.

The Flownex® model's compressor is already set up with the K31 compressor maps, from which initial performance results are produced. Following that, the new impeller design's compressor maps are imported into the Flownex® model to produce new results that are used to evaluate the engine's overall performance improvement.

3. Centrifugal Compressor Design

According to the previously mentioned design methodology, the geometry of the existing centrifugal compressor impeller is measured and replicated in a three-dimensional (3D) modelling tool. This reverse engineering technique is used to provide a baseline design for testing and future improvements. Following that, a one-dimensional (1D) mean line code is applied to iteratively develop a new impeller design based on desired running points.

3.1. Current Impeller

The current K31 compressor consists of an impeller and a vaneless diffuser, which means that the diffuser is simply an open passageway. The basic dimensions of the impeller, such as diameters and axial lengths, are measured manually with a vernier calliper. The remainder of the impeller's dimensions, particularly the blade profiles, have a very complex geometry that necessitates a more sophisticated 3D measuring technique.

The geometry of the impeller, including the complex blade profiles, is captured using a structured light 3D scan method. It works by projecting light in a grid pattern, which becomes distorted when reflected off an object, and cameras catch the reflections to form the model. The EinScan Pro 2X 3D scanner, developed by [8], is used to carry out this task. This device used is housed and administered by [9], located in the Stellenbosch University library. Fig. 5 exhibits the 3D scanner scanning the impeller.

Fig. 5. EinScan Pro 2X 3D scanner

The turntable, on which the impeller is mounted, turns in small increments as cameras record its geometry. The computer program, interacting with the scanner, builds a point cloud of millions of points resembling the impeller. The point cloud is then refined into a solid mesh that replicates the impeller's geometry. From this mesh, exact x, y, and z coordinate point measurements can be captured along all the blade profiles and imported into a 3D modelling program such as Autodesk Inventor® Professional where the blade geometries can be built. Fig. 6 shows the existing K31 impeller alongside the 3D scanned impeller.

(a) **(b)**

Fig. 6. (a) K31 impeller and (b) scanned impeller result

The Einscan Pro 2X claims to deliver a scan accuracy of 0.04 mm, which was validated and proven to be within range. This was accomplished by comparing the basic dimensions of the physical measurements to the same dimensions in the Inventor® 3D model.

3.2. New Impeller and Diffuser Design

The 1D mean-line code is based on a centrifugal compressor design procedure developed by [10]. It has been optimised further, providing users with more control over designing a compressor based on design specifications. It is currently used to assist in the design of centrifugal compressor components such as the impeller and diffuser, and it additionally provides the required geometry file to conduct a computational fluid dynamic (CFD) analysis. A user-friendly graphical user interface (GUI) application (App) in Matlab® for the 1D mean-line code was developed by [11] for assisting users with initial compressor designs. The 1D App follows a logical procedure featuring user inputs and is divided into five steps according to [11], which are listed below:

- Inlet Thermodynamic Conditions: Here, the atmospheric conditions and the fluid characteristics of air are set.
- Impeller Design: The impeller's geometrical inputs are specified at a desired operating speed and output performance. The two-dimensional (2D) blade profile can also be modified, and calculated preliminary performance results can be compared to the intended performance.
- Diffuser Design: Similar to the Impeller Design, geometrical inputs are specified to achieve a desired output performance. The 2D blade profile can be modified, and preliminary performance results are calculated.
- Overall Performance Results: The performance of the impeller and diffuser is calculated at specified operating points, enabling users to validate their initial design.
- CFD Output: The geometry of the impeller and diffuser is exported as a .geomTurbo file, which specifies the blade profiles and operating points. The .geomTurbo file is imported into Numeca FINE™/Turbo software for CFD analysis.

These five steps are performed in an iterative procedure where more than one compressor is designed. CFD simulations provide more accurate results that must be compared and validated to determine the optimal design. The chosen impeller and diffuser generated by the 1D App from the preceding five steps are shown in Fig. 7 below.

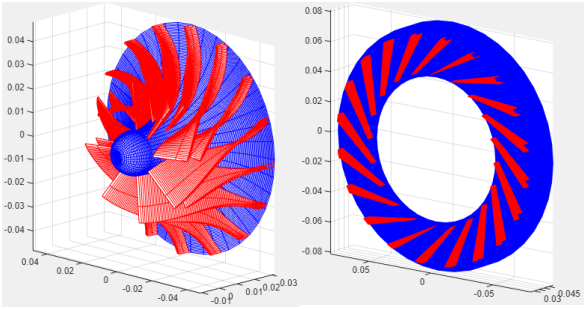

(a) **(b)**

Fig. 7. (a) Impeller and (b) diffuser 1D App design

The characteristics of this final design were chosen to perform at a higher pressure ratio and efficiency. To aid in this, the tolerance of the gaps between the impeller and its housing is increased to the highest manufacturing tolerance achievable with standard machinery. As a result, the new design's housing gap was decreased from the K31 impeller's 0.65 mm to 0.3 mm. The new impeller design includes an additional main and splitter blade to help reduce a blade loading parameter. In comparison to the vaneless diffuser in the K31 compressor, the new compressor design has a 20-blade vaned diffuser to improve the pressure ratio even higher.

The new design aims to increase the output power of the micro gas turbine (MGT) while improving overall engine efficiency. It intends to achieve this by running the compressor at an ideal operating point based on the compressor maps illustrated from Fig. 4.

4. CFD Analysis

A computational fluid dynamic (CFD) simulation is essential because it gives valuable data that aids in understanding the compressor's performance. It provides the total-to-total pressure ratio and efficiency performance curves that the Flownex® model requires. The CFD software used in this study is Numeca FINE™/Turbo v16.1, which is ideally suited for turbomachinery and functions well with the one-dimensional (1D) application (App).

4.1. Setup

The Reynolds-Averaged Navier-Stokes (RANS) Equations are solved using the Spalart-Allmaras turbulence model in this CFD simulation. In comparison to the two equation models, $k-\varepsilon$ and $k-\omega$, Spalart-Allmaras, a one equation model developed by [12], is chosen for its improved boundary layer prediction in the presence of adverse pressure gradients. Its initial intended use for aerofoil applications has resulted in its popularity for modelling turbomachinery applications.

The CFD simulation requires a mesh configuration, which entails dividing the domain into a grid. Before the three-dimensional (3D) mesh is generated, the grid pattern and number of points along the blades are adjusted in a two-dimensional (2D) blade-to-blade (B2B) mesh. This process is necessary to ensure that the grid achieves a good quality, where its orthogonality, aspect ratio, and expansion ratio are all within a particular range. Table 1 lists the recommended requirements for these in accordance with [13], along with the worst results and the percentage of these "bad cells" that were obtained.

Table 1. Mesh quality results

Quantity	Criteria	Worst Value	% Bad Cells
Orthogonality	> 25°	22°	0.098%
Aspect ratio	< 2500	519	0%
Expansion ratio	< 1.8	2.4	0.999%

Further quality optimisation steps are performed on the mesh to guarantee that it meets the Spalart-Allmaras criteria for the non-dimensional distance, y^+, at the walls. The y^+ distribution mostly stayed within the required range of 1 to 10, with minimum and maximum values of 0.142 and 11.172 at non-critical locations. The size of the grid cells is checked for mesh independence, where the results of a coarse, medium, and fine mesh are compared. This is accomplished by generating a performance curve from simulations of each of the three meshes at a particular operating speed, as shown in Fig. 8.

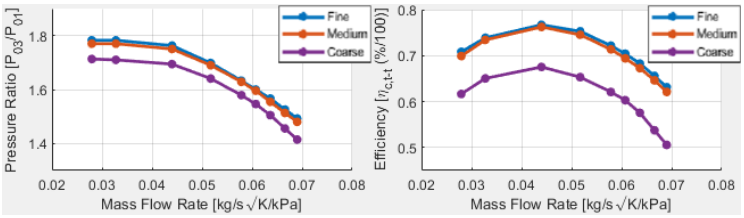

(a) **(b)**

Fig. 8. (a) Pressure ratio and (b) efficiency mesh independence performance curves

The performance curve produced by the coarse mesh differed from the curves generated by the medium and fine meshes. Whereas the performance curves generated by the medium and fine meshes were almost exact. Therefore, mesh independence is achieved because any further increase in mesh density will not significantly improve the results.

The remainder of the CFD setup entails establishing the domain and its boundary conditions, as well as setting the necessary output variables to be analysed. The inlet, outlet, periodic, and solid boundaries make up the domain's boundary conditions. The inlet and outlet boundaries denote the locations where air flows into and out of the domain. The inlet boundary is set up to replicate atmospheric air conditions of 100 000 Pa and 298 K, while the outlet boundary is defined as a mass flow imposed,

which specifies a particular mass flow rate for the simulation to run at. Finally, the solution's convergence is monitored and approved when the inlet and outlet mass flow rates are equal. It is limited to a maximum of 6 000 iterations, giving the solution sufficient time to converge and meet this condition.

4.2. CFD Results

The CFD simulations are used to generate the compressor maps, as shown in Fig. 4, which are required by the Flownex® model. This is done by simulating various mass flow rate points along the operating range, and then assessing the results to calculate the pressure ratio and efficiency from Eq. (1) and Eq. (2) respectively. Lowering the mass flow rate until the pressure ratio reaches a maximum value determines the stall point, or lower mass flow rate boundary. The choke point, or upper mass flow rate boundary, is defined as the point where the pressure ratio curve becomes vertical and no further increase in mass flow rate is possible. The choke point is found by specifying an unrealistically low outlet pressure and then running the simulation to determine the choke mass flow rate. These curves are constructed at various operating speeds to collect adequate data for the Flownex® model.

To begin, the scanned replica impeller is simulated in CFD to obtain its compressor maps, which are then compared to those of the K31 to validate the CFD accuracy. These curves are shown in Fig. 9 below, with the scanned replica impeller's curves superimposed on the K31 curves.

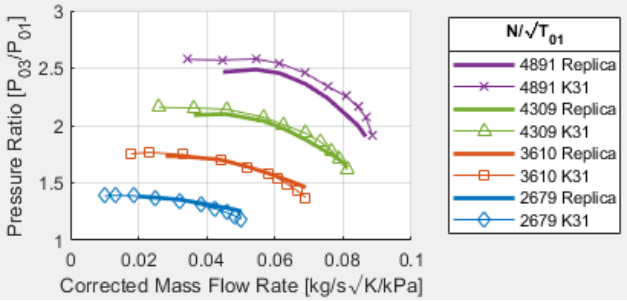

(a)

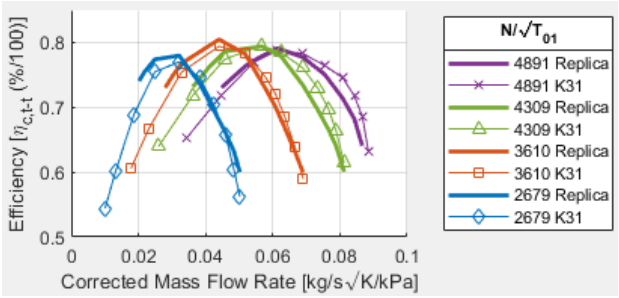

(b)

Fig. 9. (a) Pressure ratio and (b) efficiency compressor maps of scanned replica and K31 impeller

The curves of the scanned replica mostly match those of the K31, with maximum deviations of 6.5% and 6.8% for the pressure ratio and efficiency, respectively. It is concluded that a minor deviation is to be expected because the K31 maps are obtained from actual test runs where more losses are present. Because actual test runs on the compressor allow for pushing further boundary points than a CFD simulation can produce, the stall point of the K31 maps occurs further to the left, as expected.

The new designed impeller and diffuser were subject to the same CFD simulation conditions and method of constructing the performance curves. The compressor map curves of the new design are compared to those of the scanned replica in Fig. 10.

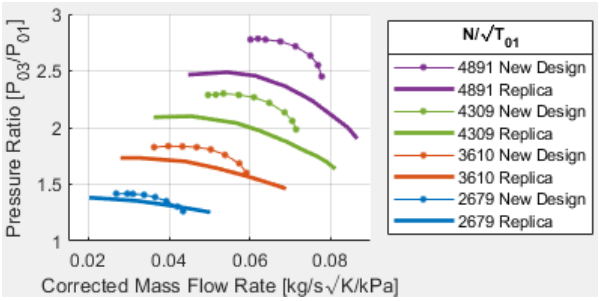

(a)

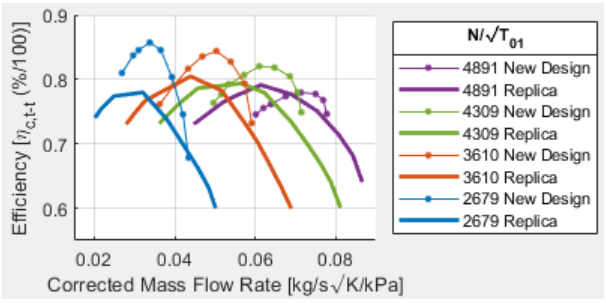

(b)

Fig. 10. (a) Pressure ratio and (b) efficiency compressor maps of new design and scanned replica impeller

The new design displays a narrower operating range compared to the replica due to one additional impeller main and splitter blade and the addition of the vaned diffuser, causing choking to occur earlier. However, it produces a higher pressure ratio and efficiency at each of the engine speeds' optimal operating point, indicating that it can provide better performance for the micro gas turbine (MGT).

5. Results

The K31 compressor maps are first configured to the compressor in the Flownex® model, and the MGT is simulated to obtain initial results. The compressor maps of the scanned replica impeller are then configured to the compressor of the Flownex® model to verify how closely they match. Subsequently, the

compressor maps of the Flownex® model are replaced with maps of the new compressor design to determine the improvements in performance. A constant engine speed of 53 000 rpm is chosen because this is the observed speed at which all the compressors run at peak efficiency. The compressor and overall operating performance results of the Flownex® model are listed in Table 2.

Table 2. Flownex® model MGT results

	$PR_{C(tt)}$ [-]	$\eta_{C(tt)}$ [%]	$\dot{m}_C$ [kg/s]	$\dot{W}_{out}$ [kW]	η_{MGT} [%]
K31	1.477	77.8	0.218	17.8	8.86
Replica	1.482	78.3	0.219	18.078	8.93
New design	1.55	84.2	0.241	22.186	9.96

The replica's design results match the operating point of the K31 compressor with a minor variance, resulting in a total output power that is 1.56% higher. This was expected given that the scanned replica impeller's compressor maps are based on a CFD simulation executed under ideal conditions, whereas the K31's are based on actual test runs. The compressor results of the new design enhance the pressure ratio and efficiency operating points, boosting the MGT engine output power by 22.7% above the scanned replica's performance.

6. Discussion and conclusion

This paper presents the redesign of a centrifugal compressor for an MGT engine used for a solar-hybrid application. A Flownex® model of this MGT is examined where its performance can be predicted, and its compressor stage is defined by compression performance charts. The geometry of the existing impeller is replicated in software, which was done by a 3D scanner. The 1D App was used to aid in the development of a new impeller and diffuser design. CFD simulations are performed on both the scanned replica and the new design to generate performance charts for further modelling the MGT's performance in the Flownex® model.

The compressor maps of the scanned replica exhibited a small variance when compared to the K31 compressor maps. The MGT's overall output power deviates from 17.8 kW, when configured with the K31 maps, to 18.078 kW, when configured with the scanned replica's maps. Modelling the new design's compressor maps yield a substantially higher compressor operating point at which the engine's power improves by 22.7% from 18.078 kW, of the scanned replica impeller, to 22.186 kW.

This modification to the MGT improves overall performance by enabling the MGT's compression stage to offer an optimal operating point. The new compressor not only boosts the output power of the solar-hybrid MGT configuration, but it also allows for future modifications in other stages of the engine to extract the maximum performance achievable from this system.

Acknowledgements

This project was partially funded by the National Research Foundation (NRF) of South Africa (Grant Number 141891).

References

[1] SolarGIS, 2020. Direct Normal Irradiance (DNI). [Online] Available at: https://solargis.com/maps-and-gis-data/download/south-africa [Accessed 19 April 2022]

[2] Kröger, D., 2011. The Stellenbosch University Solar Power Thermodynamic cycle. [Online] Available at: https://sterg.sun.ac.za/wp-content/uploads/2011/05/SUNSPOT-2.pdf [Accessed 19 April 2022].

[3] Ssebabi, B., 2020. Development of a Micro Gas Turbine for Central Receiver Concentrating Solar Power Systems, Stellenbosch: PhD, Stellenbosch University.

[4] Hummel, S., 2014. Berechnung und Konstruktion einer Brennkammer für eine Mikrogasturbine, s.l.: Final year project, University of Stuttgart.

[5] Saravanamuttoo, H., Cohen, H. & GFC, R., 2009. Gas Turbine Theory. 5th ed. s.l.:Pearson Education

[6] Dixon, S. & Hall, C., 2010. Fluid Mechanics and Thermodynamics of Turbomachinery. 6th ed. s.l.:s.n.

[7] Afeltra, M., 2022. The Development of a Recuperator for a Solar Hybrid Micro Gas Turbine System, Stellenbosch: Masters, Stellenbosch University.

[8] 3D, S., 2023. About SHINING 3D. [Online] Available at: https://www.shining3d.com/about-us/ [Accessed 30 March 2023].

[9] Service, S. L. a. I., 2023. Makerspace: 3D Scanning. [Online] Available at: https://libguides.sun.ac.za/makerspace [Accessed 30 March 2023].

[10] Aungier, R., 2000. Centrifugal Compressors, New York: ASME Press.

[11] Van Eck, H., 2020. Development of a One-Dimensional Code for the Initial Design of a Micro Gas Turbine Compressor Stage, Stellenbosch: Masters, Stellenbosch University.

[12] Spalart, P. R. & Allmaras, S. R., 1994. A one-equation turbulence model for aerodynaic flows, s.l.: s.n.

[13] De Villiers, L., 2013. Numeca Manual for the Design of a Centrifugal Compressor, s.l.: Stellenbosch University.

FEASIBILITY STUDY ON THE USE OF A WATER-COOLED SHELL AND TUBE HEAT EXCHANGER FOR A SCO_2 BRAYTON RECOMPRESSION CYCLE IN CSP APPLICATIONS

Mubenga C. Tshamala[1], Michael Owen[2], Craig McGregor[3], and Zinhle Dlamini[4]

[1] Stellenbosch University, Mechanical and Mechatronic Department, Joubert Street, Private Bag X1, Matieland 7602, South Africa; Phone: + 27 21 808 4243; E-mail: mctshamala@sun.ac.za

[2] Stellenbosch University; E-mail: mikeowen@sun.ac.za; [3] Stellenbosch University; E-mail: craigm@sun.ac.za

[4] Stellenbosch University; E-mail: zdlamini00666@gmail.com

Abstract: The Rankine cycle has been a leading power generation cycle for years. Recently however, the Brayton cycle, specifically the recompression configuration, has proven to be more efficient when using sCO_2. Studies have demonstrated that if the compressor inlet temperature and pressure of sCO_2 are maintained near the critical values, the cycle's efficiency can be improved. For this project, the goal was to design a water-cooled shell and tube heat exchanger (STHE) that can cool sCO_2 to within a range of 30°C to 33°C for a Brayton recompression cycle and evaluate its performance when used with CSP. The STHE was designed iteratively using the Bell Delaware method and TEMA standards. With FLOWNEX, a simulation of the Brayton recompression cycle with an inventory control system was conducted using DNI collected in the Upington area on the hottest day of the year. For this simulation, it was found that a minimum heat input of 35MW was required for accurate results. It was shown that even when the dew point temperature varies, the heat exchanger can maintain the required outlet temperature. However, it transpired that this could not result in the predicted 51.5% efficiency, but cycle temperatures revealed to be stable even during transient operation. To achieve the above efficiency, a combination of pressure ratio, split ratio, and main compressor inlet temperature (CIT) to the recommended range is required to ensure efficiency increase.

Keywords: Supercritical carbon dioxide Brayton cycle; Compact heat exchangers; Recompression cycles; Concentrated Solar Power.

1. Introduction

According to the International Energy Agency [1], the world energy demand is expected to continue its rise for the foreseeable future. The Stated Policies Scenario (STEPS) predicted an annual growth of 1% between 2022 and 2030, while the Announced Pledges Scenario (APS) predicted a 0.2% annual growth. However, it is necessary to highlight that these predictions account for the current energy crisis, leading to a 3.3% drop from the previous 2030 predicted GDP. In the South African context, about 80% of carbon emission derives from the energy sector, of which 50% is from electricity generation [2]. In-light of the above, there is a drive to further develop alternative sources of energy to feed the power generation industry to adequately respond to challenges of energy demand growth, high prices as well as the reduction of emissions. As such, in the search for alternative solutions, the Department of Mineral Resources and Energy of South Africa has embarked on a journey to diversify the energy supply for 2030 and beyond [2]. For instance, one of South African most attractive regions, the Upington region, with a recorded long-term annual average of 2816 kWh/m^2 of Direct Normal Irradiance (DNI) and 2282 kWh/m^2 of Global Horizontal Irradiance (GHI); is an under-utilized energy source that could potentially alleviate the strain on existing power plants because the area is exposed to relatively high solar irradiation that can greatly contribute to the power generation sector.[3]

However, these regions are often characterized by a combination very little to no rain, which results in water shortages, and very high ambient temperatures. It is recorded that the annual average rain can be as little as 83.3 mm and ambient temperatures, reaching maximum of 45.3°C between 1991 – 2020 [4]. The above constitutes a significant challenge when it comes to the design of effective heat rejection units for thermal power plants. The traditional steam Rankine cycle has been used for many years in thermal power generation for its ability to produce power at high efficiencies. In recent years, however, variations of the Brayton cycle are under investigation as they have shown potential for achieving competitive efficiencies, when operated using supercritical carbon dioxide (sCO_2) as working fluid [5]. The density of sCO_2 near the critical state resembles that of a liquid. Thus, the use of sCO_2 in a Brayton cycle offers reduced compression power and increases the cycle's overall efficiency [6]. In the early 2000s Dostal [7] investigated different sCO_2 cycle layouts to discover that the recompression layout is the most efficient layout of all.

To further improve the performance of the sCO_2 Brayton recompression cycle (BRC), it is important to analyse how the individual components can affect the overall efficiency. While there is much research on all the other power block components, there is unfortunately very limited research on heat rejection system design, as well as the impact of this system on the cycle's overall performance. Most plants attempt to avoid operating near the critical point of sCO_2 because the carbon dioxide thermo-physical properties are very sensitive to change in temperature or pressure is unstable in this region [8]. Specifically, there are rapid fluctuations in the fluid properties that affect the compressor performance. A 2℃ difference in the main compressor inlet temperature (CIT) can result in a 10% drop of adiabatic efficiency of the compressor [9]. Despite of the above, Ehsan [10] showed that if the CIT can be 35℃ or below, a BRC could operate at efficiencies higher than 49%. Attaining such lower temperature after the heat rejection unit in regions characterized by high ambient temperature as discussed earlier present many challenges; hence, it was recommended to investigate multiple cooling system designs to ensure delivery of CIT of below 35°C. Hence, for this study, a shell-and-tube heat exchanger (STHE) was identified as a suitable candidate due to its compactness, affordability, ability to sustain high pressure ranges and wide range of operating temperatures [11].

2. Aim

The objective of this study is thus to investigate the dynamic response of a water-cooled sCO_2 BRC for concentrated solar power (CSP) applications to simultaneous variations of solar resource, direct normal irradiation (DNI), and ambient temperatures. A previous study by Tshamala *et al.* [12], considered a concentrated solar powered sCO_2 BRC fitted with inventory control system, subjected to daily variation of DNI. The above cycle was simulated to predict the required cooling capacity of the heat rejection unit that would maintain the CIT constant at 35°C. The inventory control, however, was introduced to regulate and maintain the turbine inlet temperature (TIT) through cycle's mass flow rate control. Whilst the above study assumed a hypothetical heat rejection unit, in this study, a water-cooled shell-and-tube heat exchanger (STHE) is designed and integrated to the 1-D Flownex simulation model of the sCO_2 BRC and daily ambient temperatures are used as input to the STHE. This STHE is designed to deliver a CIT ranging between 30 – 33°C, aiming at improving the power block overall efficiency. It is essential to highlight that since the study of the turbomachinery is not part of the current scope, the built 1-D model simulation model used centrifugal pumps in place of compressors; this was decided in anticipation that in the transcritical region the fluid exhibits liquid-like properties, especially as its temperature continues decrease [13]. Simulation of the complete power block is performed to determine the overall cycle dynamic response and performance assessment is presented. However, the current investigation assumes that the cooling water is provided at ambient wet-bulb temperature in the Upington. The designed STHE will be used in ongoing research which will consider performance assessment of dry, wet and hybrid systems in an indirect cooling configuration.

3. sCO_2 BRC cooling method and design.

3.1. Brayton Recompression Cycle description

The original BC (Fig. 1) comprised three primary components. The compressor, combustion chamber and the turbine. Atmospheric air (State 1) would enter the compressor and be pressured to state 2 and then heated to state 3 to increase its specific volume to ensure greater power output in the turbine where it is expanded to state 4. After the turbine the exhaust gas is released into the atmosphere [6]. This is a very basic form of the BC when compared to the Brayton recompression cycle (BRC) (Fig. 2) which comprises two compressors, two recuperators, a turbine, a heater, and a cooler. The working fluid enters the main compressor (MC) at state 1 where the fluid is pressurised to state 2. The fluid is then heated in the low temperature recuperator (LTR) (2 – 3), as well as the high temperature recuperator (HTR) (4 – 5) using heat from the hot exhaust gases.

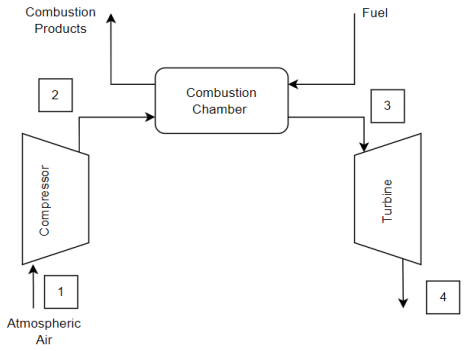

Fig. 1. Original Brayton Cycle Layout

Additional heat is added from an external source, CSP in this case, lifting the temperature to state 6 where the fluid enters the turbine. The fluid is expanded to state 7, producing work, and then directed into the HTR (7 – 8) and LTR (8 – 9) to reject heat. The fluid at state 9 splits into the cooler and the auxiliary compressor where a percentage of the fluid is pressurised to the cycle's highest operating pressure. The remainder of the fluid is directed to the cooler (heat rejection unit), where it is cooled to targeted CIT (state 1) before returning to the main compressor.[14]

3.2. sCO_2 BRC heat rejection unit

The heat rejection unit is an essential part of any cyclic heat engine whose role is to ensure effective energy transfer from the heat engine to the surrounding. According to Carnot, operating the heat rejection unit at low temperatures may contribute to enhancing to the overall power cycle's efficiency. Considering the above, a prior investigation was conducted to advise on the operating temperature of the sCO_2. This investigation took foundation from Ehsan [10], revealed that the sCO_2 BRC has the potential to achieve greater efficiencies for higher overall pressure ratios, around 2.5, for CITs ranging between 30 – 35 °C as showed in fig. 3 below. Therefore, 32 °C is used as targeted CIT for the heat rejection unit.

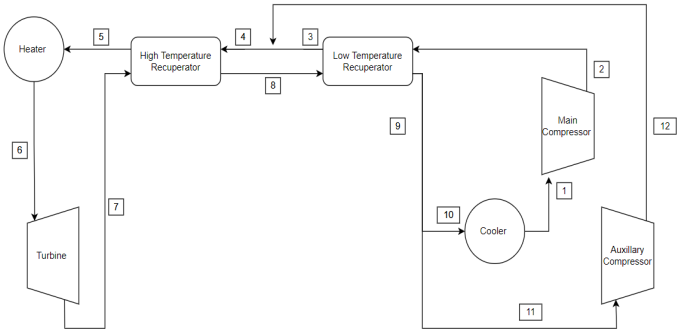

Fig. 2. Brayton Recompression Cycle Layout. [14]

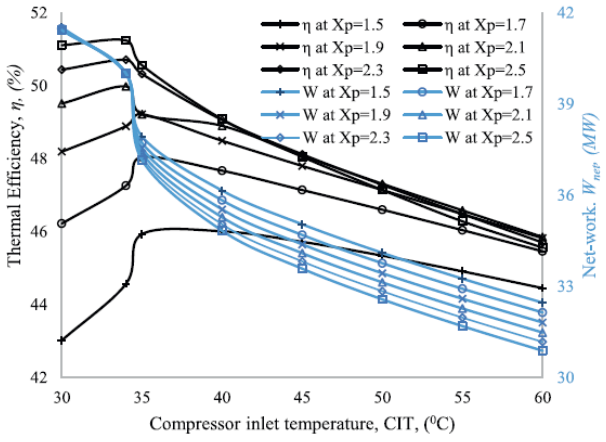

Fig. 3. s-CO_2 BRC efficiency and net power as function of pressure ratio CIT. [10]

To determine the heat rejection cooling capacity, a Flownex simulation model of a 20 MW sCO_2 BRC was built and simulated by Tshamala *et al.* [12] using 32 °C as CIT. This simulation revealed that to maintain a constant 32 °C CIT in an environment affected by daily variations in DNI, the heat rejection unit should be able to effectively transfer 20.36 MW of heat. Thus, this cooling duty together with the heat rejection unit inlet temperatures and the CIT are therefore used to advise the design of the heat rejection unit heat exchanger.

3.3. sCO_2 BRC Shell-and-tube heat exchanger design considerations

3.3.1.STHE physical configuration

The current shell-and-tube heat exchanger (STHE) was sized using the approach prescribed in the Tubular Exchanger Manufacturers Association (TEMA) standards [15]. This approach is used to ensure compliance with best practices and safety regulations. Hence, based on TEMA standards, the STHE design specifications such as shell type, tubes bundle type, tubes layout, tubes material, baffles type, spacing and cut, front-end head type, and rear-end type were selected as presented in Table 1. The above assisted to define to SHTE physical configuration. Choices resulting in the STHE physical layout are generally made with respect to specific criteria such as pressure requirements, cleaning method, cost of production, etc. However, for the purpose of the current STHE design, to maintain the carbon dioxide in supercritical region, the current design suggested to use 7.45 MPa as cycle's lowest pressure [14]. This value has been arbitrary chosen to ensure that at all time, the carbon dioxide remain in supercritical conditions, and not too high to ensure relatively effective gas expansion in turbine. This value will therefore be accounted for when selecting the tube size and thickness.

Table 1. Selected heat exchanger [15]

Front-end Head:	B-type
Shell Type:	E-type
Rear-end Head:	S-type
Tube Bundle Type:	Floating head type
Baffle Type:	Single segmental baffle
Baffle Cut:	25%
Baffle Spacing:	40% of the shell diameter
Tube Fluid:	sCO_2
Shell Fluid:	H_2O
Tube Layout:	30°
Tube Material:	Copper

3.3.2.STHE design methodology

At this stage of the design process, the required cooling duty, the operating pressure of the STHE, the sCO_2 inlet temperature to the STHE, and mass flowrate have been approximated based

on thermodynamic cycle analysis; the cooling water inlet temperature approximated to ambient wet bulb temperature, since we operate on the assumption that a wet cooling tower is used to refresh the cooling water. The desired sCO_2 outlet temperature known (set to 32°C), and the sCO2 inlet temperature was set as 120°C which is the highest value established in Tshamala *et al.* [12]. The mass flowrate of the cooling water can be estimated using equations from basic heat transfer. The above assumed maximum 7 °C temperature difference between the inlet and the outlet temperature of the cooling water across the STHE [16]. Although both the e-NTU procedure as well as a LMTD method could be used for the sizing of the current STHE, for simplicity a decision for made to use only the LMTD method for sizing of the STHE. The above was done using equation (1) to define the overall heat transfer area.

$$Q = U A_o F \Delta T_{lm} \qquad (1)$$

In the above equation (1), Q, U, A, F, and ΔT_{lm} represent the cooling duty, the overall heat transfer coefficient, the total heat transfer area, the temperature correction factor, and the mean log temperature difference across the STHE. Equation (2) was used to evaluate the temperature correction factor introduced in equation (1).

$$F = \frac{\left(\sqrt{R^2+1}\right) \ln\left(\frac{1-S}{1-RS}\right)}{(R-1) \ln\left[\frac{2-S\left(R+1-\sqrt{R^2+1}\right)}{2-S\left(R+1+\sqrt{R^2+1}\right)}\right]} \qquad (2)$$

Where S is a measure of the temperature efficiency of the heat exchanger, and R is the thermal capacities ratio between the shell side and the tube side; calculated as below:

$$R = \frac{T_{CO2in} - T_{CO2out}}{T_{wout} - T_{win}} \quad (3) \quad \text{and} \quad S = \frac{T_{wout} - T_{win}}{T_{CO2in} - T_{win}} \quad (4)$$

With T_{win}, T_{wout}, T_{sCO2in} and $T_{sCO2out}$ representing the water inlet, water outlet, sCO_2 inlet and sCO_2 outlet temperatures respectively [17]. The ΔT_{lm} was obtained from the temperatures given above, while U, was estimated using an iterative approach. At first, both the shell-side and the tube-side heat transfer coefficients (h_w and h_{sCO2}) are guessed as 5000 W/m^{2}K on shell-side (water) and 500 W/m^{2}K (gas) on the tube-side [18]; using in conjunction equations (5) and (1), the heat transfer area A_o is obtained. In equation 3, the fouling resistances for both make-up water and sCO_2 were approximated by Kakac et *al.* [18]. To define the tubes configuration, equations (6) and (7) were used to determine the number of tubes (N_T) as well as shell diameter (D_s) of the STHE.

$$U_{fc}^{-1} = \frac{1}{h_w} + R_{fs} + \frac{d_o}{2k} \ln\left(\frac{d_o}{d_i}\right) + R_{ft} + \frac{PR}{h_{CO2}} \qquad (5)$$

In equation 5, R_{fs}, R_{ft}, k, d_i, d_o and PR are the shell-side fouling factor, the tube-side fouling factor, tube material thermal conductivity, the tubes inside diameter, tubes outside diameter and representing tube outside to inside diameter ratio.

$$D_s = 0.637 \sqrt{\frac{CL}{CTP}} \left[\frac{A_f \, SO \, PR^2 \, d_o}{L_T}\right]^{1/2} \qquad (6)$$

$$N_t = \text{round}\left[0.785 \frac{CTP}{CL} \frac{D_s{}^2}{(PR \, d_o)^2}\right] \qquad (7)$$

Where CL represents the tube layout constant; CTP, the tube count calculation constant; L_T, the tubes active length, SO surface overdesign, and A_f, the heat transfer areas. [18]

According to literature, the optimum ratio between the tubes length and the shell diameter should be kept between 5 – 10, since it is a trade-off between the pressure drop on the shell side and manufacturing costs [18]. Engineering Equation Solver (EES) was used solve simultaneously all equations described in the model for variety of tube diameter. For each tube diameter, a parametric study was conducted to determine the corresponding tube length that would balance the heat transfer equation between the tube and shell sides of the STHE. The result of the parametric study is presented in Fig. 4 and Fig. 5, for only four diameters; hence for the purpose of this project a conservative approach suggested that a length-to-shell diameter of 5.31, using 22.225 mm tube outside diameter.[19]

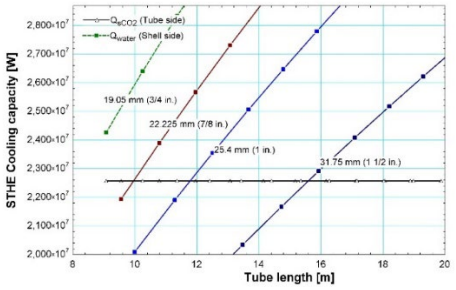

Fig. 4. STHE cooling capacity vs tube length for various tube diameters.

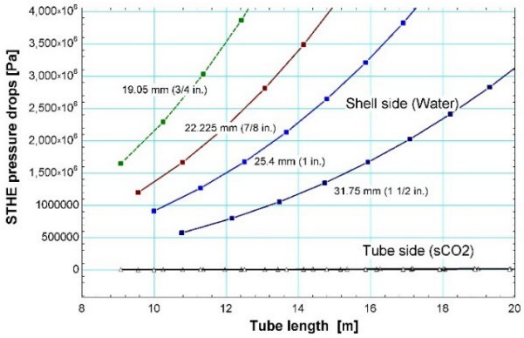

Fig. 5. STHE pressure drops vs tube length for various tube diameters.

In Fig. 4 above, the tube side heat transfer was found using the enthalpy change of sCO_2 between the inlet and the outlet of the STHE, while the shell side heat exchanger was found using equation 1. The shell side heat transfer coefficient was obtained using equation 8, while equation 10 approximated the tube side heat transfer coefficient. [18]

$$\frac{h_w D_e}{k_{mw}} = 0.36 \left[\frac{D_e G_w}{\mu_{mw}}\right]^{0.55} \left[\frac{cp_{mw}\,\mu_{mw}}{k_{mw}}\right]^{1/3} \left[\frac{\mu_{mw}}{\mu_w}\right]^{0.14} \quad (8)$$

$$D_e = \frac{4\left(\frac{P_T^2\sqrt{3}}{4} - \frac{\pi d_o^2}{8}\right)}{\frac{\pi d_o}{2}} \quad (9)$$

$$h_{sCO2} = \frac{k_{sCO2}}{d_i}\left[\frac{\frac{f_D}{8}(Re_{sCO2} - 1000)\,Pr_{sCO2}\left[1 + \left(\frac{d_i}{L_T}\right)^{0.67}\right]}{1 + 12.7\left(\frac{f_D}{8}\right)^{0.5}\left(Pr_{sCO2}^{0.67} - 1\right)}\right] \quad (10)$$

Where:

$$f_D = [0.79\,\ln(Re_{sCO2}) - 1.64]^{-2} \quad (11)$$

In equation 8, D_e is the hydraulic diameter applicable on the shell side for triangular tube configuration, G_w is the water mass flux; cp_{mw}, k_{mw}, and μ_{mw} are the water specific heat, thermal conductivity, kinematic viscosity expressed at mean temperature respectively, μ_w the water kinematic viscosity at well temperature. And in equation 10, f_D represents the friction factor on the tube side; Re_{sCO2}, Pr_{sCO2}, and k_{sCO2} are the Reynolds number, the Prandtl number, and the thermal conductivity of sCO_2, respectively. Hence, the results of the above approximation converged to 416.2 W/m^{2}K on the tube-side (h_{sCO2}) and 10307 W/m^{2}K on the shell-side (h_w). The subscript m in the thermophysical properties refers to the thermophysical properties evaluated at mean temperature, while w refers to water. Although tube side pressure drops were not described as one of the driving factors of decision for STHE sizing, it was found necessary to estimate them and present them in Fig. 6 below (Tube side of Fig.5 enhanced).

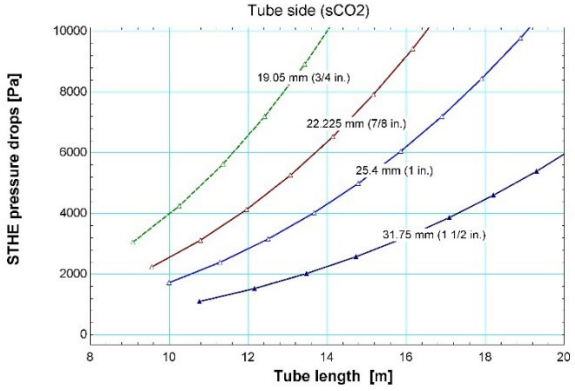

Fig. 6. STHE tube side pressure drops vs tube length for various tube diameters.

From Fig 5 and Fig. 6, it could be seen that at 22.225 mm tube outside diameter and 9.95 m tube length, the corresponding pressure drops on the shell side and the tube are 1.4 MPa and 2.5 kPa.

For the rating of the designed STHE, five methods were investigated, including the traditional e-NTU, the Kern, the Taborek, the Bell, and the Bell Delaware. It was found that although the first four could approximate the heat transfer coefficient and pressure drops with reasonable accuracy, the Bell Delaware method considers most of the fluid complexities as the fluid passes for baffle to tubes and vice versa, hence was found to be the most accurate. [20]

3.3.3.STHE rating – The Bell Delaware method

This method suggests that the designer initially start by estimating the tube size, the tube length, the heat transfer coefficient, the baffle spacing as well as the pitch ratio. Using an iterative approach, the pressure drops as well as the heat transfer coefficient was computed iteratively to convergence for the shell side fluid flow as well as the tube side fluid flow with the equations listed in Table 2. This process was repeated for a variety of tube sizes and lengths to approximate the appropriate heat exchanger dimensions.

Table 2. Pressure drop and heat transfer equations [18]

Shell Side (Water)	
Pressure drops:	$\Delta P_s = \frac{f_s G_w^2 D_s (N_b+1)}{2\,\rho_{mw} D_e \Phi_s}$ (12)
Heat transfer coefficient:	$h_B = h_{id} J_c J_l J_b J_s J_r$ (13) Where: $h_{id} = J_i\, cp_{mw}\, G_w \left[\frac{k_{mw}}{cp_{mw}\mu_{mw}}\right]^{2/3} \Phi_s$ (14)
Tube side (sCO_2)	
Pressure drops:	$\Delta P_{ft} = \left[\frac{4 f_D N_P L_T}{d_i} + 4 N_P\right] \frac{G_{CO2}^2}{2\,\rho_{mCO2}}$ (15)
Heat transfer coefficient	Use equations 10 and 11

In table 2, f_s, N_b, Φ_s, ρ_{mw}, N_P, G_{CO2}, and ρ_{mCO2} are shell-side friction factor, number of baffles, water density at mean temperature, number of tube passes, carbon dioxide mass flux, and carbon dioxide mean density. J_i, J_c, J_l, J_b, J_s, and J_r are the corresponding correction factors for Colburn j-factor, baffle cut and spacing, baffle leakage, baffle spacing at inlet/outlet, bundle bypassing and Reynolds number correction.

4. Sensitivity analysis and cycle simulation

This simulation was done in Flownex. It was also important to determine whether the designed heat exchanger could maintain the temperature in the specified range. Table 3 presents overall cycle performance for CIT of 32 °C which is within the recommended target and 35 °C which aligned with the model verification discussed in the previous project [12].

Table 3 values were obtained through steady state simulation of the sCO_2 BRC assuming CIT at 35°C and at 32°C, for 10.4 MW and 20 MW net power. Table 3 values were obtained through steady state simulation of the sCO_2 BRC assuming CIT at 35°C and at 32°C, for 10.4 MW and 20 MW net power. Hence, to run the dynamic simulation of the complete cycle, it was necessary to integrate the designed STHE to the steady state model and implement variations in the solar DNI, ambient air temperature and wet bulb temperature.

Table 3. s-CO_2 BRC simulation model results

Targeted CIT [°C] / Plant size [MW]	**35 / 10.4**	**35 / 20**	**32 / 20**
MC Power [MW]	1.87	3.61	3.27
AC Power [MW]	2.31	4.44	4.35
Turbine Power [MW]	14.59	28.05	27.57
Net Power [MW]	10.44	20.00	19.87
Heat input [MW]	21.78	41.88	40.23
Efficiency [%]	47.76	47.77	49.4
Cooling Duty [MW]	11.34	21.88	20.36

The solar DNI was obtained from SOLARGIS, while the ambient air temperature as well as wet bulb temperature were sourced from the South African weather services for a typical hot day of the year 2022.

At this stage, it is necessary to specify that the sizing discussed in section 3 allowed to determine all other dimensions of the STHE as shown in Table 4. Information provided in Table 4 are used to build the STHE in Flownex, and the STHE simulation model was integrated in the sCO_2 BRC to close the loop and finally enabling the overall cycle dynamic response analysis.

Table 4. STHE design characteristics

Tube Outer Diameter (d_o)	mm	22.225
Tube pitch ratio (PR)	-	1.25
Tube Inner Diameter (d_i)	mm	17.78
Tube Length (L_T)	m	16
Tube Pitch (P_T)	mm	27.78
Baffle Cut (BC)	%	25
Number of Tubes (N_T)	-	4258
Shell Diameter (D_S)	m	2

5. Results and discussion

Two scenarios were investigated. The first being the ideal scenario where the heat input to the cycle was constant and secondly the heat input to the cycle was allowed to track the daily variation of the DNI. The 20 MW net power solarized sCO_2 BRC was designed using a solar field capable of supplying 44 MW thermal as peak capacity while for the second simulation, the cycle heat addition was simulated using the DNI and ambient temperature daily profiles. In both cases, the cooling water mass flow rate is maintained constant, and its temperature was approximated to the daily variation of the wet bulb temperature in the Upington. According to Uvarov *et al.* [21], knowing the ambient temperature, one could approximate the wet bulb temperature; however, for the current simulation this temperature was measured and supplied by the SAWS. A varying ambient temperature for a typical hot day in Upington, March 10th, 2022, was used. The results of both simulations are shown and discussed in the next few paragraphs.

With the first scenario (Figure 5 and 6), it can be observed that the heat exchanger can deliver a CIT ranging within the recommended values. The produced net power and the cycle efficiency are close to the predicted steady state values, 20.7 MW and 46% for mass flow rate approaching the designed maximum mass flow rate for the turbine used. The sCO_2 mass flow distribution between the two compressors depends on the split ratio (SR), which is the ratio of the secondary compressor mass flow to the total mass flow in the turbine. For this case, the SR fluctuates at about 30%. Regardless of the wet bulb temperature hourly variations, the CIT was effectively maintained to a maximum of 31.6 °C, which is well below the 35 °C where sCO_2 properties become unstable.

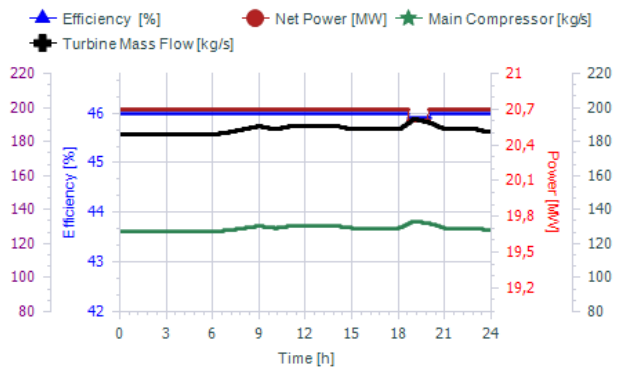

Fig. 5. Cycle efficiency, Net power, Main compressor mass flow, and turbine mass flow for constant heat load

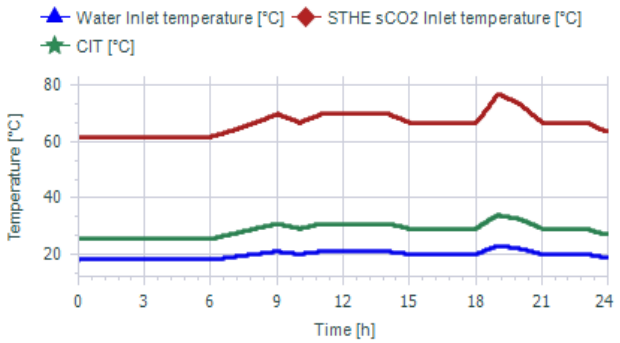

Fig. 6. CIT, Cooling water inlet temperature and STHE sCO_2 inlet temperature for constant heat load

The efficiency curve of the original cycle with the CIT of 35 ℃ is shown in Figure 7. This graph shows that at 35 °C CIT, the efficiency was recorded as 45.6% regardless of the DNI variation (Heat input). This efficiency slightly increased to about 46% when the CIT drops to 31.6 °C. according to literature, the efficiency is expected to be at its best value at 33 °C. [10]

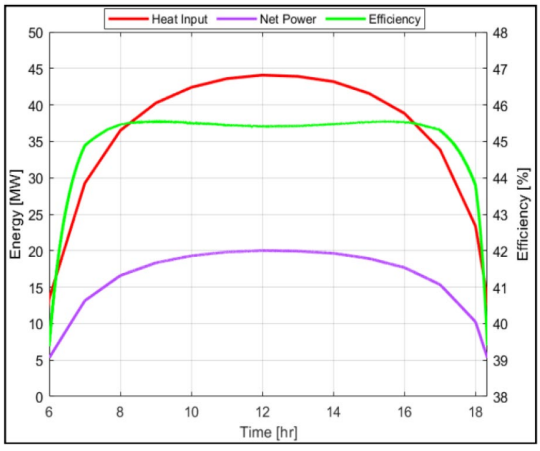

Fig. 7. Heat input, Net power, Efficiency for 35°C CIT cycle [12].

However, in the study of efficiency increase, two other parameters are critical to ensure best values. Figure 8, discussed by Ehsan [10] shows that there is a strong correlation between the split ratio with the cycle thermal efficiency, which was not part of the current investigation. Hence, it is believed that pressure ratio and split ratio may play a significant role for the efficiency improvement to achieve performances predicted in Ehsan [10] as it can be seen in Figure 8.

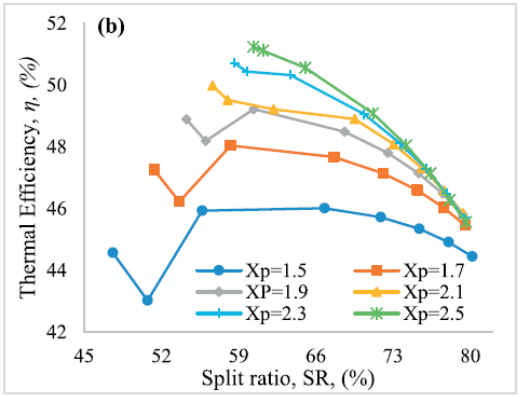

Fig. 8. Thermal efficiency variation with split ratio and pressure ratio of a sCO_2 BRC [10]

The second scenario, the full dynamic simulation of the sCO2 BRC power block with STHE integrated to the loop, was performed using input variables presented in Figure 9. The ambient temperature and the DNI were used to estimate the heat input to the system, while the wet bulb temperature is used as input at the STHE, representing the heat rejection unit.

Figure 10 is a display of the full cycle response to variation in weather conditions and solar energy. The efficiency still starts at 6am at 47% but slightly decreases to 46% when the full heat input is applied, then rises again as the heat input decreases. Many reasons could be responsible for the observed changes, since operating with many variables. However, the heat input variations can be highlighted as one of the many reasons. As the heat input increases, the turbine inlet temperature (TIT) in figure 11 tends to rise, however, the inventory control system constantly attempts to maintain the TIT at 700 °C by adjusting the total mass flow through the turbine. The above is believed to be the main reason for severe fluctuations observed in the TIT as well as the efficiency from around 13h00 through the after until sunset as shown in figure 11.

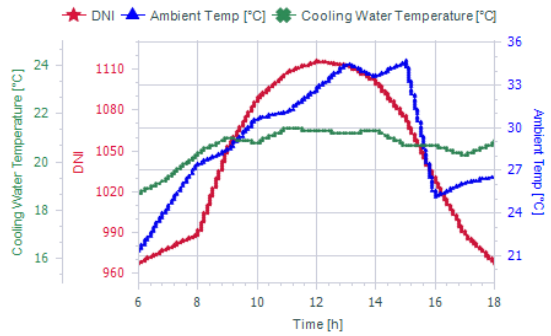

Fig. 9. Upington selected DNI, ambient temperature and wet bulb temperature [22] [4]

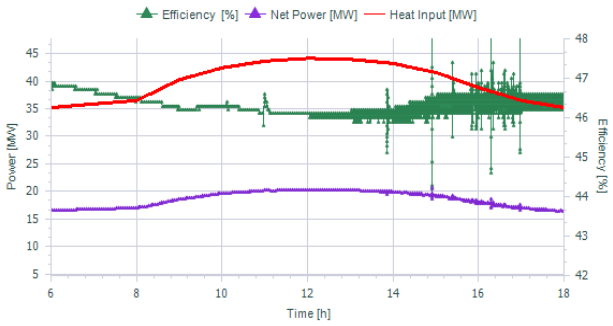

Fig. 10. sCO_2 BRC cycle efficiency and net power for variable heat load

In figure 10, the heat input is observed to rise as the day progresses in the morning times and decreases progressively in the afternoon. With it, the net power of the cycle increases to reach the power block's rated capacity when the heat input reaches it maximum. On the heat rejection site, it can be observed in figure 12 that the cooling load also follows the heat input trend, with a little deviation due to ambient conditions changes.

Another important observation is made on the CIT which starts just about 26 °C (compressed liquid), then increases, reaching its maximum when the heat input reaches its maximum, then decreases progressively in the afternoon. The above is due to a combined effect of the variation of the sCO_2 mass flow in the cycle induced by the inventory control system, the low wet bulb temperature early in the day and late in the afternoon, as well as the unchanged mass flow of the cooling water through the STHE for the duration of the simulations. Figure 11 also shows the STHE sCO_2 inlet temperature, which changes because of feedback introduced by the STHE in the cycle.

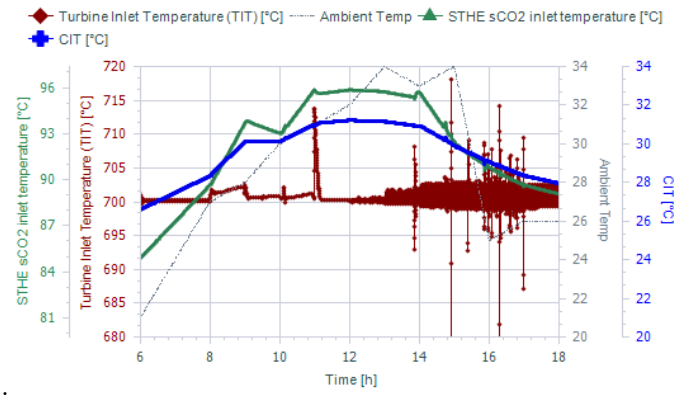

.

Fig. 11. Turbine inlet temperature, CIT, STHE sCO_2 inlet temperature and ambient temperature fluctuations for variable heat load.

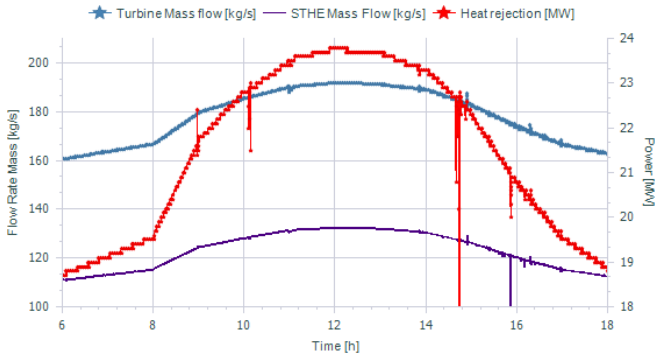

Fig. 12. STHE cooling load, mass flow through the turbine and main compressor variation for variable heat load.

6. Conclusion

The aim of this project was to design a STHE with capacity to service a sCO_2 BRC powered by CSP, then investigate the overall cycle dynamic response to variable heat input as well as ambient temperatures. A water cooled STHE was designed using the traditional mean-log temperature difference approach during the first iteration sizing, which was enhanced using the Kern approach to refine the optimum dimensions, and Bell-Delaware considered for rating. Industry recommendations were used to make final decisions on the STHE design parameters accounting for the balance between manufacturing cost and pressure losses. The designed heat exchanger was then used in a simulation of a sCO_2 BRC at both constant heat load as well as variable heat load. The simulation results of the sCO_2 BRC have shown that the designed STHE adequately performed, maintaining the CIT below 32 °C, however the efficiency remained lower than the targeted 52%. The above revealed that decreasing the CIT alone is necessary to enhance the stability of the power cycle, however other aspects such the pressure ratio and split ratio are critical to further improve the

overall cycle efficiency.

Acknowledgements

Authors would like to acknowledge the support received from the Solar Thermal Research Group (STERG) and the Centre for Renewable and Sustainable Energy Studies (CRSES) for the funding and administration support which enabled the authors to present the findings of this study at the Southern African Sustainable Energy Conference (SASEC 2023). These acknowledgements are also extended to the Mechanical and Mechatronic department staff for their support and guidance.

References

[1] I. E. Agency, "World Energy Outlook," 2022.

[2] S. G. Mantashe, "Integrated Resource Plan," 2019.

[3] T. Cebecauer, A. Skoczek, J. Betak, and M. Suri, "Site Assessment of Solar Resource Upington Solar Park," 2011.

[4] SAwS, "Annual State of the Climate of South Africa 2020," *Annu. State Clim. South Africa 2020*, vol. 1, no. 1, p. 30, 2021, [Online]. Available: https://www.weathersa.co.za/Documents/Corporate/Annual State of the Climate 2019.pdf.

[5] V. T. Cheang, R. A. Hedderwick, and C. McGregor, "Benchmarking supercritical carbon dioxide cycles against steam Rankine cycles for Concentrated Solar Power," *Sol. Energy*, vol. 113, pp. 199–211, 2015, doi: 10.1016/j.solener.2014.12.016.

[6] Y. A. Cengel, M. A. Boles, and M. Kanoglu, *Thermodynamics: An Engineering Approach*, 9th Editio. Mc Graw Hill Education, 2019.

[7] V. Dostal, P. Hejzlar, and M. J. Driscoll, "High-performance supercritical carbon dioxide cycle for next-generation nuclear reactors," *Nucl. Technol.*, vol. 154, no. 3, pp. 265–282, 2006, doi: 10.13182/NT154-265.

[8] A. Yu, W. Su, X. Lin, and N. Zhou, "Recent trends of supercritical CO2 Brayton cycle: Bibliometric analysis and research review," *Nucl. Eng. Technol.*, vol. 53, no. 3, pp. 699–714, 2021, doi: 10.1016/j.net.2020.08.005.

[9] P. Jiang, B. Wang, Y. Tian, X. Xu, and L. Zhao, "Design of a Supercritical CO2Compressor for Use in a 1 MWe Power Cycle," *ACS Omega*, vol. 6, no. 49, pp. 33769–33778, 2021, doi: 10.1021/acsomega.1c05023.

[10] M. M. Ehsan, S. Duniam, J. Li, Z. Guan, H. Gurgenci, and A. Klimenko, "Effect of cooling system design on the performance of the recompression CO2 cycle for concentrated solar power application," *Energy*, vol. 180, pp. 480–494, 2019, doi: 10.1016/j.energy.2019.05.108.

[11] G. B. Eke and C. A. Ebieto, "Performance Analysis of Shell and Tube Heat Exchangers : A case study," *J. Emerg. Trends Eng. Appl. Sci.*, vol. 3, no. 5, pp. 899–903, 2012.

[12] M. C. Tshamala, C. Govender, T. M. Hans, C. McGregor, and M. T. F. Owen, "Thermodynamic Analysis of a 20 MW Concentrated Solar-Powered Supercritical Carbon Dioxide Brayton Recompression Cycle," Proceedings of the 16th International Conference on Heat Transfer, Fluid Mechanics and Thermodynamics HEFAT-ATE 2022, pp. 984–995.

[13] M. T. White, G. Bianchi, L. Chai, S. A. Tassou, and A. I. Sayma, "Review of supercritical CO2 technologies and systems for power generation," *Appl. Therm. Eng.*, vol. 185, no. November 2020, 2021, doi: 10.1016/j.applthermaleng.2020.116447.

[14] K. Brun, P. Friedman, and R. Dennis, *Fundamentals and applications of supercritical carbon dioxide (sCO2) based power cycles*, 1st Editio. Woodhead Publishing, 2017.

[15] R. C. Byrne, "TEMA Standards of the Tubular Exchanger," 2019.

[16] P. Roy, I. N. Rao, T. R. Martha, and K. V. Kumar, "Discharge water temperature assessment of thermal power plant using remote sensing techniques," *Energy Geosci.*, vol. 3, no. 2, pp. 172–181, 2022, doi: 10.1016/j.engeos.2021.06.006.

[17] G. Towler and R. Sinnott, *Chemical Engineering Design Principles , Practice and Economics of Plant and Process Design Second Edition*. .

[18] S. Kakaç, H. Liu, and A. Pramuanjaroenkij, *HEAT EXCHANGERS: Selection, Rating and Thermal Design*. 2012.

[19] G. Towler and R. Sinnott, *Chemical Engineering Design: Principles, Practice and Economics of Plant and Process Design, Second Edition*. 2012.

[20] S. Y. Kulkarni, S. B. Jagadish, and M. B. Manjunath, "Analysis Comparing Performance of a Conventional Shell and Tube Heat Exchanger Using Kern, Bell and Bell Delaware Method," *Int. J. Res. Eng. Technol.*, vol. 03, no. 15, pp. 486–496, 2014, doi: 10.15623/ijret.2014.0315093.

[21] A. V. Uvarov, N. A. Sakharova, and N. A. Vinnichenko, "Effect of natural convection on the current-voltage characteristic of a DC discharge in neon at intermediate pressures," *Plasma Phys. Reports*, vol. 37, no. 12, pp. 1046–1052, 2011, doi: 10.1134/S1063780X11110092.

[22] Weatherspark, "Weather history at Upington Airport," 2022. https://weatherspark.com/h/d/148468/2022/1/22/Historical-Weather-on-Saturday-January-22-2022-at-Upington-Airport-South-Africa#Figures-Temperature (accessed May 04, 2023).

TESTING BASIC SOLAR IRRADIANCE MODELS ON MEASUREMENTS AT SOUTHERN AFRICAN LOCALITIES

Sindiswa M. Figlan[1], and Hartmut Winkler[2]

[1] Dept. Physics, University of Johannesburg; E-Mail: sindiswafiglan@gmail.com

[2] Dept. Physics, University of Johannesburg, PO Box 524, 2006 Auckland Park, Johannesburg, South Africa; Phone: +27-115594417; Fax: +27-115592327; E-Mail: hwinkler@uj.ac.za

Abstract: Five clear-sky models have been investigated to determine the accuracy of the model to fit the calculated solar irradiance measured over an eight-year period (2014-2021). The main forms of solar irradiance that were investigated were: Direct normal irradiance (DNI), which is used in solar PV and CSP, Diffuse horizontal irradiance (DHI) and Global horizontal irradiance (GHI), which are important for solar PV systems. The Haurwitz, Chràcicki, Meinel, Power law, and Logarithmic (newly proposed) models were used to investigate GHI, the Archer, Sharma, Meinel, Power law, and Logarithmic models for DNI; and the ASHRAE, Power law, Fritz, Daneshyar, and Logarithmic (newly proposed) models for DHI. All models are regarded as simple clear-sky models due to only depending on the zenith angle and having two scaling parameters used for linear regression analysis. The data, measured at one-minute intervals, was taken from the five stations (Richtersveld, Vanrhynsdorp, Graaff-Reinet, Gaborone, and Windhoek) found in South Africa, Namibia and Botswana which were supplied by the SAURAN network. The influence of station elevation will also be evaluated.

Keywords: solar irradiance; solar models; solar irradiance components; airmass.

1. Introduction

Research into renewable energy has increased over the last decade as countries around the world are looking for more sustainable ways of generating electricity. In 2020 South Africa was the 7th largest coal producer in the world and 85% of its electricity was produced from coal plants. With the trend away from coal due to the impact carbon emissions have on climate change, the country has begun to consider more eco-friendly ways of decreasing the amount of strain placed onto the grid [1].

South Africa receives solar radiation of 2.4 MWh/m^2 per annum at its sunniest locations in the country's north west, and even the areas with the least sunshine, along the southern and eastern coastal belt, get as much as 1.5 MWh/m^2 solar radiation per annum [2], thus making solar energy a very effective source of renewable energy. Understanding the solar resource is important for the optimization of solar energy production, and this can be achieved through the application of simple solar irradiance models. Electricity is largely generated from solar energy in two forms in South Africa: photovoltaic systems and thermal concentrated solar power [3]. The performance of these systems can be estimated from the solar irradiance. Solar irradiance has traditionally been represented by three interlinked quantities: Global, Direct and Diffuse Irradiance.

2. Solar irradiance modelling

2.1. Airmass

When solar radiation travels through the earth's atmosphere, the radiation encounters molecules and particles with different optical properties and varying concentrations. The ratio of the path travelled by the solar beam through the atmosphere relative to the vertical path is known as the airmass.

Assuming that the effect due to the earth's curvature is negligible, the relative airmass m is defined in terms of the solar zenith angle ζ as follows:

$$m = \frac{1}{\cos\zeta} \quad (1)$$

This quantity should not be confused with the absolute airmass, which is obtained by multiplying m by the ratio of the site atmospheric pressure to the sea level atmospheric pressure.

2.2. Solar irradiance types

The total amount of solar radiation which is incident on a horizontal surface on the earth is referred to as the Global Horizontal Irradiance (GHI).

This is made up of two components (see eq.3, [4]). Firstly, there is the fraction of solar beam radiation that reaches the surface

after attenuation in the atmosphere. When measured in the direction towards the Sun this is referred to as Direct Normal Irradiance (DNI). Then there are the photons which experienced scattering by gases and aerosols (dust, pollen, water vapour, etc.) in the earth's atmosphere and are now directed towards the detector from all parts of the sky. When measured on a horizontal surface this is referred to as Diffuse Horizontal Irradiance (DHI).

These three measures of irradiance are related to each other by the equation:

$$G = B\cos\zeta + D \qquad (2)$$

where G, B, D represent the GHI, DNI and DHI respectively.

If we define the above equations in terms of the airmass m and the irradiance at the top of the atmosphere B_0, equation 2 can be expressed as follows:

$$\frac{Gm}{B_0} = \frac{B}{B_0} + \frac{Dm}{B_0} \qquad (3)$$

2.3. Existing solar irradiance models.

Comprehensive lists of solar irradiance models of varying degrees of complexity have been summarised elsewhere [5, 6]. This study specifically restricts itself to models where the irradiance only depends on one easily determinable variable, the solar zenith angle. Furthermore, our models all contain a maximum of two parameters that should be constant for set heights above sea level provided skies are aerosol-free. These parameters can however be expected to vary mildly with altitude above sea level and atmospheric turbidity. Such models are very basic and have for most purposes been superseded by advanced models with many more parameters that may also depend on further meteorological variables like temperature and humidity. The one variable, two parameter models explored in this study are however still very useful precisely because of their simplicity if they can reproduce measured irradiance reasonably. This is because meteorological measurements are often not available, and because their straightforward mathematical formulation eases computational application.

The solar irradiance models examined in this study are listed and defined in Table 1. The form of the model equations and the associated analytic tools are well illustrated by the example of the Haurwitz model for GHI [7]:

$$G = B_0 A e^{-qm}\cos\zeta \qquad (4)$$

Each model is defined by two scaling parameters, A and q. The amplitude parameter A defines the vertical scale of the irradiance fitted by model and q defines the spread of the model. The exact significance of these two parameters however varies from model to model. For example, in the Haurwitz model defined by Equation 4, q is a measure of the turbidity, while A would be the fraction G/B_0 at the zenith as the turbidity tends to zero.

Table 1. Irradiance models investigated.

Model name	Model equation
GHI models	
Haurwitz [7]	$Gm/B_0 = A\,e^{-qm}$
Chràcicki [8]	$Gm/B_0 = A/(1+qm)$
Meinel [9]	$Gm/B_0 = A^{m^q}$
Power law [10]	$Gm/B_0 = A\,m^q$
Logarithmic	$Gm/B_0 = A - q\ln m$
DNI models	
Archer [11]	$B/B_0 = A\,e^{-qm}$
Sharma [12]	$B/B_0 = A/(1+qm)$
Meinel [9]	$B/B_0 = A^{m^q}$
Power law [10]	$B/B_0 = A\,m^q$
Logarithmic [13]	$B/B_0 = A - q\ln m$
DHI models	
Power law [10]	$Dm/B_0 = A\,m^q$
ASHRAE [14]	$Dm/B_0 = Am\,e^{-qm}$
Fritz [15]	$Dm/B_0 = A(1-e^{-qm})$
Daneshyar [16]	$Dm/B_0 = Am(1-q\sec^{-1}m)$
Logarithmic	$Dm/B_0 = A - q\ln m$

Linearizing Equation 4 by taking logarithm on both sides and substituting the definition of the airmass, we get the expression:

$$\ln\frac{Gm}{B_0} = -qm + \ln A \qquad (5)$$

A standard linear regression analysis of a plot of the measured $\ln(Gm/B_0)$ vs. m thus yields a slope of $-q$ and a y-intercept $\ln A$, from which q and A can immediately be determined. Similar linearization can also be constructed for the other relationships given in Table 1, from which the A and q parameters for the other models are then derived accordingly.

2.4. New proposed Logarithmic model

We also tested a model that has seemingly never been proposed before, given by:

$$G\ (\text{or } D) = B_0(A - q\ln m)\cos\zeta \qquad (7)$$

This model appeared suitable to describe both GHI and DHI, and

bears the same form as a model suggested for DNI by Williams [15]. We will refer to this form as Logarithmic models. Here the scaling parameter A represents the fraction of G, B or D to the top of the atmosphere irradiance B_0 when the sun is directly overhead (i.e. m = 1). As in other models, the q-parameter defines the shape of the decline in the irradiance with the change in airmass.

3. Data and methodology

3.1. The SAURAN network

The solar irradiance data for this project was obtained from the Southern African Universities Radiometric Network (SAURAN) [17]. Most stations belonging to this network collect both radiometric data (GHI, DHI, DNI) and meteorological data such as site temperature and atmospheric pressure. The data, which normally has a resolution of 1 minute, can be freely downloaded from the SAURAN website.

The instruments used to collect solar irradiance on the SAURAN network are as follows: A radiometer mounted on a SOLYS tracker including a CHP1 pyrheliometer, to measure DNI. A CMP11 pyranometer under a shading ball which measures the DHI, while an exposed CMP11 pyranometer measures the GHI [17]. If required, DNI can also be calculated from the GHI and DHI using Equation 2. Given that measurement uncertainties, multiple scattering, refraction and horizon topography all significantly degrade irradiance data quality near sunrise and sunset, we only used irradiance measurements taken where the solar zenith angle ζ did not exceed 80°.

We estimated the random error in the GHI and DHI data to be 0.1% and 0.3% respectively by determining the fluctuations in the 20-minute period around noon, when the change in solar zenith angle is minimal. Systematic errors caused by sensitivity degradation and similar effects are likely to exceed these amounts, and may account for some of the offsets of the parameters for each site derived later.

3.2. Site and day selection

We chose five sites in areas known to have above-average solar irradiance that had data archives spanning several years, and that furthermore spread over a wide range of altitudes above sea level. The selected sites are listed in Table 2. Exact site coordinates are available on the SAURAN website.

We identified approximately 20 clear days for each site where visual inspection of the irradiance curves over the course of the day suggested minimal losses due to cloud or other solar beam interference. An example of the days meeting these criteria is illustrated in Figure 1.

Table 2. SAURAN stations selected for this study with their altitude above sea level.

Station name	Country	Site coordinates	Altitude
Richtersveld	S. Africa	16.761E, 28.561S	141 m
Vanrhynsdorp	S. Africa	18.738E, 31.617S	130 m
Graaff Reinet	S. Africa	24.586E, 32.485S	660 m
Gaborone	Botswana	25.934E, 24.661S	1014 m
Windhoek	Namibia	17.075E, 22.565S	1683 m

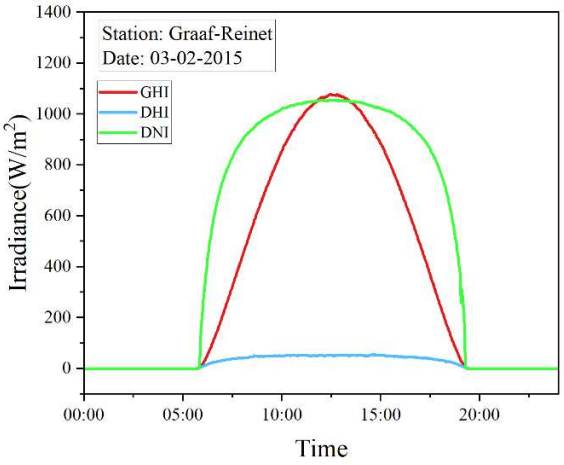

Fig. 1. GHI, DHI and DNI plots: Graaff Reinet, 03/02/22

We note that, despite the cloud-free conditions, some days experienced high aerosol concentrations, which weaken the DNI, but also increase the DHI. This is best exhibited by comparing the behaviour of the DHI over time for various days, as is done in Figure 2, where the amplitude and irregularity of this irradiance form clearly points to higher aerosol levels.

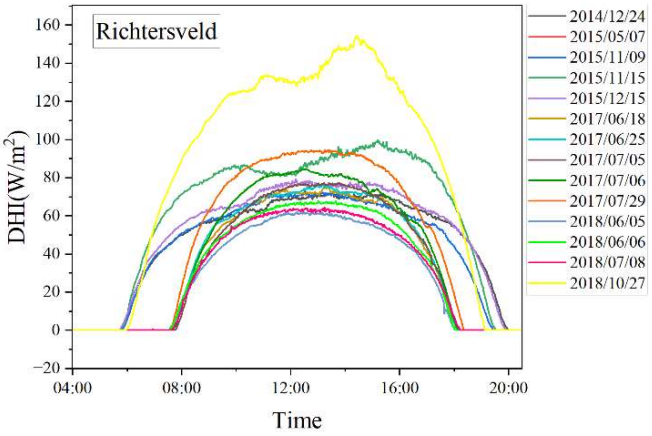

Fig. 2. Daily DHI curves from the Richtersveld station.

4. Results

For each considered day and site, we plotted the graphs for the quantities projected to be linearly related according to each of the model formulae in Table 1 and determined the model parameters A and q for that daily data set accordingly. Examples of these plots are illustrated in Figures 3-9. We furthermore determined the correlation statistic R^2 for each graph, which is an indicator of the goodness of the fit with a linear relationship. Averages over all days at a station, as well as the combined average R^2 for each model, are detailed in Table 3.

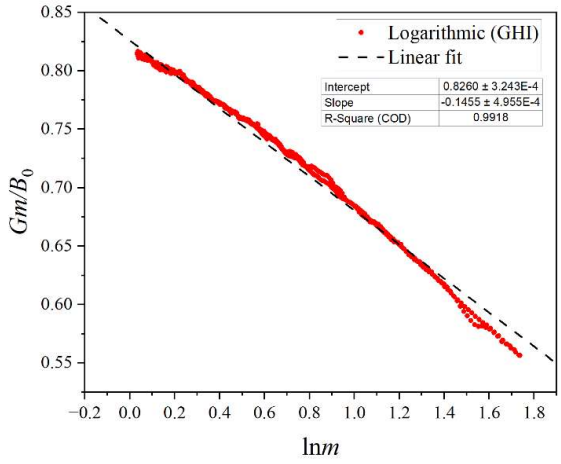

Fig. 3. GHI Logarithmic model fit: Graaff Reinet, 03/02/22

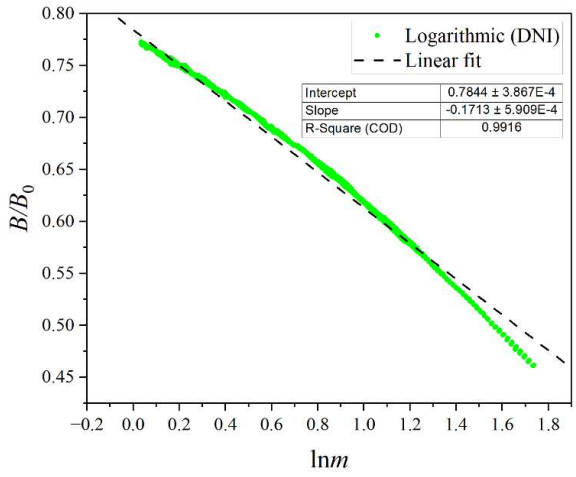

Fig. 4. DNI Logarithmic model fit: Graaff Reinet, 03/02/22

In Figures 3-5, we illustrate the performance of the new Logarithmic model for GHI, DNI and DHI. While the model at least matches and to some extent even exceeds the performance of the relatively widely used power law model (see Figures 6-8), it does not attain the superb fits achieved with the two models that this study finds to be the best suited for the GHI and DNI,

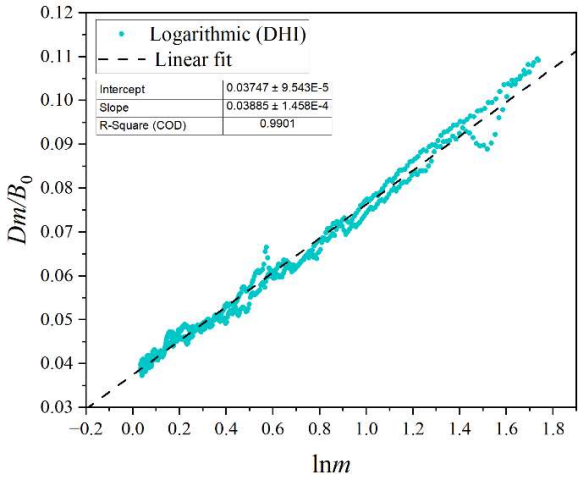

Fig. 5. DHI Logarithmic model fit: Graaff Reinet, 03/02/22

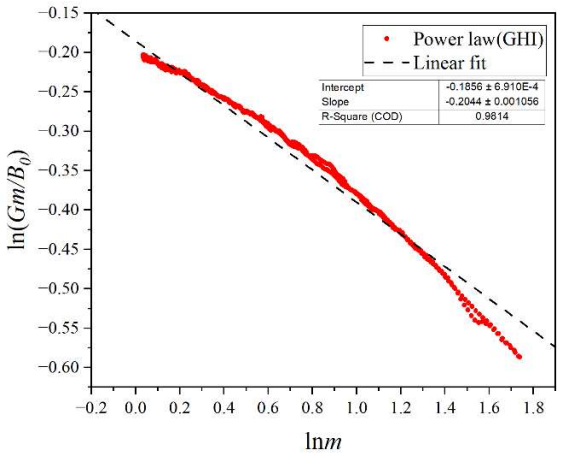

Fig. 6. GHI Power law model fit: Graaff Reinet, 03/02/22

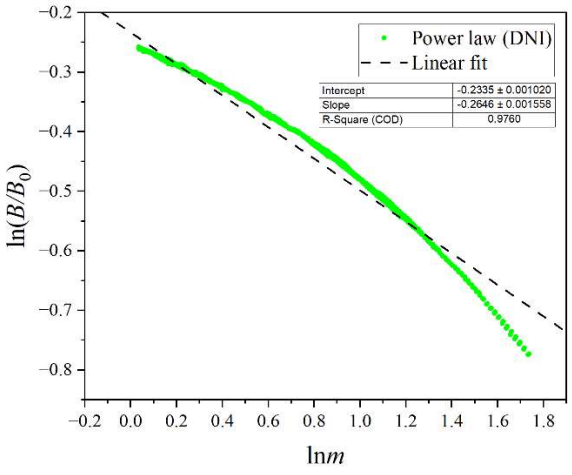

Fig. 7. DNI Power law fit: Graaff Reinet, 03/02/22

which are the Meinel model (see Figure 9) and the Chràcicki / Sharma model. For the diffuse irradiance, however, the

Logarithmic model performed best of all models studied here.

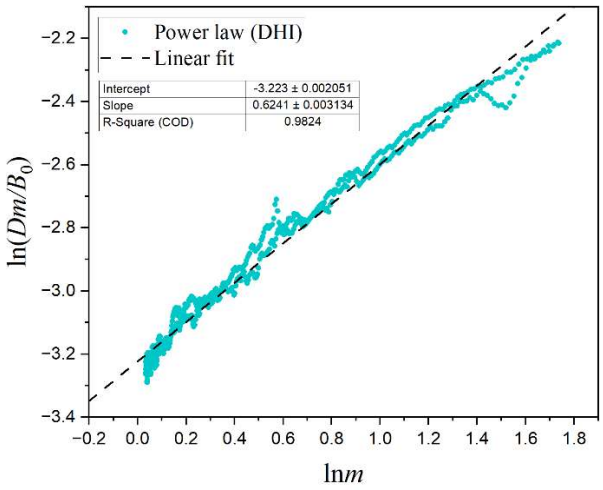

Fig. 8. DNI Power law model fit: Graaff Reinet, 03/02/22

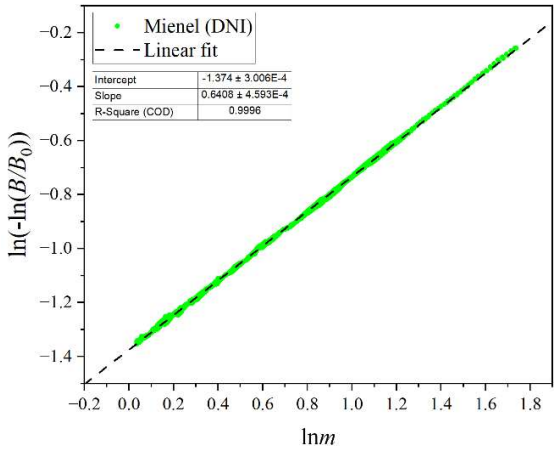

Fig. 9. DNI Meinel model fit: Graaff Reinet, 03/02/22

After determining the average A and q parameters for each site, we plotted these as a function of altitude above sea level for all models. Examples of these plots, here for the Logarithmic model parameters, are shown in Figures 10 and 11. These display a clear trend for almost every model, as expected. The offset of the point at 1014 m representing Gaborone is due to higher levels of aerosols there. The analysis of these plots and the full dependence of these parameters on height above sea level and turbidity will form the subject of another paper.

5. Discussion

This study builds on a growing number of initiatives to characterise the solar irradiance over Southern Africa, the impact of which is important for establishing the local solar energy resource. While previous studies have often focused on the global irradiance [18, 19, 20], we have here also attempted to establish the most suitable basic models for the DNI and DHI.

Table 3. R^2 average value of the model plots.

Station name	Global Horizontal Irradiance				
	Haurwitz	**Chràcicki**	**Meinel**	**Power**	**Logarithmic**
Richtersveld	0.9878	0.9936	0.9967	0.9865	0.9933
Vanrhynsdorp	0.9892	0.9941	0.9961	0.9830	0.9905
Graaff Reinet	0.9879	0.9939	0.9961	0.9844	0.9919
Gaborone	0.9901	0.9947	0.9938	0.9775	0.9869
Windhoek	0.9865	0.9926	0.9953	0.9830	0.9896
average R^2	0.9883	0.9938	0.9956	0.9829	0.9904
	Direct Normal Irradiance				
	Archer	**Sharma**	**Meinel**	**Power**	**Logarithmic**
Richtersveld	0.9878	0.9910	0.9938	0.9779	0.9910
Vanrhynsdorp	0.9909	0.9959	0.9962	0.9815	0.9926
Graaff-Reinet	0.9868	0.9902	0.9932	0.9754	0.9888
Gaborone	0.9888	0.9917	0.9933	0.9739	0.9892
Windhoek	0.9876	0.9937	0.9939	0.9785	0.9895
average R^2	0.9884	0.9925	0.9941	0.9774	0.9902
	Diffuse Horizontal Irradiance				
	ASHRAE	**Power law**	**Fritz**	**Daneshyar**	**Logarithmic**
Richtersveld	0.9463	0.9650	0.9143	0.8834	0.9685
Vanrhynsdorp	0.9339	0.9649	0.9057	0.8773	0.9636
Graaff-Reinet	0.9160	0.9615	0.8978	0.7979	0.9583
Gaborone	0.9525	0.9669	0.9155	0.8932	0.9709
Windhoek	0.9377	0.9660	0.9136	0.8186	0.9764
average R^2	0.9373	0.9648	0.9094	0.8541	0.9676

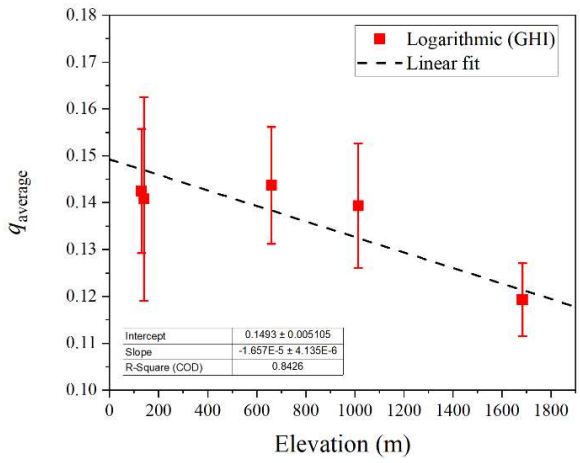

Fig. 10. Average scaling parameter q vs station elevation for the GHI Logarithmic model

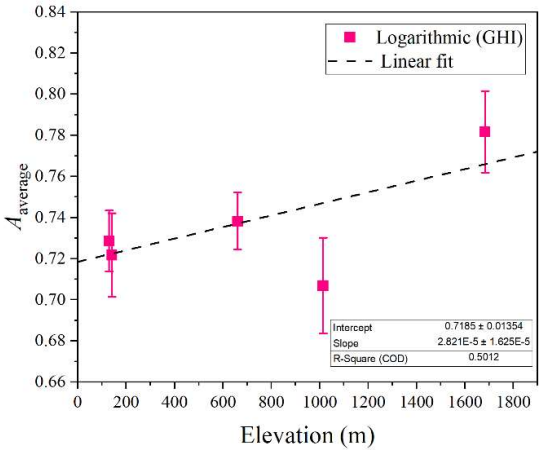

Fig. 11. Average amplitude scaling parameter *A* vs station elevation for the GHI Logarithmic model

The Meinel model provides the best model fits for GHI and DNI with very high correlation R^2 values of 0.996 and 0.994 respectively. The performances of the Chràcicki model and the mathematically similar Sharma models follow very closely to the Meinel models in accuracy, and these three models are hereby confirmed as the recommended models of a simple formulation for describing the global and direct irradiance. The newly proposed Logarithmic model did best when modelling for DHI, with an R^2 value of just under 0.971. As seen in Figure 5, the lower correlation is not so much due to lack of linearity, but rather caused by small-scale fluctuations that are in part probably also due to the much lower photon counts. The model itself describes the overall relationship between the DHI and the airmass quite well. The Power law model performed noticeably worse for GHI and DNI than even the Logarithmic model, which is perhaps surprising given its comparatively wide usage. The Daneshyar model performed the worst for DHI with an R^2 value of only 0.854. This model was formulated based on irradiance data collected in Tehran, Iran, [16] a site expected to exhibit evidence of high dust levels and smog, so it is not surprising that the relationships displayed there are dissimilar to what obtains at much clearer localities. Out of all the simple clear sky solar irradiance models, the DHI models exhibited the lowest degree of correlation. This is not unexpected, due to the assumptions made when simplifying the Rayleigh and Mie scattering equations to make the models computable. The overall satisfactory fits obtained with the Logarithmic models show that this class offers a suitable alternative to the currently established models.

Considering the thinner atmosphere above the sites at greater altitude above sea level, as well as the nature of the *A* parameter as a vertical scaling factor (which was the case for all models), it was expected that the latter would increase with increased elevation. This was found to be true for all stations apart from the Gaborone station which had lower scaling parameter values than expected. When analysing this, it was found that Gaborone had the highest scatter in the values for A, whereas Richtersveld had the highest scatter for the q scaling parameter. We also note that these two stations exhibited higher DHI values compared to the other stations (90-140 W/m^2), as shown in Figure 2. The higher level of aerosol concentration in Richtersveld is due to the station being located in the desert [21] while Gaborone is in a semi-desert region. The cause for these elevated aerosol levels is still being investigated. This shows that other factors such as aerosol concentrations and geographical altitude should be taken into consideration in addition to cloud coverage when establishing defining clear day model parameters.

6. Conclusion

Our analysis shows the Meinel model to perform best when modelling for GHI and DNI, closely followed by the Chràcicki model for GHI and the analogous Sharma model for the DNI. The newly proposed Logarithmic model performs best when modelling for DHI. The Power law and Haurwitz / Archer models are shown to be less effective, but still usable. The ASHRAE, Fritz and Danyeshar models, which were developed as fits to DHI data that was likely strongly affected by aerosols, do not match the clean sky DHI nearly as well as the other models examined.

Acknowledgements

We gratefully acknowledge use of the data generated by the Southern African Universities Radiometric Network (SAURAN).

References

[1] O. K. Akinbami, S. R. Oke, O. M. Bodunrin, “The state of renewable energy development in South Africa: An overview” *Alexandria Engineering Journal*, vol. 60, pp. 5077–5093, 2021.

[2] J. G. Wright, T. Bischof-Niemz, J. R. Calitz, C. Mushwana, R. van Heerden, “Long-term electricity sector expansion planning: A unique opportunity for a least cost energy transition in South Africa”, *Renewable Energy Focus*, vol. 30, pp. 21-57, 2019.

[3] J. G. Wright, J. R. Calitz, “Statistics of utility-scale power generation in South Africa”, CSIR [http://hdl.handle.net/10204/11865], 2021.

[4] H. Winkler, “The suitability of clear sky diffuse irradiance models for South African atmospheric conditions” in *South African Solar Energy Conference*, Durban, 2018.

[5] V. Badescu, C. A. Gueymard, S. Cheval, C. Oprea, M. Baciu, et al., “Computing global and diffuse solar hourly irradiation on clear sky. Review and testing of 54 models”, *Renewable and Sustainable Energy Reviews*, vol. 16, pp. 1636-1656, 2021.

[6] F. Antonanzas-Torres, R. Urraca, J. Polo, O. Perpiñán-Lamigueiro, R. Escobar, “Clear sky solar irradiance models: A review of seventy models”, *Renewable and Sustainable Energy Reviews*, vol. 107, pp. 374-387, 2019.

[7] B. Haurwitz, “Insolation in relation to cloudiness and cloud density”, *J. Meteorology*, vol. 2, pp. 154-166, 1945.

[8] W. Chràcicki, “Solar climate of the Swedish territory. Selected problems”, *Tellus*, vol. 23, pp. 232-246, 1971.

[9] Meinel A.B., Meinel M.P., (1976). ‘Applied Solar Energy: An Introduction. Addison-Wesley series in physics, Addison-Wesley Publishing Company’.

[10] A. J. Biga, R. Rosa, “Contribution to the study of the solar radiation climate of Lisbon”, *Solar Energy*, vol. 23, pp. 61-67, 1979.

[11] R. E. Schultze, ‘A physically based method of estimating solar radiation from sun cards”, *Agric. Meteorol.*, vol. 16, pp. 85-101, 1976.

[12] M. R. Sharma, R. S. Pal, “Interrelationships between total, direct, and diffuse radiation in the tropics”, *Solar Energy*, vol. 9, pp. 183-192, 1965.

[13] J. G. Williams, “Change in the transmissivity parameter with atmospheric pathlength”, *J. Appl. Meteorol.*, vol. 15, pp. 1321-1323, 1979.

[14] ASHRAE, “Handbook of Fundamentals. American Society of Heating, Refrigerating and Air-Conditioning Engineers”, 1972.

[15] L. D. Williams, R. G. Barry, J. T. Andrews, “Application of computed global radiation for areas of high relief”, *J. Appl. Meteorol.*, vol. 11, pp. 526-533, 1972.

[16] M. Daneshyar, “Solar radiation statistics for Iran”, *Solar Energy*, vol. 21, pp. 345-349, 1978.

[17] M. J. Brooks, S. Du Clou, W. L. van Niekerk, P. Gauché, C. Leonard, et al., “SAURAN: A new resource for solar radiometric data in Southern Africa”, *J. Energy Southern Africa*, vol. 26, pp. 2-10, 2015.

[18] E. Zhandire, “Predicting clear-sky global horizontal irradiance at eight locations in South Africa using four models”, *J. Energy Southern Africa*, vol. 28, issue 4, pp. 77-86, Nov 2017.

[19] L. Javu, H. Winkler, K. Roro, “Validating clear–sky irradiance models in 5 South African locations”, in *South African Solar Energy Conference*, Mpekweni, 2019.

[20] B. Mabasa, M. D. Lysko, H. Tazvinga, N. Zwane, S. J. Moloi, “The performance assessment of six Global Horizontal Irradiance clear sky models in six climatological regions in South Africa”. *Energies*, vol. 14, 2583, 2021.

[21] R. Román, M. Antón, A. Valenzuela, J. E. Gil, H. Lyamani, et al., “Evaluation of the desert dust effects on global, direct and diffuse spectral ultraviolet irradiance”, *Tellus B: Chemical and Physical Meteorology*, vol. 65, issue 1, 19578, 2013.

COMPARISON AND VALIDATION AGAINST IN-SITU MEASUREMENTS OF THE SARAH-3 SOLAR IRRADIANCE SATELLITE ESTIMATES OVER THE SOUTH WEST INDIAN OCEAN

Christella Igihozo[1], Béatrice Morel[2], Mathieu Delsaut[3], Chao Tang[4], Patrick Jeanty[5], Morgane Goulain[6], Jörg Trentmann[7], Jean-Pierre Chabriat[8], and Amine Ouhechou[9]

[1] University of Reunion, ENERGY-Lab, 20 avenue Hippolyte Foucque 97744 St Denis Cedex 9, Reunion Island (France);
Phone: +33779714669; E-mail: igihchrist01@gmail.com

[2] University of Reunion, ENERGY-Lab, 15 avenue René Cassin CS 92003 97744 St Denis Cedex 9, Reunion Island (France);
Phone: +26226293822; Fax: +262262938673; E-Mail: beatrice.morel@univ-reunion.fr

[3] University of Reunion, ENERGY-Lab; E-mail: mathieu.delsaut@univ-reunion.fr

[4] University of Reunion, ENERGY-Lab; E-mail: chao.tang@univ-reunion.fr

[5] University of Reunion, ENERGY-Lab; E-mail: patrick.jeanty@univ-reunion.fr

[6] SPL Horizon Reunion; E-mail: morgane.goulain@spl-horizonreunion.com

[7] Deutscher Wetterdienst; E-mail: joerg.trentmann@dwd.de

[8]University of Reunion, ENERGY-Lab; E-mail: jean-pierre.chabriat@univ-reunion.fr

[9]University of Grenoble;E-mail: amine.ouhechou@univ-grenoble-alpes.fr

Abstract: The solar resource has by far the highest energy potential on Earth, leading to an increased attention to climate data sets of surface solar radiation (SSR) as an important source of information for solar energy assessment. Such an assessment is essential for solar energy project policy and planning. The present work aims to evaluate the skill of satellite-based estimates of solar global horizontal irradiance (GHI) from the new "Surface Solar Radiation Data Set–Heliosat edition 3" SARAH-3 at 0.05° spatial resolution and 30min temporal resolution over the South West Indian Ocean, using 1-min pyranometer GHI measurements (in-situ) recorded at different stations of the Indian Ocean Station network (IOS-net) during the year 2020. Both data have been arithmetically averaged to different time scales from the annual means to hourly means for comparison. The data have also been classified into 4 clusters by the use of an unsupervised method of machine learning, "K-means clustering", to depict the 4 types of solar regimes. Validation results show that SARAH-3 reproduces fairly in the shapes of seasonal cycles and diurnal cycles with different amplitudes compared to the in-situ measurements. Stations with higher GHI estimates in SARAH-3 also depict more clear days and fewer overcast days than the in-situ measurements.

Keywords: renewable energy; surface solar radiation; surface observation; satellite-based estimates; South West Indian Ocean.

1. Introduction

Island regions suffer from structural disadvantages related to their insularity, which permanently affect their economic and social development [1]. The recent upward trend in oil prices also suggests that the global oil market has entered a depletion phase caused by the conflicting effects of accelerated growth in global oil consumption due to the rise of emerging economies and the freeze in supply that has led to a slowdown in oil production. This global energy price increase could have profound effects on the weak economic structure of tropical islands [2]. In addition, the need for a green environment to reduce carbon emissions and mitigate climate change is indispensable [3]. Consequently, the use of renewable energy (RE) is the best way forward for these tropical islands [4].

Solar energy is claimed to be the cleanest and most abundant renewable energy source available [5]. However, the availability of reliable, high-quality in-situ measurement of Surface Solar Radiation (SSR) is a prerequisite for efficient planning and operation of solar energy systems [6]. The Indian Ocean Station network (IOS-net) provides SSR measurements at different locations on the territories of the South West Indian Ocean (SWIO; [7]). However, the network of stations over the SWIO region territories remains loose, pointing out the scarcity of in-situ measurements.

Satellite-based SSR has grown in importance over the last few decades. They represent the second-best option after the ground measurements [8]. The real concern is the validation of these satellite estimates against the quality-controlled in-situ measurements to evaluate their characteristics. Several studies have compared satellite-based estimates to ground measurements so far over Africa (e.g., Central Africa: [9], Morocco: [10], Ghana: [11], but to the authors' knowledge, none has ever made the comparison over the whole SWIO. Mialhe et al. [12] compared the SSR satellite estimates of CM SAF SARAH-E with in-situ measurements performed by Météo-France but over La Réunion island only.

This study aims to compare and assess the coherence and accuracy of the CM SAF SARAH-3 SSR estimates against the in-situ measurements from the IOS-net radiometric network and the analysis of their spatial and temporal variation from diurnal circles to seasonal cycles over the South West Indian Ocean Islands (La Réunion, Mauritius (Rodrigues including), Seychelles, Madagascar, and Comoros). Section 2 is dedicated to the description of the datasets, 3 methodology, 4 results analysis, 5 discussion, and 6 conclusions.

2. Data

The variable of interest in this study is the global horizontal component of the incoming surface solar radiation, namely the Global Horizontal Irradiance (GHI) expressed in W/m^2.

2.1 IOS-net in-situ measurements

GHI in-situ measurements are from the Indian Ocean Station Network (IOS-net, [7]), which covers Comoros, La Réunion, Madagascar, Seychelles, and Mauritius (including Rodrigues). Those measurements are taken from Delta-T Devices SPN1 pyranometers, which provide data in 1-min resolution. The data collected either as NetCDF or CSV files is freely available and usable as Open Data on https://galilee.univ-reunion.fr/ and for different years depending on when the station was established. For this study, the data for 2020 was used, collected from 1st January 00:00 up to 31st December 23:00 for all the analysis at different locations in the SWIO for which data was available (Fig.1).

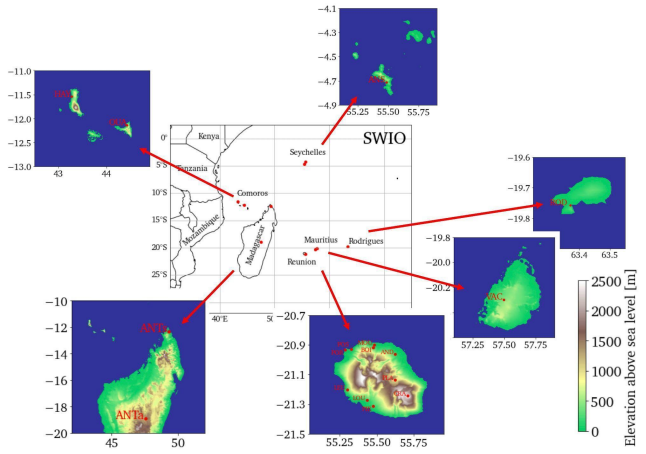

Fig.1. Location of the IOS-net stations in SWIO used in the study with their elevation (see table 1 for full names).

2.2 CMSAF SARAH-3 satellite estimates

The EUMETSAT Satellite Application Facility on Climate Monitoring (CM SAF, [13]) generates and distributes high-quality long-term climate data records (CDR) of energy and water cycle parameters, which are freely available through the CMSAF Web User Interface (https://wui.cmsaf.eu/). A new version of the "Surface Solar Radiation data set – Heliosat – Edition 3" (SARAH-3) was recently released [14]. As with the previous editions, the SARAH-3 climate data record is based on satellite observations from the first and second METEOSAT generations and provides various surface radiation parameters, including global radiation, direct radiation, sunshine duration, photosynthetic active radiation, and others. SARAH-3 covers the time period 1983 onward and offers 30-minute instantaneous SSR data as well as daily and monthly means on a regular 0.05° x 0.05° lon/lat grid. For this specific study the 30-min instantaneous SSR data were used as they provide high resolution and facilitate the analysis on a sub-daily time scale.

3. Methodology

3.1 Data quality control of IOS-net data

The World Meteorological Organization (WMO) Baseline Surface Radiation Network (BSRN) has established globally physical possible limits as well as extremely rare limits for surface radiation measurements, which is included in the quality control (QC) testing [15]. As a continuation to [15], Baronnet and Delsaut [16] developed Python tools available on https://github.com/LE2P/PyBsrnQC that were used in this study to identify erroneous data and hence discard them.

3.2 Data pre-processing

The analysis was done on different time scales, from the annual means to diurnal cycles. It should be noted that SARAH-3 data have been taken after the time of transition (2006) from MVIRI to SEVIRI instruments, hence the variable time difference SEVIRI was added to the UTC time in data to derive the acquisition time of the instantaneous data. For this very reason, 30 min resolution was upscaled to the hourly resolution to ensure an accurate comparison for the analysis on the sub-daily time-scale. The same data for in-situ (1 min) and for SARAH-3 (30 min instantaneous) has been used to derive long term averages (annual and monthly). Because the SWIO spans several time zones, the UTC time was kept for both IOS-net and SARAH-3 data. All the analysis was performed in Python (version 3).

3.3 Diurnal cycles' classification

To perform the analysis on a daily time scale, a diurnal cycles' classification was made on both in-situ measurements and satellite estimates of SSR. K-means clustering, as in [9], was applied to each station and the corresponding pixel separately to allocate a set of points into 4 clusters: Clear, AM clear, PM clear, and Overcast [17], in such a way as to minimize the sum of squares of distances from a point to the cluster. 200 runs with 4 different centroid seeds were launched, with 300 as the maximum number of iterations for the K-means algorithm to allocate each day (either at the station or pixel) into the 4 clusters and to define their respective centroids. It should also be noted that data were first smoothed using the Savitzky-Golay filter to deal with high-frequency variations in diurnal cycles.

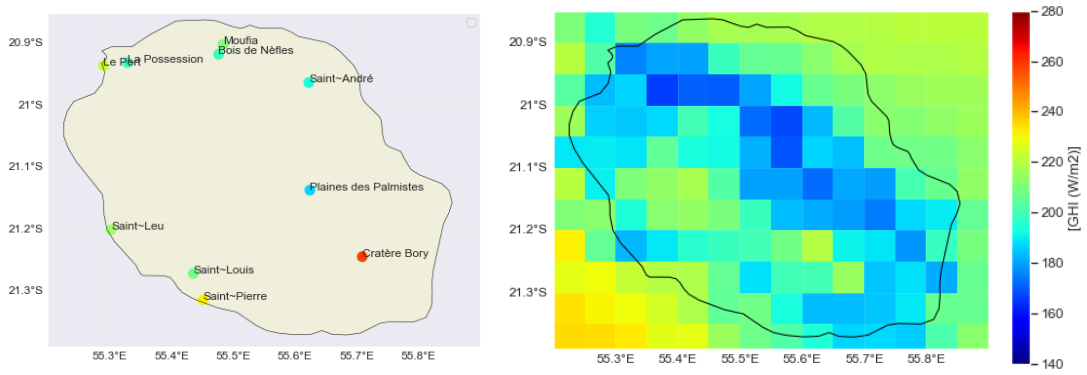

Fig.2. Mean annual GHI fields (W/m^2) of a) the stations at La Réunion b) SARAH-3. Fields were computed for a common period of 2020.

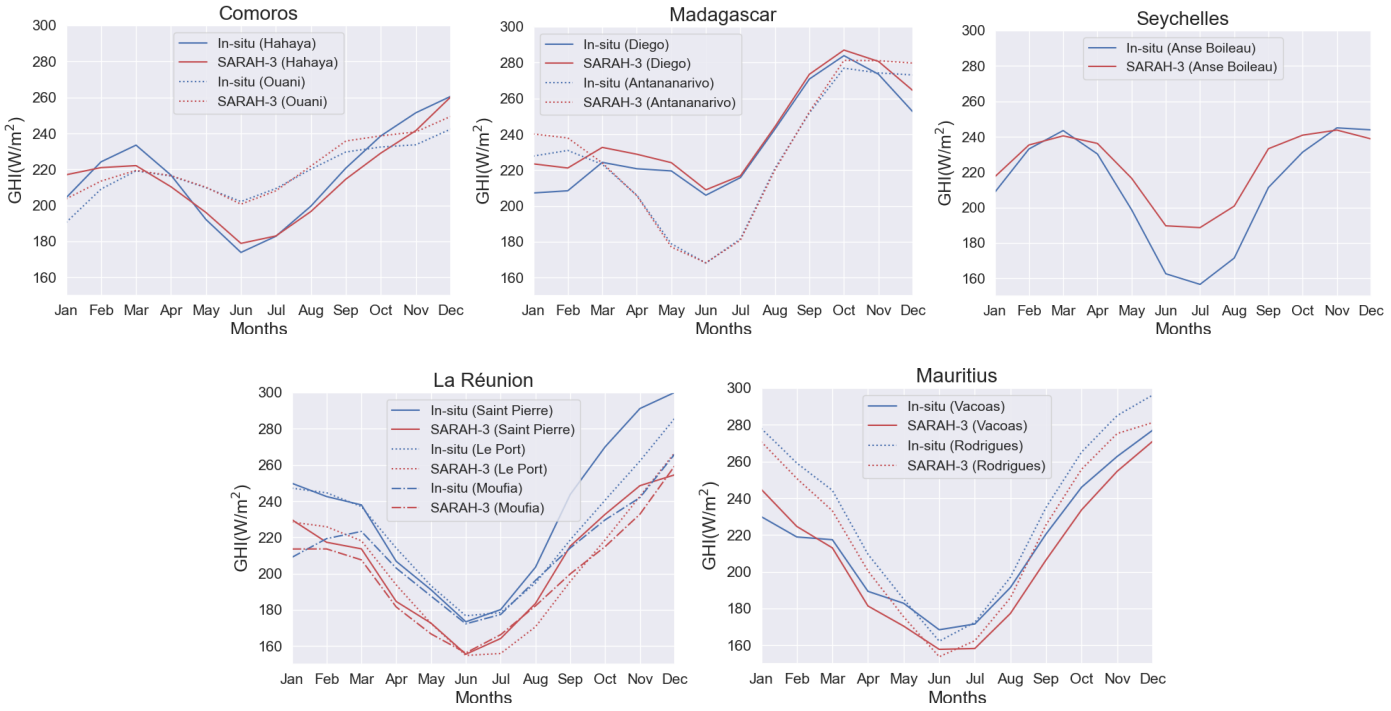

Fig.3. Seasonal cycles of GHI of selected stations in each territory in the South West Indian Ocean (Fig.1) and their respective satellite (SARAH-3) estimates.

Differences in 4 types of diurnal cycles between in-situ measurements and satellite estimates were analyzed along with their frequency distribution throughout the year.

3.4 Measures of accuracy

There are a number of statistical metrics that have been used to measure the accuracy of the SARAH-3 solar irradiance satellite estimates against in-situ measurements. Those include: the bias (taken as the mean error), the Root Mean Square Error (RMSE), the Pearson correlation coefficient R, and the skewness coefficient, which indicates the degree of skewness of a distribution.

4. Results

4.1 Comparison at the annual time-scale

As a first step of comparison, the annual mean GHI for IOS-net measurements and SARAH-3 estimates are presented in Fig.2 while bias values between the two are provided in Table 1. As expected, La Réunion has a very pronounced spatial variability due to its complex topography [12]. The western part receives more GHI than the eastern part. Le Port, La Possession, Saint-Leu, and Saint-Pierre stations all display higher values of GHI as they are located on the coast, which indicates less cloud cover, though SARAH-3 tends to underestimate the GHI values at these stations up to ~ 32W/m^2 at St-Leu (Table 1). Moufia and Bois de Nèfles stations are very close but with varying altitudes (Table 1), which explains their difference in GHI values. Both stations are negatively biased, though Bois de Nèfles displays the smallest bias (~ –0.3W/m^2) of all the stations. Saint-André and Plaines des Palmistes stations have lower annual mean GHI because the east part experiences the strongest intermittency due to its high cloud weather and higher precipitation than other places [17]. Generally, the annual mean representation appears realistic in SARAH-3 except for Cratère Bory, which stands out with the largest mean annual GHI value (~258W/m^2) at the

station and hence the largest negative bias compared to SARAH-3. This is due to the fact that Cratère Bory is the highest of all the stations (2584m; see Fig 1), and the cloud development (both orographic and those driven by synoptic systems) is limited by the thermal inversion, the height of which ranges from 1700 to 3100m over La Réunion, with an average value of 2000m [12]. Apart from stations of La Réunion, other stations of SWIO display an annual mean bias that doesn't exceed 13 W/m^{2,} and this implies a favorable performance of satellite-based estimates of the Surface Solar Radiation (SSR).

4.2 Comparison at the monthly time scale

The annual mean gives little information as it does not convey the evolution of GHI values across the annual cycle, so as a second step of comparison, the seasonal cycles of GHI are displayed for the 10 stations selected across the SWIO region (Fig.3). The stations closer to the equator like Anse Boileau tend to display a bimodal seasonal cycle with two GHI maxima in February-March and October-November, while those in the south part of the region like Rodrigues display a unimodal cycle with one peak in December-January. At all stations, minimum GHI values are observed in June-July. Compared with the in-situ measurements, SARAH-3 tends to reproduce the shape of the seasonal cycles fairly. However, we observe a quite changing behavior for the satellite-based estimates at different stations.

At the stations of La Réunion, namely Saint-Pierre, Moufia and Le Port Mairie, SARAH-3 underestimates the GHI evolution for all stations across the whole year (Fig.3). This also applies to stations at Mauritius (Vacoas and Rodrigues) where satellite estimates are lower compared to the in-situ measurements (Fig.3) with the lowest bias in the austral winter ranging from July to August (Figure not shown). The satellite estimates at stations in Madagascar (Diego & Antananarivo) show a close agreement with the in-situ measurements. Antananarivo stands out with a lower bias of ~ 2.7W/m^2 and the highest correlation coefficient (Table 1), which suggests a strong, positive association between the two. Anse Boileau station has a peculiarity in the sense that the satellite strongly overestimates the GHI values and, more precisely, during the mid-year when GHI values are lower. This may be because this station is located near the ocean, and the nearest pixel from which the satellite estimates GHI values captures a larger part of the ocean rather than the land hence resulting in higher values of GHI estimated at this station. For the Hahaya station in Comoros, GHI values are overestimated by the satellite in May-July and underestimated for the rest of the year.

4.3 Comparison and validation on a daily time-scale

After the comparison on a monthly basis, it is wise to look closely at the daily means as well as the sub-daily cycles. To that aim, the frequency distribution of daily GHI data for each station was computed using both in-situ measurements and satellite estimates. These distributions are presented in Fig.5 for each station separately and their corresponding skewness coefficients.

The stations exhibit different distributions of GHI values due to the spatial variability of GHI data, as it has also been observed in annual mean values (Fig.2). For stations in Comoros and Seychelles (resp. Hahaya and Ouani, and Anse Boileau), more than 70% of daily GHI values range between 100-300W/m^2. SARAH-3 tends to underestimate the frequency of days with GHI levels between 40-200W/m^2 but overestimates the days with GHI levels in the range 200-300W/m^2. In addition, the distributions at these 3 stations are moderately skewed to the left, as shown in Fig.5, with SARAH-3 having a narrower distribution compared to the in-situ measurements. This is consistent with results in Fig.4, which depicts lower interquartile range (i.e., less variability) in SARAH-3 data than in the in-situ measurements.

Stations on Madagascar (Diego and Antananarivo) all depict a positive and small annual mean bias as shown in Table 1, which suggests a close agreement between the two datasets. SARAH-3 overestimates days with GHI values in the range of 230-260W/m^2 and 300-350W/m^2 at Diego and overestimates days with GHI values in range of 190-230W/m^2 as well as those in the range of 280-370W/m^2 at Antananarivo (Fig.5). The interquartile range of both datasets at these stations shows no significant differences with the median displayed around the same level as per Fig.4, this suggests that satellite estimates are able to capture both the mean and the variability as in the measurements.

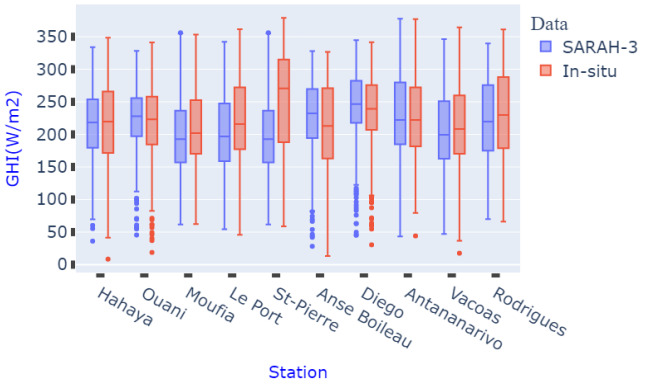

Fig.4. Boxplots of mean daily values of GHI (W/m^2) at IOS-net stations and their respective SARAH-3 estimates.

For La Réunion stations (Moufia and Saint-Pierre), the distributions are moderately skewed to the right except for satellite estimates at Saint-Pierre (Fig.5). This is due to the fact that at this station, GHI measurements reach higher levels than in satellite estimates. At Moufia, SARAH-3 overestimates the frequency of days with GHI values ranging between 70-180W/m^2 and underestimates days with GHI values between 180-350 W/m^2 (see Fig.5).

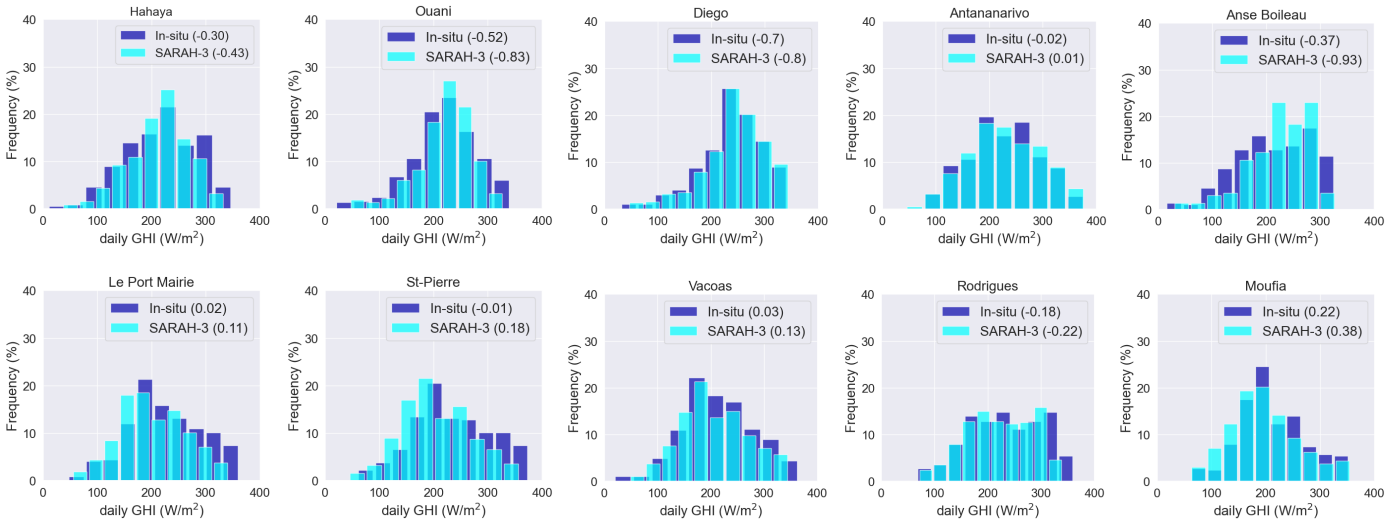

Fig.5. Frequency distribution of daily GHI values at 10 IOS-net stations and their respective pixels in SARAH-3. The skewness coefficient of the distribution for each dataset is provided right next to the legend of the figure.

Both stations are characterized by negative bias (Table 1) and the median distributed at higher level in-situ measurements than in satellite estimates (Fig.4).

At Mauritius stations (Vacoas and Rodrigues), SARAH-3 has narrower distribution compared to the in-situ measurements (Fig.5) and the mean is lower in SARAH-3 than in in-situ measurement. Days with GHI values ranging between 170-350 W/m^2 are underestimated by SARAH-3 at Vacoas, as illustrated in Fig.5.

4.4 SARAH-3's ability to reproduce diurnal cycles

SSR is subjected to variations during the day, and it is important to assess the performance of SARAH-3 on a sub-daily basis and its ability to reproduce the diurnal cycles. By the use of K-means clustering, the 4 types of diurnal cycles were obtained; "Clear", "Overcast", "AM clear", and "PM clear" days as per [9].

The four types of days are represented in Fig.6 for just one station (Hahaya) as an example, and their frequency of occurrence throughout the year for all the selected stations in Fig.7. It should also be noted that the 4 types of days illustrated in Fig.6 are not the data for any day picked but rather the centroids of the 4 clusters. SARAH-3 reproduces the shapes of the diurnal cycles, especially for the clear sky conditions (Clear and AM clear), For overcast and PM clear days, the amplitude of the satellite estimates is almost the same level as the in-situ measurements, but it can overestimate in other stations (not shown), especially around noon (local time). For all types of days, it is right to notice that the GHI values from in-situ measurements are underestimated during most hours of the day, especially in the morning (see Fig.6).

SARAH-3 doesn't accurately picture the frequency of the 4 types of days as in the in-situ measurements. However, in coherence with the previous analysis on the annual mean (Fig.2) and seasonal cycles (Fig.3), Saint-Pierre, Moufia, Le Port, Vacoas and Rodrigues stations at which GHI values are underestimated, SARAH-3 depicts fewer clear days than in-situ measurements (Fig.7). On the other hand, stations like Anse Boileau where we observe a significant overestimation of GHI measurements (Fig.3), the frequency of clear days is greater for SARAH-3 than in-situ measurements while the frequency of overcast days is underestimated as shown in Fig.7.

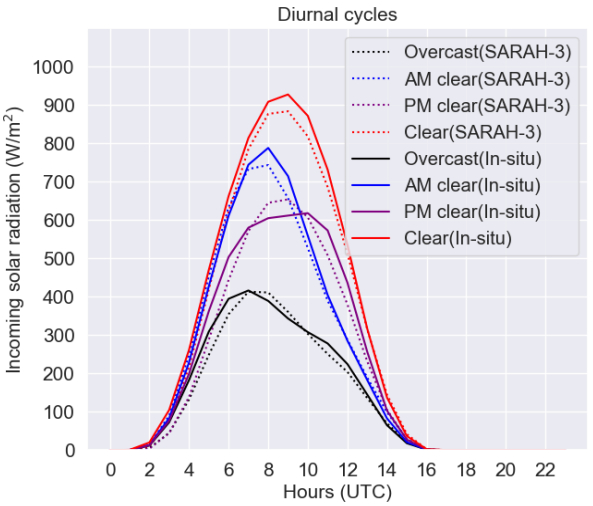

Fig.6. Comparison between the four types of diurnal cycles of GHI (Clear, AM clear, PM clear and Overcast) extracted thanks to K-means clustering applied separately to IOS-net stations and their respective estimates from the nearest pixel in SARAH-3. The figures shown are for Hahaya station.

5. Discussion

In the quest to assess the performance of SARAH-3 to estimate the SSR, various analyses have been done on different scales from annual means to diurnal cycles in comparison with in-situ measurements. As per the results in section 4, SARAH-3 revealed quite changing behaviour at

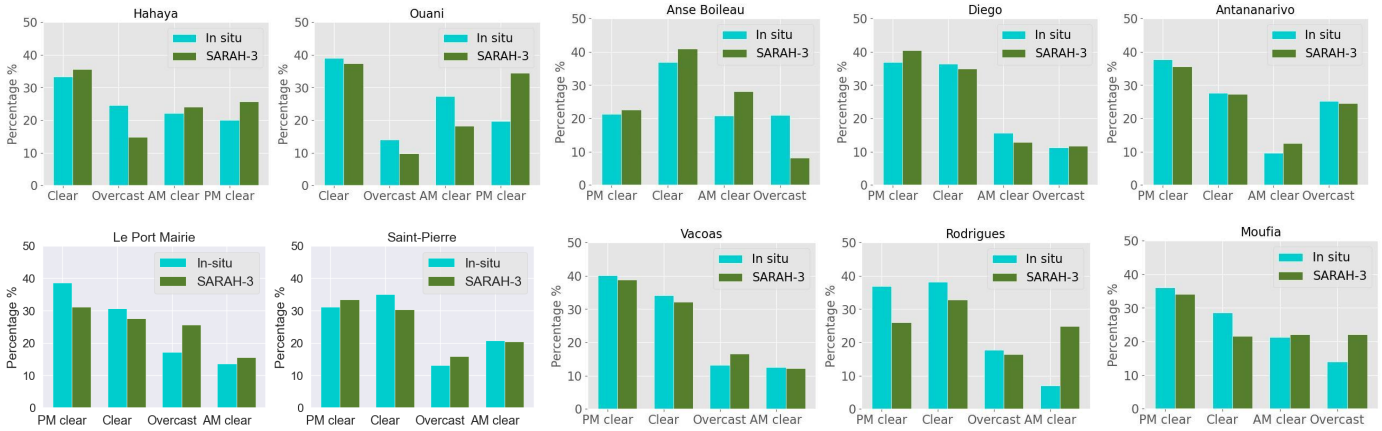

Fig.7. Frequency of occurrence (in percentage) of the 4 types of days in both in-situ measurements and SARAH-3 at the IOS-net station.

different stations. At the annual time-scale (Fig.2), stations of La Réunion have been analysed and revealed that the eastern part receives lower levels of GHI values than the western part, in agreement with the result of [12]. However, SARAH-E does overestimate SSR values except in September-November, which is not the case for SARAH-3 over La Réunion. The differences in GHI values observed between satellite estimates and in-situ measurements might be a result of the estimation of atmospheric input parameters of the gnu-MAGIC/SPEMAGIC algorithm used in SARAH-3, which include: aerosols, water vapor, and ozone ([18]).

The aerosol particles have a significant effect on the estimation of SSR as they scatter and absorb solar radiation. SSR, in particular, is sensitive to AOD (Aerosol Optical Depth) as well as the aerosol type, and SARAH-3 uses monthly mean aerosol information SSR, which is a coarse resolution for such an important parameter. In addition, the accuracy of aerosol information is unknown in several regions due to missing ground measurements, and the stations in this study might be affected by the aerosols from sea-salt aerosols, hence affecting also the accuracy of SSR estimation. Ozone and water vapor used in the algorithm are daily means but are on a larger spatial resolution of 0.25° lat/lon and are regridded to 0.05° lat/lon to match the resolution of SARAH-3. Also, the uncertainty in effective cloud albedo leads to the same exact uncertainty in the cloud index, all mounting to the overall uncertainty in SSR estimation ([18]).

Moreover, SARAH-3 is derived from satellite images centred on Africa, and some of the SWIO territories are at the border of these images causing the pixels to be deformed and the spatial resolution greater than 0.05°. The differences we observe in the results of the study in section 4 can not only be attributed to uncertainties of the SARAH-3 but also to the quality of in-situ measurements. While data quality control removes erroneous data from in-situ measurements, some other errors may result from the calibration or poor maintenance of the instruments (SPN1) and cannot be detected by quality control. The temporal resolution of aerosol load and composition is the main source of uncertainty in the Meteosat satellite retrievals, and improving this resolution from monthly to daily mean might lead to a significant decrease of bias that is observed.

Table 1. Correlation coefficient (R), mean Bias, and the Root Mean Square Error (RMSE) of the stations (Fig.1 for names) and their corresponding pixel in SARAH-3 derived from daily data.

Stations	R	Mean Bias (W/m^2)	RMSE (W/m^2)
Moufia(MOU)	0.93	-12.43	26.56
Bois de nèfles(BOI)	0.88	-0.28	31.72
Le Port Mairie(POR)	0.94	-20.79	31.46
La possession(POS)	0.80	-21.77	44.59
Cratère bory(CRA)	0.80	-68.78	88.10
St-Leu(LEU)	0.70	-32.03	58.62
St-Pierre(PIE)	0.92	-26.65	38.41
Hahaya(HAY)	0.82	-3.02	37.35
Ouani(OUA)	0.80	3.44	36.08
Anse Boileau(ANS)	0.87	12.08	36.02
Diego(ANTs)	0.95	6.52	20.16
Antananarivo (ANTa)	0.97	2.73	16.24
Vacoas(VAC)	0.94	-7.18	23.56
Rodrigues (ROD)	0.96	-9.75	22.49

6. Conclusion

This study aimed at comparing and assessing the coherence and accuracy of the CM SAF SARAH-3 SSR estimates against the in-situ measurements from the IOS-net radiometric network and the analysis of their spatial and temporal variability over the South West Indian Ocean Islands (La Réunion, Mauritius, Seychelles, Madagascar, and Comoros).

To achieve this aim, the satellite estimates of SSR have been compared to the in-situ measurements at different time scales spanning from annual to diurnal circles. While SARAH-3 fairly reproduces the shape of the seasonal circles, the amplitude differs from those of in-situ measurements at each station. At diurnal cycles, not only the

shapes of the cycles have been analyzed but also the classification of the 4 types of days (Clear, AM clear, PM clear, and Overcast) have been conducted thanks to K-means clustering. This also has allowed the comparison of their frequency of occurrence at each station. The assessment on a daily time-scale showed a high correlation above 0.8 at all stations, suggesting a good resemblance of the satellite estimates and in-situ measurements at this time scale. However, SARAH-3 underestimates the SSR annual mean at some stations and overestimates at some others because the spatial resolution of 5 km implies that non-negligible variations are to happen inside each pixel of 25 km^2. The main source of uncertainties for SARAH-3 is believed to be the accuracy of the detection of aerosols and cloud index in order to estimate SSR values. The refinement of the temporal resolution of aerosol from monthly to daily mean and spatial resolution of SARAH-3 from 5 km to 1 km would improve the estimation of SSR values. Additionally, the use of adaptation techniques can be used to improve satellite-derived SSR estimates so as to reduce the biases with the local in-situ measurements.

Finally, this study has just focussed on one year (2020), which might not give enough information on the performance of SARAH-3. Moreover, there are few stations available in territories of SWIO, which doesn't allow a deeper analysis of the performance of SARAH-3 on special variability in the specific territories. This poses a limitation to this study and creates a room for future improvements.

Acknowledgments

This work was supported by the Regional Council of La Réunion in the framework of the European INTERREG V Indian Ocean (2014–2020) and the Indian Ocean Commission Energies programmes (GURDTI/ 20181274 – 0016015 convention). The authors gratefully acknowledge C. Brouat, Y. Hoarau, and L. Oddoz for their technical assistance in the set up and maintenance of the IOS-net stations.

References

[1] Georgios Tzanes, D. Zafirakis, C. Makropoulos, J.K. Kaldellis, and A. I. Stamou, "Energy vulnerability and the exercise of a data-driven analysis protocol: A comparative assessment on power generation aspects for the non-interconnected islands of Greece," *Energy Policy*, vol. 177, pp. 113515–113515, Jun. 2023, doi: https://doi.org/10.1016/j.enpol.2023.113515.

[2] J. P. Praene, M. David, F. Sinama, D. Morau, and O. Marc, "Renewable energy: Progressing towards a net zero energy island, the case of Reunion Island," *Renewable and Sustainable Energy Reviews*, vol. 16, no. 1, pp. 426–442, Jan. 2012, doi: https://doi.org/10.1016/j.rser.2011.08.007.

[3] Panel, "Renewable Energy Sources and Climate Change Mitigation," Cambridge University Press, USA, 2012.

[4] IRENA, "A Path to Prosperity : Renewable Energy for Islands," Nov. 2016. Accessed: Sep. 30, 2023. [Online]. Available: https://www.irena.org/-/media/Files/IRENA/Agency/Publication/2016/IRENA_Path_to_Prosperity_Islands_2016.pdf?rev=cecf22f9f1e047399a31d364edb6789d

[5] Solar Energy Industries Association, "About Solar Energy | SEIA," *SEIA*, 2022. https://www.seia.org/initiatives/about-solar-energy

[6] R. Müller and U. Pfeifroth, "Remote sensing of solar surface radiation – a reflection of concepts, applications and input data based on experience with the effective cloud albedo," *Atmospheric Measurement Techniques*, vol. 15, no. 5, pp. 1537–1561, Mar. 2022, doi: https://doi.org/10.5194/amt-15-1537-2022.

[7] B. Morel, P. Jeanty, M. Delsaut, N. Hassambay, A. Graillet, and J.-P. Chabriat, "Surface measurement of total solar and ultraviolet irradiance and ancillary meteorological data at the South-West Indian Ocean Solar network (IOS-net) stations," *Data in Brief*, vol. 37, p. 107136, Aug. 2021, doi: https://doi.org/10.1016/j.dib.2021.107136.

[8] J. Polo *et al.*, "Preliminary survey on site-adaptation techniques for satellite-derived and reanalysis solar radiation datasets," *Solar Energy*, vol. 132, pp. 25–37, Jul. 2016, doi: https://doi.org/10.1016/j.solener.2016.03.001.

[9] Amine Ouhechou *et al.*, "Inter-comparison and validation against in-situ measurements of satellite estimates of incoming solar radiation for Central Africa: From the annual means to the diurnal cycles," *Atmospheric Research*, vol. 287, no. 106711, pp. 106711–106711, Mar. 2023, doi: https://doi.org/10.1016/j.atmosres.2023.106711.

[10] M. Marchand, A. Ghennioui, E. Wey, and L. Wald, "Comparison of several satellite-derived databases of surface solar radiation against ground measurement in Morocco," *Advances in Science and Research*, vol. 15, pp. 21–29, Apr. 2018, doi: https://doi.org/10.5194/asr-15-21-2018.

[11] A. D. Quansah *et al.*, "Assessment of solar radiation resource from the NASA-POWER reanalysis products for tropical climates in Ghana towards clean energy application," *Scientific Reports*, vol. 12, no. 1, Jun. 2022, doi: https://doi.org/10.1038/s41598-022-14126-9.

[12] P. Mialhe *et al.*, "On the determination of coherent solar climates over a tropical island with a complex topography," *Solar Energy*, vol. 206, no. 508–521, pp. 508–521, Aug. 2020, doi: https://doi.org/10.1016/j.solener.2020.04.049.

[13] J. Schulz *et al.*, "Operational climate monitoring from space: the EUMETSAT Satellite Application Facility on Climate Monitoring (CM-SAF)," *Atmospheric Chemistry and Physics*, vol. 9, no. 5, pp. 1687–1709, Mar. 2009, doi: https://doi.org/10.5194/acp-9-1687-2009.

[14] D. D. W. Germany, "CM SAF Web User Interface // DOI // Details," *wui.cmsaf.eu*. https://wui.cmsaf.eu/safira/action/viewDoiDetails?acronym=SARAH_V003 (accessed Jul. 29, 2023).

[15] C. N. Long and Y. Shi, "An Automated Quality Assessment and Control Algorithm for Surface Radiation Measurements," *The Open Atmospheric Science Journal*, vol. 2, no. 1, pp. 23–37, Apr. 2008, doi: https://doi.org/10.2174/1874282300802010023.

[16] M. Baronnet, "Determination of coefficients for quality control of BSRN data," 2021.

[17] Q. Li and P. Li, "Intermittency study of global solar radiation under a tropical climate: case study on Reunion Island," Scientific Reports, vol. 11, no. 1, Jun. 2021, doi: https://doi.org/10.1038/s41598-021-91639-9.

[18] U. Pfeifroth and J. Trentmann, "EUMETSAT," *Algorithm Theoretical Basis Document SARAH-3*, vol. SAF/CM/DWD/ATBD/SARAH, no. 3.5, Feb. 2023, doi: https://doi.org/10.5676/EUM_SAF_CM/SARAH/V003.

INTERCOMPARISON AND VALIDATION OF ERA5, ERA5-LAND AND AROME AGAINST IN-SITU MEASUREMENTS FOR WIND ENERGY APPLICATIONS OVER REUNION ISLAND

Liliane Uwajeneza[1], Béatrice Morel[2], Chao Tang[3], and Bamba Sylla[4]

[1] University of Reunion, ENERGY-Lab, 15 avenue René Cassin, CS 92003, 97744 Saint-Denis Cedex 9, Reunion Island (France); Phone: +262693610183; Fax: +262262938673; E-mail: liliane.uwajeneza@univ-reunion.fr

[2] University of Reunion, ENERGY-Lab; E-mail: beatrice.morel@univ-reunion.fr

[3] University of Reunion, ENERGY-Lab; E-mail: chao.tang@univ-reunion.fr

[4] AIMS Rwanda; E-mail: sylla.bamba@aims.ac.rw

Abstract: To ensure energy autonomy, initiatives aiming at mitigating emissions of greenhouse gases in the energy sector rely on the development of renewable energy sources (RES). However, integrating electric RES into the energy mix represents an important challenge due to the variations they undergo, which induce variations in electricity production that are not always in phase with demand. The key goal of the present study is to provide a wind resource assessment over Reunion, a small island located in the South West Indian Ocean (SWIO) aiming to become self-sufficient for its electricity with RES by 2030. Currently, wind energy comes from two farms. An increased reliance on wind energy could help reach the 100% RES target, including new offshore and onshore wind turbine capacity installations. In this study, the wind data from a variety of gridded datasets, including climate reanalysis ERA5 at ~25 km spatial resolution and ERA5-Land at ~9 km spatial resolution, along with the Météo-France AROME model at ~2.5 km spatial resolution are compared and validated against in-situ measurements from different Météo-France sites across Reunion over the period 2017–2020. All datasets are recorded at 10 m height with an hourly temporal resolution. The validation was performed over different time scales, from annual means to diurnal cycles, and statistical metrics such as correlation, bias, and root-mean-square error were computed to measure errors. Logarithmic law was used to extrapolate wind speed at hub heights in order to obtain the wind power density at those heights. The results reveal that the AROME is highly accurate and reliable, especially in complex terrain where lower biases are obtained in comparison to the ones with the reanalysis datasets. The wind power potential is high at 50 m and 100 m, especially in the northeast parts of the island, which appear to be suitable for onshore wind farm installation.

Keywords: Renewable energy; Logarithmic law; Wind power density; Reunion Island; model estimates; surface observation.

1. Introduction

According to the Intergovernmental Panel on Climate Change (IPCC), temperature will rise by roughly 1.5°C by the end of the 21^{st}century under the best-case scenario. Continued greenhouse gas (GHG) emissions will cause additional warming and long-term changes in all components of the climate system; therefore, limiting climate change requires a reduction in those emissions [1]. In the context of the energy sector, climate change mitigation policies rely on the development of Renewable Energy (RE) to ensure energy autonomy. Transitioning to a sustainable energy supply using RE sources (RES) is even more important for island territories as they do not have any connection to continental grids. This is especially the case of Reunion island, a French overseas department located at 20°8S and 55°5E in the South West Indian Ocean (SWIO), which has turned to RE sources as a sustainable replacement for some of its energy supply [2]. The island aims to achieve energy autonomy by 2030 based on greater energy efficiency and RE alternatives such as solar, wind, geothermal, ocean, biomass, and hydropower energy [3]. In 2017, RE provided almost 32% of electricity production, with about 14% coming from hydropower, 9% from biomass, and 9% from solar, wind, and biogas [4]. Thus far, the electricity produced from wind over Reunion comes from two farms located at the east of the island. Significant growth in wind power in Reunion is expected to meet the 2030 target, with the installation of both offshore and onshore wind turbines. This will require the assessment and characterization of the available wind resources, considering the island's context.

The wind potential is usually investigated using the wind at the hub height of the wind turbine (e.g., 50 or 100 m). In the absence of such measurements, a power or logarithmic law can be used to first extrapolate wind speed at 10 m to different hub heights [5, 6, 7, 8] and then convert the wind speed at these heights into wind power density. Given the small size of the island and the scarcity of the in-situ measurements (only ~15 Météo-France stations measuring the wind at 10 m), the characterization of the variability of the wind resource at high spatial and temporal resolution requires the use of gridded simulated datasets, provided that they are capable of representing the wind fields at 10 m.

In a recent study conducted in France, Jourdier compared wind speeds from various simulated datasets (AROME, ERA5, MERRA-2, COSMO-REA6, and NEWA) with observed wind speeds. The wind speed was then converted into wind power. The findings revealed that AROME and COSMO-REA6 exhibited superior performance in complex areas, characterized by lower bias and higher correlation, compared to the other models. This was attributed to their higher spatial resolution [5].

The objectives of this study are to compare and validate

gridded datasets (ERA5 and ERA5-Land climate reanalysis, AROME numerical weather prediction model) against in situ measurements, to (1) determine the average wind field, (2) examine the spatial and temporal variations from the diurnal to the seasonal time scales, and (3) compute the wind power density at different hub heights. The paper is structured as follows: section 2 covers the data and methodology, and section 3 provides the results. Finally, section 4 presents the discussion and conclusion.

2. Case study, Data and Methodology

2.1 Description of Reunion case study

Reunion is a small island (2512 km^2) with complex topography: it has two significant peaks, the Piton des Neiges (3071 m) and the Piton de la Fournaise (2632 m), linked by a plateau at an altitude of about 1500 m (Fig.1). The island's mountain slopes experience sudden changes in elevation, which can significantly impact wind patterns [9]. The presence of updraft caused by atmospheric stability and the interaction with the surrounding topography can lead to increased gusting due to turbulence intensity and integral length scale turbulence. The island is characterized by a humid tropical climate that is tempered by the oceanic impact caused by trade winds blowing from east to west with a speed of up to 4 m/s throughout more than 60% of the year [10]. Wind acceleration is observed in the southeast and northeast due to the trade-wind direction and high relief of the island. Trade winds are usually weaker in the rainy season (November to April) than in the dry season (May to October). In the rainy season, Reunion is exposed to strong cyclones [11]. that reach wind speeds of more than 200 km/h.

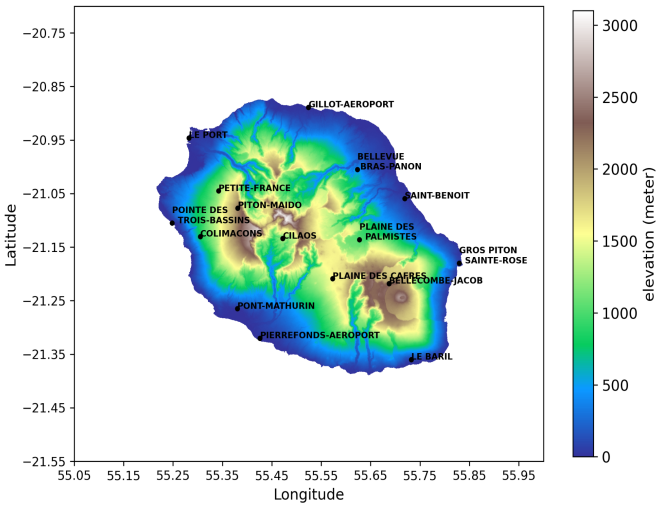

Fig.1. Topography of Reunion Island along with the stations from Météo-France measuring wind speed and direction at 10 m.

2.2 Data

2.2.1 In-situ measurements

In this study, we used quality-controlled hourly wind speed and direction measurements from 16 Météo-France stations (Fig.1) recorded between 2017 and 2020 at a height of 10 m above ground level. The stations can be classified into three categories based on their location: east, highs, and west.

2.2.2 Gridded datasets

Gridded datasets used in this study include two global climate reanalysis produced by the European Center for Medium-range Weather Forecast (ECMWF), namely ERA5 at a spatial resolution of ~25 km [12] and ERA5-Land at a spatial resolution of ~9 km [13], which are available for free and accessible on https://cds.climate.copernicus.eu/cdsapp#. These two datasets are produced by combining observations with simulated data in order to obtain the most realistic possible description of meteorological phenomena by using the laws of physics. ERA5 provides the wind data for land and ocean at a height of 10 m and 100 m, while ERA5-Land provides the wind data only for land at a height of 10 m. Both have the same temporal resolution (hourly). In addition, the outputs of the Météo-France numerical weather prediction model, AROME, at a spatial resolution of 2.5 km are used [14]. This dataset is available with permission from Météo France. All datasets provide zonal and meridional wind data at a height of 10 m, with the exception of ERA5, which also provides wind data at 100 m.

2.3 Methodology

2.3.1 Extrapolation of wind speed at different hub heights

Wind speed and direction from the gridded datasets were computed from the zonal and meridional components of the wind field at different hub heights. The logarithmic law is used to derive the wind data at different hub heights, 50 and 100 m, following [15]:

$$v_2 = v_1 \frac{ln(z_2/z_0)}{ln(z_1/z_0)} \qquad (1)$$

where z_1=10 m, z_2=50 m or 100 m, v_1 is the wind speed at z_1, v_2 is the wind speed at z_2, and z_0 is the surface roughness length which varies according to terrain types.

The surface roughness is estimated from equation (1) as:

$$z_0 = exp\left[\frac{v_2(ln(z_1) - v_1(ln(z_2)}{v_2 - v_1}\right]$$

using ERA5 wind data at 10 m (v_1) and 100 m (v_2). Equation (1) is then applied to the wind data at 10 m from the other datasets [16].

2.3.2 Comparison and validation of simulated and observed wind speed

The following basic performance metrics are used to determine the accuracy of the three gridded datasets. These include:

- The Mean Bias Error (MBE, or Bias) captures the average deviation between modelled and observed data.

$$MBE = \frac{1}{N}\sum_{i=1}^{N}(S_i - O_i) \qquad (2)$$

where N is the total number of observations, and S_i is the simulated value and O_i the observational value at point i.

- The Root Mean Square Error (RMSE) is used to measure the difference between modelled and observed data.

$$RMSE = \sqrt{\frac{1}{N}\sum_{i=1}^{N}(S_i - O_i)^2} \qquad (3)$$

- The Pearson Correlation (R) is used to measure the linear relationship between two variables.

$$R = \frac{\sum_{i=1}^{N}(S_i-\bar{S})\ (O_i-\bar{O})}{\sqrt{\sum_{i=1}^{N}(S_i-\bar{S})^2 \sum_{i=1}^{N}(O_i-\bar{O})^2}} \qquad (4)$$

where $\bar{S}$ the average simulated value and $\bar{O}$ is the average observational value.

2.4 Wind power density (WPD)

The wind power generated by wind turbines, or Wind Power Density (WPD), is related to the cube of wind speed V in m/s and the air density ρ in kg/m^3. WPD (W/m^2) is expressed as:

$$WPD = \frac{1}{2}\rho V^3 \qquad (5)$$

$$\rho \cong \frac{353.4\left(1-\frac{Z}{45271}\right)^{5.2624}}{273.15+T}$$

where Z is the altitude in m and T is the surface temperature in $°C$. These variables are available in the Météo France dataset. The air density was computed at the point and height of interest from [8].

3. Results and Discussion

3.1 Comparison of simulated and observed annual wind speed

Fig.2. depicts the 10-m wind speed for land and ocean over the Reunion domain on annual means from 2017 to 2020 for the three gridded datasets (ERA5, ERA5-Land, and AROME) and the observations (all stations provided). Focusing on the latter, we can see that the annual mean wind speed varies from 1.2 to 6.0 m/s. High annual average wind speeds are found at Gillot Aéroport, Pierrefonds Aéroport, and Gros Piton Sainte Rose, as well as at the stations located on the coastline of the island, whereas the lowest annual average wind speed (~1.2 m/s) is found at Cilaos (Fig.2a). ERA5 and AROME display higher annual mean wind speeds on the ocean compared to the land (Fig.2b, 2d). The data for ERA5 and AROME on the ocean could be used for assessing the wind resource to identify the best locations for the installation of offshore wind farms. Over land, the annual mean wind speed varies from ~2.3 to 3.0 m/s in ERA5, from ~1.5 to 4.3 m/s in ERA5-Land, and from 1.0 to 6.0 m/s in AROME (Fig.2b, 2c, 2d). In all datasets, it appears that the northeast part of the island displays a higher annual mean wind speed compared to the other parts, in agreement with the mean direction of the trade winds over the region. Fig.3 depicts the seasonal and diurnal cycles of wind speed at 10 m for all datasets. The wind speed is clearly higher and more variable throughout the year in the observational data compared to the gridded datasets. Higher wind speeds are found in June and July (Fig.3a). The monthly mean wind speed peaks in July in the observations and AROME and in June in ERA5 and ERA5-Land. This is consistent with the strengthening of the trade winds in wintertime. At diurnal timescales (Fig.3b), wind speed peaks during the day and declines slowly at night. Compared to the other gridded datasets, the average wind speed from AROME is closer to that from the observations, which indicates that it gives better performance on this island when compared to the observations than the climate reanalyses.

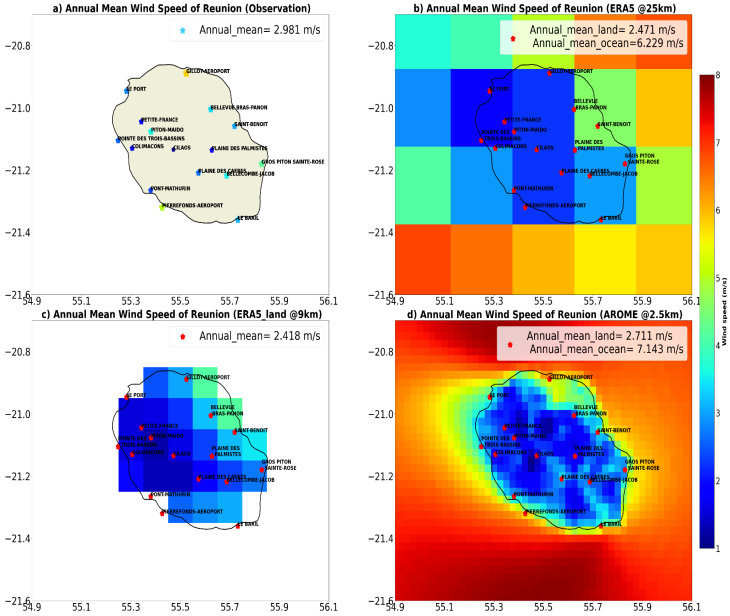

Fig.2. Spatial distribution of the annual mean wind speed at 10 m over the Reunion domain from stations (Météo-France) and gridded (ERA5, ERA5-Land, AROME) datasets for the period 2017-2020. For each dataset, the spatial average is indicated at the top right corner of the graph.

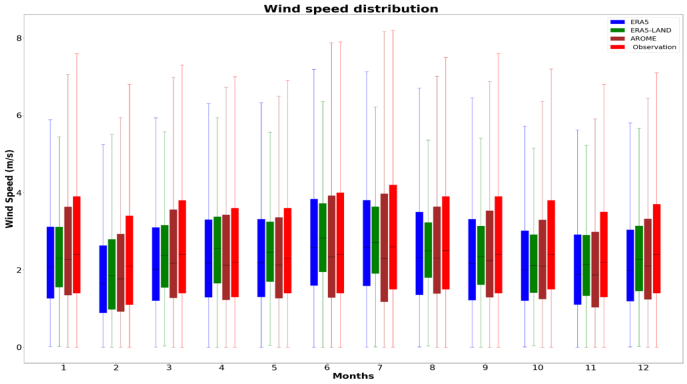

(a)

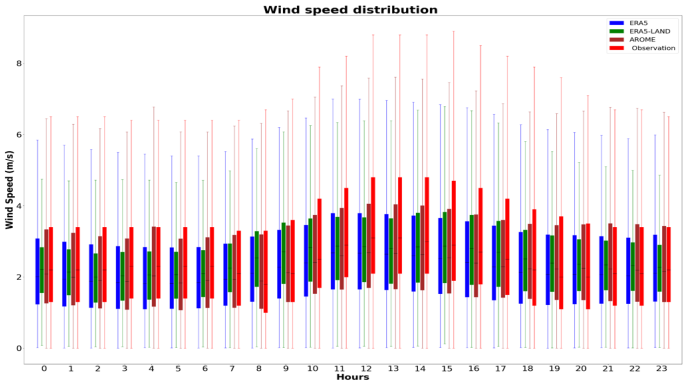

(b)

Fig.3. Box plots of the (a) monthly- and (b) hourly-mean 10-m wind speed for 16 Météo-France stations over Reunion (red) along with the nearest pixels in ERA5 (blue), ERA5-Land (green) and AROME (brown).

3.2 Wind rose and wind speed validation for eight stations over Reunion Island

In this section, we use wind rose diagrams to describe both the speed and the direction of winds at locations of interest. Hopuare used wind roses to determine which winds were dominant in French Polynesia at different sites [17]. Eight stations over Reunion Island were organized into two groups depending on their location: Bellevue Bras-Panon, Saint-Benoît, and Gros Piton Sainte-Rose on the eastern coast of the island, and Piton-Maïdo, Plaine des Cafres, Petite-France, Bellecombe-Jacob, and Plaine des Palmistes on the highs (Fig.1). Fig.4 shows the wind roses for the chosen locations.

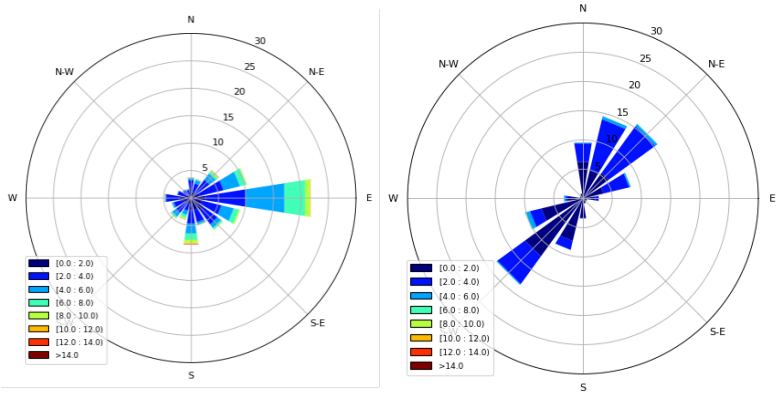

a) Piton-Maïdo **b) Plaine des Palmistes**

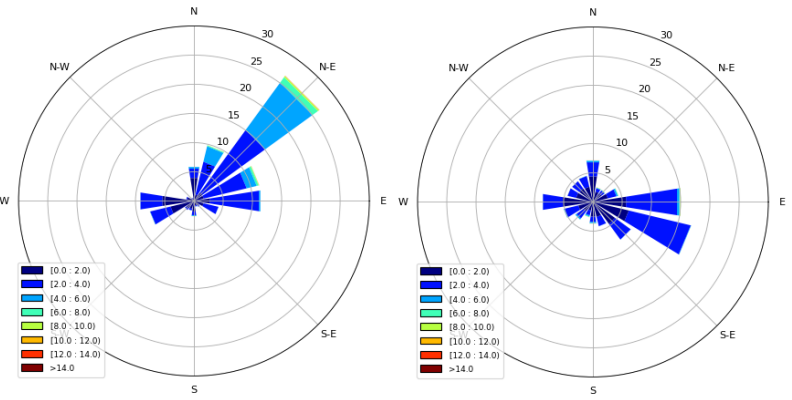

c) Plaines des Cafres **d) Petit-France**

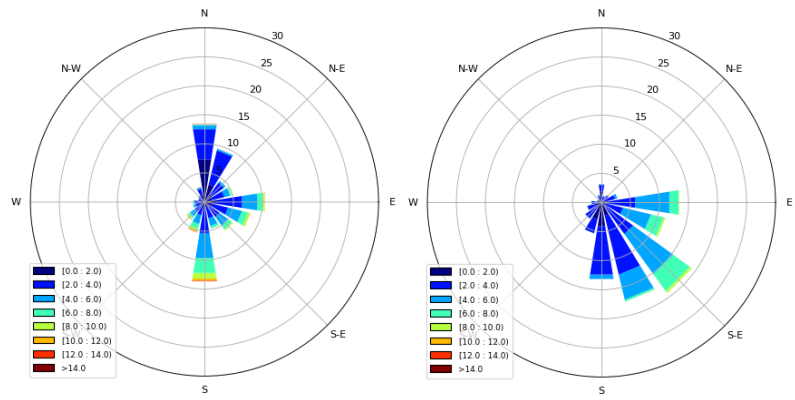

e) Bellecombe-Jacob **f) Bellevue Bras-Panon**

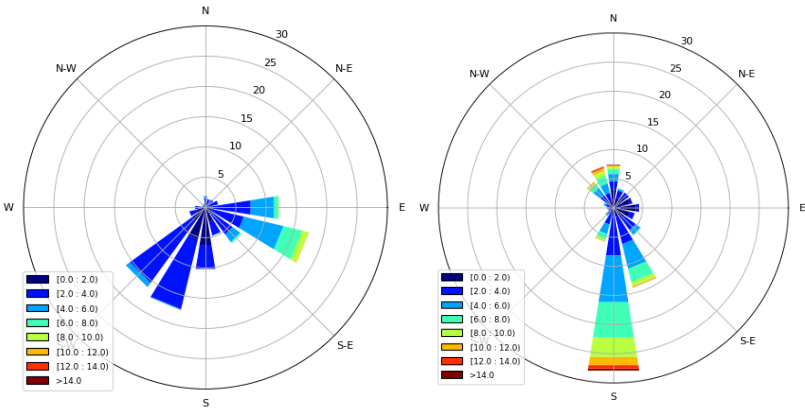

g) Saint-Benoît **h) Gros Piton Sainte-Rose**

Fig.4. Wind direction and speed frequency at 10 m for eight Météo-France stations for the period 2017-2020. The circles indicate the frequency and a colour band indicates the range of wind speeds in m/s.

The wind roses in Fig.4 illustrate the frequency and speed of wind blowing from each direction at each location. According to Fig.4a, we find that at Piton-Maïdo, easterly winds are predominant, and only about 1% of all winds exceed 8 m/s. The lowest wind speeds, less than 4 m/s, are seen at the Plaine des Palmistes (Fig.4b). At the Plaine des Cafres (Fig.4c), northeasterly winds showing a speed below 6 m/s are observed. Lower wind speeds, often less than 6 m/s, are found at Petite France, where the wind comes predominantly from the southeast (Fig.4d). Southerly and northerly winds are frequently observed at Bellecombe-Jacob (Fig.4e), where they often reach 8 m/s. The two stations in the highs of the mountain peaks (Bellecombe_jacob, Plaine des Palmistes) are the only ones that have two opposite predominant wind directions. Fig.4f, shows that Bellevue Bras-Panon winds are predominantly blowing from the southeast, with wind speed values up to 8 m/s. Fig.4g shows that at Saint-Benoît, the predominant wind blows from east to south-east, it often reaches 8 m/s. Gros Piton Sainte-Rose (Fig.4h) shows higher wind speed values than the other locations, reaching 14 m/s, and a predominant wind direction from the south. There is a wind farm in Reunion located at this site. The northwest winds are infrequent in (Fig.4b, 4c, 4g, 4f). The most predominant winds at those sites are easterly, southeasterly, and southerly. Furthermore, in comparison to stations located over the highs, stations on the east exhibit the highest wind speed, particularly in Gros Piton Sainte-Rose.

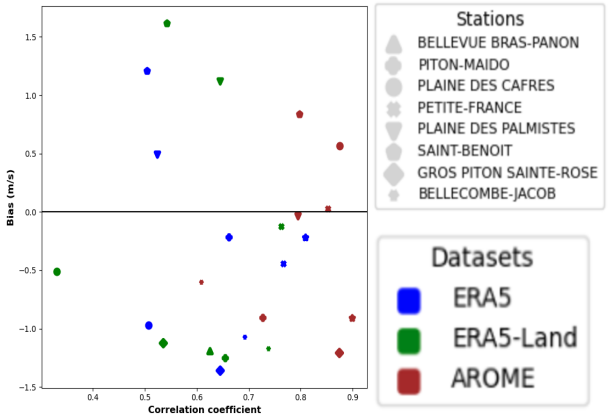

Fig.5. Correlation coefficient between the 10-m wind speed at the nearest pixel of the gridded dataset and that at the station as a function of bias (in m/s) at eight Météo-France stations. Results are given in blue for ERA5, in green for ERA5-Land and in brown for AROME.

Table 1. Calculated Root Mean Square Error (m/s) values at 8 stations.

Stations	Datasets		
	ERA5	ERA5-Land	AROME
Bellevue Bras-Panon	1.19	0.24	0.91
Piton-Maïdo	1.27	-2.23	-0.91
Plaine des Cafres	0.54	0.99	0.58
Petite-France	0.17	0.45	0.13
Bellecombe-Jacob	1.18	1.08	0.63
Plaine des Palmistes	1.12	0.50	0.08
Saint-Benoît	1.62	1.22	0.85
Gros Piton Sainte-Rose	1.17	1.22	1.22

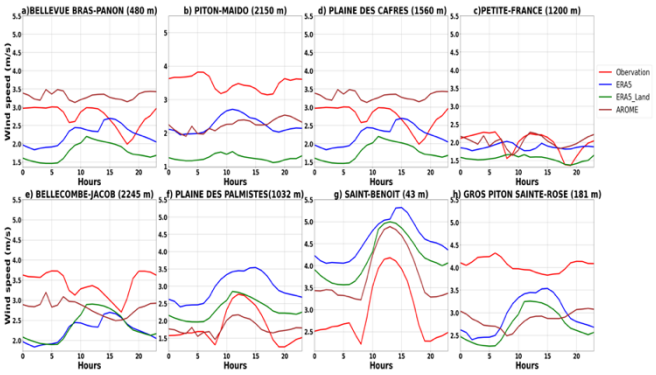

Fig.6. Diurnal evolution of the 10-m wind speed (in m/s) at 8 Météo-France stations over Reunion for the period 2017-2020 (in red) along with that from the nearest pixel of the gridded datasets (AROME in brown, ERA5-Land in green, ERA5 in blue).

In Fig.5, which depicts the bias vs the correlation coefficient for the gridded datasets in comparison to the observations (only 8 sites at the east and over highs are used here due to the availability of ERA5-Land), the AROME model has a high correlation (>0.7) for all stations with the exception of Bellecombe-Jacob, which displays a correlation of 0.6 and a small bias of -0.59 m/s. In addition, stations with the highest correlation (above 0.8) are Gros Piton Sainte-Rose, Bellevue Bras-Panon, Plaine des Cafres, and Petite-France. Petite-France, for all datasets, shows a low bias, an absolute value lower than 0.5 m/s, and a high correlation. AROME depicts that Plaines des Palmistes and Petite-France have a low bias close to 0 m/s. Table 1 shows the calculated RMSE values. The lowest RMSE found at Plaine des Palmistes (AROME) is around 0.08 m/s. In ERA5-Land, the highest correlation is found for Bellevue Bras-Panon and is associated with a low bias (absolute value below 0.3 m/s) and low RMSE around 0.23 m/s. In ERA5, higher correlation is obtained in Petite-France (0.76) and Bellevue Bras-Panon (0.73), where the absolute values of bias are 1.17 m/s and 0.12 m/s, respectively. Plaine des Cafres in ERA5 shows the lowest correlation, around 0.33, with a low bias**.** At the diurnal scale (Fig.6f), AROME at this location closely follows the observation, with a sharp increase of the wind speed from 9 a.m. up to 3 p.m. and a slow decrease during the night, in contrast to the two other gridded datasets in which the mean hourly wind speed is overestimated. In ERA5 and ERA5-Land, the diurnal cycle shows a tendency to increase during the day for all sites, unlike observations and AROME, where the diurnal cycle is sometimes less marked in Piton-Maïdo (Fig.6b), Plaine des Cafres (Fig.6c), Petite-France (Fig.6d), and Gros Piton Sainte-Rose (Fig.6h). At Bellevue Bras-Panon (Fig.6a), we observe a decrease in the intensity of the wind during the day, unlike ERA5 and ERA5-land. Compared to the other gridded datasets, the AROME model well represents the diurnal cycle of average wind speed in the mountainous area.

3.3 Wind power density for eight stations at 10, 50 and 100 m in Reunion Island

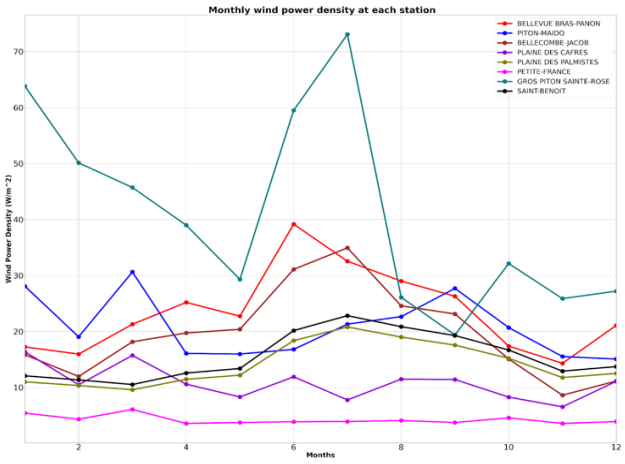

(a)

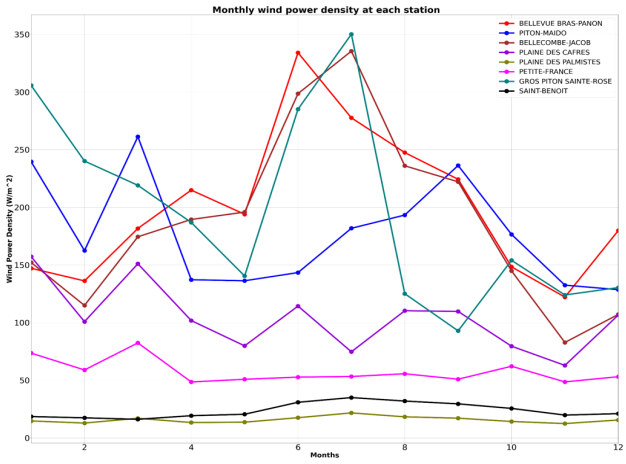

(b)

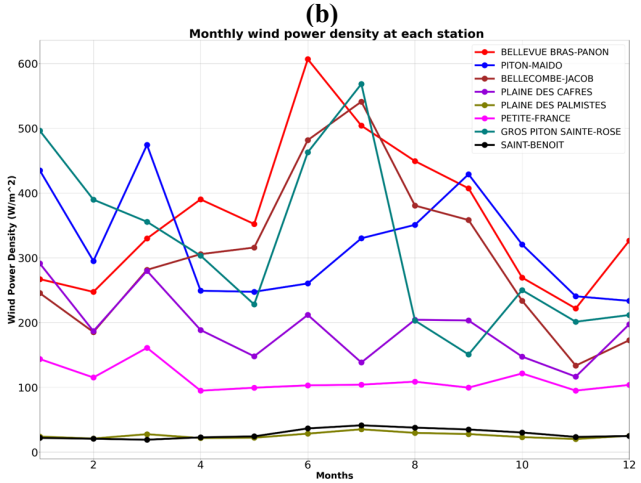

(c)

Fig.7. Monthly wind power density in W/m² at the height of (a) 10 m, (b) 50 m and (c) 100 m for eight Météo-France stations over Reunion for the period 2017-2020.

Fig.7 shows the monthly Wind Power Density (WPD) at 10 m, 50 m and 100 m for the eight Météo-France stations over Reunion Island. At 10 m (Fig.7a), the WPD never exceeds 100 W/m^2 for all stations. We observe that Gros Piton Sainte-Rose at the east displays higher WPD values compared to the other stations in all months except August and September, with a peak at approximately 75 W/m^2 in July. In contrast, Petite-France over the western highs has the lowest WPD values (below 10 W/m^2) for all months. By considering the logarithmic atmospheric boundary layer profile, the wind speed tends to increase due to reduced surface roughness, which leads to an increase in WPD at higher elevations. At 50 m (Fig.7b), high WPD is found at three stations at the east, Gros Piton Sainte-Rose, Bellevue Bras-Panon and Bellecombe-Jacob, with the highest value at 350 W/m^2 once again at Gros Piton Sainte-Rose in July. In addition, Piton-Maïdo over the western highs displays a maximum WPD at ~260 W/m^2 in March. The lowest WPD is found at Saint-Benoît and Plaine des Palmistes with values less than 50 W/m^2 in all months. At 100 m (Fig.7c), a maximum value of ~600 W/m^2 is found in June at Bellevue Bras-Panon. At this location, WPD remains above 230 W/m^2 for all months. As for the 50-m hub height, the minimum values at 100 m are observed at Saint-Benoît and Plaine des Palmistes. According to the results, maximum values in June and July indicate higher WPD in austral winter. Furthermore, Gros Piton Sainte-Rose has the highest wind resource potential, followed by Bellevue Bras-Panon, Bellecombe-Jacob and Piton-Maïdo. This indicates that these locations have a higher wind speed and are more suitable for wind power projects.

4. Discussion and Conclusion

For assessing the wind resource in Reunion Island, we used different methods described in section 2.3. The comparison between model outputs at different spatial resolutions and observations showed that the northeast part of the island has a higher annual wind speed compared to the other parts due to the fact that the wind trades over the island blows largely from the northeast part. The AROME model compared to gridded datasets indicates a high annual wind speed of around 2.71 m/s at 10 m for only land. Furthermore, the AROME model also indicates that there is a higher annual wind speed along the coastline and in some parts of the middle of the island. This is due to the fact that the model has a higher resolution compared to the other gridded datasets, showing more pixels that provide more detailed information with a resolution (~2.5 km). Additionally, this model exhibits a strong correlation above 0.7 for all stations, particularly for Gros Piton Sainte-Rose, Bellevue Bras-Panon, and Plaine des Cafres, which have correlations above 0.8. The spatial and temporal variability was quantified at the seasonal and diurnal timescales. The mean wind speed is higher in June and July in the wintertime. At the diurnal scale, the peak of average wind speed is found during the day and slowly decreases during the night, due to the differential heating of the Earth's surface during the daily radiation cycle [16]. At the eight stations used, the wind rose maps (Fig.4) showed the predominant winds over the island to be easterly, northeasterly, and southerly, depending on the stations. For instance, Piton-Maïdo experiences easterly winds of 8 m/s, suggesting wind farms should be oriented eastward direction to maximize their efficiency. It is important to take account both frequency of high winds and direction in which their blow. The wind potential density (Fig.7) was estimated at different heights. At 10 m, the WPD never exceeds 100 W/m^2 for all stations used. It increases at 50 m and 100 m, with the highest WPD values notably found at stations located in the northeast part of the island, such as Gros Piton Sainte-Rose and Bellevue Bras-Panon. The wind power density at 50 m and 100 m shows the high potential, where the maximum reached 350 W/m^2 and 600 W/m^2, respectively. Additionally, Bellevue Bras-Panon and Piton-Maïdo display WPD above 220 W/m^2 throughout the year. Furthermore, Gros Piton Sainte-Rose displays lower intra-daily variation compared to the other stations with wind speeds above 3.7 m/s throughout the day. In addition, Bellevue Bras-Panon also has a mean wind speed above 3 m/s for all hours and a higher mean speed than the other stations from 12 p.m. to 15 p.m. Then, the highest wind resources over Reunion could be found at those stations. These sites could be considerable for the installation of new wind farms. Gros Piton Sainte-Rose, for instance, should be directed south in order to take advantage of the strong and frequent south winds, while Bellevue Bras-Panon should be oriented southeast.

The aim of this study was to compare and validate modelled (ERA5, ERA5-Land, AROME) and observed wind data. To achieve this aim, we used statistical metrics to validate the models, which include R, RMSE, and MBE. Wind energy potential was investigated in Reunion Island using hourly data from 2017–2020 for eight stations at 10 m above ground level. The wind speed at 50 m and 100 m was extrapolated using logarithmic law. Our results show that all datasets have high mean wind speeds in the north-east and east parts of the island and along the coast. Among those modelled datasets, the AROME model demonstrated that it has a higher annual wind speed than the gridded datasets used in this study. In addition, it shows the lowest bias with a high correlation in comparison with the observations than the other datasets over complex terrain. It also exhibits low biases relative to other models, with biases that are particularly low for the Plaines des Palmistes and Petite-France. According to the annual mean wind speed, the northeast, east, and coastal parts of the island have high wind potential, especially in lower latitudes. Gros Piton Sainte-Rose, Bellevue Bras-Panon, Piton-Maïdo, and Bellecombe-Jacob were found to have a higher WPD compared to other sites considered. Furthermore, the AROME model demonstrated that it has better skill on this island compared to other gridded datasets, as it provides more information on mean wind speed from a regional to a local scale due to its higher resolution.

In this study, we used 4 years and 8 stations to determine the wind potential of the island. We would therefore suggest using more than 4 years of data with high resolution, at most 5 km, as required to determine the wind resource assessment on a complex topography such as that of Reunion.

Acknowledgements

This work is funded by the French Embassy in Rwanda. The authors would like to thank Météo France for providing the dataset used in this study. Finally, thanks to ECMWF for storing the dataset and making it accessible through their website.

References

[1] IPCC, "Summary for Policymakers — Global Warming of 1.5 °C," *IPCC*, 2018. https://www.ipcc.ch/sr15/chapter/spm/

[2] J. P. Praene, M. David, F. Sinama, D. Morau, and O. Marc, "Renewable energy: Progressing towards a net zero energy island, the case of Reunion Island," *Renewable and Sustainable Energy Reviews*, vol. 16, no. 1, pp. 426–442, Jan. 2012, doi: https://doi.org/10.1016/j.rser.2011.08.007.

[3] S. Selosse, S. Garabedian, O. Ricci, and N. Maïzi, "The renewable energy revolution of reunion island," *Renewable and Sustainable Energy Reviews*, vol. 89, pp. 99–105, Jun. 2018, doi: https://doi.org/10.1016/j.rser.2018.03.013.

[4] "Energy balance 2018 EDITION Reunion Island 2017." Available: https://energies-reunion.com/wp-content/uploads/2015/01/BER-2017-ed-2018-english.pdf

[5] B. Jourdier, "Evaluation of ERA5, MERRA-2, COSMO-REA6, NEWA and AROME to simulate wind power production over France," *Advances in Science and Research*, vol. 17, pp. 63–77, Jun. 2020, doi: https://doi.org/10.5194/asr-17-63-2020.

[6] G. Gualtieri, "Reliability of ERA5 Reanalysis Data for Wind Resource Assessment: A Comparison against Tall Towers," *Energies*, vol. 14, no. 14, p. 4169, Jul. 2021, doi: https://doi.org/10.3390/en14144169.

[7] G. Gualtieri and S. Secci, "Methods to extrapolate wind resource to the turbine hub height based on power law: A 1-h wind speed vs. Weibull distribution extrapolation comparison," *Renewable Energy*, vol. 43, pp. 183–200, Jul. 2012, doi: https://doi.org/10.1016/j.renene.2011.12.022.

[8] W. Sawadogo *et al.*, "Current and future potential of solar and wind energy over Africa using the RegCM4 CORDEX-CORE ensemble," Jul. 2020, doi: https://doi.org/10.1007/s00382-020-05377-1.

[9] D. Lesouëf, F. Gheusi, R. Delmas, and J. Escobar, "Numerical simulations of local circulations and pollution transport over Reunion Island," *Annales Geophysicae*, vol. 29, no. 1, pp. 53–69, Jan. 2011, doi: https://doi.org/10.5194/angeo-29-53-2011.

[10] J. Badosa, M. Haeffelin, N. Kalecinski, F. Bonnardot, and G. Jumaux, "Reliability of day-ahead solar irradiance forecasts on Reunion Island depending on synoptic wind and humidity conditions," *Solar Energy*, vol. 115, pp. 306–321, May 2015, doi: https://doi.org/10.1016/j.solener.2015.02.039.

[11] M.-D. Leroux, J. Meister, D. Mekies, A.-L. Dorla, and P. Caroff, "A Climatology of Southwest Indian Ocean Tropical Systems: Their Number, Tracks, Impacts, Sizes, Empirical Maximum Potential Intensity, and Intensity Changes," *Journal of Applied Meteorology and Climatology*, vol. 57, no. 4, pp. 1021–1041, Apr. 2018, doi: https://doi.org/10.1175/jamc-d-17-0094.1.

[12] H. Hersbach *et al.*, "The ERA5 global reanalysis," *Quarterly Journal of the Royal Meteorological Society*, vol. 146, no. 730, Jun. 2020, doi: https://doi.org/10.1002/qj.3803.

[13] J. Muñoz-Sabater *et al.*, "ERA5-Land: a state-of-the-art global reanalysis dataset for land applications," *Earth System Science Data*, vol. 13, no. 9, pp. 4349–4383, Sep. 2021, doi: https://doi.org/10.5194/essd-13-4349-2021.

[14] O. Bousquet *et al.*, "An evaluation of tropical cyclone forecast in the Southwest Indian Ocean basin with AROME-Indian Ocean convection-permitting numerical weather predicting system," *Atmospheric Science Letters*, vol. 21, no. 3, Mar. 2020, doi: https://doi.org/10.1002/asl.950.

[15] J. D. Holmes, *Wind Loading of Structures*. CRC Press, 2001.

[16] J. F. Manwell, J. G. Mcgowan, and A. L. Rogers, *Wind energy explained : theory, design and application*. Chichester, U.K.: John Wiley & Sons, Ltd, 2011. Available: https://www.wiley.com/en-us/Wind+Energy+Explained%3A+Theory%2C+Design+and+Application%2C+2nd+Edition-p-9780470015001

[17] M. Hopuare, T. Manni, V. Laurent, and K. Maamaatuaiahutapu, "Investigating Wind Energy Potential in Tahiti, French Polynesia," *Energies*, vol. 15, no. 6, p. 2090, Mar. 2022, doi: https://doi.org/10.3390/en15062090.

AN OVERVIEW OF AVAILABLE RENEWABLE ENERGY RESOURCES AND TECHNOLOGIES FOR THE LIMPOPO PROVINCE

Pfesesani Netshilonwe[1], Fhulufhelo Nemangwele[2], Mukovhe Ratshitanga[3]

[1] University of Venda, Faculty of Science, Engineering, and Agriculture, Department of Physics, Private Bag X5050, Thohoyandou, Limpopo, South Africa, 0950, 17008248@mvula.univen.ac.za

[2] University of Venda, Faculty of Science, Engineering, and Agriculture, Department of Physics, Private Bag X5050, Thohoyandou, Limpopo, 0950, nemangwele@univen.ac.za

[3] Cape Peninsula University of Technology, Faculty of Engineering and the Built Environment, Department of Electrical Engineering, Electronics and Computer Engineering, P.O Box 1906, Bellville, 7535, ratshitangam@cput.ac.za

Abstract: In South Africa, the energy transition from fossil fuels to renewable energy is advancing. The advancement is essential to meet affordable, reliable, and sustainable energy. Replacing fossil fuels with renewable energy has been unfolding at an average rate due to gradual improvements in renewable energy technologies and insufficient awareness of those technologies. Improvements in renewable energy technologies will protect the environment, improve the socio-economic lives of people, and promote clean economic growth in rural areas. This paper presents an overview of available and potential renewable energy resources in Limpopo province to evaluate their technologies concerning the availability of energy sources and their technological criteria. Renewable energy resources assessed were solar PV, biomass, hydropower, geothermal, and wind energy. Two renewable energy resources (solar PV and biomass) are the top utilized energy resources in the province and the remaining resources are potential resources. Favorable geographic location and affordability are the drivers behind solar PV demand. Biomass waste availability and waste treatment plant availability drive the utilization of biomass technology. Satisfying renewable energy performance consequence an economical reliable energy supply, lower harmful gas emissions, and reduced energy poverty.

Keywords: Renewable energy technologies; solar PV; Biomass; Biogas; Micro-grids.

1. Introduction

In Sub-Saharan Africa, approximately 13% of the population dwells in areas with limited access to electricity [1]. This challenge is arising in areas with enormous potential for renewable energy development and implementation. Limpopo province in South Africa falls under that area scenario where some areas do not have access to electricity and some with limited electricity reliability [2]. People who have access to national utility electricity face annual electricity price hikes, and this puts their socio-economic life under difficulties. An alternative way to supply reliable cheap-priced electricity is needed and that can be achieved through the combination of various renewable energy resources technologies in the province. Favorably Limpopo province has available renewable energy resources. In this paper, the overview of different renewable energy technologies both available and potential which include: solar PV, biomass, hydropower, geothermal, and wind turbine [2] is presented, to achieve qualities of renewable energy resources such as sustainability and durability and technological criteria such as continuity, availability and predictability of energy sources assessment. This will answer the question of what technologies are being utilized in the province and whether those technologies are successful in supplying sufficient energy to end-users. To the author's knowledge, this subject of study has been conducted in various parts of the world but there exists limited literature on the subject in Limpopo province. To this effect, different technologies are assessed to determine why certain technologies are implemented and others are not. In areas where they utilize some of those renewable energy systems, there is a socio-economic development [3].

2. Literature review

This literature review will examine both available and potential renewable energy resources. Solar PV, wind turbine, hydropower, biomass, and geothermal are the renewable energy technologies assessed.

2.1. Solar PV technology

The study conducted by [4] utilized a model created on MATLAB R2020a to simulate the performance of a solar system. The study showed that the climate of Limpopo maintains satisfactory performance and reliable utilization of solar PV. [5] Identified types of renewable energy resources used in the province through surveys and questionnaires. It was supported that Limpopo has favorable weather conditions suitable for any solar PV technology. [6] assessed small-scale renewable energy resources, utilizing empirical models and the NASA database for solar estimation. The study acknowledged that the effects of solar radiation and territorial climatological measurements in the Vhembe district are satisfactory for solar PV energy generation. The assessment study conducted by [7] used the solar radiation H-S model to investigate the effects of seasonal change on solar PV power performance in the Vuwani area. Seasonal changes do impact the performance of solar PV as temperature intensity changes. [8] conducted a study that discussed various methods and technologies to solve Sub-Saharan Africa's electrification challenges. The geographical climate and load profiles of the study area support that on top of the list, solar PV technology is an employable technology in the region. An assessment by [9] analyzed the performance of solar PV for a groundwater pumping system utilizing a community engagement process and solar-powered irrigation system toolbox. The solar system generates power, which benefits the locals of Giyani with domestic and farming water security. An assessment conducted by [10] and [11] continued to promote that efficient solar system technologies are essential as they can satisfy the load, especially for large-scale projects. A report given by the Limpopo provincial government acknowledged that the province is home to the biggest solar power plants in the country [12]. [13] presented the successful operation of the Soutpan solar plant which feeds the national grid. A review paper by [14] supported that not only the Soutpan solar plant was a success but also the Witkop solar park, which generates 33MW of power that is fed to the national grid, has been successful and satisfactory. The satisfaction of large solar PV plants has been further supported by [15], who assessed the successful operation of the 66MW Tom Burke solar plant.

2.2. Biomass and biogas technology

An investigation study conducted by [16] indicated that Limpopo province sits in 2nd position in terms of utilizing biomass energy in the country. Biomass is converted to biogas using anaerobic digestion and its availability and consumption have been studied by [17] to exhibit the advantages and benefits of using biogas energy. A review paper authored by [18] provided perspective on Africa's energy transition and the commitment of various locations towards transitioning into the green economy through biogas technology. An evaluation conducted by [19] used a field survey and logit regression model to evaluate basic factors the biogas technology awareness and perceptions towards its adoption and utilization at the household level in Limpopo and the study showed that the adoption of biogas technology has a positive impact in the province. [20] Continued to study effects of human perspective towards biogas energy implementation. A study conducted by [21] observed the operation of fixed dome biogas digesters, intending to exhibit development success brought by biogas energy in rural areas. Biogas energy was found to be a system that saves the environment by reducing greenhouse gases and serving as a waste management solution [22]. A study by [23] addressed the implementation of suitable biogas technology in rural areas of the Vhembe district, where fixed dome digesters are utilized. [24] supported that biogas technology can enhance communities' economic development. [25] said that it is important to implement small bio-digesters for household' usage. An assessment conducted by [26] showed that barriers to popularizing and implementing biogas digester technologies dwell on technical, economic, and sociocultural constraints. [27] continued to narrate to provide solutions on barriers behind the low adoption of biogas technology in some areas. An evaluation conducted by [28] demonstrated the advantages of utilizing biogas technology, including health, environmental, and economic benefits. The agricultural benefits of using green manure legumes in maize production have been studied by [29] to lengthen the advantages of biomass utilization.

2.3. Hydropower

The hydropower development report prepared by [30] showed that there is a 1500MW pumped storage hydropower built by ESKOM in Tubatse municipality, Limpopo. [31] went on to show that small, decentralized hydropower stations can play a role in supplying electricity to rural areas. The evaluation study presented by [32] described the development of South African hydropower opportunities and the study showed that stakeholders in hydropower need to be made aware of its positive outcomes. A study conducted by [33] addressed barriers of lack of information by providing an overview status of small hydropower in South Africa. The study showed that a small hydropower capacity can be installed for Limpopo, Mpumalanga, KZN, and Free State provinces. [34] examined problems and challenges in hydropower development in South Africa. Studies showed that lack of finance is the main hindrance to hydropower development. This means that the province has hydropower potential.

2.4. Geothermal

Geothermal energy is a renewable resource that has potential in Limpopo province. A brief study conducted by [35] explored various renewable sources of energy and their applications. Geothermal was found to be one of the potential renewable energies in Limpopo province but its exploration is moderate. [36] presented an exploration study utilizing magnetic and seismic methods to describe requirements for geothermal exploration In South Africa. The study explored ancient plate boundaries known as mobile belts and greenstone belts. Unfortunately, little exploration has been done on geothermal energy, though the study area has its potential. Evaluation conducted by [37] supported that low enthalpy geothermal energy can be alternative energy in Namaqua-natal mobile belt and Limpopo belt. Binary-circle geothermal plants were proposed. Low enthalpy geothermal energy was further investigated in Limpopo province by [38] to harness it. The study utilized hydraulic fracturing and magneto-telluric methods to show that a 75MW geothermal system can be implemented. [39] employed mathematical modeling and numerical simulations on MATLAB to show that geothermal can generate 66.6% efficiency of power and there is room for development.

2.5. Wind turbine energy

Implementing wind plants requires careful planning to position wind turbines. Wind speed and wind direction is also an important aspect to observe [40]. A study conducted by [41] indicated that areas with good wind potential have an average wind speed of 4m/s for small wind turbines and 5.8m/s for utility-scale turbines. A study conducted by [42] utilized a scale temporal-spatial data approach to point out that Limpopo province has a low potential for utility wind turbines as the province has an annual average wind speed which is less than 4 m/s. [43] supported that Limpopo province like has low potential for wind turbine as it has an average annual wind speed of 3.05m/s, which is not enough for even small scale wind turbine. Another factor is that wind turbines function successfully in locations with dense air flow and those locations are found near oceans and Limpopo is in high altitudes [44].

3. Methodology

3.1. Description of the selected site

Limpopo province is found in the northern part of South Africa. The province shares borders with Mozambique, Zimbabwe, and Botswana [45]. The province has the potential for geothermal energy [38], wind turbines [46] and hydropower [47]. The site mainly utilizes solar PV and biomass as renewable energy resources.

3.2. Models of available and potential renewable energy resources

Table 1 describes the principles of operation for existing renewable energy technologies and potential renewable energy technologies in Limpopo province. The principles of operation show the models for output power of solar PV, biomass energy, hydropower, wind turbine, and energy and efficiency generated by geothermal technology.

Table 1. Models of available and potential renewable energy resources

Technologies	Models
Solar PV	$P_{PV} = \eta_{PV} * A_{PV} * I_{PV}$ (1)
Biomass	$P_{biomass} = \frac{BQ_{LHV}\,\eta\eta_{biogas}}{3600}$ (2)
Hydropower	$P_{ht} = \eta_{ht} * \rho_w * g * \psi_{net} * Q_t$ (3)
Geothermal	$\eta_T = \frac{W_T}{W_{TS}} = \frac{\dot{m}_{ref(h_1-h_2)}}{\dot{m}_{ref(h_1-h_{2s})}}$ (4) $W_t = \dot{m}_{wf}(h_1 - h_2)$ (5)
Wind turbine	$P_{wtg} = \frac{1}{2}\rho A v^3 C_p \eta_g \eta_b$ (6)

Table 1 describes the available and potential renewable energy technologies and their models. The model's symbols are described as follows: On solar PV, P_{pv}, η_{pv}, A_{pv} and I_{pv} are the power output of PV, PV module efficiency, surface area of the PV system, and solar irradiance. On wind turbine,P_{wtg}, ρ, A, V, C_p, η_g , η_b are wind power output, air swept density, swept area, speed, coefficient performance, generator efficiency, and gear efficiency. On hydropower, P_{ht}, η_{ht}, g, ρ_w, ψ_{net}, Q_t are power output of hydropower, HT efficiency, gravitational acceleration, density of water, net head, and flow rate [48] . On biomass energy B is biomass materials consumed, Q_{LHV} is the low calorific value of biogas, η is biogas generator efficiency, η_{biogas} is gasification efficiency and P_{biogas} is biogas output power [22] . On geothermal, η_T, W_T, W_{TS}, h_4, and h_{4s} are turbine isentropic efficiency, turbine power, and isentropic turbine power, refrigerant enthalpy at outlet turbine/inlet condenser and refrigerant isentropic enthalpy at outlet turbine/inlet condenser [39].

4. Review of available and potential renewable energy technologies

4.1. Existing renewable energy technologies

The following section assesses the performance of existing renewable energy technologies. Those technologies include solar PV and biomass.

4.1.1. Solar PV

In the village of Mpheni, the sizing of a solar PV system has been done. The village has a population density of about 50 houses. One house is estimated to have a load of 7.846 kWh which means the generated power of 372 kW is satisfactory [49]. A 31 MW solar PV plant in Soutpan solar plant generates about 61 000MWh/year, feeding 22kV to the Eskom distribution grid system and serving about 13 000 South African homes. A 33MW Witkop Solar plant commissioned in 2014 generates 62 000MWh/year of electricity for the utility grid [50]. A 66MW Tom Burke solar plant is a successful operating plant in Limpopo. The plant generates a capacity of 66 MW and can generate up to 122 000 MWh/year of energy. [15]. The village of Gwakwani has about 40 houses. One house has an estimated load of 126Wh per day [10]. Schneider Electric and the University of Johannesburg donated and installed 750 W solar panel water irrigation systems, a 12V rooftop PV system capable of lighting and charging a cell phone at home. A 15kW solar PV runs in the local bakery [11]. A solar system in Vuwani Science Center has been assessed using estimated global solar irradiation. A solar system assessed generates power of 225W. The system is operational in the Vuwani Science Resource Center [7].

4.1.2. Biomass and biogas

Limpopo province is ranked 2nd for biomass usage in the country [51]. Therefore, we have about 100 installed bio-digesters in the province [22] and [52]. In Vhembe district, fixed dome bio-digesters have been built with the support of the South African National Energy Development Institute (SANEDI) in Chavani village for agricultural waste-to-energy conversion [23]. The Mafuneko solution project at Gawula village near Giyani uses cow dung as feed material for a fixed dome digester that generates biogas sold to locals at low prices. The project has created employment and skills, and commuters use biogas for cooking [53]. The waste-to-energy technology project in Capricorn district, driven by the University of Venda in collaboration with UNIDO (United Nations Industrial Development Organization) to turn waste into biogas energy is successful [54]. Biogas technology in Limpopo dairies uses project feedstock type of dairy waste.

The digester technology is IBR (Induced Bed Reactor). The di-gestate is then used as a wet or solid fraction and supplied to farmers for land fertilization [54]. Tzaneen municipality utilizes a fixed dome bio-digester for wastewater treatment, and it is responsible for producing dried sludge for farmers for land application [55]. Two fixed dome bio-digesters have been built at Makhado military bases for cooking and waste management. Those bio-digesters are advantageous as they eliminate waste leftovers from the kitchen and produce manure for farmers [56]. Humphries methane recovery and electricity generation project utilized anaerobic digestion swine wastewater treatment to generate methane gas the community uses for cooking and heating [57].

4.2. Potential renewable energy technologies

The following section assesses the performance of potential renewable energy technologies. Those potential technologies include geothermal, wind turbines, and hydropower.

4.2.1. Hydropower

Tubatse hydroelectric plant is the pumped storage hydropower built by Eskom and it is anticipated to generate 1500MW of power. The plant hasn't been commissioned yet [58]. This shows that with the flowing rivers, the province has hydropower potential.

4.2.2. Geothermal

In three regions in Limpopo (Waterberg, Drakensberg, and Soutpansberg) there are about 23 thermal springs [59]. According to the Council for Geosciences, one of the most promising areas for drilling for geothermal energy is in the thermal spring of Tshipise. The spring has a temperature of 58^0C and a flow rate of 10 L/s [37]. There is a potential for a 75 MW geothermal plant at Makuleni, the area falls under the Limpopo belt [38].

4.2.3. Wind Turbine

Wind turbine energy is less potential renewable energy in the province as the province has a high altitude and that makes wind less dense to have the capacity to rotate wind turbine blades sufficiently [60]. [61] Layered out each province's available and potential renewable energy and wind potential in Limpopo is at low reference. A study conducted by [42] utilized a mixed-scale temporal-spatial data approach to point out that Limpopo province has low potential for utility wind turbines as the province has an annual average wind speed which is less than 4m/s. [43] supported that Limpopo province has a low potential for wind turbines as it has an average annual wind speed of 3.05m/s, which is not enough for even small-scale wind turbines.

5. Conclusion

This paper has reviewed publications on available and potential renewable energy technologies for Limpopo province. Two questions were responded to. The 1st question addressed technologies behind available and potential renewable energy resources. The evaluation showed that Solar PV and biomass are the most utilized renewable energy in the province. The demand behind solar PV is due to its affordability, costs that account for manufacturing and installations only, and favorable geographical location. The reason behind biomass usage is the availability of biomass material in various locations and the impact minimization of energy costs for households. The 2nd question addressed the successful integration of available renewable energy. The evaluation showed that most solar PV projects implemented, operate at expected efficiency, but some small-scale solar systems failed to deliver due to negligence and poor maintenance by customers.

This paper finally acknowledges the availability of potential renewable energy resources: wind turbine, hydropower, and geothermal energy though they are not yet fully implemented due to financial constraints.

Future work in this study field will look at the economic analysis of those renewable energy resources in the Limpopo province. More attention will be on their economic feasibility based on Net Present Costs and Costs of Energy.

Acknowledgment

The authors would like to express special thanks to the Department of Higher Education and Training for financial support through the Nurturing Emerging Scholar Programme (NESP).

References

[1] Emília Inˆes Come Zebra, "A review of hybrid renewable energy systems in mini-grids for off-grid electrification in developing countries, 2021.

[2] Solomon Eghosa Uhunamure, "Evaluating Biogas Technology in South Africa: Awareness and Perceptions towards Adoption at Household Level in Limpopo Province," in Renewable Energy - Resources, Challenges and Applications, 2020.

[3] C. Budischak, "Cost-minimized combinations of wind power, solar power and electrochemical storage, powering the grid up to 99.9% of the time," Journal of Power Sources, 225, pp. 60-74, 2013.

[4] S. Arend, "Design of a solar home system for an unelectrified household in a rural community in the province of Limpopo, South Africa," 2020.

[5] KE Masekoameng, "Household energy needs and utilization patterns in the Giyani rural communities of Limpopo Province, South Africa," Journal of Energy in Southern Africa • Vol 16 No 3 • August 2005, 2005.

[6] Clement Matasane, "Solar Radiation Estimations Using the Territorial Climatological Measurements in Vhembe District, Limpopo Province for Solar Energy Potential Estimation and Use," 2019 IEEE PES/IAS PowerAfrica, 2019.

[7] E. N. Maluta, "Assessment of photovoltaic power output using the estimated global solar radiation at Vuwani Science Resources Centre," Masevhe & Maluta, Cogent Engineering (2022), 9: 2105031, 2022.

[8] Q. Liu, "Microgrids As A Service for Rural Electrification in Sub-Saharan Africa," Computers, Materials & Continua, 63(3), 2019.

[9] N. Jovanović, " Feasibility of Solar-Powered Groundwater Pumping Systems in Rural Areas of Greater Giyani Municipality (Limpopo, South Africa)," Applied Sciences, 13(6), p. 3859, 2023.

[10] S. Solms, "A Socio-Technical System for Rural Community Engagement: the Gwakwani project," 2022.

[11] N. Rene and M. Johan, "Impact assessment to measure the success of implementation of rural community engagement projects. A case study," IEEE African, 2017.

[12] M. John, "Polokwane Green Goal Energy Strategy Update and Implementation Plan 2016," 2016.

[13] T. Fraser, "Does social capital boost or block renewable energy siting? South African solar politics in comparison, 2021.

[14] P. F. Husvu, "Photovoltaic system with multilevel converter coupled to a compressed air energy storage system for grid integration," 2014.

[15] G. power, "The Tom Burke solar plant, South Africa," https://www.enelgreenpower.com/our-projects/operating/tom-burke-solar-plant, 2017.

[16] M. R. Shuma, Investigating calorific values and emissions of loose biomass feedstock in South Africa. University of Johannesburg, South Africa, 2018.

[17] K. Semenya, "Factors that influence firewood use among electrified Bapedi households of Senwabarwana Villages, South Africa, 2019.

[18] G. Mutezo, "A review of Africa's transition from fossil fuels to renewable energy using circular economy principles., 2021.

[19] Nethengwe and D. Tinarwo, "Correlating the factors influencing household decisions on adoption and utilization of biogas technology in South Africa. 2019.

[20] E. E. Netshiozwi, "The Role Of Renewable Energy To Address The Climate Change Phenomena: The South African Context, 2018.

[21] A. Roopnarain, "Current status, hurdles and prospects of biogas digestion technology in Africa, 2017.

[22] T. E. Rasimphi, "Assessment of the Biogas Potential in the Vhembe District of Limpopo: A Case Study of Waste-to-Energy Conversion Technology," Springer International Publishing AG 2018, 2018.

[23] Te Rasimphi, "Biogas Technology Implementation In Rural Areas: A Case Study Of Vhembe District In Limpopo Province, South Africa," 2012.

[24] Nthaduleni Samuel Nethengwe, "Potentials of Biogas as a Source of Renewable Energy: A Case Study of South Africa, 2018.

[25] M. Mondal, "Drivers, barriers, and strategies for implementation of renewable energy technologies in rural areas in Bangladesh—An innovation system analysis," Energy Policy, pp. 4626-4634, 2010.

[26] R. M. Situmeang, "Technological, economic, social and environmental barriers to adoption of small-scale biogas plants: a case of Indonesia., 2022.

[27] J. Mwirigi, "Socio-economic hurdles to widespread adoption of small-scale biogas digesters in Sub-Saharan Africa: A review, 2014.

[28] M. Gao, "Biogas potential, utilization and

countermeasures in agricultural provinces: A case study of biogas development in Henan Province, China," Renewable and Sustainable Energy Reviews, 99, pp. 191-200, 2019.

[29] M. Liebman, "Use of legume green manures as nitrogen sources for corn production, 2012.

[30] S. Vuuren, "Conduit Hydropower Development Guide," 2014.

[31] W. Karanitsch, "South Africa's hydropower options," 2011.

[32] A. Bekker, "The Development Of The South African Hydropower Atlas," Sancold Conference 2021: "Resilient Dams In A Challenging Environment", 2021.

[33] W. J. Klunne, "Small hydropower in Southern Africa – an overview of five countries in the region," 2014.

[34] E. Kalitsi, "Problems and Prospects for Hydropower Development in Africa," 2013.

[35] O. Ikumapayi, "A brief study into renewable energy technologies," 2023.

[36] D. Johnson, "Exploration of South Africa's Geothermal Resources," 2013.

[37] E. Tshibalo, "Evaluation of the Geothermal Energy Potential for South Africa," 2015.

[38] T. Dhansay, "Evaluation for harnessing lo-enthalpy geothermal energy in South Africa based on a model pilot plant in the Limpopo mobile belt," AEON, 2012.

[39] E. Nshimyumuremyi, "Geothermal reservoir heat transfer, temperature modeling and electrical power potential estimation, 2020.

[40] M. elgendi, "A review of wind turbines in complex terrain," International Journal of Thermofluids, 2023.

[41] P. Mukumba, "An overview of renewable energy technologies in the EC province and rural households energy poverty coping strategies," Challenges, 2023.

[42] E. C. Meren, "The evaluation of wind energy potentials in SA," Energy and Power, 2022.

[43] T. Nemirini, "Improving the performance of horizontal axial wind turbines using bioinspired," 2021.

[44] C. Marumuthu, "A critical review of facts affecting wind turbine and solar cell system power production," 2014.

[45] J. Rebecca O. Adeeyo, "Determinants of Solid Fuel Use and Emission Risks among Households: Insights from Limpopo, South Africa, 2022.

[46] N. Marisa, Energy Catalyst, UK: Innovate UK KTn, 2022.

[47] A. N. Tiago, "Evaluation of potential sites for the construction of hydropower plants in the Revuboe River," 2016.

[48] Temitope Adefarati, "Application of renewable energy resources in a microgrid power system," The Journal of Engineering, 2018.

[49] Davhana M. Khonani, "Optimal Sizing of Stand-Alone Photovoltaic Systems for Rural Electrification," 2nd Energy and Human Habitat Conference 2021, 2021.

[50] energy, "Witkop solar park," https://sturdee-energy.com/witkop-and-soutpan-solar-parks-30mw-28mw/, 2014.

[51] H. K. Olanrewaju, "A review of renewable energy technologies for sustainable development: Case Study-South Africa, 2022.

[52] Mansour Al Qubeissi, Renewable Energy - Resources, Challenges and Applications, London: Intechopen, 2020.

[53] R. Pasman, "Constructing of biogas digesters in South Africa: planning and risks in building biogas digesters," 2014.

[54] UNIDO, "Promoting organic waste-to-energy and other low-carbon technologies in small and medium and micro-scale enterprises.

[55] P. Mukumba, " Biogas technology in South Africa, problems, challenges and solutions 2016.

[56] Dod, SanedI insights book 2023, 2023.

[57] M. Waqas, "Composting Processes for Agricultural Waste Management: A Comprehensive, 2023.

[58] G. e. monitor, "Tubatse hydroelectric plant," 2022.

[59] E. Ekose, "Hydrogeochemical setting of geothermal spring in Limpopo Africa," 2015.

[60] E. Merem, "The evaluation of wind energy potentials in South Africa," Energy and power, pp. 9-25, 2022.

[61] T. J. Petterson, "State of renewable energy in South Africa," 2015.

[62] Shilpi Jain, "The rise of Renewable Energy implementation in South Africa," Energy Procedia, 2017.

TOWARDS IMPROVED SOLAR PV MODULE CHARACTERISATION: CORRELATING ELECTROLUMINESCENCE IMAGE DEFECTS WITH I-V CURVE CHARACTERISTICS USING A SEMANTIC SEGMENTATION-BASED MULTI-DEFECT DETECTION ALGORITHM

Frank Zandamela[1], Lawrence Pratt[1], May Siyasanga[1], Wisani Mkasi[1], and Thabang Mabeo[1]

[1] CSIR, Smart Places, Energy Research Centre, Pretoria 0001, South Africa; E-Mail: fzandamela@csir.co.za

[1] E-mail: lpratt@csir.co.za, smay@csir.co.za , hmkasi@csir.co.za, rmabeo@csir.co.za

Abstract: There has been significant research on the relationship between current-voltage (I-V) curve characteristics and electroluminescence (EL) module defects. Current methods use EL image pixels to develop features, which are then correlated with module I-V curve characteristics. In most cases, image thresholding is used to gather pixel information. These approaches have two major limitations. First, they lack generalisability, as imaging conditions may vary from module to module, and thresholding algorithms are often developed for specific types of defects or imaging conditions. Second, the correlation between specific types of defects and I-V features cannot be studied because all defects are grouped into one high-level defect detected by a sharp change in pixel intensity. In this paper, we conduct a correlation study between EL defects and I-V curve characteristics of photovoltaic (PV) modules that were exposed to accelerated stress testing. We correlate power loss and two common EL defects. The defects are detected and quantified using a prediction model based on semantic segmentation in which each pixel is assigned to one of multiple classes. Results obtained indicate that the defect detection tool can be used to correlate power loss with dark cells and cell cracks. A significant amount of variability in output power delta can be explained by defects detected by the prediction model (r^2 = 72%).

Keywords: Cell cracks; Electroluminescence image defect detection; I-V curve characteristics*; deep learning; PV module; semantic segmentation.*

1. Introduction

The ongoing adoption and installation of solar PV with the intention of moving to sustainable energy generation has necessitated the need to understand module lifetime performance and gain insights into the mechanisms causing module degradation [1]. Current-voltage (I-V) curve tracing and electroluminescence (EL) imaging are two of the commonly used techniques for characterising a PV module. I-V curve tracing performs a complete electrical sweep from short circuit current to open circuit voltage of an illuminated PV module [2]. The I-V curve characteristics alone cannot be used to determine specific degradation mechanisms leading to power loss. However, EL imaging rich spatial information that can help to understand the performance and condition of a module [3]. Due to the vital role that both I-V curve tracing and EL imaging play in the characterisation of a PV module, there has been a huge research effort aimed at finding the correlation between I-V curve characteristics of a PV module and the module defects found on the corresponding EL image [1]–[6]. Such studies can aid the development of algorithms that can estimate the I-V characteristics of a module. The ability to estimate module I-V features from EL images can enable high-speed in-situ power estimation for fielded PV modules and a framework for understanding large-scale mechanistic degradation of PV modules at high resolution. In addition, such a framework can be used across different facets of the PV community to improve speed, quality, and usefulness of cell and module-level image-based characterisation.

A host of the existing approaches use the EL image pixel intensities to derive hand-crafted features that describe the defects found on the EL image of the module. Approaches that use hand-crafted features derived from image pixel information have two major limitations. First, the approaches have limited or lack of generalising ability because imaging conditions may change from module to module and the thresholding algorithms are often developed for specific type of defects or imaging conditions. Second, the correlation between specific type of defects and the I-V features cannot be studied because all defects are grouped into one high-level defect that is detected by sharp

change in pixel intensity. Studying the correlation between specific defects and I-V features can help us understand low-level details about the performance of a module.

In this paper, we conduct a correlation study between two specific EL defects and I-V curve characteristics of PV modules that were exposed to accelerated stress testing at the CSIR PV Module Quality and Reliability Lab (PVQRL). The I-V data was measured on the indoor sun simulator and the EL defects were detected using a deep learning semantic segmentation-based model that was trained to detect and quantify common defects in solar cells.

2. Related work

The correlation of I-V curve characteristics and EL defects has received a lot of attention in the literature. The first work that investigated the impact of EL defects on module performance was presented by Köntges *et al.* [7]. In the paper, the direct impact of micro-cracks on the module power and the consequences after artificial aging were analysed. According to the results of the experiment, artificially initiated micro-cracks in the silicon wafer did not impair the electrical contact between cell fragments and did not reduce solar power generation by more than 2.5 %. It was found that cracked cells are correlated with power degradation after the accelerated ageing test, and that power loss follows a linear pattern over time. Since then, there has been significant research effort directed at investing the correlation of EL defects with I-V curve characteristics.

Existing methods investigate correlation between I-V curve characteristics and EL defects that are quantified using the pixel intensities of EL images. The I-V curve characteristics are typically obtained using a sun simulator. Typical characteristic values measured and derived from the module I-V curve include maximum power (Pmp), fill factor (FF), current at maximum power (Imp), voltage at maximum power (Vmp), current at short circuit (Isc), voltage at open circuit (Voc), series resistance (Rs), and shunt resistance (Rsh) [2]. To quantify EL defects, some researchers convert the EL images to grayscale and use the raw pixel intensities to calculate the median, mean, and standard deviation [2], [8]. For example, Karimi *et al.* [8] demonstrated the quantification of generalized and performance mechanism-specific EL image features using pixel intensity-based and machine learning classification algorithms. The research employed two stress testing methods: 3000 hours of damp heat exposure with measurements at 500-hour intervals for 15 modules, and 600 cycles of thermal cycling with measurements taken every 200 cycles for another 15 modules. This yielded 11,700 EL images from the 30 modules tested. Each cell-level image was analysed, resulting in four hand-crafted features being extracted, including the busbar corrosion ratio (BBCR). The research reported strong correlations between the features extracted from EL images and I-V characteristics. The study also uses a convolutional neural network to classify cells by the severity of busbar corrosion. In addition, researchers developed models to predict PV module I-V features from EL image characteristics, especially ribbon corrosion.

Some researchers [4], [9] also use image thresholding and edge detection techniques to enhance and localise module cracks. The area of a crack is then used to quantify the crack defect. For example, Wu *et al.* [4] used MATLAB's "im2bw(I, level)" function to perform image thresholding using different "level" values to capture and quantify module dark areas (cracks and inactive areas) using pixel intensity percentages. In their results, total pixel weight percentage of EL image dark areas and fill factor demonstrated a linear correlation with an r^2 value of 86.5 %. Likewise, Whitaker *et al.* [9] conducted a correlation study between I-V curve characteristics and EL image defects. The EL defects were quantified using an image thresholding algorithm called black top-hat transform. The black top-hat filter enhances dark cracks in a bright background; thus, it isolates darker pixels from brighter neighbouring pixels.

In this paper, we use a deep learning semantic segmentation EL defect detection tool to detect and quantify defects on EL images taken before and after accelerated stress testing. A study is then conducted to investigate possible correlations between the quantified defects and I-V curve characteristics of the PV modules. To the best of our knowledge, there is no study that investigates the correlation between EL defects quantified by a deep learning semantic segmentation algorithm.

3. Methodology

3.1. Solar cell defect detection overview

Solar cell defect detection (SCDD) on EL images is performed using a deep learning semantic segmentation model called Deeplabv3 [10]. The model was adapted for the task of defect detection on EL images using the source code provided by the authors on their official GitHub repository. The model was adapted using the three-step development process shown in Fig. 1. The reader is encouraged to refer to our previous work [11], [12] for details on the implementation and training details as they are beyond the scope of the current work.

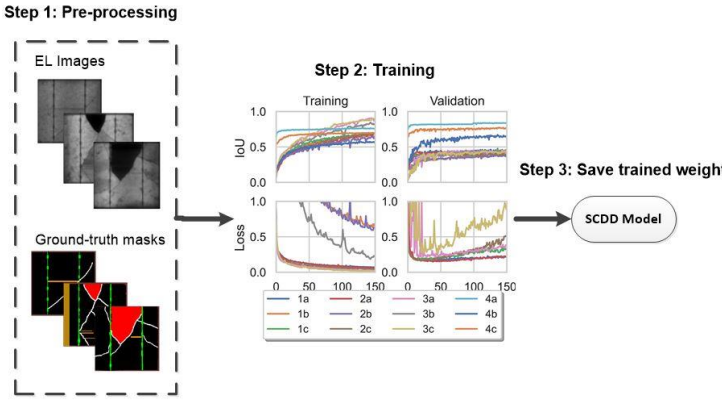

Fig. 1. Three-step development process of the SCDD model.

3.2. EL defects vs I-V curves correlation

The EL images and I-V curves were collected during a PV module reliability program conducted in 2019-2020 at the CSIR [13]. PV modules with four different 'bill-of-materials' (BOMs) were subjected to a series of accelerated stress tests according to the methods described in the IEC 61215:2016 international standard for PV module design qualification and type approval. The accelerated stress tests are designed to simulate real-world stresses in a controlled lab environment for certification testing. The PV Module Testing Protocol for Quality Assurance Programs described in the ANSI C450-18 is a public standard designed for long-term reliability testing of PV modules based on the IEC 61215 series in which the certification tests are conducted repeatedly. For example, a certification test per IEC 61215 requires 200 thermal cycles and the C450 requires 600 thermal cycles with a characterization sequence every 200 cycles. The characterisation sequence includes EL images and I-V measurements. The characterization sequence was conducted on each module as received at the lab and again after each step in the stress testing sequence, generating nearly 200 EL images and IV curves (Fig. 2).

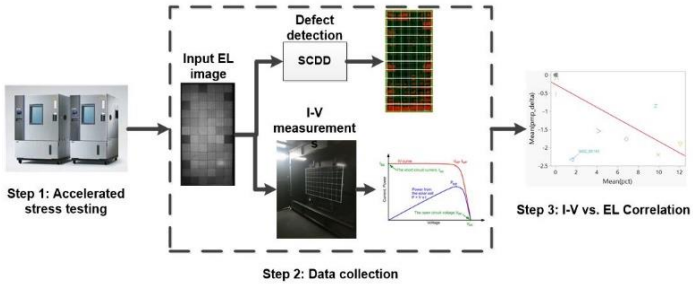

Fig. 2. Methodology used for the EL defects vs. I-V correlation study.

The I-V curves were generated on an indoor sun simulator at the CSIR PVQRL. The sun simulator is designed to measure the electrical characteristics over a range of temperatures and irradiance levels. A module is loaded into the integrated temperature chamber (Fig. 3) to control temperature while the irradiance level is controlled by the energy applied from a capacitor bank to the xenon arc lamp. The temperature chamber has a glass door to allow the light to hit the module and the irradiance level is monitored by a reference cell that is co-planar with the PV module. During a C450 reliability sequence, most I-V curves are conducted at standard test conditions (STC) defined as 1000 W/m^2, 25 °C cell temperature, and a light spectrum consistent with the natural sunlight at an airmass of 1.5.

Fig. 3. PV module mounted inside the sun simulator thermal chamber with glass door.

The correlation analysis was conducted using simple linear regression and summarized by the coefficient of determination, or the square of the Pearson's Correlation Coefficient (r^2). The dataset consisted of matched pairs for each module at each characterization step. The pairs consisted of an IV characteristic and an output from the SCDD model. Table 1 shows a subset of the data used in this study. Row 1 shows a record for the 'dark cell' defect on Module 1 at the initial inspection. The initial maximum power (Pmp) serves as the reference point for subsequent IV measurement, so the delta to initial = 0. The percentage defective shows the output of the SCDD model averaged over all the cells in the module. At this stage, the SCDD model did not detect any 'dark cell' defects in any of the cells. The second row shows the results on the same module after the potential inducted degradation (PID) stress test. The module power decreased by 6.8% and the SCDD model predicted 1.77% of the pixels were likely from dark cells, on average. The bottom half of the table shows a similar example for one module after the thermal cycling sequence. After 600 thermal cycles (TC600), the module power decreased by 1.1 % and the percentage defective increased to 0.52 %. This study focuses on maximum power measurements (Pmp) versus dark cells after PID and cracks after thermal cycling.

Table 1. Sample records of the dataset used for the correlation analysis.

Defect	Module ID	Sequence	Pmp Delta to Initial (%)	Percentage Defective (%)
Dark cell	1	Initial	0.0	0.00
Dark cell	1	Post PID	6.8	-1.77
Dark cell	2	Initial	0.0	0.00
Dark cell	2	Post PID	9.9	-2.19
Crack	1	Initial	0.0	0.06
Crack	1	Post TC200	-0.2	0.07
Crack	1	Post TC400	-0.5	0.48
Crack	1	Post TC600	-1.1	0.52

The r^2 value from the linear regression quantifies the proportion of the variation in the dependent variable (y-axis) explained by the independent variable (x-axis). For example, Fig. 4 shows the least squares line for maximum power (Pmp) versus current at maximum power (Imp) for a subset of the modules analysed in this research. The r^2= 0.99, meaning 99 % of the variability in the Pmp can be explained by the variability in Imp. While correlation does not prove causation, in the case of I-V characteristics this relationship does imply causation because a higher current output will lead to higher power output.

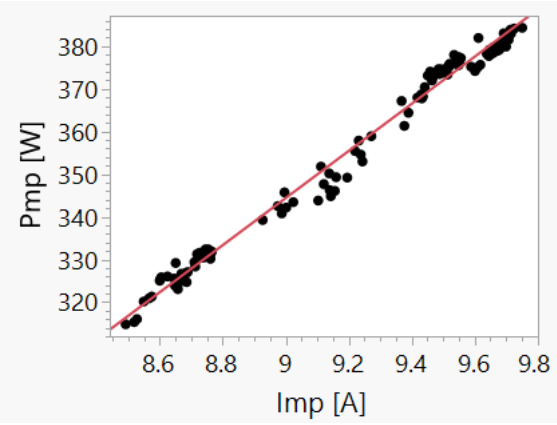

Fig. 4. Simple linear regression of maximum power (Pmp) delta to initial versus current at maximum power (Imp) delta to initial (r^2 = 0.99).

Table 2 shows the key statistics for the analysis of variance from the linear regression model. The sum of squares error (SSE) quantifies the residual errors, specifically the value represents the sum of the squared residuals. The sum of squares total (SST) quantifies the variance in the Pmp, specifically the value represents the sum of squared differences between the Pmp and the average of the Pmp. The sun of squares model (SSM) is the difference between the SST and the SSE. The ratio of the SSM over SST equals the r^2. In this case, 99 % of the variability in the Pmp is explained by the Imp.

Table 2 Analysis of variance summary statistics for the linear regression analysis.

Description	Value
Error Sum of Squares (SSE)	350 223
Model Sum of Squares (SSM)	31 562 191
Total Sum of Squares (SST)	31 912 413
R^2	0.99

4. Results and analysis

4.1. Module output power vs. dark cells post PID

Fig. 5 shows the correlation between module power loss (delta to initial Pmp) and the percentage of dark cell pixels predicted by the SCDD model. A subset of the dataset was described in Section 3.2 for clarity. An r^2 value of 55% was obtained from the analysis of variance table as described in Table 2. This indicates that 55% of the decrease in Pmp can be explained by the increase in the dark cell percentage. The point representing SASC_00145 module was an outlier with respect to the regression model. With the outlier excluded, an r^2 value of 78% percentage was obtained. This demonstrates the significant impact the outlier had on the correlation analysis. Further investigations were made to understand the behaviour of the SASEC_00145 observation.

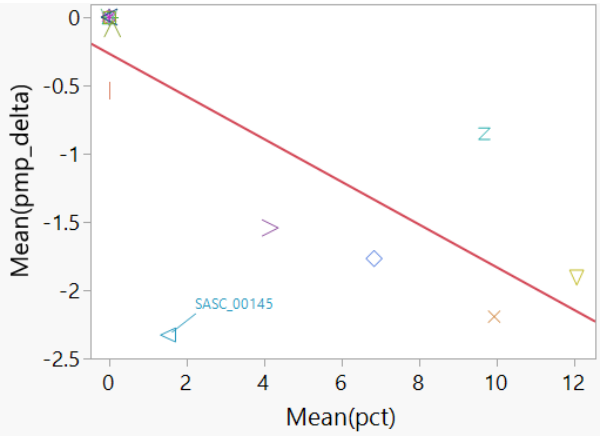

Fig. 5. Regression analysis between delta output power and percentage of dark cells predicted by SCDD.

We investigated the effect of pre-processing methods applied to the EL images before prediction by the SCDD tool to better understand the SASEC_00145 outlier. Specifically, we studied the influence of the brightness of an EL image on the ability of the SCDD tool to predict and quantify dark cells. Fig. 6 shows the correlation between the module power loss (delta to initial Pmp) and the percentage of dark cell pixels predicted by the SCDD model after reducing the brightness of the original EL image of the SASEC_00145 PV module by 50%. The percentage of dark cell pixels predicted by the SCDD model increased after reducing the brightness, and the resulting r^2 value increased by 17% (from 55% to 72%). This suggests that pre-processing methods that change the brightness of EL images impact the prediction of dark cells.

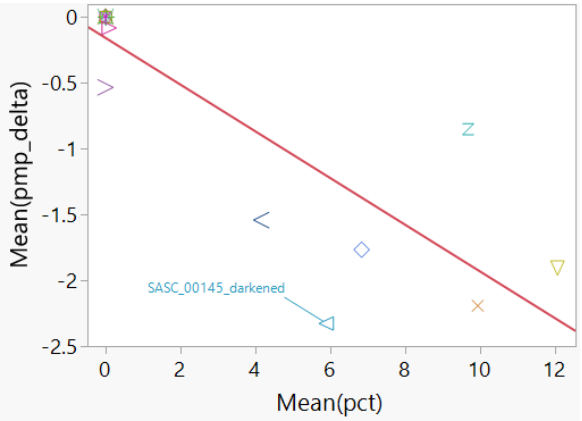

Fig. 6. Regression analysis between delta output power and percentage of dark cells predicted by SCDD after darkening the PV module.

The bias current applied during EL imaging can also impact pixel brightness. Fig. 7 shows the change in the percentage of dark cell pixels in the pre- and post-stress EL images recorded at 100 % of Isc current and in the post-stress EL image at 10 % of Isc current. The percentage of pixels predicted as dark cells increases significantly when the current bias is decreased from 100 % of Isc current to 10 % of Isc current, as per the international standard. The IEC TS 62804-1 describes the test methods for the detection of potential-induced degradation. In that technical specification, the test sequence includes EL imaging at both 100 % of Isc current and 10 % of Isc current because the PID degradation is more easily seen to the human observer at the low bias setting It follows that the SS model would also detect more dark cell pixels in images taken at low bias. Unfortunately, the pre-stress EL images at 10% of Isc were not available to assess the percentage of dark cell pixels at that bias current prior to the stress.

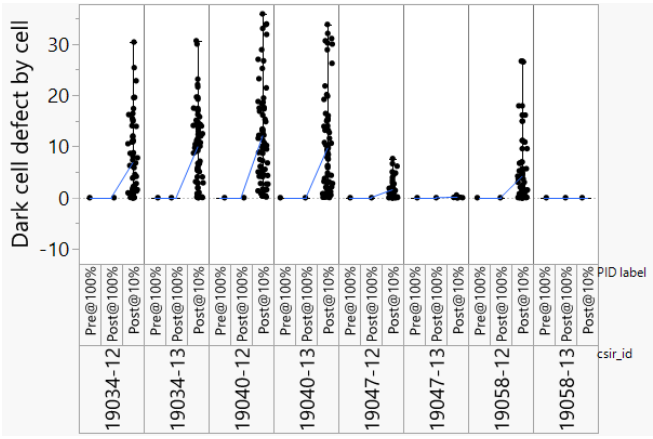

Fig. 7. Percentage of dark cells post PID at different levels of bias current.

4.2. Module output power vs. cracks after thermal cycling

Fig. 8 shows the correlation between module power loss (delta to initial Pmp) and the percentage of crack pixels predicted by the SCDD model for each module from one BOM that was subjected to thermal cycling. Based on the Pmp delta and cracked cell percentage values, an r^2 value of 55% was obtained. This indicates that 55% of the change in Pmp can be explained by the change in the percentage of crack pixels predicted by the SCDD model.

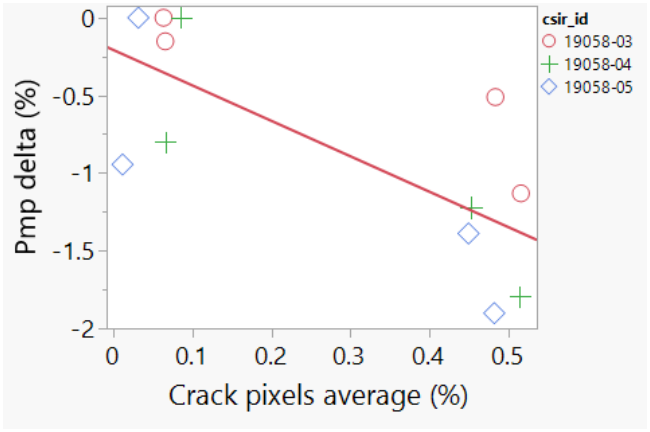

Fig. 8. Regression analysis between Pmp delta and crack pixels average post thermal cycling.

Fig. 9 shows the evolution of cell cracks on the three PV modules from one BOM during 600 hours of thermal cycling, using steps of 200 thermal cycles. From this figure, it can be observed that all three PV modules developed cracks after TC400. This was not expected since thermal cycling does not typically cause cracks, and none of the modules from the other three BOMs developed significant cracks. Interestingly, the cracks showed a similar pattern across all three modules with long, 45 ° diagonal cracks developing in the top left and bottom right corners.

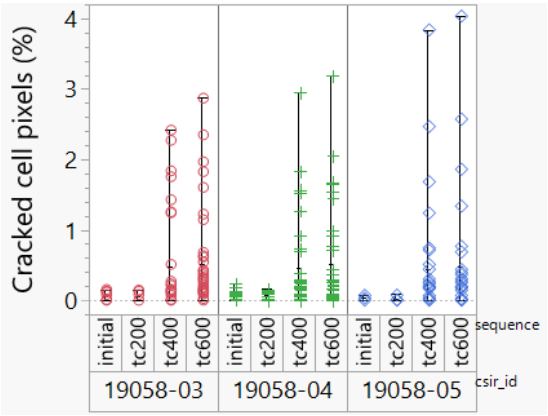

Fig. 9. Variation of the percentage of cracked cells at 0, 200, 400, and 600 thermal cycles.

The sensitivity of crack detection to brightness post thermal cycling was also investigated. It was found that crack detection is robust to any brightness changes applied to the original image during pre-processing.

5. Conclusion

This work investigated linear correlations between the output of a semantic segmentation model trained to detect defects in EL images and the corresponding IV characteristics of PV modules exposed to accelerated stress testing. The output power of PV modules that were subjected to damp heat and thermal cycling was correlated to the percentage of dark cells and the percentage of cracks, respectively. The results suggest that a significant amount of variability in output power loss can be explained by defects detected by the SCDD tool, although causation should not be implied. In addition, it was found that the prediction of dark cells using the SCDD tool is susceptible to brightness changes in the EL image made during post-processing and the electrical current bias applied during imaging. In contrast, crack detection is robust to brightness changes.

Future work will include further investigations on the sensitivity of predictions using the SCDD model to image preprocessing.

Acknowledgements

The authors wish to thank the CSIR and the Centre for High Performance Computing (CHPC) for measurement equipment, test samples, and computing resources. The authors also wish to thank David Torpey for technical support in the development of the SCDD model.

References

[1] R. Asadpour, D. B. Sulas-Kern, S. Johnston, J. Meydbray, and M. A. Alam, “Dark Lock-in Thermography Identifies Solder Bond Failure as the Root Cause of Series Resistance Increase in Fielded Solar Modules,” IEEE Journal of Photovoltaics, vol. 10, no. 5, pp. 1409–1416, Sep. 2020.

[2] J. S. Fada et al., "Correlation of I-V Curve Parameters with Module-Level Electroluminescent Image Data Over 3000 Hours Damp-Heat Exposure," 2017 IEEE 44th Photovoltaic Specialist Conference (PVSC), Washington, DC, USA, 2017, pp. 2697-2701.

[3] A. M. Karimi et al., "Generalized and Mechanistic PV Module Performance Prediction From Computer Vision and Machine Learning on Electroluminescence Images," in IEEE Journal of Photovoltaics, vol. 10, no. 3, pp. 878-887, May 2020.

[4] Wu, Jiawei, et al. "Durability evaluation of PV modules using image processing tools." New Concepts in Solar and Thermal Radiation Conversion and Reliability. Vol. 10759. SPIE, 2018. vol. 1075915, no. September 2018, p. 36, 2018.

[5] M. Hoffmann et al., “Deep-learning-based pipeline for module power prediction from electroluminescense measurements,” Progress in Photovoltaics, vol. 29, no. 8, pp. 920–935, May 2021.

[6] V. Kumar and P. Maheshwari, “Advanced analytics on IV curves and electroluminescence images of photovoltaic modules using machine learning algorithms,” Progress in Photovoltaics: Research and Applications, Sep. 2021.

[7] M. Köntges, I. Kunze, S. Kajari-Schröder, X. Breitenmoser, and B. Bjørneklett, “The risk of power loss in crystalline silicon based photovoltaic modules due to micro-cracks,” Solar Energy Materials and Solar Cells, vol. 95, no. 4, pp. 1131–1137, Apr. 2011.

[8] A. M. Karimi *et al.*, “Generalized and Mechanistic PV Module Performance Prediction from Computer Vision and Machine Learning on Electroluminescence Images,” *IEEE J. Photovoltaics*, vol. 10, no. 3, pp. 878–887, 2020.

[9] C. M. Whitaker, B. G. Pierce, A. M. Karimi, R. H. French, and J. L. Braid, “PV Cell Cracks and Impacts on Electrical Performance,” *Conf. Rec. IEEE Photovolt. Spec. Conf.*, vol. 2020-June, pp. 1417–1422, 2020.

[10] L. C. Chen, Y. Zhu, G. Papandreou, F. Schroff, and H. Adam, “Encoder-decoder with atrous separable convolution for semantic image segmentation,” *Lect. Notes Comput. Sci. (including Subser. Lect. Notes Artif. Intell. Lect. Notes Bioinformatics)*, vol. 11211 LNCS, pp. 833–851, 2018.

[11] L. Pratt, J. Mattheus, and R. Klein, “A benchmark dataset for defect detection and classification in electroluminescence images of PV modules using semantic segmentation,” *Systems and Soft Computing*, vol. 5. 2023.

[12] L. Pratt, D. Govender, and R. Klein, “Defect detection

and quantification in electroluminescence images of solar PV modules using U-net semantic segmentation," *Renewable Energy*, vol. 178. pp. 1211–1222, 2021.

[13] L. Pratt, M. B. Ayanna, S. I. May, W. Mkasi, L. Maweza, and K. Roro, "PV MODULE RELIABILITY SCORECARD - ROUND 1," pp. 1–7.

Photovoltaic Module Fault Classification Using Optical and Thermal Imagery

Edward James Westraadt[1], Chantelle Clohessy[2], Warren Brettenny[3], and E Ernest van Dyk[4]

[1] Nelson Mandela University, University Way, Summerstrand, Gqeberha; Phone: 083 771 1163;
E-mail: s215052064@mandela.ac.za

[2] Nelson Mandela University; E-Mail: chantelle.clohessy@mandela.ac.za

[3] Nelson Mandela University; E-mail: warrenb@mandela.ac.za

[4] Nelson Mandela University; E-mail: ernest.vandyk@mandela.ac.za

Abstract: Photovoltaic module faults can arise due to several factors including damage caused during the manufacturing, transportation or installation processes, as well as damage caused by outdoor operational conditions such as bad weather. Such faults cause degradation of the PV system, and can result in major power loss and even fire hazards. This study compares the results of both optical and thermal image data for module-based PV fault classification. This classification is done according to a framework of twelve, IEC-aligned fault categories. These categories are based on the size, shape, intensity and pattern of faults, as seen mainly in thermal images.

The results are obtained for both types of image data (optical, and thermal) using five pre-coded convolutional neural network architectures, namely: InceptionV3, ResNet50, Xception, MobileNet and VGG16. By comparing these two types of image data as input for classification analysis, results can be used to determine the best overall image data type for this task. It will also outline and emphasize the advantages to using each type of image data individually.

Keywords: Photovoltaic Fault Detection; Photovoltaic Systems; Deep Learning; Convolutional Neural Networks

1. Introduction

Due to the imminent and growing threat of global warming, a shift towards renewable energy in recent decades aims to reduce carbon dioxide emissions worldwide. Photovoltaic (PV), or solar power, systems are one of the main sources of renewable energy production [1]. PV energy production offers both environmental and commercial advantages, and the maintenance of such systems is of paramount importance to reap the greatest rewards possible. The maintenance on large-scale PV plants, with regards to fault detection and classification, can be extremely cost and labour intensive. Undetected PV faults that are left for an extended period of time can cause substantial power loss and safety breaches [2]. If left undetected, without proper maintenance, these faults can drastically reduce the power production output and, in turn, the plant's overall profits.

Past research [3, 4] has shown that using convolutional neural networks (CNNs) and thermal imagery to detect and classify PV faults is both efficient and accurate when compared to feature-based approaches using machine learning techniques such as support vector machines and random forests. As a result, five pre-coded CNN architectures were chosen for this study, mainly due to their good performance in past studies [3, 4], as well as their performances in past ImageNet Large Scale Visual Recognition Challenges (ILSVRC). The selected architectures are: InceptionV3 [5], ResNet50 [6], Xception [7], MobileNet [8], and VGG16 [9]. Pre-coded CNNs are usually pre-trained on general items such as people, animals and objects, using large datasets. Making use of these pre-trained models and their associated weights is known as transfer learning, and it may benefit researchers by decreasing training times, as well as lowering generalization errors [10]. The difference between training CNN models from scratch and using the above transfer learning approach is also investigated.

2. Related Work

2.1. Renewable Energy and Photovoltaic Systems

The rapid growth of the global population has resulted in an exponential demand for energy. Non-renewable sources of energy such as coal and other fossil fuels are still, however, the main contributors to the energy sector [11]. Greenhouse gases, such as carbon dioxide, methane, and nitrous oxide, are emitted in large quantities during the combustion process of fossil fuel, all of which contribute heavily to the ever-growing problem of climate change [11]. A transition to renewable energy resources

will reduce greenhouse gas emissions, and reduce the effects of climate change as a whole. One type of renewable energy resource is solar power, where energy is harvested from the sun and converted into electricity. This is a reliable and environmentally sustainable method of producing electricity which emits little to zero greenhouse gases [12]. Solar energy, produced by PV systems, falls under the category of mainstream renewable energy sources, due to its popularity in both the public and private sectors across the globe [11].

2.2. Photovoltaic Faults and Infrared Thermography

Mansouri et al. [13] categorizes PV module faults into five common groups, namely: mismatch faults, bypass diode faults, connectivity faults, ground faults, and partial shading faults. Depending on the type of fault present in an affected module, various heating patterns and intensities can be observed. This is where PV module fault detection and classification using thermal (or infrared) image data can be applied. By analysing the heating patterns, temperature intensities and shapes of faults found in thermal images of PV modules, researchers are able to use deep learning techniques such as CNNs or artificial neural networks to detect and classify faults according to a classification schema or framework. The framework used and investigated in this study is an adaption of that of Bommes et al. [14], which adheres to the International Electrotechnical Commission's guidelines [15]. This framework compromises of fourteen PV module fault classes, including a non-faulty class, and is based on the shapes, patterns, intensities and overall maintenance issues relating to each fault class.

2.3. Convolutional Neural Networks

Convolutional neural networks, or CNNs, are a type of deep learning algorithm that started gaining popularity in 2012 [16]. This was largely due to the effectiveness of CNNs in reducing the number of parameters without losing on the quality of models [17]. They have since become the most successful algorithm in the field of image processing, including image classification, recognition, semantic segmentation, and machine translation [18]. Although more complex CNN architectures require large amounts of computational power and resources, they have been shown to produce reliable results that are both useful and beneficial in real world problems [19]. The main advantage of CNNs when compared to other deep learning techniques is that they are able to detect significant features independently, without any human supervision [20]. Robust CNNs should be trained using large datasets of images and their associated classification labels [21], for example: thermal images of PV modules and their associated fault types (as labels).

2.4. Photovoltaic Fault Classification

Once fully trained, the CNNs can interpret unseen data and predict or classify the data according to the framework used during training. Past research into this topic [3] investigated a three-class PV fault problem using thermal images of modules, and produced classification accuracies of 92% using pre-coded CNNs. Another study [4] investigated a four-class PV fault problem using thermal images, and obtained a k-fold average accuracy of 89.5% for classification with CNNs. Herraiz et al. [21] used region-based CNNs to automatically detect relative hot regions of solar plants. This study produced an automatic detection accuracy of 99.02% for the binary fault/no-fault problem, and showed that thermal imagery is a good choice for PV fault detection analysis. Another study by Prajapati et al. [22] used thermal imagery for the detection of faults in PV modules, using the YOLO architecture for real-time fault detection and identification. The study achieved a maximum average accuracy of 83.86% for a five-class problem. Haidari et al. [23] made use of thermal images for a three-class PV fault classification problem, including a non-faulty class using the VGG16 model, and obtained an accuracy of 98.00%.

Other studies have used CNNs for PV fault classification using electroluminescence (EL) data [24, 25]. Akram et al. [24] presented a novel approach for the automatic detection of PV cell faults using a light CNN architecture and EL images. This approach required low computational power and time, and produced an average accuracy of 93.02% for fault detection. Deitsch et al. [25] presented a tuned-version of the VGG19 architecture used for the detection of faulty PV cells in high-resolution EL images. This CNN model achieved an average accuracy of 88.42%, which was higher than the 82.44% obtained by a support vector machine model investigated in the same study. Standard electroluminescence image data must, however, be captured at very controlled conditions, making it non-viable for large-scale PV systems with hundreds of thousands of PV modules. Due to the relative ease in which both thermal and optical image data of such PV systems can be captured, they were chosen as the main focus in this study.

Although thermal and EL imagery have been the main focus of PV classification research in the past, there have been a few studies which investigate the use of optical images too. Cavieres et al. [26] makes use of optical image data for the detection and classification of soiling and partial shading faults in PV modules. This study proposes a custom CNN which produces a maximum accuracy of 73.00%. Although this study is promising, it is noted by the authors that a greater range of image data is required for more robust testing. Another study by Espinosa et al. [27] makes use of CNNs and optical image data for both PV fault detection and classification. This approach produces maximum accuracies of 75.39% for fault detection and 70.00% for fault classification. The authors, once again, refer to the dataset as being small, and

more data being beneficial for future work and results. It is conjectured that including optical images may improve on classification results, due to the extra information obtained for some of the PV fault classes from this type of data, namely: soiling, shading, and vegetation.

3. Data and Methodology

3.1. Data and Classification Framework

The thermal image data for this study was collected at ten large-scale PV systems in South Africa. The locations of these PV plants cannot be disclosed due to a privacy agreement with the supplier. Both the thermal and optical images were collected in the same manner. An unmanned aerial vehicle (or UAV) equipped with both optical and thermal imaging cameras was flown over the PV plants, and images were captured at a high level. This means each image taken and stored by the UAV shows multiple PV modules. Once these high-level images were captured and stored, they were then cropped to show individual PV modules, resulting in a larger dataset of individual modules. The images were named according to an ID given to each module on the PV site where they are located. A total of 9 028 thermal images were collected, where 1 562 were non-faulty modules and 7 470 were faulty modules. Similarly, a total of 9 028 optical images were collected. The thermal images were then categorized and sorted into the twelve, IEC-aligned classes as given in the classification framework. Thereafter, the optical data was matched to its corresponding thermal data using the name IDs, and was sorted into its respective classification framework classes for analysis. This resulted in two datasets for analysis, one thermal and one optical, which matched each other in their structure and sorting. The class composition of these two datasets is given in Table 1.

Table 1. Class composition of the thermal and optical datasets (9 028 images each)

Fault Class	Number of Images	Percentage
Warm Cells (C)	193	2.12 %
Hot Spot (Chs)	244	2.68 %
Hot Cell Multi (Cm+)	542	5.95 %
Diode Overheat (D)	2 063	22.66 %
Junction Box (J)	357	3.92 %
Module Short Circuit (Mp)	170	1.88 %
Non-faulty (N)	1 562	17.16 %
Soiling and Shading (S)	1 067	11.74 %
Substring Open Circuit (Sh)	816	8.96 %
Hot Cell Single (Sm+)	733	8.05 %
Substring Short Circuit (Sp)	478	5.26 %
Vegetation (V)	803	8.82 %

As mentioned previously, this framework was adapted from the study of Bommes et al. [14], which proposes fourteen fault classes according to their shape, heat intensities and overall maintenance issues. It also includes a non-faulty class, which assists PV maintainers in knowing which modules are functioning correctly. This framework was further adjusted to a twelve-class framework, due to the low amounts of data for two of the fourteen classes, namely: Module Open Circuit (Mh), and Potential Induced Degradation (PID).

3.2. Classification Methods and Implementation

Five pre-coded CNNs were chosen as the main focus of this classification analysis. In order to employ these CNN architectures within Python 3.6.5, the *tensorflow* package was used. This package was first developed by machine learning engineers from the Google Brain team within Google's AI organization [28], as a means to implement deep learning techniques and artificial neural networks in Python. Tensorflow has become increasingly popular for machine and deep learning research over the last decade due the relative ease in which it can be implemented. The inclusion of being able to use transfer learning in CNNs makes this package extremely beneficial for this study.

The InceptionV3 CNN architecture was introduced to the *Keras* [29] library in 2015, where the 'V3' refers to it being the third version of the Inception architecture released by Google [5]. InceptionV3 was designed for higher computational efficiency, and having notably fewer parameters than the original model. The ResNet50 (or ResNet) architecture was introduced by Microsoft in 2015 [6]. This architecture makes use of 'shortcut' paths, allowing it to learn identity functions which ensure performance is at least as good as the normal path layer [30]. The Xception architecture was proposed by the creator and chief maintainer of the *Keras* library, François Chollet, in 2017 [7]. The Xception model is an extension and adjusted version of the Inception model, where the standard Inception modules are replaced by depth-wise separable convolutional layers [31]. The MobileNet architecture, was first introduced by Google engineers in 2017 [8]. This architecture was designed with two main goals: less parameters and less complexity, meaning fewer calculations during training [32]. Lastly, the VGG16 (or ConvNet) architecture, was first introduced by engineers from the University of Oxford in 2014 [9]. This architecture has only 16 layers, and was created to reduce learnable weight layers and

parameters [33]. VGG16 proposed the use of a very small receptive filters throughout the entire network with the stride of 1 pixel each time [34]. These five CNN architectures were analysed using *tensorflow*, as well as the *Keras* packages in Python. This analysis was performed on a workstation at Nelson Mandela University. The specifications of the workstation are given in Table 2.

Table 2: Computational / workstation specifications

Workstation Components	Specifications
Processor (CPU)	AMD Ryzen Threadripper 1950X
Operating System (OS)	64-bit Windows 10 Enterprise
RAM	128 GB
Hard Drive	2 TB SSD
Graphics Card (GPU)	NVIDIA GeForce RTX3090

The workstation available to this study should not have any performance-related issues in implementing the proposed methodology and analysis.

4. Results

All classification analysis was performed over 100 epochs for each CNN, as this is where the model accuracies seem to stabilize during training. The use of both transfer learning (i.e. using Imagenet, or pre-trained, weights) and initializing the model weights is also investigated. The classification was performed separately using the two datasets, namely: optical, and thermal. The *k*-fold average accuracies, where $k = 5$, as well as the training and validation testing times, are provided for each data type and weighting approach (i.e. pre-trained/initialized) used. The value of $k = 5$ was chosen as this value of *k* has been shown empirically to yield test error rate estimates that do not suffer from high bias nor high variance [35].

4.1. Optical Photovoltaic Fault Classification

The optical dataset consisting of 9 028 optical images was analysed according to the methods described and the classification results for the pre-trained CNN architectures are provided in Table 3.

From Table 3 it can be seen that the classification accuracies for the optical image data using the 12-class framework were poor, with no average accuracy exceeding 40%. Table 4 provides the optical classification results for the initialized CNN architectures, where no pre-trained weights are used.

Table 3: Optical classification results (pre-trained weights)

CNN	k-Fold Average Accuracy	Training Time	Validation Time
InceptionV3	36.67 %	14h 27m 20s	22m 05s
ResNet50	39.99 %	14h 24m 25s	16m 53s
Xception	39.25 %	14h 28s 35s	18m 00s
MobileNet	35.39 %	14h 01m 48s	12m 33s
VGG16	23.26 %	14h 12m 54s	24m 06s

Table 4: Optical classification results (initialized weights)

CNN	k-Fold Average Accuracy	Training Time	Validation Time
InceptionV3	28.35 %	14h 23m 40s	20m 10s
ResNet50	26.53 %	14h 29m 59s	24m 28s
Xception	30.31 %	14h 24m 12s	14m 58s
MobileNet	22.99 %	14h 18m 16s	15m 01s
VGG16	23.77 %	15h 06m 33s	15m 56s

The classification accuracies for the optical image data using the initialized weights were lower than those obtained using the pre-trained model weights. Using pre-trained weights, or transfer learning, provides models with a starting point for a problem, and allows for faster training. Transfer learning also offers a higher learning rate, and, in turn, higher accuracies after training since the model converges at a higher performance level [36]. The best-performing CNN architecture from the optical image analysis was the pre-trained ResNet50 model, which made use of transfer learning. By using its bottleneck design and 'shortcut' paths [30], the ResNet50 model is able to be trained faster than other CNNs [37]. This could be one of the reasons it is the best-performing model in the optical analysis. This model is shown in Table 3, and obtains an average k-fold classification accuracy of 39.99%. The pre-trained models in Table 3 seem to outperform the initialized models in Table 4 slightly, having higher average accuracies four out of five times. The VGG16 model seems to perform fractionally better when trained using initialized weights as opposed to using pre-trained weights, but its overall accuracies are sub-par. It should be noted that using initialized weights may take longer for the model to converge, and thus extra or additional epochs may be required. For the purpose of this study and results, however, the number of epochs was kept constant at 100 epochs.

4.2. Thermal Photovoltaic Fault Classification

The thermal dataset consisting of 9 028 thermal images was analysed next. Table 5 provides the thermal classification results for the pre-trained CNN architectures.

Table 5: Thermal classification results (pre-trained weights)

CNN	k-Fold Average Accuracy	Training Time	Validation Time
InceptionV3	80.09 %	12h 21m 14s	19m 14s
ResNet50	82.56 %	12h 40m 37s	25m 33s
Xception	82.78 %	12h 44m 33s	19m 29s
MobileNet	77.83 %	12h 22m 17s	12m 18s
VGG16	44.60 %	12h 19m 05s	28m 08s

Table 6 provides the thermal classification results for the initialized CNN architectures, where no pre-trained weights are used.

Table 6: Thermal classification results (initialized weights)

CNN	k-Fold Average Accuracy	Training Time	Validation Time
InceptionV3	71.47 %	12h 38m 46s	24m 44s
ResNet50	75.10 %	12h 44m 07s	41m 20s
Xception	74.77 %	12h 48m 56s	26m 50s
MobileNet	60.83 %	12h 27m 58s	12m 11s
VGG16	61.63 %	12h 33m 31s	15m 37s

The best-performing CNN architecture from the thermal image analysis was the pre-trained Xception model in Table 5, which makes use of transfer learning. As an extension of the Inception model, the Xception makes use of depth-wise separable convolutional layers, which have been shown to improve classification performance [7]. This model obtained an average *k*-fold classification accuracy of 82.78%. It can also be noted that the pre-trained models in Table 5 outperform the initialized models in Table 6 four out of five times, which indicates that the use of transfer learning in this type of classification using thermal image data is beneficial to the model accuracies. The VGG16 model seems to perform better when trained from scratch as opposed to using pre-trained weights. When compared to the optical image data results, it is clear that, as expected, thermal image data should be preferred for this type of PV fault classification, with accuracy results roughly doubling in value.

4.3. Image Data Type Comparison

When comparing the results obtained in Table 3 to Table 5, the pre-trained Xception architecture using thermal image data in Table 5 seems to be the best choice for PV fault classification, obtaining a *k*-fold average accuracy of 82.78%. This is followed closely by the pre-trained ResNet50 architecture using thermal image data in Table 6 as second-best, obtaining a *k*-fold average accuracy of 82.56%. It can also be noted that the pre-trained CNN models seem to perform better than the initialized models across both data types. Using the thermal images, the five pre-trained CNNs have an average classification accuracy of 73.57%, while the initialized models have an average accuracy of 68.76. This shows that using the pre-trained weights when training the CNN models is beneficial for future prediction and accuracy purposes in PV fault classification analysis, providing an average accuracy increase of 4.81%. When comparing training times, it should be noted that although the optical training seems to take longer than the thermal training, this is somewhat expected as the optical images are captured at a higher resolution than the thermal images and, as such, the associated image data is larger in size than the thermal image data. Currently, the best FLIR thermal cameras record thermal images at a resolution of 1024 x 768 [36], which is much smaller than most optical images, which have a resolution of up to 8688 × 5792 [39].

5. Conclusion

The primary aim of this research was to assess the accuracy of CNNs in classifying PV module faults using two different types of image data, namely: optical, and thermal. The classification analysis was performed using five pre-coded CNNs, comparing the difference between using pre-trained and initialized weights. From the results obtained, it was clear that using the thermal image data outperformed the optical image data in all analysis scenarios. The thermal image data type can therefore be noted as the best choice for PV module fault classification.

When comparing the difference between using pre-trained weights and initialized weights, it is clear that for the better-performing CNN architectures, the pre-trained weights aid in increasing the models' classification accuracies. For the best-performing, ResNet50 model in Table 3, we can also note a classification accuracy increase of 13.46% when using pre-trained weights instead of initialized weights (in Table 4) for the optical data type. It can be noted that even though one expects the use of pre-trained weights to decrease the training and validation times, there is no indication that this is true when compared to the initialized weights training and validation times. The use of initialized weights would require more epochs for convergence, thus providing lower average accuracies overall

when compared to the pre-trained models. To train the initialized models up to the same level of accuracy obtained using pre-trained weights, one would need to increase the number of epochs quite drastically, increasing the training and validation times immensely. With regards to these computational times, it is therefore clear that the use of transfer learning, or pre-trained models, does in fact improve the convergence time.

Future work will investigate a third type of image data, termed "opti-thermal", which will be a combination of both optical and thermal image data. This will be done by layering the optical images over the thermal images, in an effort to improve information fed into the CNNs during training, since certain faults and issues such as vegetation, soiling and shading can be easily identifiable on the inspection of optical images. This, in conjunction with the thermal information, is envisioned to improve classification accuracies overall.

Acknowledgements

The financial assistance of the Centre for Renewable and Sustainable Energy Studies (CRSES) and the Department of Science and Innovation (DSI) towards this research is hereby acknowledged. Opinions expressed and conclusions arrived at are those of the authors and are not necessarily to be attributed to the CRSES and DSI. The workstation used was funded through NRF Grant SFH180517331201. The authors would also like to thank Nelson Mandela University for their financial support through the Postgraduate Research Scholarship (PGRS) programme.

References

[1] Y.-Y. Hong and R. A. Pula, "Methods of photovoltaic fault detection and classification: A Review," Energy Reports, vol. 8, pp. 5898–5929, 2022. doi:10.1016/j.egyr.2022.04.043

[2] E. Garoudja et al., "Statistical fault detection in photovoltaic systems," Solar Energy, vol. 150, pp. 485–499, 2017. doi:10.1016/j.solener.2017.04.043

[3] E. J. Westraadt, W. J. Brettenny, and C. M. Clohessy, "Deep learning for photovoltaic defect detection using variational autoencoders," South African Journal of Science, vol. 119, no. 1/2, 2023. doi:10.17159/sajs.2023/13117

[4] C. Dunderdale, W. Brettenny, C. Clohessy, and E. E. van Dyk, "Photovoltaic defect classification through Thermal Infrared Imaging using a machine learning approach," Progress in Photovoltaics: Research and Applications, vol. 28, no. 3, pp. 177–188, 2019. doi:10.1002/pip.3191

[5] C. Szegedy, V. Vanhoucke, S. Ioffe, J. Shlens, and Z. Wojna, "Rethinking the inception architecture for computer vision," 2016 IEEE Conference on Computer Vision and Pattern Recognition (CVPR), 2016. doi:10.1109/cvpr.2016.308

[6] K. He, X. Zhang, S. Ren, and J. Sun, "Deep residual learning for image recognition," 2016 IEEE Conference on Computer Vision and Pattern Recognition (CVPR), 2016. doi:10.1109/cvpr.2016.90

[7] F. Chollet, "Xception: Deep learning with depthwise separable convolutions," 2017 IEEE Conference on Computer Vision and Pattern Recognition (CVPR), 2017. doi:10.1109/cvpr.2017.195

[8] A. G. Howard et al., "Mobilenets: Efficient convolutional neural networks for mobile vision applications," arXiv preprint, vol. 1704:04861, 2017.

[9] K. Simonyan and A. Zisserman, "Very deep convolutional networks for large-scale image recognition," arXiv preprint, vol. 1409:1556, 2014.

[10] J. Brownlee, "Transfer learning in Keras with computer vision models," MachineLearningMastery.com, https://machinelearningmastery.com/how-to-use-transfer-learning-when-developing-convolutional-neural-network-models/ (accessed Jun. 18, 2023).

[11] A. G. Olabi and M. A. Abdelkareem, "Renewable energy and climate change," Renewable and Sustainable Energy Reviews, vol. 158, p. 112111, 2022. doi:10.1016/j.rser.2022.112111

[12] A. Hussain, S. M. Arif, and M. Aslam, "Emerging renewable and sustainable energy technologies: State of the art," Renewable and Sustainable Energy Reviews, vol. 71, pp. 12–28, 2017. doi:10.1016/j.rser.2016.12.033

[13] M. Mansouri, M. Trabelsi, H. Nounou, and M. Nounou, "Deep learning-based fault diagnosis of photovoltaic systems: A Comprehensive Review and enhancement prospects," IEEE Access, vol. 9, pp. 126286–126306, 2021. doi:10.1109/access.2021.3110947

[14] L. Bommes et al., "Computer vision tool for detection, mapping, and fault classification of photovoltaics modules in aerial IR videos," Progress in Photovoltaics: Research and Applications, vol. 29, no. 12, pp. 1236–1251, 2021. doi:10.1002/pip.3448

[15] International Electrotechnical Commission, "IEC everywhere for a safer and more efficient world," IEC, https://www.iec.ch/homepage (accessed Jun. 18, 2023).

[16] N. D. Girsang, "Literature study of Convolutional Neural Network Algorithm for batik classification," Brilliance: Research of Artificial Intelligence, vol. 1, no. 1, pp. 1–7, 2021. doi:10.47709/brilliance.v1i1.1069

[17] P. Mishra, "Why are convolutional neural networks good for image classification?," Medium, https://medium.datadriveninvestor.com/why-are-convolutional-neural-networks-good-for-image-classification-146ec6e865e8 (accessed Jun. 21, 2023).

[18] R. Xin, J. Zhang, and Y. Shao, "Complex network classification with Convolutional Neural Network," Tsinghua Science and Technology, vol. 25, no. 4, pp. 447–457, 2020. doi:10.26599/tst.2019.9010055

[19] M. Rastegari, V. Ordonez, J. Redmon, and A. Farhadi, "XNOR-net: ImageNet classification using binary convolutional Neural Networks," Computer Vision – ECCV 2016, pp. 525–542, 2016. doi:10.1007/978-3-319-46493-0_32

[20] L. Alzubaidi et al., "Review of Deep Learning: Concepts, CNN Architectures, challenges, applications, Future Directions," Journal of Big Data, vol. 8, no. 1, 2021. doi:10.1186/s40537-021-00444-8

[21] Á. Huerta Herraiz, A. Pliego Marugán, and F. P. García Márquez, "Photovoltaic plant condition monitoring using thermal images analysis by convolutional neural network-based structure," Renewable Energy, vol. 153, pp. 334–348, 2020. doi:10.1016/j.renene.2020.01.148

[22] N. Prajapati, R. Aiyar, A. Raj, and M. Paraye, "Detection and identification of faults in a PV module using CNN based algorithm," 2022 3rd International Conference for Emerging Technology (INCET), 2022. doi:10.1109/incet54531.2022.9825452

[23] P. Haidari, A. Hajiahmad, A. Jafari, and A. Nasiri, "Deep learning-based model for fault classification in solar modules using infrared images," Sustainable Energy Technologies and Assessments, vol. 52, p. 102110, 2022. doi:10.1016/j.seta.2022.102110

[24] M. W. Akram et al., "CNN based automatic detection of photovoltaic cell defects in electroluminescence images," Energy, vol. 189, p. 116319, 2019. doi:10.1016/j.energy.2019.116319

[25] S. Deitsch et al., “Automatic classification of Defective Photovoltaic module cells in electroluminescence images,” Solar Energy, vol. 185, pp. 455–468, 2019. doi:10.1016/j.solener.2019.02.067

[26] R. Cavieres, R. Barraza, D. Estay, J. Bilbao, and P. Valdivia-Lefort, “Automatic soiling and partial shading assessment on PV modules through RGB images analysis,” Applied Energy, vol. 306, p. 117964, 2022. doi:10.1016/j.apenergy.2021.117964

[27] A. Rico Espinosa, M. Bressan, and L. F. Giraldo, “Failure signature classification in solar photovoltaic plants using RGB images and convolutional neural networks,” Renewable Energy, vol. 162, pp. 249–256, 2020. doi:10.1016/j.renene.2020.07.154

[28] M. Abadi et al., “Tensorflow: Large-scale machine learning on heterogeneous distributed systems,” arXiv preprint, vol. 1603.04467, 2016.

[29] F. Chollet et al., “Keras: Deep Learning for Humans,” GitHub: Keras, https://github.com/fchollet/keras (accessed Jun. 18, 2023).

[30] P. Dwivedi, “Understanding and coding a ResNet in Keras,” Medium, https://towardsdatascience.com/understanding-and-coding-a-resnet-in-keras-446d7ff84d33 (accessed Jun. 18, 2023).

[31] A. Rosebrock, “ImageNet: Vggnet, ResNet, inception, and xception with keras,” PyImageSearch, https://www.pyimagesearch.com/2017/03/20/imagenet-vggnet-resnet-inception-xception-keras/ (accessed Jun. 18, 2023).

[32] J. Rodriguez, “The evolution of Google’s MobileNet architectures to improve computer vision models,” Medium, https://medium.com/dataseries/the-evolution-of-googles-mobilenet-architectures-to-improve-computer-vision-models-ffb483ffcc0a (accessed Jun. 18, 2023).

[33] Great Learning, “Everything you need to know about VGG16,” Medium, https://medium.com/@mygreatlearning/everything-you-need-to-know-about-vgg16-7315defb5918 (accessed Jun. 18, 2023).

[34] A. Thite, “Introduction to VGG16: What is VGG16?,” Great Learning Blog, https://www.mygreatlearning.com/blog/introduction-to-vgg16/ (accessed Jun. 18, 2023).

[35] J. Brownlee, “A gentle introduction to k-fold cross-validation,” MachineLearningMastery.com, https://machinelearningmastery.com/k-fold-cross-validation (accessed Jun. 21, 2023).

[36] “Benefits of Transfer Learning: Data Science and Machine Learning,” Kaggle, https://www.kaggle.com/general/291011 (accessed Jun. 21, 2023).

[37] “ResNet-50: The basics and a quick tutorial,” Datagen, https://datagen.tech/guides/computer-vision/resnet-50/#:~:text=The%2050%2Dlayer%20ResNet%20uses,faster%20training%20of%20each%20layer. (accessed Jun. 21, 2023).

[38] “Technical note - Teledyne FLIR,” FLIR, http://support.flir.com/appstories/AppStories/Electrical&Mechanical/Testing_solar_panels_EN.pdf (accessed Jun. 21, 2023).

[39] “Canon EOS 5Ds SLR Camera Body,” Icecat, https://icecat.biz/p/canon/0581c002/eos-digital+cameras-4549292037791-5ds-26432223.html (accessed Jun. 21, 2023).

SENSITIVITY ANALYSIS OF AEROSOL OPTICAL DEPTH AND OZONE IN SPECTRAL MISMATCH ESTIMATIONS FOR THREE SOUTH AFRICAN LOCATIONS

Francisca M. Daniel-Durandt[1] and Dr Arnold J. Rix[2]

Electrical & Electronic Engineering, Stellenbosch University, Banghoek Rd, Stellenbosch, 7600, South Africa

E-mail: [1]18296033@sun.ac.za, [2]rix@sun.ac.za

Abstract: This paper assesses the sensitivity of the spectral mismatch for three South African locations for two atmospheric conditions: aerosol optical depth at 500nm (AOD_{500}) and ozone (O_3). Spectral data remains scarce, and this paper aims to determine how to substitute the data when no spectral data is available, specifically in South Africa. The initial investigation identified that AOD_{500} has a more significant effect on spectral irradiance than O_3, which will also be more pronounced in spectral mismatch calculations. Three corresponding SAURAN and AERONet databases were combined to assess the spectral mismatch sensitivity. The investigation showed that an estimated ozone value with the measured O_3 had a negligible error in spectral mismatch calculations, which prompted the second part of this investigation: to identify a way of predicting AOD_{500} using a lookup table using air mass, the clearness index or a combination of the two for different intervals. The investigation showed that a lookup table did not improve the error of estimating spectral mismatch using a constant AOD_{500} of 0.123. Spectral irradiance and mismatch can be determined with reasonable accuracy using an estimated O_3 and constant AOD_{500} when no spectral irradiance measurements are available.

Keywords: Spectral Mismatch; Aerosol Optical Depth; Ozone; Sensitivity Analysis

1. Introduction

The solar spectral irradiance at ground level is influenced by many atmospheric variables [1]. The spectrum influences the output of photovoltaic (PV) modules. Solar spectral irradiance is becoming more prevalent in atmospheric studies and solar energy [1].

Most of the Sun's incident radiation on the top of Earth's atmosphere is distributed over the 290 to 3000 nm wavelengths. The spectral distribution of solar radiation depends on both local environmental conditions and the Sun's position [1]. The solar spectral irradiance is described using Bird's model [2], which requires input variables, such as air mass (AM), aerosol optical depth at 500 nm (AOD_{500}) and ozone (O_3). In this paper, AOD at 500 nm will be referred to as AOD_{500}.

The relative spectral responses (SR) differ for PV technologies because different PV modules absorb the solar spectral irradiance differently between different wavelengths [3]. In addition, the short-circuit current I_{SC} is dependent on the spectrum [4]:

$$I_{SC} = \int SR(\lambda) \cdot G_{tot}(\lambda) d\lambda \qquad (1)$$

where $SR(\lambda)$ is the spectral response of the module, and $G_{tot}(\lambda)$ is the combination of the irradiance sources on the module surface. Therefore, spectral irradiance and SR directly impact a PV module's performance [3, 4].

Spectral mismatch (MM) is defined as

$$MM = \frac{\int_{\lambda_1}^{\lambda_2} E(\lambda) \cdot SR(\lambda) d\lambda \int_{\lambda_3}^{\lambda_4} E_{ref}(\lambda) d\lambda}{\int_{\lambda_1}^{\lambda_2} E_{ref}(\lambda) \cdot SR_r(\lambda) d\lambda \int_{\lambda_3}^{\lambda_4} E(\lambda) d\lambda}. \qquad (2)$$

λ_1 and λ_2 are the lower and upper wavelength limits of spectral absorption of the PV module. λ_3 and λ_4 are the wavelength limits of the spectrum [3]. E_{ref} and SR are the reference spectral irradiance at standard testing conditions (STC) and the spectral response of the PV module, respectively. E_{meas} is the measured solar spectral irradiance [5]. MM accounts for the spectrum's influence on PV performance. The interpretation of MM is that the PV module undergoes a spectral loss when MM is less than unity and undergoes a spectral gain if MM is greater than unity [3].

On-site spectral data is scarce and expensive due to the cost and care needed for spectroradiometers [6]. However, the AErosol RObotic NETwork (AERONet) has multiple stations worldwide, providing global observations of AOD_{500} and O_3 [7]. The Southern African Universities Radiometric Network (SAURAN) provides solar radiometric data from locations across Southern Africa [8]. The combination of these two separate databases can be used to address the spectral data scarcity in Southern Africa. Using overlapping data periods can

be extremely useful to estimate spectral variables with reasonable accuracy.

To the authors' knowledge, a study has yet to be done to assess the sensitivity of the spectral mismatch regarding AOD_{500} and O_3. Further, based on the sensitivity of these variables, is there a simple and inexpensive computational manner to estimate AOD_{500} and O_3 for spectral mismatch evaluations? Is it necessary to have accurate and expensive spectral measurements if there is a more straightforward solution? This study aims to quantify how much of an impact AOD_{500} and O_3 will have on MM and propose what modelling assumptions can be made for South African locations when these measurements are unavailable.

2. Spectral Irradiance

2.1. Irradiance Components

Tilted irradiance or global plane-of-array irradiance, which is the total spectral irradiance, is defined as:

$$G_{s\lambda} = G_{bs\lambda} + G_{ds\lambda} + G_{rs\lambda}. \quad (3)$$

$G_{bs\lambda}$ is the beam or direct tilted irradiance, $G_{ds\lambda}$ is the sky diffuse tilted irradiance, and $G_{rs\lambda}$ is the ground-reflected diffuse tilted irradiance [9]. $G_{bs\lambda}$ is determined using Direct Normal Irradiance (DNI), $G_{ds\lambda}$ using Diffuse Horizontal Irradiance (DHI) and $G_{rs\lambda}$ using Global Horizontal Irradiance (GHI).

2.1.1.Direct Normal Irradiance

Direct irradiance on a surface normal to the direction of the Sun at ground level for wavelength λ ($G_{d\lambda}$) is given as [2]:

$$G_{d\lambda} = H_{o\lambda} D T_{r\lambda} T_{a\lambda} T_{w\lambda} T_{o\lambda} T_{u\lambda} \quad (4)$$

where $H_{o\lambda}$ is the extraterrestrial irradiance at the mean earth-sun distance for wavelength λ, D is the correction factor for earth-sun distance, T is the transmittance functions of the atmosphere at wavelength λ, $T_{r\lambda}$ is the Rayleigh transmittance, $T_{a\lambda}$ is the aerosol attenuation transmittance, $T_{w\lambda}$ is the water vapour absorption transmittance, $T_{o\lambda}$ is the ozone absorption transmittance and $T_{u\lambda}$ is the uniformly mixed gas absorption transmittance. The interested reader is referred to [2] for more detail.

Ozone absorption is described by:

$$T_{o\lambda} = \exp(-a_{o\lambda} O_3 M_O) \quad (5)$$

$$M_O = (1 + h_O/6370)/(\cos^2 Z + 2h_O/6370)^{0.5} \quad (6)$$

where $a_{o\lambda}$ is the ozone absorption coefficient, O_3 is the ozone amount (atm-cm), M_O is the ozone mass, and h_O is the height of the maximum ozone concentration, approximately 22 km.

Ozone can be estimated using:

$$O_3 = 235 + \big(100 + 30\sin[0.9865(n + 152.625)] + 20\sin\big(2(L - 75)\big)\big) \cdot (\sin^2(1.5\phi_L)) \quad (7)$$

where O_3 is measured in matm-cm, n is the day of the year (1 Jan = 1), L is the longitude and ϕ_L is the longitude [10]. Equation (12) has not been validated for the Southern Hemisphere [10].

2.1.2.Diffuse Horizontal Irradiance

Diffuse irradiance on a horizontal surface or the total scattered irradiance $G_{s\lambda}$ is given as [2]:

$$G_{s\lambda} = G_{r\lambda} + G_{a\lambda} + G_{g\lambda} \quad (8)$$

where $G_{r\lambda}$ and $G_{a\lambda}$ refer to the Rayleigh and aerosol scattering components, respectively, and $G_{g\lambda}$ is the multiple reflection of irradiance between ground and air. These equations are explained in detail in [2].

2.1.3.Global Horizontal Irradiance

GHI, $G_{T\lambda}$, is given as a combination of $G_{s\lambda}$ and $G_{d\lambda}$:

$$G_{T\lambda} = G_{d\lambda} \cos Z + G_{s\lambda} \quad (9)$$

AM, AOD_{500} and O_3 impact the $G_{d\lambda}$ and as contribute more than the $G_{s\lambda}$ to GHI.

2.2. Influences on Spectral Irradiance

This section illustrates AM, AOD_{500} and O_3's effects on the spectral irradiance. STC for atmospheric conditions is defined as a spectrum at an Air Mass of 1.5 (AM1.5), water vapour of 1.42cm, O_3 of 0.344 atm-cm and AOD_{500} at 500nm of 0.27 [11]. The spectral irradiance is simulated in Figure 1 to Figure 3 using Bird's model [2].

Solar irradiance at different AM is shown in Figure 1 with STC atmospheric conditions for water vapour, O_3 and AOD_{500} and the STC conditions of 37° tilt angle, 180° azimuth angle, 37° latitude and −100° longitude. Figure 1 clearly shows the impact of AM on the spectral solar irradiance.

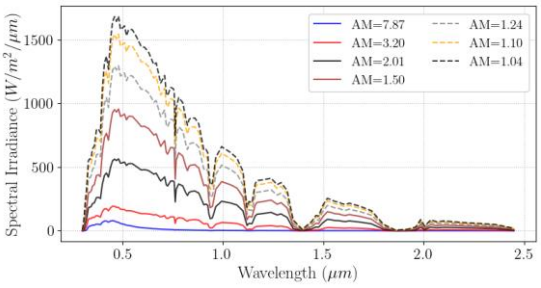

Figure 1. Solar spectral irradiance at varying AM indicates a significant effect on the irradiance

Figure 2 visualises the effect that the change in AOD_{500} has on the spectral irradiance. The STC conditions are kept constant; however, AOD_{500} varies. Figure 2 indicates how AOD_{500} has a moderate effect on the irradiance. The spectral irradiance was slightly decreased across the wavelengths as the AOD_{500} increased.

Figure 3 visualises the effect of the change in O_3 on spectral irradiance. The simulation indicated no noticeable changes after 1 µm, which is not shown in Figure 2 and Figure 3. Similarly, to Figure 2, the STC conditions are kept constant; however, in this scenario, O_3 varies. Changes in the spectral irradiance were noted in the 0.3-0.35 and 0.5-0.65 µm wavelengths, which had a much less pronounced overall effect than AOD_{500}. These results align with O_3 being more effective at absorbing at lower wavelengths where irradiance is also lower, being the Hartley absorption band at 0.195 to 0.35 µm and the Chappuis band between 0.42 to 0.83 µm [12].

As discussed previously, significant changes in the spectral irradiance were noted for changes in AM, moderate sensitivity for AOD_{500} and very little sensitivity in O_3. The conclusion is that AOD_{500} has a more significant impact than O_3, where the spectral irradiance is concerned. As the spectral mismatch is dependent on spectral irradiance, the hypothesis is that MM will be more sensitive to AOD_{500} than O_3.

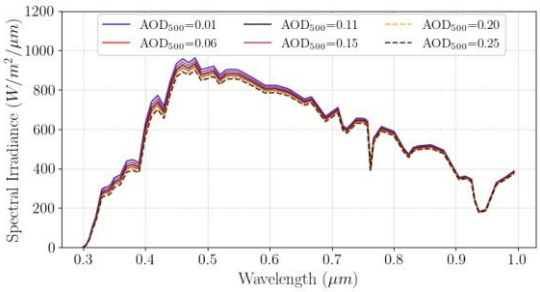

Figure 2. Solar spectral irradiance at varying AOD_{500} indicates a moderate effect on the irradiance

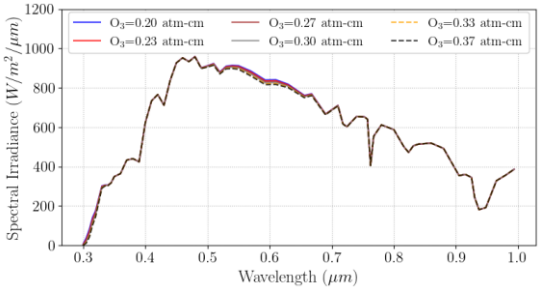

Figure 3. Solar spectral irradiance at varying O_3 indicates a mild effect on the irradiance

3. Sensitivity Analysis

3.1. Data

Three locations within South Africa were identified with proximity between the SAURAN and AERONet stations and overlapping data periods, and are indicated in Figure 4 and Table 1. The AERONet database's Durban, Simon's Town and Pretoria stations were selected to be paired with the SAURAN University of KwaZulu-Natal Howard College (KZH), Stellenbosch University (SUN) and UPR (University of Pretoria) stations respectively. The coordinates for the Durban, Stellenbosch and Pretoria sites are (-29.871, 30.977), (-33.935, 18.867) and (-25.753, 28.229), respectively. Further, the three sites have varying elevations of 150 m, 122 m and 1,410 m for Durban, Stellenbosch and Pretoria, respectively. The tilt angle is assumed to be 30° for all three sites and north-facing (0° azimuth angle).

Table 1 indicates the corresponding stations and the overlapping period identified for this study. The GHI and pressure measurements from the SAURAN database are used for this study. Level 2.0 quality assured data from AERONet is used in this study.

The SAURAN database has minutely-resolution data available, however, the AERONet database only has one-minute data available as it observes at approximately 15 minutes [13]. Figure 5 shows a visual explanation where the SAURAN and AERONet datasets combination indicates no AOD_{500} and O_3 datapoints for some of the corresponding SAURAN timestamps. The available datapoint is then set as the corresponding AOD_{500} and O_3 for the pre- and proceeding two minutely timestamps of the available AERONet data point. Therefore, the two datasets were combined by a forward- and backwards-filling procedure with a 2-minute limit to ensure more data points are available for this study.

The mean O_3 for the Durban, Stellenbosch and Pretoria sites are 0.275 atm-cm, 0.271 atm-cm and 0.287 atm-cm, respectively. The mean AOD_{500} for the three sites are 0.164, 0.161 and 0.077 for Durban, Stellenbosch and Pretoria, respectively. Figure 6 and Figure 7 show the statistical distributions of the three AERONet sites, for both AOD_{500} and O_3, respectively.

Figure 4. AERONet and SAURAN sites with overlapping data periods [7, 8]

Table 1. Database summary

Dataset name	SAURAN station	AERONet station	Overlapping period	Data Points available
Durban	KZH	Durban	24-01-2016 to 07-03-2019	30,776
Stellenbosch	SUN	Simon's Town	02-06-2020 to 03-01-2022	31,998
Pretoria	UPR	Pretoria	02-01-2019 to 29-12-2020	36,863

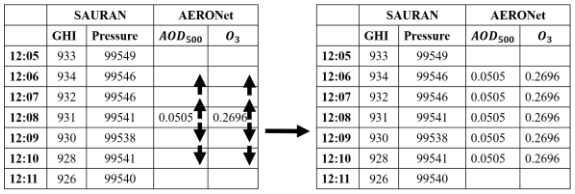

Figure 5: Forward and backwards filling principle

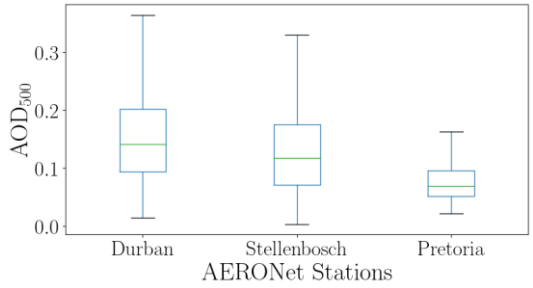

Figure 6: AOD_{500} statistical distribution

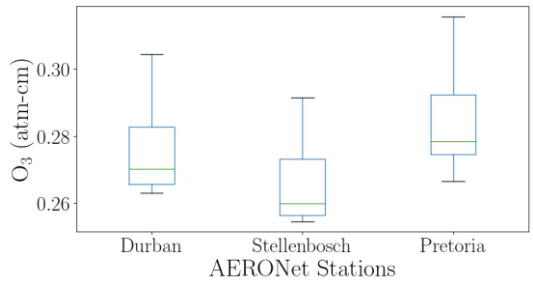

Figure 7: Ozone statistical distribution

The sites closer to the coast and lower altitudes have a higher mean AOD_{500} than the higher altitude, inland Pretoria site, whereas the O_3 shows the opposite. The statistical distribution does indicate that there is flunctations in the data, contributed to the variability inherent to changing of seasons.

Figure 8 shows the MAE and RMSE, expressed as a percentage of the mean O_3 for comparing the estimated O_3 using Equation (12). The results indicate that the Pretoria site has a higher percentage error than the lower altitude sites (Stellenbosch and Durban). However, as seen in Figure 2 and Figure 3, the changes in the spectral irradiance when these values differ has a minimal effect, which will carry over to a minimal effect on the spectral mismatch calculations. Overall, the estimation of O_3 yields a 3.8% MAE and 4.9% RMSE, which should be noted when using an alternative when no O_3 measurements are available.

The SAURAN datasets were processed using the quality control procedure proposed in [14]. Further, only daytime values, i.e., after sunrise and before sunset, were used for this study. The data processing results in 99,637 total datapoints with a temporal resolution of 1 minute available. The dataset consists of 30.9% data from the Durban station, 32.1% from the Stellenbosch station and 37% from the Pretoria station, described in Table 1.

3.2. Spectral Response of Polycrystalline Module

Figure 9 shows the simulated spectral response (SR) of a polycrystalline PV module, which will apply to all three location scenarios to determine spectral mismatch.

3.3. Comparison Metrics

The comparison metrics used in this study are the mean absolute error (MAE), root mean square error (RMSE) and coefficient of determination R^2. The error is calculated as the difference between the predicted and simulated MM.

3.4. Sensitivity Analysis

An initial sensitivity analysis was done using three different combinations of data to determine MM:

1. Measured AOD_{500} with the estimated O_3 using Equation (12)
2. Measured O_3 with a constant AOD_{500} value of 0.123;
3. And a constant AOD_{500} value (0.123) with the estimated O_3.

AOD_{500} of 0.123 is the mean of the total combined datasets, including Upington as an additional AERONet dataset; thus, the mean value of measurements from Stellenbosch, Durban, Pretoria and Upington. Due to no overlapping period for the corresponding Upington SAURAN and AERONet databases, the Upington station is not included in the spectral mismatch sensitivity analysis.

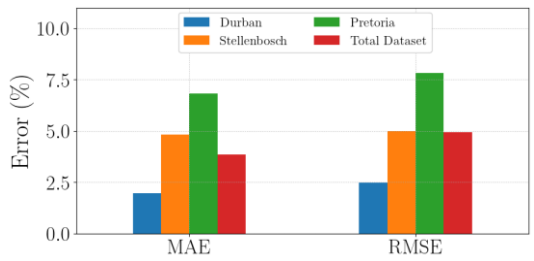

Figure 8. MAE and RMSE of using estimated ozone

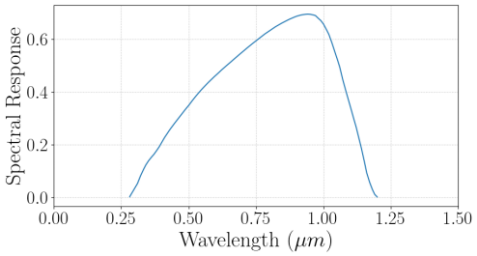

Figure 9. Simulated spectral response of a polycrystalline PV module

Figure 10 shows the distribution of the spectral MM for the three stations with the constant AOD_{500} with estimated O_3 compared to the measured values to estimate MM. The results show that the Durban site's mean MM is very close to unity, whereas Pretoria and Stellenbosch are slightly less than unity, i.e. slight spectral loss. The normal distribution changes slightly between the measured MM and the estimated MM. The estimated MM's peak is more clustered around the mean than the measured MM. The measured O_3 with a constant AOD_{500} showed almost no difference in the distribution and was not included in Figure 10. However, the distribution shows that the estimated MM will deviate more from the mean when the MM has a spectral gain or loss and is not unity.

Figure 11 shows the subsequent results, which indicate the sensitivity of spectral MM towards O_3 and AOD_{500} for the three sites and the total dataset. When the measured AOD_{500} was used to determine MM with the estimated O_3 value, there was very little error for all three locations.

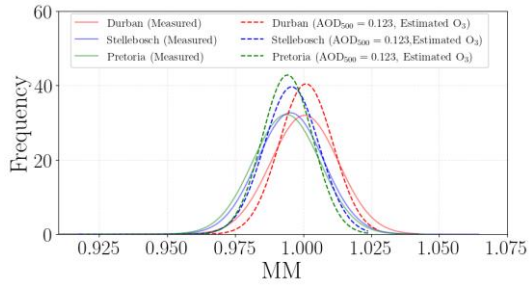

Figure 10. Spectral MM frequency distribution of three stations

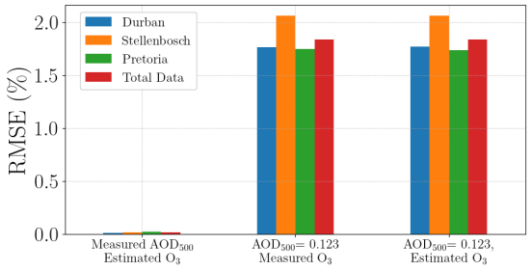

Figure 11. Spectral MM RMSE using a combination of constant and measured values.

However, the spectral MM showed noticeably higher errors for all three sites in the scenarios where AOD_{500} was a constant value instead of the measured value. The conclusion is made that the spectral MM is more affected by AOD_{500} than O_3, and an estimated O_3 value is acceptable if no measured O_3 is available. Therefore, the second part of this paper is to determine a methodology in which AOD_{500} can be predicted with reasonable accuracy that will improve this error.

4. Aerosol Optical Depth Estimations

4.1. Irradiance and Solar Components

The relative AM is expressed by [15]

$$\mathrm{AM} = [\cos\theta_Z + 0.5057(96.080 - \theta_Z)^{-1.634}]^{-1} \quad (10)$$

where θ_Z is the solar zenith angle.

The clearness index K_t was defined in [16] as

$$K_t = \frac{GHI}{I_{0n}\cos\theta_Z} = \frac{G_{T\lambda}}{I_{0n}\cos\theta_Z} \quad (11)$$

The extraterrestrial irradiance on a normal surface I_{0n} is based on the day of the year and is described as:

$$I_{On} = SC\left(1 + 0.033 \cdot \cos\left(\frac{360 \cdot n}{365}\right)\right) \quad (12)$$

where SC denotes the solar constant (usually 1367 $\mathrm{W/m^2}$).

4.2. Aerosol Optical Depth

4.2.1. Baseline Model

The baseline model is selected as AOD_{500} value (0.123) with an estimated O_3 value using Equation (12).

4.2.2. Lookup Tables for Aerosol Optical Depths

Three lookup tables were selected to determine AOD_{500}: an AM-only, K_t-only and a two-dimensional (2D) lookup table which consists of AM and K_t-intervals. The values are generated by taking the mean value of the training set with the corresponding interval of AM and K_t. The data is split into 60:40 training and testing sets for each dataset, and then a larger training and testing

datasets are combined with the three sites. Table 2 describes the AM-lookup table, Table 3 the K_t lookup table and Table 4 the 2D lookup table. AM refers to relative AM.

Table 2. AM lookup table

AM	AOD_{500}
[0, 1.5)	0.127
[1.5, 3)	0.138
[3,6)	0.128
[6, ∞)	0.119

Table 3. K_t lookup table

K_t	AOD_{500}
[0, 0.2)	0.098
[0.2, 0.5)	0.127
[0.5, 0.7)	0.143
[0.7, ∞)	0.118

Table 4. 2D lookup table

		K_t			
		[0, 0.2)	**[0.2, 0.5)**	**[0.5, 0.7)**	**[0.7, ∞)**
AM	**[1, 1.5)**	0.072	0.111	0.15	0.118
	[1.5, 3)	0.096	0.137	0.145	0.118
	[3,6)	0.126	0.147	0.125	0.104
	[6, ∞)	0.105	0.125	0.107	0.127

4.3. Spectral Irradiance Simulation

Simulation is done in Python using the pvlib spectrum library [17]. The O_3 values were calculated using Equation (12). Input variables such as the angle of incidence, θ_Z and AM can be empirically determined. The ground albedo was selected as 0.2. The location variables were set as described in Section 3.1. The spectral irradiance was simulated accordingly, and the spectral mismatch was calculated using the spectral response.

5. Results

Figure 12 shows the frequency distribution of the measured MM and is compared with the baseline model and three lookup tables. The mean of all the models stays the same; however, the frequency distribution has a higher peak than the measured MM.

Figure 13, Figure 14 and Figure 15 show, respectively, the RMSE, MAE and R^2 results of the three sites, as well as the total dataset, of the errors between the actual and predicted MM with differently estimated AOD_{500}. In Figure 13 and Figure 14, the baseline model is not significantly outperformed by the other lookup tables. The K_t-only lookup table shows the worst performance.

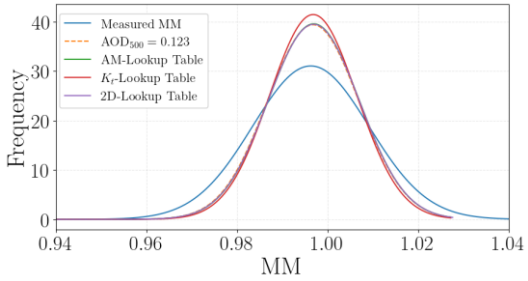

Figure 12. Spectral MM frequency distribution of the total dataset

Figure 15 shows the R^2 results of the total dataset, i.e., all three sites, for different intervals of AM and K_t. The three sites show that the Pretoria site has the lowest errors, whereas the Stellenbosch site shows the highest. The RMSE for all the stations is small, all under 1% RMSE error rate. The MAE is also very low, ranging between 0.26% for Stellenbosch and 0.17% for Pretoria.

The MAE and RMSE using a constant AOD_{500} with the estimated O_3 were 0.21% MAE and 0.75% RMSE for the total dataset. The small margin of error using these estimated values indicates that the proposed method in this paper is an appropriate substitution when no spectral data is available. The overall dataset (including all three sites) shows no significant outperformance from the baseline model using the three lookup tables. Further, Figure 16 shows the overall test dataset baseline model MM with the percentage error from the measured MM.

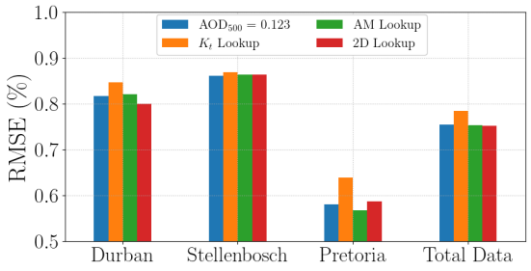

Figure 13. RMSE results

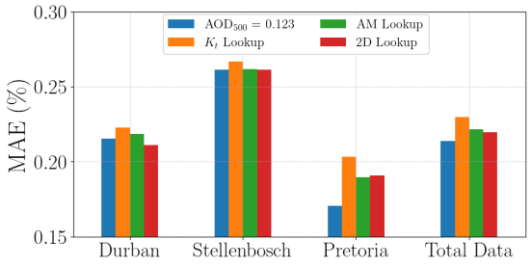

Figure 14. MAE results

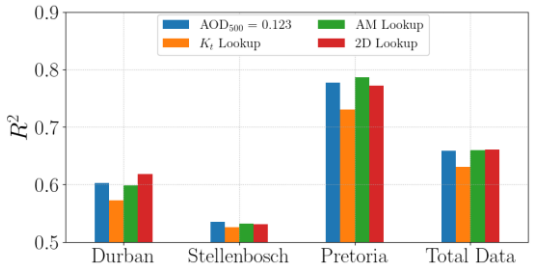

Figure 15. R^2 results

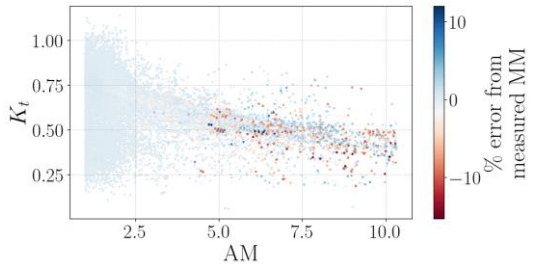

Figure 16. Percentage error of measured vs. estimated MM with constant AOD_{500}

From AM4 and higher, the percentage error is more prominent. However, most of the test dataset (97.9%) falls within a 2% error from the MM compared to the estimated MM. Figure 16 also indicates that the baseline MM slightly underestimates the MM more than it overestimates.

6. Conclusion

A sensitivity analysis of aerosol optical depth at 500nm and ozone for spectral mismatch of three South African locations was performed. This paper addresses a data scarcity issue: Are precise spectral measurements for AOD_{500} and O_3 necessary, specifically for spectral mismatch estimations, when a simpler alternative is available? Three South African sites with corresponding AERONet and SAURAN locations were combined to assess the spectral mismatch sensitivity. The results indicated that AOD_{500} has a more pronounced effect on spectral irradiance than O_3, which subsequently proved to have a more pronounced effect on spectral mismatch. The results indicated that an estimated ozone value with measured AOD_{500} generates a negligible error for spectral mismatch calculations. Therefore, the paper's objective was to determine a methodology to predict AOD_{500} using a lookup table. Three lookup tables were proposed with AM, K_t and a 2D-lookup table, which combined AM and K_t intervals. The results indicate that spectral mismatch can be simulated using an estimated O_3 with a constant AOD_{500} with a relatively minimal effect on spectral mismatch simulations. A constant AOD_{500} of 0.123 for South Africa is suggested to determine spectral irradiance and spectral mismatch with reasonable accuracy when no spectral data is available.

References

[1] A. Marzo, J. Ballestrín, J. Alonso-Montesinos, P. Ferrada, J. Polo, G. López and J. Barbero, "Field Quality Control of Spectral Solar Irradiance Measurements by Comparison with Broadband Measurements," *Sustainability*, vol. 13, 2021.

[2] R. E. Bird and C. Riordan, "Simple Solar Spectral Model for Direct and Diffuse Irradiance on Horizontal and Tilted Planes at the Earth's Surface for Cloudless Atmospheres," *Journal of Climate and Applied Meteorology*, vol. 25, pp. 87-97, 1986.

[3] J. A. Caballero, E. F. Fernández, M. Theristis, F. Almonacid and G. Nofuentes, "Spectral Corrections Based on Air Mass, Aerosol Optical Depth, and Precipitable Water for PV Performance Modeling," *IEEE Journal of Photovoltaics*, vol. 8, pp. 552-558, 2018.

[4] M. P. Brennan, A. L. Abramase, R. W. Andrews and J. M. Pearce, "Effects of spectral albedo on solar photovoltaic devices," *Solar Energy Materials and Solar Cells*, vol. 124, pp. 111-116, 2014.

[5] K. Takeguchi, J. Chantana, K. Nakayama, Y. Kawano, T. Nishimura, Y. Hishikawa and T. Minemoto, "Accurate estimation of outdoor performance of photovoltaic module through spectral mismatch correction factor under wide range of solar spectrum," *Current Applied Physics*, vol. 28, pp. 59-71, 2021.

[6] G. Nofuentes, C. Gueymard, J. Aguilera, M. Pérez-Godoy and F. Charte, "Is the average photon energy a unique characteristic of the spectral distribution of global irradiance?," *Solar Energy*, vol. 149, pp. 32-43, 2017.

[7] AErosol ROBotic NETwork (AERONet), 2023. [Online]. Available: https://aeronet.gsfc.nasa.gov/.

[8] SAURAN, 2023. [Online]. Available: https://sauran.ac.za/.

[9] C. A. Gueymard, "The SMARTS spectral irradiance model after 25 years: New developments and validation of reference spectra," *Solar Energy*, vol. 187, pp. 233-253, 2019.

[10] T. Van Heuklon, "Estimating Atmospheric Ozone For Solar Radiation Models," *Solar Energy*, vol. 22, pp. 63-68, 1979.

[11] C. A. Gueymard, D. Myers and K. Emery, "Proposed reference irradiance spectra for solar energy systems testing," *Solar Energy*, vol. 73, pp. 443-467, 2002.

[12] J. Brion, A. Chakir, J. Charbonnier, D. Daumont, C. Parisse and J. Malicet, "Absorption Spectra Measurements for the Ozone Molecule in the 350–830 nm Region," *Journal of Atmospheric Chemistry*, vol. 30, pp. 291-298, 1998.

[13] C. A. Gueymard and D. Yang, "Worldwide validation of CAMS and MERRA-2 reanalysis aerosol optical depth products using 15 years of AERONET observations," *Atmospheric Environment*, vol. 225, p. 117216, 2020.

[14] F. Daniel-Durandt and A. Rix, "The Automation of Quality Control for Large Irradiance Datasets," in *2022 International Conference on Electrical, Computer, Communications and Mechatronics Engineering (ICECCME)*, 2022.

[15] F. Kasten and A. T. Young, "Revised optical air mass tables and approximation formula," *Appl. Opt.*, vol. 28, p. 4735–4738, November 1989.

[16] B. Y. H. Liu and R. C. Jordan, "The interrelationship and characteristic distribution of direct, diffuse and total solar radiation," *Solar Energy*, vol. 4, pp. 1-19, 1960.

[17] W. Holmgren, C. Hansen and M. Mikofski, "pvlib python: a python package for modeling solar energy systems," *Journal of Open Source Software*, vol. 3, p. 884, September 2018.

INITIAL EXPERIMENTAL TESTING OF A SOLAR SALT THERMAL ENERGY STORAGE UNIT COUPLED TO A SOLAR DISH

Tlou S. Mokobodi[1] and Willem G. Le Roux[1]

[1] Department of Mechanical and Aeronautical Engineering, University of Pretoria, Private Bag X20, Hatfield, 0028, Pretoria, South Africa; Phone:+27 12 420 5367; E-Mail: tlou.mokobodi@up.ac.za, willem.leroux@up.ac.za

Abstract: Ongoing efforts in the development of thermal energy storage (TES) systems coupled with concentrating solar power systems show potential for matching increasing energy demand. A solar dish and tubular receiver coupled to a short-term TES unit are currently being investigated at the University of Pretoria (UP) over a full range of mass flow rates and using concentrated solar energy as the source of heat input. This paper reports the findings from initial experimental results evaluated in lower-range mass flow rates using a blower with air as the heat transfer fluid (HTF). During the experimental evaluation, 151 kg of solar salts was charged and discharged in a TES unit. The full cycle of charging the system was achieved over three sunny days (which included two unavoidable overnight heat loss processes) whereafter one overnight discharging process was performed. A maximum average temperature of 222.6 ℃ was achieved in the TES unit. During the charging process, an average uncontrolled air mass flow rate of 0.0132 kg/s was supplied. Results show that 17.51 kWh of energy was stored during the 13-hour intermittent charging process and 9.81 kWh was recovered from the TES during the 17-hour discharge process. Lastly, the system displayed substantial parasitical energy losses – recommendations are suggested for the next round of mid-range and higher-range mass flow rate testing.

Keywords: Concentrating solar power (CSP); solar salts; solar dish; thermal energy storage.

1. Introduction

The need to explore alternative energy sources is important as the mismatch in energy supply and demand continues while the global population increases. Furthermore, one could argue that the unfriendly environmental impact associated with fossil fuels and the high associated cost of consumption of fossil fuels propagates global socio-economic imbalances [1, 2]. Whilst some of these problems can be resolved, the depletion of fossil fuels has been forecasted [3].

In the search for an alternative energy source, sustainable and renewable sources (such as biomass, solar, hydropower and wind) tick many boxes as attractive solutions. This paper focuses on solar energy as it is fundamentally Earth's energy source [4] and the energy available from the sun in one hour is typically enough to meet all annual energy demands globally [5, 6].

1.1. Opportunity

The global energy crisis affects Africa in multiple ways owing also to the injustices of the past on Africa. Currently, it is estimated that 940 million people do not have access to electricity globally, and a large percentage of these people live in Africa [7]. Sub-Saharan Africa (SSA) [8] amounts to more than two-thirds of the world's population with no access to electricity. Many factors contribute to why Africa is left behind in closing this gap. One such reason is that the national grid infrastructure is not sufficient to electrify the population using centralised power distribution methods [9]. As a result, while the rest of the world is transitioning to renewable and sustainable energy, access remains a challenge to SSA. Solar energy is an attractive source of renewable energy as it can also address the distribution of energy to isolated communities via the use of microgrids [10].

1.2. Concentrating Solar Power

Concentrating solar power (CSP) for power and heat generation has shown great potential in providing solutions to the multi-faced energy crisis [10]. Several methods have been developed to actively capture and convert energy derived from the sun. A major shortcomings in deploying solar power has been intermittency [11]. To mitigate the associated risks, many studies have shown that the integration of TES in CSP plants can increase their power availability. Furthermore, the inclusion of TES would render CSP a more dispatchable source of energy, as this would improve the reliability and availability of power plants.

1.3. Thermal Energy Storage

In the search for a suitable TES method, numerous studies have suggested that eutectic solar salts are the best candidate for these applications, due to their superior properties [12]. Furthermore, eutectic salts are attractive as a phase change material (PCM) for heat storage because they display stable characteristics [13]. When solar salts are used as PCM material for TES, the solid-to-liquid phase change is achievable at high temperatures and liquid phases are maintained over a wider range of temperatures [14-16]. Material handling is also simplified because of small changes in volume at phase change [17]. In addition, PCM storage offers an added advantage in being deployed for both sensible heat (SH) (in the solid and liquid phases) and latent heat (LH) [18]. Considering the available literature on the various benefits of different mixture ratios of solar salts for different storage applications, the focus of this paper is on $40_{wt}\%\, KNO_3 - 60_{wt}\%\, NaNO_3$ [19]. The TES was previously evaluated under a controlled charging process with input heat generated by flue gases from the combustion process as described by Humbert et al. [19].

2. Methodology

This paper presents the initial experimental evaluation of an existing solar dish, as designed and developed at the University of Pretoria (UP) [20, 21], coupled to an existing TES unit which was designed for heat recovery from the exhaust of a micro-turbine (see Humbert et al. [18]). For the present work, the temperature response of the TES from solar energy input is evaluated. The setup uses ambient air as the heat transfer fluid (HTF).

2.1. Heat input

The heat input to the system is provided by the solar dish, with the central receiver located at the focal point of the parabolic dish to maximise the heat transferred to the HTF [22, 23]. The available solar power is calculated using Equation 1 below [24]:

$$\dot{Q}_s = A_d \times DNI \times \eta_s \tag{1}$$

where $\dot{Q}_s$ is the solar power input at the receiver, DNI ($\mathrm{W/m^2}$) is the direct normal irradiance of the sun, A_d is the total reflective area of the dish and η_s is the reflectivity of the reflector material.

2.2. Heat losses

There are several heat loss mechanisms associated with the solar dish system. These are found at the dish, receiver, process piping, and TES. The mechanisms include conduction, convection, and radiation [23]. In this paper, these losses were not monitored, however, they were calculated from the measured energy gains associated with the system components.

2.3. The process heat input to the system

The rate of heat gained or lost by the HTF as it undergoes the process is calculated using Equation 2 [25]:

$$\dot{Q}_t = \dot{m}_{air} C_{p,air} (T_{out} - T_{in}) \tag{2}$$

where $\dot{Q}_t$ is the power gained or lost, $\dot{m}_{air}$ is the mass flow rate of the process air in kg/s, and $C_{p,air}$ is the specific heat capacity of air. The properties of the HTF are evaluated at the bulk mean temperature. T_{out} and T_{in} are the exit and inlet air temperature values respectively across the specific component of interest.

2.4. Thermal energy storage analysis

Fully understanding the TES's response to the current system will enable controlled variation of parameters and prediction of the TES's performance. From the literature, the use of eutectic solar salts, $40_{wt}\%\, KNO_3 - 60_{wt}\%\, NaNO_3$, has advantages: large-temperature-range stability, high C_p value, as well as sensible and latent heat storage [17]. The melting point of this mixture, as reported by Humbert et al., is around 222 ℃, and the solar salts remain stable in the liquid phase to temperatures of up to 600 ℃. Furthermore, eutectic solar salts can be used as both a storage medium and HTF [10].

To evaluate the response of the TES, the energy balance for the HTF process line and the solar salts bath was evaluated.

2.4.1.Energy balance: TES-process side

Across the TES inlet and outlet, energy is transferred from the HTF (Equation 3) to the solar salts and to the environment as heat loss through the insulation of the TES.

$$\dot{Q}_{TES,air} = \dot{m}_{air} C_{p,air} \left(T_{TES,in} - T_{TES,out}\right) \tag{3}$$

In Equation 3, a time stamp of 1 minute was used as inherited from the SAURAN station at UP [26], whose DNI data was used to analyse the results. The other measurements were taken at a sampling rate of 3 seconds and averaged over 20 data points to result in minute samples for analysis.

2.4.2.Energy balance: TES-storage material side

In using solar salts as energy storage material, SH (solid: *sol*), LH, and SH (liquid: *liq*) can be stored (see Equations 4, 5, 6, and 7 below).

$$Q_{sen,sol} = m \times C_{p,salt} (\Delta T_{sol}) \tag{4}$$

$$Q_{latent} = m \times \lambda_{sol-liq} \tag{5}$$

$$Q_{sen,liq} = m \times C_{p,salt} (\Delta T_{liq}) \tag{6}$$

$$Q_{tot,stored} = Q_{sen,sol} + Q_{latent} + Q_{sen,liq} \tag{7}$$

Note that ΔT represented the change in temperature of the solid and the liquid during charging or discharging. The LH value $\lambda_{sol-liq}$ was taken from Ref. [27] as 96 kJ/kg.

2.4.3. Heat losses around the TES during charging.

The TES experiences heat losses during both the charging and discharging periods. The total heat loss rate in the TES is calculated using the difference between the total amount of heat delivered to the TES by the air and the energy stored in the TES.

$$\dot{Q}_{TES,losses} = \dot{Q}_{TES,air} - \dot{Q}_{tot,stored} \quad (8)$$

Equation 8 is applicable for charging and discharging, as there are energy losses associated with both processes.

3. Experimental setup

The solar dish for this experiment contained uncontrolled HTF flow. The HTF was supplied by a domestic application 3.3 kW Trimtech leaf blower with only one power setting. The flow rate through the system varied continuously throughout the charging and discharging cycle. The variations were due to changing air properties (affecting the friction factors) at the blower, in the solar receiver and in the TES due to changing wind conditions, humidity, ambient temperature and DNI. A low-range air mass flow rate (0.01 kg/s to 0.02 kg/s) was evaluated in the current work. These initial results can be used to systematically characterise the experimental performance of the solar dish system, even though the theoretical desired receiver performance is described by Le Roux et al. to be around the optimum mass flow rate of 0.07 kg/s [23]. The schematic diagram of the dish setup is shown in Fig. 1.

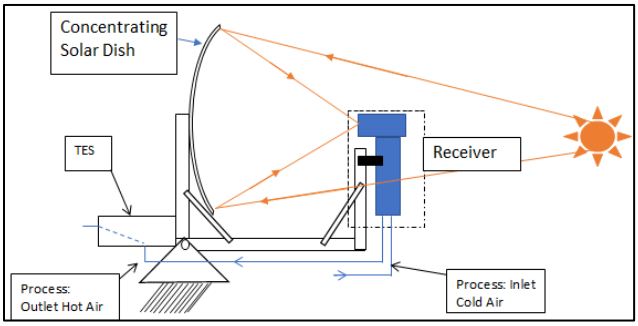

Fig. 1. Solar dish and TES layout

The results presented in this paper, came from measurements taken from three consecutive days of testing in the lower mass flow rate range. The charging process started on the morning of the 18th of April 2023 and ended on the 20th of April 2023, and the discharging process started on the evening of the 20th of April 2023 and ended on the morning of the 21st of April 2023.

3.1. Charging process

During the charging cycle, the system starts from a cold state, in which it heats the process piping, receiver, and the TES. The system's average temperature increases and the mass flow rate decreases as the resistance increases due to an increase in friction. During discharge, the opposite is the case. For the discharging process, the process started immediately after the end of charging on Day 3 and therefore started hot.

The same process path line for charging and discharging according to path 2 is used. Path 1 and 3 was not used for this setup. See Fig. 2 below showing path 2: Fan > flowmeter (fm) > Receiver (*ab*) > Down piping (*bc*) > TES (*cd*) > Outlet.

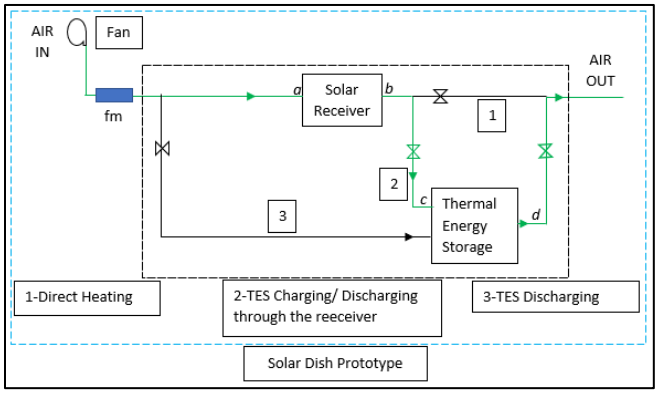

Fig. 2. The charging and discharging path 2

The actual system setup is shown in Fig. 3 below.

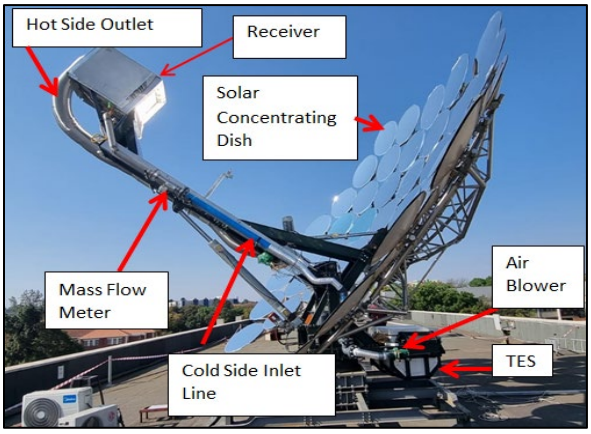

Fig. 3. Solar dish setup

The solar dish system's design consists of a reflective area of 23.95 m^2 and assumed reflectivity of 0.85, with a receiver aperture area of 0.25 × 0.25 m, as detailed by Roosendaal et al. [20, 21]. The TES was constructed as a coil immersed in solar salts (see Ref. [19]). The coil consists of 6 loops, adjacent to each other, with the first loop situated at the hot air inlet side and the last loop at the outlet of the TES. The experiments were performed in an uncontrolled environment to observe a true response. The mass flow rate was measured using a SUTO

S421 mass flow meter. The TES was fitted with thermocouples for temperature response readings. Some of the thermocouples were welded to the surface of the coils (ST_1-ST_6), and some were immersed in the solar salts between the coils (PT_1-PT_5) (see Fig. 4 below).

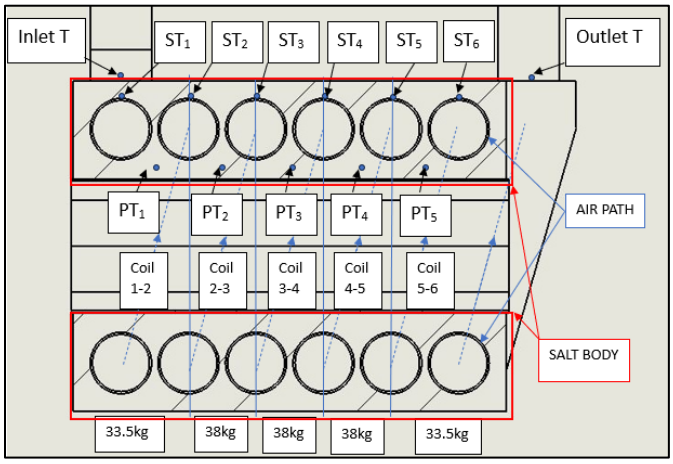

Fig. 4. Thermocouple positions and IDs

The positions of the thermocouples are described by Humbert et al. [19]. The thermocouples were connected to an Agilent Keysight 34901A module connected to a suitable Agilent data logger. The measurements were manually observed on a computer to track the real-time response of the setup.

The TES mass is divided into 5 sub-mass components to accommodate the 5 immersed temperature probes (PTs). Due to the complex bath shape on the inlet and outlet sides, the mass of the solar salts surrounding the first and last coils are assumed to be 33.5 kg each, whilst the middle coils are assumed 28 kg each (see Fig. 4). The average temperature of the two adjacent coils' surface temperature (ST) and probe temperature reading were used in analysing the heat transfer from the HTF to the PCM locally in each coil section. This approach was opted to accommodate the immersed probes' thermocouples in the PCM as there were only five.

4. Results

The system was tested for three consecutive days by charging and by discharging across Day 3 into Day 4. The experimental mass flow rate is shown below in Fig. 5. The average mass flow rate of 0.032 kg/s is calculated for charging whilst the average mass flow rate of 0.0175 kg/s is calculated for discharging.

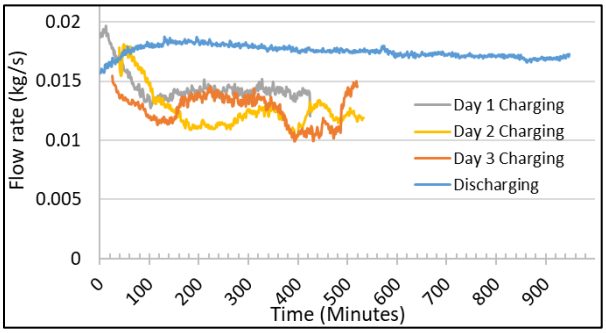

Fig. 5. System's mass flow rate

4.1. Combined TES response (charging)

Over the three consecutive days, the TES experienced overnight heat losses during the first two nights (see Fig. 6). At the start of the second day, the system started with an undesired process discharge as the TES and the piping system were warming up. On the third day, to enhance the charging process, the TES was bypassed until the inlet temperature to the TES was reading the same as the TES's surface thermocouple 1. The average salt bath temperature drop overnight for both days 1 and 2 is calculated below in Table 1.

Table 1. Charging conditions (averaged values) to calculate temperature drop during the first (*) and second (**) night.

			Temperature (℃)		
	Start Type		Start	End	Temp. Drop
Day 1	Cold	Probes	16.22	*164.19	
		Surface	16.23	168.33	
Day 2	Hot	Probes	*119.09	**200.05	*44.29
		Surface	116.85	205.82	
Day 3	Hot	Probes	**158.58	219.75	**41.24
		Surface	158.58	223.58	

These temperatures drop values amount to an average heat loss rate of 0.172 kW. To evaluate the overall TES response, a conservative approach was used to select the data and combine it for overall analysis. The data points selected for analysis were based on the average temperature of the TES, such that different sections of overlapping temperatures were taken to allow continuity of temperature in the TES over the 3 days of charging. In Fig. 6 below, for Day 1's measurements, the selected data ranges from ambient temperature to 150 ℃, for Day 2 the selected data ranges from 150 ℃ to 200 ℃, and for Day 3 the data ranges from 200 ℃ to the maximum temperature. Using the average temperature of the five probes (PT_1-PT_5) in the TES, the corresponding data indexing for a specific day was identified.

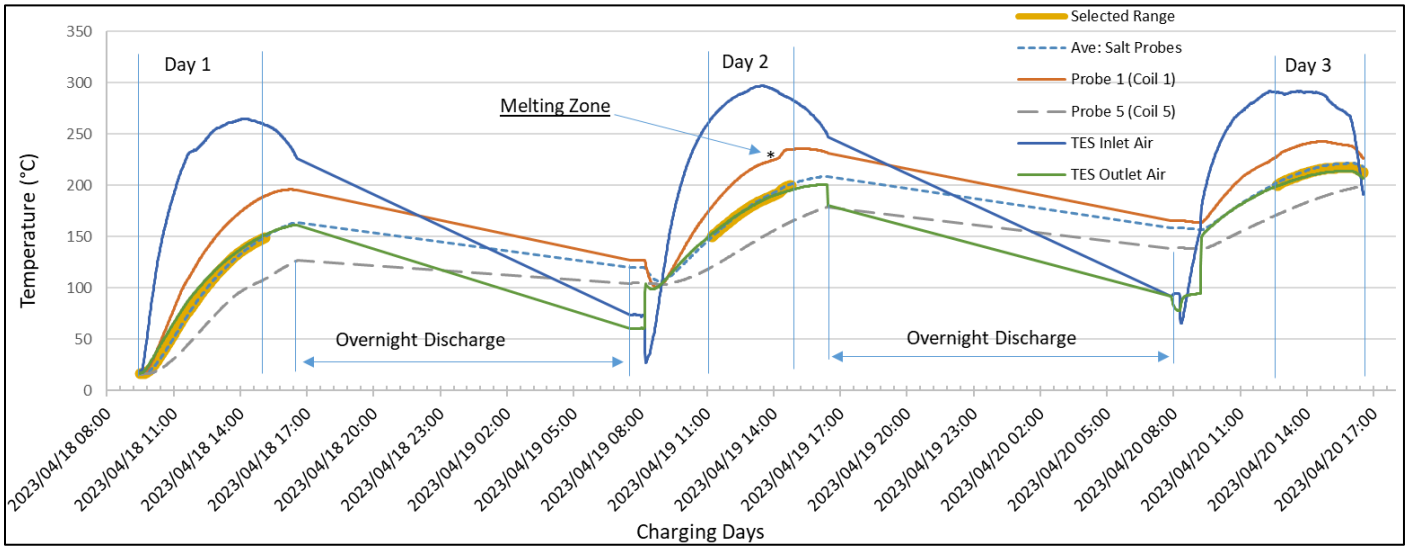

Fig. 6. Three days charging temperature results for selected thermocouples and averaged data for analysis.

4.1.1.HTF (charging)

To evaluate the charging process on the HTF side, Equations 1, 2, and 3 above were employed. The results for the performance in the receiver and the TES are shown below in Fig. 7.

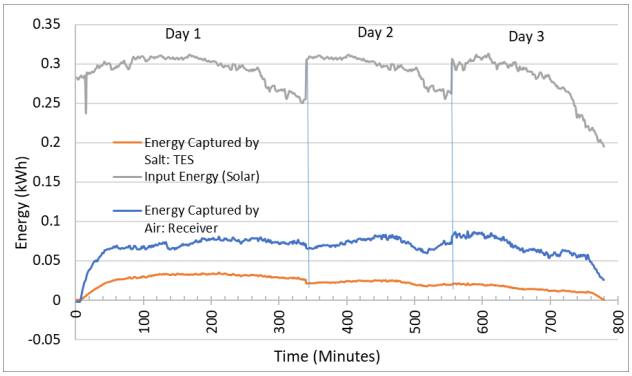

Fig. 7. Three days charging processes (HTF results). Note that the time step is 1 minute.

4.1.2.PCM (charging)

The design of the TES and the nature of the HTF resulted in the stratification of temperatures along the coils of the TES. The salts surrounding coils 1 and 2 reached the liquid phase on days 2 and 3 of testing. As a result, the energy analyses for these two coils consisted of sensible solid, sensible liquid, and latent energy analyses. Equations 4, 5, 6, and 7 were used to calculate the stored energy during the charging cycles. Table 2 below summarises the response of the TES during charging.

Table 2. Overall TES performance (charging)

Charging		[kWh]
E_{HTF}	Convective TES	**17.51**
E_{PCM}	Sensible Solid TES	12.76
	Latent TES	1.64
	Sensible Liquid TES	0.38
	Total	**14.78**

The difference (2.73 kWh) in the energy provided by the HTF and the energy gained by the PCM is assumed to be due to heat transfer to the environment during the charging process. This value corresponds to the average heat loss rate calculated from Table 1 ($0.172 \times 779/60 \approx 2.23$ kWh).

4.2. TES Response (discharging)

The evaluation of TES discharge cycles was evaluated both on the HTF side and on the PCM side. This approach offers a comparison method to evaluate the energy balance around the TES based on the results from both analyses.

4.2.1.HTF (discharging)

The system discharge cycle started hot, and the discharge process is along path 2 (same as charging). As a result, the energy restored from the system includes that which is also stored in the hot receiver and process piping at the end of Day 3's charging period.

The temperature response of the TES on the air side is shown below in Fig. 8.

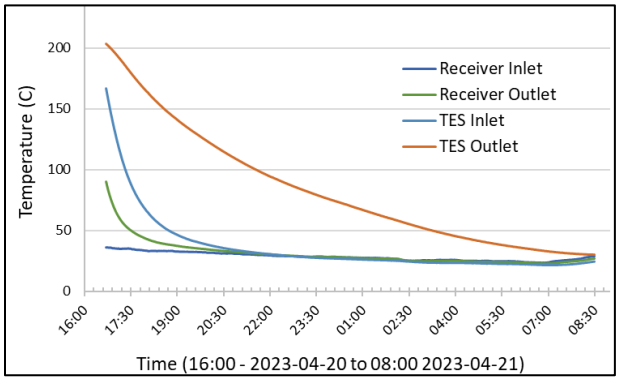

Fig. 8. The discharge temperature response for the solar receiver and the TES

The energy balance performed in this regard considers the energy restored from process piping. Using the applicable thermocouples, the heat recovered by the HTF was specifically calculated considering the source it was restored from. Fig. 9 below shows the HTF energy profile during discharge.

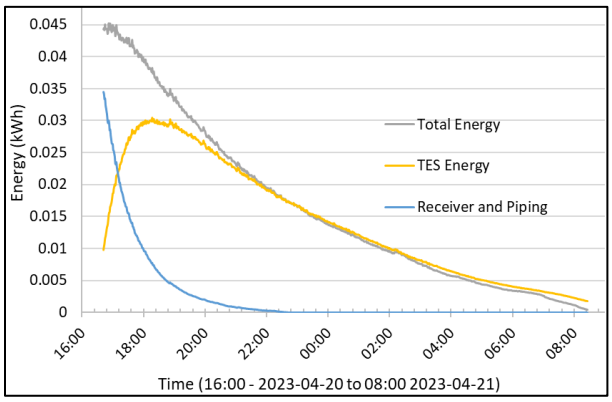

Fig. 9. Energy recovered from the TES, solar receiver, and piping during discharge. Note that the time step is 1 minute.

4.2.2.PCM (Discharging)

It was found that the thermocouples (PT_1-PT_5) did not successfully read the data during the first 10 minutes of the discharge process. During this time, the blower continued pushing air through the TES (discharging it). As a result, the PCM temperatures were only recorded in the sensible solid region even though coils 1 and 2 were charged to the sensible liquid region. The results are presented in Table 3 below.

Table 3. Overall TES performance during discharge

Discharge		[kWh]
E_{PCM}	Sensible Solid TES	**11.62**
E_{HTF}	Convective TES	9.81
	Heat recovered: hot receiver and piping	2.22
	Total	**12.04**

It must be noted that the receiver and piping energy restored by the HTF during discharge (2.22 kWh) is not accounted for in the PCM energy in this process. It is assumed that the difference (of 1.81 kWh) in the energy recovered from the PCM (11.62 kWh) and the energy captured by the HTF (9.81 kWh) during this process resulted from heat losses to the environment, and, the 10 minutes of the lost data at the start of the discharging process.

5. Discussion and conclusions

The experimental work presented in this paper investigated the response of the short-term TES in the low mass flow rate region. The energy balance of the process in the charging and discharging showed that the TES can successfully store and release a useful amount of energy. The current dish configuration consists of multiple components that expose the system to parasitical heat losses. Even with this in hand, the TES was able to store more than 80 % of the energy from the HTF and it was able to discharge more than 80 % of the thermal energy it had stored. During the discharge process, it was also found that a significant amount of energy can be recovered from the hot piping. With this finding, it is recommended that the discharge process always start through the hot process piping to extract useful energy. As Fig. 9 shows that the receiver's useful energy could only be extracted until about 22:00, it would be beneficial to switch the flow path and discharge the TES via path 3 in Fig. 2 with less flow resistance.

The results in Fig. 7 show that the performance of the overall system is very low, with efficiency of less than 10 %. The authors associate this performance with a large amount of solar spillage at the receiver due to incorrect facet calibration (individual mirror facets were not correctly aimed or vacuumed according to specifications before testing); however, the focus of this paper was on the TES and not on the performance of the solar dish. It is worth mentioning though, that the dish has the potential for very low amounts of spillage (see Ref. [20]) after careful calibration. Furthermore, the piping contributed to extra heat losses after the receiver and low mass flow rates (below design point) also affected the efficiency of the solar receiver. Identified aspects contributing negatively to the system are being investigated and continuous improvements are implemented for future work.

Acknowledgments

The authors would like to acknowledge the financial support from Innovate UK for the project “Solar-Turbo CHP” that helped construct the solar dish setup and the TES. Furthermore, the authors would also like to acknowledge the involvement of the team of engineers, technicians, and postgraduate students who were involved in the process of testing the system.

References

[1] K. Bekhrad, A. Aslani, and T. Mazzuca-Sobczuk, "Energy security in Andalusia: The role of renewable energy sources," Case Studies in Chemical and Environmental Engineering, vol. 1, p. 100001, 2020/05/01/ 2020, doi: https://doi.org/10.1016/j.cscee.2019.100001.

[2] L. Kumar, M. Hasanuzzaman, and N. A. Rahim, "Global advancement of solar thermal energy technologies for industrial process heat and its future prospects: A review," Energy Conversion and Management, vol. 195, pp. 885-908, 2019/09/01/ 2019, doi: https://doi.org/10.1016/j.enconman.2019.05.081.

[3] P. Zhang, X. Xiao, Z. Meng, and M. Li, "Heat transfer characteristics of a molten-salt thermal energy storage unit with and without heat transfer enhancement," Applied Energy, vol. 137, pp. 758-772, 2015.

[4] M. S. Ali, R. A. Tuhin, and M. S. H. Khan, "Chapter 1 - Sun: The main source of ground energy and power," in Advances in Clean Energy Technologies, A. K. Azad Ed.: Academic Press, 2021, pp. 3-18.

[5] J. Barber, "Photosynthetic energy conversion: natural and artificial," Chemical Society Reviews, vol. 38, no. 1, pp. 185-196, 2009.

[6] P. Denholm, E. Drury, R. Margolis, and M. Mehos, "Chapter 10 - Solar Energy: The Largest Energy Resource," in Generating Electricity in a Carbon-Constrained World, F. P. Sioshansi Ed. Boston: Academic Press, 2010, pp. 271-302.

[7] H. Ritchie, M. Roser, and H. Rosado, "Energy," Our World in Data, 2022. [Online]. Available: https://ourworldindata.org/energy-access.

[8] B. O. Menyeh, "Financing electricity access in Africa: A choice experiment study of household investor preferences for renewable energy investments in Ghana," Renewable and Sustainable Energy Reviews, vol. 146, p. 111132, 2021/08/01/ 2021, doi: https://doi.org/10.1016/j.rser.2021.111132.

[9] G. Falchetta, S. Pachauri, E. Byers, O. Danylo, and S. C. Parkinson, "Satellite Observations Reveal Inequalities in the Progress and Effectiveness of Recent Electrification in Sub-Saharan Africa," One Earth, vol. 2, no. 4, pp. 364-379, 2020/04/24/ 2020, doi: https://doi.org/10.1016/j.oneear.2020.03.007.

[10] M. K. Abdelrazik, S. E. Abdelaziz, M. F. Hassan, and T. M. Hatem, "Climate action: Prospects of solar energy in Africa," Energy Reports, vol. 8, pp. 11363-11377, 2022/11/01/ 2022, doi: https://doi.org/10.1016/j.egyr.2022.08.252.

[11] C. de Castro, M. Mediavilla, L. J. Miguel, and F. Frechoso, "Global solar electric potential: A review of their technical and sustainable limits," Renewable and Sustainable Energy Reviews, vol. 28, pp. 824-835, 2013/12/01/ 2013, doi: https://doi.org/10.1016/j.rser.2013.08.040.

[12] B. D. Iverson, S. T. Broome, A. M. Kruizenga, and J. G. Cordaro, "Thermal and mechanical properties of nitrate thermal storage salts in the solid-phase," Solar Energy, vol. 86, no. 10, pp. 2897-2911, 2012/10/01/ 2012, doi: https://doi.org/10.1016/j.solener.2012.03.011.

[13] A. S. Caldwell, G. Itskos, and K. H. Sandhage, "Air-stable, earth-abundant molten chlorides and corrosion-resistant containment for chemically-robust, high-temperature thermal energy storage for concentrated solar power," Materials Today, vol. 46, pp. 9-17, 2021/06/01/ 2021, doi: https://doi.org/10.1016/j.mattod.2021.02.015.

[14] S. Kalogirou, "The potential of solar industrial process heat applications," Applied Energy, vol. 76, no. 4, pp. 337-361, 2003/12/01/ 2003, doi: https://doi.org/10.1016/S0306-2619(02)00176-9.

[15] T. Bauer, N. Pfleger, D. Laing, W.-D. Steinmann, M. Eck, and S. Kaesche, "20 - High-Temperature Molten Salts for Solar Power Application," in Molten Salts Chemistry, F. Lantelme and H. Groult Eds. Oxford: Elsevier, 2013, pp. 415-438.

[16] P. d. C. Jose and E. Philip, "Thermal energy storage for low and medium temperature applications using phase change materials – A review," Applied Energy, vol. 177, pp. 227-238, 2016/09/01/ 2016, doi: https://doi.org/10.1016/j.apenergy.2016.05.097.

[17] K. Pielichowska and K. Pielichowski, "Phase change materials for thermal energy storage," Progress in Materials Science, vol. 65, pp. 67-123, 2014/08/01/ 2014, doi: https://doi.org/10.1016/j.pmatsci.2014.03.005.

[18] A. Dinker, M. Agarwal, and G. D. Agarwal, "Heat storage materials, geometry and applications: A review," Journal of the Energy Institute, vol. 90, no. 1, pp. 1-11, 2017/02/01/ 2017, doi: https://doi.org/10.1016/j.joei.2015.10.002.

[19] G. Humbert, C. Roosendaal, J. K. Swanepoel, H. M. Navarro, W. G. Le Roux, and A. Sciacovelli, "Development of a latent heat thermal energy storage unit for the exhaust of a recuperated solar-dish Brayton cycle," Applied Thermal Engineering, vol. 216, p. 118994, 2022/11/05/ 2022, doi: https://doi.org/10.1016/j.applthermaleng.2022.118994.

[20] C. Roosendaal, J. K. Swanepoel, and W. G. Le Roux, "Performance analysis of a novel solar concentrator using lunar flux mapping techniques," Solar Energy, vol. 206, pp. 200-215, 2020/08/01/ 2020, doi: https://doi.org/10.1016/j.solener.2020.05.050.

[21] C. Roosendaal, J. K. Swanepoel, and W. G. Le Roux, "OPTICAL MODELLING OF A VACUUM-MEMBRANE SOLAR DISH BASED ON ELLIPTICAL TELEVISION ANTENNA," presented at the Southern African Sustainable Energy Conference (SASEC) Cape Town, November 2021, 2021.

[22] K. J. Craig, M. Slootweg, W. G. Le Roux, T. M. Wolff, and J. P. Meyer, "Using CFD and ray tracing to estimate the heat losses of a tubular cavity dish receiver for different inclination angles," Solar Energy, vol. 211, pp. 1137-1158, 2020/11/15/ 2020, doi: https://doi.org/10.1016/j.solener.2020.10.054.

[23] W. G. Le Roux, T. Bello-Ochende, and J. P. Meyer, "The efficiency of an open-cavity tubular solar receiver for a small-scale solar thermal Brayton cycle," Energy Conversion and Management, vol. 84, pp. 457-470, 2014/08/01/ 2014, doi: https://doi.org/10.1016/j.enconman.2014.04.048.

[24] M. Villarini, R. Tascioni, A. Arteconi, and L. Cioccolanti, "Influence of the incident radiation on the energy performance of two small-scale solar Organic Rankine Cycle trigenerative systems: A simulation analysis," Applied Energy, vol. 242, pp. 1176-1188, 2019/05/15/ 2019, doi: https://doi.org/10.1016/j.apenergy.2019.03.066.

[25] M. Schmitz, G. Ambrosetti, T. Cooper, and A. Steinfeld, "On-sun optical characterization of a solar dish concentrator based on elliptical vacuum membrane facets," Solar Energy, vol. 153, pp. 732-743, 2017/09/01/ 2017, doi: https://doi.org/10.1016/j.solener.2017.06.009.

[26] M. J. Brooks et al., "SAURAN: A new resource for solar radiometric data in Southern Africa," Journal of Energy in Southern Africa, vol. 26, pp. 2-10, 2015.

[27] S.-C. Costa et al., "Solar Salt Latent Heat Thermal Storage for a Small Solar Organic Rankine Cycle Plant," Journal of Energy Resources Technology, vol. 142, no. 3, 2019, doi: 10.1115/1.4044557.

MAGNETITE THERMAL ENERGY STORAGE FOR CSP PLANTS

Muhammad Sheik[1], Tshiamo Segakweng[2], and Karabelo Sekhuthe[3]

[1] CSIR, Meiring Naude Road, Brummeria, Pretoria, South Africa; Phone: 012 841 4132; Email: MSheik@csir.co.za

[2] CSIR; E-mail: TSegakweng@csir.co.za

[3] CSIR; E-mail: KSekhuthe@csir.co.za

Abstract: The Department of Mineral Resources and Energy estimates that the industrial sector is the largest consumer of energy in South Africa. Approximately 66% of energy end-use in industry is for heat generation during manufacturing. South African industry has been previously developed in the context of low energy prices for coal and electricity. This has resulted in a wide range of industrial processes that are inefficient and carbon intensive. With rising fuel prices, the prospect of fossil fuel depletion, and the continuous global effort to minimise environmental impact, it is necessary to develop alternate energy sources for heat generation. A significant portion of thermal energy can be generated using solar technology. However, solar energy supply is variable in nature and does not always match demand. It is therefore necessary to integrate thermal energy storage systems into solar plants to ensure availability. Thermal energy can be stored in three main ways namely, sensible, latent and thermochemical heat form. Magnetite is a material that undergoes an antiferromagnetic phase change at ~570 °C. This causes a reversible spike in the heat capacity of the material. This is highly advantageous for thermal energy storage applications and allows it to store more heat than other typical sensible storage media. Magnetite is widely available in South Africa and is often a waste product of other production processes. A lab-scale prototype was developed to analyse the thermal storage characteristics of magnetite in an open (non-pressurised) system with air as the working fluid. The magnetite was heated using a gas burner in a packed bed reactor and discharged using ambient air. Magnetite has the ability to store heat up to 1000 ºC which makes it suitable for CSP plants. The experimental results will be used to validate a CFD model to inform future CSP plant designs and for industrial process heating applications.

Keywords: Thermal Storage; Magnetite; Packed Bed Reactor

1. Introduction

With the world moving towards renewable energy, recent years have also seen advances in a range of storage technologies. It has been argued that because thermal energy storage (TES) has a combination of high power density and low energy costs making it an interesting option as a long-term storage technology. Thermal energy can be stored in three main ways namely; sensible, latent and thermochemical heat form. Sensible heat is the simplest method to store thermal energy and depends on the temperature change, mass of storage material and specific heat capacity of the material. TES technology is advancing, and it is imperative to use a low-cost thermal energy storage material (TESM), so as to stay economically relevant in a new growing field [1].

TES systems use electricity/heat to heat up a material. The heated material is then stored in an insulated container to store the energy until it is needed. The heat can be converted back to electricity through a power conversion device, or it can be used directly for process heating applications in industry.

One of the central issues associated with thermal energy storage is the development of a working body that has desirable properties (i.e., thermal conductivity, heat capacity, density, price, availability, and eco-friendliness). The main issue of a great number of current technologies is the excessive capital cost, which can prevent them from being successful in a market with no incentive schemes.

The International Energy Agency has drawn up categories that a thermal energy storage material is supposed to satisfy, the list is as follows [2]:

- Low commercial cost
- Acceptable eco-balance
- Stable up to 1000 °C
- Large thermal storage capacity (higher than 2.6 $MJ/m^3.K$)
- Available in industrial quantity
- Important lifetime (over 25 years)
- Compatibility with the HTF; and
- Easy implementation.

Magnetite is a common iron oxide (Fe_3O_4) mineral found in

rocks. It is the most commonly mined iron ore [3]. Magnetite is recognized as an inert compound that is almost entirely nontoxic to all living organisms [4], and its thermophysical properties have been researched and seem to be suitable and stable for TES applications.

Magnetite has been shown to have many advantages such as high availability, low cost, ecological friendliness, and non-flammability [1]. The one disadvantage of magnetite is its low thermal conductivity, and for this reason it has not been studied extensively for TES applications.

The most interesting characteristic of magnetite is the heat capacity which makes it an attractive material for TES. At approximately 570 °C it undergoes an antiferromagnetic phase transition which is reversible. This causes a spike in the heat capacity (refer to Figure 1) of the material. This is highly advantageous for thermal energy storage applications as heat is not only stored sensibly but also in latent form. Therefore, magnetite can store more heat than typical sensible heat storage materials such as rock and sand.

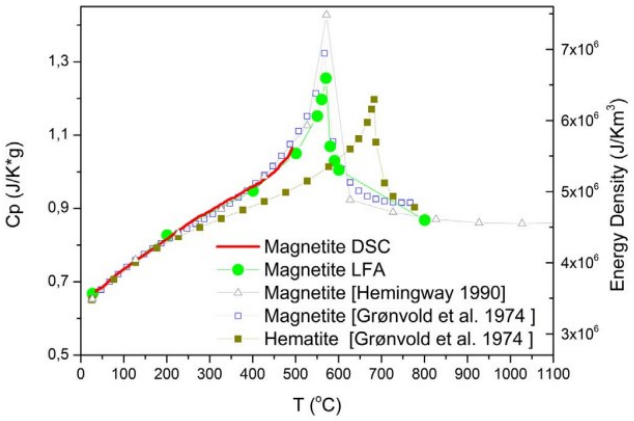

Figure 1. Heat capacity and energy density of magnetite [1]

Thermal energy storage is a crucial component of CSP systems, allowing them to generate electricity beyond daylight hours [5]. Excess thermal energy generated during sunny periods is stored as heat in various storage mediums with high heat retention properties. This stored thermal energy can then be used to continue producing steam and electricity during periods when the sun isn't shining, allowing them to provide reliable electricity output, thereby contributing to renewable energy generation with reduced intermittency. Magnetite has the ability to store heat up to 1000 ºC which makes it suitable for CSP plants [6]. Magnetite could be integrated into a thermal storage system of a CSP plant. During the charging phase, when the CSP plant is producing excess heat, the heat could be used to heat up the magnetite, storing thermal energy in the material. During the discharging phase, when electricity generation is required but there is no sunlight, the heat stored in the magnetite can be released to produce steam and drive turbines for electricity generation [7]. The system used in this investigation was regenerated at approximately 750 ºC (which is achievable by concentrated solar collectors) and the experimental results are presented and used to validate a CFD model.

There is limited research on the applications of magnetite for heat storage currently. The aim of this paper is to investigate the performance of magnetite for high-temperature thermal storage applications.

2. Experimental Apparatus

2.1. Test Rig

A packed bed thermal storage rig was developed at the Council for Scientific and Industrial Research (CSIR). The major components include a blower, LPG burner and packed bed reactor. The setup is shown in Figure 2.

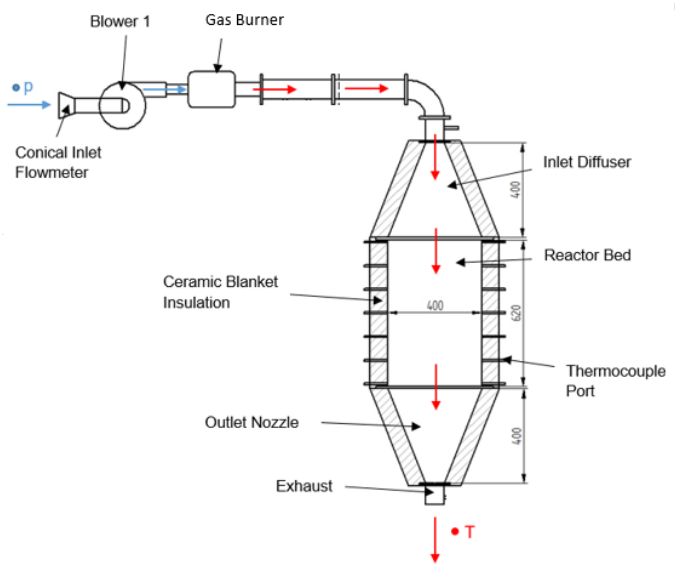

Figure 2. Diagram of packed bed test rig

For the charging cycle, the blower draws in air from the environment, through the conical inlet flow meter. The pressure differential at the throat of the conical inlet is measured to determine the mass flow through the rig. The air is then heated by the gas heater where the temperature is increased to ~750 ºC. The arrows in Figure 2, represent the flow path of the air moving through the system. Blue is representative of ambient air while red is representative of hot air. The hot air, exiting the burner, is supplied to the packed bed reactor.

The cylindrical packed bed reactor has a diameter of 400 mm and a height of 620 mm which constitutes an active volume of approximately 78 litres. A diffuser is attached to the inlet of the packed bed to distribute the air more evenly. A nozzle is attached to the exit of the packed bed to allow a smoother flow of air through

the rig. To minimise heat losses to the environment, the reactor wall is insulated with a ceramic fibre blanket of 75 mm thickness.

2.2. Temperature Sensor locations

The reactor comprises of several thermocouple ports to determine the temperature profiles through the packed bed. The thermocouples were positioned at 100 mm increments (refer to Figure 3) along the axis of the reactor.

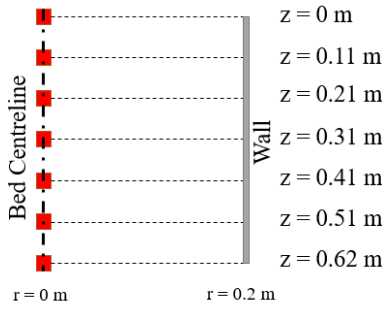

Figure 3. Thermocouple locations in packed bed reactor

2.3. Magnetite Samples

Approximately two hundred kilograms of Fine grade Magnetite (80-86% passing 45 μm) was purchased from a local supplier with a magnetite content of ≥95% and a density of >4500 kg/m^3. The powder was then compacted, at 'CERadvance Engineering Ceramics' to form 20x20 mm cylinders (refer to Figure 4) to allow for packing into a reactor for testing. The cylinders were randomly packed into the reactor.

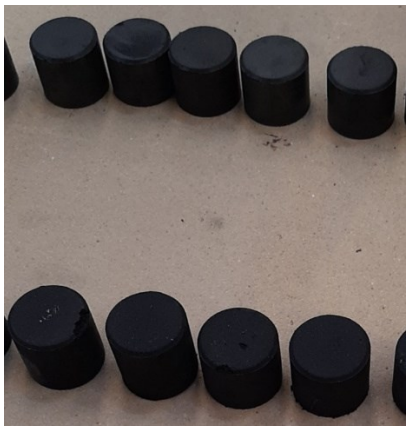

Figure 4. Magnetite samples at CERadvance

3. Experimental Results

The magnetite was heated from the top of the packed bed reactor and left to stand, for approximately 15 minutes, during which the flow direction was reversed. Ambient air was then supplied to the reactor until the heat was completely discharged. The primary type of thermal storage is sensible heat storage which is a direct form of heat storage and is a function of the temperature, heat capacity of the storage medium, and the mass of the storage medium. However, at a temperature of approximately 570 ºC, a phase change occurs in magnetite which causes a spike in the heat capacity of the magnetite. This is referred to as an antiferromagnetic change which allows additional heat (latent heat) to be stored in the medium.

3.1. Temperature

The temperature profiles achieved during testing are presented in Figure 5. The air temperatures were measured using K-type thermocouples, which were calibrated by 'Repair and Metrology Service (Pty) Ltd,' with a maximum deviation of 0.2 ºC. In region 1 (between t=0 h and t=1.75 h), the temperature of the air, entering the reactor (z=0 m), was ramped up to 750 ºC using a gas burner. The temperature was transferred from the upper layers to the lower layers as depicted by the thermocline moving through the packed bed. The burner and blower were shut off (at t=1.75 h) when the outlet temperature approached 250 ºC. This was due to a temperature limitation on the thermal plastic exhaust hose. However, at this point in time, at least half the reactor (z=0.3m) was heated to above 600 ºC which is beyond the antiferromagnetic phase change which occurs at ~570 ºC. This would have enabled the magnetite to store some latent heat in addition to the sensible heat stored. Between t = 1.75 h and t=2 h (region 2) the bed was left to stand, to change the system configuration, to reverse of the flow direction for discharging the heat stored. In region 3 (t=2 h to t=5 h) ambient air (at approximately 20 ºC) was supplied until the entire packed bed was cooled.

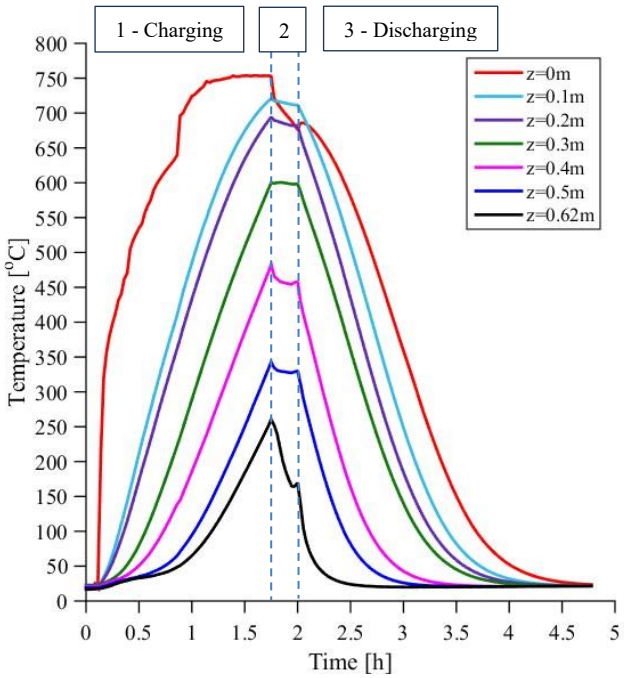

Figure 5. Temperature profiles

3.2. Mass flow rate

The mass flow rate results are presented in Figure 6. Between t=0 and t=1h the gas flame was not consistent which caused the air flow rate to fluctuate. The blower speed was carefully controlled to ensure that the temperature achieved was adequate for heating up the magnetite. As the temperature was ramped up the flow rate did stabilise at approximately 96 kg/h for the charging cycle. In region 2 the blower was switched off and therefore the flow rate was 0 kg/h. For the discharging cycle, since there were no limitations on flow rate it was increased to 115 kg/h.

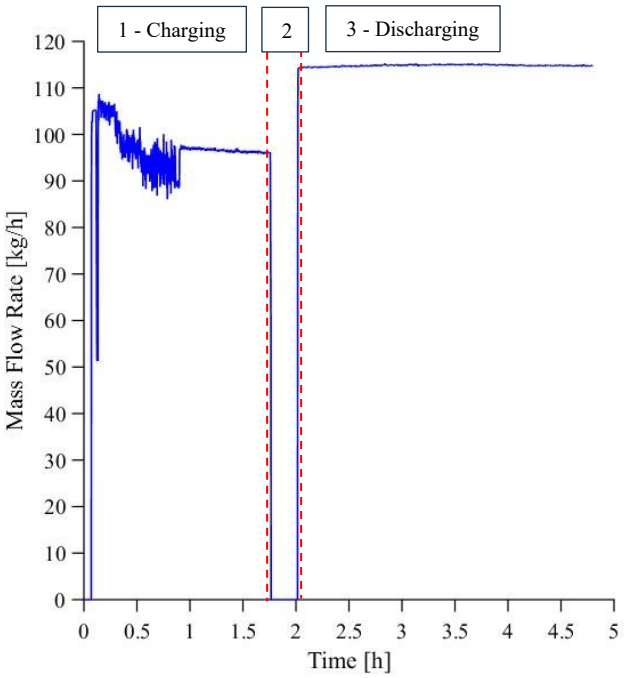

Figure 6. Mass flow rate

3.3. Heat Stored and Discharged

The amount of energy stored and released is presented in Figure 7. This was calculated from the product of the mass flow rate, specific heat capacity and temperature difference between the inlet and outlet of the reactor. By integrating the curves shown (in MATLAB) it was calculated that 25.05 kWh was absorbed by the magnetite during charging and 22.55 kWh was released from the reactor during discharging. This equates to an overall efficiency on 90%. This can be improved by increasing the thickness of the insulation surrounding the reactor.

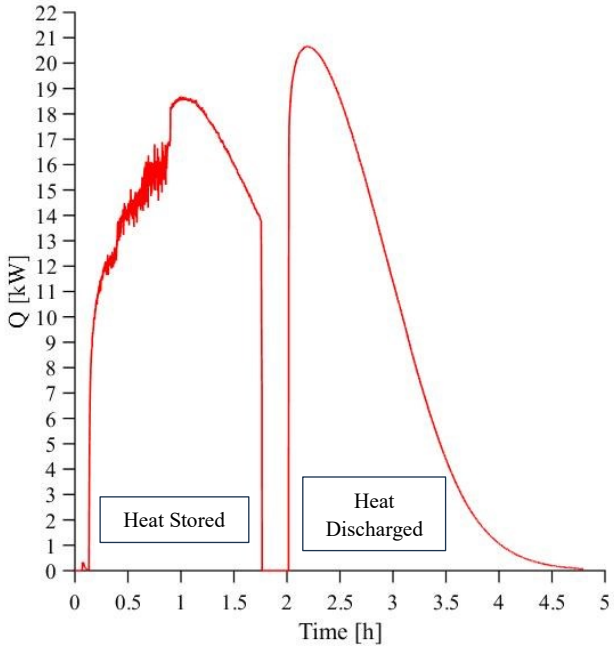

Figure 7. Heat stored and discharged

4. CFD Model

A CFD model was set up in FloEFD to model the heat storage in magnetite. The steps taken to set up the model are described in the next sections.

4.1. Solid Materials

- Packed bed walls and inlet and outlet cones: Inconel (selected from database)
- Insulation: Ceramic Fibre Blanket (User defined)

4.2. Assumptions

- Density of Magnetite powder: 4500 kg/m^3
- Void fraction: 0.5 (Calculated based on magnetite mass, density and reactor volume)
- The packed bed can be modelled as a porous medium

4.3. Steps taken to define porous medium

4.3.1. Pressure Drop

The Eisfeld and Schnitzlein equation was used to determine the pressure drop through the packed bed, with respect to flow rate, and can be calculated from equation 1 [8]. This equation is based on experimental data and accounts for particle shape, effect of Reynolds number on coefficients and wall effects. The results agree with the widely used Ergun equation [9] for lower mass flow rates (between 0 and 0.035 kg/s) as shown in Figure 8.

$$\frac{\Delta P}{Z\rho_f {U_z}^2}\mathrm{D}\frac{\varepsilon^3}{(1-\varepsilon)} = \frac{190{A_w}^2}{Re_{Erg}} + \frac{A_w}{B_w} \quad (1)$$

Where:

$$Re_{Erg} = \frac{\rho_f U_z D}{\mu_f(1-\varepsilon)} \quad (2)$$

$$A_w = 1 + \frac{2}{3(D_r/D)(1-\varepsilon)} \quad (3)$$

$$B_w = [2(D_r/D)^2 + 0.77]^2 \quad (4)$$

$$D = \frac{6\sum V_p}{\sum A_p} \quad (5)$$

Z: Height of packed bed (m)

ΔP: Pressure drop through packed bed (Pa)

U_z: Superficial fluid velocity (m/s)

ε: Bed void factor

ρ_f: Density of fluid flowing through packed bed (kg/m^3)

μ_f: Viscosity of fluid flowing through packed bed (Pa.s)

D: Particle size (m)

D_r: Diameter of reactor (m)

V_p: Particle volume (m^3)

A_p: Particle surface area (m^2)

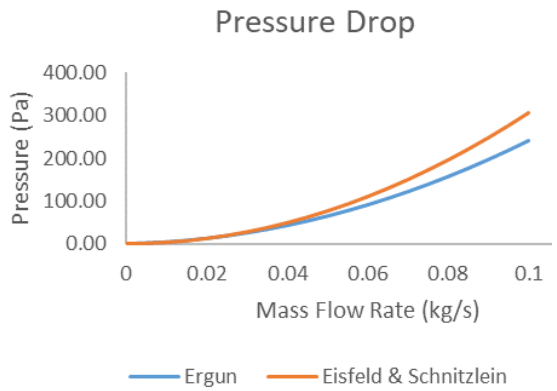

Figure 8. Pressure drop vs mass flow rate

4.4. Boundary Conditions

4.4.1.Charging

- Inlet (top): Experimental inlet temperature and mass flow rate
- Outlet (bottom): Ambient pressure

4.4.2. Discharging

- Inlet (bottom): Ambient temperature (~20 ºC) air at flow rate of ~0.032 kg/s
- Outlet (top): Ambient pressure

4.5. Running the model

During the charging cycle, approximately half the packed bed was heated to at least 600 ºC which took 1.75 h. The bed was left standing for 0.25 h as was done in during experimental testing. The discharging cycle was run thereafter by supplying air at approximately 20 ºC, until the entire packed bed cooled to ambient, which also took approximately 2.5 h. The temperature distribution through the packed bed is shown in Figure 9 at a time of 1.75 h.

4.6. Validation of model against experimental data

The experimental results and the CFD temperature profiles are plotted on the same set of axes in Figure 10. There is a good correlation between the two. Figure 11 shows the energy stored and discharged for CFD Model and experimental testing on the same plot. The results agree within 5% which is generally acceptable in literature [10]. The deviation could be due to the fact that the magnetite was mixed with approximately 5 wt% binder, before compacting, which could have affected the thermal properties and density slightly. The reactor also contains several thermocouple ports which could have led to leaks and heat losses, although great care was taken during testing to ensure that the ports were sealed.

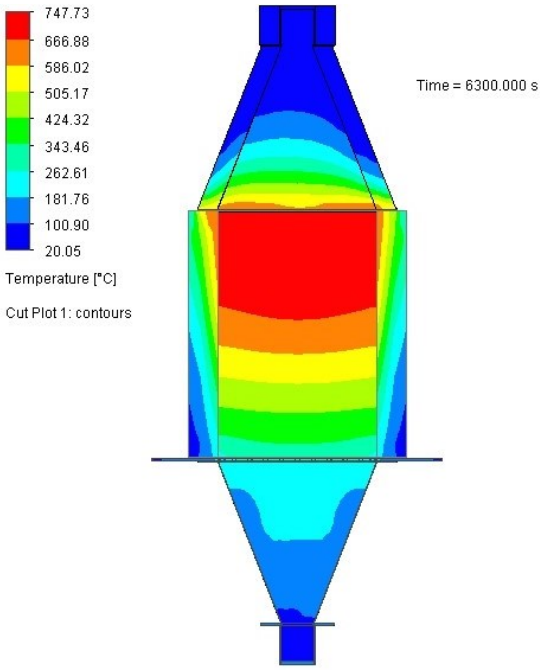

Figure 9. Magnetite packed bed CFD model

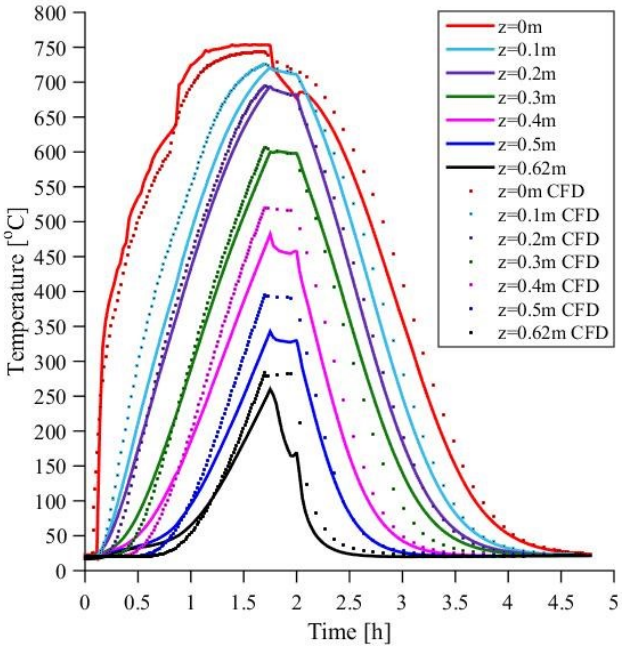

Figure 10. Experimental and CFD temperature profiles

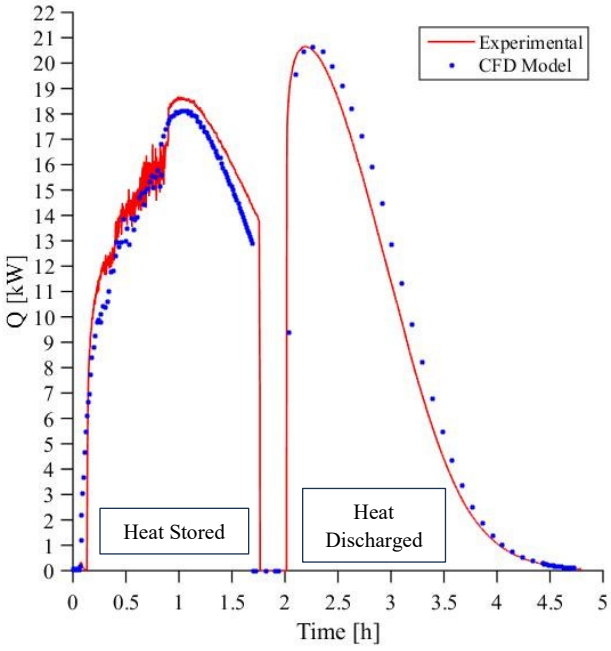

Figure 11. Energy stored and discharged in experimental and CFD model

5. Conclusion

Magnetite is a promising material for thermal storage and has the ability to store heat up to 1000 ºC, which makes it suitable for CSP plants and industrial regenerators. A lab-scale prototype was setup to investigate the performance of magnetite for high-temperature thermal storage applications. Since the antiferromagnetic phase change occurs at ~570 °C, the magnetite in the upper half of the reactor was heated to above 600 ºC. The entire packed bed could not be heated due to temperature limitations on the exhaust of the reactor. After heating the magnetite, ambient air was supplied to discharge the heat stored. From the experimental results, it was calculated that 25.05 kWh was absorbed by the magnetite during charging. This equates to an energy storage density of 320 kWh/m^3. During discharging 22.55 kWh was released from the reactor which results in an overall efficiency of 90% which is higher than a typical sensible heat storage system of 70% [11]. A CFD model was developed to inform future CSP plant designs and for industrial waste heat recovery applications. The experimental results were used to successfully validate the CFD model.

References

[1] Y. Grosu, A. Faik, I. Ortega-Fernández and B. D'Aguanno, "Natural Magnetite for thermal energy storage: Excellent thermophysical properties, reversible latent heat transition and controlled thermal conductivity," *Solar Energy Materials & Solar Cells,* no. 161, pp. 170-176, 2017.

[2] Y. F. Baba, H. Ajdad, A. . A. Mers, Y. Grosu and A. Faik, "Multilevel comparison between magnetite and quartzite as thermocline energy storage materials," *Applied Thermal Engineering,* vol. 149, pp. 1142-1153, 2019.

[3] H. M. King, "Magnetite and Lodestone," Geology News and Information, [Online]. Available: https://geology.com/minerals/magnetite.shtml. [Accessed June 2022].

[4] B. Kalska-Szostko, U. Wykowska, D. Satula and P. Nordblad, "Thermal treatment of magnetite nanoparticles," *Beilstein Journal of Nanotechnology,* vol. 6, pp. 1385-1396, 2015.

[5] M. Mehos and H. Price, "Concentrating Solar Power Best Practices Study," June 2020. [Online]. Available: https://www.nrel.gov/docs/fy20osti/75763.pdf. [Accessed 14 August 2023].

[6] H. Qiu, W. Y, H. Chen, R. Wang, J. Yu and Y. Lin, "Influence of SiC on the thermal energy transfer and storage characteristics of microwave-absorbing concrete containing magnetite and/or carbonyl iron powder," *Construction and Building Materials,* vol. 366, no. 0950-0618, p. p.130191, 2023.

[7] U.S. Department of Energy, "Concentrating Solar-Thermal Power Basics," Solar Energy Technologies Office, [Online]. Available: https://www.energy.gov/eere/solar/concentrating-solar-thermal-power-basics. [Accessed 14 August 2023].

[8] K. G. Allen, T. W. von Backström and D. G. Kröger, "Packed bed pressure drop dependence on particle shape, size distribution, packing arrangement and roughness," *Powder Technology,* vol. 246, pp. 590-600, 2013.

[9] D. Thornhill, "Flow Through Packed Beds," University of Washington, [Online]. Available: https://faculty.washington.edu/finlayso/Fluidized_Bed/FBR_Fluid_Mech/packed_beds_fbr.htm. [Accessed 14 August 2023].

[10] "What is the suitable and acceptable error variations between the CFD results and experimental data?," ResearchGate, [Online]. Available: https://www.researchgate.net/post/What-is-the-suitable-and-acceptable-error-variations-between-the-CFD-results-and-experimental-data. [Accessed 26 September 2023].

[11] A. H. Abedin and M. A. Rosen, "Closed and open thermochemical energy storage: Energy- and exergy-based comparisons," *Energy,* vol. 41, pp. 83-92, 2012.

INVESTIGATION OF SODIUM ACETATE TRIHYDRATE AS A LOW-GRADE HEAT STORAGE MATERIAL IN SOUTH AFRICAN DOMESTIC WATER HEATING

Cayley Hillier[1], Glen C. Snedden[2], Christian I. Basson[3], Matthew D. Brown[4], Graham Smith[5]

[1] Mechanical Engineering, University of KwaZulu-Natal, Howard College Campus, Durban, 4001, hillierc@ukzn.ac.za

[2] Mechanical Engineering, University of KwaZulu-Natal, Howard College Campus, Durban, 4001, Email: sneddeng@ukzn.ac.za

[3] Mechanical Engineering, University of KwaZulu-Natal; Email: bassonc@ukzn.ac.za

[4] Electrical Engineering, University of KwaZulu-Natal; Email: brownm1@ukzn.ac.za

[5] Mechanical Engineering, University of KwaZulu-Natal; Email: smithg@ukzn.ac.za

Abstract: With South Africa amidst an energy crisis, there is a need to re-evaluate current domestic water heating technology by implementing more efficient water heating systems, not only to help relieve excess pressure on the national power grid but to reduce consumer costs. Thermal energy storage (TES), more specifically the use of latent heat storage systems, provides a unique solution with the ability to take advantage of excess renewable energy, off-peak electricity tariffs and waste heat from industry which can be stored for later use. Latent heat storage is achieved using phase change materials (PCMs), specifically solid-liquid PCMs. These are classified into organic and inorganic substances that store and release energy when needed. Inorganic salt hydrates, specifically sodium acetate trihydrate (SAT) and its mixtures are presented in the following study. The high energy density, melting temperature of 58°C and relative stability in a supercooled state make SAT an ideal PCM candidate for TES and domestic water heating applications. Through small-scale experiments, including a Modified T-History method and simple heat loss method, the thermophysical and behavioural properties of SAT and its mixtures with excess water and Xanthan Gum were analysed. The T-History method confirmed that the latent heat of fusion of the SAT supplied was 248.7 kJ.kg. The simple heat loss method determined that the heat content of SAT with excess water decreased with an increasing percentage of additional water. It was also observed that the addition of Xanthan Gum of between 0.4-0.5 wt.% increased the heat content although not as significantly as in the comparative literature. However, a decrease in phase separation and spontaneous nucleation was observed with the Xanthan Gum stabilizing the solution. The results indicated that SAT shows potential as a viable alternative for on-demand domestic hot water applications in South Africa.

Keywords: Thermal energy storage; Phase change material; Sodium acetate trihydrate; Domestic water heating

1. Introduction

Electric water heating accounts for roughly 40% of the energy consumed by South African households [1]. It is estimated that of the 17 million South African households, 5.4 million use electric geysers amounting to 40 GWh of electricity usage daily. At peak times, it is noted that these water heaters account for drawing an estimated 12% (4 GW) of the power grid's operating capacity [2]. Implementation of the most appropriate PCMs and efficient heat exchanger designs are two key aspects to developing a successful TES system for domestic use.

1.1. SAT as a TES material

SAT or $NaCH_3COO \cdot 3H_2O$ is an inorganic salt hydrate that releases heat when crystalizing and changing phase between liquid and solid. It is a compound of water, acetic acid and sodium consisting of 60.3 wt.% sodium acetate and 39.7 wt.% water. Some of the most attractive properties include a high energy density with a heat of fusion of 264 kJ/kg, a melting temperature of 58°C (falling in the ideal temperature range for domestic hot water heating) and the ability to supercool and remain stable at ambient temperatures. Aside from being a mild skin irritant, SAT is also non-toxic, not flammable and is a relatively low-cost material which is available in large quantities. [3], [4], [5], [6], [7]

1.1.1. Associated challenges using SAT

One of the primary problems of using SAT is incongruent melting which causes phase separation where anhydrous sodium acetate precipitate forms. The anhydrous crystals settle at the bottom of the container and are unable to react with the water which settles at the top due to differing densities. As the amount of precipitate increases with every cycle, over time the heat storage capacity is reduced.

There are several ways to help combat incongruent melting and consequential phase separation. One way is in the container design itself. Dannemand *et al.* [8] found that phase separation was reduced when decreasing the height of the material by designing SAT containers with reduced heights. Another way includes altering the mixture itself with additives such as extra water and thickening agents. The extra water principle reduces

the formation of anhydrous crystals maintaining a saturated solution. However, negative impacts of this method include a decrease in volumetric heat storage capacity and a potential decrease in thermal conductivity [4], [9]. Finally, numerous thickening agents have been widely tested throughout the literature including Carboxy-Methyl Cellulose, Xanthan Gum and solid and liquid polymer additives [7], [10], [11]. The addition of Xanthan gum was a focus in the following experiments due to availability and the ability to increase the heat content of the storage material.

1.1.2. Triggering SAT

As SAT has the ability to supercool up to 90°C below its nucleating temperature, this means that nucleation must be initiated by a "triggering method". Implementing triggering methods brings about additional complexities as it must be reliable over hundreds if not thousands of charging and discharging cycles [11]. Methods of activation include introducing a SAT crystal (seed crystal) into to the supercooled mixture, creating a "cold spot" using liquid carbon dioxide or using a Peltier device to initiate cooling below the maximum degree of supercooling for SAT. The advantage of using a material that can be triggered is that heat can be stored and discharged only when needed.

2. SAT applications for domestic water heating

SAT storage can be applied to South African domestic water heating in several ways. Several studies have incorporated PCMs into standing hot water tanks [6]. As seen in Fig. 1a), one way is by submerging the PCM which is encapsulated in tubes or spheres to maintain the internal hot water temperature. Another way, in Fig. 1b) is by creating an outer layer around the geyser tank which can be triggered, helping to reduce heat loss to the surroundings, thus maintaining the internal water temperature and reducing reheat time. Both these methods above aim to reduce standing losses.

Another application seen in Fig. 1c) focuses on creating an on-demand water heating vessel. The concept includes a modular storage vessel with heat exchange pipes where cold water enters a module where the PCM has been triggered and the number of activated modules will depend on the user demand. *SUNAMP*, a company based in the United Kingdom, currently offers a modular heat storage battery utilizing a SAT-based PCM which replaces boilers for water and space heating [12]. Water is heated as needed by the consumer using a heat exchanger and the PCM, *Plentigrade P58*. Once fully discharged the PCM is then recharged using an immersed heating element.

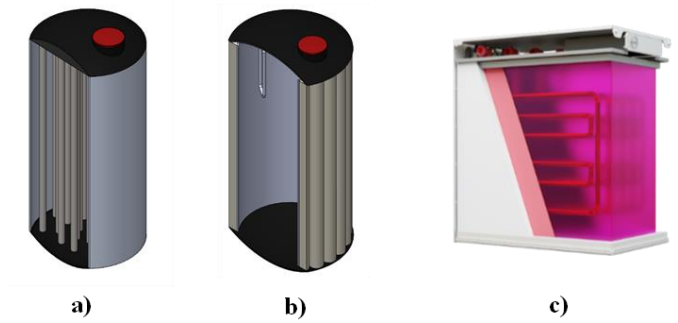

Fig. 1. a) Hot water tank with PCM encapsulated in tubes b) Hot water tank with outer layer of PCM c) Picture showing the internal structure of the *SUNAMP Thermino* heat battery [12]

In the above-mentioned concepts, thermal cycling of the PCM, the power sources for reheating and the related consumption needed to achieve this is crucial for ensuring that the storage system is energy efficient. For example, *SUNAMP* thermal batteries offer integration for reheating with one or multiple power sources which are interchangeable, including grid power, heat pumps and solar technology. Due to the proprietary nature of *SUNAMP's* SAT-PCM mixture, it is necessary to conduct research on the development of a material and system unique to South Africa's heating needs and power supply challenges.

3. Experimental Method

Two experiments were conducted to validate the properties and observe the behaviour of SAT. The SAT was purchased from *Thermo Fisher Scientific*. The experiments include the T-History Method developed by Zhang *et al*. [13], Modified T-History Method by Hong *et al*. [14], [15] and a simple heat loss method (SHLM) by Kong *et al*. [7].

3.1. T-History Method

Zhang *et al.* [13] developed the original T-history method in the 1990s which was later modified in 2003 by Hong *et al* [14], [15] to improve accuracy. The experiment was used to determine the specific heat capacity of SAT in both solid and liquid states as well as the latent heat of fusion. The experiment was set up as seen in Fig. 2.

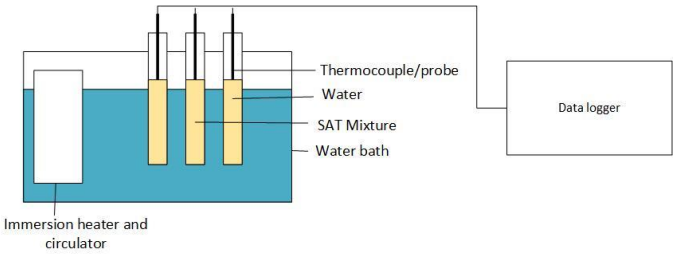

Fig. 2. Schematic diagram of the T-History experiment setup

Eight SAT samples were tested over four experiments. The procedure consisted of filling and heating three 150 x 16 mm test tubes to 80°C using a hot water bath. Two tubes were filled to 80 mm (15 grams) with SAT and one to 80 mm (±12 ml) with water. When thermal equilibrium was reached, the tubes were removed from the bath and exposed to the ambient temperature. Once cooled to ± 48°C, the SAT samples were triggered with an SAT crystal and then allowed to cool to room temperature as seen in Fig. 3. Temperature readings for each sample and the ambient temperature were taken throughout the cooling process.

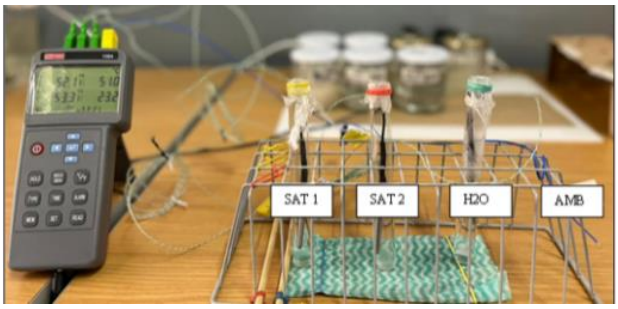

Fig. 3. T-History experimental setup

Fig. 4 and Fig. 5 represent the cooling process for SAT and water respectively, and the calculation of the inflection point. The cooling curves were used to extract specific points which were substituted into the energy equations, Equations (1)-(6) derived in Hong *et al*. [14]. The validity of the method is based on the Biot number ($Bi = hr/k$) which should be less than 0.1. By meeting these criteria, the lumped capacitance method is applicable and the temperature distribution inside the test tubes can be regarded as uniform.

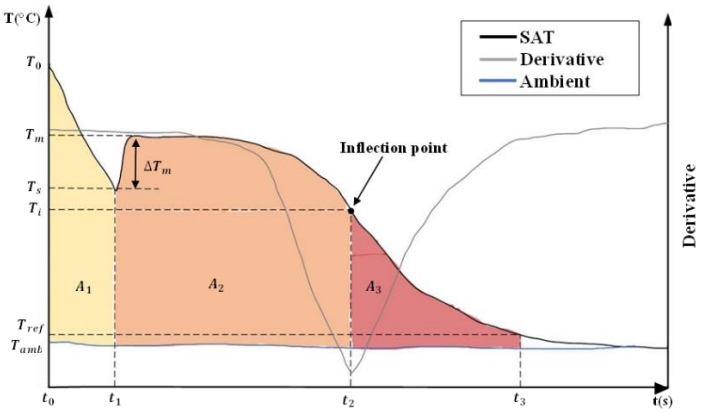

Fig. 4. Representation of a modified T-History curve during cooling of SAT (adapted from Hong *et al.* [14], [15])

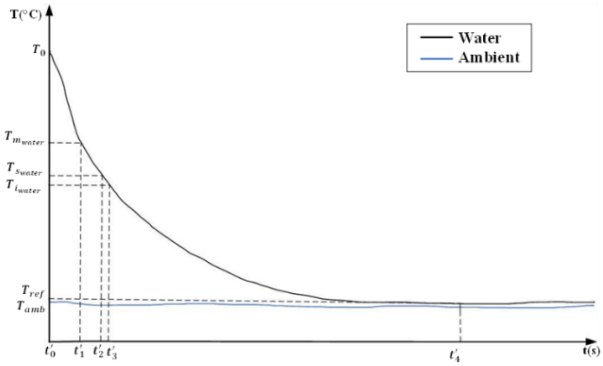

Fig. 5. Representation of a modified T-History curve during cooling of water (adapted from Hong *et al.* [14], [15])

$$\left(m_{tube}c_{p_{tube}} + m_{SAT}c_{p_{SAT(L)}}\right)(T_0 - T_s) = hA_{tube}A_1 \quad (1)$$

$$\left(m_{tube}c_{p_{tube}} + m_{SAT}\left(\frac{c_{p_{SAT(L)}} + c_{p_{SAT(S)}}}{2}\right)\right)(T_m - T_i) + m_{SAT}H_{SAT} = hA_{tube}A_2 \quad (2)$$

$$\left(m_{tube}c_{p_{tube}} + m_{SAT}c_{p_{SAT(S)}}\right)(T_i - T_{ref}) = hA_{tube}A_3 \quad (3)$$

$$\left(m_{tube}c_{p_{tube}} + m_{water}c_{p_{water}}\right)(T_0 - T_s) = hA_{tube}A_{w,1} \quad (4)$$

$$\left(m_{tube}c_{p_{tube}} + m_{water}c_{p_{water}}\right)(T_m - T_i) = hA_{tube}A_{w,2} \quad (5)$$

$$\left(m_{tube}c_{p_{tube}} + m_{water}c_{p_{water}}\right)(T_i - T_{ref}) = hA_{tube}A_{w,3} \quad (6)$$

Where $A_1 = \int_{t_0}^{t_1}(T - T_{amb,\infty})\,dt$. Table 1 describes the other area ranges corresponding with Fig. 4 for SAT and Fig. 5 for water which apply through Equations (1)-(9).

Table 1. Area ranges used in Equations (1)-(9)

	SAT		Water	
Temperature Range	**Area**	**Time Range**	**Area**	**Time Range**
$T_0 - T_s$	A_1	$t_0 - t_1$	$A_{w,1}$	$t_0' - t_2'$
$T_m - T_i$	A_2	$t_1 - t_2$	$A_{w,2}$	$t_1' - t_3'$
$T_i - T_{ref}$	A_3	$t_2 - t_3$	$A_{w,3}$	$t_3' - t_4'$

Using Equations (1)-(6), the equations for the specific heat in the solid and liquid phase as well as the latent heat of fusion can be derived as follows:

$$C_{p_{SAT(S)}} = \frac{m_{water}c_{p_{water}} + m_{tube}c_{p_{tube}}}{m_{SAT}} \times \frac{A_3}{A_{w,3}} - \frac{m_{tube}}{m_{SAT}}c_{p_{tube}} \quad (7)$$

$$C_{p_{SAT(L)}} = \frac{m_{water}c_{p_{water}} + m_{tube}c_{p_{tube}}}{m_{SAT}} \times \frac{A_1}{A_{w,1}} - \frac{m_{tube}}{m_{SAT}} c_{p_{tube}} \quad (8)$$

$$H_{SAT} = -\left(\frac{m_{water}}{m_{SAT}} c_{p_{tube}} + \frac{c_{p_{SAT(L)}} + c_{p_{SAT(S)}}}{2}\right)(T_m - T_i) + \frac{m_{water}c_{p_{water}} + m_{tube}c_{p_{tube}}}{m_{SAT}} \times \frac{A_2}{A_{w,2}}(T_m - T_i) \quad (9)$$

3.2. Simple heat loss method (SHLM)

Kong *et al*. [7] developed the SHLM to evaluate the heat content of SAT. The method used a heated water sample to determine the heat loss coefficient (UA) of a well-insulated box. The coefficient was then used to determine the heat content (HT) of the supercooled SAT samples under the same conditions.

Fig. 6 below shows a schematic diagram of the experimental setup. Glass jars with lids containing the sample were placed into the well-insulated wooden box. Four thermocouples were used to take temperature measurements during cooling, three were attached to the outer surface of the jar and one was used to measure the ambient temperature.

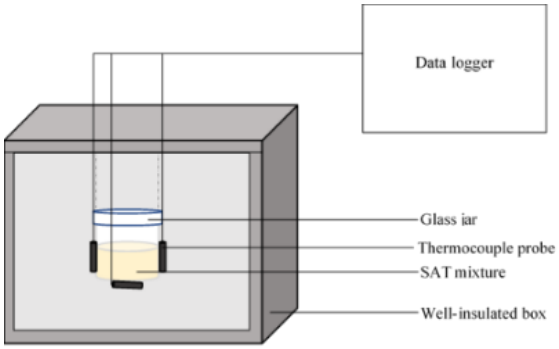

Fig. 6. Schematic diagram of the SHLM experimental setup

3.2.1.Determining the heat loss coefficient UA (W/K)

Using the well-known properties of water, the heat loss coefficient $UA\,(W/K)$ was determined by cooling down a heated sample of 150 ml of water to ambient temperature. UA was then calculated from the derived logarithmic equation below [7]. The masses and specific heat values which make up the total heat capacity (mc_p) of the sample include the glass jar, lid and water. The time period, Δt, was the time interval of the point calculated for the UA value. The points calculated for each time interval were then plotted against the sample temperature and a quadratic equation for the trendline was regressed with an appropriate R-square value.

$$UA = \frac{mc_p}{\Delta t} ln \left|\frac{T_{end} - T_{amb}}{T_{start} - T_{amb}}\right| \quad (10)$$

To attain the measurements for the SAT samples, eight samples were prepared. The first four samples had 150 grams of SAT mixed with increasing amounts of water (0 ml, 6 ml, 14.5 ml and 17.5 ml), the final weight percent of each being 40 wt.%, 42 wt.%, 45 wt.% and 46 wt.% respectively. The remaining four samples were carefully mixed with 150 grams of SAT and increasing amounts of Xanthan Gum powder (0.3 g, 0.45 g, 0.6 g and 0.75 g), the final weight percent of each being 0.2 wt.%, 0.3 wt.%, 0.4 wt.% and 0.5 wt.% respectively. These samples were melted and cooled to ambient temperature in glass jars and left in a supercooled state for between 7 and 40 days. A sample was then placed into the well-insulated box and the solution was triggered using a SAT crystal. The temperature data was recorded as the sample cooled back down to room temperature. Equation (11) was then used to determine the heat content (HT).

$$HT = \int_t^{t+\Delta t} UA(t)[T_{SAT}(t) - T_{amb}(t)]dt/m_{SAT} \quad (11)$$

4. Results

4.1. Modified T-History Method

The following results were attained from the four experiments and Fig. 7 shows an example of the resulting T-History curve and derivative curve from one of the experiments. From the differentiate the inflection point was determined for each experiment and the other relevant temperature points were taken from the recorded data.

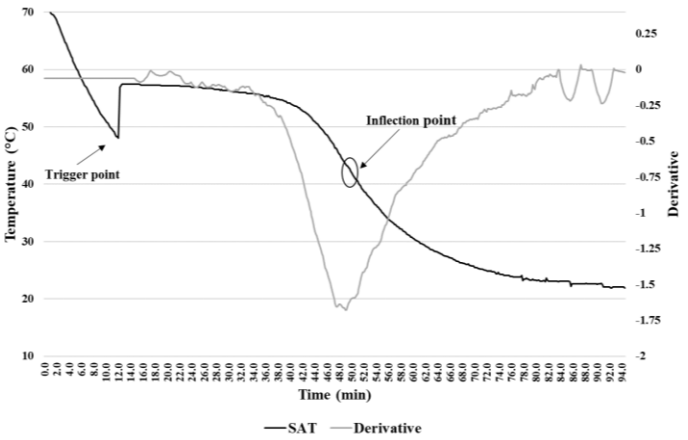

Fig. 7. T-History curve and inflection point of SAT

Table 2 summarizes the results from the eight samples and compares them to results attained in the literature.

Table 2. Results comparison of H_m, Cp_s and Cp_l

Sample	Cp_s ($kJ/kg{\cdot}K$)	Cp_l ($kJ/kg{\cdot}K$)	Hm (kJ/kg)
1A	2.58	3.33	237.23
1B	2.52	3.21	240.14
2A	2.20	3.54	268.14

2B	2.48	3.38	227.70
3A	2.32	3.26	254.30
3B	2.34	3.25	255.51
4A	2.35	3.11	252.27
4B	2.41	3.03	253.88
Average	**2.40**	**3.26**	**248.65**
Reference value [6]	1.68	2.37	266
Reference value [14]	2.25	3.77	245
Reference value [15]	2.26	3.74	245

Table 3 shows the temperatures at triggering (T_s), the maximum temperature reached after triggering (T_m) and the temperature of the inflection point (T_i).

Table 3. Temperature comparisons

Sample	Tm	Ts	Ti	$Tm - Ti$	$Ts - Ti$
1A	57.8	47.6	46	11.8	1.6
1B	57.8	47.9	46.9	10.9	1
2A	57.8	47.5	45.7	12.1	1.8
2B	57.6	47.2	46.4	11.2	0.8
3A	57.7	47.5	46.8	10.9	0.7
3B	57.9	48.3	44.9	13	3.4
4A	57.5	48	43.3	14.2	4.7
4B	57.9	47.7	47.6	10.3	0.1
Average	**57.8**	**47.7**	**46.0**	**11.8**	**1.8**
Reference [14]	58.0	47.3	44.1	14.0	3.3

4.2. SHLM

The following results were attained for the SHLM experiments. A 60-minute (3600s) time interval was used to calculate each point shown in Fig. 8 using Equation (10).

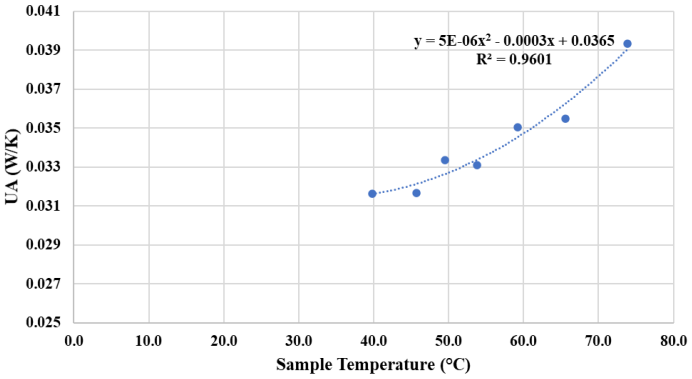

Fig. 8. An example of the regressed UA curve with quadratic equation

Three tests were repeated for each of the eight samples and the temperature data was used to calculate the heat content using Equation (11). Fig. 9 shows the results for the samples with the tested percentages of extra water and Xanthan Gum.

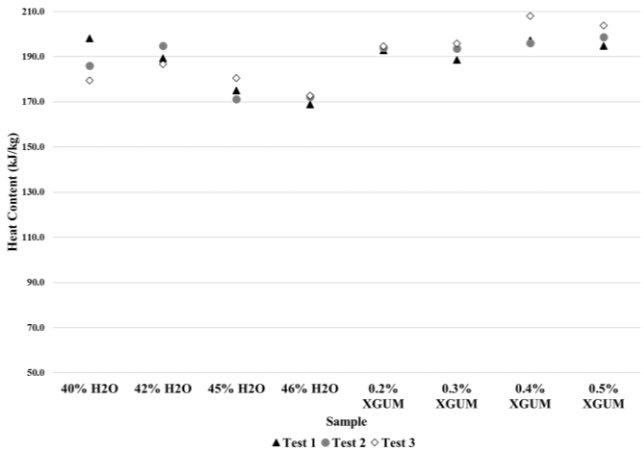

Fig. 9. Graph showing the heat content of the samples with extra water and Xanthan Gum

5. Discussion

5.1. Modified T-History Method

The results obtained for the Modified T-History method are seen in Table 2. With an average latent heat of fusion of 248.7 kJ/kg, this falls within 2% of the results obtained by Hong *et al.* [14], [15] and within 6.5% of the results obtained from differential scanning calorimetry (DSC) with a value of 266 kJ/kg [6]. There are several factors which can influence the experimental results including any variation in ambient temperature or air velocity in the room during cooling which would contribute to variance in the convective heat transfer coefficient. Another reason for deviation could also be in determining the point of inflection which in turn is used to determine the boundary between the sensible and latent heat released during cooling. The average temperature at the point of inflection (T_i) across all eight experiments was 46°C, nearly 2°C higher than the 44.1°C average attained by Hong *et al.* [14]. The increased temperature at the inflection point could decrease the area calculated for the heat released between the temperature points T_s and T_i thus reducing the latent heat of fusion (H_m). The latent heat of fusion is an important parameter to evaluate as it indicates how much energy is absorbed and released during the phase change of a PCM. This may vary depending on the supplier and purity of the PCM therefore determining baseline values using the T-History method aids in developing mixtures with different additives.

5.2. SHLM

5.2.1.Phase separation

Exploring ways to reduce phase separation is an important step in developing a TES system which operates successfully over hundreds if not thousands of cycles. Fig. 10 a) shows how phase separation occurs in a SAT sample with 42 wt.% water over 48-hours. After being supercooled for 48-hours an accumulation of sediment is seen at the bottom of the jar with a layer of water on

top. The supercooled SAT sample with 45 wt.% water in Fig. 10 b) shows no crystal accumulation due to the increased excess water ensuring a constantly saturated solution. Comparing the heat content calculated in Fig. 9 for each sample, an average decrease in the heat content of 14.7 kJ/kg between the 42 wt.% and 45 wt.% samples is observed. Therefore, although there is reduced phase segregation with increased extra water, there is a substantial decrease in the sample heat content. Despite that, for the SAT samples with lower water percentages, increased build-up of anhydrous crystal sediment occurs which cannot be dissolved also reducing the heat content over time.

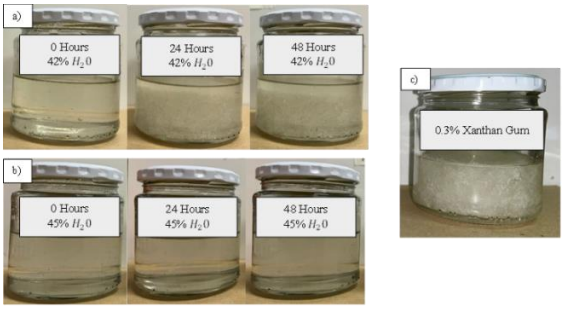

Fig. 10. a) Phase separation of SAT samples with 42 wt.% H_2O, b) Phase separation of SAT samples 45 wt.% H_2O and c) SAT sample with 0.3 wt.% Xanthan Gum

The use of Xanthan Gum as an additive aims to combat phase separation and increase heat content in the SAT samples. Fig. 10 c) shows the change in the consistency of a sample which is mixed with 0.3 grams of Xanthan Gum. The sample took on a more gelatinous texture during heating as the Xanthan Gum was carefully stirred in. After cooling, the sample showed a coarse but uniform texture throughout with no accumulation of water or crystals on the top or bottom of the container. It was noted however that during heating and reheating the Xanthan Gum accumulated in the top of the jar and needed to be stirred before cooling. Upon closer observation, small air bubbles seemed to be trapped within the gelatinous layer causing it to float to the top. In application, this would be a problem because at a larger scale the material cannot be manually stirred, and the separation may negatively impact the thermal performance and cyclability of the system.

5.2.2.Heat content of SAT with additional water

The heat content for SAT samples with 40 wt.%, 42 wt.%, 45 wt.% and 46 wt.% water were tested. The samples were prepared and supercooled for between 7 and 40 days with tests repeated a total of three times for each sample. Fig. 9 shows a graph with the heat content plotted for each sample. The highest average heat content at 190.3 kJ/kg was for the 42 wt.% mixture, however this mixture displayed significant phase separation. The sample with the lowest measured heat content was the 46 wt.% sample at 171.4 kJ/kg which showed no phase separation after all three tests. The 40 wt.% sample which had no extra water added shows a clear decrease in heat content after each test as seen in Fig. 9. This indicates that increasing phase separation occurring after each cycle does decrease the heat content which further emphasise the benefit of including additives to improve SAT mixtures.

5.2.3.Heat content of SAT with Xanthan Gum

The heat content for SAT samples with 0.2 wt.%, 0.3 wt.%, 0.4 wt.% and 0.5 wt.% Xanthan Gum were tested and like with the additional water samples, the samples were also supercooled for a period of between 7 and 40 days and the tests were repeated three times. Fig. 9 shows the resulting heat content measurements. The 0.4 wt.% sample had the highest average heat content at 200.5 kJ/kg after three tests. Generally, the average heat content for the 0.3 wt.%, 0.4 wt.% and 0.5 wt.% samples was between 10-25 kJ/kg lower compared to the results attained by Kong *et al*. [7]. Factors which may have contributed to achieving lower results include fluctuations in the ambient temperature as the tests were conducted over several weeks with the ambient temperature averaging between 17.5°C and 22°C. Deviations in ambient temperature affect the calculation of the area under the cooling curve used in Equation (11). Higher ambient temperatures result in decreased areas and a subsequent decrease in the heat content calculated.

6. Conclusion

Both the Modified T-History Method and SHLM were used to determine and verify the thermophysical and behavioural properties of SAT. The results attained from the Modified T-History Method allowed for the specific heat capacity in both the solid and liquid phase and the latent heat of fusion to be obtained. The values were comparable with the literature with latent heat of fusion averaging at 248.7 kJ/kg. The SHLM was used to determine and compare the heat content of SAT samples with excess water and Xanthan Gum. For the samples with extra water, the heat content was greatest in the 42 wt.% samples averaging at 190.3 kJ/kg however significant phase separation occurred over 48 hours. The 45 wt.% and 46 wt.% water samples had no phase separation but a much lower heat content averaging at 175.6 kJ/kg and 171.4 kJ/kg respectively. The addition of Xanthan Gum resulted in a solution with a more uniform texture throughout with no evidence of phase separation in any of the mixtures after supercooling in all three tests. Analysis of the heat content revealed that there was an increase in the Xanthan Gum sample mixtures with the highest average heat content in the 0.4 wt.% sample at 200.5 kJ/kg. However, the heat content overall for the Xanthan Gum mixtures was significantly lower compared to the results attained in the literature with a potential cause being a fluctuation in the ambient temperature during cooling. One

other shortcoming was the accumulation of the Xanthan Gum at the top of the container during heating and reheating. This was rectified during the experiments by stirring the mixture thoroughly before supercooling which would not be an appropriate solution in practical application. Overall, SAT shows promise as a candidate PCM in TES for domestic hot water heating in South Africa. Given that SAT can be supercooled and remain stable before being triggered on demand provides a great opportunity to offset the demand placed on the grid during peak consumption periods. Furthermore, SAT could reduce standing losses in geysers by helping maintain the hot water temperature for extended periods. Moving forward, SAT mixtures with extra-water in the region of 42-43 wt.% will be used to conduct further research on the most appropriate heating configurations. The intention is to reduce phase separation sufficiently without significantly compromising on heat content to draw more accurate conclusions on the prospect of TES scalability using SAT. However, further research needs to be done on refining the PCM mixture, additives, preparation and containment methods to ensure the storage unit can operate over hundreds if not thousands of cycles.

Acknowledgements

This research was supported by the J W Nelson fund.

Nomenclature

m	Mass (kg)
c_p	Specific heat capacity (kJ/kg.)
T	Temperature (°C)
h	Convective heat transfer coefficient (W/m²K)
k	Thermal Conductivity (W/m. K)
A_{tube}	Convective heat transfer area of a tube (m²)
A	Designated area under the curve
H_m	Latent heat of fusion (kJ/kg)
r	Tube radius (m)
E	Heat content (kJ/kg)
UA	Heat loss coefficient (W/K)
HT	Heat Content (kJ/kg)
t	Time (s)

Subscript

l	Liquid	i	Inflection point
s	Solid/solidification	ref	Reference point
amb	Ambient	m	Melting point
w	Water	XGUM	Xanthan Gum

References

[1] M. Kakaza and K. Folly, "Effect of solar water heating system in reducing household energy consumption," *IFAC - PapersOnLine,* vol. 48, no. 30, pp. 468-472, 2015.

[2] M. Booysen, "Smart water heating could help in South Africa's Energy Crisis," The Conversation, 2 February 2020. [Online]. Available: https://theconversation.com/smart-water-heating-could-help-in-south-africas-energy-crisis-130726#:~:text=The%20estimated%205.4%20million%20electric,electricity%20grid%20at%20peak%20times.. [Accessed 17 January 2022].

[3] I. Dinçer and M. A. Rosen, Thermal Energy Storage; Systems and Applications (2nd Edition), John Wiley & Sons, Ltd, 2011.

[4] B. K. Purohit and V. S. Sistla, "Inorganic salt hydrate for thermal energy storage application: A review," *Wiley: Energy Storage,* pp. 1-26, 2020.

[5] S. D. Sharma and K. Sagara, "Latent Heat Storage Materials and Systems: A Review," *International Journal of Green Energy,* vol. 2, pp. 1-56, 2005.

[6] J. Pereira da Cunha and P. Eames, "Thermal energy storage for low and medium temperature applications using phase change materials – A review," *Applied Energy,* vol. 177, pp. 227-238, 2016.

[7] W. Kong, M. Dannemand, J. B. Johansen, J. Fan, J. Dragsted, G. Englmair and S. Furbo, "Experimental investigations on heat content of supercooled sodium acetate trihydrate by a simple heat loss method," *Solar Energy,* vol. 139, pp. 249-257, 2016.

[8] M. Dannemand, W. Kong, J. Fan, J. Johansen and S. Furbo, "Experimental investigations on prototype heat storage units utilizing stable supercooling of sodium acetate trihydrate mixtures," *Applied Energy,* vol. 169, pp. 72-80, 2016.

[9] S. Furbo and S. Svendsen, "Report on Heat Storage in a Solar Heating System Using Salt Hydrates," Technical University of Denmark: Department of Civil Engineering, Lyngby, Denmark, 1977.

[10] P. Hu, D.-J. Lu, X.-Y. Fan, X. Zhou and Z.-S. Chen, "Phase change performance of sodium acetate trihydrate with AIN nanoparticles and CMC," *Solar Energy Materials and Solar Cells,* vol. 95, pp. 2645-2649, 2011.

[11] D. Oliver, A. Bissell, X. Liu, C. Tang and C. Pulham, "Crystallisation studies of sodium acetate trihydrate – suppression of incongruent melting and sub-cooling to produce a reliable, high-performance phase-change material," *The Royal Society of Chemistry: CrystEngComm,* vol. 23, pp. 700-706, 2021.

[12] SUNAMP, "SUNAMP UK," June 2022. [Online]. Available: https://sunamp.com/en-gb/wp-content/uploads/sites/2/2022/06/Sunamp-Thermino-Brochure-JUNE-2022-v2.2.pdf. [Accessed 7 September 2022].

[13] Y. Zhang and Y. Jiang, "A simple method, the T -history method, of determining the heat of fusion, specific heat and thermal conductivity of phase-change materials," *Measurememnt Science and Technology,* vol. 10, pp. 201-205, 1999.

[14] H. Hong, C. H. Park, J. H. Choi and J. H. Peck, "Improvement of the T-History Method to Measure Heat of Fusion for Phase CHange Materials," *International Journal of Air-Conditioning and Refrigeration,* vol. 11, no. 1, pp. 32-39, 2003.

[15] H. Hong, S. K. Kim and Y.-S. Kim, "Accuracy improvement of T-History method for measuring heat of fusion of various materials," *International Journal of Refrigeration,* vol. 27, pp. 360-366, 2004.

WIND POWER FORECASTING: A REVIEW

Schalk W van der Merwe[1], Armand A du Plessis[2], Arnold J Rix[3]

Department of Electrical and Electronic Engineering, University of Stellenbosch, Stellenbosch, 7600, South Africa

[1] 22569081@sun.ac.za, [2] armandd@sun.ac.za, [3] rix@sun.ac.za

Abstract: Due to the stochastic behaviour of wind power generation, accurately predicting wind speed and power generation is fundamental to the reliable and large-scale adoption of wind power integration onto the electrical grid. In this research paper, a compact review is presented on wind power forecasting, which focuses on the classification of methods and the evaluation thereof. Specific factors related to wind speed and power prediction have also been highlighted. To further ensure the relevance of this paper, the literature review has been limited to research published within the last 5 years. Based on the most common research trends, future recommendations are made to improve accuracy and aid development in underexplored researched domains. This review ultimately provides a framework for enhancing the implementation of wind power forecasting. This, in turn, leads to improvements in ancillary service provision through wind energy, resulting in the optimal integration of wind energy into the electrical grid.

Keywords - Wind Power; Wind Power Forecasting; Traditional Statistical Models; Physical Models; Neural Networks; Hybrid Models; Machine Learning.

1 Introduction

The global economy and human living standards have experienced substantial growth in recent years, leading to a corresponding surge in energy demand [1]. Traditionally, this demand has been met with fossil fuels, like coal, oil and natural gas. However, these sources of energy production have gained a negative reputation due to the pollutants released [1], [2]. Furthermore, fossil fuels are limited in reserves, so renewable energy sources are preferred if feasible [3]. As set out by the Paris Agreement, two-thirds of the global energy demand must be supplied by renewable energy to limit the global temperature increase to less than 2° [2], [4]. Of all the renewable energy types, like solar photovoltaic and bioenergy, wind energy has become very popular due to its high efficiency, abundance and low environmental impact and the ability to produce energy during the night [2] [5].

Wind energy is increasing in popularity globally. As shown by the statistics in the *Global Wind Report 2023*, the total installed wind capacity in 2022 was 907 GW, an increase of 9% compared to 2020 [6].

With the increasing energy demand and subsequent rise in renewable energy integration, like wind energy, additional challenges emerge. The challenges encompass, market design, real-time grid operations, ancillary service requirements and costs, competitive technologies, power system reliability and stability as well as transmission capacity upgrades and standards [7]. Another major challenge with integrating wind energy into the electrical grid is the stochastic behaviour of the wind [1], [2]. This stochastic behaviour causes challenges with wind power management, as a balance between power and demand is highly desired in distribution networks [2]. Forecasting, however, is considered to be an effective solution to many of these problems.

This review article will discuss literature regarding state-of-the-art wind power forecasting. Section 3 elaborates on forecasting literature specifically for wind energy. The literature discusses how sources classify forecasting models, some of the frequently used comparison metrics, and the advantages and disadvantages of each method. In Section 4, there is a brief discussion of two model enhancements. Section 5 briefly summarises some state-of-the-art models and methods used and their respective pros and cons. With the literature from the state-of-the-art models and methods, shortcomings in the current models will be identified to make future recommendations for improving wind power forecasting in Section 6. With the knowledge gained from this review, forecasting models can be used and developed to best suit the provision of ancillary services from renewable energy sources, specifically wind farms.

2 Methodology

Machine learning is a major topic of interest in multiple research fields globally. Due to this popularity, a multitude of research papers were available online and adequate filtering was required. Google Scholar and Stellenbosch University's SUN-Scholar were used as internet filters for searching through research databases, ensuring appropriate articles were found. Forecasting-

specific research was desired, specifically wind power forecasting, therefore, most searches contained the term forecasting. Frequently used search terms included, but were not limited to: *Wind Power Forecasting, Renewable Power Forecasting, Solar Forecasting, Forecasting Methods*. The sources were then evaluated with the following criteria.

1. The article should entail forecasting methodologies with an emphasis on machine learning.
2. The article should have been published in the last 5 years.
3. Higher impact factor journals were preferred.

The evaluation criteria ensured high-quality sources were obtained, contributing to the relevance of this review.

3 Forecasting Literature

3.1 Wind Speed and Wind Power

Traditionally, there are two ways to perform wind power forecasting. The first is to forecast wind power with given historical wind power data [1]. The second method involves predicting the wind speed, and then forecasting the wind turbine power according to wind turbine power curves. These curves reflect the power generated at different wind speeds [8], [9]. Therefore, research is commonly found on wind speed and wind power forecasting.

The two main factors influencing the power output of a wind turbine are wind speed and wind direction. Wind speed and wind direction further depend on other atmospheric conditions and location [11]. The relationship between wind speed and wind power can be given by Equation 1, where ρ is the air density ($\frac{kg}{m^3}$), which depends on air pressure and air temperature, A (m^2) is the area of the wind passing through the turbine and v ($\frac{m}{s}$) is the wind speed.

$$P_A = \frac{1}{2}\rho A v^3 \tag{1}$$

P_A (watt) is the theoretical available power in the wind, but wind turbines cannot fully extract all the power in the wind. The realistic power extraction is demonstrated with Equation 2, where C_p is the power coefficient. The power coefficient is determined by the tip angle, blade design and the relationship between wind speed and rotor speed, with an upper-efficiency limit for all turbines called the *Betz limit*, which is 0.593 (59.3 %) [23].

$$P_R = C_p P_A \tag{2}$$

This brief summary highlights that an error in wind speed prediction will result in a cubic error in wind power prediction, emphasizing why accurate wind speed predictions are important [11].

3.2 Time Horizon Classification

Wind power or wind speed forecasting models can be grouped into different time scales [1]. These time scales are determined from the various functional requirements and can be divided into four categories, as seen in Figure 1(a). These time scales include very short-term (a few minutes to 30 minutes), short-term (30 minutes to 6 hours), medium-term (6 hours to 1 day) and long-term (1 day to a week or more) [1],[2], [10]. The time-scale classification of wind power forecasting models is relatively indistinct, but most agree with the time ranges listed above. In summary, very short-term forecasting is mainly used for turbine control, real-time grid operations and regulation control [2]. Short-term forecasting is used for load dispatch planning and load intelligent decisions [2]. Medium-term forecasting is used for operational security in the energy market, energy trading and online and offline generating decisions [2]. Lastly, long-term forecasting is used for scheduling maintenance, optimal operating costs and operation management [1],[2], [11]. It is worth noting, as discussed in [2], that wind power forecasting errors increase with longer time horizons.

3.3 Applied Methodology Classification

Applied methodologies are another way of classifying wind power forecasting models. As depicted by Figure 1(b), applied methodologies can be divided into four categories, physical models, statistical models, machine learning (ML) models and hybrid models [1], [2].

Physical models, like numerical weather prediction (NWP) and weather researcher forecasting (WRF), usually take environmental conditions into consideration [1]. These factors consist of surface roughness, terrain, wake effect, humidity, pressure and temperature [2],[12]. All of these variables are then used in a complex mathematical model to predict the wind speed for that specific area. This wind speed will then be used to predict the wind power with the turbine wind power curve. Therefore, it can be said this forecasting method does not need to be trained with historical data but requires physical data [2]. Studies have shown physical prediction models to have better performance compared with traditional statistical models in medium-term and long-term wind speed prediction, however, this comes at the cost of being computationally complex, needing more computational resources [2], [5].

Unlike physical models, historical data is used with statistical methods to find linear and non-linear relationships between weather and power output. These relationships are used to make predictions for future power outputs [1],[2]. Generally, this method is easy to model

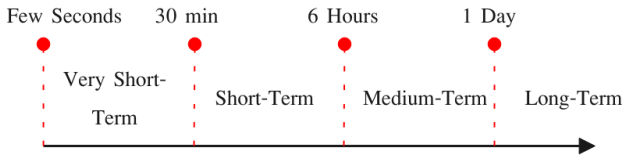

(a) Forecasting Time Horizon Classification

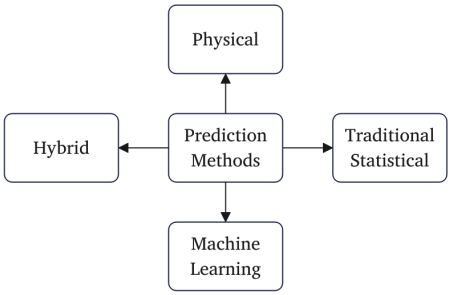

(b) Applied Methodologies Classification

Fig. 1. Forecasting Classification

and requires less computational resources than physical models, but the forecasting error increases with a larger time horizon [2]. Statistical models can be divided into two main sub-classifications, which are: the traditional statistical model, like time series forecasting and ML approaches, like artificial neural networks [2]. Time series forecasting is easier to formulate and the models have a low computational time, they are, however, more susceptible to errors when the time series data is not stationary [14]. In recent years, computer science advancements have led to the widespread utilization of ML models in wind speed and wind power forecasting [1]. The main soft computing approaches include artificial neural networks (ANN) and fuzzy systems [17]. Additionally, models like support vector machines (SVM) [15], extreme learning machines (ELM) [16] and Kalman filters [26] have also been successfully implemented. Examples of implemented AANs include back propagation neural networks (BPNN) [18], multi-layer perception (MLP) [19], Wavelet neural networks (WNN) [18] and the Elman networks [20]. These ML models have attracted considerable attention in wind speed and wind power forecasting due to their superior ability to deal with complex non-linear problems. The ML models tend to show better performance in predicting wind speed and wind power compared to conventional statistical models [1]. Although ML models generally perform better, their accuracy also depends on additional factors like data pre-processing, data structure, learning method and the connections between input and output data [2],[22].

When different forecasting methods are combined, for example, ANNs and fuzzy logic models, then we collectively refer to these as hybrid forecasting models [2]. The goal of these models is to keep the advantages of each individual model and therefore improve the accuracy of the combined prediction [1], [21]. Ensemble modelling is a more advanced type of hybrid model, where diverse predictive models are often created by employing and combining multiple algorithms and using different training data sets [2]. This process of combining forecasting models does not always guarantee better performance, but it has proved to have fewer risks in most situations. As demonstrated by the sources in Section 5, there is no universal hybrid solution and the selection of which individual models to use is problem-specific.

3.4 Key Factors to Compare Different Methods

Instead of comparing individual model algorithms, the focus of this review is on comparing methods (or model classifications) as a whole. To achieve this, studies and research of individual models and methods, under each category represented in Figure 1(b), are done to determine the advantages and disadvantages of each. As stated by [23], it is also important to note that it is difficult to measure the performance of models only using the output plots. Predictive performance can be quantified with evaluation/statistical metrics [23]. From the sources, [1] -[2], [8], [9], [24], the following statistical metrics are commonly used: root mean square error (RMSE), mean absolute percentage error (MAPE), mean absolute error (MAE), the coefficient of determination (R^2). Table 1 shows how these metrics would be calculated during experiments. All the studies listed in this paragraph agree to the use of the evaluation metrics and use at least two of them listed in Table 1.

Table 1. Equations for Common Evaluation Metrics

Metric	Equation
RMSE	$\sqrt{\frac{1}{n}\sum_{i=1}^{n}(y_i-\hat{y}_i)^2}$
MAE	$\frac{1}{n}\sum_{i=1}^{n}\lvert y_i-\hat{y}_i\rvert$
MAPE	$\frac{1}{n}\sum_{i=1}^{n}\left\lvert\frac{y_i-\hat{y}_i}{y_i}\right\rvert\times 100\%$
R^2	$1-\frac{\sum_{i=1}^{n}(y_i-\hat{y}_i)^2}{\sum_{i=1}^{n}(y_i-\bar{y}_i)^2}$

3.5 Method Comparison

Table 2 summarizes a few advantages and disadvantages of each method. Using the information from the literature review above, a comparison can be made between

Table 2. Wind Forecasting Methods Summary

Method	Advantages	Disadvantages
Physical Forecasting Methods	• Physical methods are usually more accurate when making medium-term and long-term predictions. • Physical methods are good for tailored site specific predictions.	• These methods are computationally complex, needing plenty of computational resources. This makes them unsuitable for very short-term and short-term forecasting.
Traditional Statistical Methods	• Simpler than physical models, therefore, better performance for very short-term and short-term forecasting. • Flexibility in handling different data sources.	• Susceptible to errors when the time series data is not stationary. • Struggles with non-linear features.
Artificial Intelligence Methods	• These models can handle complex non-linear problems, whether the relationships between features are known or not. • Adaptability to change with conditions. • Continuous learning and improvement.	• Susceptible to error if the data processing is not done correctly. • Could have overfitting problems due to insufficient amount of data.
Hybrid Forecasting Methods	• Integrating the best features of each individual model to obtain a better-performing final model.	• Hybrid models are designed to solve specific problems, and could, therefore, show less promising results if applied to another situation [25].

the discussed methods for wind power forecasting. A qualitative comparison is done using the various sources in the literature review.

4 Model Enhancements

The modern-day importance of delivering accurate wind power forecasts has led to most of the recent research efforts having less regard for computational expense and more regard for low prediction errors. [2]. Some of these enhancements have proven effective and are briefly discussed below.

4.1 Kalman Filtering

The Kalman filter is a group of mathematical formulas that offers a computationally and recursive method to estimate the state of a process. The goal of the Kalman filter is to minimize the mean squared error of the estimation process [2], [27]. The strength of the filter is that it can support the prediction of past, present and future states, even when the exact formulation of the prediction model is unknown [27]. In [28], the author found the Kalman filter to improve the prediction accuracy when used with an intelligent hybrid model.

4.2 Data Processing Applications

Preparing the data to improve the accuracy of predictions has become an essential part of wind power forecasting (and other forms of forecasting) [22]. These applications could be split into pre-processing or post-processing applications. Examples of data processing applications are decomposition, feature selection, feature extraction and outlier detection [10].

5 Current Forecasting Time Line

Machine learning and hybrid models have gained more attention than traditional statistical and physical methods in recent years. This was determined by evaluating sources limited to the most recent 5 years. Interestingly, hybrid models are discussed most, as many sources combine ML approaches with other models to form the hybrid models [2], [21], [24]. Deep learning models have been established to outperform traditional neural networks [21]. This is primarily attributed to the increased computational efficiencies and abilities, readily available to forecasting practitioners. In Table 3, brief summaries are given of articles containing research on state-of-the-art models and reviews.

Table 3. Current Forecasting Models Summary

Source	#	Method/s	Summary
[1]	2021 218 11.446	Deep Neural Networks (DNN)	This article is a comprehensive review of various deep learning models for each stage of wind speed and wind power forecasting. It was concluded that for feature extraction, (CNN) are used to extract deep features, for relationship learning recurrent neural networks (RNN) are popular, and often include LSTM modules. This article also states that certain hybrid models, specifically stacking-based and weight-based approaches, could provide better forecasting performance by taking advantage of different DNN properties.
[22]	2018 302 11.446	Artificial Neural Network (ANN)	ANNs have proven to be effective for predicting wind speed and wind power over short intervals, but the accuracy decreases with longer time intervals. In this article, the author also highlights the ability of ANNs to cope with different data sets, making them robust and often preferred for control tasks, as they are more efficient than PID controllers.
[29]	2021 143 8.634	Deep learning and Gated-recurrent Neural Network (GRNN)	This article discusses the implementation of LSTM and GRU deep learning neural networks. The forecasting models were developed independently of wind turbine properties, ensuring that the prediction models could be used for supplementary wind farms/turbines. The authors then conclude that the GRU neural network outperforms the LSTM neural network in accuracy, whilst having a shorter training time.
[30]	2021 10 7.985	Deep Learning	Various deep learning-based models are introduced in this article, namely, CNN, RNN and restricted Boltzmann machine (RBM). Many of these models were also combined with LSTM modules and gated recurrent units (GRU) to form hybrid models as in [1]. This article also concludes that RNNs are better at extracting dependencies and CNNs are better at extracting correlation between multiple time series.
[37]	2020 20 *	Neural Network, SVM	A comparison between neural networks, SVM, k Nearest Neighbour (kNN) and Random Forest were in this paper. The author highlighted that Neural networks and SVM were susceptible to a high computational time when there were irrelevant input features. It was determined that kNN has low computation time and low error with few features, but struggled with predicting outliers. Alternatively, Random Forest had a high error with few features and low error with many features. Random forests could ignore irrelevant input data and predict outliers. It was concluded that the models have different strengths and weaknesses. The paper also discusses the advantages of having an accurate prediction system for the TSO and the services the wind farm could provide.
[24]	2020 14 4.672	Hybrid Neurofuzzy	In this article, a comparison of two adaptive neurofuzzy interference system (ANFIS) models was done. The models were hybridised with the genetic algorithm (GA) and particle swarm optimization (PSO). The research concluded that the PSO-ANFIS model had less prediction error and compiling time than the GA-ANFIS model, making it the preferred model for short-term predictions.
[25]	2019 65 10.16	Hybrid model with Multi-objective Moth-flame Optimisation (MOMFO) Algorithm	A novel hybrid model using the MOMFO algorithm is developed and tested in the article. Multiple tests were conducted on this hybrid model and determined that it has a very high efficiency. Furthermore, it was determined that the model outperforms benchmark models, but the model is also a useful predictor for planning and managing operations. Due to the models' accuracy and robustness, the authors conclude that the model could also be used in other prediction fields, like oil price predictions.
[31]	2018 136 10.16	Hybrid model with Empirical Mode Decomposition (EMD)	This article proposes a hybrid model based on EMD with non-iterative kernel ridge regression (KRR) for short-term wind speed and wind power prediction. The study found wavelet KRR (EMD-WKRR) to exhibit superior prediction accuracy but had high execution time. Therefore, a reduced EMD-RWKRR model was also implemented, having a lower execution time and only a very small loss in accuracy.
[32]	2021 21 3.746	ML-based Hybrid models	Artificial Intelligence hybrid model applications are presented in this review article. It highlights different techniques, implementation factors, issues and constraints with these approaches. The authors concluded that certain models perform better at different time horizons. The Jaya algorithm with a SVM for short-term forecasting, the Type-2 Fuzzy Neural Network (T2FNN) for medium-term forecasts and LSTM with RNN for long-term forecasts were some of the best-performing models.
[38]	2019 75 8.634	Hybrid Model based on BMA-EL	This article proposes a hybrid wind power forecasting model based on Bayesian model averaging and Ensemble learning (BMA-EL). According to the test conducted, the BMA-EL approach reduced the uncertainty of the forecasting results of a single model. It was concluded that this proposed approach increases the reliability and precision of wind power forecasting under different meteorological conditions compared to other literature approaches.

[1] The order of # is: Date, citations and impact factor

[2] A * denotes a conference paper.

In [1] and [30], both studies concluded that different deep-learning neural networks are better at different tasks, which is why hybrid models are increasing in popularity. Recurrent neural networks (RNNs) were commonly used for extracting information regarding relationship learning, and convolutional neural networks (CNNs) are found to be more capable of extracting deep features. Hybrid models can, therefore, retain the advantages of each individual model, producing a more accurate combined model. A common theme revealed from multiple sources in Table 3, [1], [29], [30], [32] highlights that hybrid models implementing long short-term memory (LSTM) often have better prediction performance and efficiency. This could be confirmed in [33] - [35]. Most wind power forecasting models are developed for onshore wind farms, but as demonstrated in [6], offshore wind forecasting models are also implemented progressively.

The improvement in forecasting model accuracies provides more certainty to grid operators, which has allowed for the increased integration of RE sources into the electrical grid. These forecasts greatly aid in providing ancillary services to the electrical grid from renewable energy sources. Prediction horizons for ancillary services range from very short-term for frequency regulation, to medium-term for supplemental operating reserves [36]. As stated in the literature in Section 3, a larger forecasting horizon often results in a larger prediction error, therefore, future work can still be done to improve forecasting with longer time horizons. Improving this could aid with the provision of certain ancillary services such as supplemental operating reserves.

6 Future trends in Wind Power Forecasting

- As stated in [6], the amount of offshore wind farms are increasing yearly. These wind farms operate in vastly different climatic conditions than onshore wind farms and most prediction models are developed based on onshore wind farm data. It is recommended to develop models aimed at improving the accuracy of offshore wind farms as well, specifically improving feature selection in those models. This sentiment is also shared by [2].
- Controlling data imbalances (skewed class proportions) and rare event forecasting is another research domain with limited existing literature. Forecasting rare events from a time series data set would be very valuable for protecting the power system.
- A common problem for wind power forecasting is the decrease in performance with an increase in prediction horizon. Further development of accurate long-term forecasting (Figure 1(a)) could greatly aid in the provision of certain ancillary services and maintenance planning.
- The accuracy and robustness of wind power prediction with ML-based hybrid modes can be further enhanced with online wind measurement databases. The online wind measurement data could be used with cloud computing platforms (Microsoft Azure, Google Cloud and Amazon Web Services for example) to train ML/hybrid models in real-time, subsequently increasing forecasting accuracy.

7 Conclusion

With a specific focus on the most recent 5 years of published research, A state-of-the-art literature review on wind power forecasting has been presented. The classification and evaluation of new wind power forecasting models have been reviewed, together with common statistical evaluation metrics, which are predominant today. Furthermore, accurate wind power forecasting will reduce the financial and technical risks associated with the uncertainties of wind power. Collectively, it was determined that ML and hybrid models were prominent in most studies, given the increase in computing power and efficiency. From this, it was also apparent that researchers have gravitated towards the implementation of hybrid models, with LSTM models identified as a good combination with other models, due to its superior accuracy and low computational time. This literature recognised that larger time horizons often result in larger forecasting errors, therefore, some widely accepted future recommendations on wind power forecasting were made.

This paper determines that by implementing and improving wind power forecasting, easier provision of ancillary services can take place ensuring a stable grid and wide adoption of wind energy globally. There is, however, still more research to be done to aid the full integration of wind energy into the electrical grid. Therefore, this paper is beneficial towards researchers, policymakers, decision-makers and operational engineers.

References

[1] Y. Wnag, R. Zou, F. Liu, L. Shang, Q. Liu, "A review of wind speed and wind power forecasting with deep neural networks," in Applied Energy, vol 304, December 2021.

[2] S. Hanifi, X. Liu, Z. Lin, S. Lotfian, "A Critical Review of Wind Power Forecasting Methods - Past, Present and Future," in Energies, vol 13, July 2020.

[3] k.R. Abbasi, M. Shahbaz, J. Zhang, M. Irfan. R. Alvarado, "Analyze the environmental sustainability factors of China: The role of fossil fuel energy and renewable energy," in Renewable Energy, vol 187, pp. 390 - 402, 2022

[4] D. Gielen, F. Boshell, D. Saygin, M.D. Bazilian, N. Wagner, "The role of renewable energy in the global energy transformation," in Energy Strategy Reviews, vol 24, pp. 38 - 50, January 2019

[5] J. Zhang, J. Yan, D. Infield, Y. Liu, F-S. Lien, "Short-term forecasting and uncertainty analysis of wind turbine power based on long short-term memory network and Gaussian mixture model," in Applied Energy, vol 241, pp. 229 - 244, March 2019

[6] M. Dyrholm, B. Backwell, F. Zhao, E. Gannoum, C.L Mapes, "Global Wind Report", Brussels, Global Energy Council, 2023

[7] S.R. Sinsel, R.L. Riemke, V.H. Hoffmann, "Challenges and solution technologies for the integration of vrairable renewable energy sources - a review," in Renewable Energy, vol 145, pp. 2271 - 2285, 2020

[8] Y. Wang, Q. HU, L. Li, A.M. Foley, D. Srinivasan, "Approaches to wind power curve modeling: A review and discussion," in Renewable and Sustainable Energy Reviews, vol 116, December 2019

[9] J. Yan, T. Ouyang, "Advanced wind power prediction based on data-driven error correction," in Energy Conversion and Management, vol 180, pp. 302 - 311, January 2019

[10] H. Liu, C. Chen, "Data processing strategies in wind energy forecasting models and applications: A comprehensive review," in Applied Energy, vol 249, pp. 392 - 408, 2019

[11] R. Sharma, D. Singh, "A Review of Wind Power and Wind Speed Forecasting," in Journal of Engineering Research and Application, vol 8, pp. 1 - 9, July 2018

[12] X. Yuan, C. Chen, M. Jiang, Y. Yuan, "Prediction interval of wind power using parameter optimized Beta distribution based LSTM model," in Applied Soft Computing Journal, vol 82, September 2019

[13] J. Jung, R.P. Broadwater, "Current status and future advances for wind speed and power forecasting," in Renewable and Sustainable Energy Reviews, vol 31, pp. 762 - 777, January 2014

[14] Y. Zhao, L. Ye, Z. Li, X. Song, Y. Lang, J. Su, "A novel bidirectional mechanism based on time series model for wind power forecasting," in Applied Energy, vol 177, pp. 793 - 803, June 2016

[15] J. Wang, S. Wang, W. Yang, "A novel non-linear combination system for short-term wind speed forecast," in Renewable Energy, vol 143, pp. 1172 - 1192, May 2019

[16] H. Liu, X. Mi, Y. Li, "Smart multi-step deep learning model for wind speed forecasting based on variational mode decomposition, singular spectrum analysis, LSTM network and ELM," in Energy Conversion Management, vol 159, pp. 54 - 64, 2018

[17] C.A. Severiano, P.C. de Lima e Silva, M.W. Cohen, F.G. Guimaraes, "Evolving fuzzy time series for spatio-temporal forecasting in renewable energy systems," in Renewable Energy, vol 171, pp. 764 - 783, February 2021

[18] J. Song, J. Wang, H. Lu, "A novel combined model based on advanced optimization algorithm for short-term wind speed forecasting," in Applied Energy, vol 215, pp. 643 - 658, February 2018

[19] X. He, Y. Nie, H. Guo and J. Wang, "Research on a Novel Combination System on the Basis of Deep Learning and Swarm Intelligence Optimization Algorithm for Wind Speed Forecasting," in IEEE Access, vol. 8, pp. 51482-51499, 2020

[20] L. Song, Q. Xie, Y. He and P. Dang, "Ultra-short-term Wind Power Combination Forecasting Model Based on MEEMD-SAE-Elman," 2020 IEEE 4th Information Technology, Networking, Electronic and Automation Control Conference (ITNEC), Chongqing, China, 2020, pp. 1844-1850

[21] Y-Y. Hong, C.L.P.P. Rioflorido, "A hybrid deep learning-based neural network for 24-h ahead wind power forecasting," in Applied Energy, vol 250, pp. 530 - 539, May 2019

[22] A.P. Marugan, F.P.G. Marquez, J.M.P. Perez. D. Ruiz-Hernandez, "A survey of artificial neural network in wind energy systems," in Applied Energy, vol 228. pp. 1822 - 1836, July 2018

[23] Q. Chen and K. A. Folly, "Comparison of Three Methods for Short-Term Wind Power Forecasting," 2018 International Joint Conference on Neural Networks (IJCNN), Rio de Janeiro, Brazil, 2018, pp. 1-8

[24] P.A. Adedeji, S.A. Akinlabi, N. Madushele, O.O. Olatunji, "Hybrid neurofuzzy wind power forecast and wind turbine location for embedded generation," in International Journal of Energy Research, vol 45, pp. 413 - 428, May 2020

[25] P. DU, J. Wang, W. Yang, T. Niu, "A novel hybrid model for short-term wind power forecasting," in Applied Soft Computing Journal, vol 80, pp. 93 - 106, March 2019

[26] T. Ahmad, D. Zhang, C. Huang, "Methodological framework for short-and medium-term energy, solar and wind power forecasting with stochastic-based machine learning approach to monetary and energy policy applications," in Energy, vol 231, May 2021

[27] G.F. Welch, "Kalman Filter," in Computer Vision: A Reference Guide, pp. 1 - 3. December 2020

[28] H.H.H. Aly, "A Hybrid Optimized Model of Adaptive Neuro-Fuzzy Inference System, Recurrent Kalman Filter and Neuro-Wavelet for Wind Power Forecasting Driven by DFIG," in Energy, vol 239, January 2022

[29] A. Kisvari, X. Liu, "Wind power forecasting - A data-driven method along with gated recurrent neural network," in Renewable Energy, vol 163, pp. 1895 - 1909, October 2020

[30] Z. Wu, G. Luo, Z. Yang, Y. Guo, K. Li, Y, Xue, "A comprehensive review on deep learning approaches in wind forecasting applications," in CAAI Transactions on Intelligence Technology, November 2021

[31] J. Naik, P. Satapathy, P.K. Dash, "Short-term wind speed and wind power prediction using hybrid empirical mode decomposition and kernel ridge regression," in Applied Soft Computing, vol 70, pp. 1167 - 1188, 2018

[32] M.S. Hossain Lipu, MD. Sazal Miah, M.A. Hannan, A.Hussain, M.R. Sarker, A. Ayob, M.H.MD. Saad, MD. Sultain Mahmud, "Artificial Intelligence Based Hybrid Forecasting Approaches for Wind Power Generation: Progress, Challenges and Prospects," in IEEE Access, vol. 9, pp. 102460-102489, 2021

[33] R. Yu, J. Gao, M. Yu, W. Lu, T. Xu, M.Zhao, J. Zhang, Z. Zhang, "LSTM-EFG for wind power forecasting based on sequential correlation features," in Future Generation Computer Systems, vol 93, pp. 33 - 42, October 2018

[34] B. Liu,S. Zhao, X. Yu, L.Shang, Q. Wang, "A Novel Deep Learning Approach for Wind Power Forecasting Based on WD-LSTM Model," in Energies, vol 13, September 2020

[35] A. Banik, C. Behera, T.V. Sarathkumar, A.K. Goswami, " Uncertain wind power forecasting using LSTM-based prediction interval," in IET Renewable Power Generation, vol 14, pp. 2657 - 2667, October 2020

[36] The SA Grid Code Secretatiat, "GRID CONNECTION CODE FOR RENEWABLE POWER PLANTS (RPPs) CONNECTED TO THE ELECTRICITY TRANSMISSION SYSTEM (TS) OR THE DISTRIBUTION SYSTEM (DS) IN SOUTH AFRICA," in the South African Grid Code, version 3.1, January 2022

[37] K. L. Jørgensen and H. R. Shaker, "Wind Power Forecasting Using Machine Learning: State of the Art, Trends and Challenges," 2020 IEEE 8th International Conference on Smart Energy Grid Engineering (SEGE), Oshawa, ON, Canada, 2020, pp. 44-50

[38] G. Wang, R. Jia, J. Liu, H. Zhang, "A hybrid wind power forecasting approach based on Bayesian model averaging and ensemble learning," in Renewable Energy, vol 145, pp. 2426 - 2434, August 2019

Enhancing Wind Resource Allocation through Unsupervised Machine Learning: A Case Study in Coastal South Africa

Saarty Tuyakula Mikka[1] and Dr Chantelle Van Staden[2] and Theunis Oosthuizen[3]

[1] Stellenbosch University, 7600, Stellenbosch, South Africa; E-Mail: saartymikka@gmail.com

[2] Stellenbosch University, 7600, Stellenbosch, South Africa; E-Mail: cvanstaden@sun.ac.za

[3] Stellenbosch University, 7600, Stellenbosch, South Africa; E-Mail: 22541187@sun.ac.za

Abstract: This paper introduces an approach to enhancing the allocation of wind resources by leveraging unsupervised machine learning techniques. The central objective is to optimize the distribution of wind resources across geographic sites, thereby maximizing both generation profiles and overall system stability. Two distinct clustering methodologies are employed, namely temporal and statistical feature clustering. These strategies effectively cluster regions within the coastal region of South Africa and unveil the unique advantages of each approach.

Both clustering techniques harness the power of the widely utilized k-means algorithm in unsupervised learning. To comprehensively assess the characteristics of the temporal and statistical clusters, a modelling framework utilizing the Weibull distribution is implemented. This approach accounts for seasonal fluctuations and considers wind speed intervals that correspond to different temporal periods. By integrating the Weibull distribution, the modelling technique significantly enhances the accuracy of representing the characteristics of the wind resource potential.

Furthermore, this study incorporates the clustered data as inputs into an optimization model. This model serves as a guiding tool for informed decision-making regarding the strategic placement of wind power plants along South Africa's coastline. The proposed allocation methodology is adaptable, as it can easily incorporate additional critical variables such as wind direction, solar power, and green hydrogen.

Keywords: wind resource allocation; clustering; statistical feature extraction; Weibull distribution; optimisation

1. Introduction

Wind power is rapidly growing as a global Renewable Energy (RE) source [1]. Wind power energy is a popular RE source, where the efficiency of the RE generation plant is heavily influenced by its location [1]. In South Africa, where wind speed varies seasonally and geographically, developing an optimal method for placing wind resources can be highly beneficial. Evaluating the wind speed profile at each potential site is crucial for resource siting [2].

The South African power grid faces energy supply challenges exacerbated by rapid economic growth and increased demand [3]. Load-shedding measures have been introduced but haven't effectively solved the issue. To address this, South Africa is turning to Renewable Energy Sources (RES) like solar, wind, biomass, and hydropower [3].

Urgent investigation into clean, sustainable, and cost-effective energy generation methods is needed to meet electricity demand and address grid challenges. Wind power is gaining popularity, necessitating methods for planning wind power integration in South Africa. Thus, this paper proposes a method for allocating wind resources.

The study compares two clustering methodologies for wind resources. The first is temporal clustering, applying a machine-learning algorithm to raw time-series data with a Euclidean distance metric. The second method is statistical feature clustering, extracting statistical features from time series data before applying a machine learning algorithm. By comparing these approaches using the Weibull distribution, the study identifies the most efficient one. The chosen method's clusters are then used in an optimization model to maximize stability and wind speed potential, establishing optimal and robust wind farm locations in South Africa.

2. Methodology

2.1. Resource dataset and study region

This study uses data from the Wind Atlas for South Africa (WASA), encompassing wind speed and direction information from 527 locations spanning 12 years. For this study, data from 2012 at a hub height of 100m is used, given the recurring nature in the annual wind patterns. The resource has spatial resolution of 25 km² and a temporal resolution of 1 hour.

The coastal region of South Africa is selected as the focus area for the study due to the high wind speeds experienced at the coast. Fig. 1 depicts the study region, where each grid cell is represented by an averaged time-series wind speed dataset.

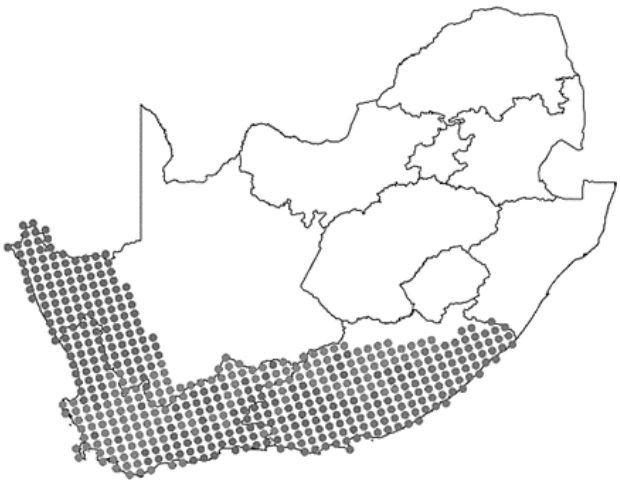

Fig. 1. Geographic coastal locations in South Africa.

2.2. Machine learning algorithms

Clustering algorithms are unsupervised machine-learning techniques used to identify distinct groups or clusters within datasets that share similar attributes. In the context of wind resource allocation, these algorithms play a crucial role in clustering geographical locations based on common wind speed traits and other relevant factors.

One widely adopted clustering technique is the k-means clustering algorithm, which divides a dataset into a predetermined number of clusters. It operates by iteratively assigning each data point to the cluster with the nearest centroid and subsequently updating cluster centroids based on the newly assigned data. K-means is efficient for large datasets but is less suited for irregularly shaped data distributions or clusters of varying sizes [4].

The primary goal of the k-means algorithm is to minimize the distance between data points and the respective cluster centroids. This is defined as reducing the intra-cluster variance, which can be achieved by employing the squared error function

$$J = \sum_{j=1}^{K} \sum_{i=1}^{N} \| x_i^{(j)} - c_j \|^2, \quad (1)$$

where J is the objective function of the cluster centroid, K is the number of clusters, N is the number of data points, c_j is the cluster centroid, and $x_i^{(j)}$ is a data point in the respective cluster.

Determining the optimal number of clusters is a challenging aspect of k-means clustering. This challenge is commonly tackled through methods like silhouette analysis and the elbow method. Silhouette analysis evaluates the cohesion and separation of clusters, yielding a score ranging from -1 to 1. Higher scores indicate more effective clustering. A score of 0 implies data points lie on or near the boundary of adjacent clusters. Conversely, negative values suggest potential misassignment of data points. The Average Silhouette Width, *ASW*, score is defined as [5]

$$ASW = \frac{1}{N} \sum_{j=1}^{K} \sum_{x_i \in C_j} \frac{(b_{x_i} - a_{x_i})}{\max(b_{x_i}, a_{x_i})}, \quad (2)$$

where a_{x_i} and b_{x_i} correspondingly denote the average intra-cluster and the smallest inter-cluster distances for data point x_i within cluster C_j. N and K denote the total number of data points and clusters, respectively.

The elbow method is another widely used approach for determining the optimal number of clusters. In this method, the Within-cluster Sum of Squares (WSS) is plotted against the number of clusters. This graphical representation helps pinpoint the optimal cluster number by identifying the point on the plot where the curve starts to level off or bend, resembling an *elbow* shape [5].

2.3. Distance metrics

Clustering algorithms rely on a distance metric to quantify the similarity between data points. The Euclidean distance is a widely used metric in data mining [6]. However, it's sensitive to time shifts and lacks invariance. Given the presence of invariants in the temporal data used in this study, an alternative distance metric is explored.

The Dynamic Time Warping (DTW) algorithm, extensively employed across various domains, optimizes alignments between time-dependent sequences by non-linearly warping them for optimal matching [7]. In this study, DTW is combined with the k-means algorithm to analyse distinctive wind speed patterns. DTW effectively accommodates time-related deformations and varying speeds inherent in time-dependent variables. Given the dimensionality of the wind dataset, DTW is adopted to compute the shortest distance between two time-series measurements.

2.4. Weibull distribution

The Weibull Probability Density Function (PDF) is a valuable modelling tool for wind speed distribution. It offers a versatile framework to characterise the probability of specific wind speeds occurring in a cluster or region [8]. The Weibull PDF encompasses two main variants: the three-parameter and two-parameter PDFs. Equation (3) represents the three-parameter PDF expression, where β is the shape parameter, α is the scale parameter, and γ is the location parameter.

$$f(x) = \frac{\beta}{\alpha} \left(\frac{x-\gamma}{\alpha}\right)^{\beta-1} e^{-\left(\frac{x-\gamma}{\alpha}\right)^{\beta}}. \quad (3)$$

By setting the location parameter equal to 0, (3) can be condensed to the two-parameter Weibull distribution function.

2.5. Optimisation

Optimization in this study involves employing mathematical and

computational techniques to identify the most favourable choice among a set of alternatives based on a specific criterion. There are three key elements to an optimization problem. Firstly, an objective function is defined, outlining the goal the optimization model aims to attain. The next step involves setting up constraints, representing the real-world limitations and prerequisites that the solution must adhere to. Lastly, the optimization process revolves around decision variables, which stand for the parameters or entities for which values are sought and act as the output of the optimization model. Considering all potential outcomes is crucial to ensure the ultimate outcome is optimal.

In this study, an optimization function is developed to determine optimal weights that simultaneously minimize risk (standard deviation) and maximize portfolio return. The portfolio consists of all of the wind clusters, where the optimal weights define the combination ratio of the summated wind profiles. Therefore, the optimised wind profile is obtained by multiplying each cluster's wind profile by its corresponding weight. The final wind profile is computed as the summation of all the adjusted weighted wind profiles. Equation (4) illustrates the derivation of this function, where achieving minimum variance involves minimizing the standard deviation of the final wind profile.

$$WP = \sum_{k=1}^{K} C_k \times W_k \quad (4)$$

Consider K as the number of clusters, n as the cluster number, C_k as the cluster profile, and W_k as the optimised weight vector.

The Sequential Least Squares Programming Optimizer (SLSQP) algorithm is utilised in this study because the function derived in (4) is nonlinear and has constraints, making SLSQP an ideal algorithm for this application. SLSQP can minimise a function that has several variables with any combination of bounds, equality, and inequality constraints [9], [10], [11].

3. Implementation and Results

3.1. Overview

Fig. 2 illustrates the clustering methodology employed in this study. Two methods will be compared in this section, temporal clustering and statistical feature clustering. The wind resource dataset for the temporal clustering is the raw wind data, while the statistical features for wind time-series data are extracted to be used in the statistical feature clustering. This statistical dataset is organised into seasons and split into morning (00:00 – 12:00) and evening (12:00 – 00:00) hours. Statistical features, namely the mean, standard deviation, and skewness, are then extracted to create a new dataset that reveals underlying patterns. In total, 24 features are extracted for each wind location, specifically the 3 features, mean, standard deviation, and skewness, calculated for the morning period and also for the evening period, repeated for each of the 4 seasons. This summates to a time series dataset that has 6 representative features per season and summates to a total of 24 features representative of each location. Both methods employ the k-means algorithm and the DTW distance metric is chosen to be used for temporal clustering method.

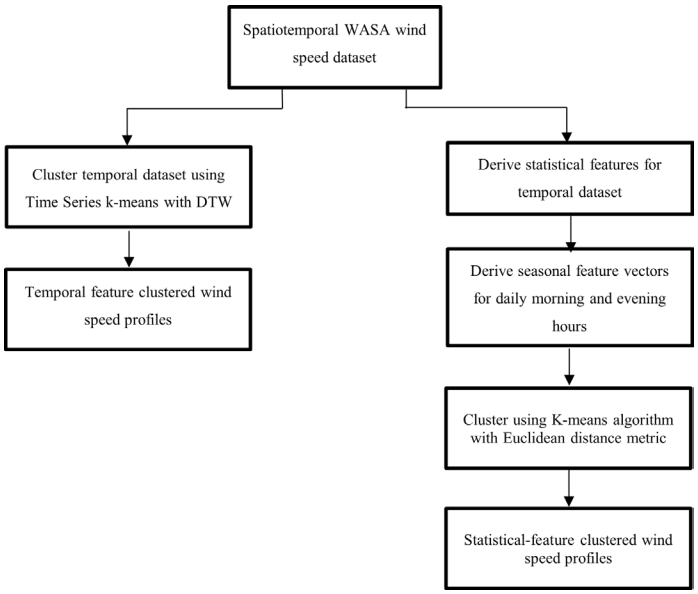

Fig. 2. The clustering methodology.

3.2. Wind resource clustering and validation

To implement the k-means clustering algorithm for classifying 527 sites along South Africa's coastal region, it is crucial to pre-select the optimal number of clusters. The elbow method and silhouette method are two commonly employed techniques to determine the ideal number of clusters. Fig. 3 and 4 showcase the elbow plot for the temporal and statistical methods, respectively, between 2 and 14 clusters. Additionally, the execution time for each cluster number is included in the figures. As noted previously, the temporal method utilizes the DTW distance metric, while the statistical method utilizes the Euclidean distance metric.

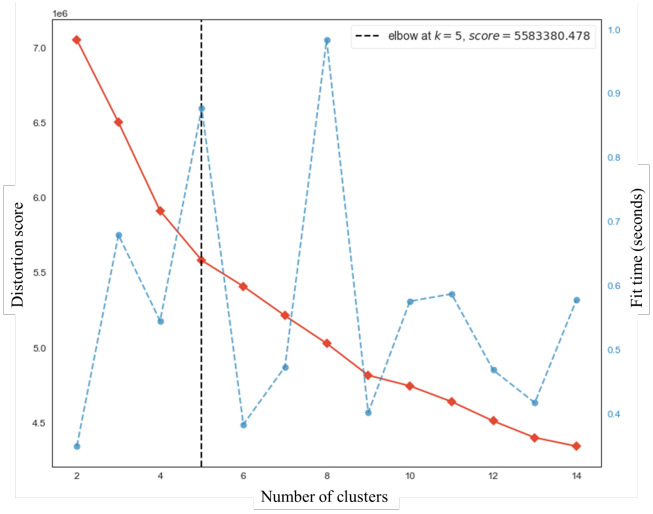

Fig. 3. Within-cluster Sum of Squares and fit time plotted against the cluster number for the temporal dataset.

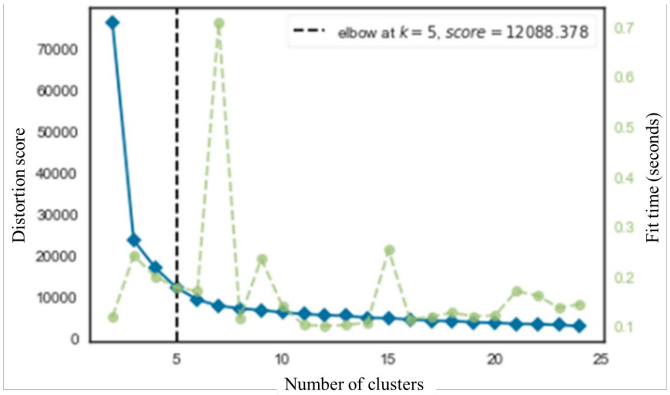

Fig. 4. Within-cluster Sum of Squares and fit time plotted against the cluster number for the statistical dataset.

The figures show that a slight change in behaviour is observed between 5 and 9 clusters for both methods. However, it is difficult to identify the optimal number of clusters since both plots are relatively smooth. For this reason, the silhouette scores for both methods are evaluated.

The average silhouette widths are calculated for clusters ranging from 5 to 9 to determine the optimal number of clusters. Table 1 showcases the silhouette scores for each cluster number for the temporal and statistical datasets. Based on these results, it was determined that 5 clusters are the most effective number for both datasets. The statistical ASW values also seem significantly higher than the temporal clusters, indicating a lower probability of locations being clustered into the wrong region. The temporal ASW values are all near 0, indicating that data points are close to the clustering decision boundary.

Table 1. Average silhouette scores for the temporal and statistical clusters.

Cluster number	ASW - Temporal	ASW - Statistical
5	0.13151	0.632
6	0.12346	0.554
7	0.12583	0.545
8	0.10809	0.375
9	0.12382	0.363

The clustering results are examined after determining the optimal number of clusters for both datasets. The cluster distribution obtained by applying k-means to the temporal and statistical datasets is shown in Fig. 5 and 6, respectively.

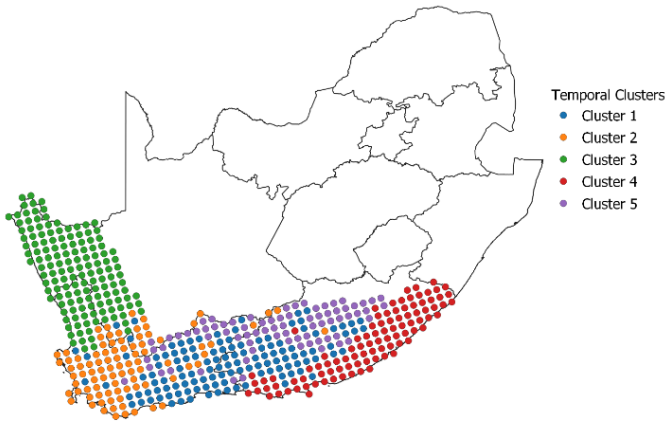

Fig. 5. Temporal cluster distribution sites of South Africa.

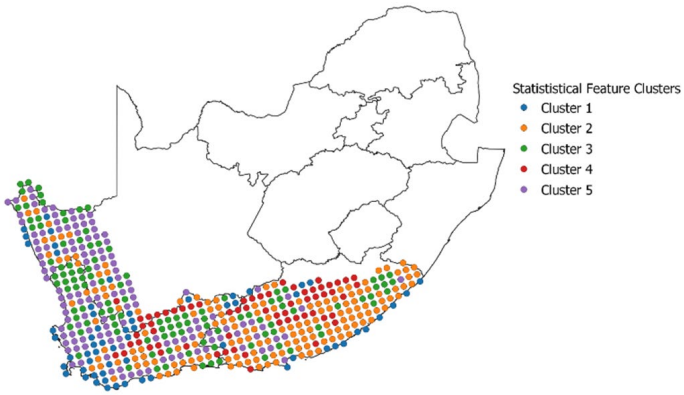

Fig. 6. Statistical cluster distribution sites of South Africa.

3.3. Comparison of the temporal and statistical clusters

This section compares and evaluates the outcomes of the two clustering methodologies to determine the most efficient and effective approach. Fig, 5 and 6 depict the clusters for both datasets obtained and mapped on a South African map. Fig. 7 and 8, depict these clusters superimposed on a heat map depicting South Africa's elevation. The cluster formations in

Fig. 7 exhibit a low degree of granularity and dispersion in relation to the underlying elevation. The cluster distribution generally corresponds to the geographic regions, with nearby locations clustered together.

Compared to the results derived for the temporal clusters, the statistical clusters depicted in Fig. 8 exhibit greater granularity and dispersion. Cluster 2 comprises the greatest number of sites, 157 in total, and each site is effectively clustered in relation to elevation. Few locations in cluster 1 are situated inland, with most of the sites located along the coast. This dispersion can also be observed in clusters 2, 3, and 5.

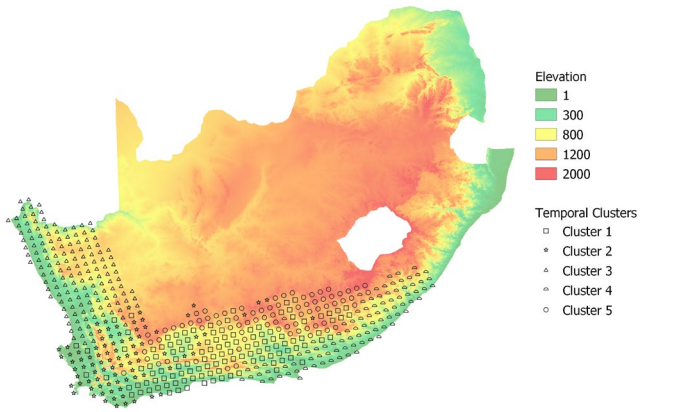

Fig. 7. Temporal cluster distribution overlayed with an elevation heatmap.

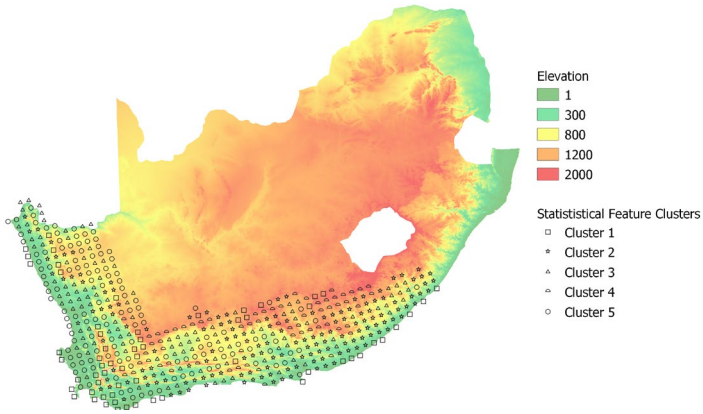

Fig. 8. Statistical cluster distribution overlayed with an elevation heatmap.

Upon comparing the clustering results achieved through both methodologies, it is observed that the two methodologies yield distinct outcomes regarding the diversity and granularity of the clusters formed. By employing (3), the Weibull distributions of the established wind speed clusters are constructed to evaluate the efficacy of both methods further. This is also done to determine the distinctions between the two methodologies and to establish which method would provide the best input for optimisation methods.

Fig. 9 and 10 depict the results of the Weibull distribution analysis corresponding to each cluster for the temporal and statistical feature-based methodologies, respectively. As indicated by the statistical clusters' distribution, a more uniform wind speed profile is observed within each cluster. In contrast, the distribution pattern of wind speed for temporal clusters appears to be shorter and with more spread. This indicates that the wind speeds within these clusters are significantly more variable. These results confirm that temporal clusters emphasise transient variations, whereas statistical clusters highlight wind profile characteristics over a longer period of time.

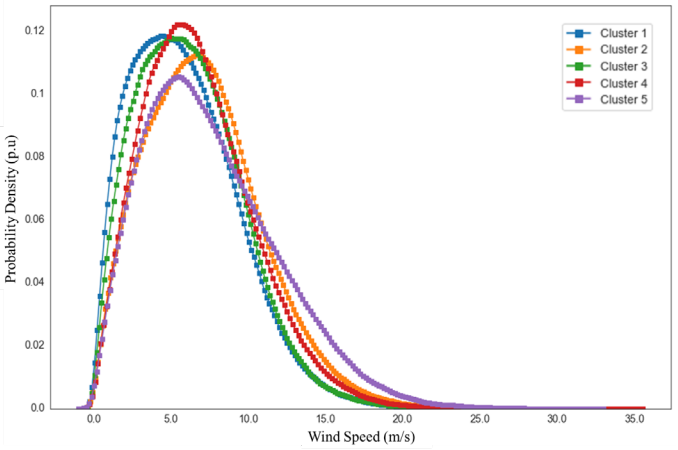

Fig. 9. Weibull distributions for the temporal clusters.

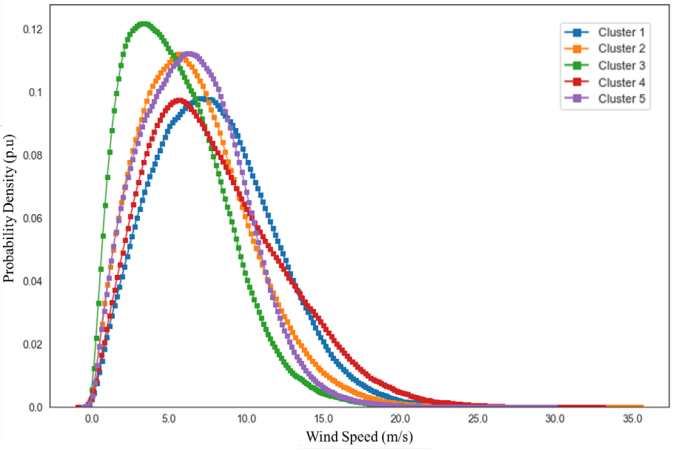

Fig. 10. Weibull distributions for the statistical clusters.

The analyses reveal additional distinctions between the distinct categories. The statistical clustering results reveal that the wind speed profiles associated with each cluster have notably higher means and lower standard deviations.

The comparative evaluation reveals clear advantages in favour of the statistical clustering method over its temporal counterpart. This choice not only significantly reduces time complexity but also ensures accurate outcomes in relation to elevation considerations. Statistical clusters demonstrate a heightened

level of certainty and consistently higher wind speed means compared to temporal clusters. Consequently, these robust statistical cluster results will be employed as the principal input for optimisation, driven by their reliability and potential to refine wind power plant placement strategies.

3.4. Optimisation of wind resource statistical clusters

Given the inherent volatility of wind energy resources, achieving optimal allocation within the necessary constraints is imperative. This section describes developing an optimal wind resource allocation model using wind speed data. Utilising a minimum optimisation algorithm, statistical cluster regions are utilised to validate the approach.

The weights are initialised randomly, and the optimisation process begins by minimising the nonlinear function described in (4). The model includes a constraint term to ensure that the cumulative sum of the weights equals 1, thereby ensuring proportional allocation. The second optimisation constraint sets the mean wind speed to the maximum average wind speed seen over all cluster formations. The standard deviation of the wind resource highlights the variation of wind speed values from the mean within each cluster's dataset. Therefore, lower standard deviations for a set mean wind speed correlate with greater stability and consistency.

3.4.1.Optimization results

The average wind speed of the resultant weighted profile is set, as an optimisation constraint, to the average wind speed of the cluster with the highest average wind speed, namely cluster 4 with an average wind speed of 7.964 m/s. The wind speed values are depicted in Fig. 11.

Table 2 presents a comprehensive breakdown of the investment allocations achieved through optimisation. This table illuminates how resources are apportioned across various cluster regions. Notably, clusters 1 and 5 emerge as recipients of the largest allocation, while cluster 3 receives the comparatively smaller allocation.

This distribution strategy correlates directly with the insights drawn from the Weibull distributions for the statistical feature-based clusters, as depicted in Fig. 10. These distributions distinctly showcase that that cluster 3's wind speed values are mainly distributed for low wind speeds compared to cluster 5, which has a high distribution for high wind speeds. Thus, it is demonstrated that using wind speed as a constraint lead to a high weight allocation in cluster 5 than cluster 3. In contrast, cluster 4's Weibull distribution reveals a lower probability density, indicating a lower degree of certainty and a higher degree of variability.

Table 2. Weight allocations for optimised wind speed profile.

Cluster number	Weight
1	0.2363
2	0.1858
3	0.1712
4	0.2035
5	0.3441

Fig. 11 displays a bar chart illustrating the average wind speeds within individual clusters. The set average wind speed for the optimised solution is 7.964 m/s. Of note, clusters 1 and 4 most resemble the optimal value.

Fig. 12 presents a bar chart that contrasts the standard deviation of each cluster with that of the optimized solution. Notably, the optimized solution boasts the lowest standard deviation of 2.540, significantly outperforming the standard deviations observed in individual clusters. This disparity emphasises the optimized solution's exceptional stability, indicating reduced risk. Consequently, clusters 3 and 5 emerge as the most efficient and reliable locations.

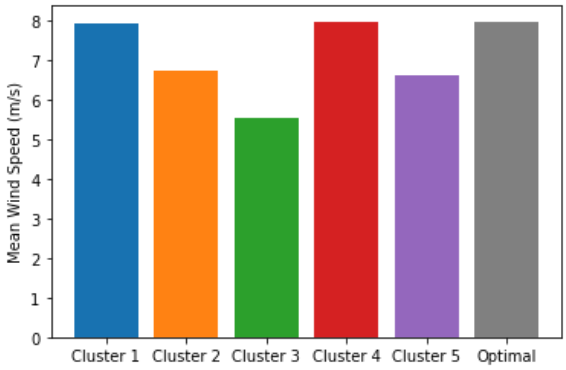

Fig. 11. Bar chart of the mean winds speeds for each cluster and the wind speed for the optimised wind profile.

Fig. 12. Bar chart of the standard deviation for each cluster and the standard deviation of the optimised wind profile.

4. Conclusion

Optimising wind resource placement is crucial for mitigating economic and technical uncertainties stemming from the inherent variability of wind energy generation. This study employed a temporal clustering methodology and a statistical feature-based clustering approach to uncover meaningful clusters within the South African region. The statistical feature-based clustering method yielded distinct clusters, where geospatial sites within each cluster shared consistent attributes and elevation characteristics.

A versatile optimisation model was employed to allocate resources across the cluster regions by utilising the average wind speed profiles of these clusters as inputs. The findings of this research underscore the potential for establishing an effective distribution of geographical sites along the South African coastline for optimal wind resource facility deployment. Consequently, this proposed strategy empowers investors to make well-informed decisions regarding the allocation of wind resources, optimising returns.

While this study was based on a one-year dataset, future implementations stand to benefit from the vast influx of data available. Using k-means, a highly efficient machine learning cluster algorithm, effectively mitigated extended execution times. This method proves especially adept at handling extensive datasets with lengthy timeframes, making it well-suited for diverse applications.

Furthermore, the optimised solution demonstrated exceptional performance, characterised by a notably reduced standard deviation for a set mean wind speed. Subsequent research could leverage the proposed methodology by translating wind speed into wind power, thereby incorporating it as an input for the optimisation algorithm. Advanced optimisation approaches, such as mean-variance portfolio optimisation, can also be used, where the performance can be compared to that of the generic optimisation used in this study. Moreover, the versatility of this approach lends itself to estimating the ideal distribution of solar resources and storage facilities, encompassing batteries and green hydrogen.

References

[1] F. Alismail, P. Xiong and C. Singh, “Optimal Wind Farm Allocation in Multi-Area Power Systems Using Distributionally Robust Optimization Approach,” *IEEE Transactions on Power Systems,* vol. 33, no. 1, pp. 536-544, 2018.

[2] M. R. Hossain, “Python based location analysis of wind mills in urban environment,” *GeoJournal,* vol. 86, no. 3, pp. 1355-1373, 2021.

[3] O. Longe, L. Myeni and K. Ouahada, “Renewable Energy Solution for Electricity Access in Rural South Africa,” in *2019 IEEE International Smart Cities Conference (ISC2)*, Johannesburg, 2019.

[4] J. MacQueen, “Some methods for classification and analysis of multivariate observations,” *Univ. Calif. Press.,* vol. 1, p. 281–297, 1967.

[5] P. J. Rousseeuw, “Silhouettes: A graphical aid to the interpretation and validation of cluster analysis,” *Journal of Computational and Applied Mathematics,* vol. 20, pp. 53-65, 1987.

[6] E. Keogh and J. Lin, “Clustering of time-series subsequences is meaningless: implications for previous and future research,” *Knowledge and Information Systems,* vol. 8, no. 2, pp. 154-177, 2005.

[7] M. Müller, Information Retrieval for Music and Motion, Berlin: Springer-Verlag, 2007.

[8] C. Y. Janse van Vuuren, H. J. Vermeulen and J. C. Bekker, “Clustering of Wind Resource Weibull Characteristics on the South African Renewable Energy Development Zones,” *2019 10th International Renewable Energy Congress (IREC),* pp. 1-7, 2019.

[9] D. Kraft, “Algorithm 733: TOMP–Fortran modules for optimal control calculations,” *ACM Trans. Math. Softw.,* vol. 20, pp. 262-281, 1994.

[10] R. Byrd, P. Lu, J. Nocedal and C. Zhu, “A Limited Memory Algorithm for Bound Constrained Optimization,” *SIAM Journal on Scientific Computing,* vol. 16, no. 5, pp. 1190-1208, 1995.

[11] J. Moré and D. Thuente, “Line Search Algorithms with Guaranteed Sufficient Decrease,” *Association for Computing Machinery,* vol. 20, no. 3, p. 286–307, 1994.

[12] P. J. Rousseeuw, “Silhouettes: A graphical aid to the interpretation and validation of cluster analysis,” *Journal of Computational and Applied Mathematics,* vol. 20, pp. 53-65, 1987.

The Value of Energy Storage in Reducing Wind Energy Forecast Error Penalty Costs in South Africa

Panduleni A. Ndengu[1], Amaris Dalton[2], and Bernard Bekker [3]

Department of Electrical and Electronic Engineering, Stellenbosch University, South Africa; Phone: +27 78 215 7648; E-Mail: [1]pandengu@sun.ac.za

Department of Electrical and Electronic Engineering, Stellenbosch University; E-Mail: [2]amaris_dalton@sun.ac.za, [3]bbekker@sun.ac.za

Abstract: The successful integration of large amounts of wind energy onto the South African network depends on reducing the uncertainties inherent in wind generation. Towards this goal, as of Bid Window 5 of South Africa's (SA's) Renewable Energy Independent Power Producer Procurement Programme independent, power producers are subjected to penalty costs for wind generation forecast errors. This paper explores the financial feasibility of adding a lithium-ion (li-ion) Battery Energy Storage System (BESS) to a wind farm to alleviate the wind forecast error penalty costs in SA. The hypothesis investigated in this study is that for a wind farm, the integration and operation of a BESS behind the meter can sufficiently alleviate the wind energy forecast errors and associated penalties to make such an integration financially feasible. An Excel-based simulation model that considers revenue, forecast penalties and the technical and financial performance of a li-ion BESS is developed. In evaluating the feasibility of the BESS integration, the net present value and internal rate of return metrics are employed. The model was tested through a case study using the Sere wind farm in SA. Feasibility was tested as a function of a number of parameters: BESS optimal size and efficiency; forecast error magnitude; BESS charging strategy; project discount rate; BESS replacement costs and wind farm size. For the case study, it was found that it is currently not financially feasible to install a li-ion BESS next to a wind farm for the sole purpose of wind energy forecast error alleviation in SA. The results of the sensitivity analysis indicate at what point such a BESS integration might become feasible given changes to input parameters. The outcome of this study is anticipated to be beneficial to wind farm owners and investors in the energy storage and wind energy domains seeking to alleviate costs associated with forecast errors.

Keywords: wind energy, forecast error, penalty cost, BESS.

1. Introduction

The share of electricity being generated from wind energy resources is the fastest growing within the electricity sector. With the increased wind energy penetration, wind energy forecasting is expected to be vital to modern power system operations [1], [2], [3]. However, there may exist a significant level of discrepancy between the wind energy forecasted and actual generation, referred to as a wind energy forecast error. These errors are influenced by many factors, including the accuracy of the weather forecast, the accuracy of the assumed power curve, wind speed, wind direction, forecasting approaches and model factors [4], [5].

With South Africa's Bid Window (BW) 5 of the Renewable Independent Power Producer Programme (REIPPPP), a forecast penalty cost due to inaccurate forecast has been introduced. Though the exact details of such penalty regimes are not, as yet, publicly available, it has been inferred that the hourly penalty cost in South Africa (SA) can be as high as 10% of the total hourly revenue [6]. Therefore these errors in wind power forecasting may lead to significant penalty costs that the wind farm is subjected to pay and can represent a substantial economic loss [7]. As such, forecast error penalty costs may pose a significant project financing risk and need to be well-understood by wind farm developers and operators [8]–[10].

Minimizing forecast errors results in minimized forecast penalty costs, which translates to profit maximization for wind farm owners [11]. The integration of a battery energy storage system (BESS) has the ability to compensate for differences between forecasted and actual wind energy generation. [12]–[18] assessed various methods and approaches in which a BESS can be employed to alleviate wind energy forecast errors in different energy markets and found that the forecast errors can be alleviated. Due to fast response, long calendar and cycle lifetime and high round trip efficiency, li-ion BESS is currently an attractive storage technology for this application [19], [20]. The financial performance and techno-economic studies for li-ion BESS carried out by [19], [21], [22] in various markets found that the integration of li-ion BESS for the sole purpose of wind

energy forecast error alleviation in the existing markets was unprofitable, unless the BESS also provides other profitable grid services.

This study aims to investigate the hypothesis that, for a wind farm in South Africa, the integration and operation of a BESS behind the meter can sufficiently alleviate the wind energy forecast errors and associated penalties to make such an integration financially feasible. To test this hypothesis, four operational strategies of the BESS are proposed, and various sensitivity analyses are performed. This paper uses the net present value (NPV) and internal rate of return (IRR) to evaluate the feasibility of integrating a li-ion BESS into a wind farm to alleviate forecast errors in SA.

The outline of this article is as follows: Section 2 provides the methodology and discusses the development of the simulation model. Section 3 introduces the description of the case studies used to test the developed approach. Section 4 presents the simulation results and discussions. Section 5 summarizes the findings and concludes the paper.

2. Methodology

2.1. Battery Energy Storage System Technical Modelling

The BESS will be used for storing the excess energy available due to under-forecasting (more energy produced than was forecasted) and will be discharged in instances of over-forecasting. A well-known SA assembled li-ion battery's specification and costing were used for this study due to its availability in the local market.

In terms of generating a technical model, the equation below was defined for charging and discharging of the BESS:

$$e\,(t) = \frac{E_a(t) - E_F(t)}{E_F(t)} \tag{1}$$

where $e\,(t)$ is the forecast error at any given hour t, $E_a(t)$ is the actual hourly energy generated and $E_F(t)$ is the hourly energy forecasted. The BESS charging and discharging is governed by the following constrains:

Charging:

$$E_i(t+1) = E_i(t-1) + E_i(t) * 0.5 * \eta_{BESS} \tag{2}$$

Discharging:

$$E_i(t+1) = E_i(t-1) - E_i(t) * 0.5 * \eta_{BESS} \tag{3}$$

where $E_i(t)$ is the energy charged or discharged at any given time step, t defined as 1 hour, $E_i(t-1)$ is the energy charged or discharged at any given time $(t-1)$ and η_{BESS} is the BESS roundtrip efficiency (assumed to have equal efficiency losses when charging as when discharging).

An important element affecting the BESS investment costs is its cycle life [23]. An iterative formula was incorporated into the model to track the BESS cycle life. This allowed the prediction of the lifespan of the BESS employed. This is determined through extrapolation of the charging and discharging cycles that the BESS is likely to employ throughout its lifecycle based on the historic generation and forecast error data. The equation below represents the iterative formula

$$C_{i+1} = C_i - \left|\frac{SOC_{i+1} - SOC_i}{2 * E_{BESS}}\right| \tag{4}$$

where C_{i+1} and C_i are the current and previous remaining number of cycles, respectively. SOC_{i+1} and SOC_i are the current and previous period's BESS state of charge (SOC, in kWh). E_{BESS} is the BESS usable capacity which is multiplied by 2 to cater for charging and discharging. This equation was deduced from similar studies by [24] and [25] to evaluate the battery life and indicate the performance of BESS by using the cycles.

2.2. Battery Energy Storage System Operation Strategies

There are multiple strategies in which the BESS can be operated that could minimize forecasting errors to various degrees of success. This paper proposes four SOC optimization strategies whose results were compared to the base case, where no BESS is integrated. These are based on setting constraints on the SOC of the BESS and how it responds to forecast errors. The objective of exploring these operational strategies was to reduce the forecast penalty costs and in turn maximize revenues.

In strategy 1, the BESS charges or discharge at any period of over -or under generation without maintaining a SOC level. Strategy 2 seeks to avoid charging and discharging when no forecast penalty was imposed, hence the constraint was on the BESS to only charge and discharge when the wind farm is subjected to a forecast penalty (i.e., $|e\,(t)| \geq 10\%$). In strategy 3, the BESS seeks to maintain a SOC level where there are no penalties imposed, in preparation for periods where there are penalties to be alleviated. Strategy 4 is an extension of strategy 3 with different SOC target levels selected to be maintained for each of the four seasons. The SOC levels were selected based on the forecast error distribution of the one-year historic data provided and for strategy 4 were selected based on the forecast error distributions for each of the four seasons.

2.3. Financial Modelling

The financial modelling accounts for all the costs incurred over the entire life of the projects.

To determine the penalty costs for inaccurate forecasting in BW 5, the penalty factors as shown in Table 1 were determined based on [6].

Table 1. Forecast Error Penalty Schedule

Forecast errors (%)	Penalty factor (w)
< 10	0
10 – 20	0.025
20 – 30	0.05
> 30	0.1

The hourly penalty cost incurred due to the forecast error ($C_{penalty}$) was calculated as:

$$C_{penalty} = w * E_a(t) * C_{gen} \quad (5)$$

where w is the penalty factor with respect to the forecast error, $E_a(t)$ is the actual wind energy generation (MWh) and C_{gen} is the feed-in tariff paid to the generator (R/ MWh). This equation was used in a similar study by [26] to determine the penalty costs for deviations.

To accurately evaluate and compare various scenarios of the project operation, a number of financial parameters were considered. The annual operational cost can be referred to as the expenses incurred to operating the part of the windfarm relating to the integrated BESS and considers the annual Operational Expenditure ($OpEx_{BESS}$) and the cost of efficiency losses of the BESS ($C_{\eta_{Loss}}$). It can be calculated as

$$Annual\ operational\ cost = OpEx_{BESS} + \sum_{t=1}^{8761} C_{\eta_{Loss}} \quad (6)$$

The hourly cost due to the efficiency losses of the BESS can be calculated as:

$$C_{\eta_{Loss}} = (SOC_{i+1} - SOC_i) * \left(\frac{1-\eta_{BESS}}{2}\right) * C_{gen} \quad (7)$$

The annual savings can be calculated as

$$Annual\ Savings = R_a - R_b \quad (8)$$

where R_b and R_a are the annual revenues before and after the interventions, respectively.

The NPV is the current value of all future cash flows (savings) over the project period, t, from year one until the last year (N) [27]. It can be calculated as

$$NPV = -CapEx_{BESS} + \sum_{t=1}^{N} \frac{R_a - R_b}{(1+r)^t} \quad (9)$$

where $CapEx_{BESS}$ is the capital expenditure of the BESS, r is the discount rate. The discount rate of 8% was selected as it reflects a representative rate for power generation technologies in SA [28].

The project's internal rate of return (IRR), which is a method of evaluating the profitability of a project based on its positive returns [29], can be calculated as follows, by setting the NPV to zero:

$$NPV = -CapEx_{BESS} + \sum_{t=1}^{N} \frac{R_a - R_b}{(1+\text{IRR})^t} = 0 \quad (10)$$

The flowchart in Fig. 1. presents the methodology used for the operation of the simulation model.

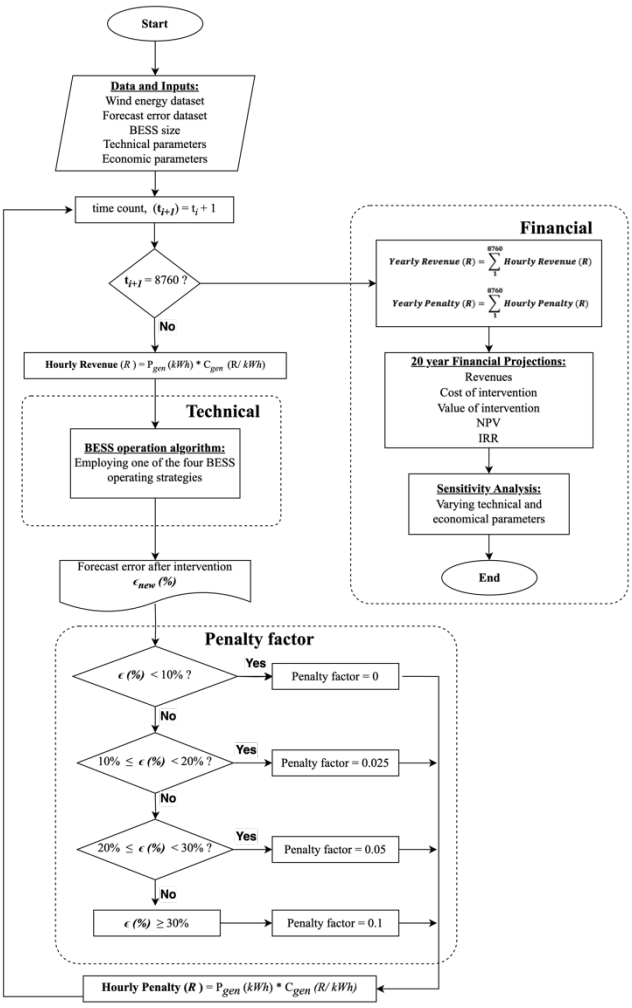

Fig. 1. Methodology flowchart of the developed simulation model

The simulation model used a range of li-ion BESS sizes between 0 MWh (Base case) and 10 MWh to determine the optimal BESS intervention size.

3. Description of Case Study

The 2018 historical wind energy generation data for the 100MW

Sere onshore wind farm was used as a case study to demonstrate the proposed methodology. As individual forecast error data was not available for South African wind farms, the clustered forecast error data for eight wind farms (which includes the Sere wind farm) between 01 January 2018 to 31 March 2021 obtained from Eskom was used. The pattern in forecast errors and the generation profile considered are assumed to be valid for the 20-year assessment. Fig. 2 illustrates the cluster that contains the Sere wind farm.

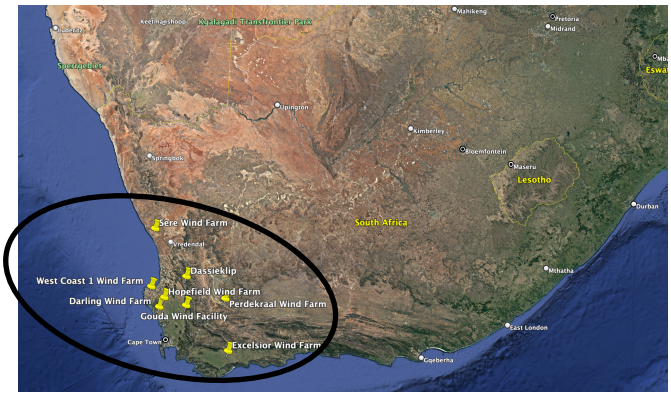

Fig. 2. Cluster region with Sere wind farm

The forecast error distribution, as seen in Fig. 3. is expressed as a percentage of the installed capacity having a slight positive bias of 0.046, median of 0.02 and standard deviation of 0.389. The negative forecast errors and positive forecast errors have means of -0.314 and 0.322, respectively.

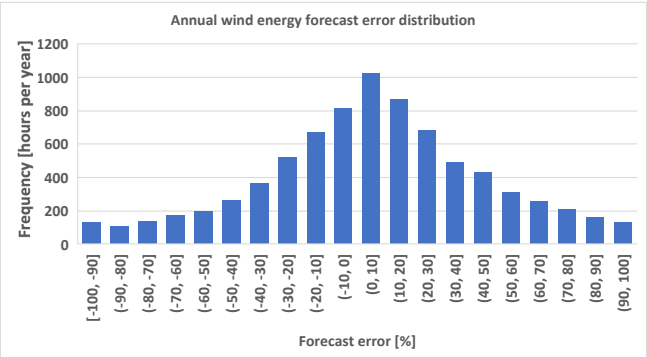

Fig. 3. Annual wind energy forecast error distribution of the clustered eight wind farms

4. Results and Discussion

4.1. Base Case: No Intervention

The base case results of the study comprised the annual penalty costs to be paid by the wind farm, with respect to different deviation factors employed as depicted in Table 2. The deviation factors were introduced to explore the impact of variation in the forecast error.

Table 2. Base Case Results for the 20 Years of Operation

Forecast deviation factor (%)	Penalty cost at end of year one (R million)
0%	9,55
10%	10,07
20%	10,57
30%	11,05

From the base case simulation results, for a 30% forecast deviation factor, it was found that a wind generator of approximately 100MW would experience a loss of about R 300 million on the net revenue due to inaccurate forecasting over the entire 20 years of operation. The energy bid price of R 494.40 / MWh used was assumed to be the average of the energy bid prices of the preferred bidders of BW5.

From the base case simulation, it was found that with the forecast errors increasing to 30%, the forecast penalty costs only increases by approximately 10% (approximately R 1 million) – this relationship is a function of the specific penalty regime.

4.2. Simulation Assumptions

Below are the assumptions made for the BESS;

- Efficiency [%] – 95
- Cycle Life [Cycles] – 6 414
- Installation Cost/CapEx [R/MWh] – 6 588
- Operation Cost [% of the CapEx] – 1.2
- Replacement Cost [% of the CapEx] – 30
- Discount rate [%] – 8
- Inflation [%] – 4.5

4.3. BESS Operational Strategies

Fig. 4. illustrates how different BESS sizes alleviate large forecast errors (30% forecast deviation factor) based on the four operational strategies tested.

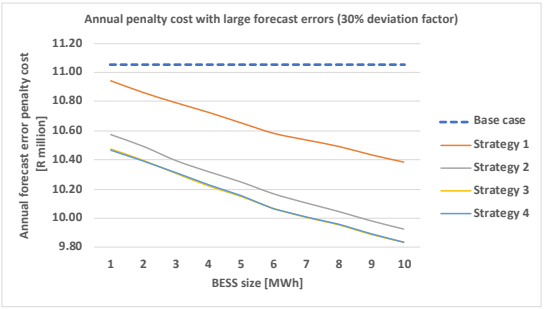

Fig. 4. Annual penalty costs of the four operation strategies with large forecast errors

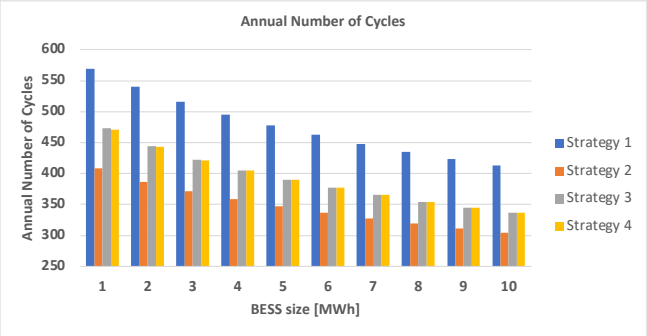

Fig. 5. Annual number of cycles of the four operation strategies with large forecast errors

As shown in Fig. 4., BESS operational strategy 4 which accounts for seasonal variations leads to the largest reduction in the case study project's penalty cost (although only slightly more than strategy 3), and should therefore lead to the highest NPV and IRR in comparison to the other strategies. Strategy 4 also resulted in the greatest penalty alleviations for both small (5.6%) and large (5.2%) forecast errors and was thus used for the rest of the calculations in this section. With this strategy, more charging than discharging was required in summer and winter and hence a SOC target of 20% was maintained during these periods. Likewise, more discharging than charging was required in autumn and spring, and hence a SOC target of 60% was maintained.

In terms of cycles, Strategy 2 has the least annual number of cycles, as depicted in Fig. 5. The reason for this relates to the fact that the BESS target SOC is not optimized for the actual operating conditions, leading to higher error penalty costs but lower battery charge/discharge cycles than other strategies.

4.4. Financial Comparison

The impact of various li-ion BESS sizes on financial viability was investigated next. As BESS size increases, the margin between the BESS CapEx and penalty cost reduction reduces as illustrated in Fig. 6. This illustrated that for the specific case study a larger BESS is less effective in alleviating the penalty costs.

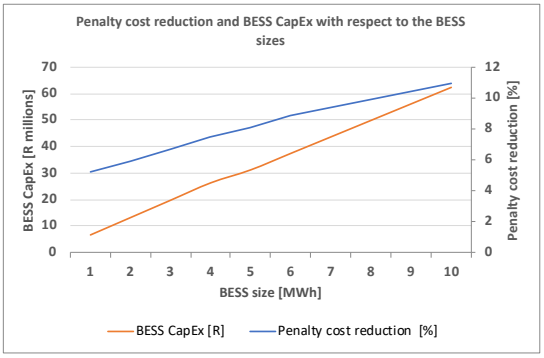

Fig. 6. Penalty cost reduction and BESS CapEx

The feasibility of the intervention was then assessed by applying the financial indicators: NPV and IRR. Fig. 7 and Fig. 8 present, respectively the project NPV and IRR of the savings (or losses) made on various BESS sizes employed in the study.

From the 2 to 6 MWh BESS, the IRR cannot be obtained due to the high replacement costs and replacement expected towards the end of the 20 years of project operation which resulted in huge losses. From 7 MWh BESS, no replacement was expected during the 20 years of operation. Larger BESS sizes further lower IRR through replacement costs.

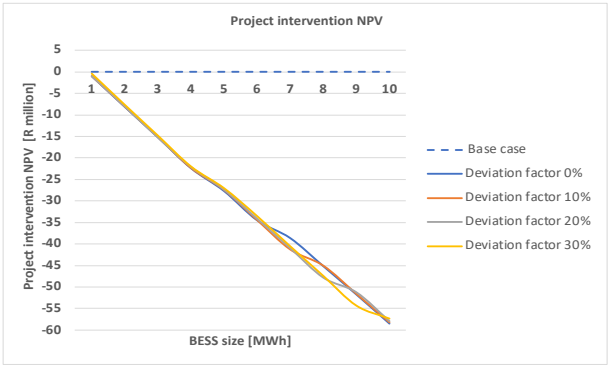

Fig. 7. NPV of the project intervention over a 20-year period

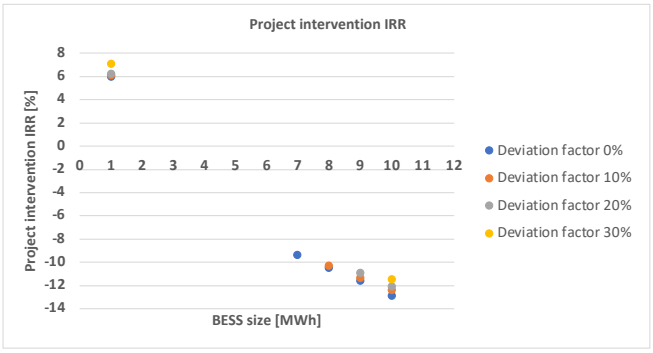

Fig. 8. IRR of the project intervention over a 20-year period

It is feasible to integrate a BESS when the NPV is positive given a required discount rate / when the IRR is greater than the hurdle rate. The hurdle rate is the minimum rate of return expected on a project to make the cash flows positive [30].

The BESS size with the highest NPV is the most attractive investment. It was found that none of the BESS sizes employed is feasible as their NPVs were all negative (NPV<0) and their IRRs were less than 8%. The 1 MWh BESS had the highest NPV of R -0.492 million and IRR of 7.07%, with financial viability decreasing as battery size increase.

4.5. Sensitivity Analysis

Sensitivity analysis was carried out to understand the influence

of variations in key technical and economic parameters for the BESS sizes employed. The 1 MWh BESS size, 0% deviation factor and strategy 4 were kept constant. The analysis aims to explore (a) forecast error and SOC, (b) battery efficiencies, (c) battery replacement costs, (d) discount rate and (e) wind farm size.

The study found that a small BESS, i.e 1 MWh is very sensitive to the size of forecast errors and BESS SOC due to the unsymmetrical nature of the forecast error, which is due to the small amount of available storage compared to the size of the error results in many instances where the BESS is not able to correct the error, in comparison to a larger BESS. Only at around 50 MWh BESS size are all error instances corrected.

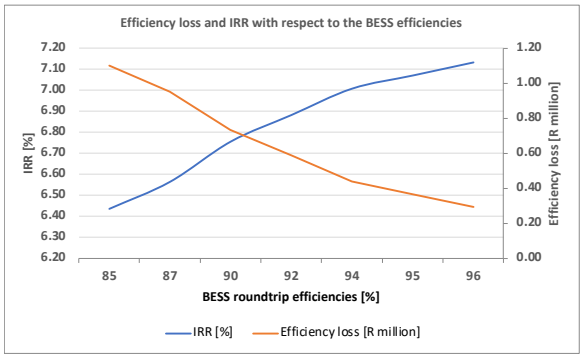

Fig. 9. Efficiency loss, IRR of various BESS efficiencies

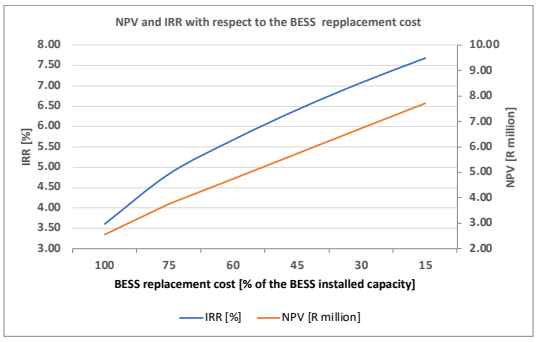

Fig. 10. IRR and NPV of various BESS replacement costs

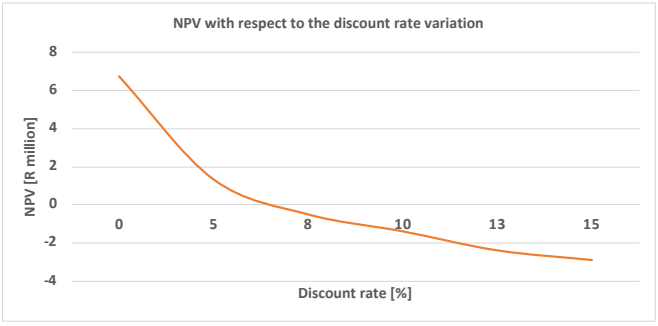

Fig. 11. NPV with respect to the discount rate variation

The financial viability of the chosen BESS is very sensitive to the BESS roundtrip efficiencies, exhibiting an almost linear relationship as illustrated in Fig. 9. The relationship between BESS efficiency-related losses over the analysis period and BESS roundtrip efficiency is also shown.

It is more financially feasible to install a 1 MWh BESS to a larger wind farm, i.e. 200 MW, as it is noted to have higher savings of R 21.38 million, higher NPV and IRR whereas there were losses made for a smaller wind farm, as noted from Table 3. The savings increase as the wind farm size increase.

Table 3. Impact of Wind Farm Size on Results

Wind farm size (MW)	Total penalty w/o BESS (R million)	Penalty reduction (%)	Savings (R million)	NPV (R)	IRR (%)
25	86,67	7.45	-4.90	-5.51	-16.6
50	173,35	5.96	-1.05	-3.86	-1.6
100	346,69	5.25	6.78	-0.47	7.1
150	520,04	4.92	14.19	2.79	12.6
200	693,39	4.73	21.38	5.95	17.6

From the above it can be seen that although the percentage of the penalty cost alleviated increases as the size of the BESS being installed increases (along with increased installation costs), the installation cost for a bigger BESS rises more than the penalty costs alleviated thus making the increase of the BESS size unfeasible.

From the obtained results, it can be inferred that the usefulness of li-ion battery technologies as BESS to support the growing penetration of wind energy which is intermittent in nature by alleviating the forecast errors as well as the respective penalty costs in SA is limited. The main reasons are the high installation costs of li-ion batteries, limited income from the BESS, BESS lifespan and the unsymmetrical nature of the forecast errors. The findings of this study align with those found in the literature [21], [22], [31].

5. Conclusion

In this paper, a methodology to incorporate BESS into a wind farm in SA was developed to allow the wind farm to alleviate the forecast errors and associated penalties. This was achieved by charging the BESS during periods of under forecasting and discharging it during periods of over forecasting. This approach was tested using the Sere wind farm actual wind energy generation data and the clustered forecast error data from eight wind farms in SA which includes Sere. Four BESS operational strategies were proposed, of which the strategy that accounts for seasonal variations was found to be optimal.

Two financial metrics (NPV and IRR) were determined to evaluate the feasibility and performance of the intervention. For the case study, the 1 MWh Li-ion BESS intervention was found to be most appropriate for this purpose as it has the highest NPV of R -0. 492 million, and IRR of 7.07% as compared to other BESS sizes used. However, due to the negative NPV and an IRR smaller than 8%, a much lower discount rate between 0 – 7.05% is required to make the NPV positive. Low-interest rate environments are therefore more conducive to such interventions.

Given the findings from the study, it was concluded that whilst the BESS can be used to alleviate the forecast errors, it is currently financially unfeasible to offset the penalty costs in SA. A BESS with a large energy capacity is required to alleviate most forecast errors due to the imbalance between positive and negative forecast errors, thus affecting the BESS performance.

Additionally, it was clear from the case study that the project viability estimation is very sensitive to the replacement cost that is assumed in the modelling, and to a lesser extent the BESS roundtrip efficiency. So, should the prices of BESS fall or cycles increase it might become viable.

References

[1] P. Pinson and G. Kariniotakis, "Optimal Prediction Intervals of Wind Power Generation," vol. 25, no. 3, pp. 1845–1856, 2010.

[2] B.-M. Hodge and M. Milligan, "Wind power forecasting error distributions over multiple timescales," *2011 IEEE Power Energy Soc. Gen. Meet.*, pp. 1–8, 2011, doi: 10.1109/PES.2011.6039388.

[3] B. Hodge *et al.*, "Wind Power Forecasting Error Distributions: An International Comparison," no. September 2012, 2012, [Online]. Available: http://www.osti.gov/bridge.

[4] J. Yan, Y. Liu, S. Han, Y. Wang, and S. Feng, "Reviews on uncertainty analysis of wind power forecasting," *Renew. Sustain. Energy Rev.*, vol. 52, pp. 1322–1330, 2015, doi: 10.1016/j.rser.2015.07.197.

[5] M. Lange, "On the uncertainty of wind power predictions - Analysis of the forecast accuracy and statistical distribution of errors," *J. Sol. Energy Eng. Trans. ASME*, vol. 127, no. 2, pp. 177–184, 2005, doi: 10.1115/1.1862266.

[6] M. Rastall, "Wind forecasting penalty under the PPA," 2022. [Online]. Available: https://www.dnv.com/Publications/wind-forecasting-penalty-under-the-ppa-214463.

[7] T. Aigner, S. Jaehnert, G. L. Doorman, and T. Gjengedal, "The effect of large-scale wind power on system balancing in Northern Europe," *IEEE Trans. Sustain. Energy*, vol. 3, no. 4, pp. 751–759, 2012, doi: 10.1109/TSTE.2012.2203157.

[8] N. Mararakanye and B. Bekker, "Renewable energy integration impacts within the context of generator type, penetration level and grid characteristics," *Renew. Sustain. Energy Rev.*, vol. 108, no. October 2018, pp. 441–451, 2019, doi: 10.1016/j.rser.2019.03.045.

[9] P. M. S. Frade, J. P. Pereira, J. J. E. Santana, and J. P. S. Catalão, "Wind balancing costs in a power system with high wind penetration – Evidence from Portugal," *Energy Policy*, vol. 132, no. October 2018, pp. 702–713, 2019, doi: 10.1016/j.enpol.2019.06.006.

[10] N. Mararakanye, A. Dalton, and B. Bekker, "Characterizing Wind Power Forecast Error Using Extreme Value Theory and Copulas," *IEEE Access*, vol. 10, no. June, pp. 58547–58557, 2022, doi: 10.1109/access.2022.3179697.

[11] H. Holttinen, J. Miettinen, and S. Sillanpää, "Wind power forecasting accuracy and uncertainty in Finland," *VTT Tech. Res. Cent. Finl.*, pp. 10–11, 2013, [Online]. Available: http://www.vtt.fi/publications/index.jsp.

[12] J. Martinez-Rico, E. Zulueta, U. Fernandez-Gamiz, I. R. de Argando-a, and M. Armendia, "Forecast error sensitivity analysis for bidding in electricity markets with a hybrid renewable plant using a battery energy storage system," *Sustain.*, vol. 12, no. 9, 2020, doi: 10.3390/SU12093577.

[13] Z. Zhang, Y. Zhang, Q. Huang, and W.-J. Lee, "Market-oriented optimal dispatching strategy for a wind farm with a multiple stage hybrid energy storage system," *CSEE J. Power Energy Syst.*, vol. 4, no. 4, pp. 417–424, 2018, doi: 10.17775/cseejpes.2018.00130.

[14] H. Bitaraf, S. Rahman, and M. Pipattanasomporn, "Sizing Energy Storage to Mitigate Wind Power Forecast Error Impacts by Signal Processing Techniques," *IEEE Trans. Sustain. Energy*, vol. 6, no. 4, pp. 1457–1465, 2015, doi: 10.1109/TSTE.2015.2449076.

[15] P. Haessig, B. Multon, H. Ben Ahmed, S. Lascaud, and P. Bondon, "Energy storage sizing for wind power: Impact of the autocorrelation of day-ahead forecast errors," *Wind Energy*, vol. 18, no. 1, pp. 43–57, 2015, doi: 10.1002/we.1680.

[16] S. Atcitty, J. Neely, D. Ingersoll, A. Akhil, and K. Waldrip, "Battery Energy Storage System," *Green Energy Technol.*, vol. 59, pp. 333–366, 2013, doi: 10.1007/978-1-4471-5104-3_9.

[17] H. Bludszuweit and J. A. Domínguez-Navarro, "A probabilistic method for energy storage sizing based on wind power forecast uncertainty," *IEEE Trans. Power Syst.*, vol. 26, no. 3, pp. 1651–1658, 2011, doi: 10.1109/TPWRS.2010.2089541.

[18] Z. Cai, C. Bussar, P. Stöcker, L. Moraes, D. Magnor, and D. U. Sauer, "Optimal Dispatch Scheduling of a Wind-battery-System in German Power Market," *Energy Procedia*, vol. 99, no. March, pp. 137–146, 2016, doi: 10.1016/j.egypro.2016.10.105.

[19] U. Datta, A. Kalam, and J. Shi, "A review of key functionalities of battery energy storage system in renewable energy integrated power systems," *Energy Storage*, vol. 3, no. 5, pp. 1–21, 2021, doi: 10.1002/est2.224.

[20] M. Świerczyński, D. I. Stroe, A. I. Stan, R. Teodorescu, and S. J. Andreasen, "Evaluation of different operational strategies

for lithium ion battery systems connected to a wind turbine for primary frequency regulation and wind power forecast accuracy improvement," *11th Wind Integr. Work.*, no. November, pp. 6–9, 2012.

[21] Y. Li *et al.*, "Design of minimum cost degradation-conscious lithium-ion battery energy storage system to achieve renewable power dispatchability," *Appl. Energy*, vol. 260, no. August 2019, p. 114282, 2020, doi: 10.1016/j.apenergy.2019.114282.

[22] A.-I. S. and R. T. Maciej Swierczynski, Daniel-Ioan Stroe, "Lifetime and economic analyses of lithium-ion batteries for balancing wind power forecast error," *Arch. Thermodyn.*, vol. 33, no. 4, pp. 23–40, 2015, doi: 10.1002/er.

[23] Y. Zhang, Y. Su, Z. Wang, F. Liu, and C. Li, "Cycle-Life-Aware Optimal Sizing of Grid-Side Battery Energy Storage," *IEEE Access*, vol. 9, pp. 20179–20190, 2021, doi: 10.1109/ACCESS.2021.3054860.

[24] S. Khunkitti, P. Boonluk, and A. Siritaratiwat, "Optimal Location and Sizing of BESS for Performance Improvement of Distribution Systems with High DG Penetration," *Int. Trans. Electr. Energy Syst.*, vol. 2022, pp. 1–16, 2022, doi: 10.1155/2022/6361243.

[25] M. Moncecchi, C. Brivio, S. Mandelli, and M. Merlo, "Battery energy storage systems in microgrids: Modeling and design criteria," *Energies*, vol. 13, no. 8, pp. 1–18, 2020, doi: 10.3390/en13082006.

[26] H. Ali, "Benefits of Battery Storage for Wind Power," pp. 11–14, 2022, [Online]. Available: https://odr.chalmers.se/server/api/core/bitstreams/72befa3f-4af5-43fd-a707-04bc9ea600db/content.

[27] N. Yimen *et al.*, "Optimal sizing and techno-economic analysis of hybrid renewable energy systems—a case study of a photovoltaic/wind/battery/diesel system in Fanisau, Northern Nigeria," *Processes*, vol. 8, no. 11, pp. 1–25, 2020, doi: 10.3390/pr8111381.

[28] W. M. Fanaian S. , Money A., Pop M., Berdellans I., Hasanovic S., Gritsevskyi A,. Stankeviciute L., Tot M., "Lecture 3: Financing Power Projects, FinPlan. Release Version 1.0.," Atomic Energy Agency, 2021.

[29] S. Pookpunt, W. Ongsakul, and N. Madhu, "A comprehensive techno-economic analysis for optimally placed wind farms," *Electr. Eng.*, vol. 102, no. 4, pp. 2161–2179, 2020, doi: 10.1007/s00202-020-01014-6.

[30] E. Koutroulis, D. Kolokotsa, and G. Stravrakakis, "Optimal design and economic evaluation of a battery energy storage system for the maximization of the energy generated by wind farms in isolated electric grids," *Wind Eng.*, vol. 33, no. 1, pp. 55–81, 2009, doi: 10.1260/0309-524X.33.1.55.

[31] M. Świerczyński, D. I. Stroe, A. I. Stan, R. Teodorescu, and S. J. Andreasen, "Evaluation of different operational strategies for lithium ion battery systems connected to a wind turbine for primary frequency regulation and wind power forecast accuracy improvement," *11th Wind Integr. Work.*, no. December 2015, pp. 6–9, 2012.

ELECTRIFICATION MODELING APPROACHES FOR RURAL AREAS OF SUB-SAHARAN AFRICA

Basilio Zeloso Salvador Tamele[1,3], Erik O. Ahlgren[2], Alberto Tsamba[1]

[1]Faculty of Sciences, Eduardo Mondlane University, Maputo City, Mozambique; cel phone: +258843017730; email: bazeta2004@gmail.com

[2]Department of Space, Earth and Environment, Chalmers University of Technology Gothenburg, Sweden

[3]Faculty of Natural and Exact Sciences, Universidade Save, Xai-Xai, Mozambique

Abstract: Energy is a major driver of social and economic development, but energy should also be provided at the right time and place and in the right amount. Thus, advance planning is required, and this planning demands accurate energy data. Energy system modeling has proven valuable for rationalizing resources and simulating and analysing energy systems prior to implementation for optimal design and during operation for improved operational decisions to be made. Due to lack of data, in particular in developing countries, energy systems studies often use aggregated statistical and/or survey data as well as data from geographic information systems (GIS). Yet, the accuracy of available statistical and survey data is debatable and may lead to over or underestimation of electricity demand and/or supply. This is particularly the case for rural areas. This calls for new modeling methods for electrification planning. Thus, this article reviews trends in modeling approaches used in studies of rural electrification in developing countries, particularly in sub-Saharan Africa, between 2012 and 2022. The majority of studies tend to optimize power generation systems based on the lowest-cost technologies and with a high degree of disaggregation of technologies. Results indicate that geospatial tools such as GIS help divide rural and urban zones, which is important for energy planning because of the different features of these different zones. Modeling electrification at the subnational level (especially in rural areas) requires higher resolution, in spatial and time variables. The models should include local variations in energy resources such as wind, biomass, and small hydro, to allow for good prediction of potential generation at different time scales and better planning of the alternatives that need to be considered for power system reliability. Besides, high-resolution population and resource data as well as high-time computational resolution would enhance the models result.

Keywords: electricity; modeling approach; sub-national, rural.

1. Introduction

Energy (and mainly electricity) access represents a key factor for the development of any country. It is a way out of poverty, increasing productivity and improving health from a population perspective. Most developing countries like sub-Saharan Africa (SSA) are characterized by a lack of access to electricity and poor power quality and reliability [1]. The reliability is related to the low or weak transmission and distribution infrastructure, and strategies to expand grid penetration (as the main source of electricity) need to acknowledge that supply and demand obstacles are important and interlinked.

With the advances in technology and innovation and increasing concern in environmental problems (due to fossil fuel-based energy and electricity generation and traditional use of biomass), there is an increased penetration of renewable energy generation through off-grids and mini-grids [2]. Strategies to combine these technologies with the existing electrical grid can contribute to expanding the access to electricity for a large part of the population living in rural and remote areas and help to improve the quality of power are necessary. This has been done through different energy modeling approaches and the results are used to help decision-makers to minimize the investment cost and possible socio-environmental impacts associated.

The prediction of energy demand and supply in developing countries is a complex task, as any expansion of electricity to new areas would create its own demand [1]. Besides, most energy (electricity) models fail to represent differences between urban and rural areas regarding socioeconomic, cultural, and structural characteristics. As variable renewable energy resources vary considerably in time and space, models must include a high spatiotemporal resolution, and some models are not applicable due to the lack or inconstancy of the input data [3].

Thus, the focus of this study is to critically review scientific papers related to modeling of electric energy systems in rural electrification planning in developing countries published within the period 2012 to 2022, to analyse and compare different approaches used, and thereby identify suitable approaches. Thus, as a guide for the study, the following research questions were formulated:

- Which energy systems modeling approaches and methodologies have been used in modeling electricity supply and demand at sub-national level in rural areas of developing countries?
- What are the main energy modeling parameters (characteristics) in energy systems at the sub-national

level in developing countries?

- Which type of energy modeling tool is preferable to represent the supply and demand of rural areas in developing countries?
- How could energy modeling approaches be improved to better capture crucial characteristics of rural areas?

2. Methodology

The purpose of this study is to identify appropriate modeling approaches for rural electrification at the sub-national level in developing countries. Existing reviews of energy models in developing countries focus on energy models at national and/or international levels ([3], [4]). However, different from national, modeling energy systems at small geographical areas requires higher spatial resolution than national. Further, the mentioned reviews focus on analysis of energy modeling tools, while our focus is to analyse and compare different approaches used and, thereby, identify suitable approaches.

The methodological approach is divided into two steps. The first step consists of the identification and selection of relevant scientific peer-reviewed papers on Google Scholar, with the help of Boolean operators (AND, NOT, OR). From a total of 134 articles, 30 were pre-selected for further review, and 14 were selected as core papers. Due to the rapid development of energy modeling tools, papers reviewed were limited to publications between 2012 and 2022.

In the second step, a critical review of the selected papers with a focus on analyses of the approaches used rather than of the models was applied. The majority of rural villages in developing countries, such as in sub-Saharan Africa, do not have access to electricity currently. Due to abundant resources, a large share of variable renewable (e.g, solar and wind) energy generation is expected when these areas are electrified together with a highly dynamic electric demand. Thus, a spatial and temporal variation analysis with high-resolution is of great importance. The terminology applied differs from paper to paper, thus the review was based on a set of criteria including the analytical approach, geographical coverage area, domain, time horizon, methodological approach, spatial resolution, and temporal resolution [5], type of input data summarized in Table 1.

The information in Table 1 allowed us to do a comparative analysis of the approaches used in the reviewed studies in terms of similarities and differences, weaknesses, and robustness. The analysis of the limitations of the different models used in the different studies allowed the identification of the critical aspects that must be considered when developing models to predict energy supply and/or demand.

In this study, main modeling approaches are identified. The most appropriate tools are identified based on the type and availability of data and their ability to cover different electrification technologies, including temporal and spatial resolution.

3. Literature Review

In the literature, electrification planning is usually carried out with the help of energy models, which are fundamental tools for the adequate exploitation of natural resources for the generation, distribution, and consumption of electricity. The use of models increases the ability of the country to anticipate and respond to the rapid changes occurring, and new issues and opportunities [1], as it allows better resource and technology management, without wasting financial and material resources, as well as time saving.

Energy models can be classified in several ways, however this study focus on: (i) the analytical approach, (ii) coverage area, (iii) domain, (iv) time horizon, (v) methodological approach, (vi) spatial resolution, and (vii) temporal resolution [6], [7]

Based on the analytical approach [6], the models can be top-down or bottom-up. Top-down models, often econometric model, use aggregate data to estimate energy demand and supply. Least-cost technologies are set by market behaviors, however, such technologies are new and thus not represented in the current system. For that reason, top-down approaches often underestimate the potential for efficiency improvements, and therefore not appropriate to identify sector-specific policies [7]. Bottom-up (often techno-economic) models disaggregate electricity supply and demand to individual technology units. They allow the user to compare the impact of a set of different technologies and to identify the optimal technologies based on the performance, technical potential, and technology efficiency [7]. Although, bottom-up approach neglects macroeconomic impacts on technology selection ([7], [3]).

The time horizons addressed correspond to the time frame for which the model is applied, and can be short-term (up to 5 years), medium-term (between 3 and 15 years), and long-term (above 10 years) ([6]; [8]). Long-term models are useful for planning expansion of generation capacity, while short-term models are usually used to analyze electricity system configurations and their future modifications [8]. Moreover, the time resolution corresponds to the time steps in which the simulation year is divided. It can be categorized into low (1 to 32 time-slices, usually 12-time slices is used in case of three-time slices per season), medium (36 to 288 time-slices, using representative days approach), and high-resolution (hourly representation, 8760-time slices annually ([3]; [8]). High-resolution models increase the computational burden but are crucial when considering variable energy generation (such as solar and wind power) as they depend on weather patterns.

Regarding the methodology, energy models are often classified as optimization or simulation models [8]. According to [6], optimization models are used to find the best solution for given variables while meeting given constraints, and in the

case of developing countries, are usually applied to find the least-cost electrification option. Simulation models are usually used to reproduce a simplified operation of an electricity system and are helpful when it is impossible or extremely costly to do experiments on the system itself.

Since the focus of this study is to analyse electrification modeling approaches for rural electrification within developing countries, especially in SSA countries, only studies conducted at the sub-national electrification level are considered in the review.

Moksnes et al. [2], used a disaggregated approach to optimize least-cost electrification among grid, mini-grid, and off-grid options in Kenya. They combined two energy optimization tools, OpeN-Source Spatial Electrification Toolkit (OnSSET) and Open-Source Energy Modeling SYStem (OSeMOSYS), using 36-time slices over the year and 1 km spatial resolution. The models consider two scenarios of electricity demand layers at the residential level. The modeling approach used in this study gave a detailed map based on the specific resource location. The same approach was used in [9], applying OnSSET to project long-term energy generation scenarios at the sub-national level in SSA, using aggregated energy demand. In this study, however, 1-hour resolution and 1 km spatial resolution are used, and the result is a disaggregated technology generation.

Li et al. [10], estimated the electric energy consumption (EPC) in China using night-time light (NTL) data from 198 cities. For data collection, consumers were disaggregated by sector. The input data include statistical data (population density, urbanization rate, employment) for each city and satellite NTL image data and administrative boundaries.

Ohiare [11], used the Network Planner (NP) model to investigate long-term electrification in Nigeria based on least-cost options. The model built in GIS tool at hourly time resolution and 1 km spatial resolution to compare hybrid solar PV linked to diesel generators, mini-grid diesel-based, and grid technologies. Required input data include electricity demand and cost, population, and other socio-economic parameters. The optimized generating plants are spatially located based on the population density and availability of resources. A disaggregated approach was used to estimate electricity demand at the community level.

A study using the LoadProGen tool was conducted by [12] to estimate the load profiles and size of a PV system with battery storage in a small community in Tanzania. The tool uses a bottom-up stochastic approach with a time resolution of 1 minute. Another work using a bottom-up approach addressed the modeling and optimization of a mix of renewable energy technologies in an unelectrified village in India [13]. The Particle Swarm Optimization (PSO) algorithm coded in Matlab tool was used for the modeling.

Guta and Borner [14], used a dynamic linear programming model (DLPM), an energy sectoral tool based on General Algebraic Modeling System (GAMS) software to identify optimal least-cost options for integrating the energy source mix in Ethiopia. The DLPM uses a bottom-up approach to analyse six different technology options (biomass, hydropower, wind, solar, and geothermal). The study considered a 100-year horizon (divided into groups of 5 years), with a time resolution of 1 hour at national and sub-national levels. Input data include daily and weekly peak and off-peak load duration, discount rate, total annual costs, CAPEX, land use, fuel cost, and availability, existing installed capacity, technology capacity factor, population and economic growth rates, power trade, and the main outputs include energy demand scenarios (peak and medium), capacity (power) and electricity, electricity price.

Tian et al. [15], used Autoregressive Integrated Moving Average (ARIMA) and the Long-Range Energy Alternative Planning (LEAP) model for long-term (2010 – 2030) forecasts of energy demand scenarios and the resultant environmental impacts in China. The study was conducted at local level using a top-down analytical approach at hourly time resolution. The building sector was disaggregated into commercial and residential, and the required data include population, energy efficiency, GDP, income level, urbanization level (building area), energy resource availability, energy export/import, energy supply, energy policy, energy technologies and resources.

Schinko et al. [16] used the Renewable Energy Pathways Simulation System (renpassG!S), a numerical partial equilibrium model, to assess the long-term techno-economic feasibility of different electricity generation portfolios in Morocco. The model uses a disaggregated approach in selecting electricity supplying technologies. Input data include load curves, meteorological and geographical data at hourly resolution, capacity/investment and running costs of existing generation technologies, grid infrastructure, and levels of demand.

Aly et al. [17] used a System Advisor Model (SAM) to investigate the techno-economic feasibility of a concentrating solar power (CSP) technology in Tanzania. This model combines bottom-up and top-down approaches to optimize cost and technology and uses a spatial resolution of 1 km^2. Simulations were done at hourly basis. The main input data include direct normal irradiance at the earth`s surface, geographical coordinates, degradation rate, collectors' geometry and optical parameters, and heat transfer fluid properties.

Moner-Girona et al. [18], used a Rural Electrification Spatial Model for Kenya (RE_RU_KE_tool) to identify the optimum electrification split between grid extension, mini-grids and stand-alone technologies for different locations within the

country. The model uses a geospatial/numerical methodological approach for the unelectrified population. The main input data include spatial data layers such as energy resources (e.g, hydro, geothermal, wind and solar), the existing energy infrastructure, population, households' number and size, income rate, and electricity costs.

Zhong [19], uses Geographically Weighted Regression GWR) model to determine a long-term (1992-2013) electric power consumption (EPC) based on DMSP/OLS night light (NTL) data in three urban areas (YREB) of China. The model runs at yearly time resolution and 1km spatial resolution. Apart from NTL, input data include annual precipitation and average temperature, sunshine hours, and socio-economic data (e.g, GDP, urbanization rate, per capita income, built-up area). Energy demand is calculated based on statistical data. The relative difference of EPC is determined by means of coefficient of variation method.

Lee et al. [20], used a Reference Electrification Model (REM) to determine a long-term cost-optimal technology mix to provide universal access to electricity in Uganda. The model has high spatial granularity and a technically detailed approach and uses hourly time resolution. Input data include consumption demand, existing grid topology, networks, and generation components. The energy supply is disaggregated into grid extension, mini-grid, and standalone technologies.

Musselman et al. [21], used a multi-period optimization model for power generation and transmission system expansion planning to analyse short and long-term impacts of the change of electrification rate and policy on the cost and resources selected for power system expansion in Rwanda. The model is based on linear programming and the analysis was conducted at district level, at hourly and yearly time resolution to capture solar variations. Input data include fuels, energy resources, costs, existing generating units and costs, transmission network, discount rate, population, and economic factors.

4. Results

The results of the reviewed papers are summarised in Table 1. From each paper was identified the modeling tools, the coverage area, the domain (supply and/or demand), time horizon and resolution, spatial resolution, analytical approach, methodology, and main parameters Table 1 shows that 13 different tools were used to model electricity at the subnational level in rural areas of developing countries. All studies were based on bottom-up methods to model either electricity supply or demand.

The time resolution varied from 1 minute, 1 hour to 1 year. Hourly resolution was mainly used for short- and medium-term studies, while yearly resolution was mainly used for long-term studies. With the exception of studies [11] and [14], all others were conducted at a 1 km spatial resolution of 1 km. Electricity demand is usually modeled in the short-term, while supply is modeled for medium and long-term horizons in most studies.

As for the methodology used, electricity supply is mainly modeled with the aim of finding the optimal technology with the least- cost. However, a few studies [13], [15] are based on simulation and optimization methods.

5. Analysis and Discussion

Most rural areas of developing countries are not yet electrified and data on electricity demand is not available. For this reason, electricity demand data is either taken from other already electrified regions with similar characteristics or collected through local surveys of end-users. Bottom-up approaches are the most used because they allow detailed information from the consumer to be obtained and reduce the risk of under/overestimation of consumption. They also help the selection of the techno-economic optimal technology mix that suits particular demands.

Moreover, due to financial constraints and the availability of energy resources, the decision to electrification option is often based on the lowest capital and operating costs, including associated emission costs.

The electrification of rural areas with low population density requires a combination of grid extension and off-grid technologies. Off-grid solutions are mainly based on renewable energy systems and their implementation depend on the availability of energy resources, the physical-geographic characteristics of the location, as well as socioeconomic factors.

The use of GIS tools when planning energy systems helps to obtain these data for a specific location without necessarily being on the ground. The studies [2], [9], [10], [11], [15], [21], [18] and [19] rely on geospatial NTL data to split electrified and unelectrified areas. Since NTL is based on remote sensing data referring to illuminated areas, it may also account for the illumination from other sources than electricity (e.g., firewood), but data accuracy can be improved using filters.

Future community energy demand should be carefully analysed. This is a complex task due to the lack of historical data. All the reviewed papers used a bottom-up approach to model energy demand basedon statistical data. The use of statical demand data means that data is based on other (already) electrified regions sharing similar characteristics, but future demand developments, including developments of economic activities resulting from electrification, are not covered. To minimize the risks imposed by those uncertainties, it is recommended to consider a dynamic energy demand, considering the effect of parameters influencing future energy demand developments [20].

Table 1. Comparison of different approaches used for rural electrification in developing countries.

Author	Model	Study area	Domain	Time horizon	Time resolution	Spatial resolution	Analytical approach	Methodology	Input parameters
[15]	ARIMA/ LEAP	Community	Demand	2010 - 2030	Yearly	-	Bottom-up	Simulation/ optimization	P, GDP, I, PG, eff, Es, Tech, D, U, ER, Fa, HH
[14]	GAMS (DLPM)	Local	Demand/ supply	2010-2110	16-slices per year	0.01 km^2	Bottom-up	Simulation	P, Ir r, CAPEX, D, Cap; Tech, Hy, W, Gt, Bio
[17]	SAM	Project	Supply	2017 and 2025	Hourly	1 km^2	Bottom-up	Optimization	Tech, CAPEX, O&M, P
[2], [9]	OnSSET/ OSeMOSYS	Subnational	Demand/ supply	2012-2040/ 2030	hourly	1 km^2	Bottom-up/ top-down	Optimization	D, P, I, GIS, HH, GDP NTL, El_P, F, Grid, CAPEX, O&M, W, S
[16]	renpassG!S	National/ sub-national	Supply	2020-2050	Hourly/ yearly	-	Bottom-up	Simulation	Tech, W, Ir grid, D, CAPEX, P, O&M
[18]	RE_RU_KE tool	Sub-national	Supply	2008-2016	Hourly	1 km	Bottom-up (GIS)	Optimization	ER, GIS, grid, Cap, P, HH, Ir, M, , Ta, Hy
[19]	DMSP-OLS	Sub-national	Demand	1992-2013	Years	1 km	Bottom-up	Forecast	NTL, Tech, grid, D, M, GDP, I, CAPEX
[10]	NPP-VIIRS/ NTL	Sub-national/ local	Demand	2017	Hourly	-	Bottom-up (GIS)	Forecast	NTL, GRP, statistical, ED
[11]	NP	National/ local	Supply	2013-2030	Hourly	25 m	Bottom-up	Optimization	El_P, HH, U, D, Ir, GIS, grid
[21]	MPLOM	National/ sub-national	Supply	2015-2046	hourly/ 5 years	1 km	Bottom-up	Optimization	F, ER, D, grid, El_P, CAPEX, P, HH, GDP
[20]	REM	National/ sub-national	Supply	Short-term	Hourly	high	Bottom-up	Optimization	D, grid, Tech, eff, F, RE
[12]	LoadProGen	Local	Demand/ supply	Short-term	1 min	-	Bottom-up	Optimization	D, Ir, CAPEX
[13]	PSO	Local	Supply	Short-term	hourly	-	Bottom-up	Simulation/ optimization	CAPEX, O&M, Ir, W, eff.,D,Bio, Hy, BAT, L

Table 1: ER- energy resources combined; Di- Diesel, F- fuel, Tech- energy technologies and their technical parameters, Cap- installed capacity, M- meteorological data, GIS- geospatial tools and data, G- existing electrical generation, grid- existing/ planned grid, eff- technology efficiency, U- urbanization/ urbanization rate; D- Demand/ demand growth; HH- Households number/Size; I- income/ income level; L- land coverage/floor space/building area; P- population, population density/growth rate, CAPEX – investment/ capital expenditure; O&M- running costs, r- discount rate, GDP-Goss Domestic Product; GRP- Gross Regional Product, Exp/Imp- energy export/import, EL_P- electricity price, and S- subsidies, Optimization.

The increasing penetration of intermittent renewable energy generation introduces great variability in power generation and, as a result, there might be unbalanced supply-demand. High resolution spatial and temporal modeling are used to overcome this problem [3]. However, increasing the model resolution leads to an increase in the time required for the model to obtain the solution, i.e., a balance between spatial and temporal resolution is required. Electricity system planning studies at the local level are typically conducted at higher spatial resolution [11], [15]) than for large areas (i.e., country, region, or global) ([16], [9], [19], [21]). Higher temporal resolution is often used for short-term planning (i.e., operations and maintenance, tariff setting), while lower temporal resolution is typically used for long-term planning (new investments).

An alternative to making the best use of distributed renewable generation is to combine it with other technologies (e.g., the electric grid or other technologies) and meet demand at all times. To achieve this, models must allow for the analysis of multiple options. For example, NP and Load ProGen consider only PV technology, but the OnSSET, renpassG!S, NP, RU_RU_KE_tools, and REM models consider multiple energy technologies.

The time horizon is very important when planning electrification at sub-national level. The longer the planning period, the more uncertain assumptions on e.g. population and GDP growth [3], [6], and demand [6] will be and accordingly, model results will be less useful. Some of the reviewed studies were carried out for both the short-term and long-term [15], [14], [18], [21], others only long-term [9], [11], [19], [16], [18], and three applied a short-term horizon ([10], [12], [13]) When a higher time resolution is considered, the models take long time to run , [13].

When modeling power systems in rural areas of developing countries, socioeconomic and cultural factors are important for technology selection in addition to known technical parameters. For example, rural populations in SSA countries that have access to electricity often rely on traditional biomass to meet their cooking and heating needs, and electricity is used only for lighting and to run some appliances because of their habits and lower ability to pay for electricity. In addition, population demographics and urbanization have a great impact on the future electricity demand development and its spatial caracteristics and, thus, for the optimal generation mix and distribution so generation capacity planning should take this into account.

There are a number of energy modeling tools that can be used for modeling supply and demand of rural areas in developing countries: from the literature review was found that OnSSET/OSeMOSYS ([2], [9]), ARIMA [15], GAMS-DLPM [14], SAM [16], renpassG!S [21], RE_RU_KE [17], NPP-VIIRS [10], GWR [18], and NP [11] are the most widely used tools. Nevertheless, these energy models have their own limitations and could be further improved. The models should include local variations in energy resources such as wind, biomass, and small hydro, to allow for good prediction of potential generation at different time scales and better planning of the alternatives that need to be considered for power system reliability. Besides, high-resolution population and resource data as well as high-time computational resolution would enhance the models result.

When addressing grid extension, factors like geographical terrain, elevation and land use can be incorporated to improve the accuracy of the models. Furthermore, the use of geospatial data is crucial to fill the data gaps when there is a lack of recorded data. As bottom-up approaches are data-intensive, the advent of GIS data allows to overcome the problem of lack of recorded data, but the accuracy of the data is limited by the satellite sensor measuring range.

6. Conclusions

This study reviews original scientific papers on electricity supply and demand modeling in rural areas of developing countries. It is concluded that the bottom-up approach is most commonly used in modeling electricity supply and demand at the subnational level in rural areas of developing countries. This approach makes it possible to obtain detailed information from consumers and reduces the risk of underestimating or overestimating consumption. In most of the studies reviewed, the main objective is to find the optimal electrification technology (or mix of technologies) based on the least-cost.

Electrification modeling at a sub-national level (e.g., in rural areas) using decentralized systems based on variable renewable energies requires the use of both spatial and time high-resolution. All the models used in the reviewed papers appear to be appropriate for modeling electricity systems at the subnational level. However, the OnSSET, renpassG!S, NP, RU_RU_KE_tools, and REM models allow the analysis of multiple energy resources and minimize the lack of data due to the use of GIS tools, and therefore are found the most suitable candidates.

To better capture the local variation factors like geographical terrain, elevation and land use can be incorporated to improve the performance of the models. In addition, socio-economic and cultural factors, and land use must be taken into account for the acceptance of the technology by the end-users.

Acknowledgements

Authors would like to thank Chalmers Univeristy of Technology and Eduardo Mondlane University for financial support to conduct this research through the bilateral cooperation program SIDA – Breemers 1.4.1. Authors also thank Universidade Save for permission to continue the studies of the leading author.

References

[1] M. Bazilian, P. Nussbaumer, H. Rogner, A. Brew-Hammond, V. Foster, S. Pachauri, E. Williams, M. Howells, P. Niyongabo, L. Musaba, B. R. M. Gallachoir och D. Kammen, "Energy access scenarios to 2030 for the power sector in sub-Saharan Africa," Utilities Policy, vol. 20, nr 1, pp. 1-16, 2012.

[2] N. Moksnes, A. Korkovelos, D. Mentis och M. Howells, "Electrification pathways for Kenya-linking spatial electrification analysis and medium to long-term energy planning," Environmental Research Letters, vol. 15, nr 129501, 2017.

[3] S. Pfenninger, A. Hawkes och J. Keirstead, "Energy systems modeling for twenty-first century energy challenges," Renewable and Sustainable Energy Reviews, vol. 33, pp. 74-86, 2014.

[4] S. C. Bhattacharyya and G. R. Timilsina, (2010), "A review of energy system models", International Journal of Energy Sector Management, vol. 4 Iss 4 pp. 494 - 518

[5] S. Selvakkumaran och E. O. Ahlgren, "Determining the factors of household energy transitions: A multi-domain study," Technology in Society, vol. 57, pp. 57-75, 2019.

[6] N. van-Beek, "Classification of Energy Models," 1999.

[7] M. G. Prina, G. Manzolini, D. Moser, B. Nastasi och W. Sparber, "Classification and challenges of bottom-up energy system models - A review," Renewable and Sustainable Energy Reviews, vol. 129, nr 109917, 2020.

[8] M. G. Prina, G. Manzolini, D. Moser, B. Nastasi och W. Sparber, "Classification and challenges of bottom-up energy system models - A review," Renewable and Sustainable Energy Reviews, vol. 129, nr 109917, 2020.

[9] D. Mentis, M. Howells, H. Rogner, A. Korkovelos, C. Arderne, E. Zepeda, S. Shahid, C. Taliotis, M. Bazilian, A. de Roo, Y. Tanvez, A. Oudalov och E. Scholtz, "Lighting the World: the first application of an open source, spatial electrification tool (OnSSET) on Sub-Saharan Africa," Environmental Research Letters, vol. 12, nr 085003, 2017.

[10] S. Li, L. Cheng , X. Liu, J. Mao, J. Wu och M. Li, "City type-oriented modeling electric power consumption in China using NPP-VIIRS nighttime stable light data," Energy, vol. 189, nr 116040, 2019.

[11] S. Ohiare, "Expanding electricity access to all in Nigeria: a spatial planning and cost analysis," Energy, Sustainability and Society, vol. 5, nr 8, 2015.

[12] S. Mandelli, C. Brivio, M. Moncecchi, F. Riva, G. Bonamin och M. Merlo, "Novel LoadProGenprocedure for micro-grid design in emerging country scenarios: application to energy storage sizing," ScienceDir, vol. 135, p. 367–378, 2017.

[13] D. P. Pathak och D. k. Khatod, "Modeling and Optimization of Integrated Renewable," 2018, IEEE 8th Power India International Conference (PIICON), India, 2018.

[14] D. Guta och J. Borner, "Energy security, uncertainty and energy resource use options in Ethiopia: A sector modelling approach," International Jourbal of Energy, vol. 11, nr 1, pp. 91-117, 2017.

[15] C. Tian, G. Freng, S. Li och F. Xu, "Scenario Analysis on Energy Consumption and CO2 Emissions Reduction Potential in Building Heating Sector at Community Level," Sustainability, vol. 11, nr 5392, 2019.

[16] T. Schinko, S. Bohm, N. Komendantova, E. M. Jamea och M. Blohm, "Moroccos's sustainable energy transition and the role of financing costs: a participatory electricity system modeling approache," Energy, Sustainability and Society, vol. 9, nr 1, 2019.

[17] A. Aly, A. Bernardos, C. M. Fernandez-Peruchena och S. S. Jensen, "Is Concentrated Solar Power (CSP) a feasible option for Sub-Saharan Africa?: Investigating the Investigating the techno-economic feasibility of CSP in Tanzania," Renewable Energy, vol. 135, pp. 1224-1240, 2019.

[18] M. Moner-Girona, K. Bodis, J. Morrissey, I. Kougias, M. Hankins, T. Huld och S. Szabo, "Decentralized rural electrification in Kenya: Speeding up universal energy access," Energy for Sustainable Development, vol. 52, pp. 128-146, 2019.

[19] Y. Zhong, A. Lin, C. Xiao och Z. Zhou, "Research on the Spatio-Temporal Dynamic Evolution Characteristics and Influencing Factors of Electrical Power Consumption in three Urban Agglomerations of Yangtze River Economic Belt, China Based on DMSP/OLS Night Light Data," Remote Sensing, vol. 13, nr 1150, 2021.

[20] S. J. Lee, E. Sanchez, A. Gonzalez-Garcıa, P. Ciller, P. Duenas, J. Taneja, F. d. C. Garcıa, J. Lumbreras, H. Daly, R. Stoner och I. J. Perez-Arriaga, "Investigating the Necessity of Demand Characterization and Stimulation for Geospatial Electrification Planning in Developing Countries," A MIT Center for Energy and Environmental Policy Research, 2019.

[21] A. Musselman, V. M. Thomas, D. Nazzal, D. J. Papageorgiou, A. Venkatesh och D. S. Mallapragada, "The impact of development priorities on power system expansion planning in sub-Saharan Africa," Energy Systems, 2021.

A REVIEW OF ELECTROLYSER MODELLING FOR HYDROGEN PRODUCTION COUPLED WITH RENEWABLE ENERGY SOURCES

Joshua Woods[1], Arnold Rix[2], and Chantelle van Staden[3]

Department of Electrical and Electronic Engineering, University of Stellenbosch, Stellenbosch, 7600, South Africa

E-mail: [1] 22690352@sun.ac.za, [2] rix@sun.ac.za, [3] cvanstaden@sun.ac.za

Abstract: Hydrogen production through water electrolysis, coupled with renewable energy sources presents a promising solution to significantly reduce carbon emissions. A substantial body of research has been conducted in the integration and modelling of these two domains, resulting in numerous models and simulation approaches being presented in the literature. However, selecting an appropriate model that accurately characterises an electrolyser is unclear, especially when renewable energy sources are integrated.

In this paper, the methodology used to review existing literature is outlined, followed by a discussion of the relevant electrolyser theory needed in order to model such a process. This work reviews various electrolyser models for both Alkaline Electrolysers and Proton Exchange Membrane Electrolysers. The models vary in complexity, ranging from simplified linear approximations to highly intricate ones that utilise experimental data.

The research focuses on evaluating the advantages and drawbacks of these models, along with identifying scenarios where the implementation of each model would be appropriate. The paper places special emphasis on essential variables including electrolyser efficiency, hydrogen production, power input, temperature affect, load range, operating states and ramp up and ramp down rates. These parameters play a crucial role in developing an accurate electrolyser model when integrated with variable renewable energy sources.

Keywords: Electrolyser; model; green hydrogen; renewable energy; review

1. Introduction

Hydrogen production powered by renewable energy sources has grown in popularity as the demand for more sustainable production processes has increased [1]. Accurately representing a system or process through a mathematical model is vital when analysing the system in both isolation and within a greater system or process. The research presented forms part of a greater research project involving green ammonia where electrolysis accounts for roughly 90% of the power consumption [2]. Accurate modelling of the electrolyser system and the power source is crucial to producing accurate results.

Water electrolysis is a mature and well-established technology, with numerous mathematical models and simulation approaches existing in the literature. This poses a challenge when selecting a suitable approach. Is it necessary to develop and use a complex model and perform experiments in order to determine model parameters, as well as validate this empirical model, or would a simple linear approximation suffice? This paper aims to outline what type of electrolyser modelling approach is necessary. It must be noted that this paper does not provide an exhaustive review of models in literature, but merely a guide and direction in which to go to simulate an electrolysis system.

This paper presents a methodology used to review various relevant papers. A brief overview and comparison of the operation of two readily available systems, alkaline electrolysers (AKE) and proton exchange membrane (PEM) electrolysers is then discussed. The different types of modelling approaches that exist are explored and presented, including how these methods are implemented in different scenarios. Finally, the scenarios are discussed and compared with a conclusion drawn.

2. Methodology

There exist numerous modelling and simulation approaches in the literature. In order to systematically review as many relevant articles as possible, a set of keywords, relevant to the research presented in this paper is selected.

Keywords: renewable energy, hydrogen production, model, modelling and (alkaline electrolyser OR proton exchange membrane)

This generated a number of results across the Engineering Village and Institute of Electrical and Electronic Engineers (IEEE) databases. The relevant results were systematically reviewed to extract pertinent information for the research review, resulting in the identification of numerous approaches. These were then categorised into their respective modelling approaches and analysed. The literature review produced limited results pertaining to electrolyser modelling, the need for this category of article is thus relevant.

3. Electrolyser Theory

3.1. Operation

This paper explores two different types of electrolysers, the alkaline electrolyser and the proton exchange membrane electrolyser.

3.1.1.Alkaline Electrolyser

Alkaline water electrolysis is the process of splitting water into gaseous hydrogen and oxygen using electrical energy. Two electrodes are submersed in an electrolyte. When a DC current is passed from the cathode to the anode, the electrolyte is split into hydrogen and oxygen ions. Figure 1 illustrates the electrolysis process:

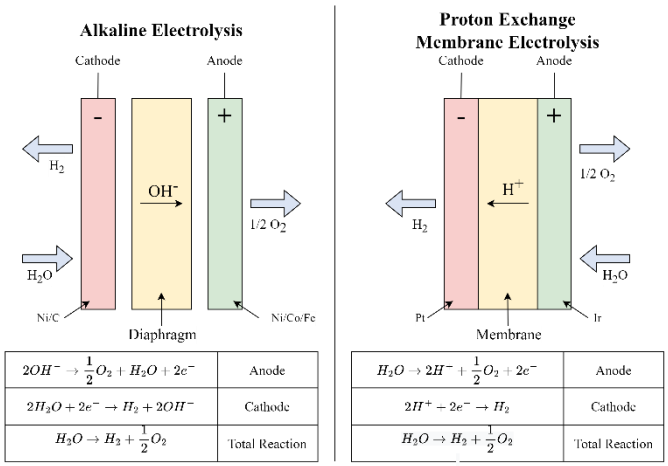

$2OH^- \rightarrow \frac{1}{2}O_2 + H_2O + 2e^-$	Anode
$2H_2O + 2e^- \rightarrow H_2 + 2OH^-$	Cathode
$H_2O \rightarrow H_2 + \frac{1}{2}O_2$	Total Reaction

$H_2O \rightarrow 2H^- + \frac{1}{2}O_2 + 2e^-$	Anode
$2H^+ + 2e^- \rightarrow H_2$	Cathode
$H_2O \rightarrow H_2 + \frac{1}{2}O_2$	Total Reaction

Fig. 1. Diagram of Electrolysis Cell Operation [3]

3.1.2.Proton Exchange Membrane

Proton Exchange Membrane Electrolysers operate on a similar principle. Water is split into oxygen, hydrogen protons and electrons. These protons then travel through the proton conducting membrane to the cathode, the electrons exit from the anode and travel though the external DC circuit to the cathode where they combine with the protons at the cathode to form hydrogen.

3.2. Key Parameters

The modelling of electrolysers, ranges in complexity from simple linear approximations to detailed models requiring specific system parameters such as electrode areas and electrolyte concentrations. Due to the intermittent nature of renewable energy, modelling the electrolyser such that the ramp up, ramp down and operating state are included.

3.2.1.Specific Power Consumption (kWh/kg)

A crucial measure of electrolyser systems performance. It is defined as the amount of power required to produce one kilogram of hydrogen [4].The electrolysis of water has a parameter known as the Higher Heating Value (*HHV*), which is the thermodynamic minimum, namely, the smallest amount of energy required to split water into hydrogen and oxygen, an electrolyser with a specific power consumption equal to its *HHV* has an efficiency of 100 %. This value gives an indication of the overall system efficiency in terms of energy consumption.

3.2.2.Efficiency (%)

There are different measures of electrolyser efficiency; Faraday's efficiency, Voltage efficiency and overall efficiency. Faraday's efficiency is based on the theoretical amount of hydrogen produced and the actual amount of hydrogen produced. Voltage efficiency is based on the thermoneutral potential and cell voltage. However, these parameters are beyond the scope of this research. Electrolyser efficiency (η_E) in this paper is regarded as the ratio between specific power consumption (P_{SP}) and the *HHV*, this is defined in Equation 1:

$$\eta_E = \frac{P_{SP}}{HHV}(\%) \quad (1)$$

3.2.3.Hydrogen Production (kg/h)

The hydrogen output of the electrolyser in kg/h. The units used are to ensure a standard measurement regardless of pressures or fluid densities.

3.2.4.Ramp Rates ($\%/s$)

The ability for an electrolyser to increase or decrease hydrogen output as the renewable energy source fluctuates is vital to maximise hydrogen output. Due to the intermittent nature of renewable energy sources, inclusion of a ramp rate in a model is paramount to ensure accurate results. Whilst the inclusion of a ramp rate when dealing with hourly resolution data is not crucial, when the time resolution of the data is in the order of seconds it becomes a crucial factor.

3.2.5.Degradation ($\%/year$)

The process of electrolysis results in the anode, cathode and membrane of an electrolyser degrading over time and eventually requires replacement. Electrolyser performance also deteriorates due to this degradation. This variable is seldom included in papers spanning less than a year, it becomes more prevalent in

longer time periods, such as greater than 5 years.

3.2.6.Load Range (%)

Renewable energy, as mentioned prior, is inherently intermittent, resulting in periods where the power available to an electrolyser falls outside of its load range and thus will not produce any hydrogen. Alkaline electrolysers exhibit slightly poorer load range ability compared to proton exchange membrane systems [5]. Incorporating the load range of the system allows for different operating states to exist, for example idle, off or operating. This adds a further degree of accuracy to the analysis.

3.3. Advantages and Disadvantages

The electrolysers reviewed in this paper, provide similar levels of performance, however there exist some differences. Table 1 discusses the major parameters:

Table 1. Comparison of Electrolyser Performance Parameters [5]– [7]

Parameter	Alkaline Electrolyser	PEM Electrolyser
Power Requirements (kWh/kg)	53.4	62.3 - 70.1
Load Range (%)	20 - 110	0 - 160
Production Range (t/day)	0.1-1.2	4.25
Efficiency (%)	< 73.8	56-73
Ramp Rate $(\%/s)$	10	20

Overall, PEM electrolysers are marginally better when coupled with renewable energy sources due to their fast ramp rates and larger load range. The ability to operate at very low levels is highly beneficial when renewable energy supply is low, as well as being able to operate at above rated conditions for short periods contribute to it being a marginally better system. However degradation of PEM electrolysis systems and capital investment cost is significantly higher [8].

4. Models Reviewed

Different approaches exist in order to model an electrolyser, these include linear, empirical and semi-empirical, static, dynamic and physical models.

4.1. Linear Model

A linear model is the simplest of the models found in the literature [3], [10-18]. It assumes the input power (P_{app}) and hydrogen output ($\dot{m}_{H_2}$) of the electrolyser are proportional, according to Equation 2, where P_{rated} and $\dot{m}_{rated}$ are defined as the rated power and hydrogen output of the electrolyser respectively.

$$\dot{m}_{H_2} = \frac{P_{app}}{P_{rated}} \dot{m}_{rated} (kg/h) \quad (2)$$

The following equation uses a more theoretical approach. The electrolyser efficiency (η_E) and higher heating value (HHV) are included.

$$\dot{m}_{H_2} = \frac{\eta_E P_{app}}{HHV} (kg/h) \quad (3)$$

Varela et. al. [9] analysed multiple electrolyser models which revealed the power input and hydrogen output are strongly correlated and thus allows for a linear approximation. It is evident this does not factor in other crucial system parameters such as temperature, pressure and electrode characteristics. This has led to linear models being a common approach in many papers found in the literature. The use of a linear model would not be suited to applications where detailed results are required or if all parameters needed in a more detailed approach are known.

4.2. Empirical & Semi-Empirical Models

Empirical and semi-empirical models are also very common in literature [3], [7]. Empirical modelling relies on experimental data available or that has been measured, whilst semi-empirical models utilise both experimental data and theoretical principles in order to characterise the electrolyser. The model generated is thus specific to one type of electrolyser and thus has poor universality [10].

The use of empirical modelling does not take into consideration the electro-chemical reaction [10], the core principle behind the electrolyser operation. This results in the model being developed to be quite restricted if applied to other systems.

In order to improve this a semi-empirical model would be used. This approach incorporates both empirical data obtained and theoretical principles. This allows for the inclusion of variables such as pressure, cell and/or stack temperature, electrode area, and various thermodynamic and heat transfer-related phenomena, however, this does increase complexity.

Hybrid renewable energy systems more often than not involve some form of optimisation, and non-linear formulae, which are common in semi-empirical and empirical models can lead to complex simulations. Careful consideration should be given as to how many aspects (thermodynamic, electro-chemical, fluid dynamic etc), are included in a model and if the increase in accuracy is necessary.

5. Model Discussion

The section to follow outlines the implementation of various modelling approaches, including a performance discussion.

5.1. Linear Model

Numerous linear modelling approaches exist and are commonly used due to simple implementation and minimal number of parameters required.

5.1.1. Constant Efficiency – Specific Power Consumption

Techno-economic studies are commonly done when using linear approaches, specifically looking at cost analysis or plant economics. However, more technical papers utilise these approaches for optimisation and sizing problems [11], the most common implementations include using the specific energy consumption with units: (*kWh/kg*). This method assumes a constant efficiency regardless of any external factors such as temperature and fluctuating loads. A paper discussing the impact of hydrogen production on the electrical grid for hydrogen-powered vehicles utilised the constant efficiency approach [12], and another analysed islanded ammonia production [5]. Both studies emphasised that this may be an overestimation and a conservative approach.

5.1.2. Varying Efficiency – Specific Power Consumption

Electrolysis systems, as it stands, will never reach an overall system efficiency of 100%. The linear model discussed prior can be seen as a more idealistic approach, utilising purely simple theoretical calculations, this could not be further from the truth. These approaches neglect the use of varying efficiency as the electrolyser's load changes. Beerbuhl et al. [13] discuss the idea quite well.

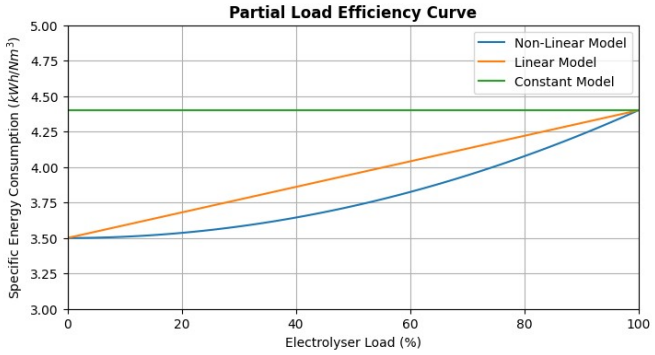

Fig. 2. Partial Load Efficiency Curve [13]

In order for an electrolyser to achieve 100% efficiency it has to approach the thermodynamic minimum, also known as its *HHV* of 39.39 *kWh/kg* or 3.54 *kWh/Nm*^{3} . This efficiency does not follow an intuitive approach, or "economies of scale" from an economic perspective, similar to what most thermal power plant efficiencies follow. Figure 2 depicts this idea, where it can be seen that at lower loads the specific energy consumption (efficiency) of an electrolyser performs better than at full load conditions. This makes it attractive for plant operators to run their systems at lower levels, whilst still maintaining a reasonable output [14]. Optimisations involving non-linear or exponential terms lead to very complex problems and are computationally expensive, hence surveying of literature revealed very few articles utilising this approach [13].

Researchers have attempted to approximate this non-linear behaviour, through piecewise linear models. Baumhof et al. [15] discusses when a more detailed operational electrolyser model is necessary, specifically for use in scheduling the electrolyser state based on the day ahead electricity price. The paper presents the idea of generating a linear piece-wise function of the non-linear efficiency curve depicted in Figure 3(b).

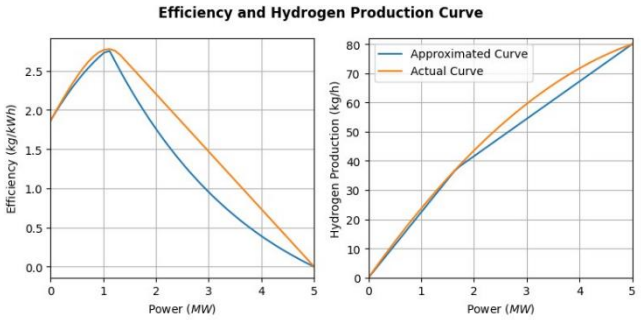

Fig. 3. Efficiency and Hydrogen Production curve [15]

The central idea behind the approach is defining how many segments are needed to linearize the efficiency curve in order to provide an accurate approximation, comprising a number of linear equation segments. As the number of segments increase, the accuracy of the model increases. The approximated curve in Figure 3(b) consists of two linear piecewise curves. It is concluded that an increase in segments greatly improves the scheduling accuracy [15].

5.1.3.Heating Value and Electrolyser Efficiency

A similar approach is used by relating efficiency (η_E) and the *HHV* with the power applied (P_{app}) to the electrolyser to determine the hydrogen output ($\dot{m}_{H_2}$), which is also constant efficiency approach.

$$\dot{m}_{H_2} = \frac{\eta_E P_{app}}{HHV_{H_2}} (kg/h) \quad (4)$$

5.2. Empirical and Semi-Empirical Models

5.2.1. Ulleberg

The most notable modelling approach under this category is the work done by Øystein Ulleberg [16]. The model is based on a combination of thermodynamics, heat transfer and static-empirical electro-chemical relationships, it also includes a dynamic thermal model. A significant proportion of papers that utilise a semi-empirical approach have used Ulleberg's model.

The model presented is complex and detailed when compared with other approaches, such as purely empirical or linear

methods, thus requiring extensive knowledge of detailed system parameters. Ulleberg has attempted to reduce the number of parameters required by the empirical relations. This allows the model to be as generic as possible as well as limiting the number of experiments that are needed and subsequently the costs involved with implementing such a model.

A fundamental aspect of electrolysers is the current-voltage relationship or I-U curve as shown in Figure 4:

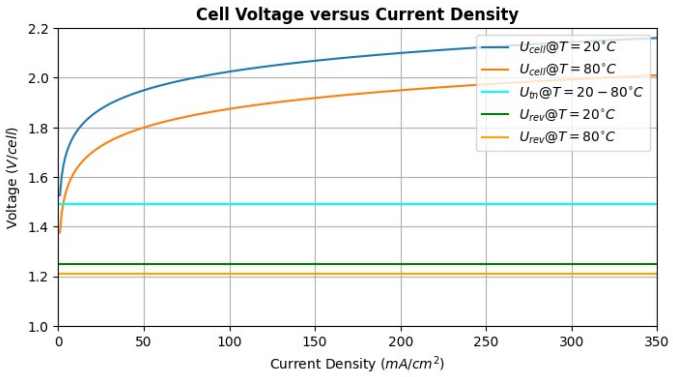

Fig. 4. Typical U-I Curve for Electrolyser [16]

The product of voltage and current produce the power of the electrolyser. The cell voltage (U) is calculated as:

$$U = U_{rev} + \frac{r_1 + r_2 T}{A} I + slog\left(\frac{t_1 + t_2/T + t_3/T^2}{A} I + 1\right) \quad (5)$$

The voltage is dependent on the electrode area (A), cell temperature (T), reversible cell voltage (U_{rev}), ohmic resistance (r) and over-voltage coefficients (s & t). Faraday's Law is the main principle behind hydrogen production. According to this law, hydrogen production in a stack ($\dot{m}_{H_2}$) is directly proportional to the transfer rate of electrons at the electrodes, which is equivalent to the external electric circuit current (I) . This results in Equation 5 with the variables Faraday efficiency (η_F), Faraday constant (F) and number of cells in a stack (η_C):

$$\dot{m}_{H_2} = \eta_F \cdot \frac{n_c \cdot I}{z \cdot F} \quad (6)$$

Ulleberg validated the proposed model through experiments over a series of days, with positive results. The predicted and measured energy demand error was less than 2%. This model is appropriate for both Alkaline and PEM electrolysers.

5.2.2. Simplified Ulleberg

A semi-empirical model based on Ulleberg's model is also common [17], [18]. The simplified approach assumes a constant temperature, pressure and voltage. This generates an equation relating the current applied (I) and Faraday efficiency (η_F).

$$\eta_F = 96.5 \cdot exp\left(\frac{0.09}{I} - \frac{75.5}{I^2}\right) \quad (7)$$

The parameters in Equation 7 above are determined from the empirical parameters discussed in Ulleberg's paper [16]. The Faraday Efficiency is then substituted into Equation 5 to determine the hydrogen output.

5.3. Dynamic Models

The models discussed up to this point, with the exclusion of the work of Ulleberg, have been static models and have not necessarily characterised the response an electrolyser may have to dynamic power fluctuations, similar to renewable energy sources [19].

5.3.1.Electronic Circuit

Researchers have attempted to generate an equivalent circuit, Figure 5 depicts a PEM electrolyser, in order to incorporate the dynamic profiles associated with renewable energy sources [19]. The circuit simulates the electrodes as a resistor-capacitor pair with a single resistor modelling the membrane, this is all connected in series to a DC voltage source (reversible potential).

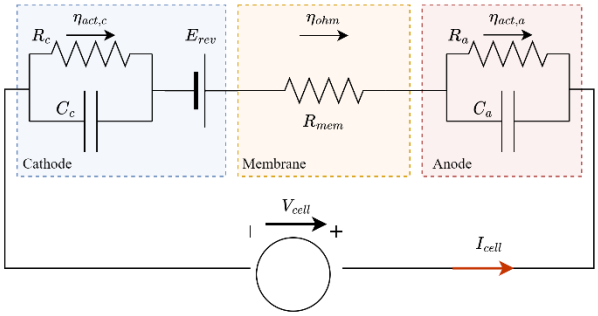

Fig 5 PEM Electrolyser Equivalent Circuit [19]

The cell voltage (V_{cell}) is calculated by summing the cathode ($\eta_{act,c}$), membrane (η_{ohm}), anode ($\eta_{act,a}$) and reversible voltage (E_{rev}).

$$V_{cell} = E_{rev} + \eta_{act,a} + \eta_{act,c} + \eta_{ohm} \quad (8)$$

This allows for the previously static current-voltage curve, i.e. in Figure 4, to be dynamic, depicted in Figure 6.

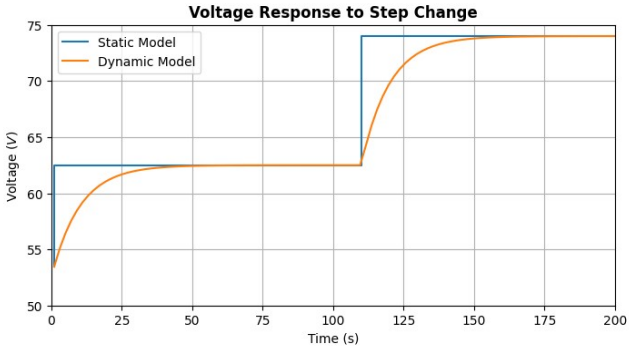

Fig. 6. Voltage Response to Step Change [20]

Author [19] proposes an accurate model. Results revealed that when a step voltage is applied to the system, a static model

produces an error of 15%, whilst the dynamic model achieves 4%, this is a significant improvement in model accuracy.

The implementation of such a model is relatively complex and requires detailed knowledge of the system, which is not always the case. Optimisation problems involving non-linear formulae are also not favoured as they are computationally expensive. Whilst the ability to accurately track sudden changes in the power supplied to the system, as is common with renewable energy, is not a very common approach.

However, a major drawback of this model is its confined operating range. Guilbert and Vitale [20] discuss validating the parameters used in [19]. It revealed that the values obtained are only applicable over a specific current range and should the model be applied outside of this region, inaccuracies and unreliability would become prevalent. This is due to the dynamics of the system changing as operating conditions change. The proposed model was regarded as being an accurate and appropriate method to emulate an electrolyser as a replacement for having to conduct an experiment.

6. Discussion and Model Selection

6.1. Discussion

It is clear that there are numerous modelling methods with varying degrees of complexity. In order to better summarise and condense the information presented, a discussion of the results follow.

Linear modelling is a simple approach to approximate hydrogen production. It requires very few parameters, whether assuming a constant specific energy consumption or assuming the power supplied to the electrolyser is proportional to the rated hydrogen output. This method is beneficial in optimisation problems as it is a simple linear approximation, thus being computationally inexpensive. It is also best suited to techno-economic research areas due to it requiring very few details about the electrolyser and its parameters, which is common when conducting feasibility studies.

The varying efficiency model is a modified linear model that incorporates the non-linear efficiency curve of an electrolyser through piece-wise approximations. This allows for the efficiency curves seen in Figures 2 and 3 to be included in the model implementation. Whilst the linear models discussed are simple and computationally inexpensive, they are static models, which do not capture the change in parameters as operating conditions change. For example, temperature greatly affects cell voltage, which subsequently affects efficiency and hydrogen output.

Semi-empirical and empirical modelling present a more detailed approach that utilises theoretical aspects and experimental data to model an electrolyser. This greatly improves the accuracy of the electrolyser model. The work of Ulleberg is a very popular method together with various models based on his work. These models are relatively simple, whilst still being detailed enough to incorporate specific parameters, such as operating temperatures and voltages.

Dynamic modelling is a complex and accurate approach, it incorporates aspects that are vital when coupled to renewable energy sources such as the system response to sudden changes in current and/or voltage. This approach is at a low/detailed system level, in order to include this flexibility in a linear or semi-empirical or empirical model, the addition of load range and ramp rate parameters is necessary.

6.2. Model Selection

Selecting the most appropriate modelling approach is purely dependent on the context in which the model is being implemented.

Linear models are simple and easy to implement, especially when very few details regarding the electrolyser are known, this makes it suitable for economic type studies (equipment costs, cost of capital etc) or high level feasibility studies that do not require high levels of accuracy. Optimisation problems benefit from more simple models as simulation times are reduced when compared with non-linear models.

Semi-empirical and empirical modelling provide a higher level of detail, compared to linear models. They require fewer parameters relative to dynamic and physical models and are still very accurate. The work of Ulleberg is a good approach if a semi-empirical model were to be employed. Numerous optimisation problems, as well as techno-economic papers, have utilised such a model.

Dynamic and physical modelling is the most complex. They are difficult to implement as they require numerous parameters that need to be determined empirically and employ multiple relations and equations to fully describe the system. This makes it difficult to implement for optimisation problems, particularly more complex types, such as multi-objective optimisation problems.

7. Conclusion

This paper offers a comprehensive overview of electrolyser modelling, encompassing both alkaline and proton exchange membrane electrolysers. The study devolves into distinct models, exploring key aspects of each. Additionally, a comparison is made among various methods, considering factors like complexity, implementation, and accuracy.

The modelling methods discussed are classified into four

different categories, linear, semi-empirical, empirical and dynamic. Within each category, several models found in the literature were presented and evaluated.

Linear methods emerge as the simplest to implement requiring minimal system parameters and are easily scalable. Conversely, empirical and semi-empirical modelling represents a significant step up and is used in more detailed analyses. Careful consideration should be given to model selection, taking into account the aspects discussed in this paper.

Although not exhaustive, this paper significantly improves the understanding of the diverse models available in the literature. While it does not analyse intricate system parameters such as electrode area or electrolyte concentrations, it serves as a guide and initial step to simulating the system.

References

[1] Y. Zheng, S. You, H. W. Bindner, and M. Munster, ¨ "Optimal day-ahead dispatch of an alkaline electrolyser system concerning thermal–electric properties and state-transitional dynamics," Applied Energy, vol. 307, p. 118091, 2022. [Online]. Available: https://www.sciencedirect.com/science/article/pii/S0306261921013751

[2] K. Verleysen, A. Parente, and F. Contino, "How does a resilient, flexible ammonia process look? robust design optimization of a haber-bosch process with optimal dynamic control powered by wind," Proceedings of the Combustion Institute, vol. 39, no. 4, pp. 5511–5520,2023.[Online].Available: https://www.sciencedirect.com/science/article/pii/S1540748922000347

[3] M. Carmo, D. L. Fritz, J. Mergel, and D. Stolten, "A comprehensive review on pem water electrolysis," International Journal of Hydrogen Energy, vol. 38, no. 12, pp. 4901–4934, 2013. [Online].Available:https://www.sciencedirect.com/science/article/pii/S0360319913002607

[4] D. Gimzauskait ˇ e, M. Aikas, and A. Tamo ˙ si ˇ unas, "Chapter 4 - recent ¯ progress in thermal plasma gasification of liquid and solid wastes," in Recent Advances in Renewable Energy Technologies, M. Jeguirim, Ed. Academic Press, 2022, pp. 155–196.[Online].Available:https://www.sciencedirect.com/science/article/pii/B9780128235324000070

[5] R. Banares-Alc ˜ antara, G. D. III, M. Fiaschetti, P. Gr ´ unewald, J. M. ¨ Lopez, E. Tsang, A. Yang, L. Ye, and S. Zhao, "Analysis of islanded ammonia-based energy storage systems," Ph.D. dissertation, University of Oxford, 2015.

[6] C. Wang, S. D. Walsh, T. Longden, G. Palmer, I. Lutalo, and R. Dargaville, "Optimising renewable generation configurations of off-grid green ammonia production systems considering haber-bosch flexibility," Energy Conversion and Management, vol. 280, p.116790,2023.[Online].Available:https://www.sciencedirect.com/science/article/pii/S019689042300136X

[7] A. Arsad, M. Hannan, A. Q. Al-Shetwi, R. Begum, M. Hossain, P. J. Ker, and T. I. Mahlia, "Hydrogen electrolyser technologies and their modelling for sustainable energy production: A comprehensive review and suggestions," International Journal of Hydrogen Energy, 2023. [Online]. Available: https://www.sciencedirect.com/science/article/pii/S0360319923017020

[8] "Thunder said energy," 2022, june 2022. [Online]. Available: https://thundersaidenergy.com/2023/01/17/green-hydrogenalkaline-versus-pem-electrolysers

[9] C. Varela, M. Mostafa, and E. Zondervan, "Modeling alkaline water electrolysis for power-to-x applications: A scheduling approach," International Journal of Hydrogen Energy, vol. 46, no. 14,pp.9303–9313,2021.[Online].Available: https://www.sciencedirect.com/science/article/pii/S0360319920347725X

[10] W. Pei, X. Zhang, W. Deng, C. Tang, and L. Yao, "Review of operational control strategy for dc microgrids with electric-hydrogen hybrid storage systems," CSEE Journal of Power and Energy Systems, vol. 8, no. 2, pp. 329–346, 2022.

[11] R. Nayak-Luke, R. Banares-Alcantara, and I. Wilkinson, "green"ammonia: Impact of renewable energy intermittency on plant sizing and levelized cost of ammonia," Industrial & Engineering Chemistry Research, vol. 57, no. 43, pp. 14 607–14 616,2018.[Online].Available:https://doi.org/10.1021/acs.iecr.8b02447

[12] K. Mahdi, C. Andrew, D. Infield, Y. Ma, and D. T. Graham, "The impact on the electrical grid of hydrogen production from alkaline electrolysers," in 45th International Universities Power Engineering Conference UPEC2010, 2010, pp. 1–6.

[13] S. S. Beerbuhl, M. Fr ¨ ohling, and F. Schultmann, "Combined scheduling ¨ and capacity planning of electricity-based ammonia production to integrate renewable energies," European Journal of Operational Research, vol. 241, no. 3, pp. 851–862, 2015. [Online]. Available:https://www.sciencedirect.com/science/article/pii/S0377221714007164

[14] C. Wang, S. D. Walsh, T. Longden, G. Palmer, I. Lutalo, and R. Dargaville, "Optimising renewable generation configurations of off-grid green ammonia production systems considering haber-bosch flexibility," Energy Conversion and Management, vol. 280, p.116790,2023.[Online].Available:https://www.sciencedirect.com/science/article/pii/S019689042300136X

[15] M. T. Baumhof, E. Raheli, A. G. Johnsen, and J. Kazempour, "Optimization of hybrid power plants: When is a detailed electrolyzer model necessary?" 2023.

[16] Øystein Ulleberg, "Modelling of advanced alkaline electrolyzers: a system simulation approach," International Journal of Hydrogen Energy, vol. 28, no. 1, pp. 21–33, 2003. [Online]. Available: https://www.sciencedirect.com/science/article/pii/S0360319902000332

[17] M. Castaneda, A. Cano, F. Jurado, H. S ˜ anchez, and L. M. ´ Fernandez, "Sizing optimization, dynamic modeling and energy ´ management strategies of a stand-alone pv/hydrogen/battery-based hybrid system," International Journal of Hydrogen Energy, vol. 38, no. 10, pp. 3830–3845, 2013. [Online]. Available: https://www.sciencedirect.com/science/article/pii/S0360319913001894

[18] M. Khan and M. Iqbal, "Dynamic modeling and simulation of a small wind–fuel cell hybrid energy system," Renewable Energy, vol.30,no.3,pp.421–439,2005.[Online].Available: https://www.sciencedirect.com/science/article/pii/S0960148104002381

[19] Angel Hern ´ andez-G ´ omez, V. Ramirez, and D. Guilbert, "Investigation ´ of pem electrolyzer modeling: Electrical domain, efficiency, and specific energy consumption," International Journal of Hydrogen Energy, vol. 45, no. 29, pp. 14 625–14 639, 2020.[Online].Available:https://www.sciencedirect.com/science/article/pii/S0360319920312271

[20] G. Damien and V. Gianpaolo, "Experimental validation of an equivalent dynamic electrical model for a proton exchange membrane electrolyzer," in 2018 IEEE International Conference on Environment and Electrical Engineering and 2018 IEEE Industrial and Commercial Power Systems Europe (EEEIC / &CPS Europe), 2018, pp. 1–6.

BIOGAS CONVERSION TO ELECTRICITY FROM FOOD WASTE AND WASTE-ACTIVATED SLUDGE DIGESTION

Selebogo M. Khune[1], Benton Otieno[2], John Kabuba[3], George Ochieng[4] and Peter Osifo[5]

[1] Vaal University of Technology, Private Bag X021, Andries Potgieter Blvd, Vanderbijlpark, South Africa; Phone: +27 725761634; E-mail: mervyn.khune@gmail.com

[2] Vaal University of Technology; E-mail: bentononyango@gmail.com

[3] Vaal University of Technology; E-mail: johnka@vut.ac.za

[4] Vaal University of Technology; E-mail: georgeo@vut.ac.za

[5] Vaal University of Technology; E-mail: petero@vut.ac.za

Abstract: An enormous amount of waste-activated sludge (WAS) and food waste (FW) is generated worldwide. Most of this waste is discarded in landfills, where it undergoes uncontrolled anaerobic digestion (AD), which emits excessive amounts of greenhouse gases, (methane and carbon dioxide), thereby contributing to global warming. Controlled digestion of WAS and FW is key for organic waste management with a positive impact on the environment and economy. In South Africa (SA) there is little uptake of biogas technology for WAS and FW management due to little research on biogas potential at small to large scale. In the current study WAS and FW was treated in both mono-digestion and co-digestion at mesophilic temperatures on a pilot scale, aided by a solar system. A complete-mix biogas pilot plant (VUT-1000C) was designed, constructed and commissioned. The materials used for constructing the pilot plant were sourced locally, including the solar geyser, to prove the applicability of the AD technology in South Africa. The biogas produced was converted to electricity using a generator. A power balance was then performed over the biogas plant for each treated feedstock. Up to 2.3 kWh power output was from 1 400 L of biogas produced during FW mono-digestion and co-digestion with WAS at an organic loading rate (OLR) of 1.6 kgVS/m^3/day. Up to 0.6 kWh of power was produced from 150 L of biogas during WAS mono-digestion indicating that the plant required 68% of the output for input. In the co-digestion of WAS with FW and mono-digestion of FW, the power output to input ratio was higher compared to WAS-only digestion. Great volumes of biogas as renewable energy are being lost in South Africa due to the lack of anaerobic technology uptake. Furthermore, the study has shown that biogas technology is readily available for South Africans as the designed biogas plant was very effective in waste-to-energy conversion.

Keywords: Anaerobic co-digestion; Biogas; Electricity; Food waste; Waste-activated sludge.

1. Introduction

There is an enormous opportunity for the recovery of energy and nutrients, water reclamation and mitigation of climate change through the effective treatment of waste-activated sludge (WAS), primary sludge and secondary sludge. WAS is the sludge that amasses at the bottom of the primary settling tank, and is an excess quantity of microbes that must be removed from the activated sludge treatment process to keep the biological system in balance thereby producing a waste product. Currently, WAS treatment and disposal account for up to 50% of the total operation cost and 40% of the total greenhouse gas emissions [1]. Anaerobic digestion (AD) is usually preferred for WAS treatment since it is more economical compared to other existing technologies [2]. AD can transform the sludge organic matter into biomethane, reduce the final amount of sludge solids, destroy most pathogens present in sludge, limit odour problems and produce energy. Thus, AD optimises treatment costs, reduces the environmental footprint of the plant, and plays an integral part in modern municipal wastewater treatment processes [3], [4]. The biogas potential of municipal waste-water treatment plants (WWTPs) can be enhanced in several ways. This technology can be enhanced by being coupled with other renewable energy sources such as solar for heating the biodigesters to mesophilic temperatures and by the introduction of other organic-rich waste streams through co-digestion. With increased biogas potential, the WWTP can become a renewable energy producer.

South Africa produces 28 million tons/year (77 million kg/day)

of food, and a third of it is discarded as waste [5]. Current methods of organic municipal waste disposal are incineration, landfills, composting and anaerobic digestion. Incineration and composting require energy, while landfilling has been considered the most practical and cheapest disposal method. However, landfills are filling up quickly, creating the need for more sites farther away from waste generation, thereby increasing costs. More than 50% of the waste disposed of in landfills rots under uncontrolled anaerobic conditions, releasing landfill gas into the atmosphere and leachate into underground water [6]–[8]. Landfill gas, also known as biogas, comprises primarily 55 – 70% methane, 30 – 45% carbon dioxide, trace amounts of hydrogen sulphide (0-2000 ppm), moisture (depending on temperature), and siloxanes [9]. Methane is 25 times more potent than carbon dioxide as a greenhouse gas. Hydrogen sulphide produces bad and unhealthy smells in the area. The disposal of organic waste in landfills contributes to 4.3% of South Africa's greenhouse gas emissions. Throughout the food supply chain to landfill, greenhouse gas emissions range between 2.8 and 4.14 t CO_2 per tonne of FW [5]. The national waste sector landfills contributed 18 773 Gg CO_2 eq to the national methane emissions in 2010 [7].

The controlled anaerobic co-digestion (AcD) of WAS with food waste (FW) is considered a key element in organic waste management due to its positive impact on the environment, economy, and energy (Kang and Yuan, 2017). AcD improves the carbon-to-nitrogen (C/N) balance of the mixture, obtaining higher biogas and methane yields and diluting potential toxic sub-stances [10]. This treatment method reduces the emissions of greenhouse gases going into the atmosphere while producing carbon-neutral renewable energy and biofertiliser. Methane, the main constituent, constitutes up to 99% of natural gas. Methane has a calorific value of 36 MJ/m^3; thus, biogas has a calorific value of 22 MJ/m^3 at 60% methane composition [11]. The calorific value of biogas can be improved by biogas purification. Biogas can be used for cooking, generating electricity in combined heat and power plants (CHP), and as a vehicular fuel. One m^3 of biogas can produce up to 2.1 kW of electricity, assuming a mechanical efficiency of 35% for the generator.

The generation of electricity from biogas is one of the most dominant future renewable energy sources because continuous power generation from organic waste can be guaranteed [12]. South Africa's primary energy source is coal, which is responsible for carbon dioxide emissions contributing to 12% of greenhouse gas emissions globally. According to Statistics South Africa [13], almost 90% of 236 TWh of electricity is generated in coal-fired power stations, 5% from nuclear, 0.5% from hydroelectricity, 2.3% from natural gas, 0.01% from wind and 1.3% from pumped storage schemes [13]. The national landfill methane emission equals 101 TWh of electricity, half of South Africa's energy generation. 3 GWh can be generated from the estimated national 9 Mt of FW (the amount of FW could be understated due to the lack of sufficient records), turning on 522 million 6W light bulbs. Power generated from biogas is carbon-neutral and thus environmentally friendly. In addition to the benefits mentioned, large biogas installations in South Africa are located at municipal wastewater treatment plants, and the digesters are often oversized and/or underutilised.

The current study aimed to (i) determine the effect of various WAS:FW mixing ratios on biogas production at the laboratory scale, (ii) optimise the pilot operation of the co-digestion of WAS with FW at the optimum mixing ratio, (iii) increase the organic loading rate during the pilot co-digestion of WAS and FW, (iv) generate electricity from the biogas produced from the pilot-scale anaerobic reactor, (iv) carry out power analysis on the pilot plant, and (v) estimate local and national biogas power potentials based on the current volumes of food waste and sludge produced in South Africa.

2. Materials

A tank made from linear low-density polyethylene (LLDPE) (1000 L), clear pipe of 8 mm internal diameter, high-density polyethylene (HDPE) pipe, polyvinyl chloride (PVC) tarpaulin, fittings, solar geyser, insulation material, biogas compressor, submersible grinder pump, pH meter (Hanna model: HI 9813-5), slaked lime, and plexiglass floating drum for the construction of a complete-mix biogas pilot plant were purchased at local hardware stores in Vanderbijlpark, South Africa. A 1.5 kW biogas generator, handheld biogas analyser, Ritter biogas meter, and ambient anaerobic digester (1 m^3) were purchased from Puxin Technology in China. Cow dung (CD) was sourced from a local farm in Vanderbijlpark. FW (mainly rice, slap chips, buns, bread, porridge, grease, raw dough, chicken, meat, vegetables, and fruits) was collected from a local restaurant, Stonehaven on Vaa; Vanderbijlpark. WAS containing sewage sludge from the primary and secondary settlers was collected from the Ekurhuleni Water Care Company (ERWAT) wastewater treatment plant based in Midvaal, South Africa.

2.1. Pilot scale digester setup

A complete-mix (VUT-1000C) anaerobic digester operated at a controlled temperature of 37 ^{o}C was used. VUT-1000C was designed and constructed from a 1000 ℓ vertical LLDPE tank with a working volume of 800 ℓ. A gas holder was made from PVC tarpaulin, and biogas was measured using a flow meter.

The substrate was mixed using a submersible grinder pump. The digester was heated using a solar geyser equipped with a temperature controller. A thermocouple was inserted inside the digester and connected to the temperature controller, which turned the hot water circulation pump on and off to maintain the desired digester temperature. The digester was insulated from cold winds. Produced biogas was stored in a 1000 ℓ tarpaulin biogas bag. An 18 W biogas compressor was used to extract biogas from the biogas bag to supply downstream processes. A 1.5 kWh generator was used for electricity generation with a conversion efficiency of 22%. The experimental setup is outlined in Fig. 1.

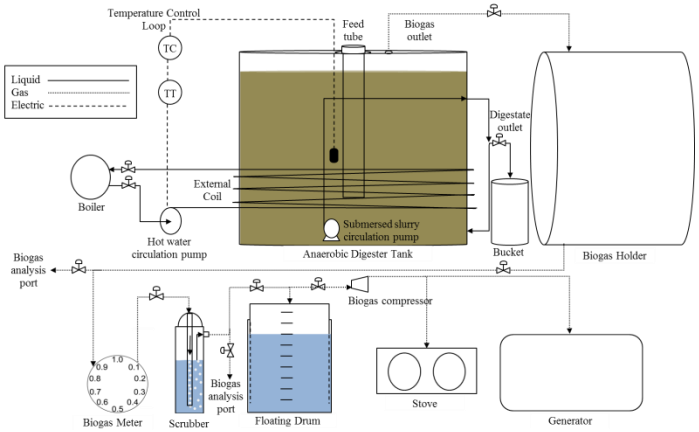

Fig. 1: Schematic representation of VUT-1000C solar heated biogas pilot plant coupled to an electricity generator.

2.2. Biochemical methane potential

Laboratory biochemical methane potential (BMP) tests were performed to evaluate the effect of various mixing ratios on biogas production. The BMP test work consisted of 6 reactor bottles with 2 L capacity and 1.7 L working volume. The inoculum-to-substrate ratio was 2:1 based on volume. The sludge to FW ratios were prepared as follows: 100:0, 80:20, 60:40, 40:60, 20:80 and 0:100, respectively, by organic loading rate at a constant organic loading rate of 2 kgVS/m^3. The digesters were incubated in a heated water bath and set to 38 ^{o}C to maintain mesophilic temperatures. Biogas production was measured and monitored periodically using water displacement collectors. All experiments were run in triplicate. Each reactor bottle was purged with N_2 (99.99%) for 3 min to remove oxygen, then sealed with a valve. A buffering agent, Sodium Hydrogen Carbonate, was added in the appropriate measure to maintain favourable pH levels to provide adequate buffering capacity.

2.3. Co-digestion of sludge with fw at the pilot scale

The optimum WAS:FW ratio obtained during the laboratory BMP test was implemented at a pilot scale using the VUT-1000C pilot plant at 0.8 kgVS/m^3/day. The pilot plant was operated using a semi-continuous feeding mode. FW collected was sorted and blended with water using a food waste disposer grinding the material to fine particle size. The solid concentration of the prepared mixtures was then determined. The blended FW in bulk was stored in a cool and shaded area near the digester. Once optimised the organic loading rate was then increased from 0.8 to 1.6 kgVS/m^3/day.

2.4. Sample analysis

The total solid (TS) and volatile solid (VS) concentrations of the inoculum and substrates were determined by drying at 105 ^{o}C to constant weight to determine TS% and then igniting at 550 ^{o}C to determine VS% [14]. An ignition test was performed to monitor methane presence. Digestate pH was measured using a pH meter (Hanna model: HI 9813-5). Critical parameters such as biogas volume, digester temperature, and digestate pH were measured and monitored daily during operation.

3. Results and discussion

3.1. Feedstock characterisation

The physical characteristics of the obtained FW and WAS are given in Table 1. The physical-chemical characteristics influence the performance of AD by affecting the methane yield and process stability, thus indicating the degree of biodegradability [15]. Both WAS and FW had high moisture contents, 93% and 87%, respectively. The average volatile solids (VS%) content obtained for WAS and FW was 4.69% and 12.35%, respectively. These are similar findings to Kuczman *et al*. [16] who obtained 13% for FW and Zahan *et al*. [17] obtained 3.13% for SS.

The VS/TS ratio is an indicator for evaluating the suitability of a substrate for biogas production; substrates with VS/TS higher than 80% are considered great candidates to be anaerobic digestion feedstock [18]–[20] In this study, VS/TS for FW was found to be 95%, an amount similar to that of Zhang *et al*. [18] of 94%. These high values indicated that the FW was rich in biodegradable matter and thus excellent for biodegradation. The VS/TS ratio for the WAS was 67%, which demonstrated that the fraction of organic matter was not too far from the suitable range as substances with values below 17.4 to 10% are considered inorganic [16]. Both the WAS and FW had an initial acidic pH value of 6.3 and 5, respectively.

Table 1: Characteristics of WAS and FW

Parameter	WAS	FW
Moisture content (MC, %)	93	87
Total solids (TS, %)	7	13

Volatile solids (VS, %)	4.69	12.35
VS/TS (%)	67	95
pH	6.3	5

3.2. BMP test on the effect of co-digestion of WAS and FW on biogas production

BMP tests were performed to evaluate the effect of various WAS:FW mixing ratios on biogas production. Fig. 2 shows the hourly and cumulative biogas production of the different ratios during the first 20 hours of digestion. Mono-digestion of WAS produced the lowest amount of biogas (160 ml) while mono-digestion of FW produced the highest (680 ml). The results indicate that biogas production increased with increasing FW composition. 100% WAS plateaued immediately after 9 hours while 100% FW only plateaued after 18 hours which is twice the time and 3 times the biogas production. Rapid biogas production began within the first 8-9 hours and thereafter started to plateau concerning the composition of FW in the mixture. The addition of FW to WAS immediately enhanced biogas production by 40% when as little as 20% FW to 80% WAS was added, and then increased by 100% with the addition of 40% FW.. The only drawback with the addition of more FW is the lack of digestate buffering capacity which required the addition of a buffering agent, consequently increasing co-digestion costs.

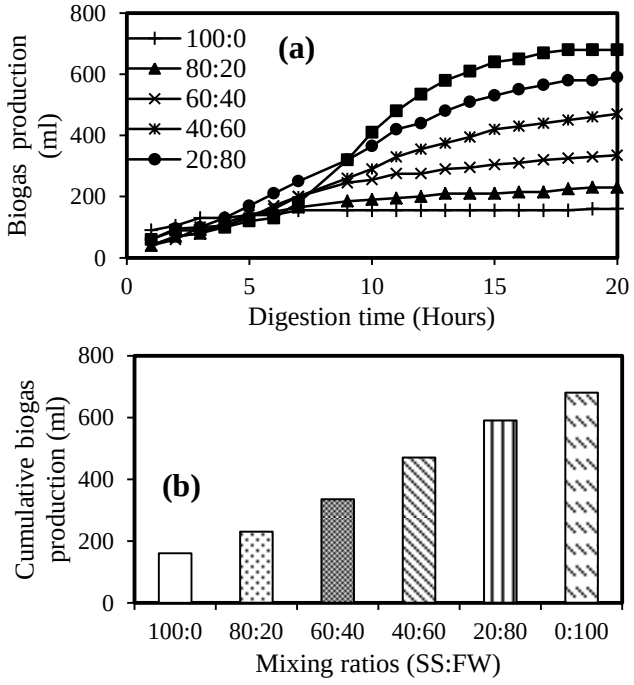

Fig. 2: Hourly (a) and cumulative (b) biogas production of the different WAS:FW mixing ratios.

3.3. Pilot codigestion of WAS with FW

Fig. 3 shows the daily biogas production of the mono-digestion of sludge and the codigestion of sludge with FW after 95 days of digestion in the solar heated pilot scale digester. Upon stabilisation of the digester, the biogas production for mono-digestion averaged 150 ℓ/day while co-digestion at 60WAS:40FW produced 650 ℓ/day, which is 4.3 times higher than that of mono-digestion. A lag phase can be observed between days 26 and 29 during the transition from mono-digestion to co-digestion. Mono-digestion took 5 days to reach stable conditions while co-digestion took 10 days. The digestate pH stabilised after 9 days for both phases (Fig. 4a). The digester temperature was also stable averaging 35 ^{o}C (Fig. 4b). This indicated the reliability of the solar geyser for digester heating. Hallaji et al., [21] also reported improvement when co-digesting WAS with FW. They assessed the activity of the main enzymes hydrolyzing organic matter, protease and cellulase, in AD. According to their findings it was indicated that codigestion of WAS with mixed fruit waste and cheese whey enhances the activity of these enzymes by 22 and 9%, respectively. Using a mixing ratio of 85:15 for WAS:FW, their cumulative methane production increased by 31% as compared to WAS monodigestion. Additionally chemical oxygen demand (COD) and VS of the feed mixture improved by 9 and 7%, respectively. Up to 270% enhanced biogas production during the codigestion of sewage sludge with 5% food waste, cheese whey and olive mill wastewater (FCO) has been reported [22].

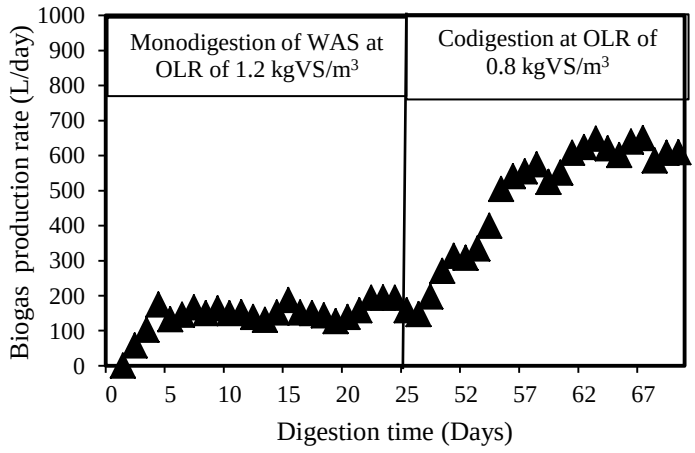

Fig. 3: Biogas production rate during the anaerobic codigestion of municipal waste-water sludge with food waste

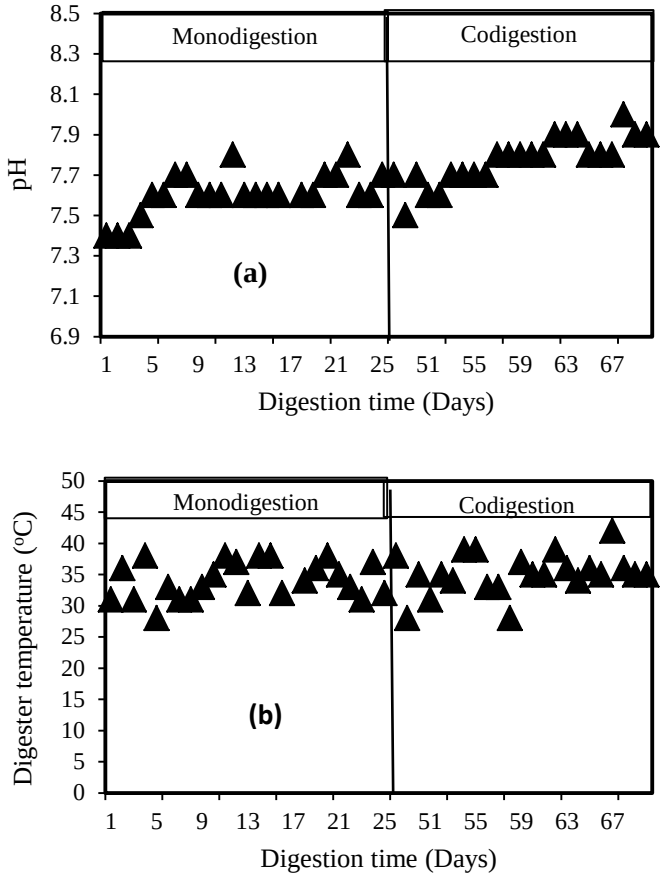

Fig. 4: (a) Anaerobic digester pH and (b) digester temperature during the anaerobic codigestion of municipal waste-water sludge with food waste

Optimisation of the pilot anaerobic codigestion of sludge with food waste at a mixing ratio of 60% WAS to 40% FS was performed. In this section, the initial organic loading rate during co-digestion at 0.8 kgVS/m^3/day was increased to 1.6 kgVS/m^3/day. Fig. 5 outlines the daily biogas production rate during mono-digestion of sludge at 1.2 kgVS/m^3/day which stabilised at an average biogas production rate of 150 ℓ/day. Upon co-digestion of WAS with FW at 60WAS:40FW biogas production rate increased to an average of 650 ℓ/day at a combined OLR of 0.8 kgVS/m^3/day. Digestion at the new OLR also took 10 days to stabilise and then remained stable for the remainder of the digestion period to an average biogas production rate of 1400 ℓ/day, which is 2 times that at 0.8 kgVS/m^3/day. By doubling the feed OLR, biogas production also doubled and thus increased by more than 9 times that of mono-digestion. The digestate pH remained stable throughout the digestion period and within the optimum range. Similarly, the digester temperature was also stable, averaging 35 °C.

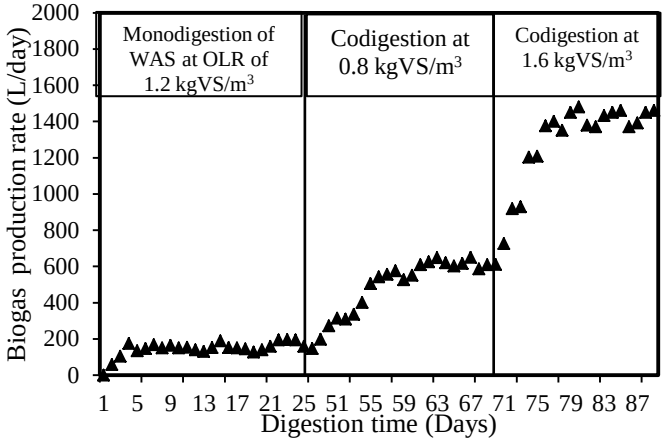

Fig. 5: Biogas production rate during the anaerobic codigestion of waste-activated sludge with food waste at different OLRs.

3.4. Biogas conversion to electricity

An electricity biogas generator connected to a combustion biogas engine was used to generate electricity. A specific volume (1000 L) of biogas was used to perform the test work, and a total of 2.3 kW was produced. The electrical output of the engine was 220 V, 50Hz, and 1.8 kWh. A maximum of 1.8 kWh was generated with an overall conversion efficiency of 22%. The biogas consumption of the generator averaged 650 L/hour. On a national scale, this electricity can light up to 300 6 W energy-saving light bulbs for an hour. Furthermore, in a rural setting with no electricity, this biogas pilot plant can provide electricity and allow the users to perform short-term energy-requiring tasks. By running the generator, a family would have a total of 2.3 kW for 1 hour and 30 minutes (1.5 – 1.8 kWh) of electricity per day from 1000 L of biogas. From 2 kWh of electricity, the family can perform one of the following tasks or a balanced mixture of these tasks for their living requirements: microwave (700 W) 32 meals, toast (800 W) 48 slices of bread, vacuum clean (1400 W) 16 rooms, run three laundry loads (800 W), iron (150 W) full laundry, bake one cake (1300 W), blend food (400 W), charge devices (36 W) and drill (650 W) and grind (650 W) for 3 hours.

3.4.1.Power balance for biogas production with different substrates

The power balance considers the energy input to run the biogas pilot plant and compares this input with the power output. The plant's power input requirements when operating on FW, WAS, and co-digestion of WAS with FW at 0.8 and 1.6 kgVS/m^3/day (60% WAS: 40% FW) were compared (Table 2). Standard to all operations, the plant temperature controllers used in this plant were operated continuously throughout the day and consumed a total of 0.024 kWh, which are the lowest power-consuming components of the plant. The two highest power-

consuming components of the plant were the food blender and the digestate circulation pump, both consumed a combined 1.14 kWh during a day's cycle. The hot water circulation pump ran continuously at start-up for two days, and then it would turn off when the set digester temperature was reached; it then ran for approximately 3 hours in the morning. On average, the hot water circulation pump used 0.024 kWh daily.

When running the generator, the biogas blower was used to pressurise the biogas, consuming 0.032 kWh. The total power input to run the entire biogas pilot plant for FW and WAS: FW was 1.22 kWh. For running WAS as the mono-substrate, 1.16 kWh power was required to run the plant. Upon evaluation of the power output of 2.3 kWh for FW and co-digestion at 1.6 kgVS/m^3/day, the biogas plant required 53% of its power output, 1.8 kWh for WAS:FW at 0.8 kgVS/m^3/day required 68%, and 0.6 kWh for WAS mono-digestion obtained 193% power consumption.

Table 2: Power consumption of equipment used in biogas production and biogas use

Component	Power rating (kW)	Hours running per day	Usage (kWh)	Usage (kWh)
VUT-1000C			Co-digestion	WAS Monodigestion
Digestate circulation pump	0.18	6	1.080	1.080
Hot water circulation pump	0.008	3	0.024	0.024
Solar geyser water level controller	0.005	3	0.015	0.015
Hot water circulation controller	0.003	3	0.009	0.009
Food blender	0.373	0.16	0.060	
Biogas blower	0.016	2	0.032	0.032
Total			**1.220**	**1.160**

These results may give guidance to the use of certain equipment in the biogas plant considering the plant's overall power balance. The contribution of the equipment used in the biogas plant to the AD process and biogas potential should be considered. Ultimately decisions regarding the final application of the biogas for either ignition in an open flame or for internal combustion may also be evaluated taking into account the conversion efficiency of each. Lastly, a combination of renewable energies such as a solar-heating promise to assist another renewable energy technology to reach its full potential.

4. Conclusions

Waste-activated sludge (WAS) has the potential for biogas production and was successfully digested as the mono-substrate. However, co-digestion of WAS with food waste (FW) significantly improved biogas production by a factor of 4 at a mixing ratio of 60% WAS and 40% FW. An increase in organic loading rate during co-digestion of WAS with FW at the pilot scale enhanced biogas production by a factor of 9 compared to WAS mono-digestion. The maximum daily biogas production during co-digestion at 0.8 and 1.6 kgVS/m^3/day was 650 and 1400 ℓ/day, respectively. No buffering agents were required during co-digestion at the pilot scale as the digester proved to have sufficient buffering capacity. Power analysis performed over the pilot digester showed that when treating WAS only the pilot plant requires additional power to support the plant obtaining 193% power consumption, while for WAS:FW co-digestion at 1.6 kgVS/m^3/day it requires 53%, and 68% WAS:FW at 0.8 kgVS/m^3/day. This shows that AD is potentially a net positive energy-producing technology. Scenarios for South Africa, ERWAT and Stonehaven on Vaal show the current lost potential for renewable energy as a result of the lack of biogas technology uptake. The novelty of a solar-heated digester was able to maintain mesophilic digester temperatures throughout digestion.

Acknowledgements

Funding: The research of this article was supported by the National Research Foundation (Grant number. 140335) under the German Academic Exchange Service (DAAD) within the framework of the climapAfrica programme with funds from the Federal Ministry of Education and Research, and the Water Research Commission (WRC, Project number. C2020/2021-00426) of South Africa. The authors are fully responsible for the contents.

References

[1] D. Cecconet and A. G. Capodaglio, "Sewage Sludge Biorefinery for Circular Economy," *Sustain.*, vol. 14,

no. 22, 2022, doi: 10.3390/su142214841.
[2] T. Liu *et al.*, "7 - Waste Biorefinery Development Toward Circular Bioeconomy With a Focus on Life-Cycle Assessment," in *Biomass, Biofuels, Biochemicals*, A. Pandey, R. D. Tyagi, and S. Varjani, Eds. Elsevier, 2021, pp. 199–230.
[3] L. Appels, J. Baeyens, J. Degrève, and R. Dewil, "Principles and potential of the anaerobic digestion of waste-activated sludge," *Prog. Energy Combust. Sci.*, vol. 34, no. 6, pp. 755–781, 2008, doi: 10.1016/j.pecs.2008.06.002.
[4] A. Leitão, D. Moni, and C. Maria, "Anaerobic co-digestion of food waste with sewage sludge from wastewater treatment plant of Sequele, Luanda-Angola," *Environ. Challenges*, vol. 9, no. May, 2022, doi: 10.1016/j.envc.2022.100635.
[5] S. H. H. Oelofse and A. Nahman, "Estimating the magnitude of food waste generated in South Africa. South Africa. Council for Scientific and Industrial Research," *Waste Manag. Res.*, vol. 31, no. 1, pp. 80–86, 2013.
[6] NWMS, "National Waste Management Strategy 2020," *Dep. Environ. Foretry Fish. - Repub. South African*, no. November, p. 71, 2020.
[7] D. of E. A. DEA, "National Waste Information Baseline," *Report*, pp. 1–21, 2012.
[8] W. de Lange and A. Nahman, "Costs of food waste in South Africa: Incorporating inedible food waste," *Waste Manag.*, vol. 40, pp. 167–172, 2015, doi: 10.1016/j.wasman.2015.03.001.
[9] G. P. S. Priebe, E. Kipper, A. L. Gusmão, N. R. Marcilio, and M. Gutterres, "Anaerobic digestion of chrome-tanned leather waste for biogas production," *J. Clean. Prod.*, vol. 129, pp. 410–416, 2016, doi: 10.1016/j.jclepro.2016.04.038.
[10] S. Borowski and M. Kucner, "Co-digestion of sewage sludge and dewatered residues from enzymatic hydrolysis of sugar beet pulp," *J. Air Waste Manag. Assoc.*, vol. 65, no. 11, pp. 1354–1364, 2015, doi: 10.1080/10962247.2015.1093564.
[11] H. Karne, U. Mahajan, U. Ketkar, A. Kohade, P. Khadilkar, and A. Mishra, "A review on biogas upgradation systems," *Mater. Today Proc.*, vol. 72, pp. 775–786, 2023, doi: 10.1016/j.matpr.2022.09.015.
[12] L. Appels *et al.*, "Anaerobic digestion in global bio-energy production: Potential and research challenges," *Renew. Sustain. Energy Rev.*, vol. 15, no. 9, pp. 4295–4301, 2011, doi: 10.1016/j.rser.2011.07.121.
[13] P. Lehohla, "Electricity, gas and water supply industry, 2013," vol. 02, no. 41, p. 35, 2013, [Online]. Available: www.statssa.gov.za.
[14] APHA, "Standard Methods for the Examination of Water and Wastewater," *Am. Public Heal. Assoc. Am. Water Work. Assoc. Water Environ. Fed.*, no. 1, pp. 1–6, 1999.
[15] R. Zhang *et al.*, "Characterization of food waste as feedstock for anaerobic digestion," *Bioresour. Technol.*, vol. 98, no. 4, pp. 929–935, 2007, doi: 10.1016/j.biortech.2006.02.039.
[16] O. Kuczman *et al.*, "Food waste anaerobic digestion of a popular restaurant in Southern Brazil," *J. Clean. Prod.*, vol. 196, pp. 382–389, 2018, doi: 10.1016/j.jclepro.2018.05.282.
[17] Z. Zahan, M. Z. Othman, and W. Rajendram, "Anaerobic Codigestion of Municipal Wastewater Treatment Plant Sludge with Food Waste: A Case Study," *Biomed Res. Int.*, vol. 2016, 2016, doi: 10.1155/2016/8462928.
[18] L. Zhang, Y. W. Lee, and D. Jahng, "Anaerobic co-digestion of food waste and piggery wastewater: Focusing on the role of trace elements," *Bioresour. Technol.*, vol. 102, no. 8, pp. 5048–5059, 2011, doi: 10.1016/j.biortech.2011.01.082.
[19] P. Illmer and G. Gstraunthaler, "Effect of seasonal changes in quantities of biowaste on full scale anaerobic digester performance," *Waste Manag.*, vol. 29, no. 1, pp. 162–167, 2009, doi: 10.1016/j.wasman.2008.02.005.
[20] C. Wang, F. Hong, Y. Lu, X. Li, and H. Liu, "Improved biogas production and biodegradation of oilseed rape straw by using kitchen waste and duck droppings as co-substrates in two-phase anaerobic digestion," *PLoS One*, vol. 12, no. 8, pp. 1–19, 2017, doi: 10.1371/journal.pone.0182361.
[21] S. M. Hallaji, M. Kuroshkarim, and S. P. Moussavi, "Enhancing methane production using anaerobic co-digestion of waste activated sludge with combined fruit waste and cheese whey," *BMC Biotechnol.*, vol. 19, no. 1, pp. 1–10, 2019, doi: 10.1186/s12896-019-0513-y.
[22] A. E. Maragkaki, I. Vasileiadis, M. Fountoulakis, A. Kyriakou, K. Lasaridi, and T. Manios, "Improving biogas production from anaerobic co-digestion of sewage sludge with a thermal dried mixture of food waste, cheese whey and olive mill wastewater," *Waste Manag.*, vol. 71, pp. 644–651, 2018, doi: 10.1016/j.wasman.2017.08.016.